

# NATIONAL INSTITUTE FOR FUSION SCIENCE

## NIFS-SWJTU JOINT PROJECT FOR CFQS — PHYSICS AND ENGINEERING DESIGN — VER. 5.1 2023. AUG.

CFQS Team

National Institute for Fusion Science, National Institutes of Natural Sciences  
Institute of Fusion Science, School of Physical Science and Technology,  
Southwest Jiaotong University  
Hefei Keye Electro Physical Equipment Manufacturing Co. Ltd.

( Received - Aug. 28, 2023 )

NIFS-PROC-126

Jan. 26, 2024

This report was prepared as a preprint of work performed as a collaboration research of the National Institute for Fusion Science (NIFS) of Japan. The views presented here are solely those of the authors. This document is intended for information only and may be published in a journal after some rearrangement of its contents in the future.

Inquiries about copyright should be addressed to the NIFS Library, National Institute for Fusion Science, 322-6 Oroshi-cho, Toki-shi, Gifu-ken 509-5292 JAPAN.

E-mail: [toshio@nifs.ac.jp](mailto:toshio@nifs.ac.jp)

**<Notice about copyright>**

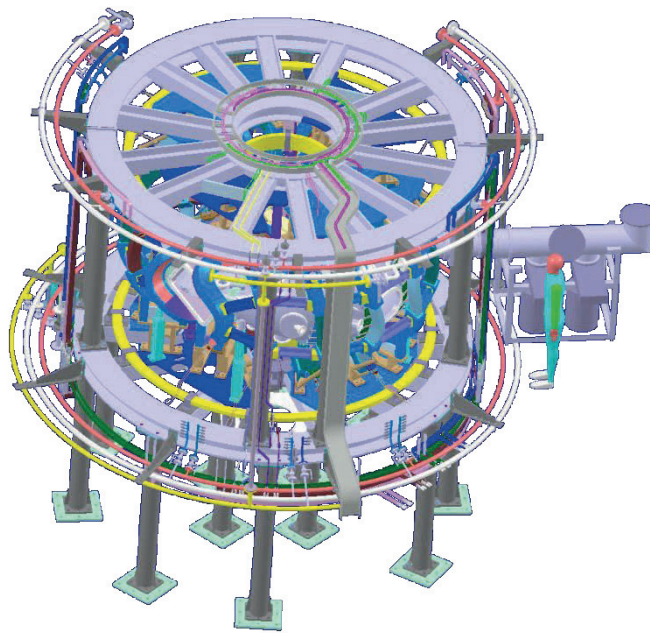
NIFS authorized Japan Academic Association For Copyright Clearance (JAC) to license our reproduction rights and reuse rights of copyrighted works. If you wish to obtain permissions of these rights, please refer to the homepage of JAC (<http://jaacc.org/eng/>) and confirm appropriate organizations to request permission.



# NIFS-SWJTU JOINT PROJECT FOR CFQS

~PHYSICS AND ENGINEERING DESIGN~

VER. 5.1  
2023. AUG.



CFQS Team

National Institute for Fusion Science, National Institutes of Natural Sciences

Institute of Fusion Science, School of Physical Science and Technology, Southwest Jiaotong University

Hefei Keye Electro Physical Equipment Manufacturing Co. Ltd.

## **NIFS-SWJTU Joint project for CFQS: Physics and engineering design Ver 5.1**

### **CFQS Team**

**National Institute for Fusion Science, National Institutes of Natural Sciences  
Institute of Fusion Science, School of Physical Science and Technology, Southwest Jiaotong  
University  
Hefei Keye Electro Physical Equipment Manufacturing Co. Ltd.**

### **Abstract**

The National Institute for Fusion Science (NIFS) and Southwest Jiaotong University (SWJTU) concluded an agreement for international academic cooperation to promote cooperative research in helical fusion plasma research on July 3, 2017. Since then, NIFS and SWJTU have continued the design study of the quasi-axisymmetric (QA) stellarator CFQS as a joint project. NIFS and SWJTU have organized the steering committee to manage this joint project. This document summarizes achievements of physical and engineering design study of the CFQS up to the 5th steering committee meeting, which was held on December 9, 2022 online, due to the effect of COVID-19.

Principal parameters of the CFQS is as follows: the major radius is 1 m, the magnetic field strength is 1 T, the aspect ratio is 4, and the number of toroidal period is 2. Magnetic field configuration is designed based on that of CHS-qa. Outstanding confinement property of CFQS in the context of neoclassical theory is achieved by its QA configuration. Appropriate feature of MHD stability is realized by its magnetic well characteristics. Magnetic field coil system is designed for the CFQS, which consists of 16 modular coils. Supporting system is designed to withstand strong electromagnetic force under 1 T operation, and it is improved to obtain wider space for heating and diagnostic systems. Analysis by using finite element method shows that the stress in the supporting structure is less than allowable level. Layout of main components, *e.g.* CFQS itself, diagnostic system, heating system, power supply in the torus hall is designed. For one of modular coils, mock up coil was already constructed in the factory of Hefei Keye Electro Physical Equipment Manufacturing Co. Ltd., and various tests, such as heat run test and voltage isolation test were performed. Construction of actual modular coils and vacuum vessel is progressing. Details of physics/engineering design, and current status of construction are reported in this document.

**Keywords:** quasi-axisymmetric stellarator, helical device, modular coil, CFQS, joint project, NIFS, SWJTU

Color figures are only available in the electric edition.

## Documentation Contributors

(Alphabetical order of family name)

HIMURA	Haruhiko	Kyoto Institute of Technology (KIT)
HUANG	Jie	Southwest Jiaotong University (SWJTU)
INAGAKI	Shinichiro	Kyoto Institute of Technology (KIT)
ISOBE	Mitsutaka	National Institute for Fusion Science (NIFS)
KANDA	Motonari	National Institute for Fusion Science (NIFS)
KINOSHITA	Shigeyoshi	National Institute for Fusion Science (NIFS)
KOBAYASHI	Sakuji	National Institute for Fusion Science (NIFS)
LI	Yangbo	Southwest Jiaotong University (SWJTU)
LIU	Hai	Southwest Jiaotong University (SWJTU)
LIU	Haifeng	Southwest Jiaotong University (SWJTU)
MURASE	Takanori	National Institute for Fusion Science (NIFS)
NAGAOKA	Kenichi	National Institute for Fusion Science (NIFS)
NAKAGAWA	Sho	National Institute for Fusion Science (NIFS)
NAKATA	Motoki	National Institute for Fusion Science (NIFS)
OGAWA	Kunirhiro	National Institute for Fusion Science (NIFS)
OKAMURA	Shoichi	National Institute for Fusion Science (NIFS)
OISHI	Tetsutaro	National Institute for Fusion Science (NIFS)
SANPEI	Akio	Kyoto Institute of Technology (KIT)
SEKI	Ryohsuke	National Institute for Fusion Science (NIFS)
SHAO	Junren	Southwest Jiaotong University (SWJTU)
SHIMIZU	Akihiro	National Institute for Fusion Science (NIFS)
SUZUKI	Chihiro	National Institute for Fusion Science (NIFS)
TAKAHASHI	Hiromi	National Institute for Fusion Science (NIFS)
TANOUE	Hiroyuki	National Institute for Fusion Science (NIFS)
VARELA	Jacobo	Carlos III University of Madrid
WAN	Yi	Hefei Keye Electro Physical Equipment Manufacturing Co., Ltd. (Keye)
WANG	Hao	National Institute for Fusion Science (NIFS)
WANG	Xianqu	Southwest Jiaotong University (SWJTU)
WU	Danni	Southwest Jiaotong University (SWJTU)
XIONG	Guozhen	Southwest Jiaotong University (SWJTU)
XU	Yuhong	Southwest Jiaotong University (SWJTU)
YAMAGUCHI	Hiroyuki	National Institute for Fusion Science (NIFS)

YANG	Lang	National Institute for Fusion Science (NIFS)
YIN	Dapeng	Hefei Keye Electro Physical Equipment Manufacturing Co., Ltd. (Keye)
YOSHIMURA	Yasuo	National Institute for Fusion Science (NIFS)
ZHU	Caoxiang	University of Science and Technology of China (USTC)

## Acknowledgements

During our work of making physics and engineering design of CFQS device and environmental utilities, we were given a lot of useful information from scientists and engineers in the experimental groups of various devices in the world. We are very grateful for their advices and supports.

Dr. Hutch Neilson, Dr. Tom Brown, and others from NCSX program in Princeton Plasma Physics Laboratory, Princeton, USA.

Prof. David Anderson, Prof. Simon Anderson, and others from HSX program in University of Wisconsin - Madison, USA.

Prof. Thomas Klinger, Dr. Lutz Wegener, Dr. Thomas Rummel, and others from W7-X program in Max Planck Institute for Plasma Physics, Greifswald, Germany.

Prof. Ge Zhuang, Tao Lan and others from KTX program in University of Science and Technology of China, People's Republic of China.

# TABLE OF CONTENTS

1	Introduction.....	8
1.1	Overview.....	8
1.2	Steering committee meeting.....	11
2	Research target.....	12
3	Physics design.....	13
3.1	MHD equilibrium.....	13
3.1.1	MHD equilibrium with VMEC code.....	13
3.1.2	MHD equilibrium with HINT code.....	17
3.2	Confinement property .....	24
3.2.1	Neoclassical property .....	24
3.2.2	Plasma parameters expected from scaling law.....	28
3.3	MHD stability .....	30
3.3.1	Mercier stability/instability .....	30
3.3.2	Ballooning mode.....	37
3.3.3	Kink mode.....	39
3.3.4	Tearing mode.....	43
3.3.5	Alfvén mode.....	44
3.3.5.1	Alfvén mode analysis by MEGA code.....	44
3.3.5.2	Alfvén mode analysis by FAR3d code.....	50
3.4	Optimization approach of anomalous transport .....	56
3.4.1	Maximum- $J$ .....	56
3.4.2	Micro instability.....	62
3.4.3	Plasma rotation.....	73
3.4.4	Study of magnetic field symmetry on the formation of plasma structure .....	78
3.5	Energetic particle .....	79
3.5.1	NBI deposition analysis .....	80
3.5.2	Feasibility study of fast ion loss diagnostics.....	83
3.5.3	Preparative study for deuterium experiment for energetic ion confinement physics ..	85
3.5.4	Predictive study of alpha particle confinement in a QAS-type reactor .....	88
3.6	ECRH deposition analysis .....	98
3.7	Modular coil design .....	102
3.7.1	Modular coil design by NESCOIL.....	102
3.7.2	Design of modular coils without torsions .....	108

3.7.3	Modular coil design by GOSPEL .....	115
3.7.4	Error evaluation using the Hessian matrix method .....	118
3.7.5	Influence of stellarator symmetric coil misalignment on magnetic field configuration 121	
3.7.6	Influence of general coil misalignment on magnetic surfaces .....	125
3.7.7	Effect of modular coil misalignment on magnetic field and particle confinement property 127	
3.8	Divertor configuration .....	140
3.9	Magnetic field control by TFC, PFC, and MC current ratio .....	150
3.9.1	Background.....	150
3.9.2	Magnetic surface and physical parameters of a standard configuration.....	152
3.9.3	Distribution of magnetic field strength .....	154
3.9.4	Rotational transform and type of boundary .....	156
3.9.5	Magnetic surface control by the PFC.....	158
3.9.6	Magnetic surface control by the TFC.....	163
3.9.7	IBD control with $m/n=5/2$ by the PFC and TFC.....	167
3.9.8	Magnetic surface control by the MC.....	169
3.9.9	Role of poloidal field for QAS equilibrium .....	172
4	Engineering design.....	178
4.1	Whole assembly .....	178
4.1.1	Specification for engineering design.....	178
4.1.2	Overall Structure .....	182
4.2	Coil system .....	186
4.2.1	System configuration .....	186
4.2.2	Modular coil system (MC).....	187
4.2.3	Poloidal field coil system (PFC) .....	191
4.2.4	Toroidal field coil system (TFC).....	192
4.2.5	Cage type support structure.....	193
4.3	Vacuum vessel.....	195
4.3.1	Structure of the main vessel .....	195
4.3.2	Cross-sectional shape of the main vessel .....	196
4.4	Related equipment .....	197
4.4.1	Limiter system .....	197
4.4.2	Vacuum pumping system .....	198
4.4.3	Wall conditioning system.....	198
4.4.4	Fuel gas supply system (Gas puff system) .....	198

4.4.5	Vacuum management system.....	199
4.4.6	Shutter system to protect the glass window .....	199
4.4.7	Vacuum test equipment .....	199
4.4.8	Compressed air supply system.....	199
4.4.9	Liquid nitrogen supply system.....	199
4.4.10	Pure water cooling system .....	200
4.5	Power supply.....	201
4.5.1	Power supply system for the 1T operation.....	201
4.6	Plasma heating system .....	202
4.6.1	Electron cyclotron resonance heating (ECRH) system .....	202
4.6.2	Neutral beam injection (NBI) heating system.....	203
4.7	Diagnostics system.....	204
4.7.1	Overview of diagnostic system .....	204
5	Research plan and schedule .....	205
5.1	Physics research plan .....	206
5.1.1	Research plan for 0.1 T operation .....	206
5.1.2	Research plan for 1.0 T operation .....	207
5.2	Construction schedule .....	207
APPENDIX-A1 (BD)	BASIC DESIGN	
APPENDIX-A2 (RD)	RESEACH AND DEVELOPMENT	
APPENDIX-A3 (DW)	DRAWING	
APPENDIX-A4 (ST)	STANDARD INFORMATION	
APPENDIX-A5 (PJ)	RELATED PROJECT	

## **1 Introduction**

### **1.1 Overview**

The controlled nuclear fusion research is one of the most important issues for human beings because it is necessary to secure stable energy resources in order to enrich human life in the future. Fusion energy does not produce hydrocarbons and hence does not contribute to the global warming, which is one of the most serious environmental problems for Earth. The source of energy are isotopes of hydrogen, which are a common resource for the world because the hydrogen isotopes are obtained from seawater.

The development of technologies so far for making controlled nuclear fusion is based on two methods, namely, magnetic confinement of high temperature plasmas and the strong compression of high density plasmas with ultra-high intensity laser. For the magnetic confinement, high technology devices with strong magnetic field produced by large currents are used. This research started from the 1950s and varieties of different designs of magnetic confinement devices were proposed. After intensive research all over the world for more than a half century, two major magnetic confinement schemes have been established as candidates for the future fusion reactor design, namely, tokamak and stellarator.

These two designs have different advantages and disadvantages. Tokamak devices have better confinement property for high temperature plasmas because of their axisymmetric configuration of the magnetic field. However, tokamaks have essential problems of suffering current disruptions, which is very hazardous for the devices, and the high cost of current drive system because a large plasma current flowing in the plasma is a necessary element for the tokamak concept. On the other hand, stellarator does not have current disruption problems and does not need high cost current drive system because it does not require plasma current as a necessary element of a magnetic confinement concept. However, because of the lack of axisymmetry of the magnetic configuration, the confinement is degraded when the plasma temperature approaches the necessary conditions for the fusion reaction.

At present, large effort toward magnetic confinement of high temperature plasmas is focused on tokamak researches. In France, ITER, the largest facility of magnetic fusion research is now under construction as an international joint project. This device is a tokamak type and it is planned to produce 10 times larger fusion reaction energy than the electric energy consumed for maintaining high temperature plasmas in the device. This program is the final goal of the long way in making good plasma confinement using tokamak type devices. As a next step of fusion research toward the power reactor, we must solve many engineering problems. One of those significant issues is technology problems related to the plasma current (disruptions and current drive). It is strongly pointed out that we should have a multi-line research strategy for the future reactor design, namely, that we should



continue the stellarator research as a safe candidate for the fusion power plant free from the plasma current problems.

When the bright news of achieving high electron temperature in the tokamak device in Russia was distributed throughout the world fusion community in 1969, all plasma experimentalists began to work on tokamak experiments, thus giving up research with their own devices with different concepts from the tokamak. Since then, the main line of magnetic confinement fusion has been based on the tokamak concept. However, there were two continuous research activities for devices with the stellarator concept. In Kyoto University, in Japan, a series of devices with the names of Heliotron (A, B, C, D, DM, DR, E, and J) were built and the plasma parameters were improved continuously. In Germany, a series of devices with the name Wendelstein (1, 2, 3, ..., 6) were producing very promising data with stellarator configuration. In the final phase of these series, Wendelstein 7-A was built in Germany and started experiments in 1975. In Japan, Heliotron E was built and started experiments in 1980. Because the impact of experimental results from these devices were very large for the world fusion community, various types of stellarator programs were initiated in many countries in the 1980s.

In Japan, the designing work for Large Helical Device (LHD) started in 1985, and the construction of the device began in 1989. In Germany, the first design workshop for Wendelstein 7-X (W7-X) took place in 1987 and the first modular coil was ordered in 1998. These two world leading stellarator devices with super-conducting magnets are now in operation for experimental research in various topics of magnetic confinement with stellarator concept. In addition to these large devices, there were two medium size stellarators in operation from the 1980s to the 2000s both in Japan and in Germany. The roles of these devices were to conduct supporting experimental research in advance of the completion of construction and starting the experiments in larger-size major devices. Compact Helical System (CHS) was in operation from 1988 to 2006 and Wendelstein 7-AS was in operation from 1988 to 2002. The experimental results obtained in these devices before starting experiments in LHD and W7-X were very useful for planning experimental program in large devices. They also produced unique scientific results available only in the smaller size devices. In addition to these two experiments, many different types of stellarators were designed and built in other countries: in the United States, Advanced Toroidal Facility (ATF) with heliotron configuration and Helically Symmetric Experiment (HSX) with quasi-helical symmetric configuration started experiments in the 1980s. TJ-II in Spain and H-1 in Australia, both having the heliac configurations, started experiments in the 1980s. Among these devices, experiments in four devices are active at present, namely, LHD, W7-X, HSX, and TJ-II. Four other devices stopped experiments (ATF, W7-AS, CHS, and H-1).

The 1980s was an exciting period for stellarator research as many devices were designed and constructed. Fortunately, four devices continue in operation. However, we notice that it is too long for scientists in active research fields to keep running experiments in old devices designed and built more than 30 years ago even though the devices are in healthy condition for the experiments. In fact, there

were two research activities for the advanced design of stellarator concept in 1990s. In Japan, when CHS completed its initial phase of experimental program, the discussion for the next device after CHS was initiated in 1995. After making surveys for the possible candidates of the next devices, a plan for building a quasi-axisymmetric (QA) stellarator CHS-qa was chosen. Based on the physics and engineering design, a proposal of CHS-qa was completed in 2000 and submitted to the National Institute for Fusion Science (NIFS). Unfortunately, the proposal was not accepted because 2000 was just after the beginning of the LHD experiments and NIFS did not have financial and personnel capability to share in two large programs.

In Princeton Plasma Physics Laboratory (PPPL), a stellarator experiment program started in 1995 for building a medium size stellarator National Compact Stellarator Experiment (NCSX) in parallel to the existing spherical torus experiment, National Spherical Torus Experiment (NSTX). The design concept was a QA stellarator similar to CHS-qa. It had  $N=3$  toroidal period number different from  $N=2$  for CHS-qa. The proposal of the device construction was approved and PPPL started to build NCSX in 2000. Unfortunately, this program was cancelled in 2008 because of the rapid increase of the construction cost, which the United States government did not accept.

The advanced concept of QA stellarator is very attractive as it is a new scheme of stellarator configuration that had not been imagined by any scientists before 1994. A toroidal device of magnetic confinement must have rotating structures of magnetic field lines in a plasma toroid which can be produced either by a plasma current or by twisting of the plasma surface. Because a twisting shape is not axisymmetric, it is not naturally possible to make a twisting system as axisymmetric. A QA stellarator is not a hybrid device of tokamak and stellarator, either. When we design a hybrid system of two different concepts, all advantageous points and disadvantageous points are mixed together in general. However, the QA stellarator combines only advantageous points from both tokamak and stellarator, thus producing a new advantageous concept. Because such a new invention of the stellarator concept was not realized in the real experimental program in 2000, we now need to recover the lost 15 years by starting a new experiment with the quasi-axisymmetric stellarator CFQS.

The present design of the CFQS device incorporates numerous experiences we have learned in CHS-qa design work. In addition, we are adding many new design points that have been learned in theoretical and computational works during the past 15 years. The divertor configuration design, which is supposed be one of the most important research issues in advanced stellarator concept, was renewed from the CHS-qa design with a new concept of the island bundle divertor configuration. For the engineering design of the device and manufacturing, we will make use of new numerical technologies of mechanical design and of new engineering facilities in order to obtain very high accuracy of the three-dimensional shape of the device.

This program is a joint project conducted by NIFS in Japan and Southwest Jiaotong University (SWJTU) in China. We concluded the MoU in 2017 on NIFS and SWJTU Joint Project (NSJP) for

CFQS experiment. In addition, we are working together with Hefei Keye Electro Physical Equipment Manufacturing Co., Ltd. in Hefei with their contribution in engineering design and manufacture of the device. Thus, in fact, the program is a joint project by three organizations in Japan and China. We have been working together for the physics and engineering design of CFQS device. SWJTU and the Keye company are primarily responsible for the engineering design and for manufacturing the device. NIFS is primarily responsible to contribute in preparing plasma heating system and diagnostic system. The experiment in the device will be conducted as international collaborations by NIFS, SWJTU and other researchers in foreign countries who will be interested in the challenging advanced stellarator program in Chengdu, China.

## 1.2 Steering committee meeting

In order to decide the policy of the joint project in each year, the steering committee meeting is regularly held. On May 30 2018, 1st steering committee meeting was held in SWJTU in Chengdu, China. In this meeting, the basic CFQS physics design, which was designed based on CHS-qa, was confirmed. Main parameters of CFQS, major radius,  $R = 1$  m, aspect ratio,  $A_p = 4$ , and toroidal magnetic field strength,  $B_t = 1$  T were decided.

On May 29 2019, 2nd steering committee meeting was held in SWJTU in Chengdu, China. In this meeting, the site for experimental building was discussed. Emei campus was one of possible sites to construct the experimental building for CFQS. Progress of engineering design was checked. And the progress of mockup modular coil construction, which was built for check of manufacturing feasibility and achieved accuracy, was confirmed. Real scale 3-D plastic model of 1/4 toroidal section vacuum chamber was made, in order to check the workability in the inside of chamber, and accessibility to plasma. On Nov. 12 2020, 3rd steering committee meeting was held by online. As the site of experiment building for CFQS, SWJTU suggested its new campus in Tianfu new district in Chengdu. The experimental building will be constructed in this site near future. The construction of mockup modular coil was completed. To check the performance of the mock up modular coil, various tests, such as heat run test, and voltage isolation test were done. On Nov. 12 2021, 4th steering committee meeting was held by online. For the initial experimental phase for CFQS, SWJTU renovated the experimental hall in Jiuli campus. Based on the experience of mockup modular coil construction, construction of actual modular coils has begun by Keye. The construction of 1/4 toroidal section of vacuum vessel has also begun.

This report summarizes the achievement of physics, engineering research, and the construction of CFQS up to 5th steering committee meeting, which is held on Dec. 9 2022. In the following sections, important items in the physics and engineering designs of CFQS will be described. We hope this report will provide give sufficient information to all researchers in the world about our CFQS program and motivate them to participate in the joint program of NSJP.

## 2 Research target

The CFQS is an international joint project between SWJTU in China and NIFS in Japan. It is the first stellarator to be manufactured and assembled by the Hefei Keye Electro Physical Equipment Manufacturing Co. Ltd. in China. Whereas in China there have been several tokamaks built by national institutions, there is no stellarator up to now. As the stellarator is technically much more complicated than the tokamak, our first target is to construct the CFQS device successfully and make it in good operation status in SWJTU. Secondly, we want to scientifically prove the major advantage of a QA stellarator in confining plasmas with reduced magnetic field ripple, and hence, neoclassical transport in comparison with previous conventional stellarators. Thirdly, for complementing the two-dimensional (2-D) tokamak physics, we will thoroughly study the intrinsic three-dimensional (3-D) physics in the CFQS stellarator to improve our understanding on related 3-D issues appeared in the tokamak, which has primarily 2-D magnetic configuration.

The main focus of the CFQS research activities is on basic physics studies under the advanced QA configuration. The scientific subjects include neoclassical transport, macro-scale magnetohydrodynamics (MHD) instabilities (interchange, ballooning, kink, and tearing modes, *etc.*), micro instabilities (electron drift wave, ion temperature gradient (ITG) and electron temperature gradient (ETG) modes, and trapped electron mode (TEM), *etc.*) and turbulence-induced transport, nonlinear interaction and energy cascading of multi-scale turbulence and zonal flows, confinement scaling and isotopic effects, plasma rotations, and edge and divertor physics. Special attention will also be paid on MHD activities arising from the neoclassical bootstrap current and the maximum- $J$  issue in the QA configuration.

### 3 Physics design

#### 3.1 MHD equilibrium

##### 3.1.1 MHD equilibrium with VMEC code

The characteristics of three-dimensional (3-D) magnetic field configuration is uniquely determined, if the geometry of last closed flux surface (LCFS), the radial profile of pressure and the toroidal current as a function of flux are given [3.1.1-1]. The equilibrium of the magnetic field configuration is obtained by the VMEC code [3.1.1-2]. This code calculates the equilibrium from the given LCFS, the pressure and the toroidal current profile. The geometry of the torus LCFS can be parameterized by the Fourier series as follows,

$$\begin{aligned} R(\theta, \phi, s) &= \sum R_{mn}(s) \cos(m\theta - N_p n\phi), \\ Z(\theta, \phi, s) &= \sum Z_{mn}(s) \sin(m\theta - N_p n\phi). \end{aligned}$$

Here,  $\theta$ ,  $\phi$ , and  $s$  are the poloidal angle, toroidal angle, and the radial flux coordinate, respectively.  $m$ ,  $n$ , are the poloidal and toroidal mode, respectively, and  $N_p$  is the toroidal periodic number of the magnetic field configuration. In other words, the geometry of the LCFS, namely, the characteristics of the magnetic field configuration equilibrium, is expressed numerically by the dataset of  $R_{mn}$  and  $Z_{mn}$ . In stellarator optimization, we consider these parameters ( $R_{mn}$ ,  $Z_{mn}$ ) as control parameters, and some specific characters of magnetic field configuration are optimized. For numerical optimization, characters of magnetic field configuration are expressed numerically. For example, the sum of non-axisymmetric components of magnetic field in the Boozer coordinates [3.1.1-3], the Mercier criteria of  $D_I$ , and the effective helical ripple  $\varepsilon_{eff}$  etc. are used for the numerical evaluation of the magnetic configuration. These values that characterize the magnetic field configuration are optimized by changing the control parameters, *i.e.*, ( $R_{mn}$ ,  $Z_{mn}$ ) by using a non-linear optimization method. The guiding center orbits of charged particles in stellarators are determined by the absolute value of the magnetic field in the Boozer coordinates [3.1.1-3,4], therefore the spectrum of magnetic field strength  $B_{mn}$  in the Boozer coordinates are important. If the magnetic field strength in this coordinate system,  $B$ , is axisymmetric, *e.g.* it depends on only the  $\theta$ , the guiding center orbits in this coordinates also become axisymmetric. This configuration is called as a QA system, because the geometry of plasma boundary is three dimensional, however, in the Boozer coordinates the particle orbit becomes axisymmetric and the good particle confinement property like tokamaks can be achieved.

As the post CHS project, the QA device, CHS-qa, was designed in NIFS [3.1.1-5]. The parameters of this device were as follows: The toroidal periodic number ( $N_p$ ) is 2, the toroidal magnetic field strength ( $B_t$ ) is 1.5 T, the major radius ( $R$ ) is 1.5 m, and the aspect ratio ( $A_p$ ) is 3.2, which is called as the 2b32 configuration. This configuration was designed to have a good QA property with good magnetic well and ballooning mode stability. Based on this configuration, new QA configuration is

designed for the CFQS.  $N_p$  of 2,  $B_t$  of 1.0 T, and  $R$  of 1.0 m are chosen for the CFQS. From the engineering point of view, the same low-aspect-ratio of the CHS-qa is not easy to realize, so the plasma size is shrunk and  $A_p$  of 4 is selected. In Fig. 3.1.1-1, the vacuum magnetic surfaces calculated by VMEC code are shown. The coefficients  $R_{mn}$  and  $Z_{mn}$  for the CFQS are shown in Table 3.1.1-1. The radial profile of the rotational transform and the magnetic well are shown in Fig. 3.1.1-2. The profile of rotational transform is characterized by low shear, and the magnetic well property is realized in the all radial region.

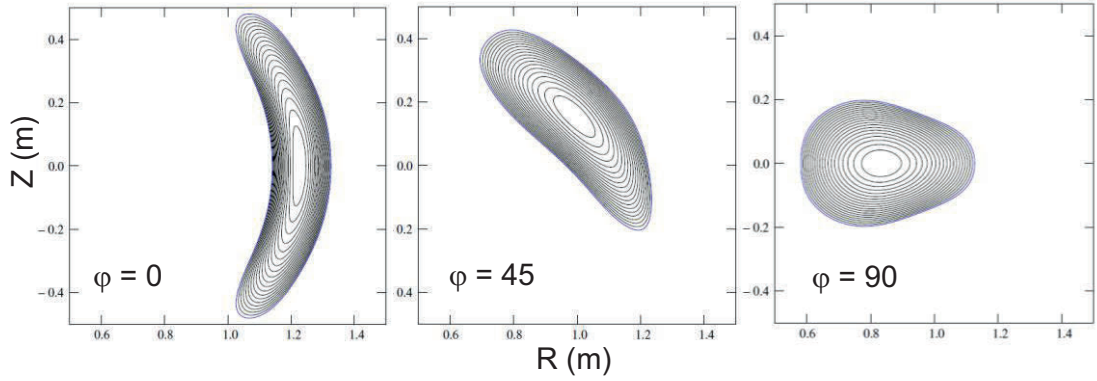


Fig. 3.1.1-1 CFQS magnetic flux surfaces in vacuum calculated by VMEC code at toroidal angles of 0, 45, and 90 degrees are shown.

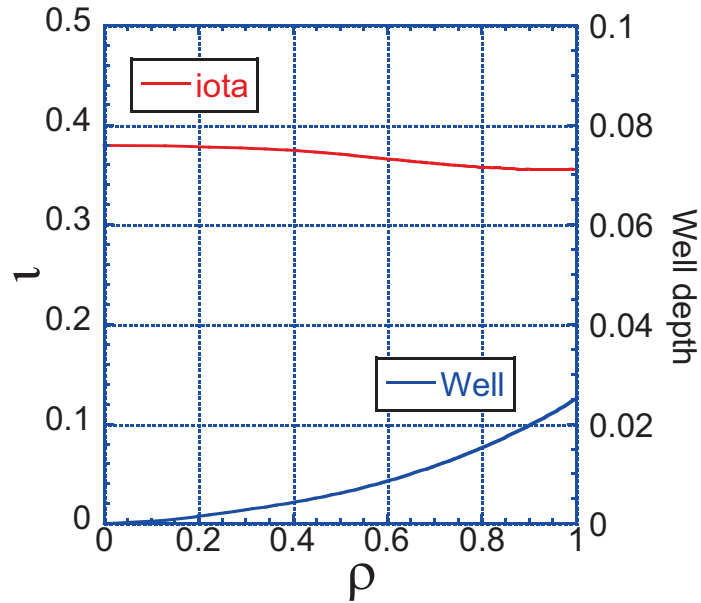


Fig. 3.1.1-2 Radial profiles of the rotational transform and magnetic well depth.

Table 3.1.1-1 Fourier components of  $R_{mn}$ ,  $Z_{mn}$  for the CFQS boundary surface.

$m$	$n$	$R_{mn}$	$Z_{mn}$
0	0	1.000000E+00	0.000000E+00
0	1	1.391875E-01	-1.041401E-01
0	2	3.510066E-03	-2.047598E-03
0	3	-1.013876E-04	1.642899E-03
0	4	-9.175025E-05	1.845669E-05
1	-4	2.798909E-05	6.083008E-05
1	-3	-8.309604E-04	-1.061025E-03
1	-2	5.350281E-04	-1.240619E-03
1	-1	3.272968E-02	3.765426E-02
1	0	1.980512E-01	3.153157E-01
1	1	-1.190292E-01	1.059881E-01
1	2	-9.839016E-03	1.600162E-02
1	3	-1.036865E-04	-1.235699E-03
1	4	-1.774901E-04	-1.233294E-05
2	-4	-1.276662E-05	1.619552E-05
2	-3	-2.212222E-04	-1.655420E-04
2	-2	2.659139E-03	9.708512E-04
2	-1	5.392748E-03	3.943360E-03
2	0	2.368458E-02	5.220414E-03
2	1	4.800571E-02	1.879457E-02
2	2	1.418504E-02	-1.281654E-02
2	3	6.331471E-04	3.229137E-03
2	4	3.216150E-04	-3.067359E-05
3	-4	-2.244352E-05	-2.337868E-05
3	-3	2.247393E-06	7.071358E-05
3	-2	1.535243E-04	-7.055294E-05
3	-1	2.756543E-03	8.833038E-04
3	0	-3.334046E-03	3.224783E-03
3	1	-7.588701E-03	-6.650261E-03
3	2	-5.415940E-03	-2.327107E-03
3	3	-1.395157E-03	2.106916E-03
3	4	3.497018E-04	-6.340033E-04
4	-4	-1.132392E-05	4.601234E-06
4	-3	2.972533E-05	2.318047E-05
4	-2	-5.763365E-06	-6.467228E-05
4	-1	-8.356260E-05	-6.036524E-05
4	0	2.323114E-05	7.077580E-04
4	1	1.594329E-03	-9.755319E-04
4	2	-1.043988E-03	-2.935019E-03
4	3	-3.632249E-05	1.253345E-03
4	4	8.926982E-05	-2.034287E-04

5	-4	-1.660390E-06	-3.428524E-06
5	-3	2.634658E-06	4.226553E-06
5	-2	2.735705E-06	-5.476804E-07
5	-1	2.253818E-05	-1.345821E-05
5	0	-6.240069E-05	9.560246E-05
5	1	2.985376E-04	3.224349E-04
5	2	2.590860E-04	-7.446490E-05
5	3	2.474033E-04	2.527979E-04
5	4	9.280067E-05	-1.552233E-04
6	-4	1.525797E-05	-1.628272E-05
6	-3	-3.190926E-06	8.024808E-06
6	-2	7.765667E-06	-1.349779E-06
6	-1	-6.667636E-06	3.234683E-05
6	0	-4.959176E-05	-2.079634E-04
6	1	2.254973E-04	4.967132E-04
6	2	-1.654727E-04	-2.109075E-04
6	3	4.065117E-06	1.641132E-04
6	4	-1.144226E-05	-2.856708E-05
7	-4	-1.117052E-05	4.973842E-06
7	-3	-2.019870E-06	2.080768E-06
7	-2	1.753082E-06	9.119779E-07
7	-1	8.999813E-06	7.420079E-06
7	0	-2.983144E-05	-4.351131E-05
7	1	7.571942E-06	1.951069E-05
7	2	1.239090E-04	1.100027E-04
7	3	-4.699164E-05	-6.161755E-05
7	4	3.831545E-05	5.227709E-05

## References

- [3.1.1-1] J. Nuhrenberg and R. Zille, Phys. Lett. **A 129** (1988) 113.
- [3.1.1-2] S. P. Hirshman and J. C. Whitson, Phys. Fluids **26** (1983) 3553.
- [3.1.1-3] A. H. Boozer, Phys. Fluids **23** (1980) 904.
- [3.1.1-4] A. H. Boozer, Phys. Fluids **24** (1981) 1999.
- [3.1.1-5] S. Okamura *et al.*, Nucl. Fusion **41** (2001) 1865.



### 3.1.2 MHD equilibrium with HINT code

The HINT code is a three-dimensional MHD equilibrium code based on the relaxation method without requiring the nested flux surface [3.1.2-1]. In this section, the typical configuration of the CFQS plasma is studied using the HINT code. A brief introduction of the code has been given here.

In the new version of the HINT code, the cylindrical coordinate  $(R, \phi, Z)$  with the right-handed system is used with a high numerical accuracy. The steady-state solution based on the relaxation method is employed to solve single-fluid nonlinear MHD equations [3.1.2-2,3,4]. The relaxation consists of the following two steps, including (A) plasma pressure relaxation and (B) magnetic field relaxation. In step A, no pressure gradient along the magnetic field is satisfied with  $\mathbf{B} \cdot \nabla p = 0$  for relaxation process of the plasma pressure ( $p$ ), where the magnetic field  $\mathbf{B}$  is fixed. In step B, magnetic field is calculated with fixed  $p$ , which is updated in the step A. The reduced MHD equations are used as

$$\frac{\partial \mathbf{v}}{\partial t} = -\nabla p + (\mathbf{j} - \mathbf{j}_0) \times \mathbf{B},$$

$$\frac{\partial \mathbf{B}}{\partial t} = \nabla \times [(\mathbf{v} \times \mathbf{B}) - \eta(\mathbf{j} - \mathbf{j}_0 - \mathbf{j}_{\text{net}})],$$

where,  $t$  is time,  $\mathbf{v}$  is plasma velocity,  $\mathbf{j}$  is the total current density,  $\mathbf{j}_0$  is the current density produced by vacuum magnetic field,  $\mathbf{j}_{\text{net}}$  corresponds to the net toroidal current like the neoclassical bootstrap current,  $\eta$  is dissipative parameter and constant plasma density is assumed. From the step B, a new magnetic field  $\mathbf{B}$  is obtained, then substituting it into step A that can yield new  $p$ . Both  $\mathbf{B}$  and  $p$  are updated via once iteration. After the multiple iteration process of the two steps, the final equilibrium is obtained when plasma velocity and magnetic field satisfy  $d\mathbf{v}/dt \rightarrow 0$  and  $d\mathbf{B}/dt \rightarrow 0$  simultaneously. The new version of HINT with the modified scheme of the pressure relaxation is efficient to calculate QAS and low shear stellarators [3.1.2-2].

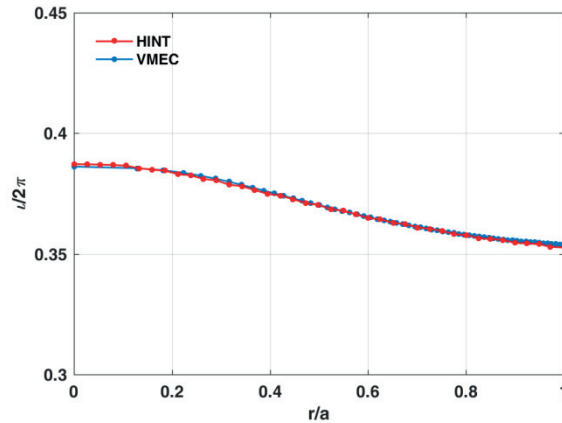


Fig. 3.1.2-1 Rotational transform ( $t/2\pi$ ) in vacuum with normalized minor radius ( $r/a$ ) for the HINT code and the VMEC code.

Fig. 3.1.2-1 shows a benchmark for CFQS equilibrium using the HINT and the VMEC code, where the rotational transform in vacuum for CFQS has been first given in previous work [3.1.2-5]. The VMEC free-boundary equilibrium result is in good agreement with the result of the HINT code for the zero pressure case. The typical rotational transform,  $t/2\pi$ , is smaller than 0.4, and this profile implies a weak shear comparing with other optimized stellarator configurations.

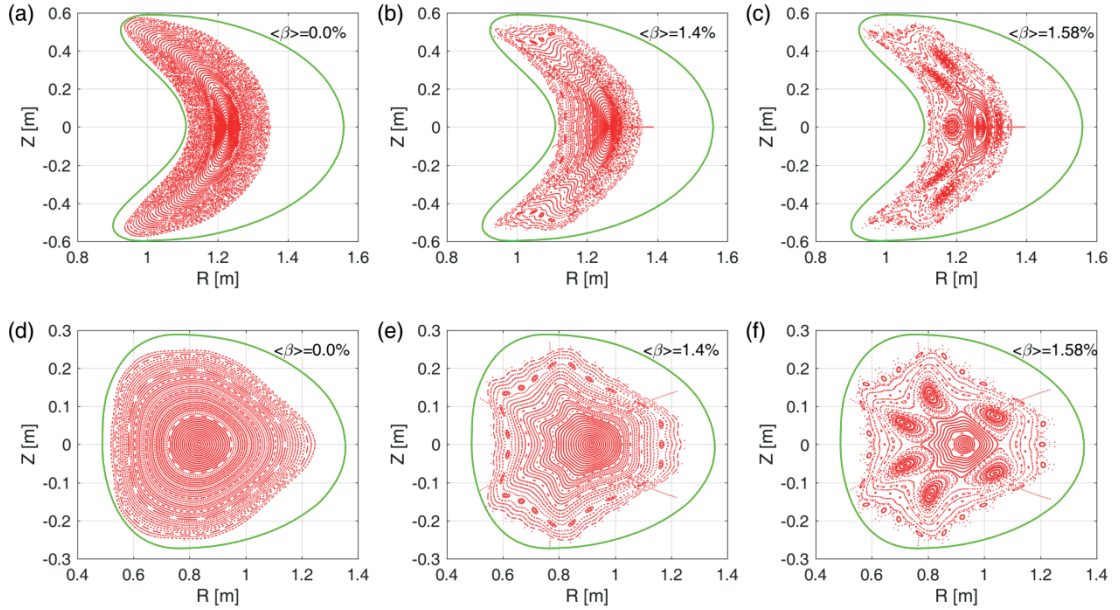


Fig. 3.1.2-2 Poincaré plots of magnetic flux surfaces calculated using HINT code for various volume averaged beta. (a)-(c)  $\langle\beta\rangle = 0.0\%$ ,  $1.4\%$ , and  $2.58\%$  at  $\phi = 0^\circ$ . (d)-(f)  $\langle\beta\rangle = 0.0\%$ ,  $1.4\%$ , and  $2.58\%$  at  $\phi = 90^\circ$ .

After the benchmark, we further calculate the finite beta equilibrium for the CFQS using the HINT code [3.1.2-6]. The Poincaré plots of magnetic surfaces are shown in Fig. 3.1.2-2, where the green line describes the vacuum vessel (VV) shape. The different volume-averaged beta  $\langle\beta\rangle$  are considered. In this calculation, a reference configuration with a general pressure profile as  $\propto (1-\psi)^2$  is employed, where  $\psi$  is the toroidal flux. Comparison of the difference  $\langle\beta\rangle$  cases shows that an ergodization of magnetic surfaces expands with  $\langle\beta\rangle$  increases in the boundary plasma ergodic region. When the plasma beta is sufficiently large, the large magnetic island generates not only on boundary but also on many low-order rational surfaces such as  $m/n = 4/2$ ,  $5/2$ , and  $6/2$ , where  $m$  and  $n$  are the poloidal and toroidal mode number, respectively. The outer ergodic region expands towards plasma center, meanwhile, flux surfaces in high- $\beta$  equilibrium tend to be more easily broken, which lead to plasma region shrinking. This suggests that the confinement of the edge plasma is significantly limited by the break of magnetic structure. On the other hand, however,  $\langle\beta\rangle$  in Fig. 3.1.2-2(b) is larger than the design value of the CFQS regular operation as  $\langle\beta\rangle = 1\%$  [3.1.2-5,7]. It is easily to predict that, in the low- $\beta$  regime of  $\langle\beta\rangle$  less than  $1\%$ , effective volume of the confinement region can be well retained

in the present equilibrium design. In order to reduce the outer magnetic surfaces loss caused by the outward shift of the surface position, an additional vertical field produced by external coils may be feasible for the CFQS to push the surface position back recovering the lost magnetic surfaces, as has been reported in reference [3.1.2-8,9].

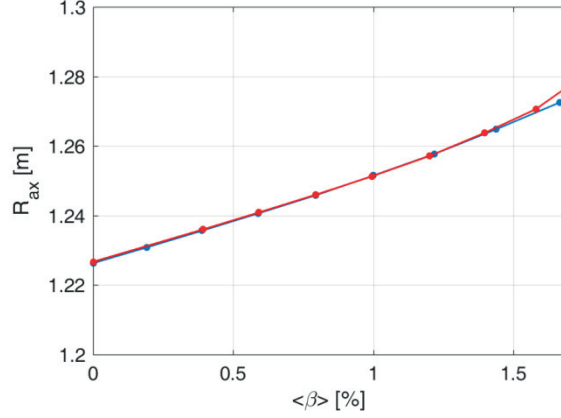


Fig. 3.1.2-3 The average position of the magnetic axis in major radius direction ( $R_{ax}$ ) as a function of  $\langle\beta\rangle$  calculated by the HINT (red line) and the VMEC code (blue line).

In fact, the finite beta effect not only on the edge, but also on every magnetic surfaces [3.1.2-2,10]. To explore the role of plasma beta and magnetic island in core region, we further calculate the magnetic axis shifts in the finite plasma beta cases by the HINT code and the VMEC code. The magnetic axis shift as a function of  $\langle\beta\rangle$  is shown in Fig. 3.1.2-3, where the pressure profile is the same as that of Fig. 3.1.2-2. It is noted that when  $\langle\beta\rangle < 1.4\%$ , the result of the HINT code is quantitatively consistent with that of the VMEC code. The  $R_{ax}$  almost linearly depends on  $\langle\beta\rangle$ . In the high- $\beta$  regimes of  $\langle\beta\rangle$  larger than 1.5%, however, the shift is accelerated as a result of the  $m/n = 6/2$  islands outward pushing. This point is confirmed in Fig. 3.1.2-2(c) and (f) in which many larger islands are produced on the left hand side of magnetic axis.

In CHS-qa, the estimated value of neoclassical bootstrap current reached to 100 kA for high- $\beta$  discharges [3.1.2-11,12]. Since the CFQS is more compact QA system, substantial neoclassical bootstrap current is expected in high- $\beta$  regime [3.1.2-7,13,14]. The HINT calculation of the equilibrium modified by neoclassical bootstrap current, therefore, is important to explore the configuration properties in detail. At first, the influence of neoclassical bootstrap current on MHD equilibrium of CFQS is investigated using the BOOTSJ code that calculates neoclassical bootstrap currents based on the drift kinetic model in non-axisymmetric magnetic configurations [3.1.2-15].

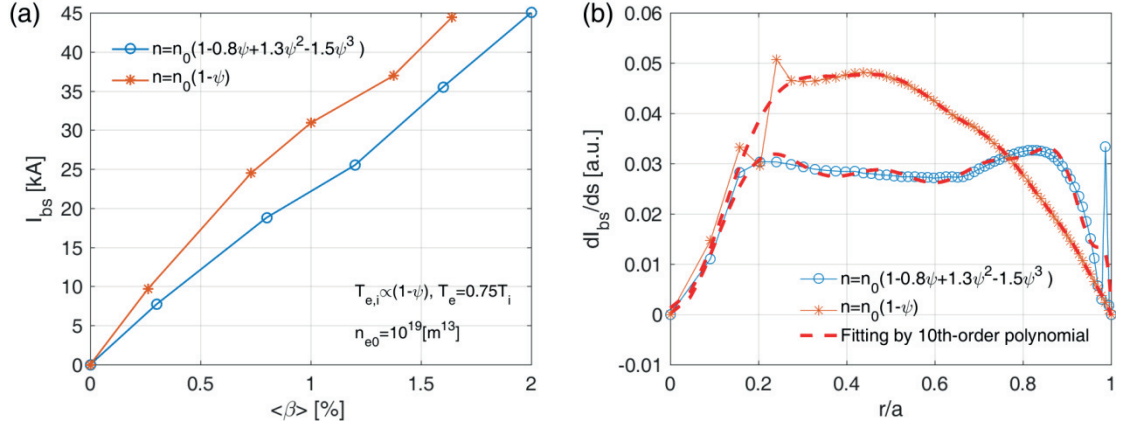


Fig. 3.1.2-4 (a) Neoclassical bootstrap current ( $I_{bs}$ ) and (b) neoclassical bootstrap current density ( $dI_{bs}/ds$ ) as a function of  $\langle\beta\rangle$  for parabolic (Case 1)  $n = n(0) \cdot (1-\psi)$  and flat  $n_e$  profile (Case 2)  $n = n(0) \cdot (1-0.8\psi+1.3\psi^2-1.5\psi^3)$  calculated by the BOOTSJ code.

To study the effect of neoclassical bootstrap current, we consider two different density profiles with the fixed temperature profile of  $T_{e,i} \propto (1-\psi)$ , corresponding to Case 1: parabolic profile ( $n = n(0) \cdot (1-\psi)$ ) and Case 2: flat density profile ( $n = n(0) \cdot (1-0.8\psi+1.3\psi^2-1.5\psi^3)$ ) as used in Fig. 3.1.2-4 (a) and (b), respectively. The parameters are the same as those used in Fig. 3.1.2-3 and then only the density profile is changed. From Fig. 3.1.2-4 (a) and (b), we can find the flattening of  $n_e$  profile can effectively reduce the neoclassical bootstrap current value and change the current density profile. The neoclassical bootstrap current almost linearly increases with  $\langle\beta\rangle$  increases. For a general design of  $\langle\beta\rangle \sim 1\%$ , the amplitudes of neoclassical bootstrap current  $\sim 20$  kA for Case 1 and  $\sim 30$  kA for Case 2 are smaller than that in CHS-qa [3.1.2-8,9,13,14]. In Case 1,  $dI_{bs}/ds$  produced by the parabolic profile has a peak at  $r/a = 0.4$  and results in the reversed magnetic shear, corresponding to advanced operation scenarios in tokamak. In Case2,  $dI_{bs}/ds$  rises toward the outer region and leads to a weak shear of  $\iota/2\pi$  profile, which is similar to the result of reference [3.1.2-7].

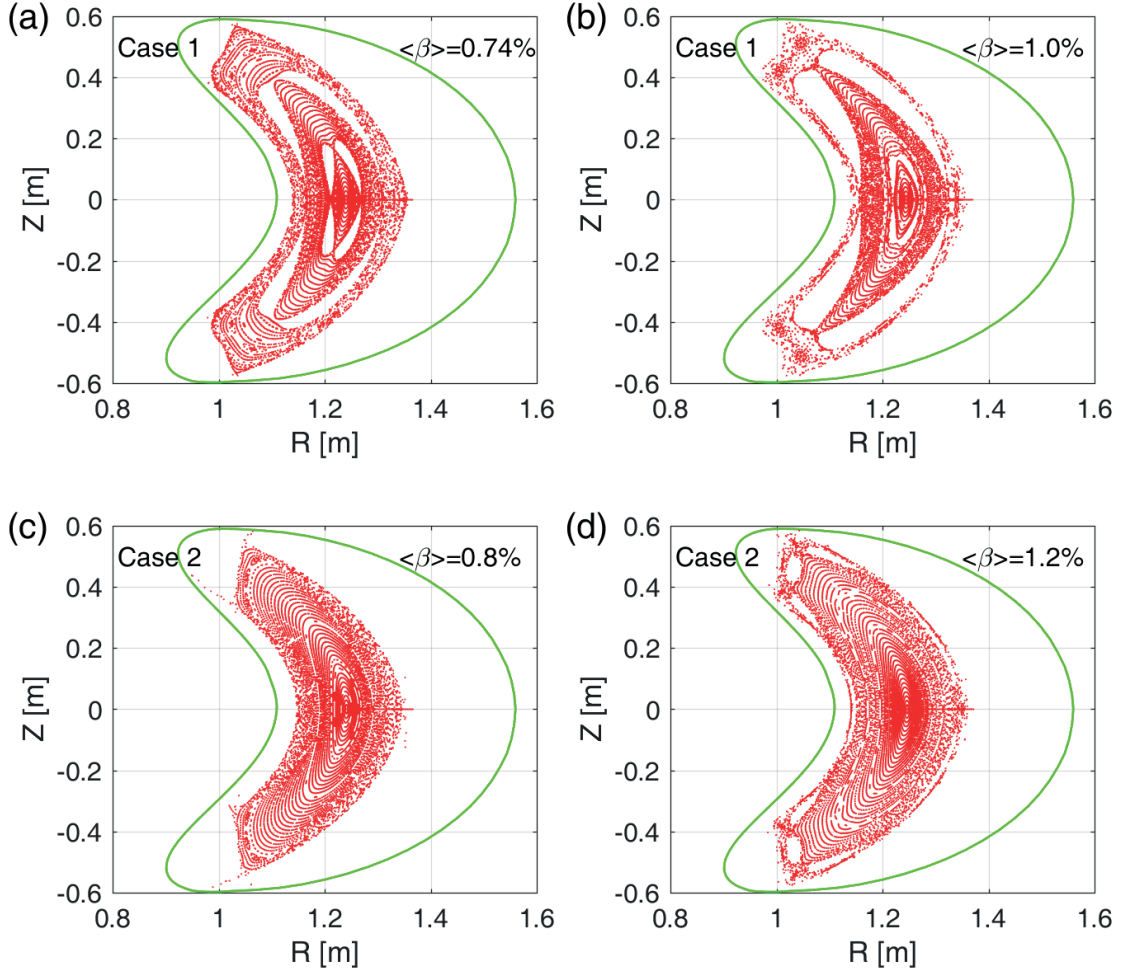


Fig. 3.1.2-5 Poincaré plots of magnetic surfaces for (a) Case 1 parabolic  $n_e$  profile with  $\langle\beta\rangle = 0.74\%$ , (b) Case 1 parabolic  $n_e$  profile with  $\langle\beta\rangle = 1.0\%$ , (c) Case 2 flat  $n_e$  profile with  $\langle\beta\rangle = 0.8\%$ , and (d) Case 2 flat  $n_e$  profile with  $\langle\beta\rangle = 1.2\%$ .

In general, in the 3-D MHD equilibrium, the magnetic island and stochastization are driven by the nonlinear 3-D equilibrium response rather than the magnetic reconnection driven by the MHD instability [3.1.2-2,3,4,10]. It means that in the CFQS the neoclassical bootstrap current can enhance the rotational transform but does not have a direct contribution on the generation of equilibrium magnetic islands. To check the robustness of boundary magnetic structure and islands, we perform the HINT calculation for the CFQS including neoclassical bootstrap current and give the Poincaré plots of magnetic surfaces in Fig. 3.1.2-5 for the two different  $n_e$  profile cases, where the parameter setting is introduced in Fig. 3.1.2-4.

For Case 1, as is shown in Fig. 3.1.2-5 (a) and (b), with increasing of  $\langle\beta\rangle$ , the shape of the LCFS is opened clearly. The edge field is ergodized as a result of the finite pressure effects. The magnetic island forms at the rational surface corresponding to  $1/2\pi = 2/4$ . For the high- $\beta$  equilibrium, the

increasing of stochastic region results in the effective volume of the confinement region shrinking to insider of islands. It implies that the force balance is not easy to maintain by residual plasma after the stochastization of magnetic field lines in the more peaked pressure configuration of Case 1.

For Case 2, as is shown in Fig. 3.1.2-5 (c) and (d), we can find in the moderate flattened pressure equilibrium with  $\langle\beta\rangle \sim 1.2\%$ , the magnetic island and stochastization are suppressed effectively. Although the boundary island remains due to increasing plasma beta, the relatively good flux surfaces are still kept over the entire plasma area. This offers the possibility to expect the high- $\beta$  equilibrium for CFQS. Meanwhile, a high effective confinement volume in high- $\beta$  operation scenarios can be realized if the density profile can be controlled by electron cyclotron resonance heating, pellet injection and so on.

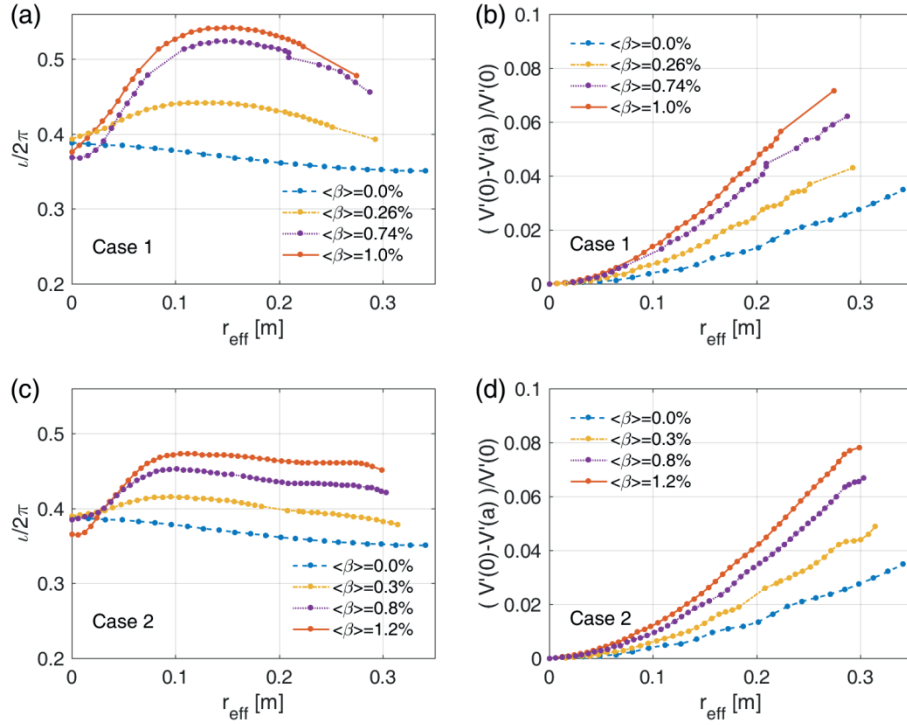


Fig. 3.1.2-6 (a) Rotational transform profiles and (b) magnetic well depth for different  $\langle\beta\rangle$  in parabolic  $n_e$  profile. (c) Rotational transform profiles and (d) magnetic well depth for different  $\langle\beta\rangle$  in flat  $n_e$  profile.

In previous works, it has been reported that the rotational transform can be enhanced by increasing the neoclassical bootstrap current in QAS [3.1.2-7,14]. Moreover, the enhanced rotational transform may play an important role in dynamics of the magnetic island. To explore the  $\langle\beta\rangle$  dependence of rotational transform including neoclassical bootstrap current consistently, we present the results of  $\iota/2\pi$  profile for various  $\langle\beta\rangle$  in Fig. 3.1.2-6 (a) and (c). The magnetic well depth defined by  $(V_p'(0) -$



$V_p'(a)/V_p'(0)$  to evaluate MHD property of QAS is shown in Fig. 3.1.2-6 (b) and (d), where  $V_p$  is the plasma volume with different effective radius and prime denotes the derivative of toroidal flux.

For Case 1, as  $\langle\beta\rangle$  increased, the rotational transform crosses  $\iota/2\pi=0.4, 0.5$ , and the  $\iota/2\pi$  profile is sensitive to the changes of  $\langle\beta\rangle$  value, particularly in the small  $\langle\beta\rangle$  regimes. On the rational surface, the modification of magnetic island near rational surface results in a vacancy region of iota profile in which the magnetic field line is closed insider islands rather than along its rotational transform. Moreover, it is also not possible to compute a  $\iota/2\pi$  value further out due to the stochasticity of magnetic field lines in plasma edge region. Using the averaged effective radial position  $r_{eff}$  [m], we can easily find the confinement plasma region shrinking which corresponds to magnetic surface plotting of Fig. 3.1.2-5 (a) and (b). Fig. 3.1.2-6 (b) shows the effect of finite  $\langle\beta\rangle$  on magnetic well depth. The magnetic well gradually rises from 3.5% to 6.7% on the LCFS, which qualitatively accords with the result of CHS-qa [3.1.2-11].

For Case 2, the iota profile flats in the intermediate region of  $r_{eff} > 0.1$  [m] due to the profile effect of neoclassical bootstrap current. In a finite beta case, the magnetic well becomes deeper than that in vacuum equilibrium. Because the modified rotational transform suppresses plasma region shrinking, the well depth ( $\sim 8\%$ ) for  $\langle\beta\rangle = 1.2\%$  is also larger than that in Case 1 even with the low  $\langle\beta\rangle = 1.0\%$ . Then the magnetic well property is achieved throughout the entire plasma region.

## References

- [3.1.2-1] S. P. Hirshman and J. C. Whitson, Phys. Fluids **26** (1983) 3553.
- [3.1.2-2] Y. Suzuki *et al.*, Plasma Phys. Control. Fusion **59** (2017) 054008.
- [3.1.2-3] Y. Suzuki, J. Geiger, Plasma Phys. Control. Fusion **58** (2016) 064004.
- [3.1.2-4] Y. Suzuki *et al.*, Contrib. Plasma Phys. **50** (2010) 576.
- [3.1.2-5] H. F. Liu *et al.*, Plasma Fusion Res. **13** (2018) 3405067.
- [3.1.2-6] X. Q. Wang *et al.*, Nucl. Fusion **61** (2021) 036021.
- [3.1.2-7] A. Shimizu *et al.*, Plasma Fusion Res. **13** (2018) 3403123.
- [3.1.2-8] K. Matsuoka *et al.*, Fusion Sci. Technol. **46** (2004) 378.
- [3.1.2-9] S. Okamura *et al.*, Nucl. Fusion **44** (2004) 575.
- [3.1.2-10] Y. Suzuki *et al.*, Nucl. Fusion **46** (2006) L19.
- [3.1.2-11] M. Isobe *et al.*, J. Plasma Fusion Res. SERIES **5** (2002) 360.
- [3.1.2-12] M. Isobe *et al.*, 28th EPS Conference on Controlled Fusion and Plasma Physics, Funchal, Portugal, 18-22 June 2001 ECA Vol.25A 761.
- [3.1.2-13] Y. Xu *et al.*, 27th IAEA Fusion Energy Conference (FEC 2018) Ahmedabad, India, 22-27 October 2018 EX/P5-23.
- [3.1.2-14] M. Isobe *et al.*, Plasma Fusion Res. **14** (2019) 3402074.
- [3.1.2-15] K. C. Shaing *et al.*, Phys. Fluids **B1** (1989) 148.

## 3.2 Confinement property

### 3.2.1 Neoclassical property

As stated above, the guiding center drift orbit is determined by the absolute value of  $\mathbf{B}$  in the Boozer coordinates, because in the guiding orbit equation, only the absolute value of  $\mathbf{B}$  appears and the vector components of  $\mathbf{B}$  do not appear. The Fourier components of the CFQS magnetic field in the Boozer coordinates are shown in Fig. 3.2.1-1. The toroidal ripple component,  $B_{10}$  is dominant for the good QA property. The contour map of magnetic field strength in the toroidal and poloidal angle plane is shown in Fig. 3.2.1-2.

Due to the QA property, the neoclassical bootstrap current is driven by the neoclassical effect. The BOOTSJ code can give us the neoclassical bootstrap current in the collision less limit [3.2.1-1]. With the BOOTSJ code, the neoclassical bootstrap current is estimated for the CFQS. Fig. 3.2.1-3 shows the dependency of the neoclassical bootstrap current on the volume-averaged plasma beta  $\langle\beta\rangle$ . Here, low-density case ( $n_{e0}=1.0 \times 10^{19} \text{ m}^{-3}$ ,  $T_e = 10 T_i$ ), and high-density case ( $n_{e0}=2.0 \times 10^{19} \text{ m}^{-3}$ ,  $T_e = T_i$ ) are considered. Radial profiles for density and temperature are assumed to be parabolic,  $n_e \propto (1-\rho^2)$  and  $T_e, T_i \propto (1-\rho^2)$ . For the beta scan,  $n_e$  is fixed, and  $T_e$  and  $T_i$  are changed. When  $\langle\beta\rangle$  reaches 1 %, the neoclassical bootstrap current of 30 kA is expected. For low-density case, the change of the rotational transform profile is shown in Fig. 3.2.1-4. The MHD instability, such as kink mode, will be studied in the future.

The neoclassical transport in the  $1/\nu$  regime can be estimated by the NEO [3.2.1-2] code. By this code, so-called the effective helical ripple  $\varepsilon_{eff}$  is estimated in this work. The neoclassical diffusion coefficient  $D$  is proportional to  $v_d \varepsilon_{eff}^{3/2}/\nu$ . Here,  $v_d$  and  $\nu$  are the drift velocity and the collision frequency, respectively. The radial profile of  $\varepsilon_{eff}^{3/2}$  are shown in Fig.3.2.1-5. The magnetic configurations of the CFQS in this figure are calculated with VMEC on fixed boundary and free boundary condition. The  $\varepsilon_{eff}^{3/2}$  of the CFQS are two or three order less than that of the CHS. Up to  $\langle\beta\rangle$  of 1.5%, the good neoclassical confinement property is kept.



Fourier spectrum of  $B$  in Boozer coordinates

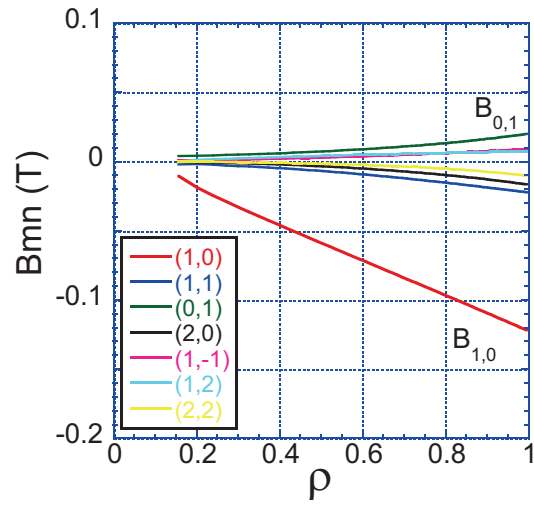


Fig. 3.2.1-1 Fourier spectrum of  $B$  in the Boozer coordinates.

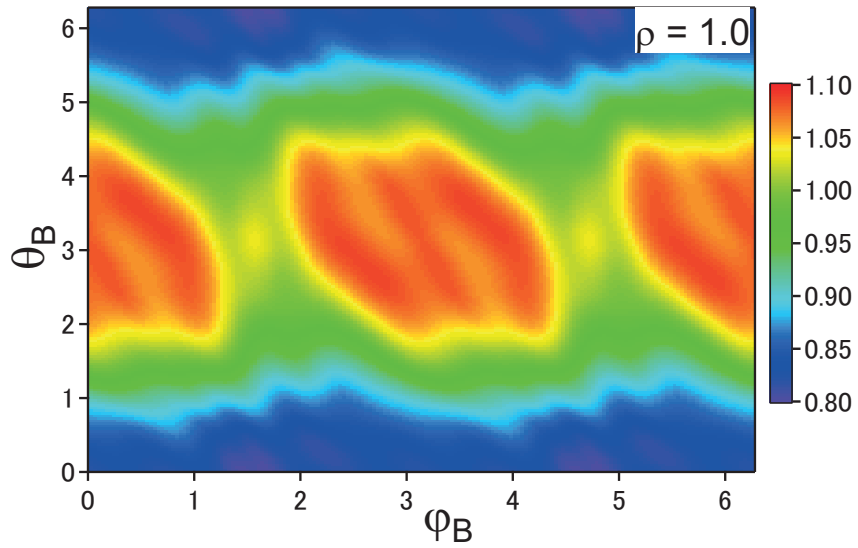


Fig. 3.2.1-2 Contour map of the magnetic field strength  $B$  in the Boozer coordinates on the LCFS of the CFQS.

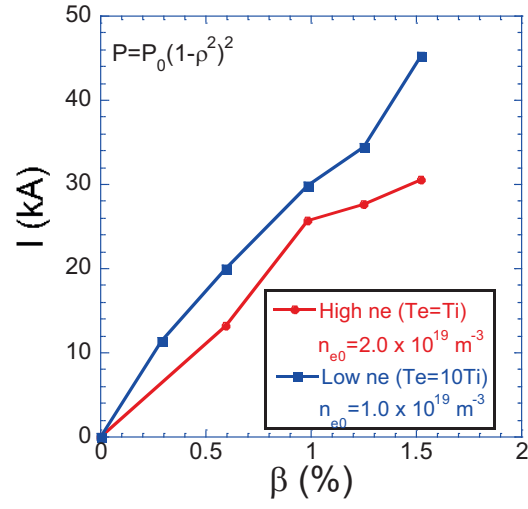


Fig. 3.2.1-3 Dependency of the neoclassical bootstrap current on the volume-averaged plasma beta.

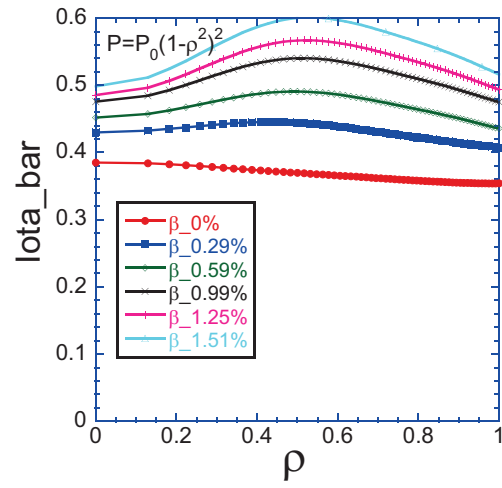


Fig. 3.2.1-4 Radial profile of the rotational transform considering the neoclassical bootstrap current.

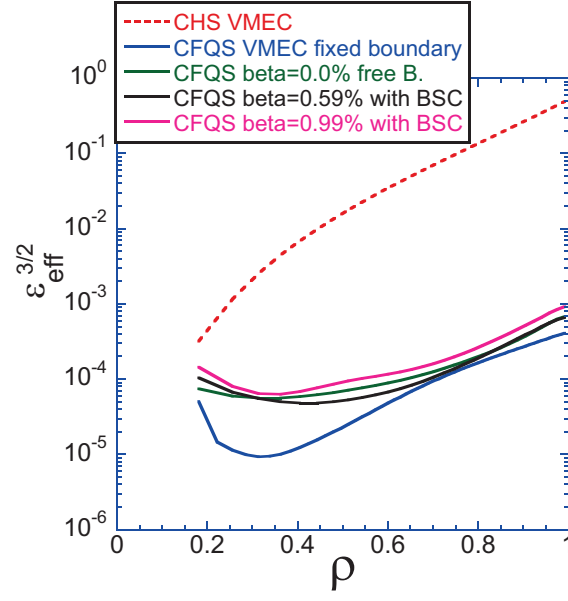


Fig. 3.2.1-5 Radial profiles of the effective helical ripple,  $\epsilon_{\text{eff}}^{3/2}$ . In the latter three cases, *i.e.*, green, black, and pink, the free-boundary calculation result of the VMEC are used to estimate  $\epsilon_{\text{eff}}^{3/2}$ .

## References

- [3.2.1-1] K. C. Shaing *et al.*, Phys. Fluids **B 1** (1989) 148.
- [3.2.1-2] V. V. Nemov *et al.*, Phys. Plasmas **6** (1999) 4622.

### 3.2.2 Plasma parameters expected from scaling law

CFQS is expected to be operated in two different heating regimes. The facility will be equipped with 1.0 MW of ECRH (54.5 GHz, on axis heating). A low density, high electron temperature case could be achieved. To analyze plasma confinement and MHD behaviors in the second ballooning stable scenario, the impact of 1.0 MW of NBI (tangential injection with beam energy  $\sim 40$  keV) and 2 MW of ICRH which is available in the 40–80 MHz range, has also been considered. This would allow access to higher density regimes than ECRH (density cut-off limited). The operational parameters of CFQS were estimated using the ISS95 scaling law [3.2.2-1]. The radial density and temperature profiles are assumed as  $T = T_0(1-\rho^2)$  and  $n_e = n_{e0} (1-0.8\rho^2+1.3\rho^4-1.5\rho^6)$ , respectively.  $T_{i0} = 2/3T_{e0}$ . The enhancement factor  $H_f = 1.0, 2.0, 2.5$ , and  $2.9$  are under consideration. The line-averaged density is  $1 \times 10^{19} \text{ m}^{-3}$  for low-density plasma heating and  $4 \times 10^{19} \text{ m}^{-3}$  for high-density plasma heating, respectively. The  $H_f = 2.9$  is similar to that in the NCSX [3.2.2-2]. For the  $B = 1.0$  T operation, the  $\beta$  and  $T_{e0}$  variations vs heating power in these two heating regimes are shown in Fig. 3.2.2-1. Concerning the low-density plasma heating, the expected  $\beta$  ranged from 0.5 % to 1.5 % at a heating power of 1.0 MW ECRH and the  $T_{e0}$  ranged from 1.0 to 3.0 keV as shown in Figs. 3.2.2-1 (a) and (b). With respect to the high-density plasma heating, the expected  $\beta$  ranged from 1.7 to 4.7 % with the range of  $T_{e0}$  from 0.7 to 2.3 keV at a heating power of 3.0 MW (1.0 MW NBI + 2.0 MW ICRH) as shown in Figs. 3.2.2-1 (c) and (d). There are numerous reasons to expect that the confinement may be enhanced in the CFQS configuration, compared with conventional stellarators and tokamaks. The robustness of quasi-symmetry should reduce neoclassical transport and suppress neoclassical toroidal viscosity, allowing development of persistent zonal flows. Furthermore, the shallow reversed/flat shear could stabilize trapped-particle modes, similar to reversed-shear advanced tokamak regimes.

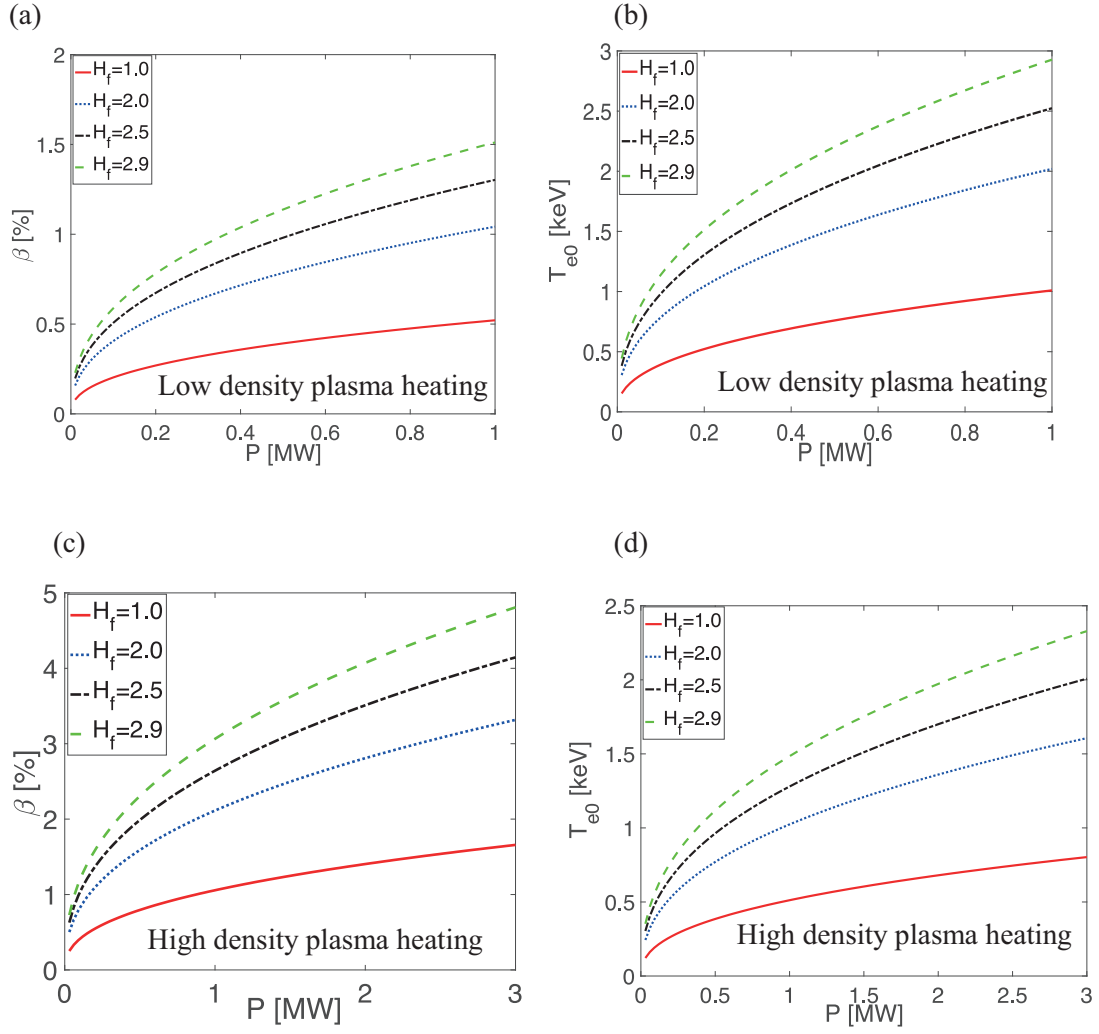


Fig. 3.2.2-1 Volume-averaged  $\beta$  (a) and electron temperature (b) for the low-density plasma heating, (c) and (d) for the high-density plasma heating estimated by the ISS95 scaling law in the  $B = 1.0$  T operation.

## References

- [3.2.2-1] U. Stroth, M. Murakami, R.A. Dory *et al.*, Nucl. Fusion **36** (1996) 1063.  
[3.2.2-2] M.C. Zarnstorff *et al.*, Plasma Phys. Control. Fusion **43** (2001) A237.

### 3.3 MHD stability

Key MHD stabilities in the design of a finite- $\beta$  QA stellarator configuration are discussed in this section. Mercier stability, ballooning mode, kink mode, and tearing mode are investigated to determination of  $\beta$  limit. These four issues are not independent. The VMEC, COBRAVMEC, BOOTSJ, and TERPSICHOE codes are executed to estimate them [3.3-1~5].

## References

- [3.3-1] S.P. Hirshman and J.C. Whitson, Phys. Fluids **26** (1983) 3353.  
[3.3-2] A. H. Boozer, Phys. Fluids **24** (1981) 1999.  
[3.3-3] K.C. Shaing *et al.*, Phys. Fluids **B1** (1989) 1663.  
[3.3-4] R. Sanchez *et al.*, J. Comput. Phys. **161** (2000) 576.  
[3.3-5] C. Mercier, Nucl. Fusion **1** (1960) 47.

#### 3.3.1 Mercier stability/instability

The Mercier criterion is a necessary condition for the stability of localized interchange modes in a toroidal plasma, according to the ideal MHD model [3.3.1-1]. These modes are localized around mode-rational surfaces, where the parallel wave vector vanishes, so as to minimize the magnetic field line bending energy. The driving force for these modes is the pressure gradient across surfaces with average unfavorable curvature. The Mercier stability criterion involves competition between the driving force and the stabilizing effect of magnetic shear. The Mercier criterion can be written as summation of four terms, corresponding to the contributions coming from the shear, magnetic well, net currents, and geodesic curvature, respectively.

Once the magnetic field coils have been designed it needs to be established that these coils actually reproduce the desired MHD equilibrium and its relevant properties. For this purpose, free boundary equilibria were computed for volume averaged  $\langle\beta\rangle=0$  and  $\langle\beta\rangle=2\%$  [3.3.1-2]. The cross sections of the plasma boundary obtained from free boundary equilibrium calculations (*i.e.* using the external magnetic field generated by the modular coils described in Sec. 4.2) are obtained. A comparison of the flux surfaces of the vacuum field and the  $\langle\beta\rangle=2\%$  solution (both VMEC) is presented in Fig. 3.3.1-1. It is observed that the Shafranov shift of the axis exists. The variation of Shafranov shift with

$\langle \beta \rangle$  is displayed in the Fig. 3.3.1-2. When  $\langle \beta \rangle$  equals to 1.7 %, the Shafranov shift is about the half of the minor radius.

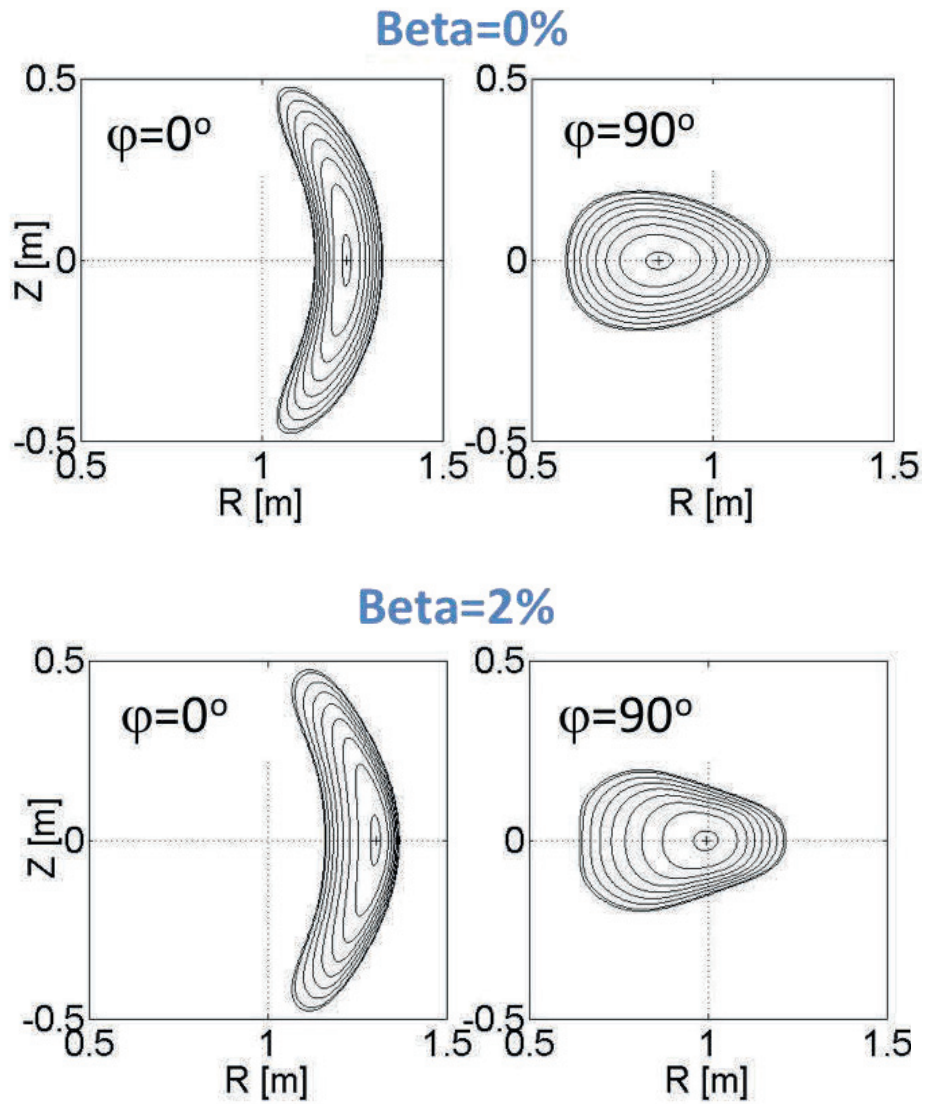


Fig. 3.3.1-1 Poloidal cross sections of the free-boundary equilibrium calculated by the VMEC code with the plasma pressure free (top panel) and  $\langle \beta \rangle = 2\%$  (bottom panel).

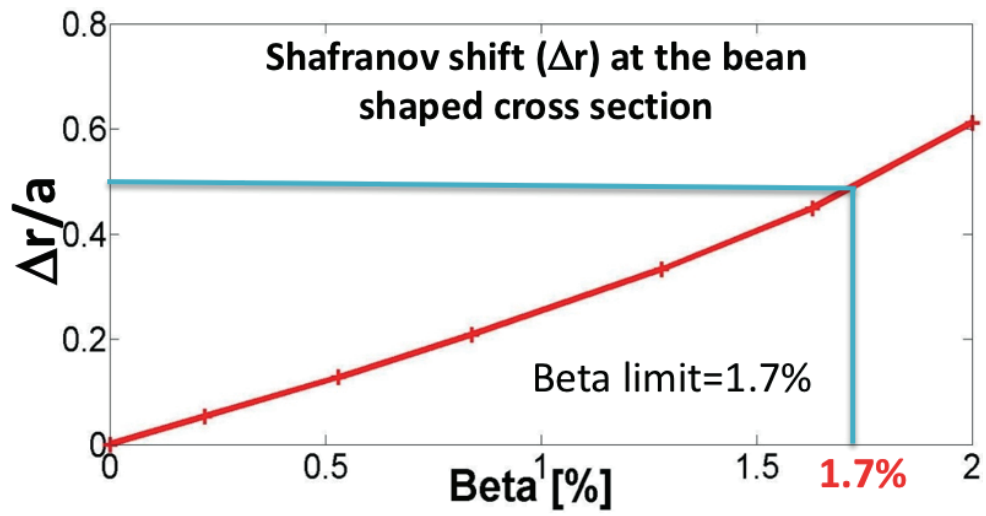


Fig. 3.3.1-2 Shafranov shift vs.  $\langle\beta\rangle$  at the bean-shaped poloidal cross section.

(a)

(b)

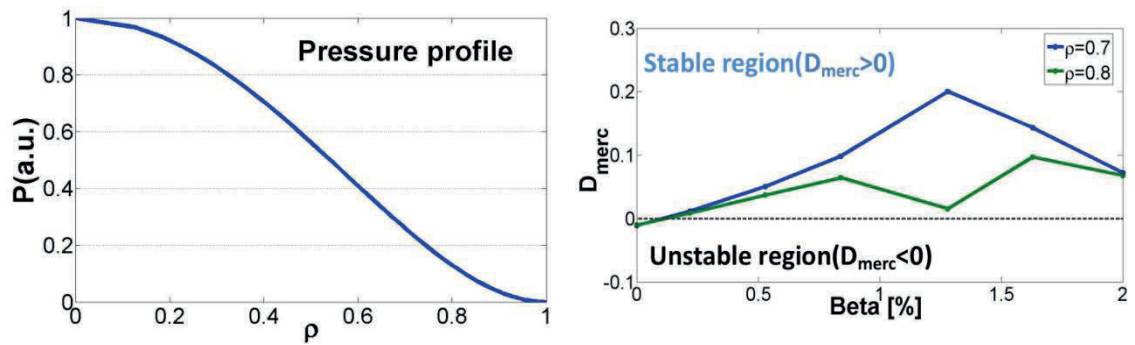


Fig. 3.3.1-3 (a) Assumed radial profile of plasma pressure (quadratic form) and (b) the variation of Mercier stability with  $\langle\beta\rangle$  at two different radial position, *i.e.*,  $\rho = 0.7$  and  $0.8$ .



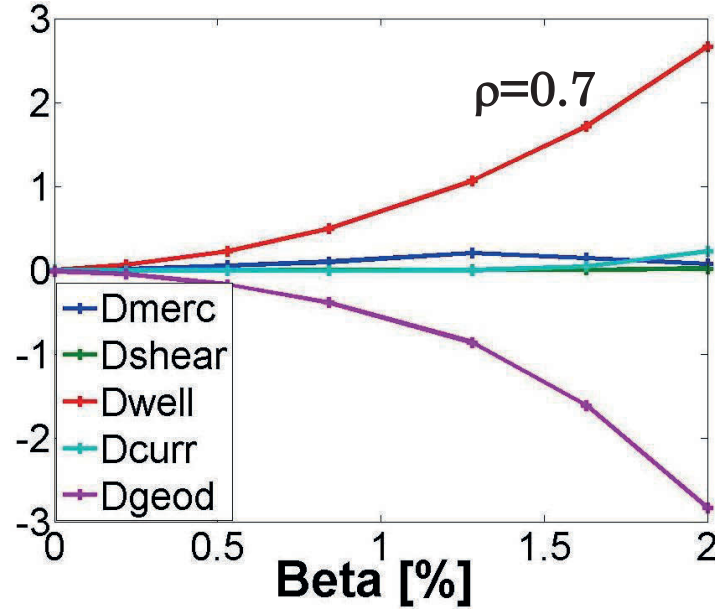


Fig. 3.3.1-4 Shear term, well term, current term and geodesic curvature term versus  $\langle\beta\rangle$  at radial position  $\rho = 0.7$ , showing stabilization from the contribution of magnetic well.

The Fig. 3.3.1-3 (a) gives the input profile of plasma pressure  $P(\rho) = P_0(1+\rho^2)^2$  for the VMEC calculation with the unfixed plasma boundary and Fig. 3.3.1-3 (b) displays the variation of Mercier stability with the volume-averaged beta at two different radial positions, *i.e.*,  $\rho = 0.7$  and  $0.8$ . It shows that the interchange mode is stable up to  $\langle\beta\rangle = 2\%$ . The Mercier criterion can be expressed as  $D_{merc} = D_{shear} + D_{well} + D_{curr} + D_{geod}$ , where these terms correspond to the contributions coming from the shear, magnetic well, net currents, and geodesic curvature, respectively. In the Fig. 3.3.1-4, the variation of these four terms versus  $\langle\beta\rangle$  at radial position  $\rho = 0.7$  is shown, which depicts the stabilizing effect from the magnetic well ( $D_{well} > 0$ ) is stronger than the destabilizing effect from the geodesic curvature term ( $D_{geod} < 0$ ).

The simulation of 3D ideal MHD equilibria is executed using the free-boundary VMEC code. The code approaches an equilibrium state by minimization of the plasma energy. The bootstrap current is estimated with the SFINCS code. A convergent iteration operation between VMEC and SFINCS codes is performed to self-consistently calculate the bootstrap current in CFQS. After several iterations a self-consistent equilibrium state is obtained. Plasma  $\langle\beta\rangle$  is scanned from 0% to 2.03 %. Problems of convergence towards an equilibrium state with VMEC arise partially due to the large Shafranov shift for  $\langle\beta\rangle > 2.03\%$ . The plasma temperature and density profiles are assumed as  $T = T_0(1 - \rho^2)$  and  $n_e = n_i = n_0(1 - \rho^2)$ , respectively and set  $T_{e0}/T_{i0} = 3/2$ .  $\rho$  represents the normalized minor radius.  $T_{e0}$  is scanned from 0 to 5.7 keV and  $n_0$  is fixed at  $1.0 \times 10^{19} \text{ m}^{-3}$ . The dependence of rotational transform (i) on bootstrap currents and bootstrap current density as a function of the normalized minor radius are shown in Figs. 3.3.1-5 (a) and (b), respectively. As the plasma  $\langle\beta\rangle$  increases to 2.03 % the bootstrap

current is enhanced to 54 kA. In the regions with  $\rho$  from 0.4 to 0.6 a peak exists in the profile of the bootstrap current density, which results in generation of magnetic shears in the bulk plasma. This could be beneficial for the stabilization of MHD modes, *e.g.*, interchange modes. Meanwhile, the rotational transform crosses the low-order rational surfaces with  $n/m = 1/2$  as  $\langle\beta\rangle$  increases to 1.0 %, which may lead to generate magnetic islands.

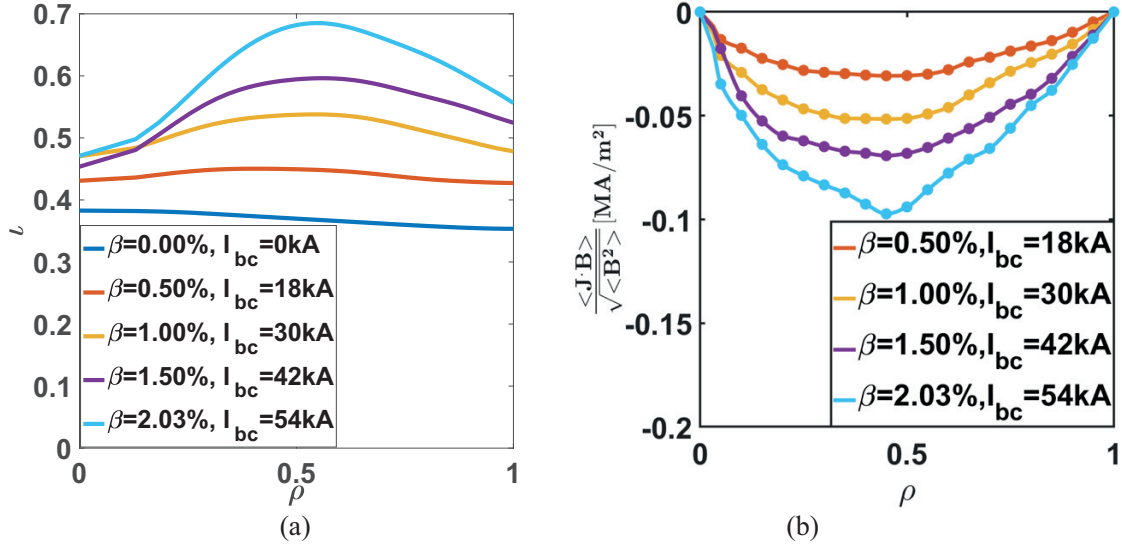


Fig. 3.3.1-5 Profiles of (a) rotational transform and (b) bootstrap current density for  $\langle\beta\rangle = 0.00, 0.50, 1.00, 1.50$ , and  $2.03$  % with plasma bootstrap current = 0, 15, 30, 42, and 54 kA, respectively. These results are obtained with the self-consistent iterations between SFINCS and VMEC codes.

The impact of increasing  $\langle\beta\rangle$  and bootstrap currents on the equilibria is shown in Fig. 3.3.1-6 which contains cross sections of magnetic flux surfaces with the bean shape in equilibrium states with various bootstrap currents and corresponding magnetic field strength spectra  $B_{m,n}$  normalized by  $B_{0,0}$  in the Boozer coordinates. In order to demonstrate clearly variation of non-axisymmetric magnetic fields, the dominant component  $B_{1,0}$  with a large amplitude is not given. Figs. 3.3.1-6 (a)-(c) show as  $\langle\beta\rangle$  is increased, the magnetic axis is shifted horizontally by the net toroidal current because the effective vertical field is changed. Meanwhile, the flux surfaces become deformed and compressed towards the outside of the torus. The core region develops a  $B_{0,1}$  symmetry breaking component from  $\langle\beta\rangle > 1.0$  % in Fig. 3.3.1-6 (e) and from  $\langle\beta\rangle > 2.0$  % the  $B_{2,1}$  term becomes significant in Fig. 3.3.1-6 (f), which indicates as  $\langle\beta\rangle$  increases beyond 2.0 %, the deformation of magnetic flux surfaces may degrade the quasi-axisymmetry of the magnetic configuration in the core.

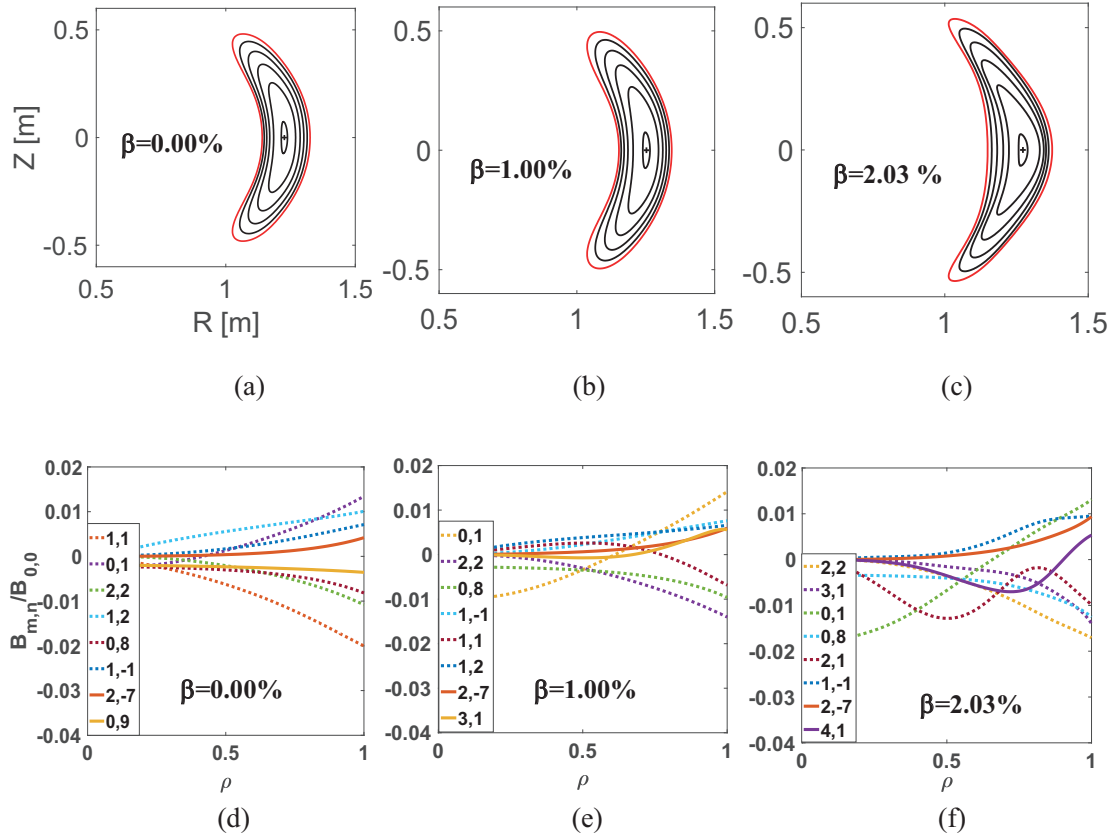


Fig. 3.3.1-6 Cross sections of magnetic flux surfaces with the bean shape and magnetic field strength spectra with  $n \neq 0$  normalized by  $B_{0,0}$  in the Boozer coordinates for three of the cases: (a) and (d) for  $\langle \beta \rangle = 0.00\%$ , (b) and (e) for  $\langle \beta \rangle = 1.00\%$  with a 30kA bootstrap current, and (c) and (f) for  $\langle \beta \rangle = 2.03\%$  with a 54kA bootstrap current.

The Mercier criterion and global linear MHD stability are estimated with the VMEC and TERPSICHORE codes. The Mercier criterion for the stable interchange modes is expressed by  $D_{merc} = D_{shear} + D_{well} + D_{curr} + D_{geod} > 0$  where they represent magnetic shear term, magnetic well term, current term and geodesic curvature term, respectively. At three different radial positions, the variations of Mercier stabilities with  $\langle \beta \rangle$  are given in Fig. 3.3.1-7 (a), which illustrates that the interchange modes are stable up to  $\langle \beta \rangle = 2.03\%$  at least. What is interesting is that in the equilibria with bootstrap currents the stabilization of interchange modes is attributed to the enhancement of magnetic shear and the magnetic well, as shown in Fig. 3.3.1-7 (b). These two stabilization effects enable to robustly suppress the destabilization effect of the geodesic curvature term. The previous study found that free boundary equilibria without bootstrap currents, they were also stable when  $\langle \beta \rangle \leq 2.0\%$  in CFQS. However, a flat  $\iota$  profile was sustained well as  $\langle \beta \rangle$  increased. Thus, interchange

modes were merely stabilized by magnetic well structures. In addition, the stabilization effect of a net toroidal current on interchange modes in heliotron plasmas was also observed. The resistive ballooning mode was also studied in CFQS and its stability is dependent on the MHD resistivity. If the resistivity is not large, the ballooning modes can be stabilized well.

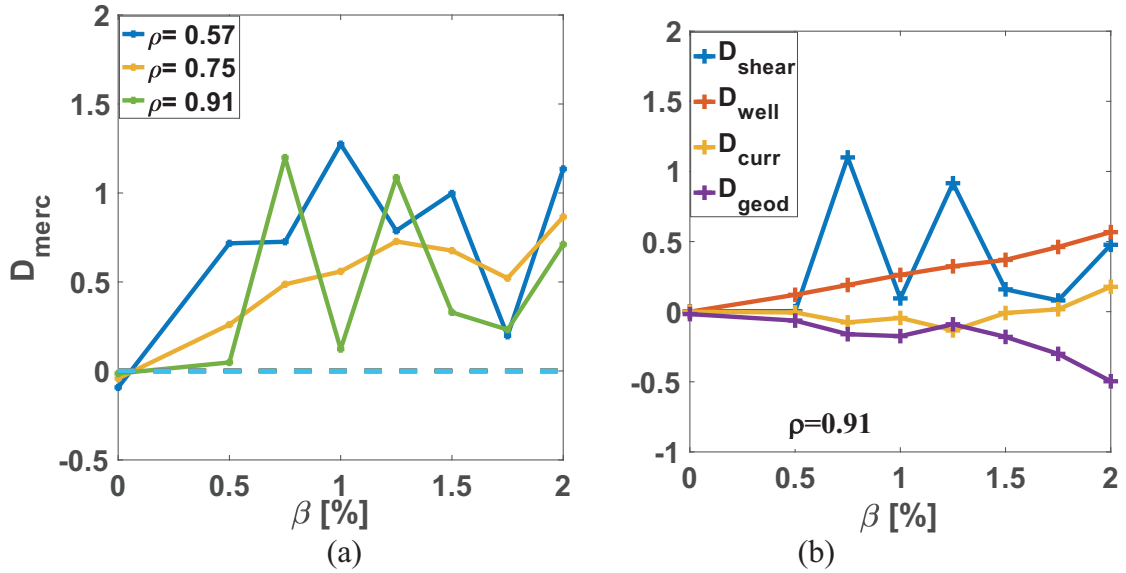


Fig. 3.3.1-7 (a) Mercier stabilities versus  $\beta$  at three different radial positions  $\rho = 0.57, 0.75$  and  $0.91$  respectively; (b) magnetic shear, magnetic well, current and geodesic curvature terms versus  $\beta$  at  $\rho = 0.91$  in various free-boundary equilibria with bootstrap currents.

## References

- [3.3.1-1] C. Mercier, Nucl. Fusion **1** (1960) 47.
- [3.3.1-2] H. Liu, *et al.*, Nucl. Fusion **61** (2021) 016014.

### 3.3.2 Ballooning mode

A principle aim of stellarator research is to understand the physical mechanisms that limit the plasma stored energy. The expectation is that pressure driven instabilities will be excited as the plasma energy increases relative to the magnetic energy. Since one of the advantages of stellarators is the avoidance of current driven instabilities, pressure driven instabilities may be critical in limiting stellarator operation. In theoretical studies of particular configurations, local criterion deduced from ideal MHD ballooning theory is often used to predict the plasma pressure limits of stellarators.

A feature related to second stability, which we call ‘self-stabilization’ for large pressure gradients after Ref. [3.3.2-1] has been observed in various stellarator experiments [3.3.2-2,3]. In these results, geometrical deformations associated with the Shafranov shift result in configurations which are stable with respect to Mercier modes as the plasma pressure increases. In this section, the COBRAVMEC code is utilized to calculate ideal ballooning stability for VMEC equilibria.

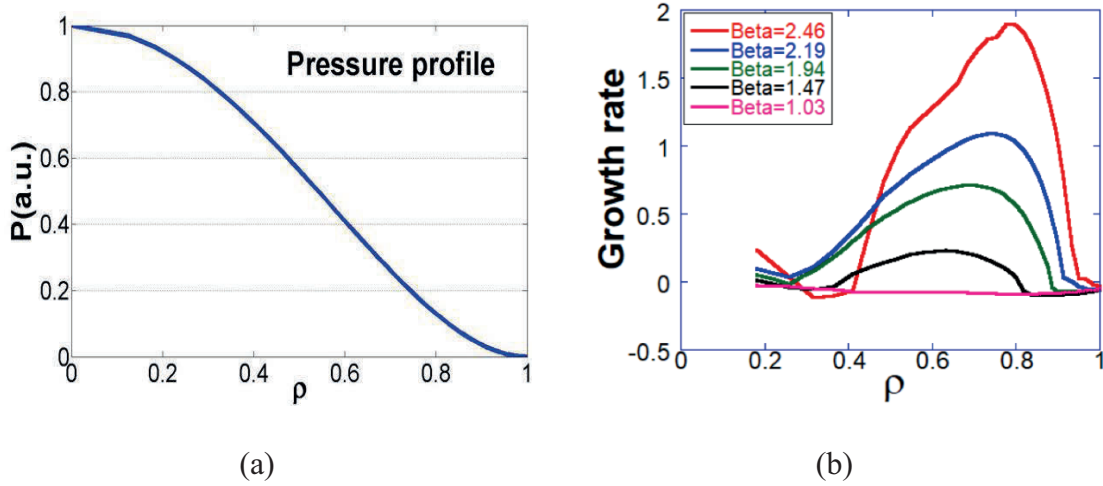


Fig. 3.3.2-1 (a) Assumed radial profile of plasma pressure (quadratic form), (b) Ballooning growth rates from COBRAVMEC as a function of the normalized flux for various volume-averaged beta, indicating the first stability boundary.

For the reference configuration, a quadratic pressure profile,  $P(\rho) = P_0(1+\rho^2)^2$  was chosen. Ballooning growth rates as a function of the normalized flux label,  $\rho$ , are shown in Fig. 3.3.2-1 (a). As the plasma pressure increases, the plasma first becomes ballooning unstable at  $\langle\beta\rangle$  of 1.03%, displayed in Fig. 3.3.2-1 (b). The region of instability grows until 3 %, where a region of second stability appears as shown in Fig. 3.3.2-2.

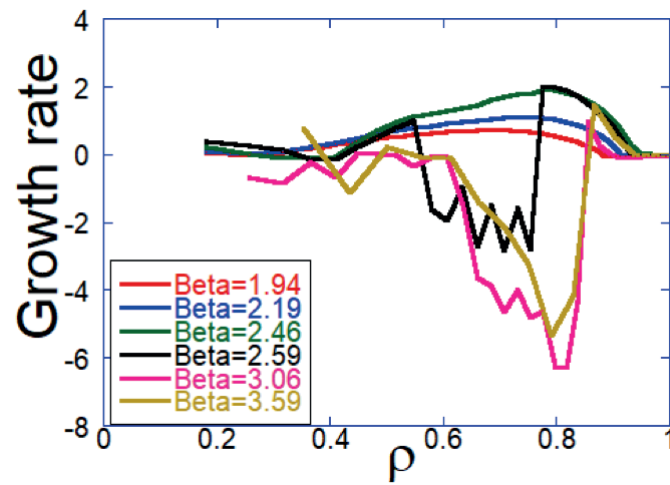


Fig. 3.3.2-2 Ballooning growth rates from COBRAVMEC as a function of the normalized flux for various volume-averaged beta, indicating the onset of second stability.

### References

- [3.3.2-1] R. D. Hazeltine and J. D. Meiss, Plasma Confinement (Addison Wesley, Redwood City, 1992), pp. 309–312.
- [3.3.2-2] C. C. Hegna and S. R. Hudson, Phys. Plasmas **9** (2002) 2014.
- [3.3.2-3] R. Hudson and C. C. Hegna, Phys. Plasmas **10** (2003) 4716.

### 3.3.3 Kink mode

In a QA configuration, larger amount of neoclassical bootstrap current (BSC) flows and increases rotational transform due to its tokamak-like magnetic field structure. Therefore, the onset of an external kink mode should be carefully assessed in the ideal MHD stability analysis including plasma current. If a BSC profile is given, global low- $n$  ideal MHD stability can be calculated with the TERPSICHOE code [3.3.3-1]. Since such a calculation for the CFQS configuration has not been performed yet, a typical example for the CHS-qa configuration [3.3.3-2] is described below.

A self-consistent BSC profile for a CHS-qa reference configuration has been calculated with SPBSC code [3.3.3-3]. We have solved finite beta equilibria including BSC assuming the fixed density and temperature profiles for three representative cases; (A)  $n_e = 1.0 \times 10^{20} \text{ m}^{-3}$ ,  $T_e = 1.04 \text{ keV}$ , (B)  $n_e = 0.2 \times 10^{20} \text{ m}^{-3}$ ,  $T_e = 5.2 \text{ keV}$ , (C)  $n_e = 1.5 \times 10^{20} \text{ m}^{-3}$ ,  $T_e = 1.04 \text{ keV}$  [3.3.3-4]. The resulting rotational transform is shown in Fig. 3.3.3-1 as a function of the normalized toroidal flux. Then the ideal global MHD stability has been analyzed with artificially changing the total parallel current while keeping its profile. The dependences of the most unstable eigenvalues on the total current are shown in Fig. 3.3.3-2 for the three representative cases. The onset of destabilization above 150 kA in the cases A and B clearly corresponds to the crossing of the edge rotational transform beyond 0.5 and 0.6. The associated amplitude of the dominant perturbation mode increases toward the edge, which clearly indicates the characteristics of an external kink instability. On the other hand, the global mode is kept stable up to 250 kA for the case C which has a different current profile. It indicates the possibility of stabilization of the external kink mode by controlling the current profile in a QA configuration.

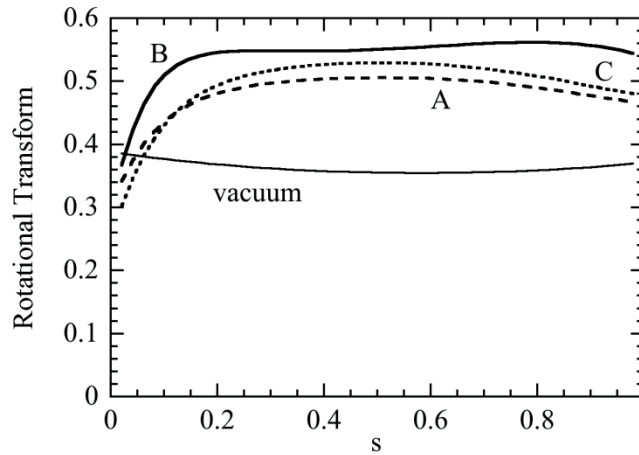


Fig. 3.3.3-1 Radial profiles of rotational transform for the three representative cases.

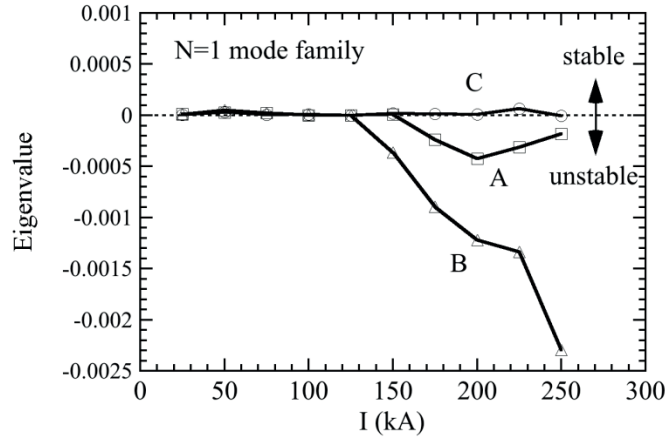


Fig. 3.3.3-2 Most unstable eigenvalues as functions of total current for the three representative cases.

A global linear MHD stability analysis of CFQS equilibria is computed with respect to  $n=1$  and  $n=2$  family of modes with the TERPSICHORE code, which evaluates the variational energy principle. Fig. 3.3.3-3 displays bootstrap currents as a function of  $\langle\beta\rangle$  and it is approximately proportional to  $\langle\beta\rangle$ . The ranges of Fourier modes for the global MHD stability analysis are  $m < 49$  and  $n < 14$  for the poloidal and toroidal modes, respectively. The typical marginal stability is represented by a threshold value of  $\lambda = -1 \times 10^{-4}$  and more negative eigenvalues than this crucial number are thought to be more unstable. The simulation results reveal that a global MHD stability is obtained for  $\langle\beta\rangle$  up to 1.35 % ( $I_{bc} = 38$  kA). The stability is determined by the rotational transform at the edge, *i.e.*, the iota value higher than 0.5 is unstable. As  $\langle\beta\rangle$  increases beyond 1.35 %, global instabilities arise. As an instance, the Fourier amplitudes of the radial component of the displacement vector ( $\xi^s$ ) profiles are displayed in Fig. 3.3.3-4 (a). In this equilibrium the plasma  $\langle\beta\rangle$  and bootstrap current are 1.75 % and 46 kA, respectively. The unstable mode structure is dominated by the  $m/n = 2/1$  term with the eigenvalue  $\lambda = -3.8724 \times 10^{-4}$ . In order to identify the category of these unstable modes, Fig. 3.3.3-4(b) shows radial profiles of surface-averaged plasma potential energy  $\langle\delta W_p\rangle$  which mainly includes two instability drive terms,  $\langle\delta W_{p\kappa^s}\rangle$  and  $\langle\delta W_{j\parallel\kappa^s}\rangle$ . The former drive term associates with ballooning modes in which the plasma pressure gradient interacts with the curvature of magnetic field lines. The latter describes kink modes which are caused by the parallel current density interacting with the local magnetic shear. In the unstable regions with  $\langle\delta W_p\rangle < 0$ , the second term completely exceeds the first term. Hence, the 2/1 mode is mainly current-driven external kink mode.



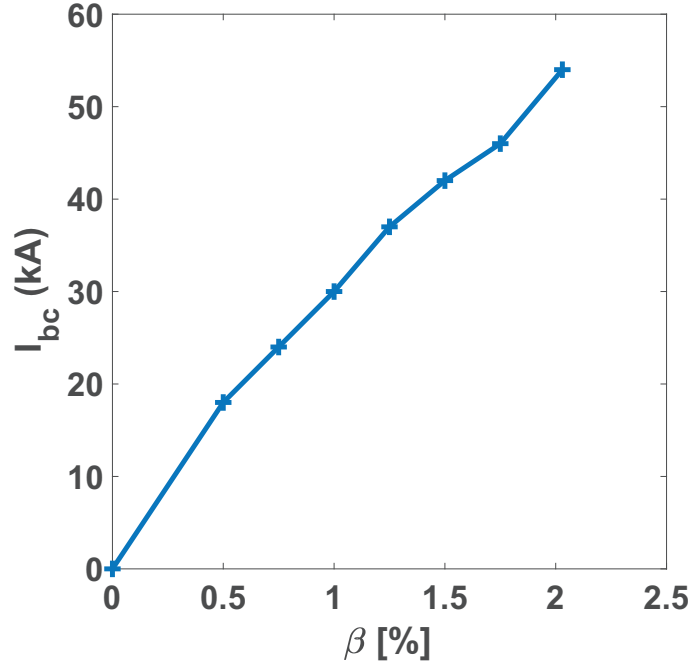


Fig. 3.3.3-3 Bootstrap currents versus  $\langle\beta\rangle$  in CFQS, calculated with the self-consistent iterations between SFINCS and VMEC codes.

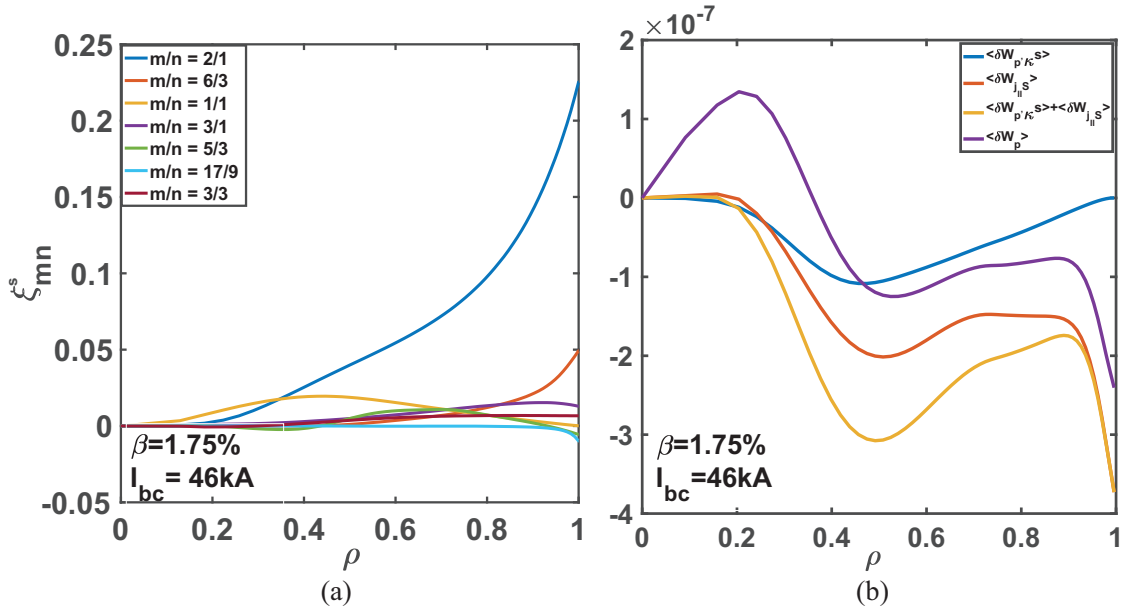


Fig. 3.3.3-4 Fourier amplitudes of the radial component of the displacement vector  $\xi^s$ (a) and surface-averaged plasma potential energy  $\langle\delta W_p\rangle$ , ballooning mode driven energy  $\langle\delta W_{p\kappa^s}\rangle$ , and kink modes driven energy  $\langle\delta W_{j\kappa^s}\rangle$  (b) as a function of  $\rho$  for  $\langle\beta\rangle = 1.75\%$  and  $I_{bc}=46\text{ kA}$ . These results are calculated with TERPSICHORE.

## References

- [3.3.3-1] D.V. Anderson *et al.*, Int. J. Supercomput. Appl. **4** (1990) 34.
- [3.3.3-2] C. Suzuki *et al.*, J. Plasma Fusion Res. SERIES **6** (2004) 519.
- [3.3.3-3] K.Y. Watanabe *et al.*, Nucl. Fusion **35** (1995) 335.
- [3.3.3-4] M. Isobe *et al.*, J. Plasma Fusion Res. SERIES **5** (2002) 360.

### 3.3.4 Tearing mode

The tearing mode stability, which is determined by  $\Delta'$ , is analyzed for existing singular point in the plasma region with the same code described in Ref. 3.3.4-1 for the CHS-qa configuration [3.3.4-2]. Here, we consider a pressure less plasma in the cylindrical system with parabolic net toroidal current density  $J_z$  and check whether the tearing mode is stable or not at the rational surface of interest with increasing  $J_z$ . The tearing mode is stable for rational surfaces  $n/m = 2/5, 3/7, 4/9$ , and  $1/2$  in the core domain (see Fig. 3.3.4-1) but the analyses indicate that it becomes unstable when singular point is in outer region ( $r/a > 0.6$ ) for  $n/m = 1/2$ .

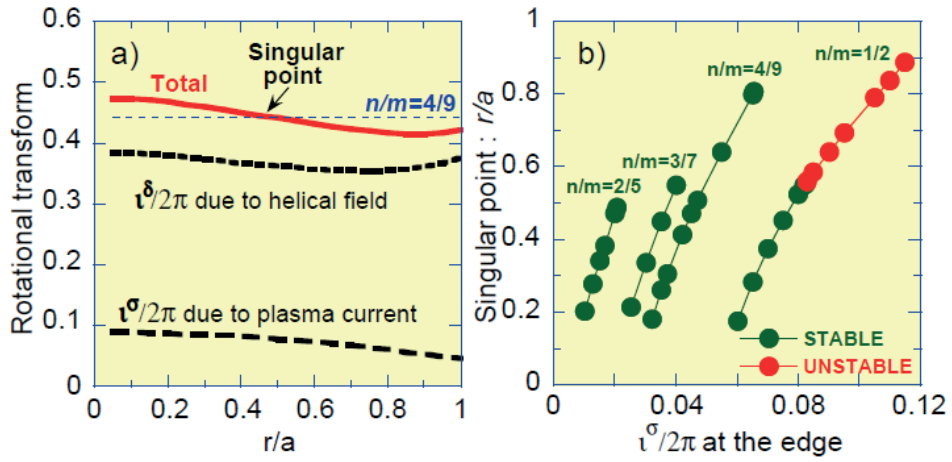


Fig. 3.3.4-1 (a) An example of rotational transform profile for tearing mode analysis for  $n/m = 4/9$ , and (b)  $\Delta'$  analysis results are shown.

### References

- [3.3.4-1] K. Matsuoka *et al.*, Nucl. Fusion **17** (1977) 1123.
- [3.3.4-2] M. Isobe *et al.*, 28th EPS Conference on Controlled Fusion and Plasma Physics, Funchal, Portugal, 18-22. June 2001, ECA Vol. **25A** (2001) 761.

### 3.3.5 Alfvén mode

#### 3.3.5.1 Alfvén mode analysis by MEGA code

To further study the MHD stability in CFQS configuration, we perform the MHD simulation by MEGA code without energetic particles. The module and equations of this code are same as that of reference [3.3.5.1-1,2]. The MHD equilibrium is calculated by HINT2 code in Fig. 3.3.5.1-1 (b) with the core averaged pressure value being  $3.7 \times 10^{-3}$ [3.3.5.1-3]. The rotational transform profile is shown in Fig. 3.3.5.1-1 (a). The random initial perturbation and small normalized dissipation coefficients ( $= 1 \times 10^{-8}$ ) are adopted. From the Fig. 3.3.5.1-2, we can find that in this configuration the MHD mode is stable with the negative growth rate defined by  $\gamma = d(\ln E_k)/dt$ .

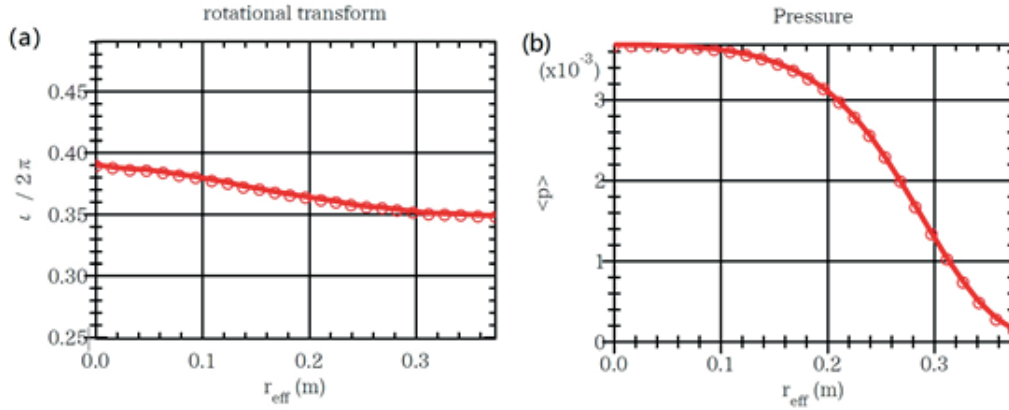


Fig. 3.3.5.1-1 MHD equilibrium profiles for (a) iota and (b) plasma pressure.

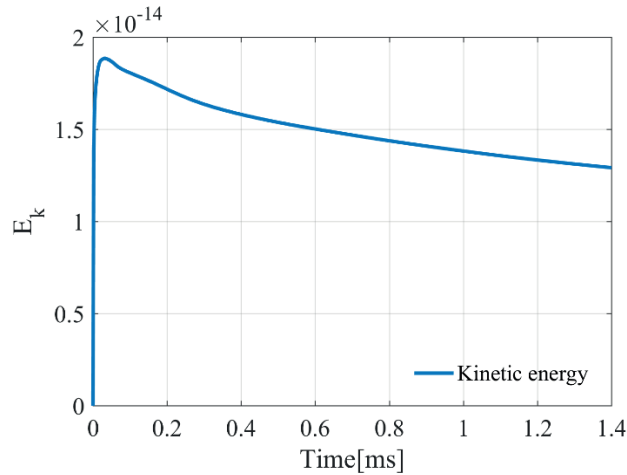


Fig. 3.3.5.1-2 Time evolution of kinetic energy.

MHD instability analysis is essential to evaluate the basic properties of QAS configuration [3.3.5.1-4~7]. Especially, the stability of external kink mode and ballooning mode has been paid close attention in the physical design and optimization of QAS. As an initial value MHD code, MEGA code is a

powerful tool to study nonlinear MHD instabilities in 3-D tokamak and stellarator [3.3.5.1-2,8,9]. Therefore, the simulations of global MHD stability have been carried out for the optimized equilibrium (Case 2) given in section 3.1.2 using MEGA code. In the simulations, the potential MHD stabilities are considered self-consistently adopting of an initial random perturbation. The plasma viscosity and diffusion coefficients are set to  $10^{-5}$  to maintain numerical stability, which are assumed to be equal to each other. The plasma resistivity are given as  $5 \times 10^{-5}$  or other values. The growth rate and mode frequency are normalized by Alfvén frequency for Case 2 equilibrium. Alfvén time is  $\sim 1.4 \times 10^{-7}$  second with plasma density being  $1 \times 10^{19} \text{ m}^{-3}$ . A Boozer coordinate system of the MHD equilibrium was constructed for the spectral analysis of the simulation results [3.3.5.1-2].

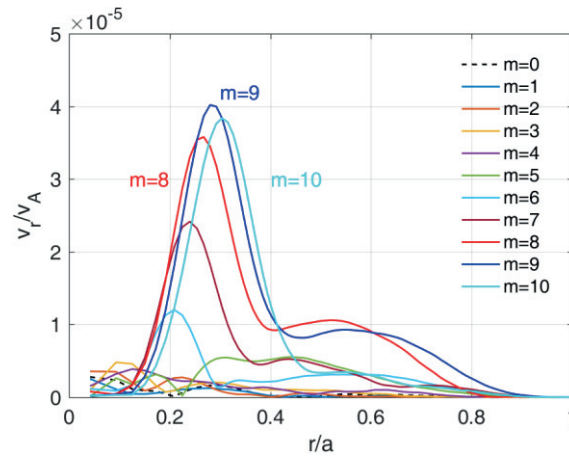


Fig. 3.3.5.1-3 The profiles of radial velocity for  $m = 0 \sim 10$  and  $n = -4$ .

The radial eigenmode structures of the unstable mode with a dominated toroidal mode number  $n = -4$  are shown in Fig. 3.3.5.1-3, where radial velocity  $v_r$  is normalized by Alfvén velocity  $v_A$ . The mode harmonics are dominated by  $m = 8 \sim 10$ . The peaking location is near the rational surface of  $\iota/2\pi = 0.5$  and also close to the weak shear regions as shown in Fig. 3.1.2-6 (c). The mode structure with a strong coupling is compared with conventional resistive ballooning modes as reported in such publications [3.3.5.1-9,10].

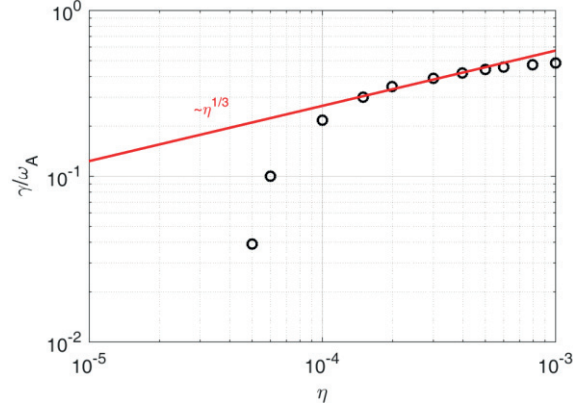


Fig. 3.3.5.1-4 The linear growth rate of the mode,  $\gamma = d(\ln Ek)/dt$ , as a function of plasma resistivity and the fitting by  $\eta^{1/3}$  with  $\langle\beta\rangle \sim 1.2\%$ .

Considering the important role of resistivity in dynamics of the MHD mode, we show the resistivity dependence of mode growth rate in Fig. 3.3.5.1-4, where the linear growth rate  $\gamma = d(\ln Ek)/dt$  is normalized by Alfvén frequency  $\omega_A$ ,  $\eta$  is plasma resistivity, and  $Ek$  is the kinetic energy. It is seen that, for the high- $\eta$  regimes, the mode is unstable with a zero mode frequency. For the low- $\eta$  regimes, the mode is stabilized in this equilibrium. In the resistivity-dominated region of  $10^{-4} < \eta < 10^{-3}$ , the  $\eta^{1/3}$  scaling of growth rates obtained from the simulations is in agreement with the theoretical result of resistive ballooning modes in stellarator [3.3.5.1-11]. This suggests that the resistive MHD mode can be excited due to the finite plasma pressure in CFQS plasmas.

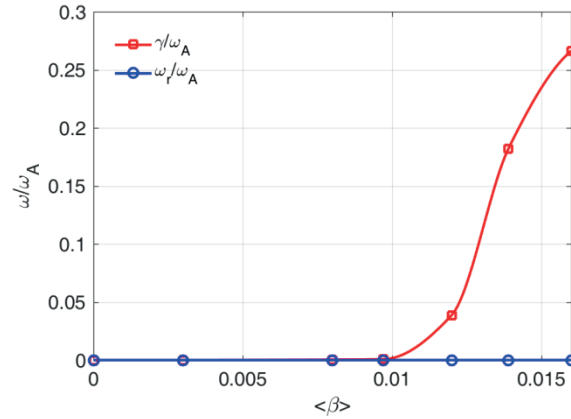


Fig. 3.3.5.1-5 Mode frequency and growth rate as a function of  $\langle\beta\rangle$ .

To clear the finite plasma pressure effects, we scan the growth rate and mode frequency as a function of  $\langle\beta\rangle$  as shown in Fig. 3.3.5.1-5. A strong  $\langle\beta\rangle$  dependence of the mode growth rate and zero mode frequency are found, corresponding to a pure MHD mode. On the other hand, the mode is stable when the  $\langle\beta\rangle$  is smaller than  $\sim 1\%$ , which suggests a beta limit for the present design of CFQS. It has to be pointed out that the ideal external kink mode as one important MHD stability in QAS [3.3.5.1-5,12,13],

we have not discussed here, may be unstable when the boundary rotational transform exceeds 0.5 [3.3.5.1-5] and should be studied in future.

Next, two different equilibrium files generated using HINT2 code are used for the simulation. They correspond to the case with magnetic islands and the case without magnetic island, as shown in Fig. 3.3.5.1-6 (a) and (b). The rotational transform  $\iota$  profile is slightly different in these two cases, as shown in Fig. 3.3.5.1-6 (c). For the case with magnetic islands,  $\iota$  profile intersects  $\iota = 1/3$  line near the plasma edge.

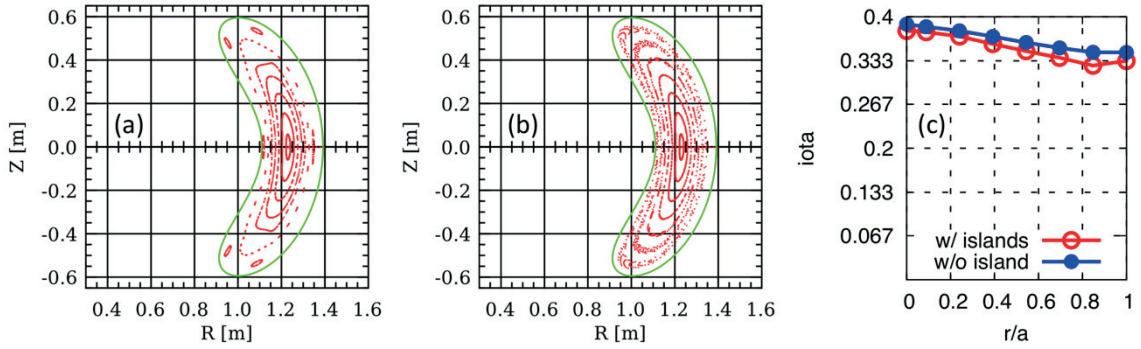


Fig. 3.3.5.1-6 Poloidal cross sections with Poincaré plots of the magnetic configurations of two cases (a) with magnetic islands and (b) without magnetic island. The  $\iota$  profile is shown in panel (c).

The instability in CFQS in three-dimensional form is shown for the first time, as shown in Fig. 3.3.5.1-7. In the toroidal direction, only 3/4 tours are shown from  $\varphi = 0$  to  $\varphi = 1.5\pi$ . The plasma from  $\varphi = 1.5\pi$  to  $\varphi = 2\pi$  is cut in order to better observe the poloidal cross section. The poloidal cross section on the left side is located at  $\varphi = 0$ , while the poloidal cross section on the right side is located at  $\varphi = 1.5\pi$ . They are bean-shaped and triangular-shaped, respectively.

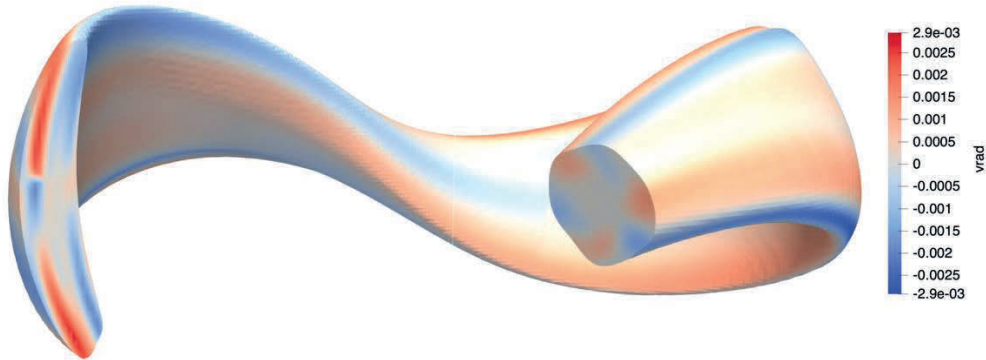


Fig. 3.3.5.1-7 Radial velocity  $v_{rad}$  of GAE in three-dimensional form.

Both global Alfvén eigenmode (GAE) and toroidal Alfvén eigenmode (TAE) are found in CFQS with and without magnetic island. The dominant mode numbers are  $m/n = 3/1$  for GAE and  $m/n = 5/2$  for TAE. Strong mode coupling is found under the condition of a very low number of field period  $N_{fp}$  value. This result is consistent with theoretical prediction [3.3.5.1-14], and it is similar to the simulation of FAR3d code [3.3.5.1-15]. For GAE, the mode frequency 79 kHz does not depend on energetic particle pressure or energetic particle beam velocity, while the growth rate increases with energetic particle pressure, as shown in the GAE case of Fig. 3.3.5.1-8. The growth rate is maximum for the energetic particle beam velocity of  $0.5v_A$  where  $v_A$  is Alfvén velocity. For TAE, similarly, the mode frequency 125 kHz does not depend on energetic particle pressure, energetic particle beam velocity, or peak value of energetic particle pitch angle. The growth rate increases with energetic particle pressure, as shown in the TAE case of Fig. 3.3.5.1-8. The growth rate is maximum for the energetic particle beam velocity of  $0.5v_A$ . The resonant condition  $f_{mode} = nf_\phi - lf_\theta$  is confirmed. For GAE,  $n = 1$  and  $l = 2$ , and for TAE,  $n = 2$  and  $l = 4$ .

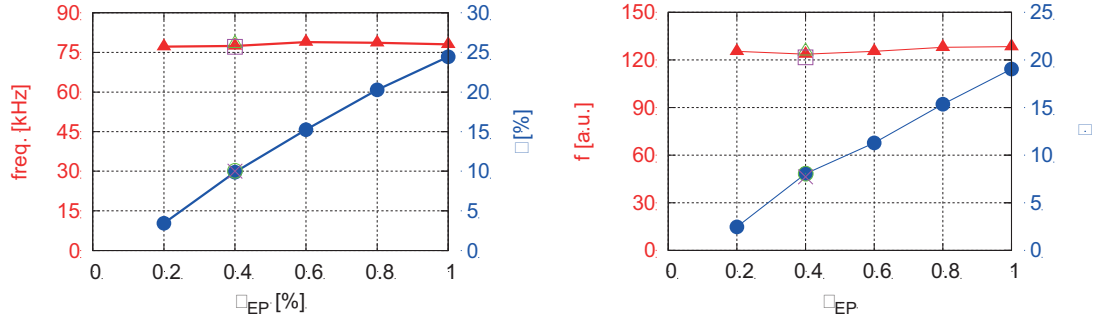


Fig. 3.3.5.1-8 The mode frequency and growth rate versus energetic particle pressure of (left) GAE and (right) TAE.

GAE frequency chirps in the nonlinear saturated phase, and TAE is similar to that, as shown in Fig. 3.3.5.1-9. Hole and clump structures are formed in the pitch angle and energy phase space. The particles comprising the hole and clump are kept resonant with the GAE or TAE during the mode frequency chirping. This is the first time to show nonlinear frequency chirping of Alfvén eigenmodes in CFQS.



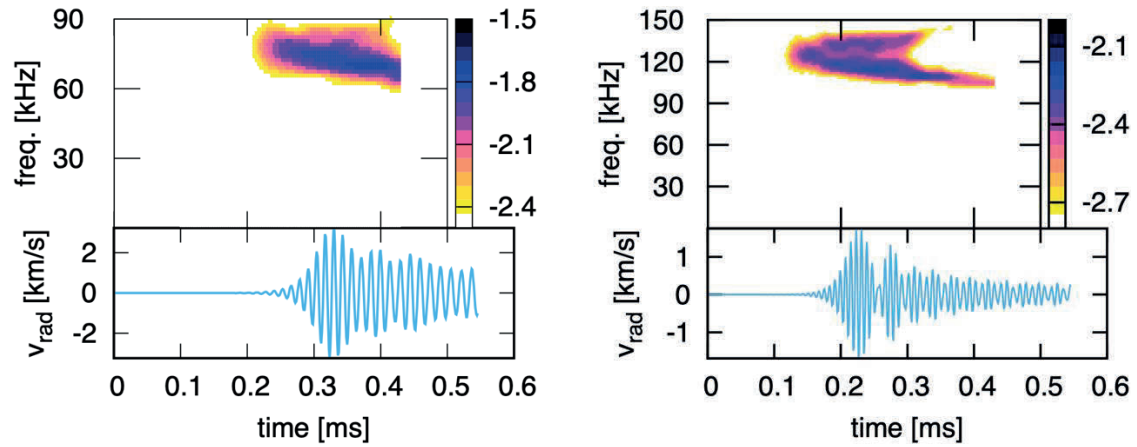


Fig. 3.3.5.1-9 The mode frequency spectrum and mode amplitude time evolution of (left) GAE and (right) TAE [3.3.5.1-16].

Finally, during the mode activities, energetic particles are lost from the core region. For the present simulation, the transport caused by GAE is stronger than that of TAE.

## References

- [3.3.5.1-1] Y. Todo *et al.*, Plasma Fusion Res. **5** (2010) S2062.
- [3.3.5.1-2] Y. Todo *et al.*, Phys. Plasmas **24** (2017) 081203.
- [3.3.5.1-3] Y. Suzuki *et al.*, Nucl. Fusion **46** (2006) L19–L24.
- [3.3.5.1-4] S. Okamura *et al.*, Nucl. Fusion **41** (2001) 1865.
- [3.3.5.1-5] M. Isobe *et al.*, 28th EPS Conference on Controlled Fusion and Plasma Physics, Funchal, Portugal, 18-22 June 2001 ECA Vol.25A 761.
- [3.3.5.1-6] G. Y. Fu *et al.*, Phys. Fluids **B 4** (1992) 1401.
- [3.3.5.1-7] S. A. Henneberg *et al.*, Nucl. Fusion **59** (2019) 026014.
- [3.3.5.1-8] Y. Todo *et al.*, Nucl. Fusion **50** (2010) 084016.
- [3.3.5.1-9] Y. Todo *et al.*, Plasma Fusion Res. **5** (2010) S2062.
- [3.3.5.1-10] M. Sato *et al.*, Nucl. Fusion **57** (2017) 126023.
- [3.3.5.1-11] W. A. Cooper, Phys. Rev. **A 32** (1985) 3124
- [3.3.5.1-12] G. Y. Fu *et al.*, Fusion Sci. Technol. **51** (2007) 218.
- [3.3.5.1-13] C. Suzuki *et al.*, J. Plasma Fusion Res. SERIES **6** (2004) 519.
- [3.3.5.1-14] D. Spong *et al.*, Phys. Plasma **10** (2003) 3217.
- [3.3.5.1-15] J. Varela *et al.*, Nucl. Fusion **61** (2021) 026023.
- [3.3.5.1-16] H. Wang *et al.*, Nucl. Fusion **62** (2022) 106010.

### 3.3.5.2 Alfvén mode analysis by FAR3d code

We analyze the stability of the AE in CFQS using the code FAR3d [3.3.5.2-1]. A set of free boundary results from the VMEC equilibrium code is calculated for the vacuum CFQS configuration ( $\beta_{th}=0$ ) and finite thermal  $\beta$  cases with  $\beta_{th}=0.01, 0.02$ , and  $0.03$ . The effect of the bootstrap current is included in the equilibria, calculated using the BOOTSJ code [3.3.5.2-2]. The magnetic field at the magnetic axis is 1 T, the toroidal field period number is 2, the averaged inverse aspect ratio is  $\iota = 0.25$  and the major radius  $R_0 = 1$  m. The energy of the injected particles by the NBI is  $T_{j0} = 30$  keV and the nominal energy of the EP resulting in an averaged Maxwellian energy equal to the average energy of a slowing-down distribution is 17 keV. Fig.3.3.5.2-1 shows the main profiles of the thermal plasma. The thermal  $\beta$  of the model increases because the thermal plasma density increases. Fig. 3.3.5.2-2 shows the EP density profiles used in the study. The energy of the EP is assumed constant, with no radial dependency, for simplicity.

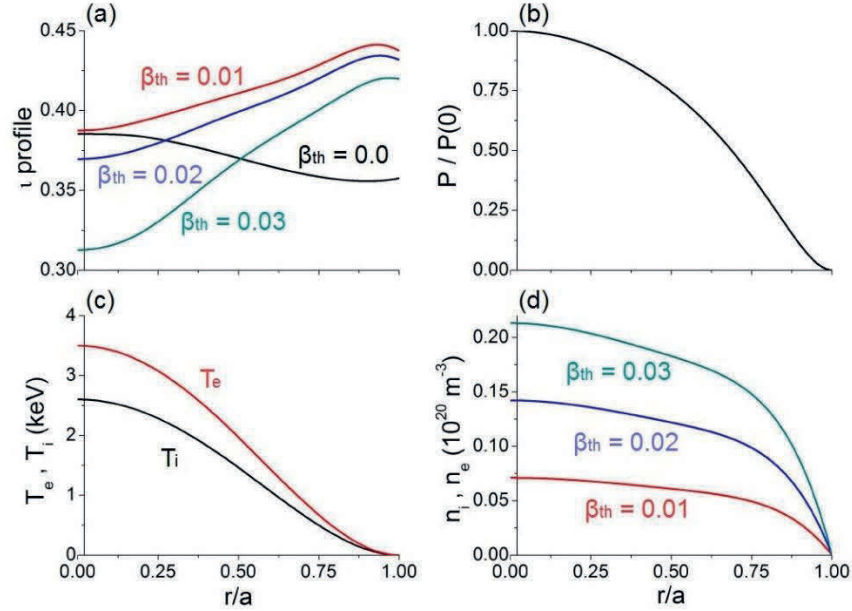


Fig. 3.3.5.2-1 (a)  $q$  profile, (b) total pressure, (c) thermal plasma temperature and (d) thermal plasma density.

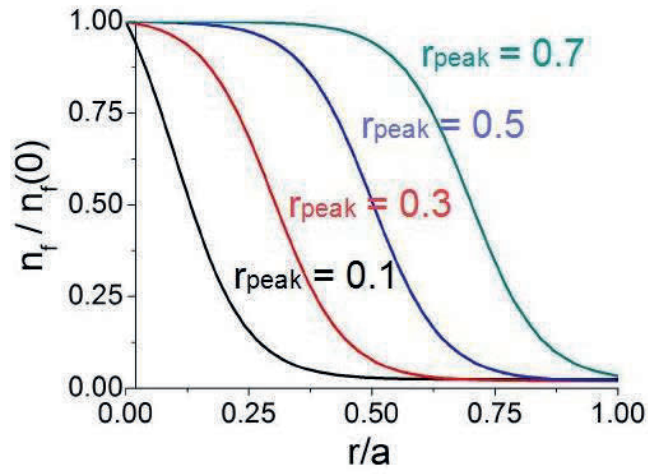


Fig. 3.3.5.2-2 EP density profiles.

Figure 3.3.5.2-3 shows the growth rate and frequency of the  $n = 1$  to 4 toroidal families for different EP  $\beta$  and energies. Fig. 3.3.5.2-4 shows the same analysis for the helical families  $n = 1, 3$  and  $2, 4$ .

The analysis of the simulations indicates the destabilization of  $n = 1$  to 4 AEs as well as  $n = 2, 4$  HAEs in NBI-heated CFQS plasma. The EP  $\beta$  threshold to destabilize AEs is calculated for EP during the slowing down process, that is to say, from weakly thermalized EP ( $T_f \geq 25$  keV) to EP at the last stage of the slowing down process ( $T_f \leq 15$  keV).

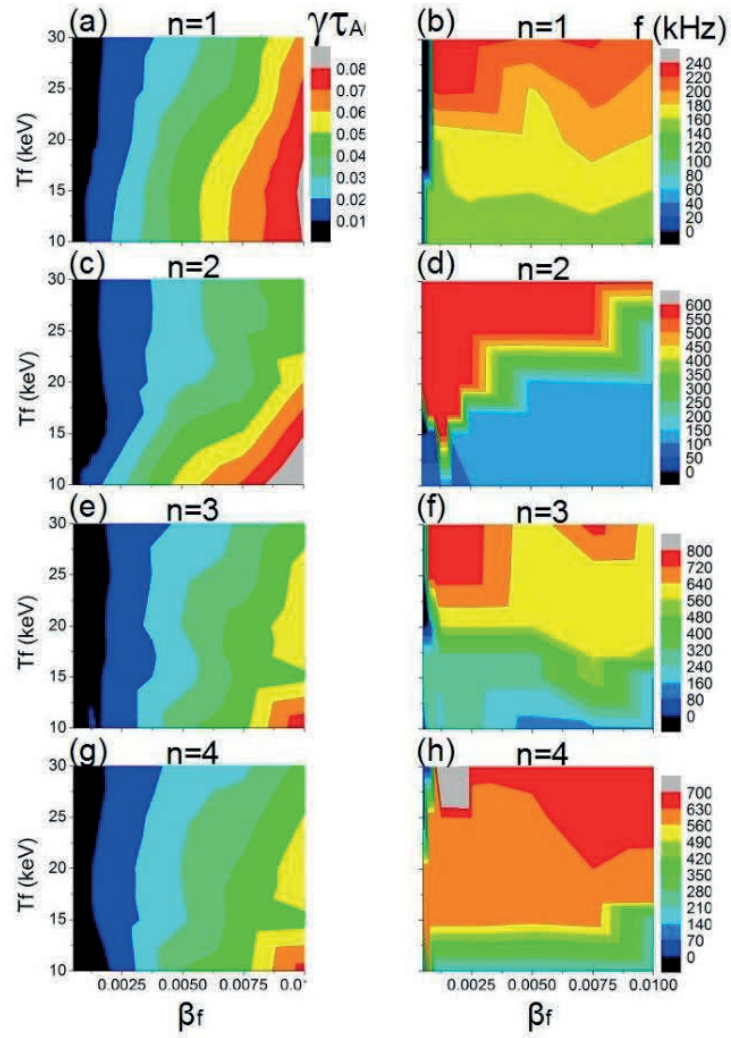


Fig. 3.3.5.2-3 Growth rate and frequency of the  $n = 1$  to 4 toroidal mode families for different EP  $\beta$  and energies.

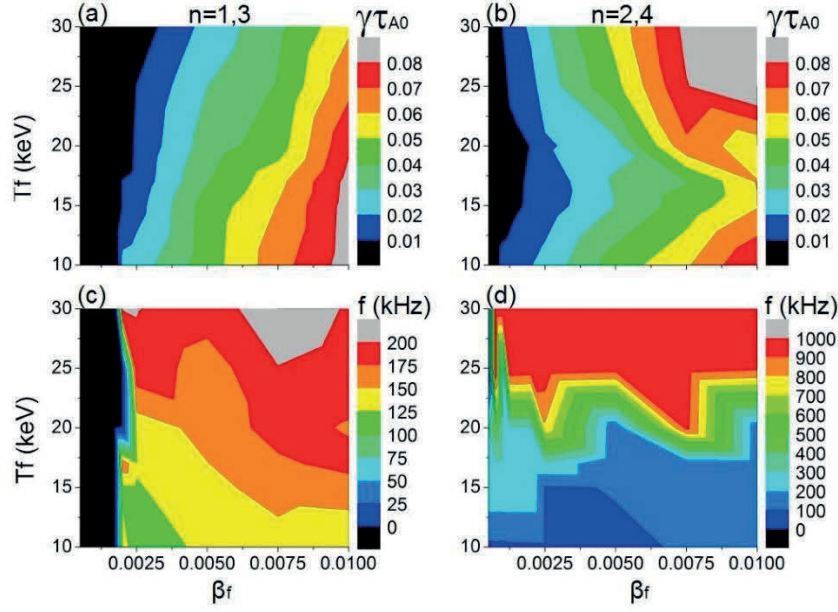


Fig. 3.3.5.2-4 Growth rate and frequency of the  $n = 1,3$  and  $2,4$  helical modes families for different EP  $\beta$  and energies.

The study of the AE destabilization threshold with respect to the EP  $\beta$  for different EP energies indicates that, an optimized operational regime of the NBI requires a power injection not exceeding EP  $\beta = 0.001$  to avoid the destabilization of high frequency AEs (EAE and NAE) by weakly thermalized EP. In addition, TAEs and BAEs that can be triggered by EPs during the slowing down process ( $T_f \leq 17$  keV) are stable if EP  $\beta < 0.0005$ . The simulations performed adding the effect of the helical couplings indicate the possible destabilization of  $2/5$  and  $2/6$  HAEs by EP with  $T_f \geq 15$  keV if EP  $\beta \geq 0.0005$ . On the other hand, the simulations show stable  $n = 1,3$  HAEs. The analysis of the Alfvén gaps indicates narrow  $n = 1,3$  HAE gaps with respect to the  $n = 2,4$  HAE gaps, thus the continuum damping is strong enough to stabilize the  $n = 1,3$  HAE.

Fig. 3.3.5.2-3 indicates the analysis of off-axis NBI models, showing no evident optimization trend with respect to an on-axis NBI injection, because the growth rate of the  $n = 1$  AE decreases although the growth rate of the  $n = 2-4$  AE increase. On the other hand, there is a transition to lower frequency AEs if the beam is deposited in the middle plasma or the periphery. It should be noted that the effect of the Shafranov shift leads to the outward displacement of the magnetic axis as  $\beta_{th}$  increases, thus the NBI deposition region changes from on-axis in low  $\beta$  operations to off-axis in high  $\beta$  operations. Consequently, a detailed analysis of the AE stability for off-axis NBI depositions is required in high  $\beta$  operations.

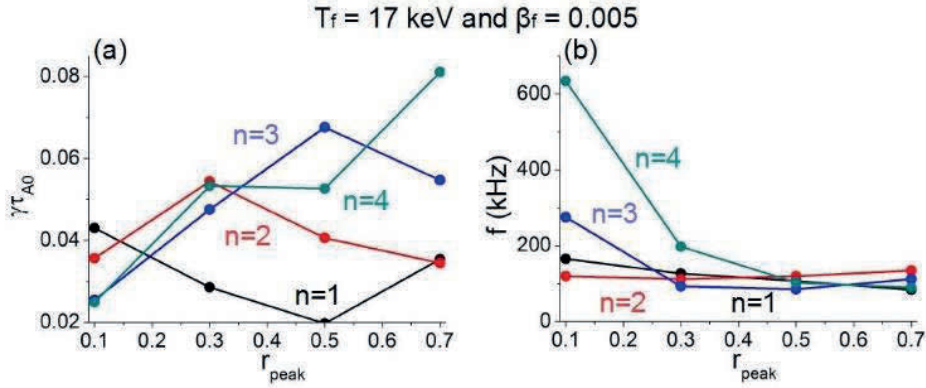


Fig. 3.3.5.2-5 (a) Growth rate and (b) frequency of the  $n = 1$  to 4 modes for different locations of the EP radial density profile gradient.

The analysis of the AE stability in models with a finite  $\beta_{th}$  indicates that CFQS operation with high  $\beta$  should have an improved AE stability with respect to low  $\beta$  discharges. High  $\beta$  operations show slender Alfvén gaps, thus the continuum damping is enhanced increasing the EP  $\beta$  threshold required to destabilize the AEs. The simulations show a decrease of the growth rate of the  $n = 1$  to 4 AEs as well as the  $n = 1, 3$  and  $2, 4$  helical families as  $\beta_{th}$  increases. It should be noted that the model assumes an increase of  $\beta_{th}$  caused by a larger thermal plasma density, thus the AE stability trend can be different if the  $\beta_{th}$  increases by a larger thermal plasma temperature. Future analysis will be dedicated to clarify the effect of the thermal plasma temperature on the AE stability in CFQS plasma.

Figure 3.3.5.2-5 shows the growth rate (a) and frequency (b) of the  $n = 1$  to 4 AEs if the location of the EP density gradient ( $r_{peak}$ ) changes from 0.1 to 0.7 (EP  $\beta = 0.005$  and  $T_f = 17$  keV). If the on-axis ( $r_{peak} = 0.1$ ) and off-axis ( $r_{peak} \geq 0.1$ ) simulations are compared, the growth rate of the  $n = 1$  AEs decreases around a 50 % if the NBI is deposited in the middle plasma region, although the growth rate of the  $n = 2$  to 4 AEs increases. In addition, the off-axis NBI injection causes a transition to a lower frequency AE family of the  $n = 1, 3$  and 4 AEs if  $r_{peak} \geq 0.3$ . It should be noted that the dominant AE changes as the location of the drive is modified, because the gradient of the EP density profile is located at different radial location where the continuum structure is different.

The simulations including the effect of the thermal ion FLR, EP FLR and e-i Landau damping indicate the stabilization of the  $n = 1$  to 4 EAE/NAEs triggered in the simulations without damping effects. Also, the  $n = 1$  to 4 BAE/TAEs show a lower growth rate and frequency relative to the simulations without damping effects, as well as the improved AE stability of CFQS operational scenarios with a high thermal  $\beta$ .

In summary, the heating efficiency of CFQS plasma heated by a tangential NBI can decrease due to the destabilization of  $n = 1$  to 4 BAE/TAEs and  $n = 2, 4$  HAEs above a given injection intensity threshold, particularly if the thermal  $\beta$  of the discharge is low. Nevertheless, the heating efficiency can

be improved by an optimized NBI operational regime with respect to the NBI voltage, injection intensity and deposition region as well as the thermal plasma parameters. The present analysis will be extended to stellarators that explores different quasi-symmetries, identifying the magnetic configurations that show an optimal AE stability, particularly for reactor-relevant plasma.

## References

- [3.3.5.2-1] J. Varela *et al.*, Nucl. Fusion **61** (2021) 026023.
- [3.3.5.2-2] K. C. Shaing *et al.*, Phys. Fluids B **1** (1989) 1663.

### 3.4 Optimization approach of anomalous transport

#### 3.4.1 Maximum- $J$

The turbulent fluctuation suppression in the CFQS has got emphasized considerably. The suppression of the turbulent transport due to the sheared flow induced fluctuation decorrelation has been widely investigated, theoretically, leading to the significant progress in the understanding of the improved confinement regime. The other possible mechanism for turbulent suppression has been proposed based on the stabilization of microinstabilities. Several kinds of microinstabilities appear when directions of the diamagnetic drift and  $\nabla B$  drift ( $B$  is the magnetic field strength) are in the same direction for trapped particles [3.4.1-1, 2]. In an axisymmetric configuration, the relevant drift is in the toroidal direction (toroidal precession). The velocity of the toroidal precession can be expressed in terms of the second adiabatic invariance  $J$  [3.4.1-3]. Also, the stability condition for microinstabilities is derived [3.4.1-4] with a scalar plasma pressure  $P$  as

$$\nabla P \cdot \nabla J > 0,$$

which is frequently called the maximum- $J$  condition; it reduces to  $dJ/dr < 0$  for a usual pressure gradient with  $dP/dr < 0$ . This indicates that microinstabilities can be stabilized or suppressed if the toroidal precession of trapped particles is in a favorable ( $dJ/dr < 0$ ) direction.

Orbits of blocked or helically trapped particles: These particles are located in the region of phase space near the locally trapped- passing boundary. These particles may be regarded as locally trapped for a few bounces but they are able to de-trap collisionlessly. A blocked particle's trajectory is not restricted to a single toroidal segment but extends to neighbouring sections. Such particles are also called transitioning [3.4.1-5]. An illustration of these three types of orbits and a comparison with particle orbits in an axisymmetric plasma is given in Fig. 3.4.1-1.

Without plasma the contour plot of  $J$  is shown as a function of the minor radius and the toroidal angle in the Fig. 3.4.1-2. The calculation of  $J$  is made by following the particle orbits starting from the outboard side of the torus with different toroidal angles.  $\zeta_N = 0$  corresponds to the vertically elongated cross section and  $\zeta_N = 0.5$  to the horizontally elongated cross section. When  $B_{ref}$  equals 0.95 T, there is no maximum- $J$  region. Whereas  $B_{ref}$  equals 0.97 T, the maximum- $J$  region comes up at the core area.

Radial profiles for density and temperature are assumed to be parabolic,  $n_e \propto (1-\rho^2)$  and  $T_e, T_i \propto (1-\rho^2)$ . When  $\langle \beta \rangle$  reaches 1 %, the neoclassical bootstrap current of 30 kA is expected. The change of the rotational transform profile with beta is shown in Fig. 3.4.1-3. As  $\langle \beta \rangle$  increases the region of the reversal magnetic shear near the magnetic axis appears and increases. In these equilibria the contour plots of  $J$  are given with  $B_{ref} = 0.91$  T in Fig. 3.4.1-4 and  $B_{ref} = 0.93$  T in Fig. 3.4.1-5, respectively. It is found that as the beta increases the region of the maximum- $J$  increases in the core region.



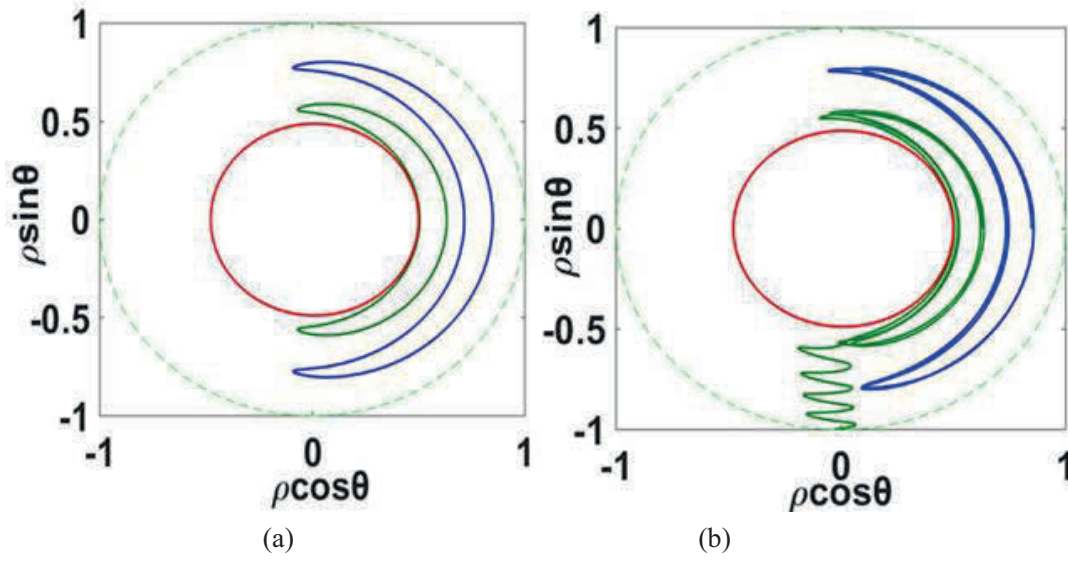


Fig. 3.4.1-1 Examples of the main orbit topologies in a perfect axisymmetric system and a CFQS. The dashed line represents the LCFS for each case. Guiding center (GC) orbits of (a) passing particle (red,  $B_{ref} = 1.5$ ) and toroidally trapped particles (green,  $B_{ref} = 0.94$  and blue,  $B_{ref} = 0.98$ ) in axisymmetric equilibrium. GC orbits of (b) passing particle (red,  $B_{ref} = 1.5$ ) and toroidally trapped particles (green,  $B_{ref} = 0.94$  and blue,  $B_{ref} = 0.98$ ) in the CFQS equilibrium. Particle (green) drifts radially due to ripple banana diffusion and is trapped in local ripple well, and is finally lost.

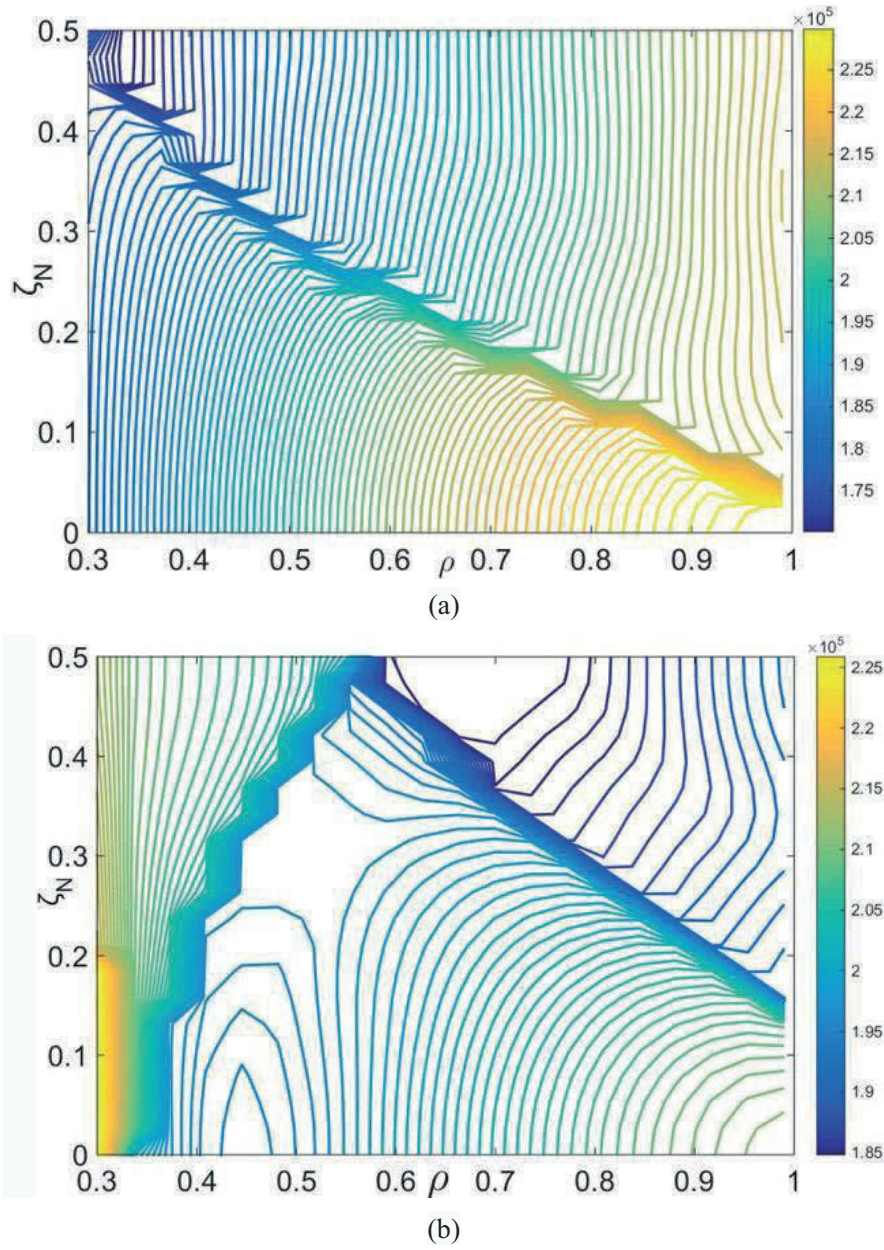


Fig. 3.4.1-2 Contour  $J$  on the  $(\rho, \zeta_N)$  plane. (a)  $B_{ref}$  equal to 0.95 T, without maximum- $J$  region (b)  $B_{ref}$  equal to 0.97 T, with maximum- $J$  region.

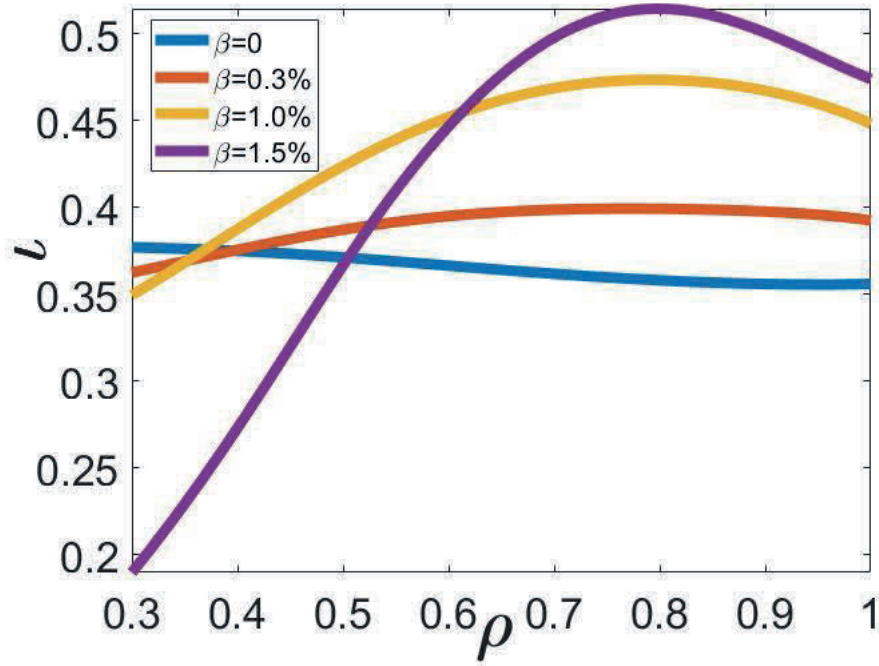


Fig. 3.4.1-3 Radial profiles of the rotational transform considering the neoclassical bootstrap current.

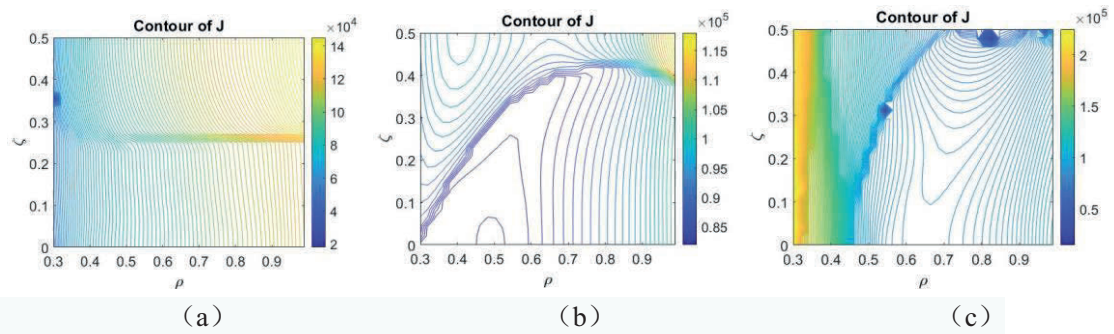


Fig. 3.4.1-4 Contour  $J$  on the  $(\rho, \zeta)$  plane,  $B_{ref}$  equal to 0.91 T,  $\langle \beta \rangle = 0.3\%$  for (a),  $\langle \beta \rangle = 1.0\%$  for (b), and  $\langle \beta \rangle = 1.5\%$  for (c).

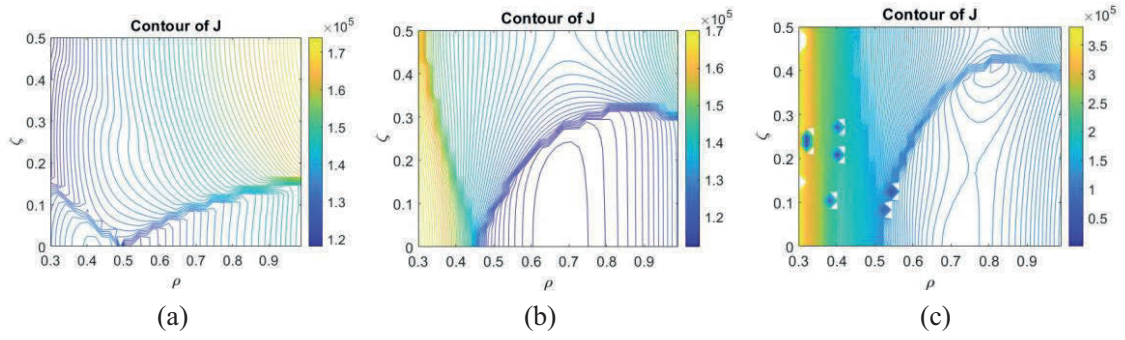


Fig. 3.4.1-5 Contour  $J$  on the  $(\rho, \zeta)$  plane,  $B_{ref}$  equal to 0.93 T,  $\langle\beta\rangle = 0.3\%$  for (a),  $\langle\beta\rangle = 1.0\%$  for (b), and  $\langle\beta\rangle = 1.5\%$  for (c).

Quasi-axisymmetry makes a stellarator as analogous as possible to a tokamak, in some sense, which is not an essential condition for achieving good plasma confinement. Mathematically, the necessary condition is to require parallel adiabatic invariant  $J = \oint m v_{\parallel} dl$  to be (approximately) constant on flux surfaces for trapped particle orbits. If the magnetic field has been written as  $\mathbf{B} = \nabla\psi \times \nabla\alpha$  and  $\psi$  measures the toroidal flux and  $\alpha = \theta - \iota\zeta$  labels the different field lines on each flux surface, a configuration with vanishing bounce-averaged drift,  $\partial J / \partial \alpha = 0$ , is called omnigenous. Meanwhile,  $J$  decreases away from the center, *i.e.*,  $\partial J / \partial \psi < 0$ , it is the so-called the maximum- $J$  condition, which is very beneficial for stabilizing trapped-particle-driven micro-instability modes. The perfectly omnigenous configurations with the maximum- $J$  property cannot be exactly achieved. Alternatively, the wave vector perpendicular to the magnetic field is expressed by  $\mathbf{k}_{\perp} = k_{\psi} \nabla\psi + k_{\alpha} \nabla\alpha$  and if  $k_{\psi}$  is very small,  $\partial J / \partial \psi < 0$  is able to suppress these micro instabilities in incompletely omnigenous configurations at least. The maximum- $J$  capability has been broadly investigated in quasi-axisymmetric and quasi-isodynamic configurations. It is of importance to evaluate the maximum- $J$  capability in CFQS.

To obtain the distribution of  $J$ , in this paper the guiding center trajectories of tracer particles are calculated in Boozer coordinates, which are reflected at the same  $B$ . The motion equations used in the simulation were expressed in Ref.[3.4.1-6]. The tracing particle energy is  $W = 10$  eV and set the magnetic field strength at the bounce point equal to 0.95 T. The initial positions of these particles are distributed in the  $(\rho, \zeta, \theta = 0)$  plane. The  $J$  contours on the  $(\rho, \zeta/\pi)$  plane are calculated in various equilibria, as shown in Fig. 3.4.1-6. The  $J$  contour values are normalized to the largest  $J$ . The color bar represents the normalized  $J$ . The areas on the left side of the red solid curve represent the maximum- $J$  criterion satisfied. In low bootstrap current equilibria with  $\beta = 0.3\%$ , the maximum- $J$  region can hardly be generated in Fig. 3.4.1-6 (a). As the bootstrap current increases, the negative magnetic shear

in the core region is enhanced in Fig. 3.4.1-6 (a), leading to a decrease of  $J$  away from the center, which is to extend maximum- $J$  regions in Figs. 3.4.1-6 (b) and (c). A similar result was also observed in reversed shear tokamaks that the maximum- $J$  region coincides with the region of the reversed  $q$  profile (negative shear). Notably, an inhomogeneity of maximum- $J$  regions in the  $\zeta$  direction arises due to the existence of the non-axisymmetry of  $B$ . Thus, it may be concluded that as plasma  $\beta$  increases, trapped-particle-driven micro-instabilities with very low radial mode numbers are mitigated in core regions of CFQS. At least according to quasilinear theory, such instabilities should not lead to large transport.

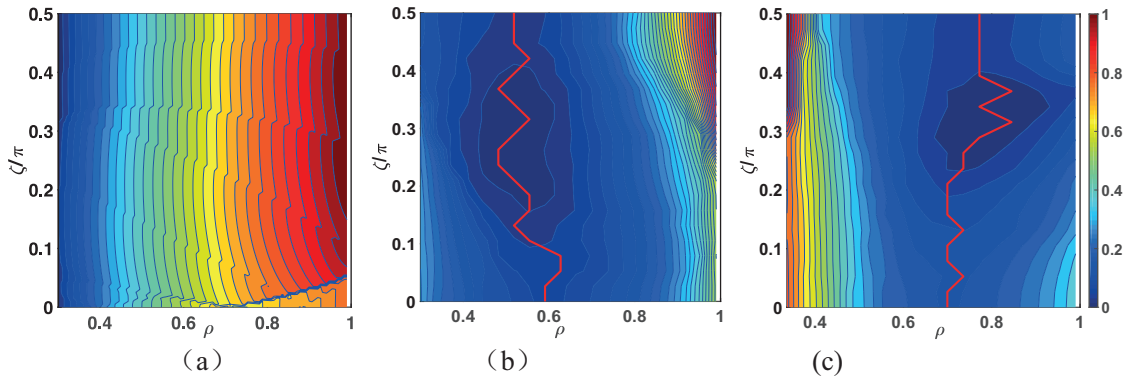


Fig. 3.4.1-6 Contours of normalized  $J$  on the  $(\rho, \zeta/\pi)$  plane for  $(\beta, I_{bc}) = (0.30\%, 11 \text{ kA})$  (a),  $(0.75\%, 24 \text{ kA})$  (b) and  $(1.50\%, 42 \text{ kA})$  (c) in CFQS configurations, respectively. The  $J$  is normalized to the largest  $J$ . The areas on the left side of the red solid curve represent the maximum- $J$  criterion satisfied.

## References

- [3.4.1-1] H. P. Furth and M. N. Rosenbluth, 1969 Proc. Conf. 3<sup>rd</sup> Int. on Plasma Physics and Controlled Nuclear Fusion Research (Novosibirsk, 1968) vol. **1** (Vienna: IAEA) p 821.
- [3.4.1-2] B. B. Kadomtsev and O. P. Pogutse, 1970 Reviews of Plasma Physics vol. **5** (New York, London: Consultants Bureau) p 249.
- [3.4.1-3] B. B. Kadomtsev and O. P. Pogutse, Nucl. Fusion **11** (1971) 67.
- [3.4.1-4] R. J. Hastie *et al.*, Ann. Phys. **41** (1967) 302.
- [3.4.1-5] C. D. Beidler *et al.*, Phys. Plasmas **8** (2001) 2731.
- [3.4.1-6] D. A. Garren *et al.*, Phys. Fluids **B 3** (1991) 2822.



### 3.4.2 Micro instability

The linear ion temperature gradient (ITG)-driven instability is examined by means of the electromagnetic gyrokinetic Vlasov simulations with GKV [3.4.2-1], where a local flux-tube at the mid-minor radius of  $\rho = 0.5$  in the vacuum equilibrium is considered. An axisymmetric limit with the same rotational transform, the magnetic shear, and the aspect ratio is compared to identify the impact of non-axisymmetric geometry on the microinstability properties, where the circular poloidal cross section is assumed for the simplicity. The linear growth rate spectra of the ITG mode at  $R_0/L_n = 0$  is shown in Fig. 3.4.2-1, where the electrons are assumed to be adiabatic here. It is found that the CFQS has more unstable ITG modes with higher growth rate  $\gamma R_0/v_{ti}$  in a wider range of the wavenumber space  $k_y \rho_i$ , compared with that in the axisymmetric limit [3.4.2-2]. The difference is mainly associated with the geometric structures appearing in the squared perpendicular wavenumber  $(k_\perp \rho_i)^2$ , which provides the finite Larmor radius (FLR) stabilization of the ITG modes. It is known that the density gradient can also affect ITG modes. The linear growth rate spectra of ITG modes at  $R_0/L_n = -2$ ,  $R_0/L_n = 2$  and  $R_0/L_n = 8$  are shown in Fig. 3.4.2-2 [3.4.2-7]. From Fig. 3.4.2-1 and Fig. 3.4.2-2, there is a critical temperature gradient for ITG modes. If  $R_0/L_T$  exceeds this critical gradient, the ITG mode is unstable. As  $R_0/L_T$  increases, ITG modes become more unstable, and as density gradient  $R_0/L_n$  increases, the  $k_y \rho_i$  of the most unstable mode shifts to a higher  $k_y \rho_i$ . Fig. 3.4.2-3 shows the relationship between the maximum growth rate of ITG modes and  $R_0/L_n$ . From the figure it is found a moderate  $R_0/L_n$  can destabilize ITG modes but for a large  $R_0/L_n$  the growth of ITG mode is strongly suppressed. If  $R_0/L_n$  is negative, *i.e.* a hollow density profile, even if  $R_0/L_n$  is small, ITG modes are suppressed. The growth rate of ITG modes almost increases linearly with  $R_0/L_T$  for any  $R_0/L_n$ . By fitting these lines, the threshold of the critical temperature gradient for ITG modes can be gotten. A negative  $R_0/L_n$  enhances this threshold, and a positive  $R_0/L_n$  can reduce the threshold firstly and then enhances the threshold as  $R_0/L_n$  increases. From Fig. 3.4.2-4, the relationship between growth rate and  $R_0/L_n$  is very clear. As  $R_0/L_n$  increases, the growth rate firstly increases and then decreases. For a negative  $R_0/L_n$ , ITG modes are always suppressed and their growth rate decreases as the absolute value of  $R_0/L_n$  increases. From the previous results, a large  $R_0/L_n$  or density peaking can strongly stabilize ITG modes [3.4.2-3].

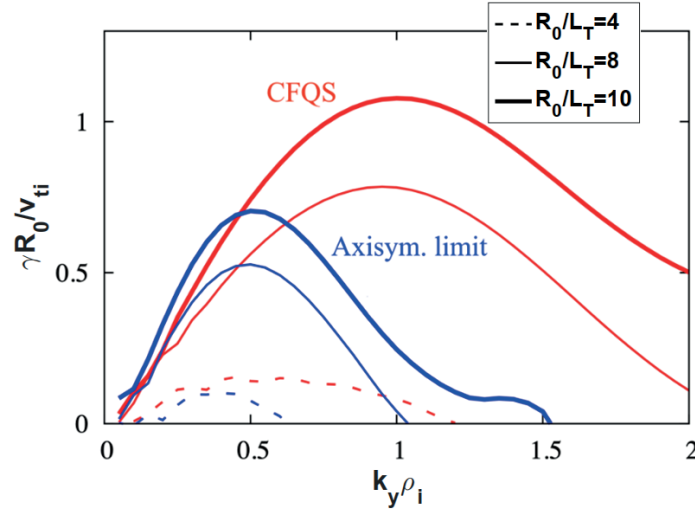


Fig. 3.4.2-1 Linear growth rate spectra for the ITG mode in CFQS and the axisymmetric limit (Axisym. limit) for several cases of the normalized ion temperature gradient parameters  $R_0/L_T = -R_0 d(\ln T)/dr$  at  $R_0/L_n = -R_0 d(\ln n)/dr = 0$ .

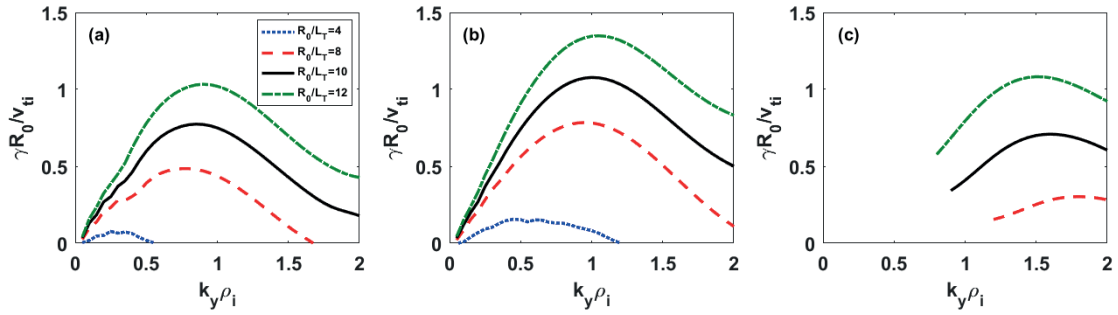


Fig. 3.4.2-2 Linear growth rate spectra for the ITG mode in CFQS for several cases of the normalized ion temperature gradient parameters  $R_0/L_T$  at (a)  $R_0/L_n = -2$ ; (b)  $R_0/L_n = 2$ ; (c)  $R_0/L_n = 8$ .

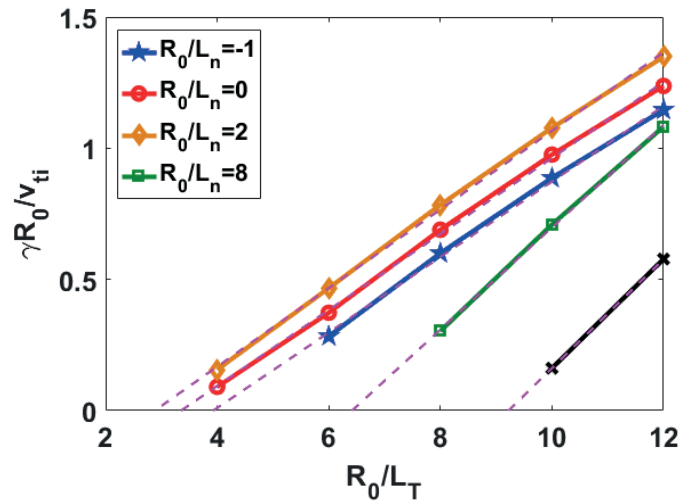


Fig. 3.4.2-3 The maximum growth rate of electrostatic ITG modes in CFQS vs.  $R_0/L_T$  for various  $R_0/L_n$ . The dashed lines are the fitted lines of the corresponding lines of growth rate.

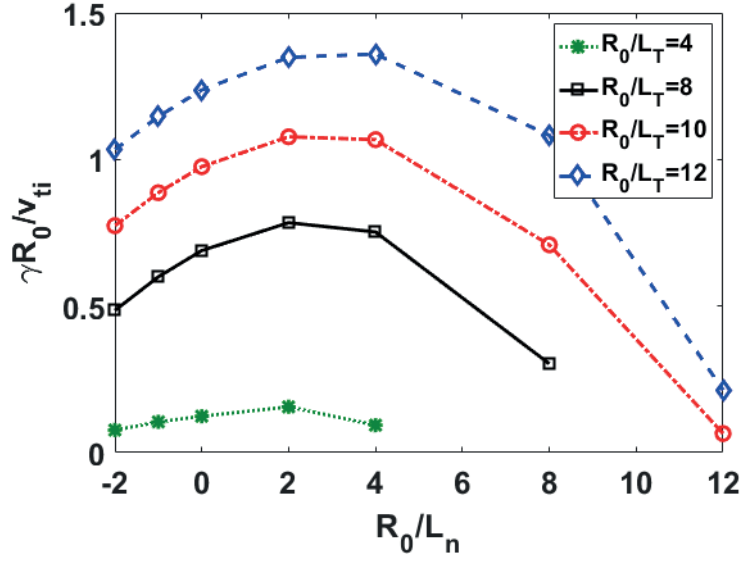


Fig. 3.4.2-4 The maximum growth rate of electrostatic ITG modes in CFQS vs.  $R_0/L_n$  for various  $R_0/L_T$ .

To scan  $R_0/L_n$  and  $R_0/L_T$ , the ITG growth rates vs.  $R_0/L_n$  and  $R_0/L_T$  are shown in Fig. 3.4.2-5. The ITG mode with the largest growth rate is located at the region with the largest  $R_0/L_T$  and a moderate  $R_0/L_n \sim 4$ . The growth of ITG mode depends on the competition between the driving of  $R_0/L_T$  and damping of  $R_0/L_n$ . To compare with the NCSX results [3.4.2-4], the relationship between the growth rate of ITG modes and  $R_0/L_T$  and  $R_0/L_n$  in CFQS and NCSX are very similar. It reveals that this relationship is rarely affected by the difference between the CFQS and NCSX magnetic configurations.

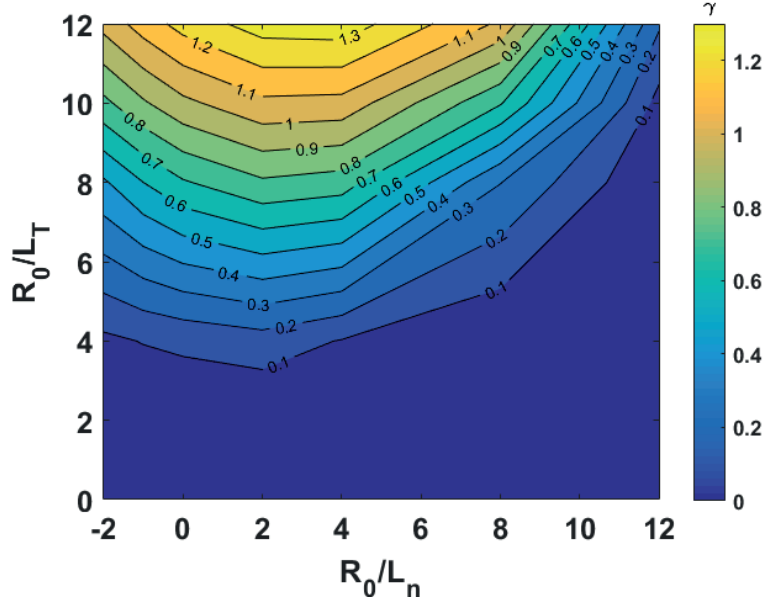


Fig. 3.4.2-5 The maximum growth rates of electrostatic ITG modes vs.  $R_0/L_n$  and  $R_0/L_T$ .



Kinetic electrons are the key factor for triggering TEMs and they also can affect ITG modes. In the cases with kinetic electrons, ITG modes and TEMs can coexist. In this subsection, we examine such electrostatic kinetic ITG-TEM modes in CFQS. Note that the trapped electron effect is excluded in the simulation model when the kinetic response of the perturbed distribution function of electron is ignored. This is the so-called adiabatic electron approximation, and such treatment is still useful for studies of the pure ITG mode and for the cross-code benchmark. The simulation results about the ITG mode in the adiabatic electron approximation are shown in the Appendix.

Fig. 3.4.2-6 shows the growth rate and the real frequency spectrum for various  $R_0/L_T$  at  $R_0/L_n = 0$ , where  $R_0$  is the major radius, and  $L_T = -(\text{dln}T_s/\text{d}x)^{-1}$ . Here,  $R_0/L_{T_i} = R_0/L_{T_e}$  is assumed. The growth rate  $\gamma$  and the real frequency  $\omega$  are normalized to  $v_{ti}/R_0$ , where  $v_{ti}$  is the ion thermal velocity. From Fig. 3.4.2-6 (a), the transition from ITG mode to TEM with the frequency switch is found, and the discontinuities in  $\omega$  and  $\gamma$  appear near the transition wavenumber. Note that the propagating directions of the ITG mode and TEM are the ion diamagnetic (the negative real frequency) and the electron diamagnetic drift directions (the positive real frequency), respectively. To compare with the adiabatic results shown in Fig. 3.4.2-2, kinetic electrons yield higher growth rate of the ITG mode. One can see that the growth rates of TEM are also proportional to  $R_0/L_T$ , but this is attributed mainly to the electron temperature gradient (cf.  $T_i/T_e = 1$ ).

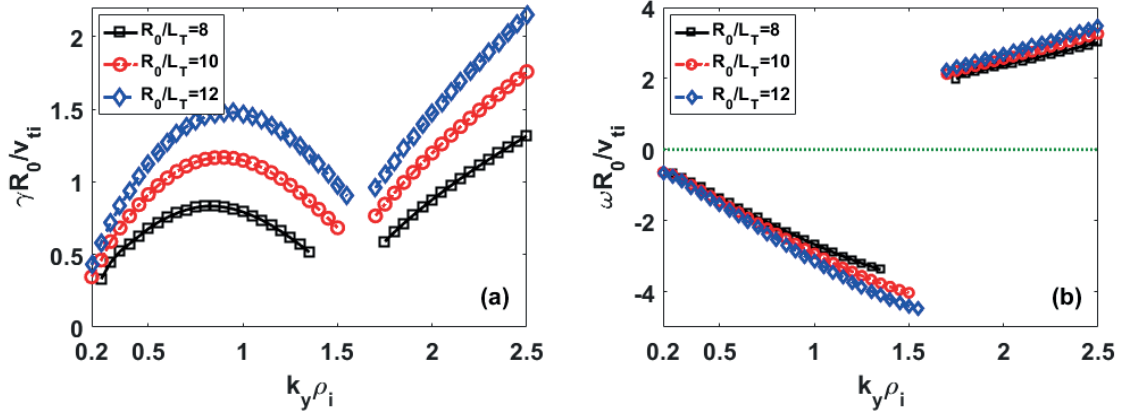


Fig. 3.4.2-6 The growth rates (a) and real frequencies (b) of the hybrid ITG-TEM modes vs.  $k_y \rho_i$  for various  $R_0/L_T$  at  $R_0/L_n = 0$ . Here,  $R_0/L_{T_i} = R_0/L_{T_e}$ .

Fig. 3.4.2-7 shows the density and temperature gradient dependence of the growth rates and real frequencies for the hybrid ITG-TEM modes at fixed  $k_y \rho_i$ . We recognize that the dominant mode at  $k_y \rho_i = 1$  is the ITG mode with the negative frequency and the dominant mode at  $k_y \rho_i = 2.5$  is the TEM with the positive frequency. In the adiabatic case, both a negative density gradient and a large density gradient can suppress ITG modes, seen in Figs. 3.4.2-3 and 3.4.2-7 (a). Similarly, in the kinetic case, a large density gradient, *i.e.*,  $R_0/L_n > 4$ , can suppress ITG modes, seen in Figs. 3.4.2-7 and 3.4.2-8. Therefore, when  $R_0/L_T < 8$  and  $R_0/L_n > 4$ , the dominant mode is TEM. On the other hand,

for  $k_y \rho_i = 2.5$ , this is smaller than the ion scale and the dominant mode is the TEM, seen in Fig. 3.4.2-7 (b). It's found that a density profile with a negative gradient, blue case in Fig. 3.4.2-7 (b), is not useful to suppress the TEM. Fig. 3.4.2-8 displays the similar results, but the horizontal axis is converted from the temperature gradient to the density gradient in order to highlight the stabilization effects by the density gradient. It is clearly shown that the ITG modes can be suppressed by a density profile with a negative gradient, seen the green and pink cases in Fig. 3.4.2-8 (a). Such ITG stabilization by hollow density profile has not been reported in the gyrokinetic analysis for QA stellarators. For high  $R_0/L_T$  cases, the similar tendency is observed for the TEM modes. These results suggest that, in CFQS configuration, the hybrid ITG-TEM modes can be suppressed when the absolute value of  $R_0/L_n$  are enough large even at some large value of  $R_0/L_T$ .

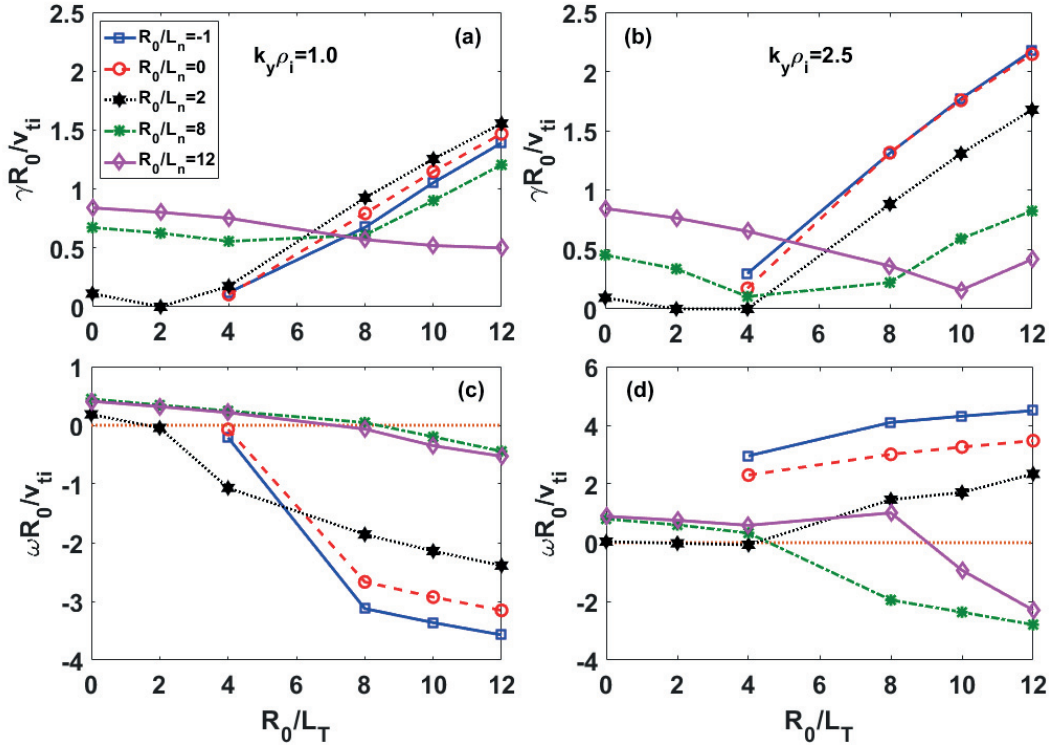


Fig. 3.4.2-7 The growth rates and real frequencies of the electrostatic hybrid ITG-TEM modes vs.  $R_0/L_T$  for several values of  $R_0/L_n$  at (a) and (c)  $k_y \rho_i = 1.0$ , (b) and (d)  $k_y \rho_i = 2.5$ .

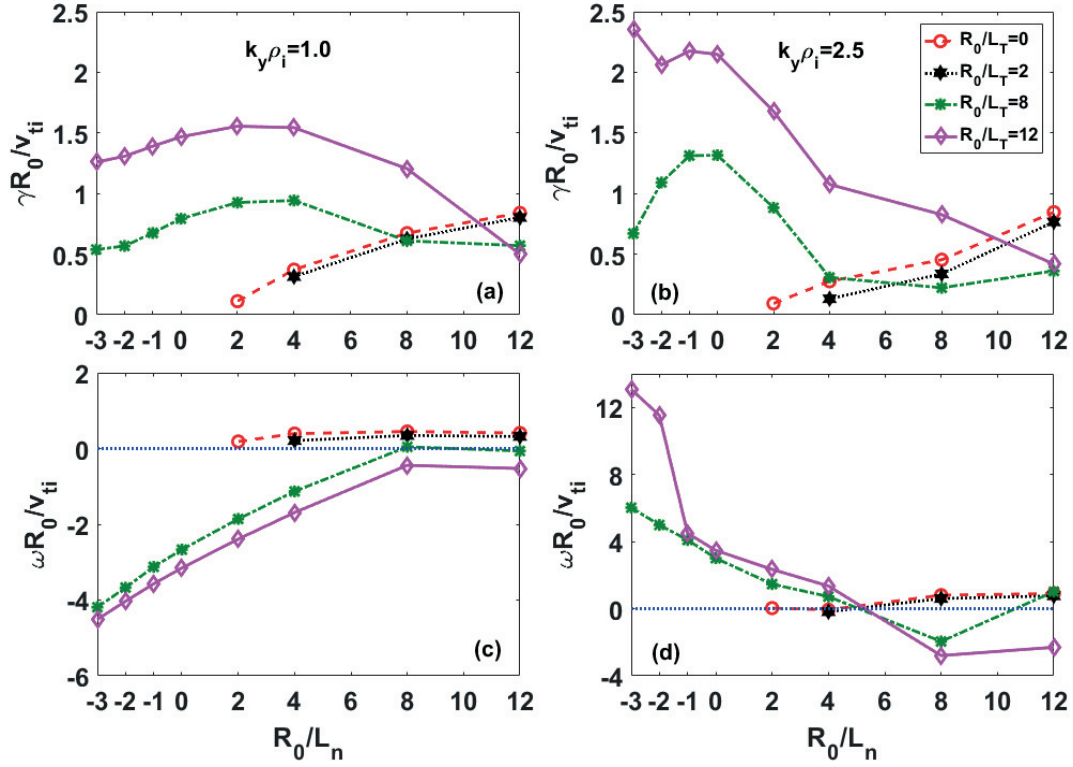


Fig. 3.4.2-8 The growth rates and real frequencies of the electrostatic hybrid ITG-TEM modes vs.  $R_0/L_n$  for various  $R_0/L_T$  at (a) and (c)  $k_y \rho_i = 1.0$ , (b) and (d)  $k_y \rho_i = 2.5$ .

The previous results are given by setting  $R_0/L_{T_i} = R_0/L_{T_e}$  in the simulations. But in experiments the electron temperature is easily changed by ECRH which causes a different value of ion temperature gradient and electron temperature gradient. In order to study such effect of the different heating scenario on hybrid ITG-TEM instabilities, the cases with a fixed electron temperature gradient are simulated here. Because the typical  $R_0/L_{T_e}$  in CFQS has not been known yet, the electron temperature gradient is set as  $R_0/L_{T_e} = 8$ , which is the typical value in the other devices like the Large Helical Device. Fig. 3.4.2-9 shows the growth rate spectrum and the real frequency spectrum of the hybrid ITG-TEM modes for  $R_0/L_{T_e} = 8$  and  $R_0/L_n = 0$ . When  $R_0/L_{T_i} \leq 4$ , the dominant instability is TEM. This is due to a large electron temperature gradient to drive a strong TEM, and  $R_0/L_{T_i} \leq 4$  is not large enough to drive a strong ITG mode. As  $R_0/L_{T_i}$  increases, ITG modes become more pronounced and dominate in the low  $k_y \rho_i$  region. It is also found that  $R_0/L_{T_i}$  can suppress TEMs.

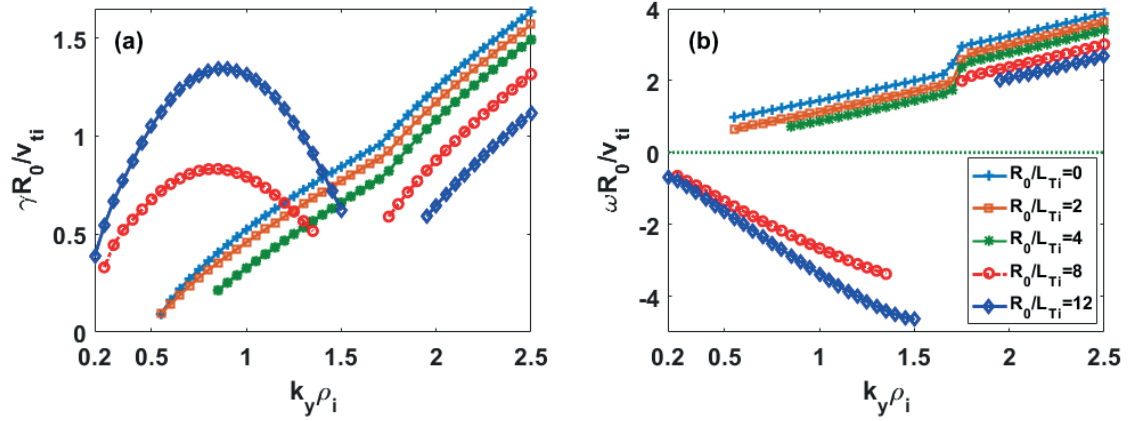


Fig. 3.4.2-9 The growth rates (a) and real frequencies (b) of the hybrid ITG-TEM modes vs.  $k_y \rho_i$  for various  $R_0/L_{Ti}$  at  $R_0/L_n = 0$  and  $R_0/L_{Te} = 8$ .

Fig. 3.4.2-10 shows the stability contour map of the growth rates of the electrostatic hybrid ITG-TEM modes with  $k_y \rho_i = 1.0, 2.5$  versus  $R_0/L_n$  and  $R_0/L_{Ti}$  for  $R_0/L_{Te} = 8$ . For  $k_y \rho_i = 1.0$ , a small density gradient or a larger density gradient can suppress ITG mode, and the density gradient can drive TEM. Therefore, the top left of Fig. 3.4.2-10 (a) is dominated by ITG and the bottom right is dominated by TEM. It is found that a stability-valley-like structure appears along the transition boundary of the ITG and TEM with  $R_0/L_n \approx R_0/L_{Ti}$ , where the growth rate is relatively low. The similar structure has also been found in the gyrokinetic analysis for the W7-X [3.4.2-5]. On the other hand, for  $k_y \rho_i = 2.5$ , the most unstable TEM is located at the region where both  $R_0/L_n$  and  $R_0/L_{Ti}$  are nearly zero. Then, one can see a significant descent of the TEM growth rate towards the transition boundary for the ITG modes. Hence, the valley-like structure no longer appears for the case in higher wavenumber.

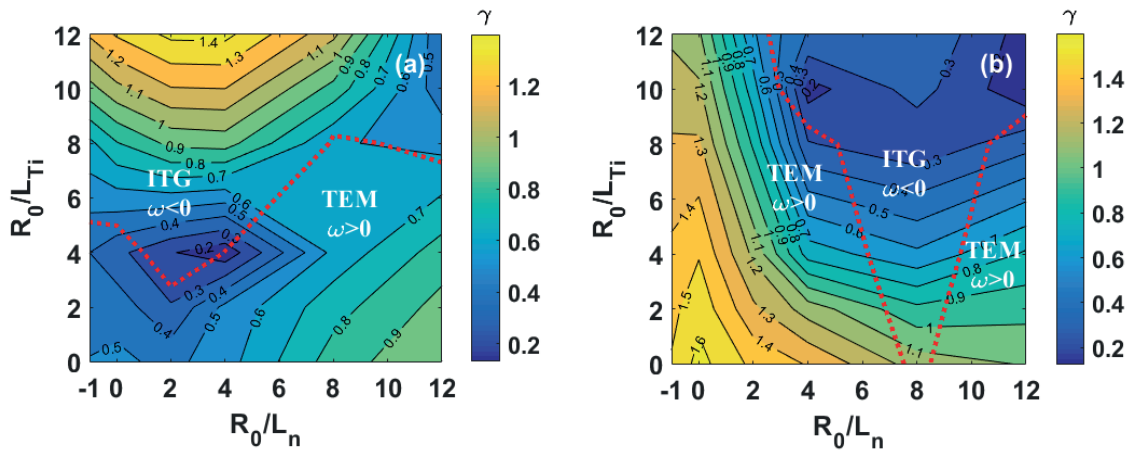


Fig. 3.4.2-10 The stability contour map of the growth rates of the electrostatic hybrid ITG-TEM modes vs.  $R_0/L_n$  and  $R_0/L_{Ti}$  for  $R_0/L_{Te} = 8$  at (a)  $k_y \rho_i = 1.0$ , (b)  $k_y \rho_i = 2.5$ . The red dashed line is the boundary of ITG modes dominant region and TEMs dominant region.

All the previous results are based on the electrostatic simulations, i.e.,  $\beta = 0$  %.  $\beta$  is defined as  $\beta = \mu_0 n_{ref} T_{ref} / B_{ref}^2$ , the ratio of the reference pressure to the reference magnetic energy density. The physical  $\beta$  enters into the Ampere equation to evolve the fluctuations of magnetic field intensity. In this subsection, we set  $\beta$  as a finite value to carry out electromagnetic simulations. Note that, in this study, the finite beta effects appear only in the fluctuations, but not in the magnetic equilibrium, and the radial derivative of  $\beta$  is ignored for simplicity. In order to identify the effect of  $\beta$  on the microinstabilities in CFQS,  $\beta$  scan of the gyrokinetic calculations is carried out, as seen in Fig. 3.4.2-11. From Fig. 3.4.2-11 (a), there are two distinct regimes before and after  $\beta = 0.3$  % for both  $k_y \rho_i$ .  $\beta = 0.3$  % is the transition point from one mode to another mode in the simulations. For  $k_y \rho_i = 1.0$ , one is dominated by ITG mode which is gradually suppressed with increasing  $\beta$ , and the other one is dominated by KBM whose growth rate increases as  $\beta$  increases. The effect of  $\beta$  on KBM have been studied in tokamaks and stellarators [3.4.2-6]. The results here are consistent with those in the references. For  $k_y \rho_i = 2.5$ , there is also a transition point at  $\beta = 0.3$  %. When  $\beta \leq 0.3$  %, the modes are TEMs which is also progressively suppressed with increasing  $\beta$ , and after the transition point the dominant mode is KBM. When  $\beta = 1.5$  %, the frequency is almost zero but positive. This is an electron mode. This might be a low-wavenumber ETG mode, which is difficult to distinguish with TEM.

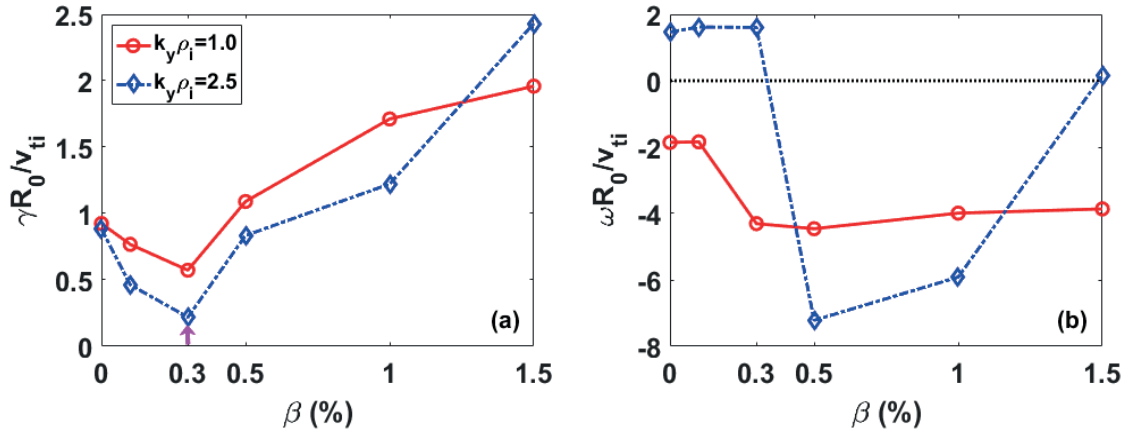


Fig. 3.4.2-11 The growth rates (a) and real frequencies (b) vs.  $\beta$  for  $R_0/L_n = 2$  and  $R_0/L_{Te} = 8$  at  $k_y \rho_i = 1.0, 2.5$ . The arrow is plotted in (a) to point the transition point from ITG to KBM.

The growth rate and real frequency spectrums for  $R_0/L_{Te} = 8$  and  $\beta = 1.0$  % are shown in Fig. 3.4.2-12. The modes with negative  $\omega$  are KBMs and the others are TEMs. From the figure, in the high  $k_y \rho_i$  region the dominant mode is TEM. The stability contour map of the growth rates versus

$R_0/L_n$  and  $R_0/L_{T_i}$  are plotted in Fig. 3.4.2-13. To compare with the electrostatic case, i.e., Fig. 3.4.2-10, these two results are qualitatively different. In  $\beta = 1.0\%$  case the dominant mode with  $k_y \rho_i = 1.0$  is KBM and the TEM only dominants in the bottom left corner where both  $R_0/L_n$  and  $R_0/L_{T_i}$  are small. When  $R_0/L_n \geq 8$ , a broad growth rate spectrum of KBM is shrunk to the low wave number region and become steeper as density gradient increases. Similarly, as temperature gradient increases, the growth rate spectrum of KBM is shrunk and become steeper. For KBMs,  $k_y \rho_i = 1.0$  is the high wave number. Therefore, because of the shrinking of the growth rate spectrum, in the right-top corner of Fig. 3.4.2-13 (a) the KBM has the smallest growth rate. On the other hand, for  $k_y \rho_i = 2.5$ , the TEM becomes more pronounced, where the growth rate almost does not depend on the  $R_0/L_T$  when  $R_0/L_n > 4$ . The upper boundary of the wave number region in our simulations is  $k_y \rho_i = 2.5$ . As density gradient increases, a more complete growth rate spectrum of TEM appears and the growth rate of TEM at  $k_y \rho_i = 2.5$  becomes smaller. Therefore, in the right side of Fig. 3.4.2-13 (b), the growth rates for  $k_y \rho_i = 2.5$  are smallest.

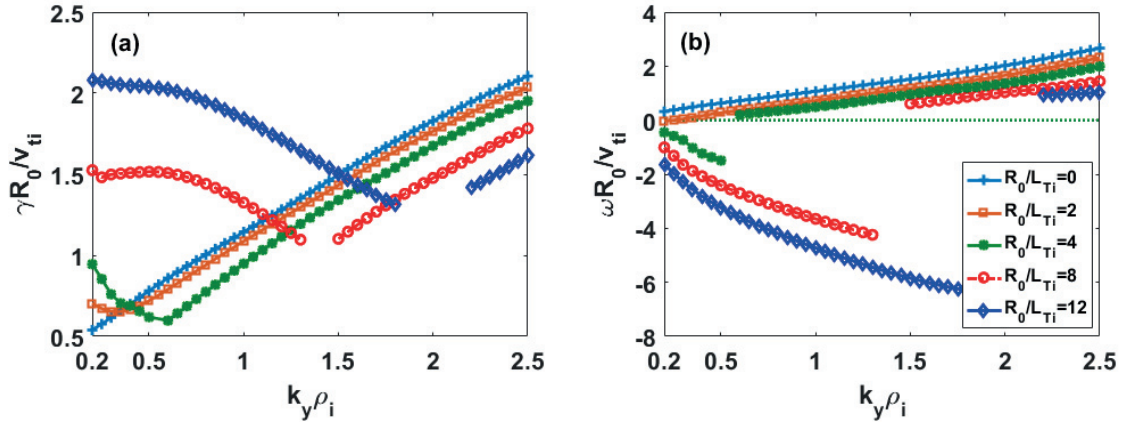


Fig. 3.4.2-12 The growth rates (a) and real frequencies (b) of the KBM-TEM vs.  $k_y \rho_i$  for various  $R_0/L_{T_i}$  at  $R_0/L_n = 0$  and  $R_0/L_{T_e} = 8$ . Here,  $\beta = 1.0\%$ .

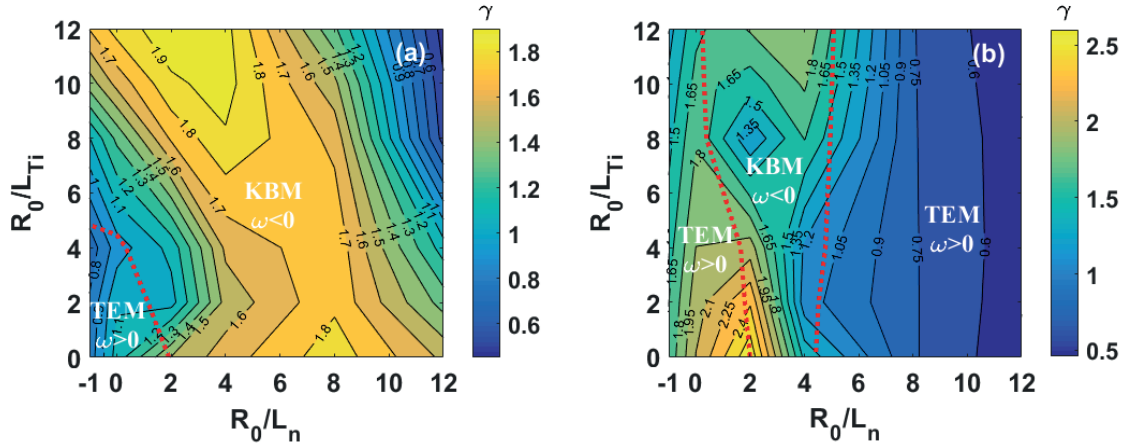


Fig. 3.4.2-13 The stability contour map of the maximum growth rates vs.  $R_0/L_n$  and  $R_0/L_{Ti}$  for fixed  $R_0/L_{Te} = 8$  at (a)  $k_y \rho_i = 1.0$ , (b)  $k_y \rho_i = 2.5$ . The red dashed lines are the boundary of KBM dominant region and TEM dominant region. Here,  $\beta = 1.0$  %.

The nonlinear ITG turbulence simulation has also been carried out. As shown in Fig. 3.4.2-14 (a), we observe that the saturated turbulent transport level  $Q_i/Q_{GB}$  in the CFQS is comparable or less than that in the axisymmetric limit. It is also found from Fig. 3.4.2-14 (b) that the CFQS indicates a relatively stronger zonal-flow generation  $W_{ZF}/W_{total}$ , in comparison to the axisymmetric limit. The magnetic fluctuations effects in the finite  $\beta$  cases, which can destabilize the kinetic ballooning modes (KBM) and micro tearing modes (MTM), will be investigated in the future works.



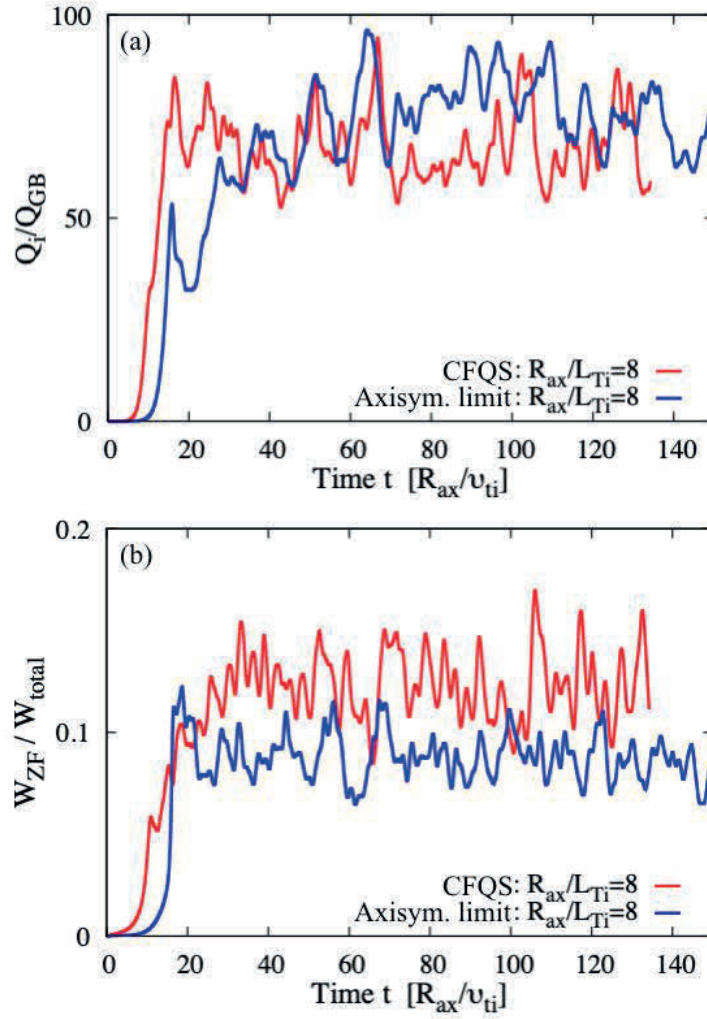


Fig. 3.4.2-14 Nonlinear GKV simulation results of (a) the ion turbulent heat flux  $Q_i / Q_{GB}$  and (b) the zonal flow energy normalized by the total energy  $W_{ZF} / W_{total}$  in the ITG-driven turbulence in the CFQS and the axisymmetric limit (Axisym. limit).

#### References

- [3.4.2-1] T. -H. Watanabe and H. Sugama, Nucl. Fusion **46** (2006) 24.
- [3.4.2-2] M. Nakata *et al.*, “Turbulent transport and zonal flow generation in quasi-axisymmetric stellarator”, The 27th International Toki Conference and the 13th Asia Pacific Plasma Theory Conference (2018) O-1.
- [3.4.2-3] M. Romanelli, C. Bourdelle, W. Dorland, Phys. Plasmas **11** (2004) 3845.
- [3.4.2-4] J. A. Baumgaertel *et al.*, Phys. Plasmas **19** (2012) 122306.
- [3.4.2-5] J. A. Alcusón *et al.*, Plasma Phys. Control. Fusion **62** (2020) 035005.
- [3.4.2-6] I. J. McKinney *et al.*, J. Plasma Phys. **87** (2021) 905870311.
- [3.4.2-7] J. Huang *et al.*, Phys. Plasmas **29** (2022) 052505.



### 3.4.3 Plasma rotation

In conventional helical devices, an impact of radial electric field on plasma confinement has extensively been investigated so far. It is one of the major issues also in a QA device because plasma rotation, which is closely related to radial electric field, can be driven more easily, and because anomalous transport can be possibly reduced by controlling plasma rotation/flow. Since the discovery of H-mode in tokamaks, the roles of shear flow on an improved confinement have been widely understood also in helical systems; *e.g.*, high ion/electron temperature modes [3.4.3-1,2]. Consequently, the reduction of anomalous transport by shear flow has become a general issue in toroidal plasmas.

Unlike tokamaks, radial electric field or plasma rotation in helical devices are determined by a solution of an ambipolar condition according to the neoclassical theory. Also, toroidal plasma rotation tends to be dissipated in conventional helical systems because of larger toroidal viscosity which originates from larger toroidal ripple of magnetic field strength [3.4.3-3]. According to theoretical studies on tokamaks, transport barriers are established by a positive feedback mechanism that reduces the transport coefficients through the increase in local pressure gradient. Radial electric field (or plasma flow), which is strongly correlated with the local pressure gradient, is a key parameter for the mechanism mentioned above. In order to promote such spontaneous growths of shear flow and pressure gradient, plasma flow should be free from any constraints.

In conventional helical devices such as CHS, plasma mainly rotates poloidally because of larger toroidal viscosity. In this situation, Pfirsch-Schlüter-type return flow should exist so as to satisfy incompressibility, which can possibly be dissipated by helical ripple [3.4.3-4]. Therefore, it is quite difficult to drive high speed plasma rotation in conventional helical systems due to large parallel viscosity both in toroidal and poloidal directions. Indeed, the radial electric field strengths observed in CHS and Heliotron-E are around 100 V/cm at most. Furthermore, the scale length of the radial electric field tends to be longer, which leads to weaker shear. Consequently, tokamak-like transition phenomena relevant to edge transport barrier have never been observed so far in helical systems.

In order to establish transport barriers, a magnetic configuration should be free from any constraints of plasma flow due to parallel viscosity. This expanded parameter range of plasma rotation is one of the reasons why we adopt the QA configuration, which is ideal for reducing toroidal viscosity as well as achieving low aspect ratio and incompressible flow at the same time.

In QA configuration, ripple trapped particles can be suppressed by reducing residual ripple. In such a situation, according to the neoclassical theory, confinement property is similar to that in an axisymmetric system. That is to say, values of radial electric field are never restricted by the ambipolar condition, which is a characteristic feature not found in the other optimized stellarators. As described below, the residual ripple in a QA configuration is drastically reduced in comparison with CHS.

In the earlier experiments in tokamaks and helical devices, it has been found that the plasma current, plasma rotation (or radial electric field) are well explained by the neoclassical theory, while particle/heat transport is dominated by anomalous transport [3.4.3-5]. The plasma rotation interpreted by the neoclassical theory gives a good hint to study the anomalous transport. Also, it is important to study the neoclassical theory itself as it is still incomplete for non-axisymmetric systems. In addition, it would be also important to investigate whether the neoclassical theory can predict neoclassical bootstrap current, toroidal viscosity and radial electric field in a QA configuration with non-axisymmetric perturbation.

Neoclassical parallel viscosity is roughly proportional to the square of the magnetic field ripple strength defined by  $\gamma^2 = \langle (\delta B / \delta s)^2 / B^2 \rangle$ , where  $\delta / \delta s$  is differential with respect to the flow direction and  $\langle \rangle$  denotes averaging on a magnetic surface. This parameter should be quantitatively evaluated from the calculations including all of the Fourier components of the field strength  $B$  because higher order mode may largely contribute to the value of  $\gamma$ . Since the calculation of  $\gamma$  for the CFQS configuration has not been carried out yet, the results for the CHS-qa configuration [3.4.3-6] are shown hereafter. In principle, similar results are expected in the CFQS.

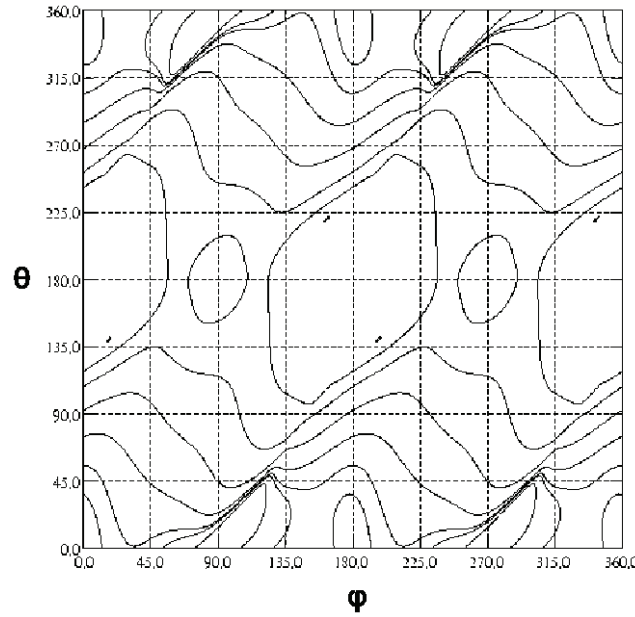


Fig. 3.4.3-1 Contour plot of  $B$  for the LCFS of CHS-qa (2w39) configuration.

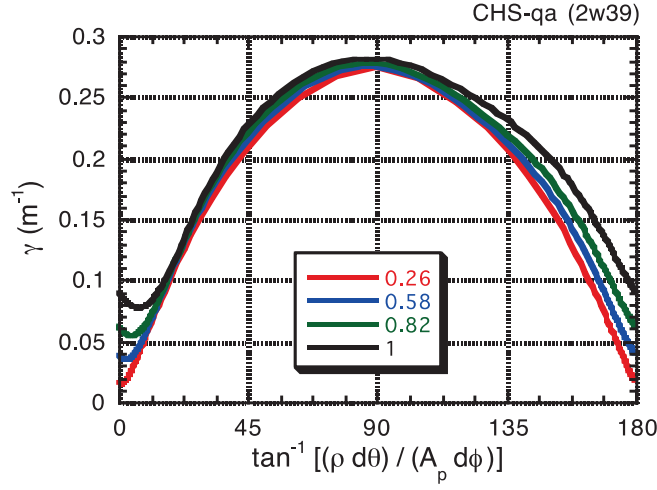


Fig. 3.4.3-2 Angle dependence of  $\gamma$  for CHS-qa (2w39) configuration.

Fig. 3.4.3-1 shows a contour plot of  $B$  on the LCFS of a reference configuration of CHS-qa (2w39). The grid data for  $B$  in cylindrical coordinates  $(R, Z, \Phi)$  are constructed from the result of VMEC code calculation. Toroidal ( $\phi$ ) and poloidal ( $\theta$ ) angles are expressed in real coordinates, and  $\theta = \tan^{-1}[(R - R_{ax})/(Z - Z_{ax})]$ , where  $R_{ax}$  and  $Z_{ax}$  are  $R$  and  $Z$  values at the magnetic axis in an equal  $\phi$  plane, respectively. This means that the effect of the excursion of the magnetic axis is ignored in the calculation. We assumed a flow direction expressed by a straight line in this  $\phi$ - $\theta$  plane. When averaging, we fixed the angle of  $\delta/\delta s$  direction with respect to the toroidal direction ( $=\tan^{-1}(r \theta / R \phi)$ ).

Fig. 3.4.3-2 shows the calculated dependence of  $\gamma$  for CHS-qa (2w39) on the flow direction at the four different flux surfaces (normalized minor radii of 0.26, 0.58, 0.82, and 1.0). As shown, the values of  $\gamma$  have peaks around 90 degrees in the QA configuration, which indicates larger parallel viscosity in the poloidal direction. In the toroidal direction,  $\gamma$  is less than 0.1 even in the LCFS, which implies that perpendicular/anomalous viscosity plays an important role for determining toroidal rotation speed in a similar way to tokamaks. Though the effect of coil ripples is not included in the present calculation, the angle minimizing  $\gamma$  is not zero but  $1.1 \sim 6.8$  degrees unlike tokamaks, which is considered to be the effect of residual non-axisymmetric components.

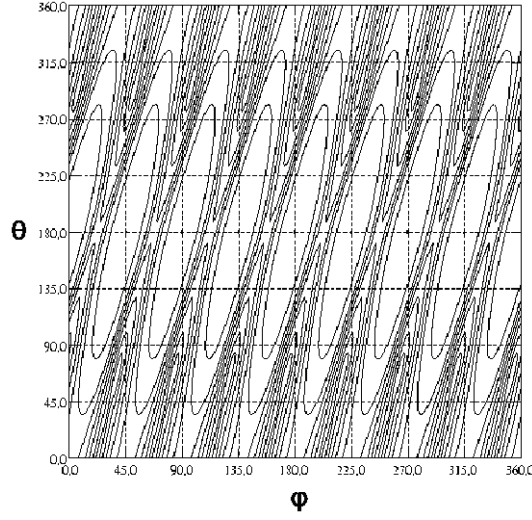


Fig. 3.4.3-3 Contour plot of  $B$  for the LCFS of CHS ( $R_{ax} = 92.1$  cm) configuration.

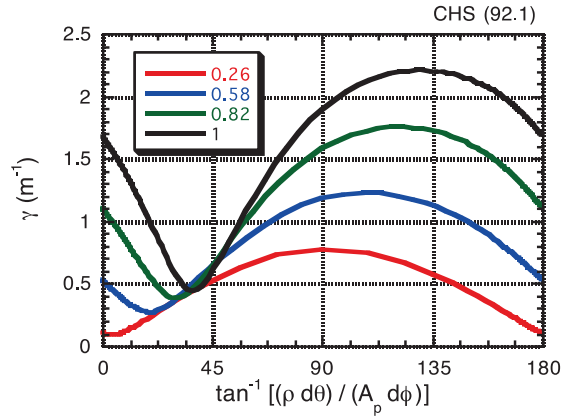


Fig. 3.4.3-4 Angle dependence of  $\gamma$  for CHS ( $R_{ax} = 92.1$  cm) configuration.

For the comparison with a conventional helical device, the calculation of  $\gamma$  has been performed for a representative configuration of CHS. The contour of  $B$  on the LCFS and the results of the  $\gamma$  calculation are shown in Fig. 3.4.3-3 and Fig. 3.4.3-4, respectively, in a similar way to the CHS-qa. The angle minimizing  $\gamma$  is around 40 degrees, which indicates that the flow tends to be driven along the helical structure ( $m = 2$ ,  $n = 1$ ) of the CHS configuration. Nevertheless, this minimum value of  $\gamma$  in CHS is still larger than the maximum value of  $\gamma$  along the poloidal direction in CHS-qa. Therefore, high-speed toroidal rotation cannot be driven in CHS because of strong toroidal viscosity, as demonstrated in the previous CHS experiment.

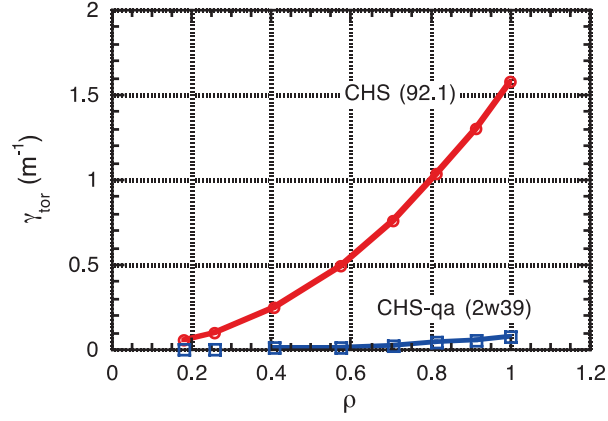


Fig. 3.4.3-5 Dependence of toroidal  $\gamma$  on minor radius for CHS-qa and CHS.

In reality, the direction of plasma flow cannot be expressed simply by a straight line in real coordinates. Experimental results in CHS suggests that the spontaneous rotation, which is driven without external momentum input (with NBI), tends to be driven along the direction minimizing parallel viscosity. In a QA configuration, this direction is the toroidal direction in the Boozer coordinates. Therefore, we have also calculated  $\gamma$  with the angle of  $\delta/\delta s$  direction fixed in the Boozer coordinates. Fig. 3.4.3-5 shows  $\gamma$  in the toroidal direction as a function of normalized minor radius for CHS and CHS-qa. As shown,  $\gamma_{\text{tor}}$  in CHS-qa is much smaller than that in CHS, which implies tokamak-like nature of a QA configuration with respect to plasma rotation.

## References

- [3.4.3-1] K. Ida *et al.*, Phys. Rev. Lett. **76** (1996) 1268.
- [3.4.3-2] A. Fujisawa *et al.*, Phys. Rev. Lett. **79** (1997) 1054.
- [3.4.3-3] K. Ida *et al.*, Phys. Rev. Lett. **67** (1991) 58.
- [3.4.3-4] S. Nishimura *et al.*, Phys. Plasmas **7** (2000) 437.
- [3.4.3-5] O. Okamoto, NIFS-PROC-**25** (1995).
- [3.4.3-6] C. Suzuki *et al.*, Plasma Phys. Control. Fusion **44** (2002) A225.

#### 3.4.4 Study of magnetic field symmetry on the formation of plasma structure

In toroidal magnetic confinement plasmas, spontaneous transition phenomena such as confinement improvement have been observed in various devices. It is widely known that flow or flow shear in plasmas significantly affects plasma confinement and stability, but the mechanisms behind the sudden flow formation and transport barrier formation observed during confinement improvement are still not fully understood. To solve this problem, it is crucial to clarify the role of magnetic field symmetry, which strongly affects the mechanisms determining the flow formation and associated electric field in toroidal plasmas. Experiments using advanced confinement devices that are capable of continuously varying the axisymmetry of the magnetic field over a wide range will allow us to examine the role of magnetic field symmetry in a series of structure-forming phenomena, such as the nonlinear interaction between flow and pressure distribution in the plasma and the resulting a new equilibrium state. In addition, the new knowledge obtained from these experiments will lead to the establishment of control methods for the transition to a confinement state with better improvement and stability.

The two main types of toroidal magnetic field confinement schemes are the tokamak type, which has good confinement performance due to its geometrical axisymmetry, and the helical type, which has essentially better characteristics of steady-state plasma sustainment. The role of magnetic field symmetry on confinement has been studied in tokamaks and helicals, respectively, but the understanding has been limited to each device because there is a discrepancy of about three orders of magnitude in the effective magnetic field ripple, an index of magnetic field asymmetry, between them. One approach to clarify the role of magnetic field symmetry in confinement is an inter-machine comparison study between the CFQS and the J-TEXT tokamak at Huazhong University of Science and Technology. Since the CFQS is equipped with QAS configuration, the symmetry of the magnetic field can be controlled continuously and over a very wide range, enabling experimental confinement studies in the magnetic field connecting tokamaks and helicals. This allows us to quantitatively and systematically demonstrate the role of magnetic field symmetry for the first time in the world, without being restricted by the device or confinement method. The J-TEXT, on the other hand, is positioned as an axisymmetric limit because of its tokamak configuration, and its plasma size and aspect ratio, as well as plasma collisionality and resistivity, which are dimensionless quantities, are comparable to those of the CFQS, making it one of the most appropriate inter-machine comparisons to ensure the universality of the results of this research.

In toroidal plasmas, the most characteristic phenomenon of the relationship between magnetic field symmetry and confinement improvement is the confinement transition with the bifurcation. When the confinement transition occurs, a large flow with shear is formed in the plasma. As a result, turbulence in the plasma is suppressed and a transport barrier is formed, thereby increasing the plasma pressure. In the transition process to the improved confinement state, it is theoretically pointed out in the viewpoint of momentum balance that the transition is triggered by the nonlinearity of ion viscosity

due to the asymmetry of the magnetic field. In other words, there are local maxima in the ion viscosity with respect to the flow velocity, and when the flow-driving force exceeds those values, the flow velocity increases rapidly, and confinement improvement is considered to occur. However, there have been very few cases in which the relationship between viscosity and flow has been experimentally evaluated and verified in comparison with transition theory.

Flow in a toroidal plasma consists of two types of flows:  $E \times B$  flow due to the radial electric field  $E$  and confinement magnetic field  $B$ , and flow driven by the pressure gradient. Both of these flows are determined as a result of the self-organization of the plasma under the influence of the symmetry of the magnetic field, interacting nonlinearly with the turbulence, so that the flow is self-consistent with the equilibrium of the plasma. Therefore, external means of controlling the flow, or radial electric field, is necessary to study the relationship between flow and confinement improvement in detail. One example of active radial field control in toroidal plasmas is the potential biasing of an electrode inserted into the plasma edge. In electrode bias experiments, the flow-driving force is obtained from the electrode current as the Lorentz force, and the ion viscosity as the flow damping force can be directly evaluated from the balance with the driving force, making comparison with theory easy. This comparative study of the relationship among confinement transitions, viscosity, and flow in the J-TEXT and the CFQS using an external control technique for the electric field is expected to advance our understanding of the role of magnetic field symmetry on structure formation in toroidal magnetic confined plasmas.

### 3.5 Energetic particle

Energetic alpha particles produced by the d-t reaction will play an essential role in sustaining a self-ignition condition in burning plasma in the future. When alpha particles are substantially lost from the plasma, the self-ignited state is easily terminated. Moreover, the localized heat load on the first wall due to the impact of the escaping alphas may seriously damage the device. Because of the reason above, a great deal of attention has to be paid to physics issues related to energetic ions such as the magnetic field ripple transport, anomalous transport and/or loss caused by MHD instabilities. Note that although neoclassical transport in CFQS is outstandingly reduced, it does not always guarantee good energetic-ion confinement. Since QAS is quite similar to tokamak in magnetic field structure, EP orbits in QAS is also quite similar to those in tokamak [3.5-1~5].

### References

- [3.5-1] M.H. Redi *et al.*, Phys. Plasmas **6** (1999) 3509.
- [3.5-2] M. Isobe *et al.*, J. Plasma Fusion Res. SERIES **6** (2004) 622.
- [3.5-3] H.W. Kugel *et al.*, Fusion Sci. Technol. **51** (2007) 203.
- [3.5-4] S. Murakami *et al.*, Proceedings of 1997 International Symposium on Plasma Dynamics in

Complex Electromagnetic Fields ~ for Comprehension of Physics in Advanced Toroidal Plasma Confinement ~, 8-11 December, 1997. **IAE-RR-98 054**, March 1998, pp. 137-140.  
 [3.5-5] D. A. Spong *et al.*, Phys. Plasmas **18** (2011) 056109.

### 3.5.1 NBI deposition analysis

To obtain high plasma parameter and to study the beam ion confinement in QA configuration, the installation of neutral beam (NB) injector is planned with CFQS. Feasibility study of NB injection on CFQS is performed using the beam deposition calculation code and the guiding center orbit following code [3.5.1-1]. Fig. 3.5.1-1 shows the schematic drawing of the CFQS with NB injector. According to the CAD modeling including the coil case, the VV, and the coil supporting structure, the possible injection angle of NBI is from 44 degrees to 52 degrees [3.5.1-2]. Here, we considered to use an NB injector operated in the CHS [3.5.1-3] with injection energy and power of 30 keV and 0.9 MW.

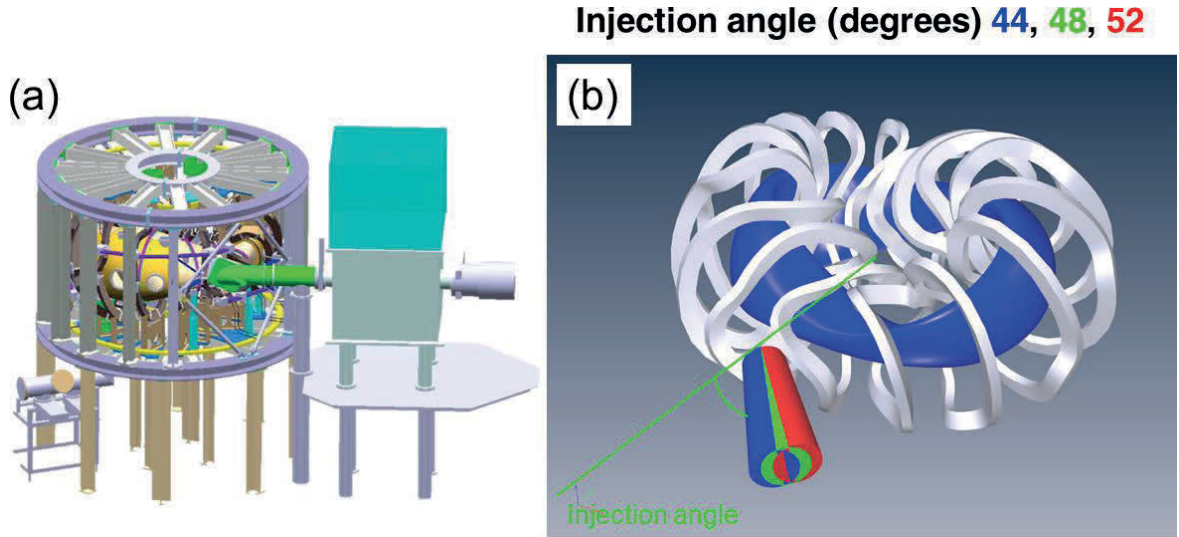


Fig. 3.5.1-1 (a) Schematic drawing of CFQS with NB injector, (b) Possible NB injection lines.

Deposition fraction on NB injection angle was surveyed by means of HFREYA code which is deposition calculation code using the Monte Carlo methods [3.5.1-4]. Here, the plasma parameter is assumed to be parabolic profile, *i.e.*,  $\sim (1-(r/a)^2)^2$ . The central electron temperature  $T_{e0}$  is given using central electron density  $n_{e0}$  with  $T_{e0} = 2.0/n_{e0}$  ( $10^{19} \text{ m}^{-3}$ ) in order to maintain the plasma stored energy. We changed NB injection angle from 44 to 52 degrees with 2 degrees steps. Fig. 3.5.1-2 shows the deposition fraction of NB injection as a function of line-averaged electron density ( $n_{e\_avg}$ ). The deposition fraction rapidly increases with  $n_{e\_avg}$  at  $n_{e\_avg}$  of less than  $4 \times 10^{19} \text{ m}^{-3}$ . The maximum deposition fraction is obtained with NB injection angle of from 44 to 48 degrees.



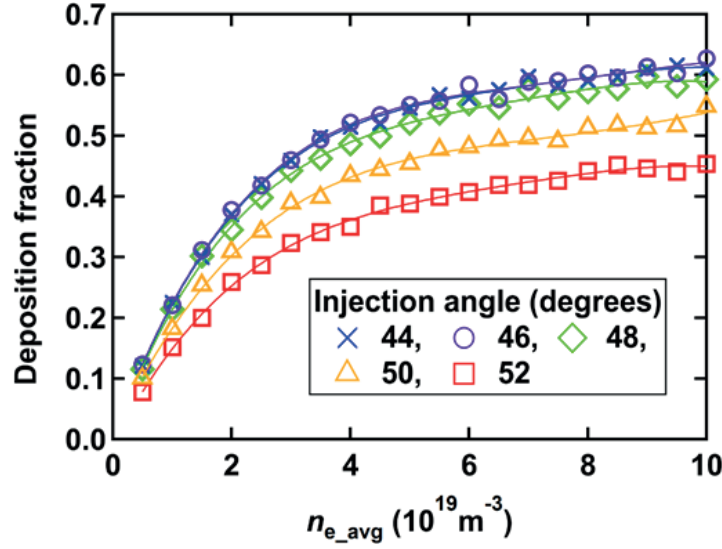


Fig. 3.5.1-2 Dependence of deposition fraction of NB on line-averaged electron density.

The beam ion orbit calculation is performed by the guiding center orbit following code in the Boozer coordinates DELTA5D [3.5-5] in order to evaluate the beam ion confinement. Fig. 3.5.1-3 shows the Poincaré plots of typical collisionless orbit of co-going transit ion ( $\text{H}^+$ ) at  $B_t$  of 1 T in toroidal angles of 90 and 180 degrees. Here, beam ion energy and pitch angle are 30 keV and 22 degrees, respectively. The deviation of orbit from the magnetic flux surfaces is relatively large due to the relatively low magnetic field strength and the relatively low rotational transform. Beam ion confinement is evaluated using DELTA5D code including beam-plasma collision. Here, we randomly choose 1000 beam ions injected by co-inject NB and followed in thermalization time of beam ions ( $\sim 50$  ms). Time evolution of loss energy of beam ions as a function of time is plotted in Fig. 3.5.1-4 (a). Here, calculation is performed with  $n_{e\_avg}$  of  $2 \times 10^{19} \text{ m}^{-3}$ . Loss energy gradually increases with time until  $t$  of 25 ms, and then is almost saturated. We obtained relatively low loss energy at the injection angle of 48 to 52 degrees. Fig. 3.5.1-4 (b) shows the loss energy at  $t$  of 50 ms as a function of  $n_{e\_avg}$ . The loss energy slightly increase with the  $n_{e\_avg}$ . The loss energy at 50 ms is relatively lower at the injection angle of 48 to 52 degrees when  $n_{e\_avg} < 4 \times 10^{19} \text{ m}^{-3}$ . This is because the fraction of beam ions deposited in smaller  $R$  region, where the confinement of co-passing beam ion seems to be worse due to the large outward deviation of orbit becomes larger with the decrease of the injection angle. It seems that the injection angle of 48 degrees is more favorable regarding deposition and beam ion confinement.

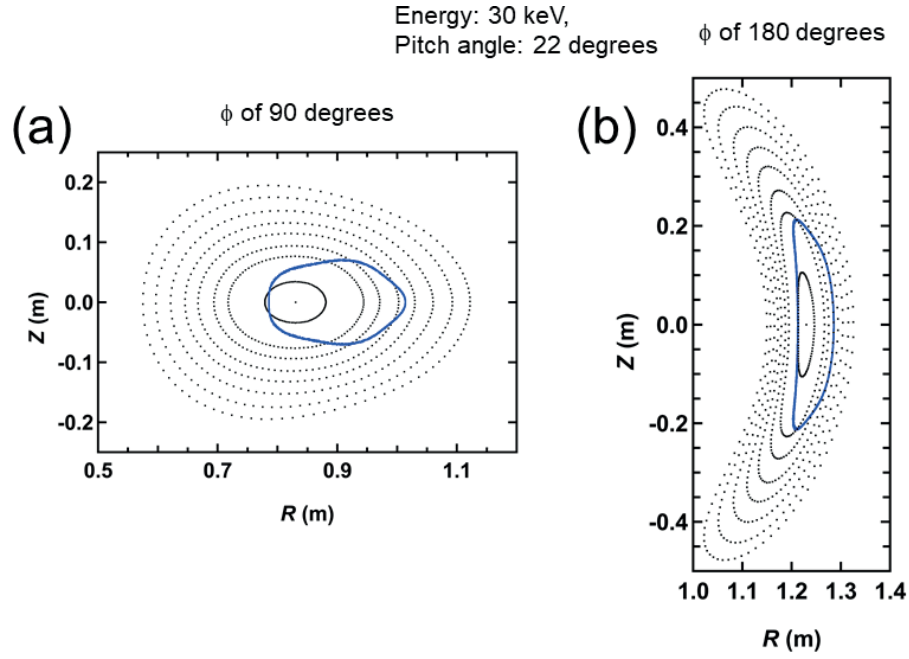


Fig. 3.5.1-3 Poincaré plots of typical co-going transit beam ion orbit at two different toroidal angles, (a) 90 degrees, and (b) 180 degrees.

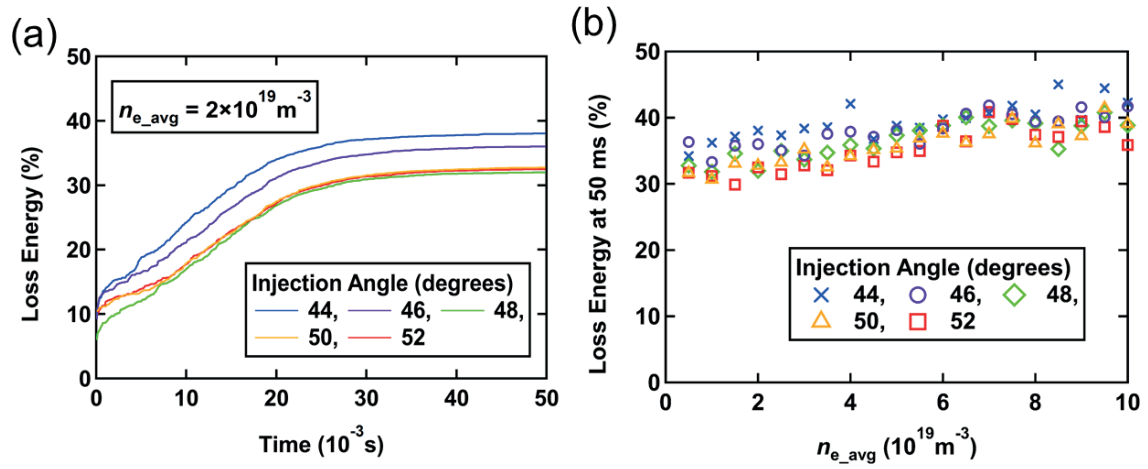


Fig. 3.5.1-4 (a) Time evolution of loss energy of beam ions. (b) Loss energy at 50 ms as a function of line-averaged electron density.

## References

- [3.5.1-1] K. Ogawa *et al.*, Plasma Fusion Res. **14** (2019) 3402067.
- [3.5.1-2] S. Kinoshita *et al.*, Plasma Fusion Res. **14** (2019) 3405097.
- [3.5.1-3] K. Matsuoka *et al.*, Plasma Phys. Control. Fusion **42** (2000) 1145.
- [3.5.1-4] S. Murakami *et al.*, Trans. Fusion Technol. **27** (1995) 256.

### 3.5.2 Feasibility study of fast ion loss diagnostics

The velocity distribution of loss flux of escaping fast ion is essential information in understanding confinement-loss boundary and fast ion transport due to MHD instabilities. Fast ion loss detector (FILD) [3.5.2-1], which provide the energy and the pitch angle of escaping fast ion, has been employed in tokamaks and stellarator/helical devices. Feasibility study of fast ion loss diagnostics has been performed using DELTA5D and LORBIT codes [3.5.2-2]. DELTA5D code is used for calculating the guiding center orbit from the birth position of NB ion including the slowing down with bulk plasma in the Boozer Coordinates until the beam ion reaches the LCFS or is thermalized. Then, LORBIT code [3.5.2-3] is utilized to calculate the collisionless Larmor orbit from the LCFS position where the beam ion reached. Fig. 3.5.2-1 shows the distribution of loss points of beam ion on the vacuum vessel. The lost points mainly appear at the upper side of the vacuum vessel due to the gradient magnetic field drift.

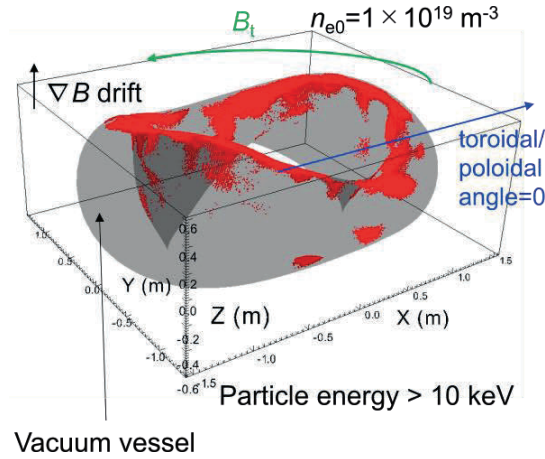


Fig. 3.5.2-1 Three-dimensional plot of beam ion loss point on the vacuum vessel at  $n_{e0}$  of  $1 \times 10^{19} \text{ m}^{-3}$ .

The candidate positions for a stacking-foil-type and scintillator-type FILDs were investigated regarding the beam ion loss distribution on the vacuum vessel. Fig. 3.5.2-2 shows the candidate location of FILDs considered in this analysis. A point at the upper side of the vacuum vessel, where relatively high beam loss flux is expected, is chosen as the candidate position for the stacking-foil-type FILD. Three different toroidal locations are selected for scintillator-based FILDs.

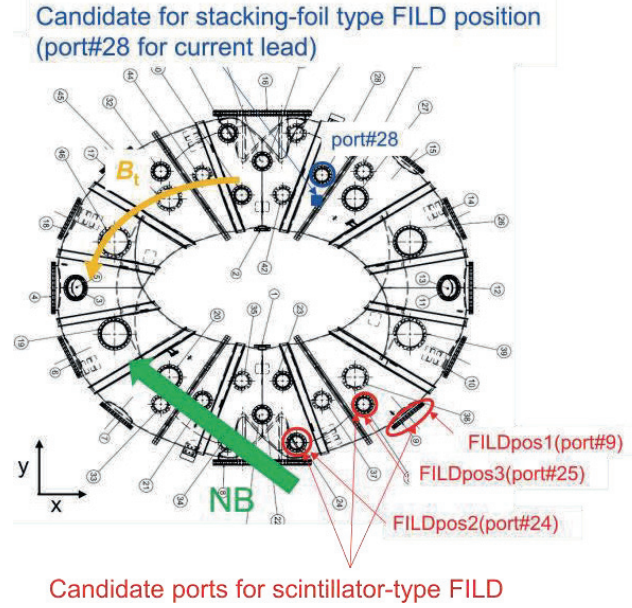


Fig. 3.5.2-2 The candidate location of FILDs.

The calculation shows that some energetic ions having an energy greater than 20 keV reaches stacking-foil-type FILD position. Fig. 3.5.2-3 shows the energy and pitch angle distributions of beam ions detected by the FILD at  $R = 1.28$  m for FILDpos1,  $Z = 0.02$  m for FILDpos2, and  $Z = 0.25$  m for FILDpos3. In these cases, the three spots that exist for energy/pitch angle are  $\sim 10$  keV/ $\sim 70$  deg.,  $\sim 10$  keV/100 deg., and  $\sim 25$  keV/140 deg. The former two spots correspond to the barely-trapped ion, whereas the third spot corresponds to the co-going ions near the injection energy. An experimental study of energy/pitch angle resolved toroidal/poloidal distribution of beam ion losses due to magnetic field ripples as well as MHD instabilities becomes prospective for the first time in QA stellarator using the multiple fast ion loss diagnostics.

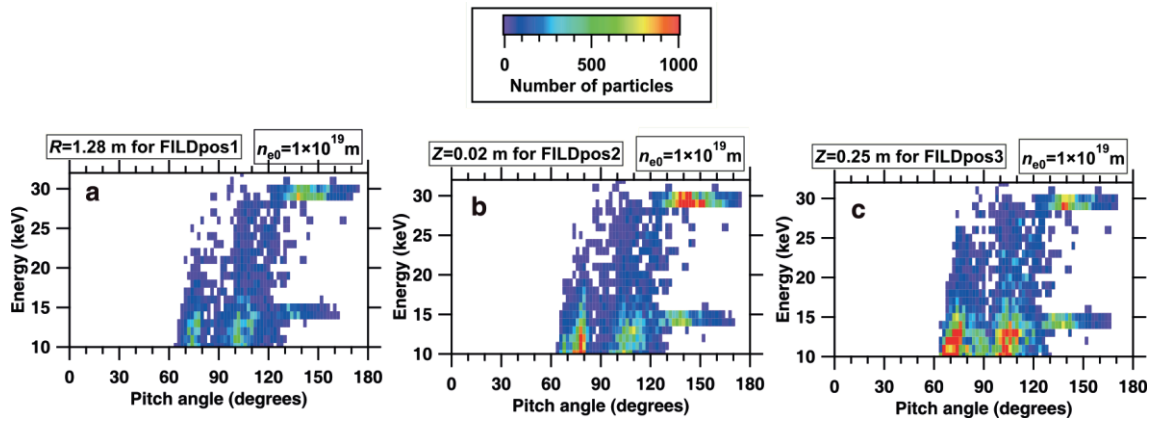


Fig. 3.5.2-3 Beam ion energy and pitch angle distribution at (a) FILDpos1, (b) FILDpos2, and (c) FILDpos3.

## References

- [3.5.2-1] S. J. Zweben, Rev. Sci. Instrum. **60** (1989) 576.  
[3.5.2-2] K. Ogawa *et al.*, J. Instrum. **16** (2021) C09029.  
[3.5.2-3] M. Isobe *et al.*, J. Plasma Fusion Res. SERIES **8** (2009) 330.

### 3.5.3 Preparative study for deuterium experiment for energetic ion confinement physics

The deuterium experiment will be one of the strategic options to investigate the isotope effect and energetic particle physics. In the deuterium experiments, 2.45 MeV neutrons are generated by nuclear fusion reactions between thermal deuterons, beam deuteron-thermal deuteron, and beam deuterons. In NB-heated CFQS plasmas, the neutron emission due to beam-thermal reaction is expected to be the main component because the injection energy of NB is much higher than the expected ion temperature. In this case, the neutron emission rate ( $S_n$ ) reflects the global confinement of beam ions. FIT3D-DD code [3.5.1-4, 3.5.3-1], which is based on a simple analytical solution for the Fokker-Planck equation, is applied to evaluate  $S_n$  and the heating efficiency in deuterium CFQS plasmas under the various temperature and density ranges [3.5.3-2]. In the FIT3D-DD code, the birth profile of beam ions is calculated by the HFREYA module, and then the beam ion orbit is traced for a short time in order to evaluate the prompt loss of beam ion using the MCNBI module. The neutron emission rate and heating profile are evaluated using the analytical Fokker-Planck equation based on the radial beam ion profile calculated by HFREYA and MCNBI modules. In this database, density and temperature profiles have a parabolic profile. The ranges of the central electron temperature, the central ion temperature, and the central electron density are set to be 0.5-4.0 keV, 0.5-1.0 keV, and  $0.5 \times 10^{19}$  -  $4.0 \times 10^{19}$  m<sup>-3</sup>, respectively. Figure 3.5.3-1 shows  $S_n$  database with the central ion temperature of 1.0 keV. The neutron emission rate monotonically increases with the electron temperature and the electron density in this plasma parameter region. The expected  $S_n$  by calculation is  $10^{12}$  (n/s) order.

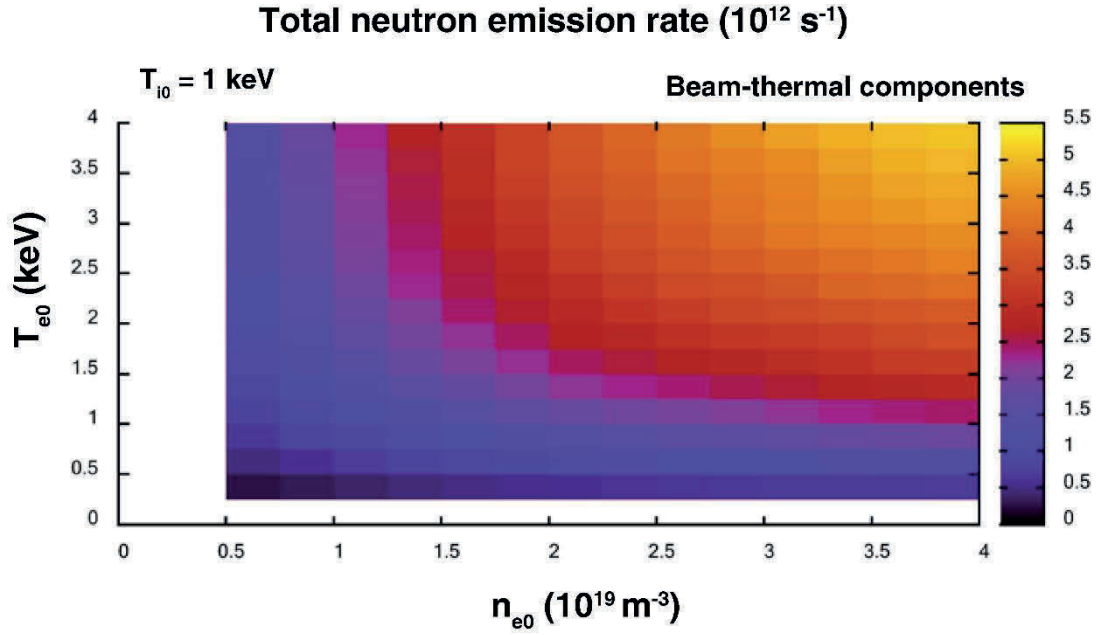


Fig. 3.5.3-1 Total neutron emission rate prediction by the FIT3D-DD code.

The comparison of neutron emissivity profiles in different densities is performed (Fig. 3.5.3-2). The peak of neutron emissivity shifts outwardly due to the increase in density. The possible reason for the shift is due to the beam ion deposition profile. In high-density cases, beam ion deposition points accumulate in the foreground, *e.g.*, outward, compared to low-density cases.

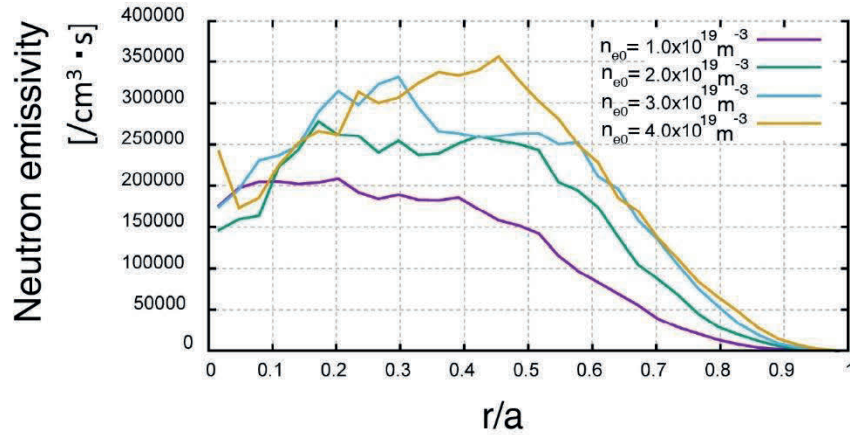


Fig. 3.5.3-2 Radial profile of neutron emissivity on different density cases.

In the deuterium experiment, 3 MeV protons are also produced with almost the same amount with 2.45 MeV neutrons. Therefore, the information of beam ions confined in a plasma core region can be obtained by 3 MeV protons. The energy Larmor radius of 3 MeV proton at the toroidal magnetic field strength of CFQS 1 T is 0.25 m, the same as the minor radius of a CFQS plasma. Therefore, the 3 MeV protons born in the plasma core region can be lost on the vacuum vessel before full gyro motion.

Therefore, the inverse transformation of the deuterium-deuterium (D-D) fusion profile is feasible using the collimated proton detector array located on the vacuum vessel. For a feasibility study of D-D profile measurement, *e.g.*, possibility of D-D fusion profile inversion by D-D-born 3 MeV proton, was performed using the FIT3D-DD code and the LORBIT code [3.5.3-3]. Here, candidate detector position is set to be  $(x, y, z)$  of (1.46 m, 0.05 m, -0.34 m). The detector direction changes from 10 degrees to 50 degrees with 5 degrees steps. Here, the angle starts from the negative  $x$ -axis. Therefore, totally nine detectors are considered. We assumed that the length of the collimator is long enough, *e.g.*, the initial velocity of the proton is set to be parallel to the detector axis. Inversion of the D-D fusion profile was conducted by solving the linear matrix equation  $\mathbf{b}=\mathbf{A}\mathbf{x}$ , where  $\mathbf{b}$ ,  $\mathbf{A}$ , and  $\mathbf{x}$  represent the signal of the detector array, weight function, and DD fusion profile, respectively. The weight function  $\mathbf{A}$  is obtained by making the dwell time of in each normalized minor radius position from the time-reversed 3 MeV proton orbit calculated by the LORBIT code (Fig. 3.5.3-3). Here, for the radial grid,  $r/a$  from 0.1 to 1.0 is divided into nine regions.

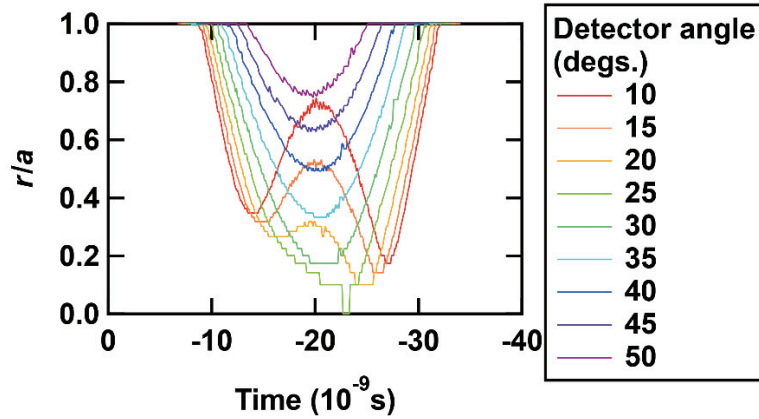


Fig. 3.5.3-3 Time trace of normalized minor radius position of 3 MeV protons. Time-reversed 3 MeV proton orbits are calculated from the candidate detector position.

The signal vector  $\mathbf{b}$  having nine components was calculated by integrating the 3 MeV proton emissivity profile obtained by the FIT3D-DD code along the proton orbit. The linear matrix equation  $\mathbf{b}=\mathbf{A}\mathbf{x}$  was solved using the NumPy linear matrix solution library (linalg.solve 1.0.4) with python3.8.2. Figure 3.5.3-4 shows the comparison of inversed D-D fusion profile to the input D-D profile. It is found that the inversed profile almost matches with the input profile except for the edge region of the plasma, *e.g.*,  $r/a > 0.8$ . The D-D fusion profile inverted by the calculated proton detector array signal shows the possibility of D-D fusion profile diagnostics by 3 MeV proton in CFQS.



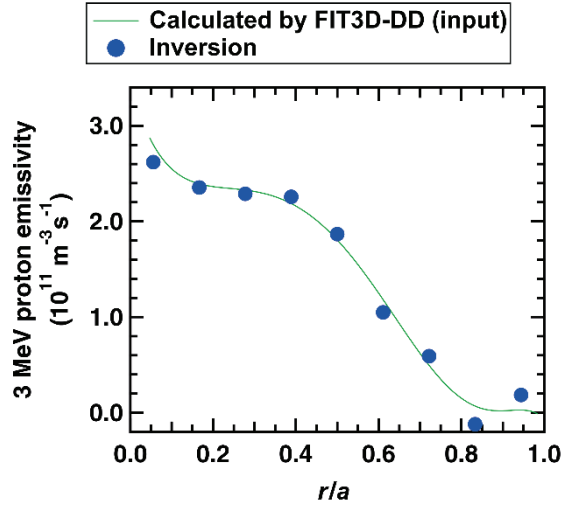


Fig. 3.5.3-4 3 MeV proton emissivity calculated by the FIT3D-DD code (input) and the inversed profile from the calculated detector signals. The inverted profile almost agrees with the input profile.

#### References

- [3.5.3-1] R. Seki *et al.*, Plasma Fusion Res. **14** (2019) 3402126.
- [3.5.3-2] R. Seki *et al.*, Plasma Fusion Res. **17** (2022) 2403063.
- [3.5.3-3] K. Ogawa *et al.*, Plasma Fusion Res. **17** (2022) 2402012.

#### 3.5.4 Predictive study of alpha particle confinement in a QAS-type reactor

Collisionless alpha particle confinement in reactor-sized Stellarator based on W7-AS and W7-X [3.5.4-1], as well as QA configuration [3.5.4-2,3] had been investigated to show the way toward a future fusion reactor. A study of alpha particle confinement in a QAS-type reactor based on the CFQS magnetic field has been initiated using a guiding center orbit code in the Boozer coordinates [3.5.4-4].

Energetic  $\alpha$ -particles with 3.5 MeV are created in the fusion reaction which are under consideration in this paper. In order to investigate their behaviors in QA stellarator reactors, the quasi-toroidally symmetric configuration is based on the CFQS stellarator, scaled up to possess the same ITER nominal magnetic field strength ( $B_t \sim 5.0\text{T}$ ) and volume ( $V \sim 800 \text{ m}^3$ ). The parameters of the scaled configuration are as follows: major radius  $R = 9.0 \text{ m}$ , minor radius  $a = 2.2 \text{ m}$ , magnetic field strength  $B_t = 5.3 \text{ T}$ , and toroidal periodic number  $N = 2$ , respectively. For simplicity, it is called the CFQS-like reactor configuration. The MHD equilibrium is calculated with the VMEC code in fixed boundary mode. Here 61 radial flux grid points, 72 poloidal modes and 23 toroidal modes are considered in the calculation. Then the magnetic field is globally decomposed in Boozer coordinates by the BOOZ\_XFORM code and the Boozer transformation error is  $< 10^{-10}$ , expressed as:

$$B(\psi, \theta_B, \phi_B) = \sum_{m,n} B_{m,n}(\psi) \cos(m\theta_B - nN\phi_B) \quad (3.5.4-1)$$



Where the coefficients  $B_{m,n}$  denotes the spectrum of the magnetic field strength. The  $\psi$ ,  $\theta_B$  and  $\phi_B$  denote the magnetic flux, poloidal and toroidal angles in the Boozer coordinates.  $N$  denotes the toroidal periodicity. Fig. 3.5.4-1 displays poloidal cross-sections of the equilibrium magnetic surfaces for the CFQS-like reactor at three different toroidal angles, which presents obvious non-axisymmetric geometric torus. In Fig. 3.5.4-2 plotted is the Fourier spectrum of the magnetic field strength normalized to  $B_{0,0}$  in the Boozer coordinates in the plasma pressure-free configuration. The dominant ten  $B_{m,n}$  components are used in this simulation. In order to clearly show the  $B_{m,n}$  spectrum and location of the quasi-axisymmetric radial position, the largest seven  $B_{m,n}$  (except  $B_{0,0}$ ) components are displayed.  $\rho$  represents the normalized minor radius  $\rho = \sqrt{\psi/\psi_{edge}}$ , with  $\psi_{edge}$  the magnetic flux at the plasma boundary. Non-axisymmetric harmonics are much lower than  $B_{1,0}$ , which indicates a quasi-axisymmetric configuration.

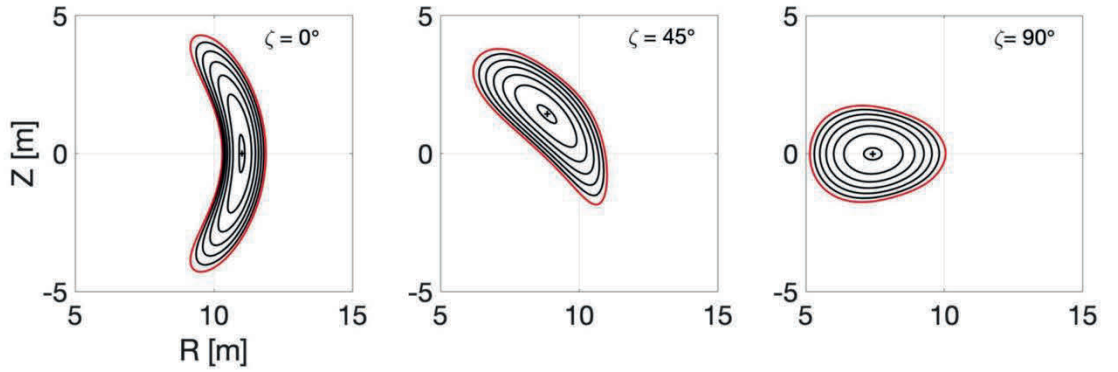


Fig. 3.5.4-1 Poloidal cross-sections of magnetic flux surfaces for the CFQS-like reactor at three different toroidal angles.

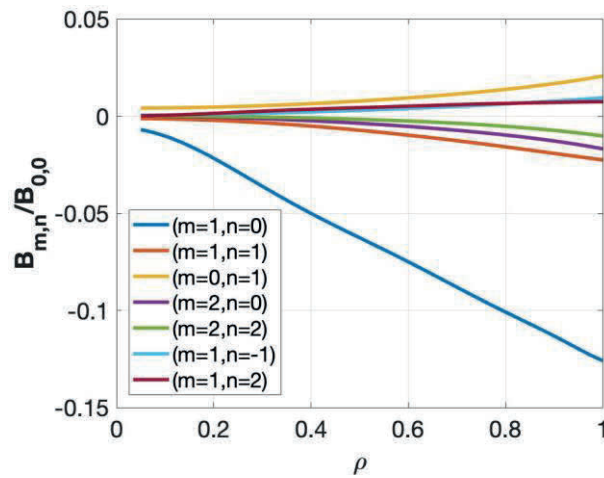


Fig. 3.5.4-2 Magnetic field strength spectrum  $B_{m,n}$  in Boozer coordinates for a vacuum case without  $B_{0,0}$  in the CFQS-like reactor. The normalized radius  $\rho = \sqrt{\psi/\psi_{edge}}$ .

In order to model the confinement of  $\alpha$ -particles produced from nuclear reactions, a fusion birth model based on the fusion cross sections is used, which is a fit to experimental data. The fit takes the expression of the equations:

$$\langle\sigma v\rangle = C_1 \cdot \theta \sqrt{\xi/(m_r c^2 T^3)} e^{-3\xi}. \quad (3.5.4-2)$$

$$\theta = T / \left[ 1 - \frac{T(C_2 + T(C_4 + T \cdot C_6))}{1 + T(C_3 + T(C_5 + T \cdot C_7))} \right]. \quad (3.5.4-3)$$

$$\xi = \left( B_G^2 / (4\theta) \right)^{1/3}. \quad (3.5.4-4)$$

$$dR/dV = n_T n_D \langle\sigma v\rangle. \quad (3.5.4-5)$$

where  $C_k (k = 1, 2 \dots, 7)$  are coefficients for different reactions,  $B_G$  is the Gamov constant,  $m_r c^2$  is the reduced mass of the particles (in keV),  $\langle\sigma v\rangle$  is the fusion reactivity. In this work it was assumed that  $T_i = T_e$  ( $T_i$  and  $T_e$  represent ion and electron temperature, respectively),  $n_T = n_D = 0.5n_e$  ( $n_D$  is the deuterium (D) isotope density,  $n_T$  is the tritium (T) isotope density,  $n_e$  is the electron density, and background plasma is a 50/50 mix of deuterium and tritium, which is done for simplicity and could be relaxed given profile modeling). Therefore, the fusion rate per volume  $dR/dV = 0.25n_e^2 \langle\sigma v\rangle$ . According to the CFQS-like reactor, the temperature and density profiles were assumed as  $T_i = T_e = T_0(1 - \rho^2 + 0.017\rho^4)$  and  $n_e = n_{e0}(1 - \rho^2 + 0.02\rho^4)$  where  $T_0 = 20$  keV,  $n_{e0} = 2 \times 10^{20}/m^3$ . The kinetic profiles are shown in Fig. 3.5.4-3 (a). Fig. 3.5.4-3 (b) depicts the birth profiles for the alpha particle populations at all radii.

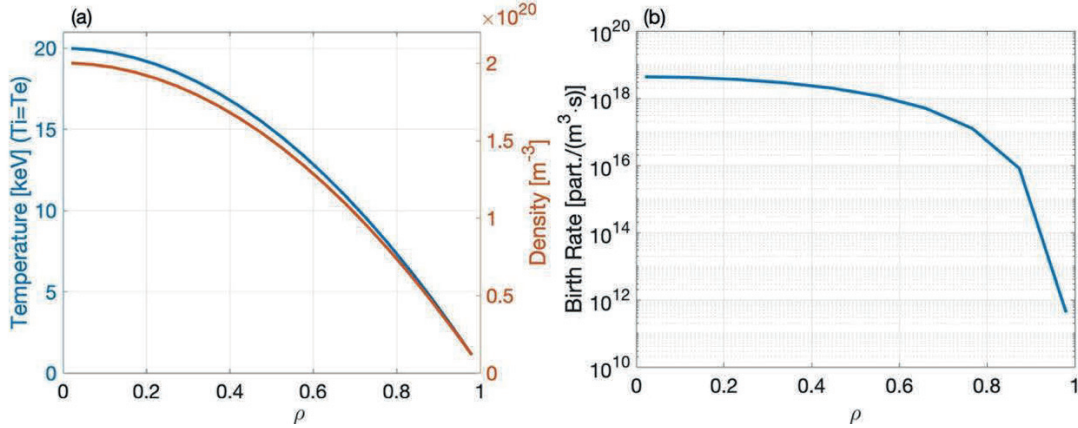


Fig. 3.5.4-3 (a) represents the temperature (blue curve) and density (red curve) profiles for the CFQS-like reactor which serve as the basis for the fusion alpha particles birth rates (b).

The loss of  $\alpha$ -particles in this configuration is estimated by ensemble averaging mono-energetic  $\alpha$ -particle trajectories, which depends on the initial conditions in the absence of collisions. In reactor conditions, the  $\alpha$ -particle confinement with high energy may not be sensitive to collisions before the fast ions slowing down and beginning to pitch angle scatter into the loss cone. Thus, in this simulation

the total time span of particles' orbits is 10 ms and the time iteration step  $\Delta t = 6.25 \times 10^{-8}$  s. An efficient way to calculate guiding center trajectories lies in solving the equations of motion in Boozer coordinates. The guiding center equations in Boozer coordinates are dependent on magnetic field strength rather than magnetic field vector. The motion equations used in the simulation are expressed by:

$$\dot{\psi} = \frac{\delta}{\gamma} \left( \frac{\partial B}{\partial \zeta} I - \frac{\partial B}{\partial \theta} g \right). \quad (3.5.4-6)$$

$$\dot{\theta}_B = \frac{g}{\gamma} \left( \delta \frac{\partial B}{\partial \psi} + e \frac{\partial \Phi}{\partial \psi} \right) - \frac{e^2 B^2}{m} \rho_c \left( \frac{\rho_c g' - l}{\gamma} \right). \quad (3.5.4-7)$$

and

$$\dot{\phi}_B = \frac{-l}{\gamma} \left( \delta \frac{\partial B}{\partial \psi} + e \frac{\partial \Phi}{\partial \psi} \right) + \frac{e^2 B^2}{m} \rho_c \left( \frac{\rho_c l' + 1}{\gamma} \right). \quad (3.5.4-8)$$

The functions  $\delta$  and  $\gamma$  are defined by  $\delta = e^2 \rho_c^2 B / m + \mu$  and  $\gamma = e[g(\rho_c l' + 1) - l(\rho_c g' - l)]$ , where  $\mu$  is the magnetic moment,  $2\pi I(\psi)$  the toroidal current, within a magnetic surface labelled by  $\psi$ ,  $2\pi g(\psi)$  the poloidal current outside a magnetic surface and  $\Phi(\psi)$  the radial electric potential,  $\rho_c = mv_{\parallel}/eB$ , respectively. The prime denotes the derivative with respect to  $\psi$ . The magnetic field strength and its derivatives are solved by the 6th order polynomial fitting. Mono-energetic  $\alpha$ -particles were evenly distributed at  $16 \times 6$  ( $N_{\theta_B} \times N_{\phi_B}$ ) positions on one period of the evaluated magnetic surface. Pitch angles of these particles cover the entire passing and trapped-particle regions.

The exact quasi-axisymmetry can only be achieved on one flux surface,  $\sum_{m,n} |B_{m,n \neq 0}(\rho_{qa})| \approx 0$ . The radial location of quasi-axisymmetry  $\rho_{qa}$  dramatically affect the spectrum of the magnetic field strength, which plays an important role on confinement of particles. Scans of the  $\rho_{qa}$  from 0 to 0.9 are carried out by vertically shifting  $B_{m,n \neq 0}$  components in the CFQS-like reactor configuration. By this method, an exact quasi-axisymmetry on a magnetic flux surface can be achieved. For example, based on the original Fourier series of the magnetic field strength components shown in Fig. 3.5.4-2, the  $B_{m,n \neq 0}$  components are vertically shifted till their values become zero at  $\rho = 0.5$  as shown in Fig. 3.5.4-4 (b). Then  $\rho_{qa} = 0.5$  is obtained. In Figs. 3.5.4-4 (a) and (b), the Fourier series of the magnetic field strength with  $\rho_{qa} = 0.2$  and 0.5 are plotted. In order to estimate the deviation of the axisymmetry on each magnetic flux surfaces, a metric is utilized to describe the error. That is:

$$QS(\rho) = \left( \sum_{m,n \neq 0} B_{m,n}^2(\rho) \right)^{1/2} / B_{0,0}(\rho). \quad (3.5.4-9)$$

In Fig. 3.5.4-4 (c), the QS deviation of the Fourier series of the magnetic field strength with different locations of  $\rho_{qa} = 0, 0.2$ , and 0.5 are plotted.

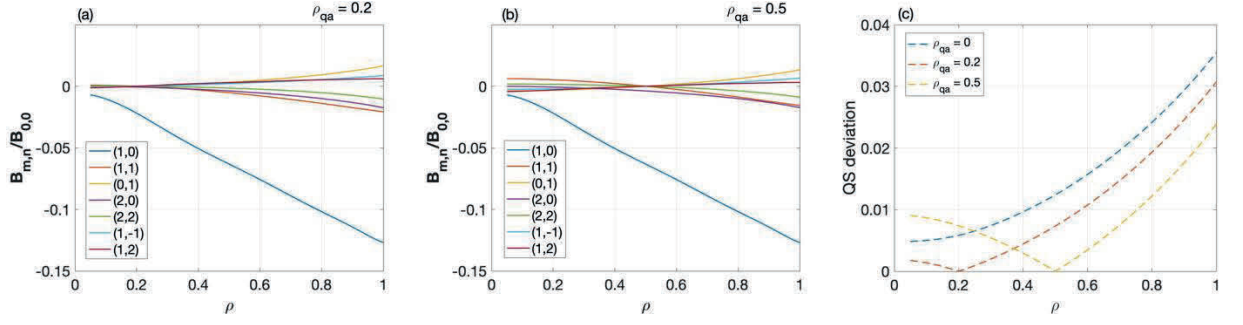


Fig. 3.5.4-4 Comparison of the Fourier spectra of the magnetic field strength for quasi-axisymmetric radial positions  $\rho_{qa} = 0.2$  (a) and  $\rho_{qa} = 0.5$  (b). (c) represents the QS deviation of  $\rho_{qa} = 0, 0.2$ , and  $0.5$ , respectively.

The radial and poloidal drifts in Boozer coordinates are expressed by Eqs. (3.5.4-6) and (3.5.4-7), respectively. If deeply trapped particles are merely concerned, the  $v_{\parallel}$  and  $\rho_c$  of particles equals zero. Consequently, the second term in the right of Eq. (3.5.4-7) can be ignored and the  $\delta$  in first term equals  $\mu$ . Therefore, the two drift equations can be simplified to

$$\dot{\psi} = \frac{\mu}{e(g+I\iota)} \left( \frac{\partial B}{\partial \zeta} I - \frac{\partial B}{\partial \theta} g \right) . \quad (3.5.4-10)$$

and

$$\dot{\theta}_B = \frac{g}{e(g+I\iota)} \left( \mu \frac{\partial B}{\partial \psi} + e \frac{\partial \Phi}{\partial \psi} \right) . \quad (3.5.4-11)$$

Eqs. (3.5.4-10) and (3.5.4-11) are of interest that the radial and poloidal drifts are determined by the equilibrium magnetic and electric potential fields. In other word, drift distributions in the spatial Boozer coordinates can be calculated analytically based on the MHD equilibrium. These expressions are different from the previous simplified equations, and can more precisely describe ion radial and poloidal drifts.

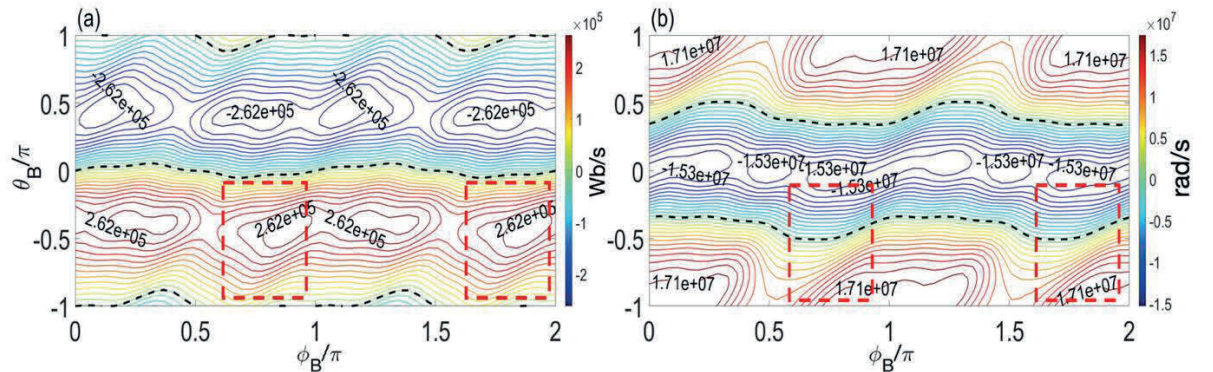


Fig. 3.5.4-5 (a) represents the contour of radial drift (on the flux surface  $\rho = 0.3$ ) with the radial location of quasi-axisymmetry  $\rho_{qa} = 0$ , and (b) represents the contour of poloidal drift for the same condition. The positions of loss channels are marked by red dashed rectangles.

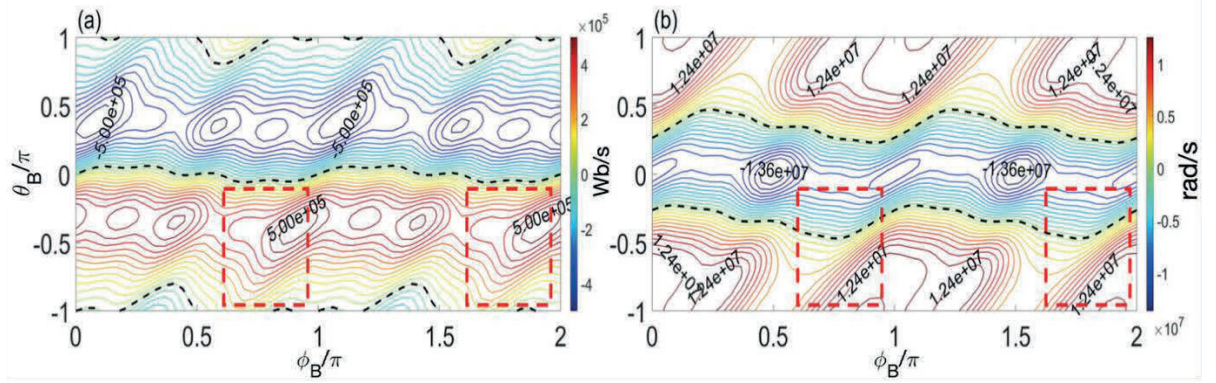


Fig. 3.5.4-6 (a) represents the contour of radial drift (on the flux surface  $\rho = 0.8$ ) with the radial location of quasi-axisymmetry  $\rho_{qa} = 0$ , and (b) represents the contour of poloidal drift for the same condition. The positions of loss channels are marked by red dashed rectangles.

Figs. 3.5.4-5 and 3.5.4-6 show the contour of radial drift (a) and poloidal drift (b) on the magnetic flux surface with  $\rho = 0.3$  and  $0.8$ , respectively, without considering electric field. The two Eqs. (3.5.4-10) and (3.5.4-11) are examined to evaluate radial (poloidal) drift for the first time. The radial drift is outward for the region with positive values and  $\alpha$ -particles will finally leak from the plasma boundary in these regions. On the contrary, if  $\alpha$ -particles remained in the region with negative values will drift inward. This paper is focused on the region with positive values. The contours of  $\dot{\psi} = 0$  and  $\dot{\theta}_B = 0$  are plotted with dashed curves. In Figs. 3.5.4-5 and 3.5.4-6, the minimum  $|\dot{\theta}_B|$  turns up close to where the maximum  $\dot{\psi}$  exists, which induces the specific loss channels generated at regions with  $\theta_B$  near  $-\pi/2$  and  $\zeta$  near  $\pi$  or  $2\pi$ , which are marked by red dashed rectangles. It considerably enables generation of localized particle orbit topologies and results in identified loss channels. Such loss channels are also revealed to exist in quasi-axisymmetric and quasi-isodynamic stellarators.

Fig. 3.5.4-7 shows the contour of radial drift (a)-(b) and poloidal drift (c)-(d) on the magnetic flux surface with  $\rho = 0.8$  and the  $\rho_{qa}$  are located at  $\rho = 0.2$  and  $0.5$ , respectively. In Figs. 3.5.4-7 (a)-(b) the positive maximum value of  $\dot{\psi}$  are,  $4.87 \times 10^5$  Wb/s and  $4.54 \times 10^5$  Wb/s around loss channels, respectively. Figs. 3.5.4-7 (c)-(d) depict the maximum  $\dot{\theta}_B$  increases as the  $\rho_{qa}$  increases. These values are,  $1.25 \times 10^7$  rad/s and  $1.26 \times 10^7$  rad/s, respectively. With an increasing of  $\rho_{qa}$ , the weak enhancement of the maximum poloidal drift and strong weakening of the maximum radial drift arise. Thus, the confinement of  $\alpha$ -particles near these loss channels have been improved as the  $\rho_{qa}$  is radially moved outward. The contours of radial and poloidal drift at core region possess the similar characteristics of those contours on the magnetic flux surfaces outside the  $\rho_{qa}$ .



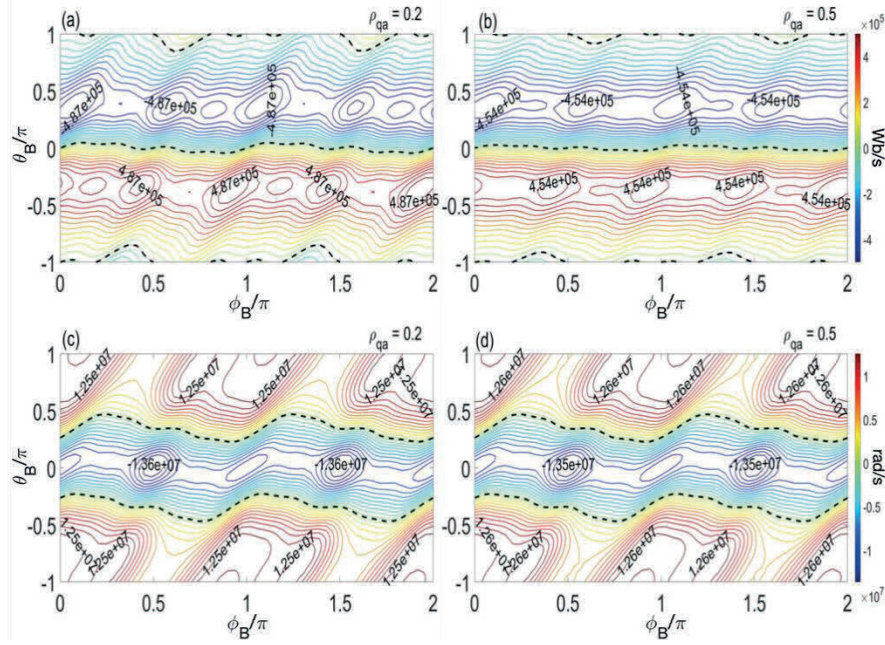


Fig. 3.5.4-7 (a)–(b) represent the contour of radial drift (on the flux surface  $\rho = 0.8$ ) with the radial location of quasi-axisymmetry  $\rho_{qa} = 0.2, 0.5$  and (c)–(d) represent the contour of poloidal drift for the same condition.

In addition, the magnetic surface-averaged drift  $\langle \dot{\psi} \rangle = \sqrt{\int_0^{2\pi} \int_0^{2\pi} \dot{\psi}^2 d\phi_B d\theta_B}$  and  $\langle \dot{\theta}_B \rangle = \sqrt{\int_0^{2\pi} \int_0^{2\pi} \dot{\theta}_B^2 d\phi_B d\theta_B}$  are evaluated on each flux surface in Figs. 3.5.4-8 (a) and (b), which can give radial and poloidal drift profiles. They are normalized by  $\langle \dot{\psi} \rangle^{org}$  and  $\langle \dot{\theta}_B \rangle^{org}$  which denote  $\langle \dot{\psi} \rangle$  and  $\langle \dot{\theta}_B \rangle$  with  $\rho_{qa} = 0$ . Figs. 3.5.4-8 (a) and (b) display  $\langle \dot{\psi} \rangle / \langle \dot{\psi} \rangle^{org}$  and  $\langle \dot{\theta}_B \rangle / \langle \dot{\theta}_B \rangle^{org}$  with various of  $\rho_{qa}$ . It implies when the radial location of  $\rho_{qa} = 0.3$ ,  $\langle \dot{\psi} \rangle / \langle \dot{\psi} \rangle^{org} > 1$  with  $\rho$  from 0 to 0.05 and  $\langle \dot{\psi} \rangle / \langle \dot{\psi} \rangle^{org} < 1$  with  $\rho$  from 0.05 to 1. As the  $\rho_{qa}$  is moved outward the region with  $\langle \dot{\psi} \rangle / \langle \dot{\psi} \rangle^{org} > 1$  extends. It seems that the confinement of energetic particles at the core region becomes weak. However, with an increasing of  $\rho_{qa}$  the  $\langle \dot{\psi} \rangle / \langle \dot{\psi} \rangle^{org}$  decreases from the mid-radius to plasma edge, which is beneficial for the confinement of fast-particles. Fig. 3.5.4-8 (b) depicts that as the  $\rho_{qa}$  is moved outward the  $\langle \dot{\theta}_B \rangle / \langle \dot{\theta}_B \rangle^{org}$  increases in global plasma region, which favorably improve fast-particle confinement. Thus, particles launched on a magnetic flux surface with bigger  $\rho_{qa}$  are clearly better than the others.

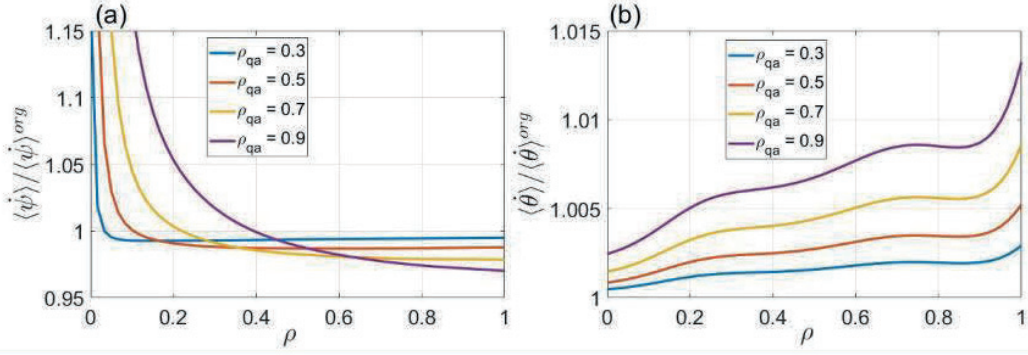


Fig. 3.5.4-8 (a) shows magnetic surface-average of radial drift on different  $\rho$  with  $\rho_{qa} = 0.3, 0.5, 0.7$ , and  $0.9$ . (b) shows magnetic surface-averaged of poloidal drift on different  $\rho$  with  $\rho_{qa} = 0.3, 0.5, 0.7$ , and  $0.9$ .

To verify the  $\alpha$ -particle loss with various  $\rho_{qa}$ , we simulate 413,664 mono-energetic  $\alpha$ -particles in each case with various  $\rho_{qa}$  and calculate their loss fraction. Fig. 3.5.4-9 show loss positions of particles with  $\rho_{qa} = 0, 0.3, 0.6$ , respectively. The red dashed rectangles emphasize the specific loss channels caused by coupling maximum radial drift and minimum poloidal drift, where  $\theta_B$  is around  $-\pi/2$  and  $\phi_B$  near  $\pi$  or  $2\pi$ . It shows that almost all of loss particles fall in these loss channels. Moreover, as  $\rho_{qa}$  increases, such lost particles decrease. This phenomenon is in good agreement with what is illustrated in Figs. 3.5.4-7 and 3.5.4-8. A correlation of a decrease of loss particles in the loss channels with an increase of  $\rho_{qa}$  could be revealed.

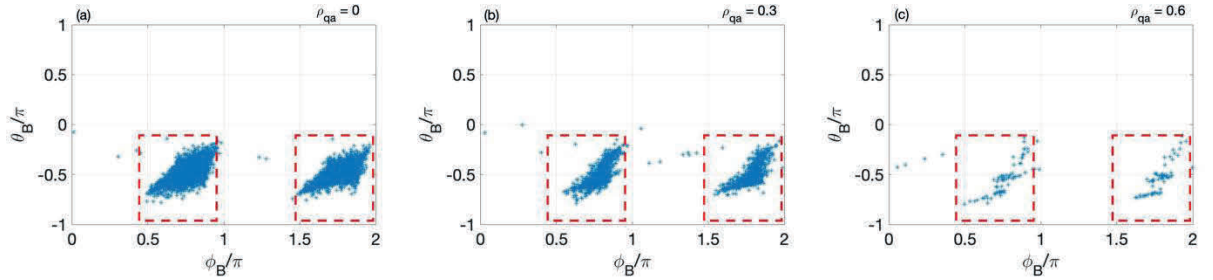


Fig. 3.5.4-9 (a)–(c) represent lost particle position (blue points) in the  $(\theta, \zeta)$  plane with the radial location of quasi-axisymmetry  $\rho_{qa} = 0, 0.3, 0.6$ . The red dashed rectangles represent specific loss channels.

Fig. 3.5.4-10 shows the time evolution of  $\alpha$ -particle loss fraction from the loss channels for the radial locations of  $\rho_{qa}$  scanned from 0 to 0.9. When  $\rho_{qa} > 0.7$   $\alpha$ -particles are well confined. This figure depicts that the particle confinement with higher  $\rho_{qa}$  are much better than the others. Figs. 3.5.4-11 (a)–(d) represent the orbit trajectories of a particle launched from different magnetic surfaces  $\rho_{launched} = 0.4, 0.5, 0.7, 0.8$ , respectively and  $\rho_{qa} = 0$ . Figs. 3.5.4-11 (e)–(h) represent the orbit trajectories of the same particle with  $\rho_{qa} = 0.6$ . The  $\rho_{qa}$  surface is described by a red solid curve

and the plasma boundary is described by a green dashed curve. The localized particles existing in the region inside the  $\rho_{qa} = 0.6$  surface is transited into blocked particles, which is favorably confined. We should reiterate that the physical process considered in this paper is different from what is considered in S.A. Henneberg *et al.* In their work, scans of radial positions of  $\rho_{qa}$  are carried out to optimize quasi-axisymmetric magnetic configuration with considering fast particle confinement. In such procedure, finite QS deviation remains at  $\rho_{qa}$  and due to the existence of QS deviation, the optimal location was found to lie between half radius and the plasma edge. In our study,  $B_{m,n}$  profiles are artificially manipulated to scan  $\rho_{qa}$ . Thus, QS deviation does not exist at  $\rho_{qa}$ . As the  $\rho_{qa}$  is set close to the plasma boundary ( $\rho = 1$ ), all  $\alpha$ -particles can be well confined except loss of blocked particles by orbit width launched at edge region. However, the important conclusion obtained in their study is qualitatively consistent with ours. Both papers obtained that, fast-particle confinement can be improved by shifting radial positions of  $\rho_{qa}$  outward.

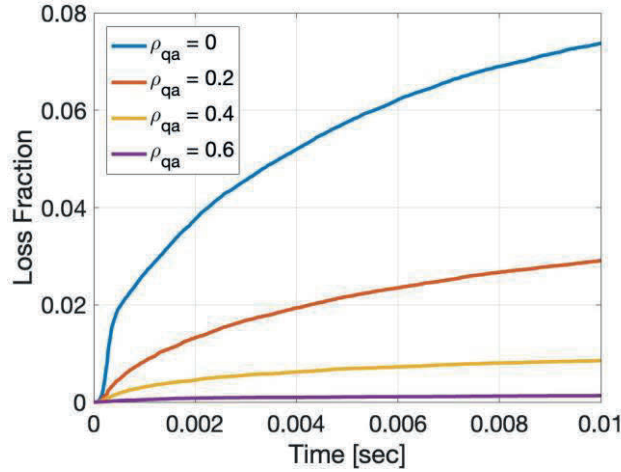


Fig. 3.5.4-10 Collisionless  $\alpha$ -particle loss from loss channels as a function of time for different  $\rho_{qa}$  on timescales of 10 ms.



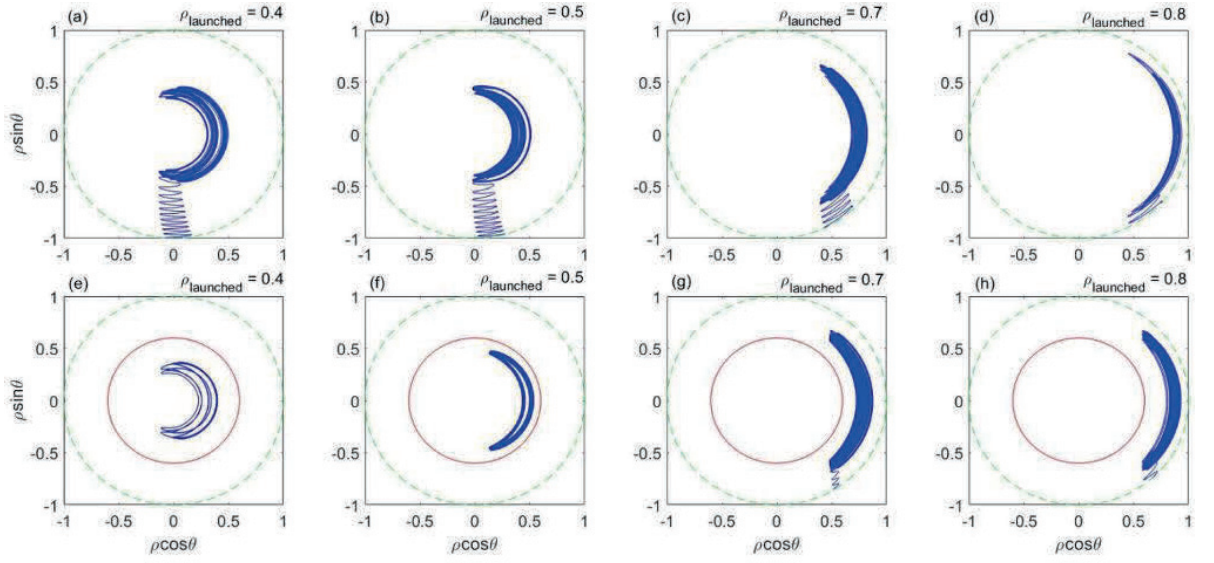


Fig. 3.5.4-11 (a)-(d) represent the orbit trajectories (blue solid curve) of a particle launched from different magnetic surfaces  $\rho_{\text{launched}} = 0.4, 0.5, 0.7, 0.8$ , respectively. (e)-(h) represent the orbit trajectories (blue solid curve) of a particle with  $\rho_{\text{qa}} = 0.6$  (red solid curve) launched from different magnetic surfaces  $\rho_{\text{launched}} = 0.4, 0.5, 0.7, 0.8$ , respectively. The plasma boundary is described by a green dashed curve.

Furthermore, in order to clarify improvement of trapped particle confinement in the QA configuration with higher  $\rho_{\text{qa}}$  the longitudinal adiabatic invariant  $J = \oint m v_{\parallel} dl$  is calculated as shown in Fig. 3.5.4-12. Input parameters  $B_{\text{ref}} = 5.23$  T and traced particle energy is 15 keV. Some “blue” points are observed which represent dramatical decreasing of  $J$ . At these regions, a blocked  $\alpha$ -particle is easily transited into a localized particle. In Fig. 3.5.4-12 (a), the  $\rho_{\text{qa}}$  equals zero. The “blue” points almost appear in global radial regions. As  $\rho_{\text{qa}}$  position is shifted outward, the “blue” points vanish in the vicinity of  $\rho_{\text{qa}}$  in Figs. 3.5.4-12 (b) and (c), which results in transition of localized particles in the region inside  $\rho_{\text{qa}}$  surface to blocked particles when these particles radially drift to  $\rho_{\text{qa}}$  position. This result is consistent with Figs. 3.5.4-10 and 3.5.4-11.

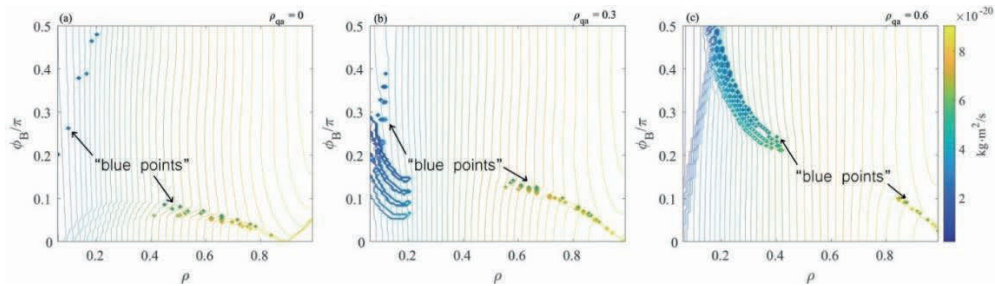


Fig. 3.5.4-12 (a)-(c) represent the longitudinal adiabatic invariant  $J$  with different radial location of  $\rho_{\text{qa}} = 0.0, 0.3, 0.6$ , respectively. The blue points represent the  $J$  value of localized particles. The arrow symbols show the blue points.

## References

- [3.5.4-1] W. Lotz *et al.*, Plasma Phys. Control. Fusion **34** (1992) 1037.
- [3.5.4-2] S. Gori *et al.*, Plasma Phys. Control. Fusion **43** (2001) 137.
- [3.5.4-3] S. Okamura *et al.*, J. Plasma Fusion Res. SERIES **3** (2000) 73.
- [3.5.4-4] Y. Zhang *et al.*, AIP Advances **12** (2022) 055214.

## 3.6 ECRH deposition analysis

Electron cyclotron resonance heating (ECRH) power deposition and electron cyclotron current drive (ECCD) are analyzed using the ray-tracing code, TRAVIS [3.6-1]. For the analysis, a CFQS equilibrium file “19-10-22.21-03\_STD.wout” was applied for the TRAVIS code. The frequency and the injected power of EC-wave in X-mode polarization are 54.5 GHz and 1 MW, respectively. As a test case, peaked electron temperature profile with  $T_{e0}$  of 3.5 keV and flat electron density profile with  $n_{e0}$  of  $1.0 \times 10^{19} \text{ m}^{-3}$  were assumed. The  $T_e$  and  $n_e$  profiles are plotted in Fig. 3.6-1.

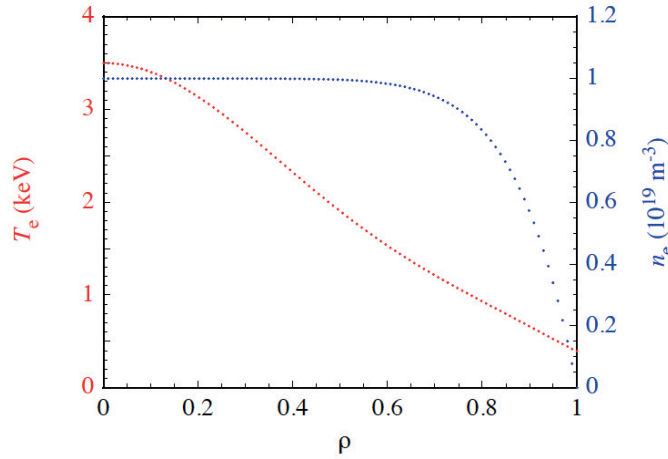


Fig. 3.6-1 Assumed electron temperature and density profiles for ECRH power deposition and ECCD analyses using the TRAVIS code.

Considering the dimension of the ECRH power injection port (CFQS O-180 port, ICF419), the size of 2-D steerable final plane mirror is determined as H247×W140 mm, the position of the center of the plane mirror is ( $R$ : major radial position = 1.694 m,  $T$ : toroidal position = 0 m, and  $Z$ : vertical position = 0.085 m) and the focused beam waist radius ( $1/e$  radius of electric field amplitude) is 30 mm at the position of  $R = 1.185$  m,  $T = 0$  m, and  $Z = 0$  m, in this analysis. Positive directions of  $T$  and  $Z$  are right side looking from outside of the torus and upper side, respectively. Using the 2-D steerable mirror, EC-wave power deposition control and ECCD can be realized.

Figure 3.6-2 shows the controllability of power deposition position by scanning beam aiming position:  $R_f$ ,  $T_f$ ,  $Z_f$ . Here,  $R_f$ ,  $T_f$ , and the magnetic field on axis at the bean-shape poloidal cross section,

$B$ , were fixed at 1.2 m, 0 m, and 0.975 T, respectively.  $Z_f$  was varied vertically as 0, 0.1, 0.2, 0.25, and 0.3 m. The vertical axis of Fig. 3.6-2 (b) is absorbed power density per volume,  $dP/dV$  ( $\text{MW m}^{-3}$ ). By the variation of  $Z_f$ , the peak position of power deposition shifts toward outside as  $\rho = 0, \sim 0.2, \sim 0.4, \sim 0.6$  and  $\sim 0.85$ , respectively. High heating efficiency of about 100 % is kept for  $Z_f$  settings up to 0.25 m, and the efficiency degrades to 75.6 % in the far off-axis case with  $Z_f = 0.3$  m.

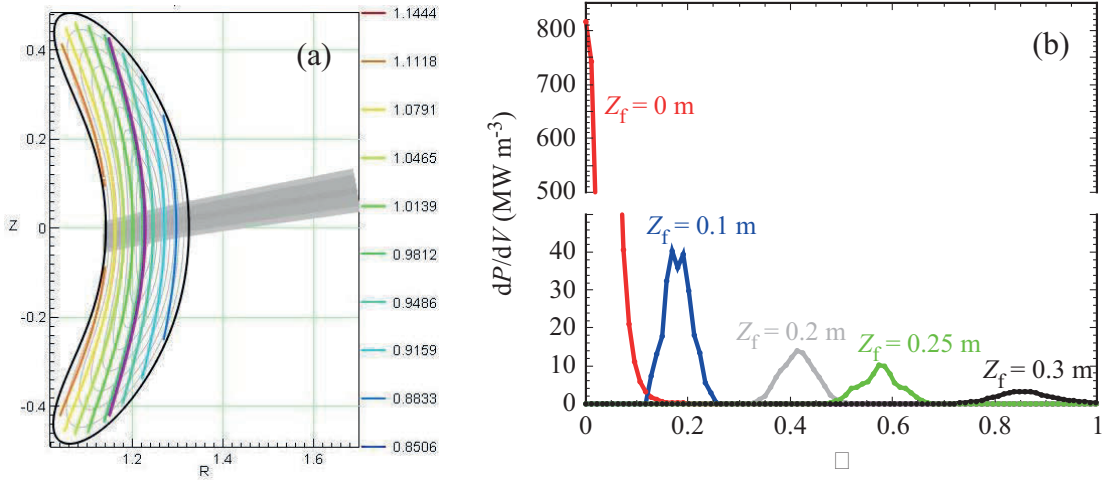


Fig. 3.6-2 (a): An example of a poloidal cross section plotted with an EC-wave beam path (here,  $Z_f = 0$  m) and (b): power deposition profiles with  $Z_f$  settings at 0, 0.1, 0.2, 0.25 and 0.3 m.

Scanning EC-wave beam direction toroidally, dependence of EC-driven current  $I_{ECCD}$  against the parameter  $T_f$  is obtained as seen in Fig. 3.6-3. Here,  $R_f$  was fixed at 1.2 m.  $Z_f$  and  $B$  were slightly adjusted at each  $T_f$ , to keep on-axis heating and center-peaked current profile. In this  $T_f$  scan, nearly all the power is absorbed by passing electrons which contribute to effective current drive.

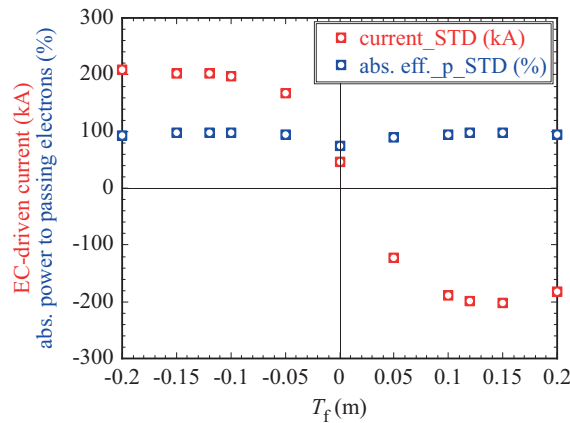


Fig. 3.6-3 EC-driven current as a function of  $T_f$ . Positive direction of current is counter-clockwise looking from top side of the torus.

The magnitude of  $I_{ECCD}$  increases up to  $\sim 200$  kA and then saturates with the magnitude of  $T_f$ . The asymmetry of  $I_{ECCD}$  about  $T_f = 0$  m comes from the upward shift of the start position of the EC-wave beams (that is, center of the final plane mirror).

Thus, the 2-D steerable EC-wave beam injection system is expected to be available for a wealth of physical experiments in CFQS which require power deposition, current, and current profile controls.

All driven current calculations described above are performed with the designed EC wave beam characteristics; circular Gaussian profile focused at the plasma center with a 30 mm waist radius. The narrow power deposition due to the focused beam is advantageous for controlling localized power deposition and current drive, and heat transport analysis. However the driven current profile is too narrow to compensate for the expected wide profile of the bootstrap current [3.6-2], as shown in Fig. 3.6-4 (a). Here, the modification of the beam profile to widen the driven current profile is investigated [3.6-3] by considering a 2D Gaussian beam with a 30 mm waist radius in the toroidal direction and a 160 mm radius in the vertical direction at the plasma center, aiming the beam direction to make the peak position of the driven current profile to be off-axis. In the investigation, realistic injected EC-wave power of 400 kW is assumed. The EC-driven current profile with the modified beam is plotted in red in Fig. 3.6-4 (a), together with the EC-driven current profile with the focused on-axis beam in blue and the typical bootstrap current profile in black. All current profiles are normalized at each maximum value. In the modified beam case, the amount of driven current is 24.1 kA with the same plasma parameters shown in Fig. 3.6-1. Figure 3.6-4 (b) shows the rotational transform profiles of CFQS standard configuration in vacuum (green), with the current of 24.1 kA driven by the modified EC wave beam (red), and with the bootstrap current assuming the amount of 24.1 kA (black). Here, the two kinds of currents are in opposite directions. A rotational transform profile with the bootstrap and modified EC-driven currents is plotted in light green. Although the procedure of compensation for the bootstrap current profile by the modified EC wave beam is not optimized in this study, because of the center-peaked beam power profile and degradation of current drive efficiency at the outer radial plasma region, sufficient compensations of the bootstrap current profile and the resultant change in the rotational transform profile would be difficult in the Gaussian beam optic framework. To perform sufficient compensation, a more sophisticated design of EC wave beam power profile by a dedicated ECH system is essential.

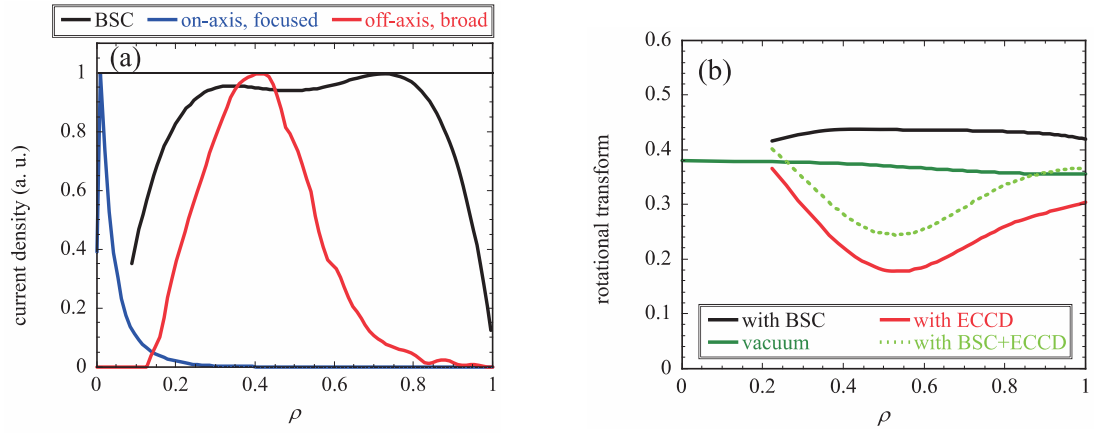


Fig. 3.6-4 (a): Normalized current density profiles in cases of bootstrap current (black), ECCD by on-axis focused beam (blue), and ECCD by off-axis broad beam (red). (b): Profiles of rotational transform in the cases of vacuum field (green), with bootstrap current (black), ECCD by off-axis broad beam (red), and bootstrap current + ECCD (light green).

## References

- [3.6-1] N.B. Marushchenko *et al.*, Phys. Plasmas **18** (2011) 032501.
- [3.6-2] A. Shimizu *et al.*, Plasma Fusion Res. **13** (2018) 3403123.
- [3.6-3] Y. Yoshimura *et al.*, Plasma Fusion Res. **17** (2022) 2402039.

### 3.7 Modular coil design

#### 3.7.1 Modular coil design by NESCOIL

Vacuum equilibrium properties of a toroidal configuration are determined by the shape of the LCFS. Generally, considering the nested magnetic flux surfaces, the VMEC code enables to solve the three dimensional MHD equilibrium accurately and efficiently. In order to achieve the target magnetic configuration, a modular coil system is necessary to be designed to reproduce the plasma boundary. Due to the Neumann boundary condition, the accuracy of the magnetic configuration induced by the coil system is dependent on the normal component of the magnetic field on the plasma boundary, which is expressed as where  $B$  is the vacuum magnetic field generated from the coil system on the plasma boundary and  $n$  is the normal unit vector of this surface. Via the minimization of on the plasma boundary, the modular coil geometry is optimized. Meanwhile, the engineering constraints are taken into account which are the minimum interval between adjacent coils and maximum curvature. This optimization process is accomplished by the NESCOIL code [3.7.1-1]. In the design of the coil system for the CFQS, the coil numbers, major radii and aspect ratio have been scanned to achieve an optimum modular coil system. The corresponding parameters of coil systems are listed in the Table 3.7.1-1. We have designed 10 magnetic configurations and 19 coil systems in total. The  $N_p$  of all configurations is the same, 2.0. Making a comparison among them, the configuration with the major radius ( $R_0$ ) = 1.0 m, aspect ratio ( $A_p$ ) = 4.0, magnetic field strength ( $B_t$ ) = 1.0 T and minor radius ( $a$ ) = 0.25 m is advantageous. In our work, the 20-coil, 16-coil, and 12-coil systems are designed. The results of filament-coil optimization are listed in the Table 3.7.1-2. In comparison of the physics and engineering constraints among them, the table indicates that the 16-coils system is preferable, which shows that the minimum interval between adjacent filament coils is the widest; the minimum radius of curvature is the largest and the magnetic flux surface generated is the closest to the target surface.

Table 3.7.1-1 Parameters for 10 magnetic configurations designed, showing the configuration with the major radius  $R_0 = 1.0$  m, aspect ratio  $A_p = 4.0$ , magnetic field strength  $B_t = 1.0$  T, and minor radius  $a = 0.25$  m.

$R_0$ (m)	$A_p$	$a$ (m)	$B_t$ (T)	Num of modular coils
1.5	3.2	0.47	1.0	20
1.5	3.9(2w39)	0.38	1.0	20
1.5	4.0	0.38	1.0	20
1.5	5.0	0.30	1.0	20
1.2	3.8	0.32	1.0	20
1.2	4.0	0.30	1.0	24, 20, 16, 12
1.2	5.0	0.24	1.0	20
1.0	3.2	0.31	1.0	20, 16, 12
1.0	3.6	0.28	1.0	20, 16, 12
1.0	4.0	0.25	1.0	20, 16, 12
Total	Number of configurations:10		Number of coil systems:19	

Table 3.7.1-2 Parameters of three different types of coil systems for CFQS-2b40.

$A_p$	$R_0$ (m)	$a$ (m)	Number of coils	Minimum distance between coils (cm)	Minimum radius of curvature (cm)	$\mathbf{B} \cdot \mathbf{n} /  \mathbf{B} $	Current per coil (MA)	Cross section of coils (cm <sup>2</sup> )
4.0	1	0.25	20	17.0	18.2	1.11 %	0.2500	17×9
4.0	1	0.25	16	18.5	21.5	0.97 %	0.3125	18×10
4.0	1	0.25	12	14.2	14.7	1.21 %	0.4167	19×13



Fig. 3.7.1-1 gives the of 16-modular coil system. Due to  $N_p = 2$  and stellarator symmetry, the whole torus consists of four symmetric sections. Therefore, the coils system possesses four different shaped modular coils. The centerline of each finite sized coil is assigned by the corresponding filament coil. The all 16 filament coils are from the results of the NESCOIL code. The coil cross section is rectangular and the area is  $13.2 \times 6.9 \text{ cm}^2$  which includes copper conductor, and insulation.

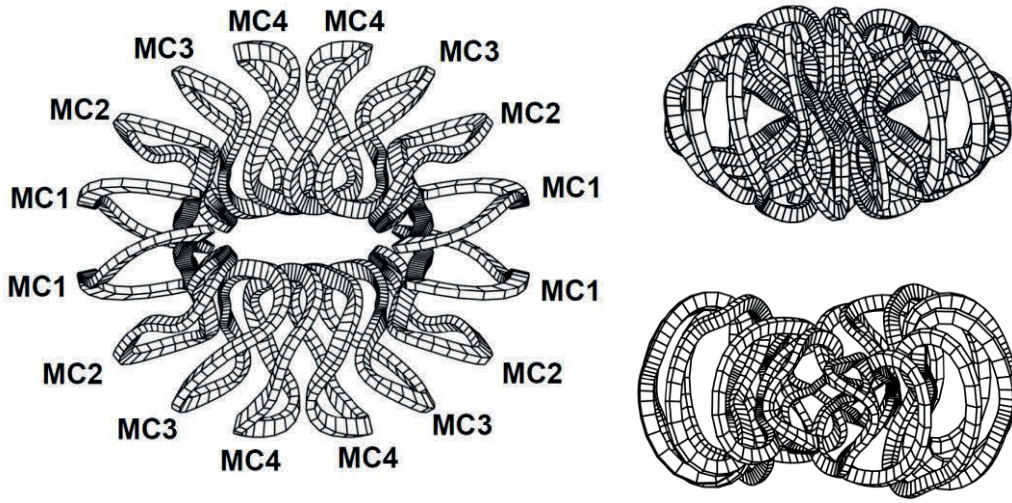


Fig. 3.7.1-1 Modular coils of the CFQS, the top view and side views at toroidal angle= $0^\circ$  (vertical elongation), and  $90^\circ$  (horizontal elongation). The serial number of coils represents the various shapes of coils. The coil system comprises of four different shape coils.

In order to estimate the accuracy of the magnetic configuration induced by the 16-coil system, the coils generated magnetic flux surfaces, rotational transform and Fourier spectrum of the magnetic field strength are calculated. In Fig. 3.7.1-2, Poincaré plots of magnetic flux surfaces and rotational transform induced by the modular coils are analyzed, assuming the coils are filament ones. At the toroidal angle=  $0^\circ$ ,  $45^\circ$ , and  $90^\circ$ , cross sections are displayed. The angle =  $0^\circ$  and  $90^\circ$  correspond to the vertically and horizontally elongated cross sections, respectively. The average of  $\mathbf{B} \cdot \mathbf{n} / |\mathbf{B}|$  on the plasma boundary is below 1%, which cannot be reduced from the viewpoint of the engineering. The rotational transform profile and magnetic well induced by coils and target profile are compared in Fig. 3.7.1-2 (d). Horizontal axis  $\rho$  in this figure represents the normalized average minor radius. The figure shows a good agreement in rotational transform profile and magnetic well depth, between coils induced ones and target ones. From Fig. 3.7.1-2 (a)-(c), they depict a good coincidence in the shapes of a magnetic flux surface and that of target plasma boundary. It should be noted that the width of outmost flux



surface produced by modular coils is larger than that of target plasma boundary, which is beneficial to raise the plasma volume by movable limiters. In order to precisely estimate the QA property of the configuration, the magnetic field strength is decomposed into a Fourier spectrum in the Boozer coordinates. Fig. 3.7.1-3 (a) depicts the spectrum of the magnetic field strength based on the target magnetic configuration. To extinguish the small-amplitude components, the largest component  $B_{00}$  is omitted. In Fig. 3.7.1-3 (a), the magnetic field strength is 1.0 T.  $B_{10}$  is the dominant component resulting from the toroidicity. Other components, such as mirror ripple ( $B_{01}$ ) and helical ripples ( $B_{11}$ ,  $B_{12}$ ), are much less than  $B_{10}$ , which indicates a tokamak-like QA configuration. In Fig. 3.7.1-3 (b), coil induced spectrum of magnetic field strength is given. On the basis of synthetical analyzation, the designed 16-coil system is well workable.

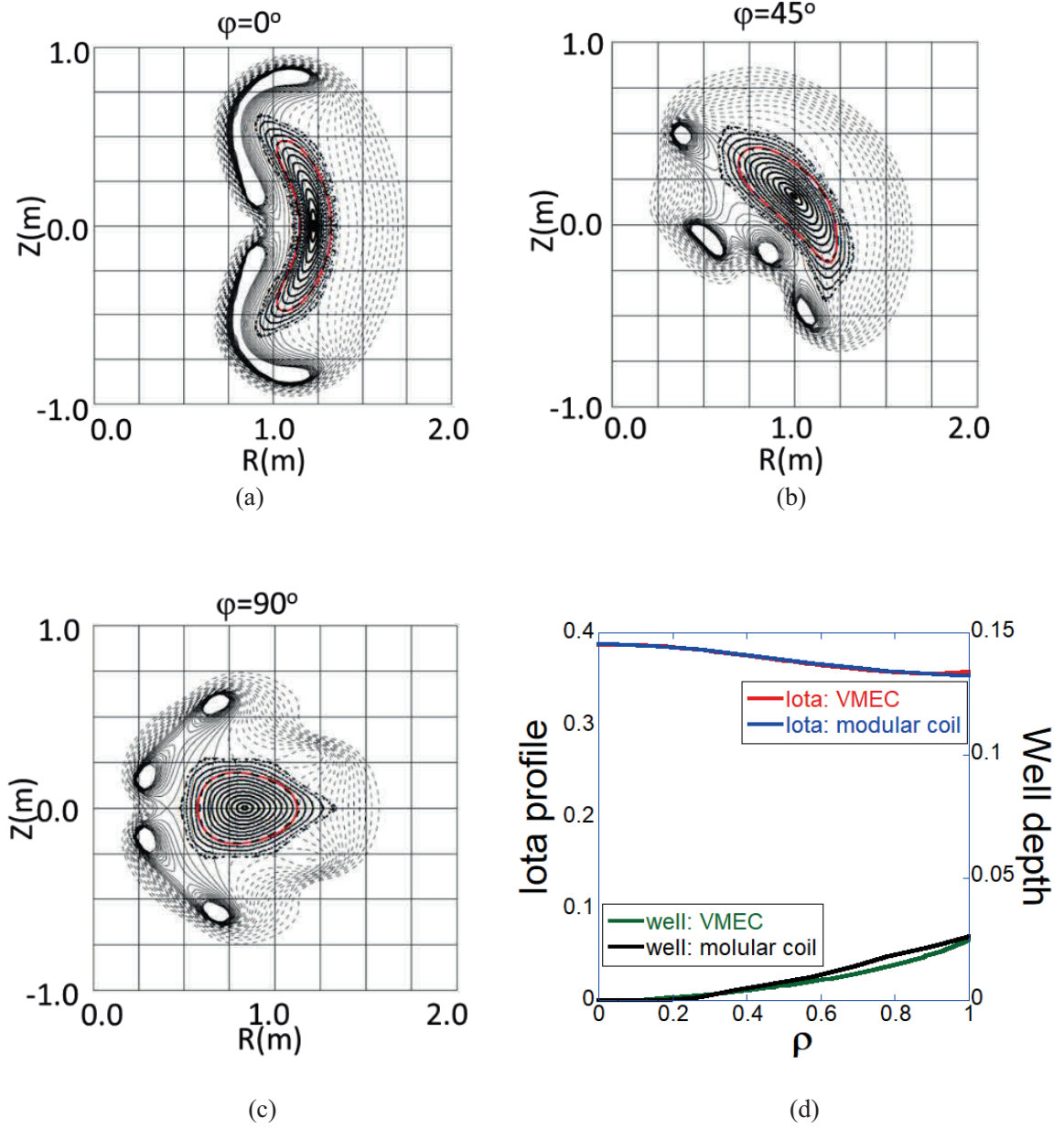


Fig. 3.7.1-2 Poincaré plots of magnetic flux surfaces at the toroidal angle  $=0^\circ$ ,  $45^\circ$ , and  $90^\circ$  for (a)-(c) respectively. The red curve represents the target plasma boundary. (d) shows the comparison of the rotational transform and magnetic well between the configuration produced by modular coils and target one.

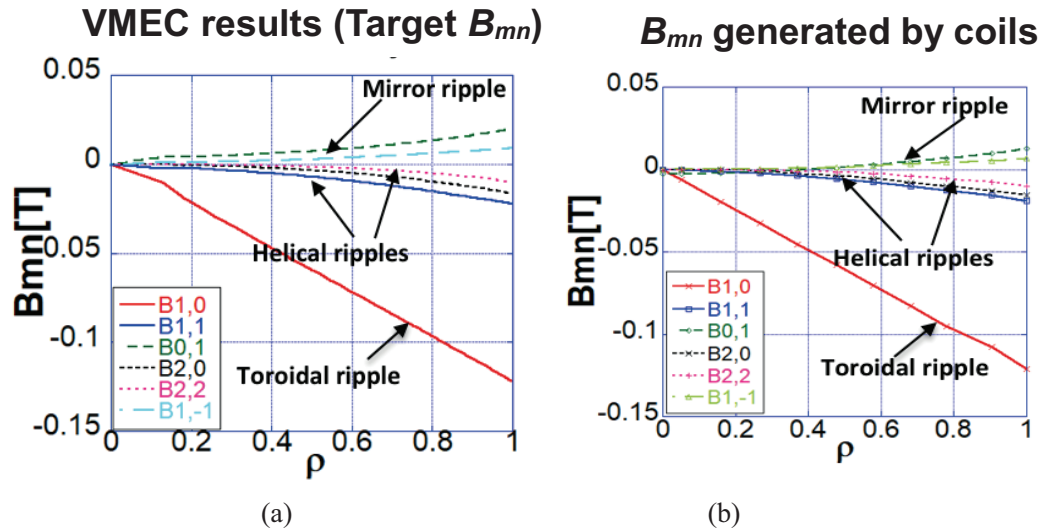


Fig. 3.7.1-3 Fourier spectrum of the magnetic field strength for the CFQS configuration in the Boozer coordinates. (a)  $B_{mn}$  from VMEC results (target spectrum), (b)  $B_{mn}$  generated by modular coils.

#### References

[3.7.1-1] M. Drevlak, Fusion Technol. **33** (1998) 106.

### 3.7.2 Design of modular coils without torsions

In the fabrication of coils, the coil's torsion has a great influence on the difficulty of manufacture. The greater the torsion, the coil is more complex. So, we have optimized the coil system by reducing the torsion.

We compute the torsion by these equations as follows:

For arbitrary point  $r_c$  in the modular coil cross section,

$$\mathbf{r}_c(l, \xi, \eta) = \mathbf{r}_G(l) + \xi \mathbf{u}(l) + \eta \mathbf{v}(l). \quad (3.7.2-1)$$

Tangential vector is as follows,

$$\mathbf{t}_c \equiv \frac{d\mathbf{r}_c}{dl_c} = \left( \frac{d\mathbf{r}_G(l)}{dl} + \xi \frac{d\mathbf{u}(l)}{dl} + \eta \frac{d\mathbf{v}(l)}{dl} \right) / \frac{dl_c}{dl}. \quad (3.7.2-2)$$

Here,  $-x_w \leq \xi \leq x_w$  and  $-y_w \leq \eta \leq y_w$ .

We define vector,

$$\mathbf{b} = \mathbf{t}_c \times \mathbf{u} \quad \mathbf{n} = \mathbf{b} \times \mathbf{t}_c. \quad (3.7.2-3)$$

Torsion,

$$\tau(l) = -\mathbf{n} \cdot \frac{d\mathbf{b}}{dl_c}. \quad (3.7.2-4)$$

We rotate the cross section of coils and calculate the torsion after each rotation. Next, we can find the minimum torsion in our calculated result. When we get the minimum in all cross section, we finish the optimization of the coil [3.7.2-1].

The following figures (Fig. 3.7.2-1~8) show the torsion of the coil without optimization and with optimization, respectively.

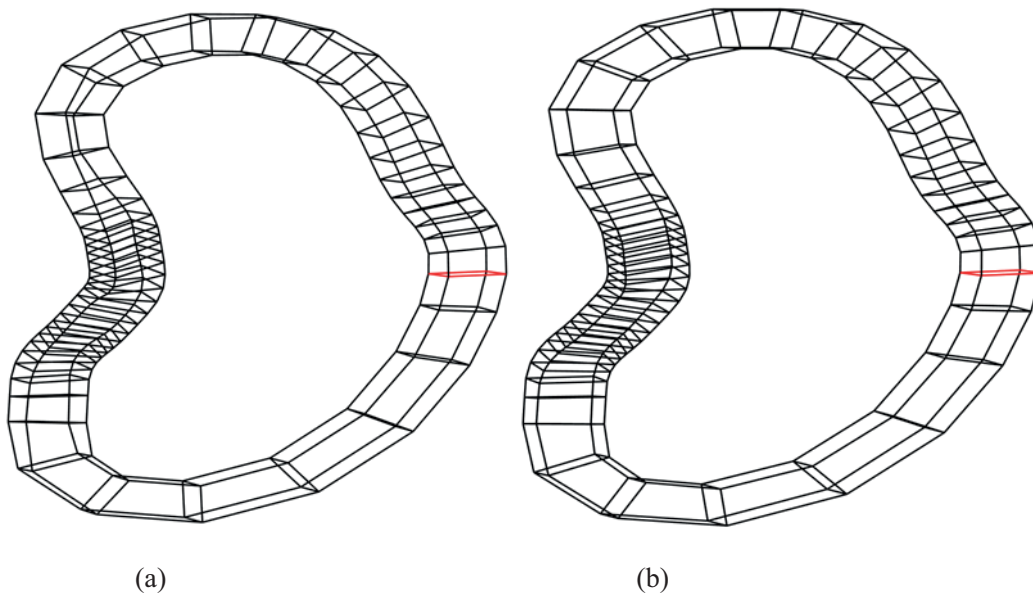


Fig.3.7.2-1 MC1 coil without optimization (a) and with optimization (b). The red line is the first cross section.

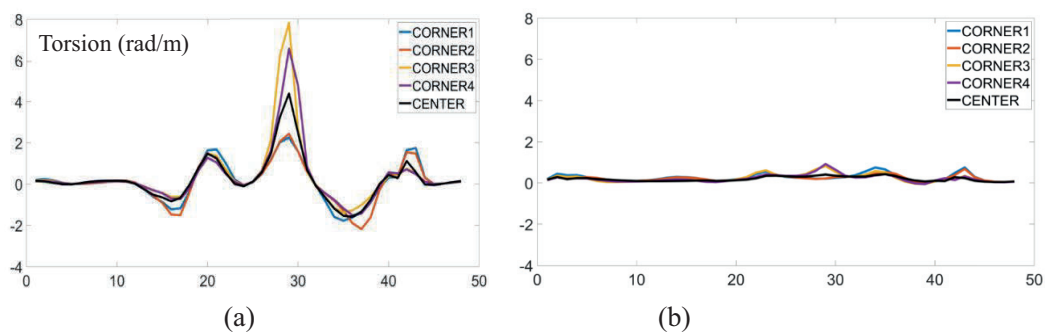


Fig. 3.7.2-2 Torsion of MC1 coil without optimization (a) and with optimization (b).

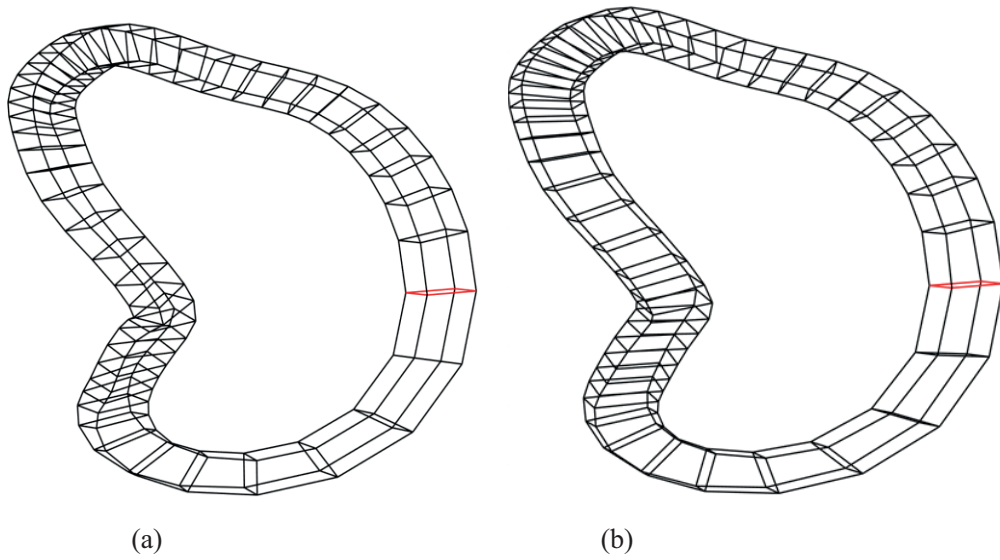


Fig. 3.7.2-3 MC2 coil without optimization (a) and with optimization (b).

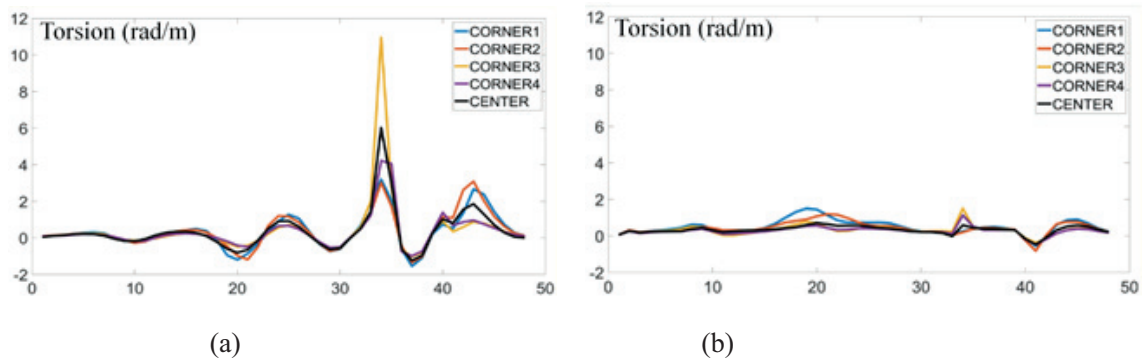


Fig. 3.7.2-4 Torsion of MC2 coil without optimization (a) and with optimization (b).

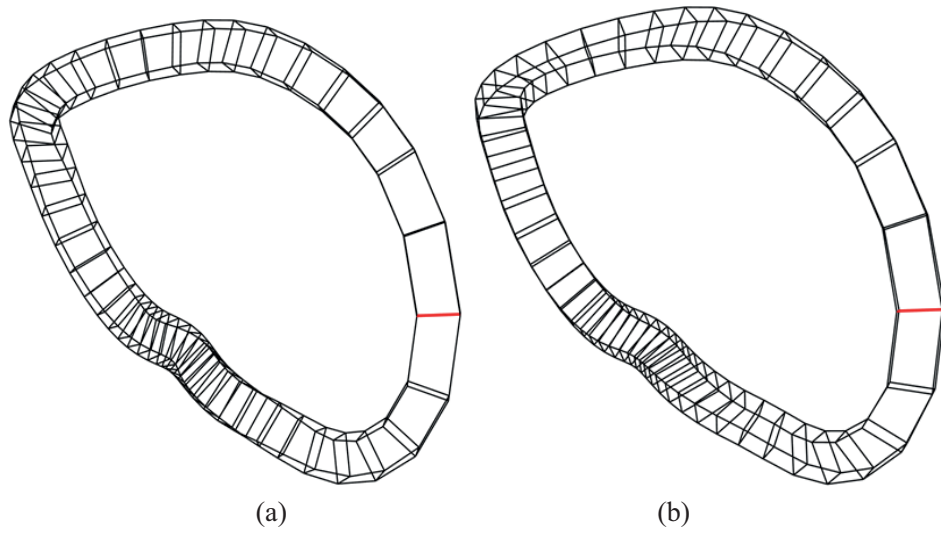


Fig. 3.7.2-5 MC3 coil without optimization (a) and with optimization (b).

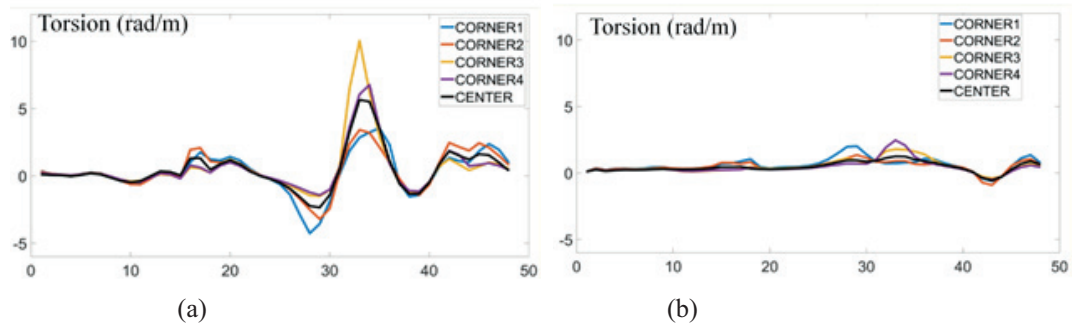


Fig. 3.7.2-6 Torsion of MC3 coil without optimization (a) and with optimization (b).

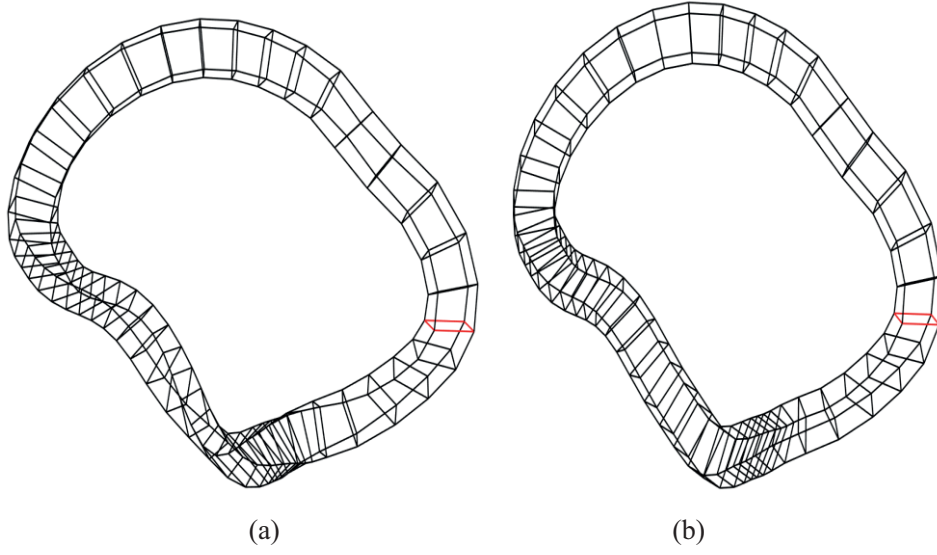


Fig. 3.7.2-7 MC4 coil without optimization (a) and with optimization (b).

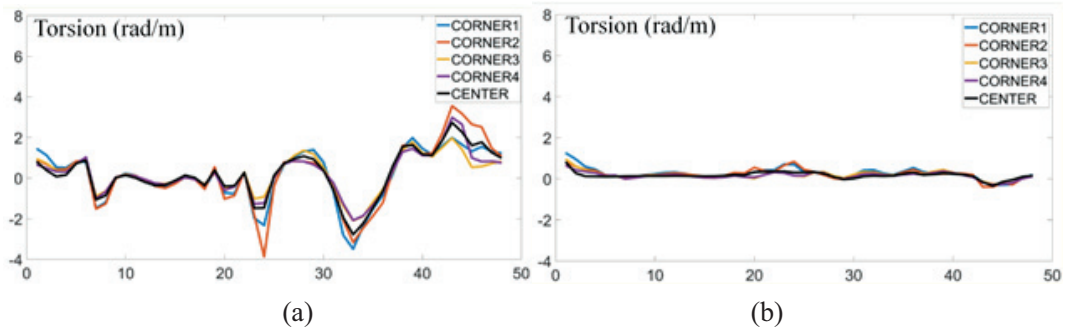


Fig. 3.7.2-8 Torsion of MC4 coil without optimization (a) and with optimization (b).

Through the figures above, it's clearly shown that the torsion has been well optimized.

In addition, curvature is also an important parameter for the coil system, of course, it is not a good parameter for the coil, the equations of curvature as follows:

$$k = \left| \frac{d\mathbf{t}_c}{dl_c} \right| = \left| \frac{d^2\mathbf{r}_c}{dl_c^2} \right|.$$

$\mathbf{t}_c$  is calculated in equation (3.7.2-2) and  $\mathbf{r}_c$  is calculated in equation (3.7.2-1).

Then, we compare the curvature of coils without optimization and with optimization, respectively.



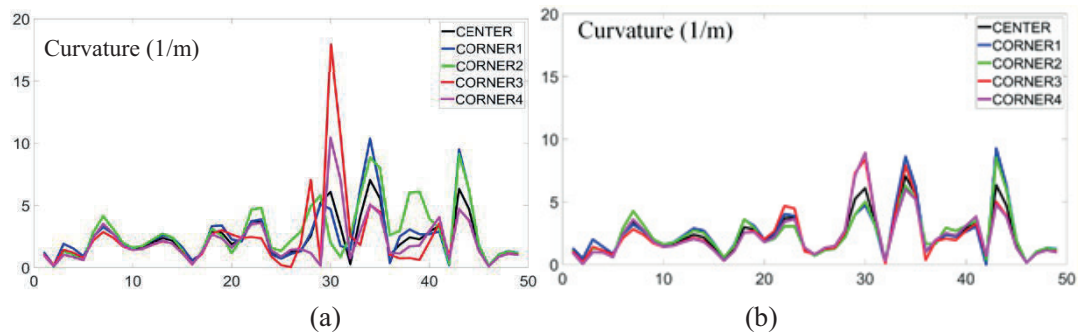


Fig. 3.7.2-9 Curvature of MC1 coil without optimization (a) and with optimization (b).

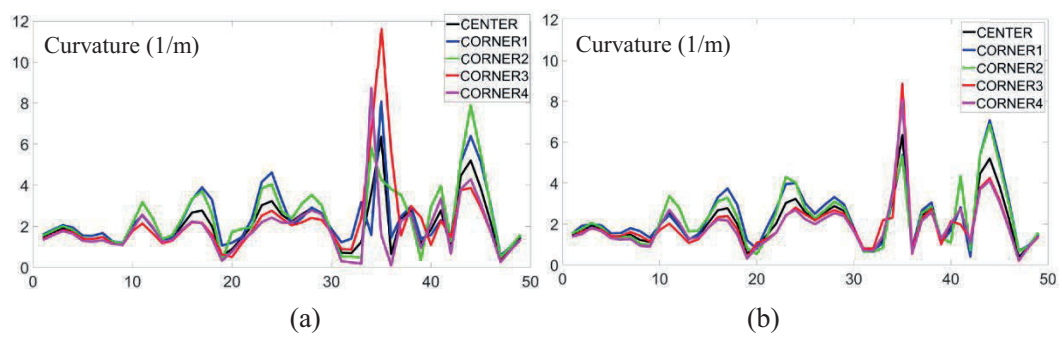


Fig. 3.7.2-10 Curvature of MC2 coil without optimization (a) and with optimization (b).

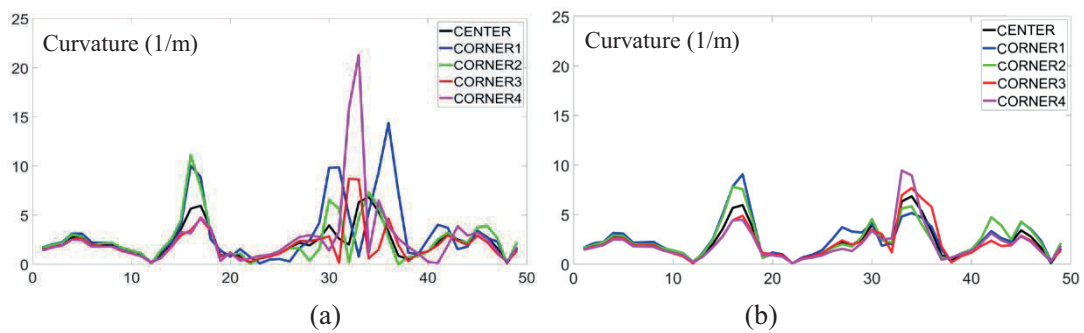


Fig. 3.7.2-11 Curvature of MC3 coil without optimization (a) and with optimization (b).

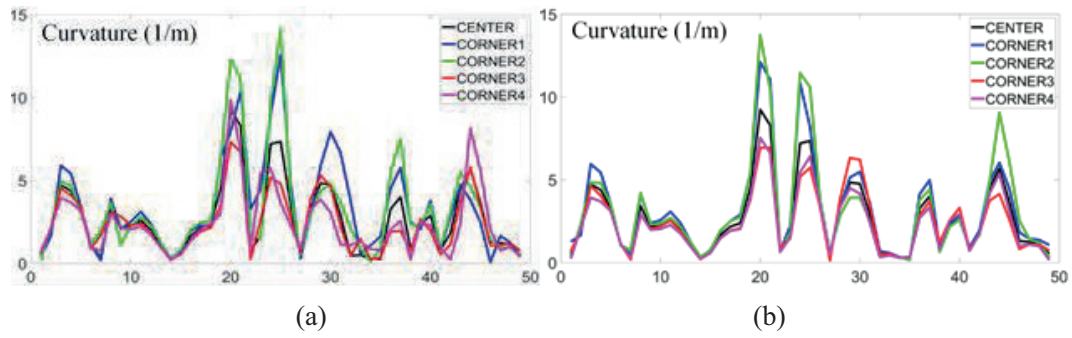


Fig. 3.7.2-12 Curvature of MC4 coil without optimization (a) and with optimization (b).

The above figures (Fig. 3.7.2-9~12) show that the coil optimization for torsion also have a good improvement in curvature. Fig. 3.7.2-13 shows the final results of modular coils with plasma boundary.

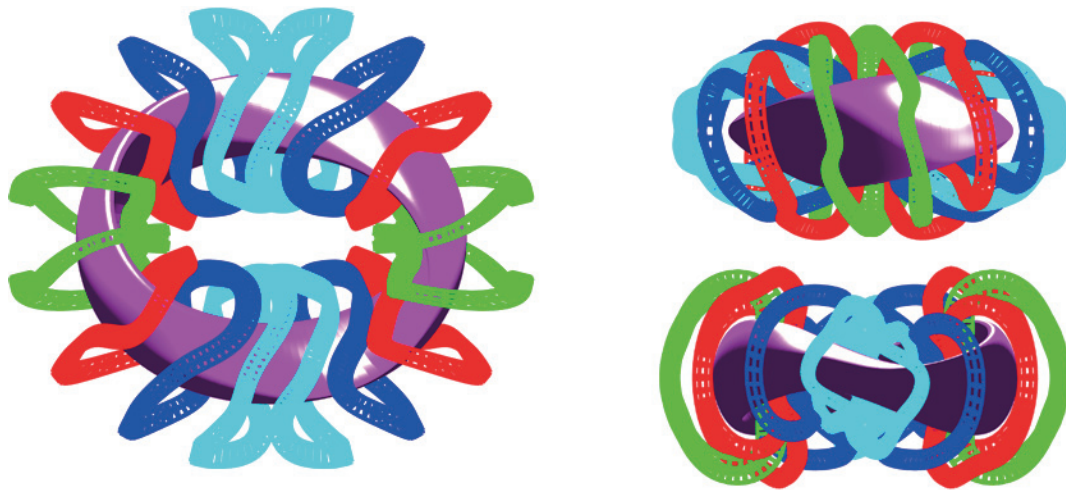


Fig. 3.7.2-13 Modular coils and plasma boundary of CFQS.

## References

[3.7.2-1] Y. Li *et al.*, Plasma Phys. Control. Fusion **62** (2020) 125004.

### 3.7.3 Modular coil design by GOSPEL

Modular and helical coil optimization for CFQS applying the newly-developed coil optimization code GOSPEL [3.7.3-1] has been done. The GOSPEL code has been developed for efficient designing of modular and helical coils using free-form curves without assuming a winding surface, neither giving a specific initial guess of the coil shape from other codes. In the GOSPEL code, a filamentary coil is assumed and expressed using cubic B-spline curve in the three-dimensional real space. The position of the control points of B-spline curve and the current for each of the coils are optimized using the algorithm based on genetic algorithm to minimize the objective function,  $f$ . The objective function includes the normal field component generated by the coils on the target magnetic surface as the primary component. In the calculations shown here, the normal field component of the objective function was defined as  $f_{bn} = (\frac{1}{M} \sum_{j=1}^M |\mathbf{b}_j \cdot \mathbf{n}_j|^2)^{1/2}$ , where  $\mathbf{b}_j$  and  $\mathbf{n}_j$  are unit vector along the magnetic field and the normal vector on the target surface, respectively, and the subscript  $j$  ( $j=1, \dots, M$ ) denotes reference points on the target surface. The engineering components regarding the coil curvature, torsion, distances between coils and target boundary *etc.* can be added to  $f$ .

The boundary magnetic surface of CFQS was chosen as one of the first targets for GOSPEL. First, coil optimization was done assuming modular coils with and without the engineering components. The number of coils, the minimum curvature radius, the minimum distance between coil center, and the maximum coil length assumed in the optimization were imported from the original coil design [3.7.3-2]. Fig. 3.7.3-1 shows the modular coils obtained by GOSPEL with 16 control points per coil considering the engineering components. Note that the coils are drawn as volume coil with square cross section just to enhance the readability of three-dimensional geometry. The coil shape by GOSPEL shows less winding sections compared to the original design by NESCOIL [3.7.3-3] although both designs have almost the same minimum coil curvature. This difference may come from the presence/absence of winding surface and different expressions of coil shape (B-spline/Fourier) employed in these two codes. The Poincare plots of the vacuum magnetic field produced by the modular coils by GOSPEL reproduced the target boundary and VMEC equilibrium well as seen in the right view graph in Fig. 3.7.3-1. The normal field component of this coil configuration was  $f_{bn} = 0.92\%$ .

Next, the optimization of continuous helical coils was done applying GOSPEL. The pattern of the coil arrangement using three helical coils and two poloidal field coils was found to reproduce the optimized stellarator configuration of the Wendelstein 7-X [3.7.3-4] well in the preliminary calculation. Fig. 3.7.3-2 (left) shows the optimized helical coil configuration for CFQS together with the last-closed magnetic surface (LCFS) generated by these coils. One of the helical coils has up-down symmetry and the remaining two helical coils creates up-down symmetry as a pair. For this helical coil configuration, the normal field component was  $f_{bn} = 1.9\%$ . Fig 3.7.3-2 (right) shows the comparison of the Poincare plots including the edge region for this helical coil configuration and the modular coils of Fig. 3.7.3-1. The field lines outside of the LCFS were traced until they reach to the

virtual wall drawn as a gray curve. The modular coils create closed magnetic surface outside of the target boundary while the helical coil create broken magnetic surfaces and divertor-leg-like structure in this region.

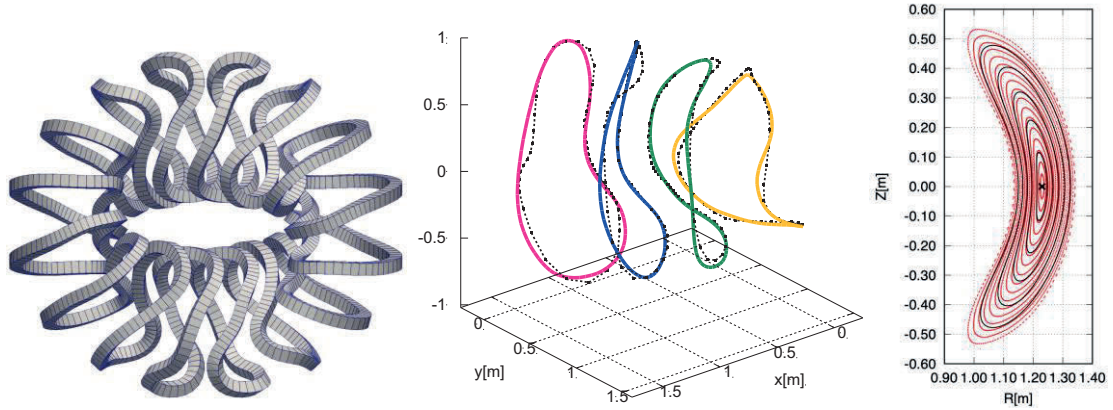


Fig. 3.7.3-1 (Left) Modular coils obtained under the engineering constraints with GOSPEL, (middle) comparison of four unique coils with the original design (symbols connected by dotted lines) in [3.7.3-2], (right) the Poincare plot of the vacuum magnetic field generated by the obtained coils (red) and the target boundary and equilibrium (black curve, magnetic axis is denoted by  $x$ ).

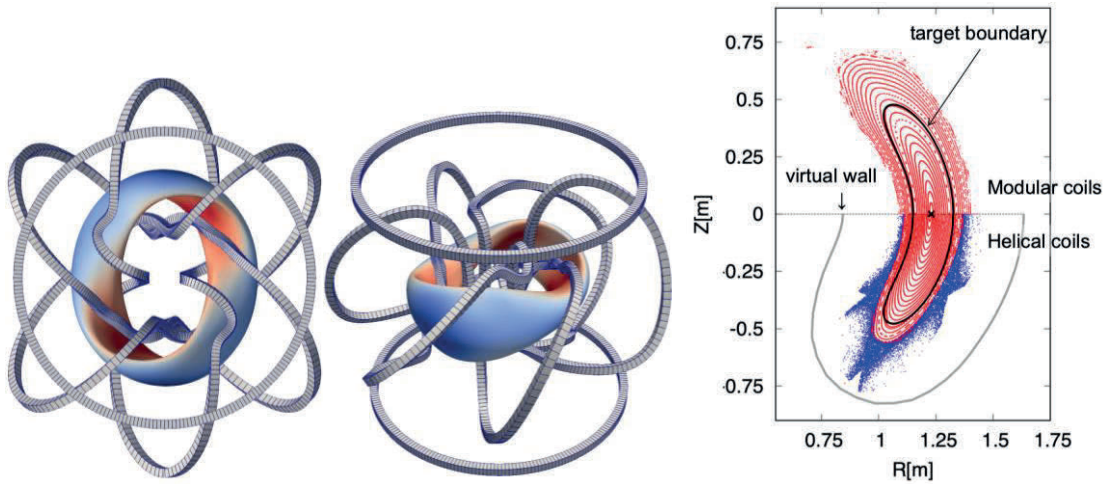


Fig. 3.7.3-2 (Left) Top and perspective views of helical coil configuration for CFQS obtained with GOSPEL. The last-closed magnetic surface generated by these coils is also drawn. (Right) The Poincare plots for the modular (top half) and the helical coil (bottom half) configurations with the target boundary and the virtual wall assumed for helical coil configuration.

## References

[3.7.3-1] H. Yamaguchi *et al.*, Nucl. Fusion **61** (2021) 2106004.

- [3.7.3-2] H. Liu *et al.*, Plasma Fusion Res. **13** (2018) 3405067.
- [3.7.3-3] P. Merkel, Nucl. Fusion **27** (1987) 867.
- [3.7.3-4] T. Klinger *et al.*, Fusion Eng. Des. **88** (2013) 461.

### 3.7.4 Error evaluation using the Hessian matrix method

Plasma performance in magnetically confined fusion devices depends on the quality of the magnetic field. Magnetic field irregularities, namely ‘error fields’, can lead to the destruction of magnetic surfaces and locked modes. One of the main sources of error field is inevitable coil deviations. The stellarator generally has more complicated coils than axisymmetric devices (like tokamaks) and the confining magnetic field predominantly arises from carefully shaped external coils. Therefore, controlling error fields during coil fabrication and assembly is crucial for stellarator construction. As-built coil geometries might differ from designed models in location, orientation or even shape. Coil deviations, as measured between designed models and final built shapes, have different effects on plasma performance. The cost and complexity of a device can increase dramatically with tight construction tolerance. Thus, it is necessary to carry out an error field sensitivity analysis for identifying important coil deviations and determining acceptable tolerance prior to machine construction.

The Hessian matrix can be used for sensitivity analysis. In [3.7.4-1], a Hessian matrix method was described to determine error field sensitivity to coil deviations. The figure of merit used was the root-mean-squared (RMS) normal field error on the target plasma boundary, which comes from the coil design code FOCUS [3.7.4-2]. A quadratic approximation indicates coil perturbation in the direction of the eigenvector corresponding to the largest eigenvalue has the most significant effect on the figure of merit. The Hessian matrix method was then applied to a CNT-like configuration as a proof of principle and the results were consistent with previous observations. The RMS normal field error represents the discrepancy between the desired magnetic field and the one produced by coils, but it does not have any particular physics meaning. In practical situations, what should be considered when evaluating the error field is plasma confinement performance. In this paper, we will implement the Hessian matrix method over the magnetic island size, which is used in most error field studies. Additionally, we would also evaluate the so-called ‘quasi-symmetry’ of the magnetic field, which is the symmetry of magnetic field strength  $|B|$ . Quasi-symmetry has been both theoretically predicted and experimentally confirmed to reduce neoclassical transport and is one of the key qualities used in today’s stellarator optimizations.

Coil optimization consists of varying coil parameters, in whatever representation, and minimizing an objective function which is the weighted summation of multiple penalty functions. Once optimal coils are found, a small change in coil shapes (and currents), which can be described as  $\delta\mathbf{x}$  in parameter space, will cause a departure in the figure of merit away from the optimum. This change can be approximated by

$$\delta F \approx \frac{1}{2} \delta\mathbf{x}^T \cdot \mathbf{H}_0 \cdot \delta\mathbf{x} , \quad (3.7.4-1)$$

where the matrix  $\mathbf{H}$  is known as the Hessian matrix (second-order derivatives). In equation (3.7.4-1), only the quadratic term is left since the linear term is zero at the optimum (stationary point) and we



are only considering a small perturbation (neglecting higher-order terms). The Hessian matrix is symmetric and its eigenvalues are positive. By perturbing coils in the direction of eigenvector,  $\delta x = \xi v_i$ , the change of the figure of merit is

$$\delta F \approx \frac{1}{2} \lambda_i \xi^2 \quad . \quad (3.7.4-2)$$

Its eigenvectors can be ordered by the magnitude of associated eigenvalues  $\lambda_i$ . The first principal eigenvector, which is the one corresponding to the largest eigenvalue, describes the most sensitive perturbation. With the information in eigenvectors and eigenvalues of the Hessian matrix, we can easily identify the sensitivity of the error field to coil deviations.

The Hessian matrix method is applied to CFQS to calculate the sensitivity of quasi-symmetry and magnetic islands to coil deviations [3.7.4-3]. The quality of quasi-symmetry (on one flux surface) can be evaluated using

$$F_{QS} = \sum_{n \neq 0} \left( \frac{B_{mn}}{B_{00}} \right)^2 \quad . \quad (3.7.5-3)$$

Note that  $F_{QS} = 0$  indicates perfect quasi-symmetry of the magnetic field on the reference flux surface. The Fourier component of magnetic field strength,  $B_{m,n}$ , is then decomposed in Boozer angles  $(\theta_B, \zeta_B)$ . The magnetic island width is proportional to the resonant perturbation on a particular rational surface,

$$w = 4 \sqrt{\frac{b_{mn}}{m \iota'_{mn}}} \quad . \quad (3.7.5-4)$$

Both quantities are analytically differentiated in FOCUS and thus the Hessian matrix can be computed. Fig. 3.7.4-1 show how the  $n/m = 4/11$  magnetic island chain changes when the coils are perturbed in the direction of the first principal eigenvector. The magnetic islands are either reduced or enlarged when the external coils are perturbed, which are both deviated from the original state. The corresponding coil perturbation can be viewed in Fig 3.7.4-2(a), where the inboard side of MC1 and MC2 coils is significantly more sensitive than other parts. Similar results can be seen in Fig 3.7.4-2(b) in which the first principal eigenvector of the quasi-symmetry with respect to coil perturbations are shown.

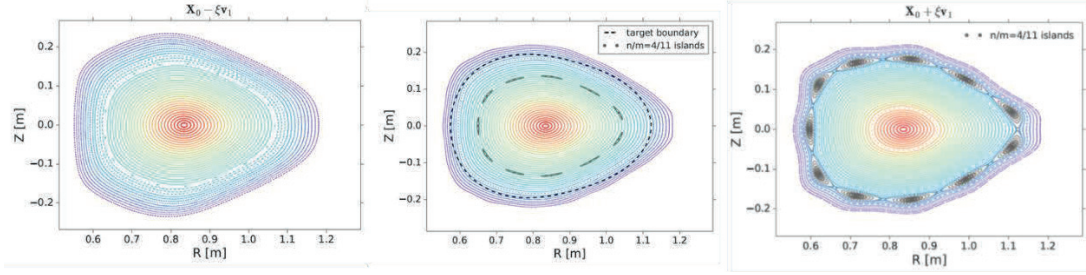


Fig. 3.7.4-1 The  $n/m = 4/11$  magnetic island chain changes with different coil deviations in the direction of the first principal eigenvector, left: negative perturbation; middle: unperturbed coils; right: positive perturbation.

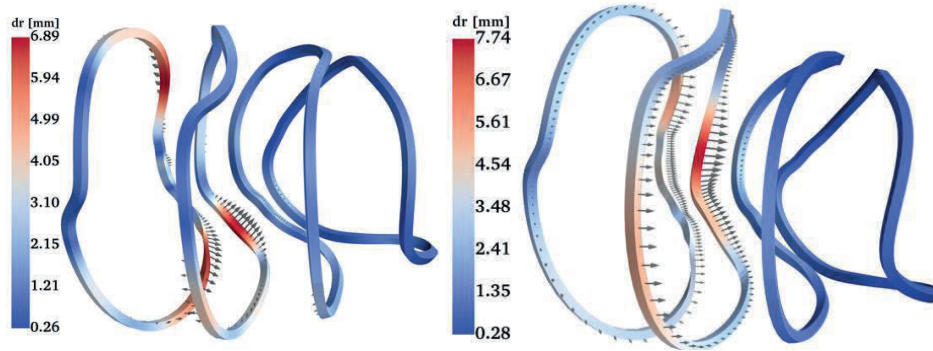


Fig 3.7.4-2 Coil deformations under the first principal eigenvector for (a)  $4/11$  islands; (b) QA quality on the half-toroidal-flux surface. Colors on coils imply the departure distance of data points in each coil and arrows demonstrate the deforming direction.

With the two new figures of merit for quantifying error fields, we have applied the Hessian matrix method to the CFQS device which is under construction. We have successfully found the most effective coil perturbation scheme that will enlarge the  $4/11$  islands. In addition, the important coil perturbations deteriorating the QA on the half-toroidal-flux surface are also identified. These results will provide insights for the upcoming coil manufacture and assembly: avoiding critical coil deformations and relaxing coil tolerance at insensitive parts. A simple estimation indicates that the maximum allowable coil deviation is about 5 mm if 10 % of QA quality deterioration is acceptable. We have also demonstrated the ability to improve coil designs towards better QA quality. This could be used in future coil optimization studies.

## References

- [3.7.4-1] C. Zhu *et al.*, Plasma Phys. Control. Fusion **60** (2018) 054016.
- [3.7.4-2] C. Zhu *et al.*, Nucl. Fusion **58** (2018) 016008.
- [3.7.4-3] C. Zhu *et al.*, Nucl. Fusion **59** (2019) 126007.



### 3.7.5 Influence of stellarator symmetric coil misalignment on magnetic field configuration

To consider the effects of misalignment of modular coils, the following three cases are considered [3.7.5-1]: Case A, where the coils move to radial direction; Case B, where the coils move to the vertical ( $Z$ ) direction; and Case C, where the coils tilt around the cylindrical  $R$  coordinate. Assumptions of these three cases are shown in Fig. 3.7.5-1. The displacement structure has stellarator symmetry for the simplicity of calculation. Herein, stellarator symmetry means that for the radial deformation,  $\Delta R(\varphi, \theta) = \Delta R(-\varphi, -\theta)$ , and for the vertical deformation,  $\Delta Z(\varphi, \theta) = -\Delta Z(-\varphi, -\theta)$  are considered. Here,  $\varphi$  and  $\theta$  are the toroidal and poloidal angles, respectively. Moreover, a toroidal periodicity of two is assumed. Hence, in Case A, eight modular coils move to the radially outward direction and another eight modular coils move to the radially inward direction. The situation in Cases B and C is similar to this. Therefore, eight modular coils move in the same direction. For the deformation, the toroidal mode number of eight is considered to investigate the effect of main highest mode. The low mode will be included in future analyses for a more comprehensive understanding of the deformation effect on magnetic field properties.

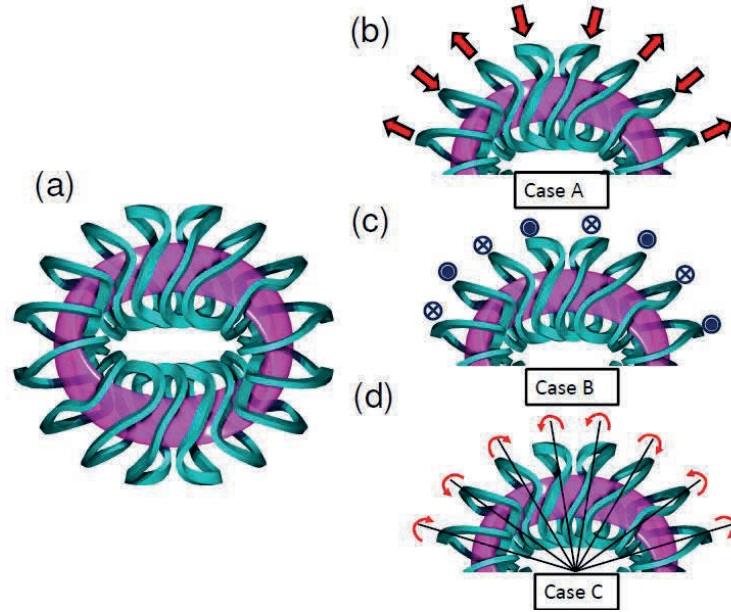


Fig. 3.7.5-1 (a) the top view of modular coil system of the CFQS. (b) assumed coil displacement of Case A, with coils moved to the radial direction. (c) Case B, with coils moved to the vertical direction, and (d) Case C, with coils tilting around the cylindrical  $R$  coordinates.

Magnetic surfaces are considered for these three types of displacements, as shown in Fig. 3.7.5-2. The displacement magnitudes are illustrated as follows: Fig. 3.7.5-2(a) depicts magnetic surfaces for the case where no displacement is considered. Fig. 3.7.5-2(b) is for  $\Delta R = 10$  mm in Case A, Fig. 3.7.5-2(c) is for  $\Delta Z = 10$  mm in Case B and Fig. 3.7.5-2 (d) is for  $\Delta\theta = 0.6$  degrees in Case C. The red line depicts the originally designed plasma boundary surface of the CFQS. Magnetic surfaces exist outside

the red line, so that the limiter in the actual experiment will determine the outermost magnetic surface. Generally, good magnetic surfaces are maintained in all cases of displacement are considered. We checked the good magnetic surfaces up to the displacement of  $\Delta R = 50$  mm,  $\Delta Z = 50$  mm, and  $\Delta\theta = 3.0$  degrees. Therefore, magnetic surfaces are very robust.

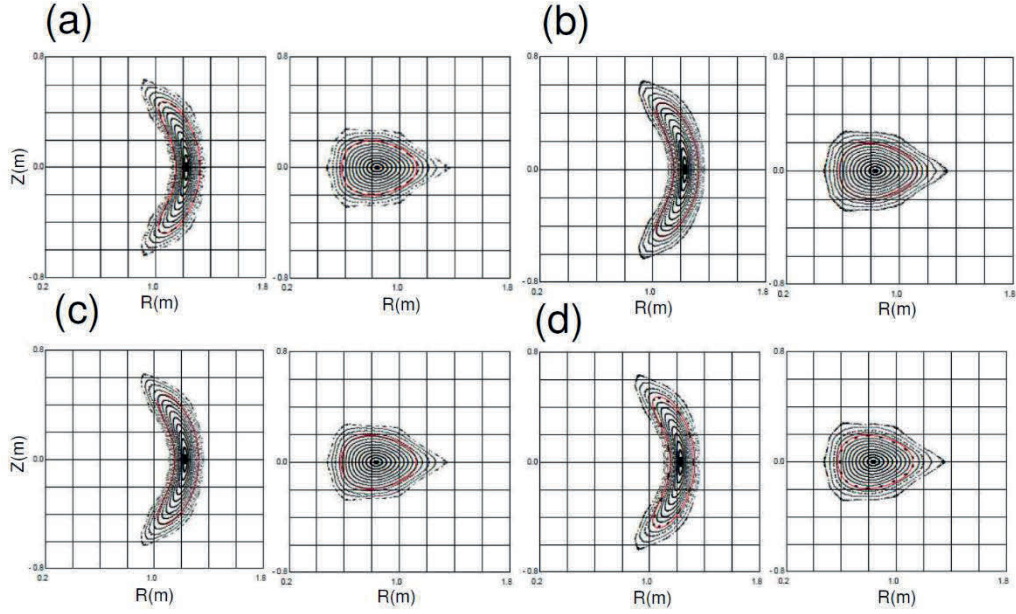


Fig. 3.7.5-2 Poincare plots with (a) no displacement of coils, (b)  $\Delta R = 10$  mm displacement in Case A, (c)  $\Delta Z = 10$  mm in Case B, and (d)  $\Delta\theta = 0.6$  degree in Case C.

Fig. 3.7.5-3 shows changes in the radial profile of rotational transform in Case A, B, and C.  $\Delta R$  and  $\Delta Z$  are scanned from 5 to 50 mm, and  $\Delta\theta$  is scanned from 0.3 to 3.0 degrees (these values of  $\Delta\theta$  correspond to the change in the maximum displacement of coil position from 5 to 50 mm). As shown in these figures, the effect of the misalignment on the rotational transform is small; therefore, islands caused by the low mode rational surface do not appear in the magnetic field configuration. Fig. 3.7.5-4 shows the change in the radial profile of the magnetic well depth. In all cases, the magnitude of change is very small.

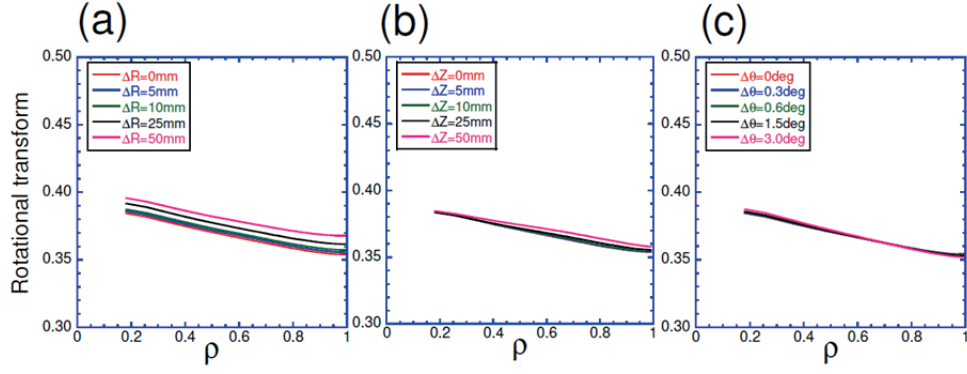


Fig. 3.7.5-3 Radial profile of rotational transform, with horizontal axis as the normalized minor radius. (a) change in the rotational transform for Case A, (b) Case B, and (c) Case C.

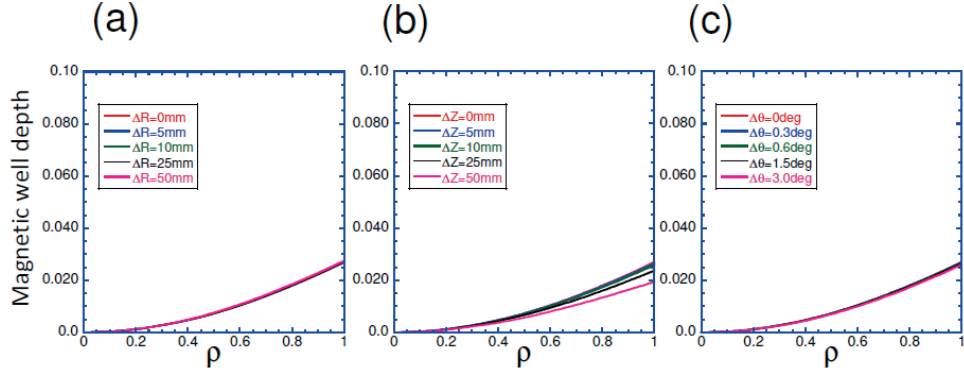


Fig. 3.7.5-4 Radial profile of magnetic well depth. (a) change in magnetic well depth for Case A, (b) Case B, and (c) Case C.

The effective helical ripple,  $\varepsilon_{eff}$ , is employed because the neoclassical diffusion coefficient in the  $1/\nu$  regime,  $D_{NEO}$ , is proportional to  $v_d \varepsilon_{eff}^{3/2} / \nu$ . Here,  $v_d$  is the drift velocity, and  $\nu$  is the collision frequency. Fig. 3.7.5-5 shows the radial profiles of the  $\varepsilon_{eff}^{3/2}$  calculated from NEO code [3.7.5-2] for the displacement in Case A (Fig. 3.7.5-5 (a)), B (Fig. 3.7.5-5 (b)), and C (Fig. 3.7.5-5 (c)). The quantitative estimation of effects of the displacement of coils on neoclassical transport becomes directly possible from these figures.

If the displacement of modular coils is less than 10 mm, the physical properties such as magnetic surfaces, the profile of rotational transform, and magnetic well depth are not significantly changed according to the calculation results. For the neoclassical diffusion coefficient estimated from  $\varepsilon_{eff}$ , the magnitude does not change. Meanwhile, if the displacement reaches 25 mm, a few factors of  $D_{neo}$  will increase. Therefore, if the displacement of coils is less than 10 mm, main physical properties such as the rotational transport, magnetic well, and QA property do not change significantly. Naturally, this

conclusion is limited to the case where the displacement structure has stellarator symmetry (and toroidal periodic number is two).

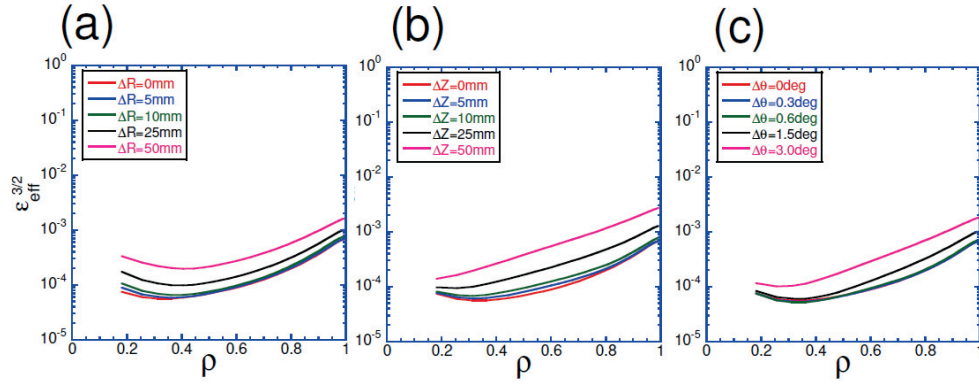


Fig. 3.7.5-5 Radial profile of effective helical ripple,  $\varepsilon_{eff}^{3/2}$  (a) change in effective helical ripple for displacement in Case A, (b) Case B, and (c) Case C.

## References

- [3.7.5-1] A. Shimizu *et al.*, Plasma Fusion Res. **14** (2019) 3403151.
- [3.7.5-2] V. V. Nemov *et al.*, Phys. Plasmas **6** (1999) 4622.

### 3.7.6 Influence of general coil misalignment on magnetic surfaces

Coil misalignment will affect magnetic field configuration. Estimating these effects are important for determining an acceptable tolerance error in a process of constructing and assembling the modular coils. We have calculated magnetic field produced by the modular coils adding some displacement to the coils and evaluated differences in the results [3.7.6-1]. We consider three directions of the coil displacement as shown Fig. 3.7.6-1 and two types of combination of the coil displacement (Case A and Case B) as shown Fig. 3.7.6-2.

According to this calculation, we found that a change of rotational transform, *i.e.*  $iota$  with displacement in  $Z$  direction tends to be larger than the other directions. Fig. 3.7.6-3 shows the  $iota$  dependence on displacement in  $Z$  direction. These are values on a magnetic surface where its average minor radius is 0.05 m. A displacement of MC2 causes larger change of  $iota$ . Therefore, we should give a priority to an accuracy of MC2 during coil assembling process. In addition, Case B also causes a larger change of  $iota$ , and magnetic islands appears with 20 mm displacement as shown in Fig. 3.7.6-4. We think more than 20 mm misalignment is supposed to have significant effect from this result. Thus, we will set an acceptable displacement to be 5 mm for potential error of coil location, because coils will be adjusted by spacer with thickness of 5 mm. For assembling accuracy of positioning, we will set it to be 5 mm, therefore the final acceptable value of total misalignment to be 10 mm.

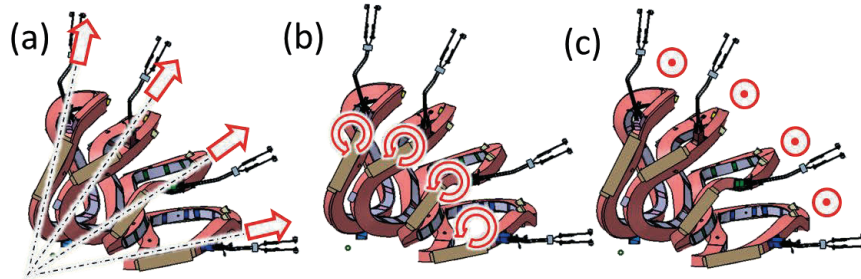


Fig. 3.7.6-1 Direction of MC displacement (a) major radius direction  $R$  (b) rotational direction around vertical axis of each coil  $\alpha$  (c) vertical direction  $Z$ .

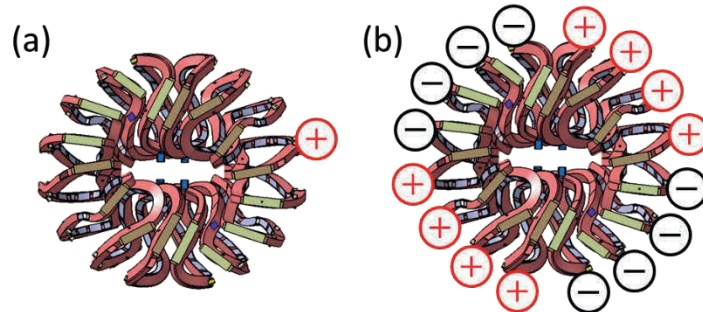


Fig. 3.7.6-2 Combination of MC displacements (a) Case A; One MC is moved (b) Case B; MCs in 90 deg. section are moved together and alternately in toroidal direction.

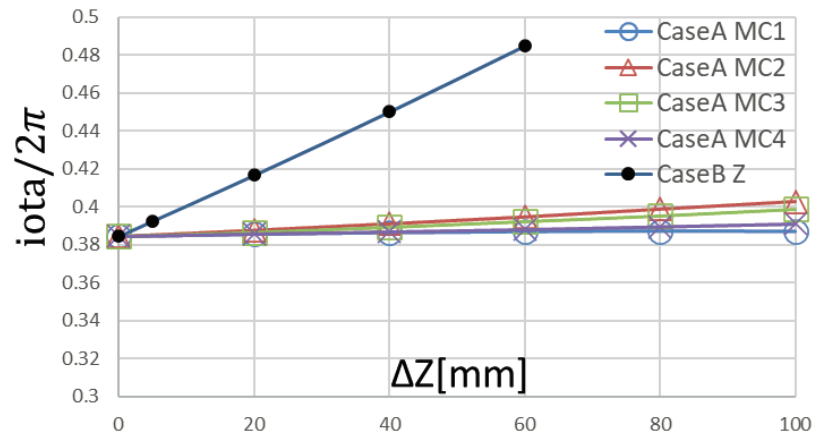


Fig. 3.7.6-3 A change of rotational transform, *i.e.* iota with displacement in Z direction.

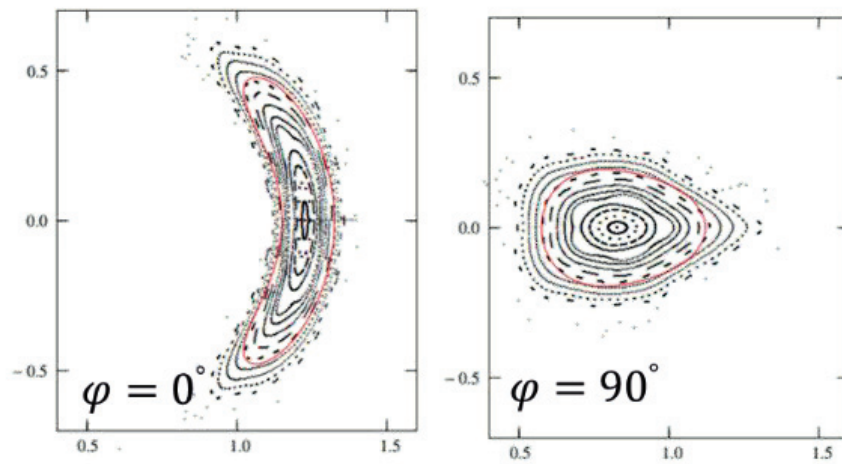


Fig. 3.7.6-4 A plot of magnetic surface in vacuum field with 20 mm displacement in Z direction in case B.

## References

- [3.7.6-1] S. Nakagawa *et al.*, The 23rd IEEE Pulsed Power Conference (PPC) and the 29th IEEE Symposium on Fusion Engineering (SOFE), online, 12-26 December 2021, Poster 366.

### 3.7.7 Effect of modular coil misalignment on magnetic field and particle confinement property

The goal of the CFQS is to realize and examine the QA configuration through experimental research. This is a challenging task since the complexity of stellarator presents numerous challenges during design and construction process. One important issue we consider in this section is the possible misalignment in assembly. The complexity of device raises the likelihood of assembly misalignment, and can lead to the error magnetic field resulting in some problems in experiment. Although the error magnetic field is not preferred in plasma physics study, minimizing the effect of misalignment and deformation is costly. In order to meet the requirement of our design purpose while saving time and resource, an appropriate tolerance for assembling error should be set up for modular coils (MCs) based on physical perspective.

In our previous research, MC misalignments were simply defined as the displacement of an entire MC body in three different directions, while keeping the stellarator symmetry, in which the magnetic field satisfies the condition  $(B_R, B_\phi, B_Z)_{(R, \phi, Z)} = (-B_R, B_\phi, B_Z)_{(R, -\phi, -Z)}$ . Note that this treatment is not very realistic because maintaining stellarator symmetry means that once misalignments in one section of the MCs are assumed, those in the other three periods are automatically determined, neglecting the randomness of misalignments. To be closer to the real situation, we adopted an additional assumption, *i.e.*, a case of breaking stellarator symmetry case.

Generally speaking, the misalignment of MCs in the assembly process is not predictable. Therefore, assuming and checking all cases of MC misalignments are time consuming and are not realistic. Here we consider a couple of possible MC misalignment cases. For simplifying the definition of MC misalignment, a cylindrical coordinate is suitable. A MC misalignment is defined on three axes of cylindrical coordinates, as depicted in Fig. 3.7.7-1.



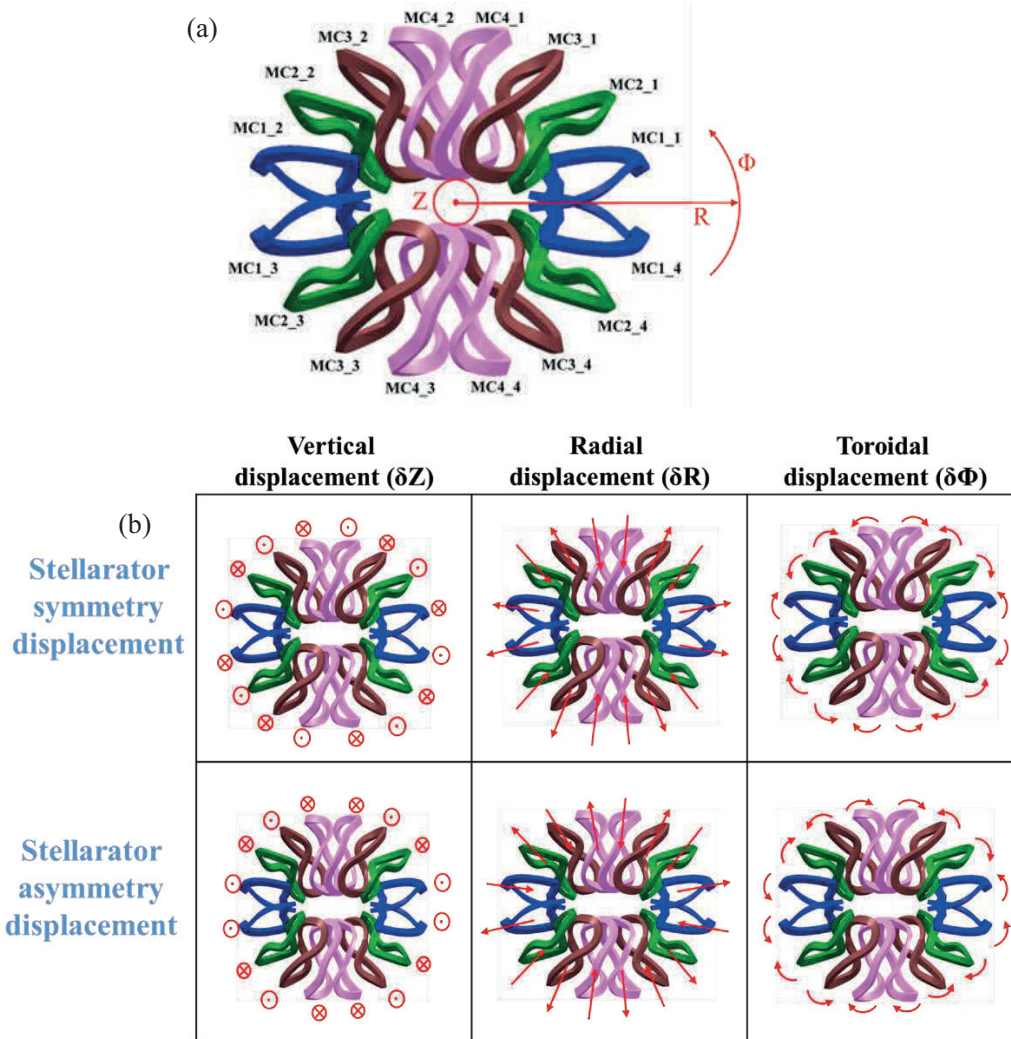


Fig. 3.7.7-1 Definition of modular coil misalignment in this work. Modular coils are displaced on certain direction with same magnitude. (a) The cylindrical coordinates for defining modular coil misalignment. (b) The examples of modular coil misalignment on different direction, with both stellarator symmetry and asymmetry misalignment cases.

To check the effect of MC misalignment on magnetic field property, we use magnetic field line tracing to construct the magnetic field and calculate some essential parameters. A comparison of rotational transform and magnetic well depth between stellarator symmetric (SS) and stellarator asymmetric (SA) misalignment cases is shown in Fig. 3.7.7-2. It is clear that the effect becomes more significant when the misalignment increases in the SS case. Meanwhile, the effect of SA misalignment is negligibly small. This situation may be caused by the coupling effect of SS misalignment and a 3-D magnetic-axis structure.

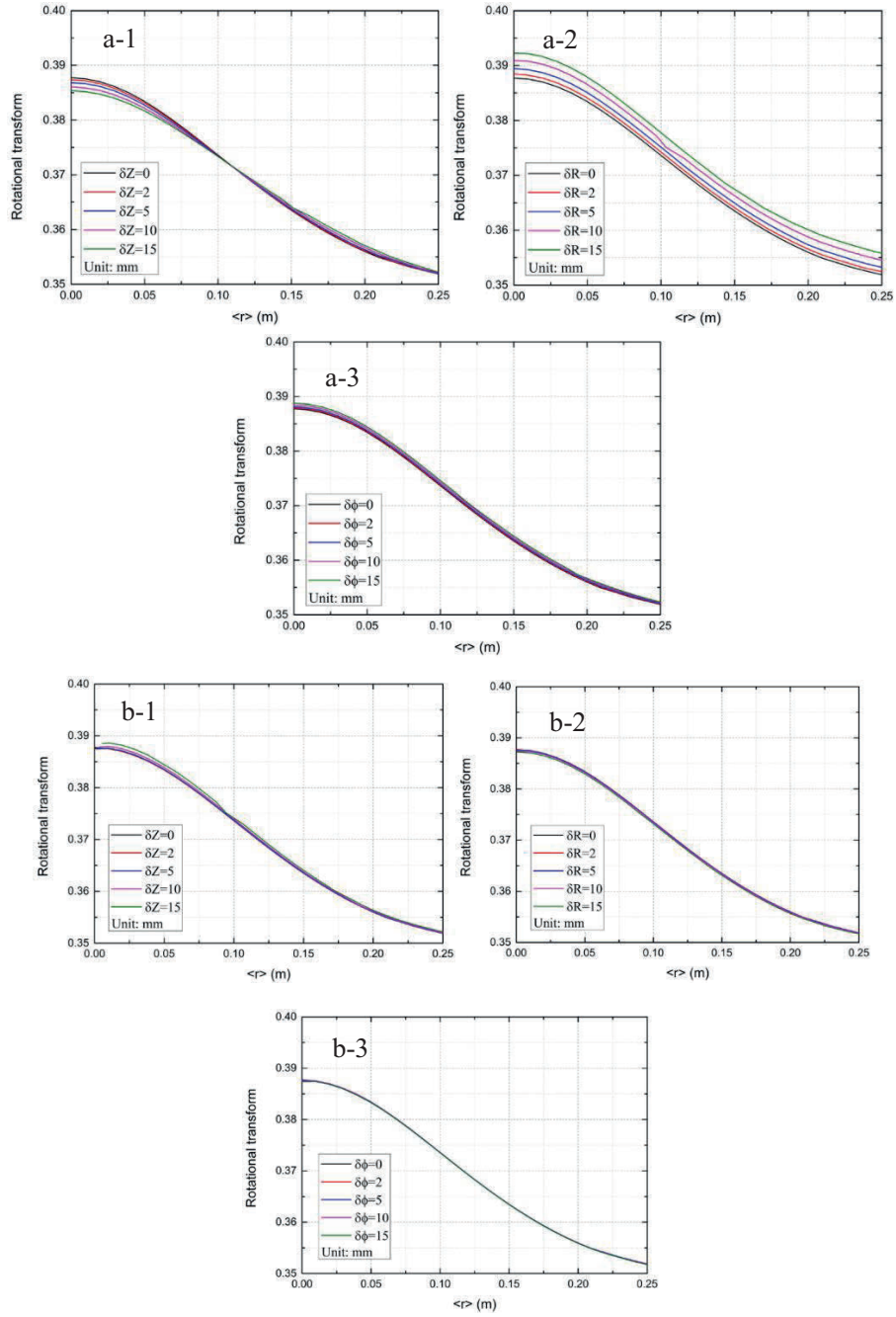


Fig. 3.7.7-2 Radial profile of rotational transform when modular coils are displaced in different directions. Profile of rotational transform in stellarator symmetry misalignment cases shown in a-1, a-2, and a-3. Profile of rotational transform in stellarator asymmetry misalignment cases shown in b-1, b-2, and b-3.

In our assumptions, there is no significant effect on the profile of rotational transform, since it does not cross any low-order rational surfaces *e.g.*,  $n/m = 2/5$  or  $n/m = 2/6$ . But the profile does cross some high order rational surfaces *e.g.*,  $n/m = 3/8$  and  $n/m = 4/11$ . To confirm the effect of MC misalignment

on a magnetic surface, drawing the Poincaré plot of magnetic flux surfaces is necessary. In Fig. 3.7.7-3, we have confirmed that there are no significant magnetic islands inside the main field, which is denoted by the red line. Here the red line represents the LCFS in the CFQS physical design. This means there is no large resonant effect between an erroneous magnetic field generated by MC misalignment and rational surfaces.

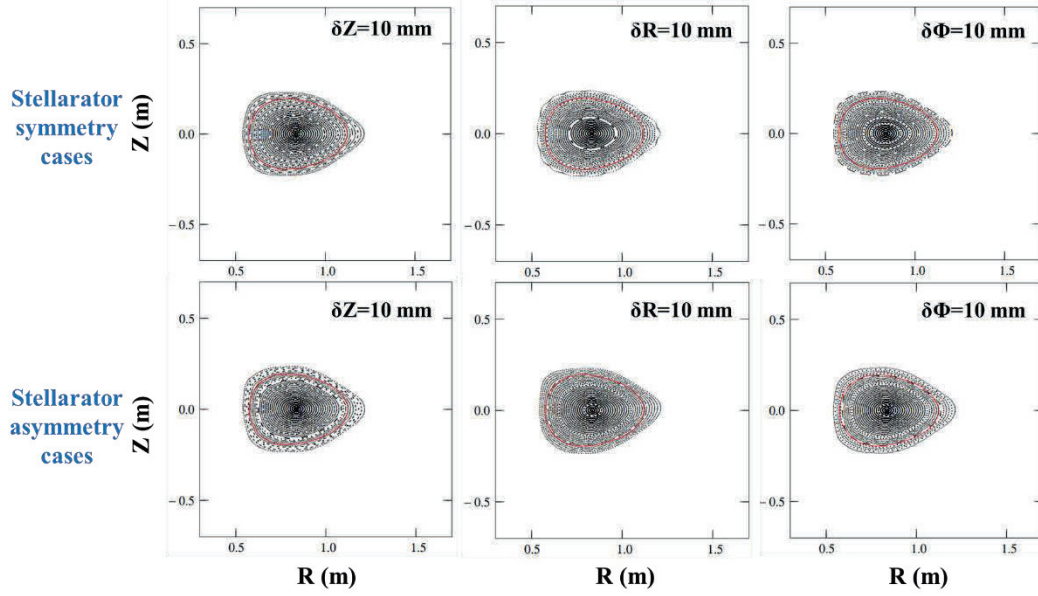


Fig. 3.7.7-3 Poincaré plots of 30 magnetic surfaces in different stellarator symmetry and asymmetry misalignment cases at toroidal angle  $\Phi=90^\circ$ . Red line represents last closed magnetic flux surface in CFQS physical design.

The profiles of magnetic well depth in different MC misalignment cases are shown in Fig. 3.7.7-4. The results indicate that the magnetic well is kept and the MC misalignment does not have a significant effect on magnetic well depth in both SS and SA misalignment cases.

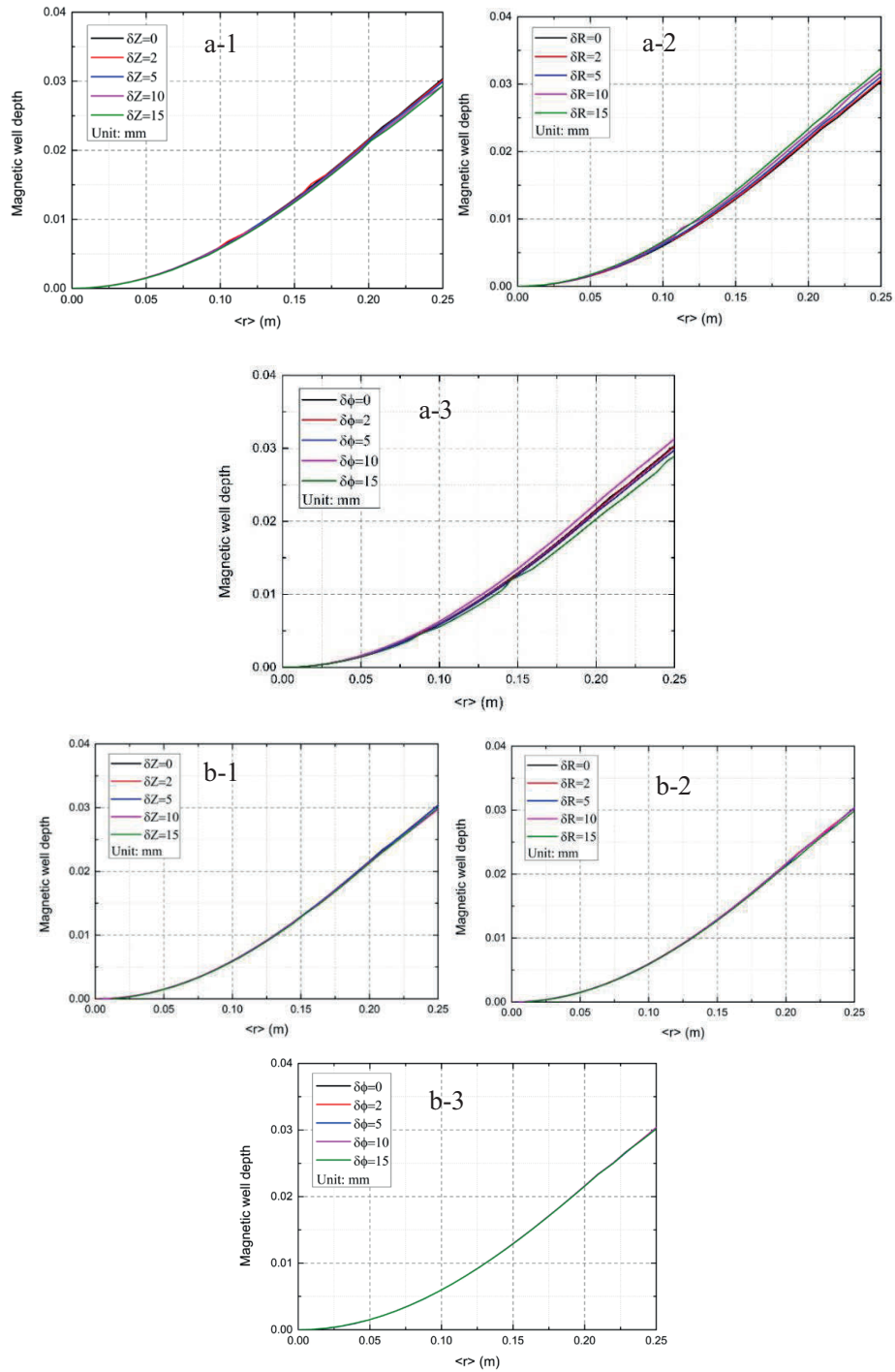


Fig. 3.7.7-4 Radial Profiles of magnetic well depth when modular coils displaced in different directions. Profiles of magnetic well depth in stellarator symmetry misalignment cases are shown in a-1, a-2, and a-3. Profiles of magnetic well depth in stellarator asymmetry misalignment cases shown in b-1, b-2, and b-3.

Our major concern is in the breaking of QA by non-axisymmetry terms. The magnetic field spectra for various MC misalignment cases are shown in Fig. 3.7.7-5. In SS misalignment cases, compared with the standard configuration, the magnetic field components do not vary significantly. Only the  $B(0,4)$  term in the toroidal SS misalignment case appears. In SA misalignment cases, the spectrum of major cosine terms remains conserved. However, some undesired sine terms appear due to the stellarator asymmetry.

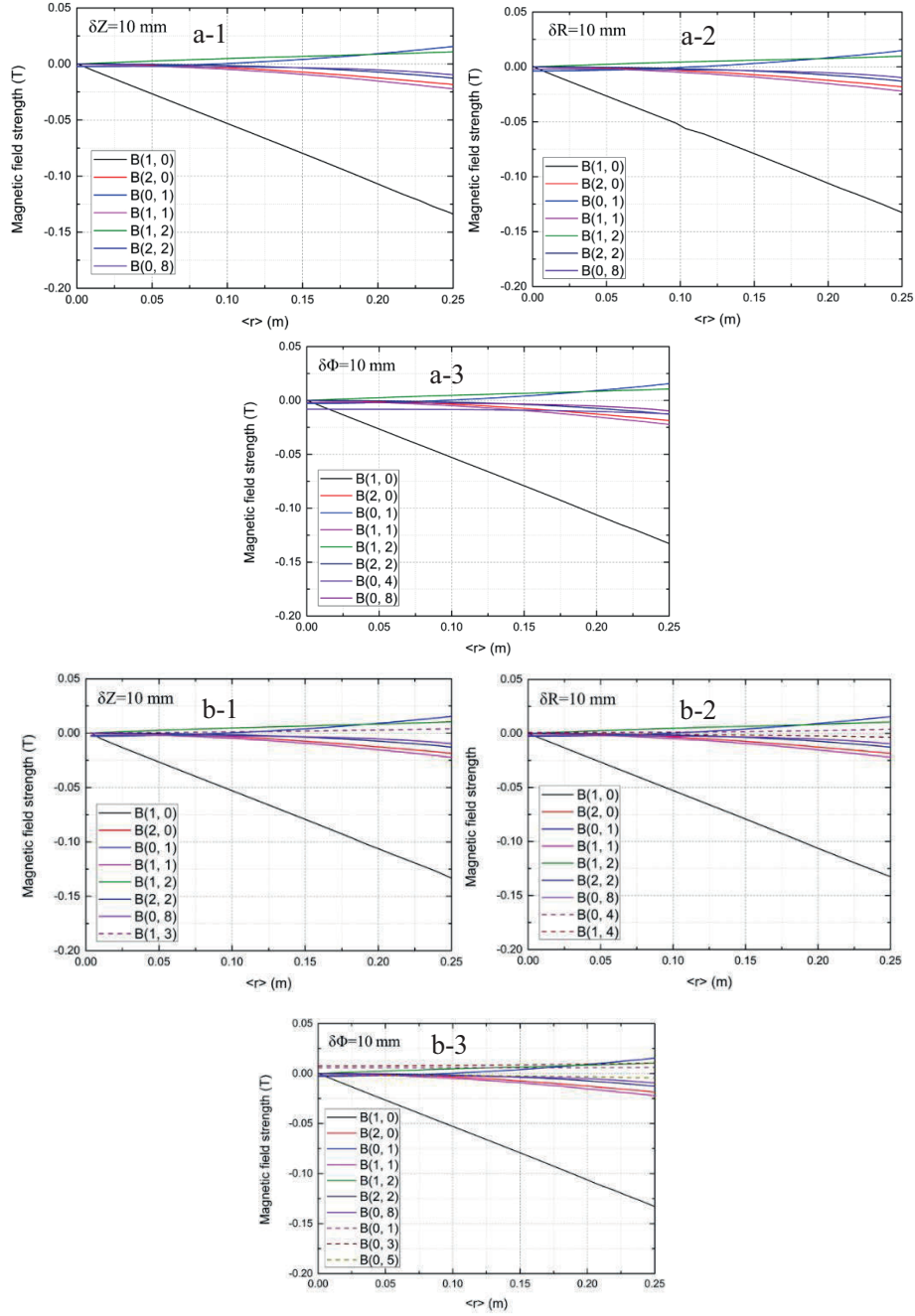


Fig. 3.7.7-5 Major components of magnetic field spectrum in different stellarator symmetry and asymmetry misalignment cases. Here terms only shown whose magnitudes are relatively large. Major magnetic field components in stellarator symmetry misalignment cases shown in a-1, a-2, and a-3. Major magnetic field components in stellarator asymmetry misalignment cases shown in b-1, b-2, and b-3. Solid lines denote major cosine components and dashed lines denote undesired sine terms in magnetic field spectrum.

In Fig. 3.7.7-5, we can observe that the dominant terms in the magnetic field spectrum are not significantly changed, but some specific ones excited by the misalignment appear, such as the unexpected sine terms. To confirm how greatly the confinement is affected due to MC misalignment, a simulation of charged particle orbits tracing is performed.

Guiding center orbit tracing is performed based on the guiding center orbit equations in Boozer's coordinates. In this paper, we considered an estimated energy confinement time ( $\tau_E$ ) to set up the orbit following time. By using the international stellarator scaling-95 law, so-called ISS95, with an assumption of  $T_i=T_e=1$  keV, NBI heating power of 0.8 MW,  $\bar{n}_e=1\times 10^{19} \text{ m}^{-3}$ , the  $\tau_E$  of the CFQS was estimated to be about 2.7 ms. Here, with an enhance factor of 1.5-2.0 in  $\tau_E$  in our consideration, we chose an orbit following time of 5 ms. As for the time step of the calculation, in order to get accurate results, it was set as 0.1  $\mu\text{s}$ . A total 200,000 protons with initial kinetic energy  $E_k=1$  keV were traced in our simulation in collisionless conditions. These protons were all initially located on the  $r/a=0.5$  surface, their position and velocity are distributed uniformly in both spatial and velocity space by use of the Monte Carlo method. The results of the magnetic field line tracing were used for forming the background magnetic field in this calculation.

By counting how many particles escape from the LCFS in the expected  $\tau_E$ , the time evolution of particle loss rate is available. Here we follow collisionless orbits. Because the purpose of orbit calculation is to check that the MHD equilibrium of the CFQS is robust against MC misalignment or not, following the collisionless charged particle orbit is good enough for our purpose. The time evolution of the particle loss rate of SS misalignment and SA misalignment cases is shown in Fig. 3.7.7-6.



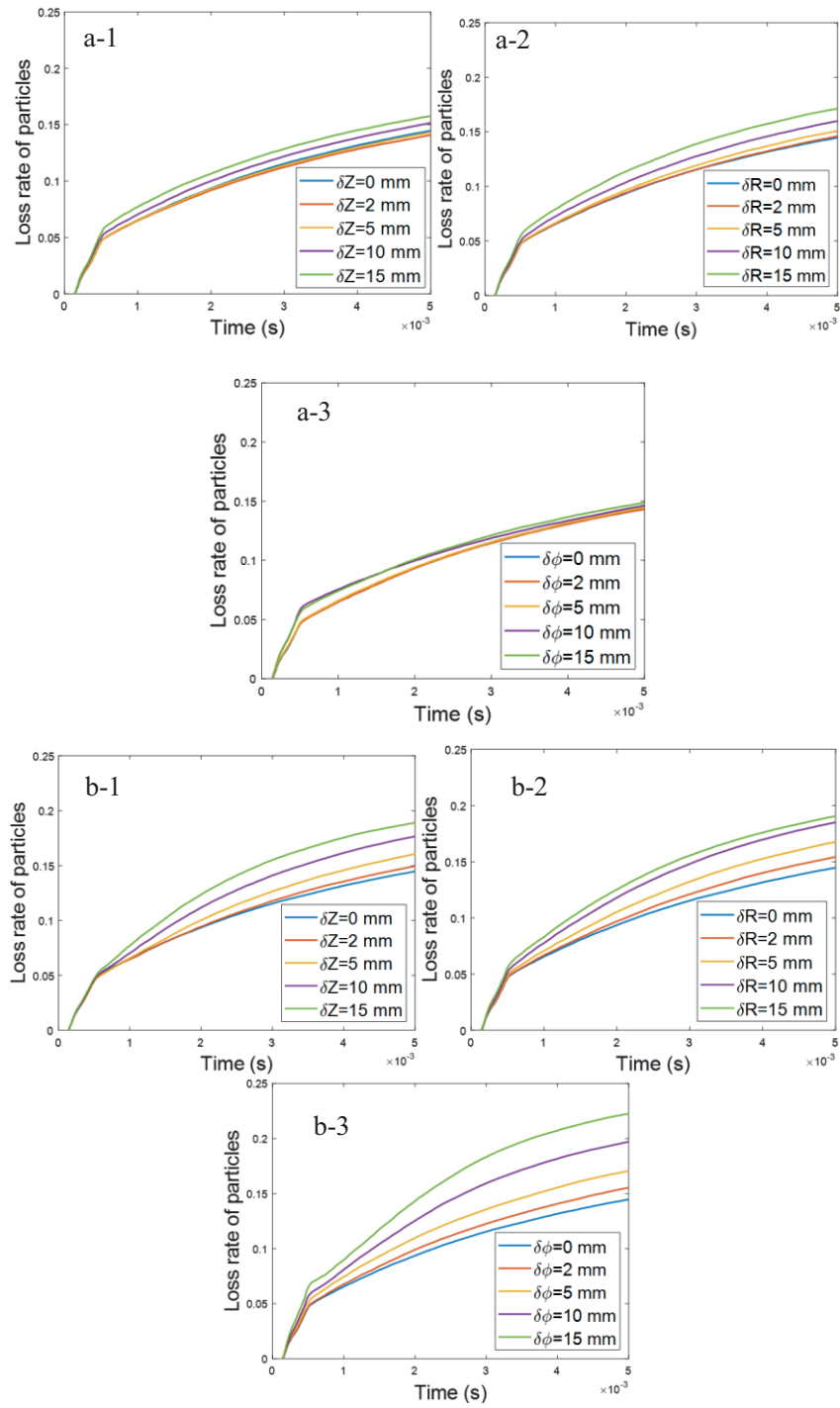


Fig. 3.7.7-6 Time evolution of particle loss rate in different stellarator symmetry misalignment and asymmetry misalignment cases. Particle loss rates in different stellarator symmetry misalignment cases shown in a-1, a-2, and a-3. Particle loss rates in different stellarator asymmetry misalignment cases shown in b-1, b-2, and b-3.

In SA misalignment cases, the loss rate increases with the MC misalignment magnitude. From one viewpoint of the magnetic field spectrum, the main difference between a SA misalignment case and a standard configuration one is in sine terms. It only appears in SA misalignment cases. Comparing SS misalignment cases with SA misalignment ones, the particle loss slightly changes in the former and not as significant as in the latter. Consequently, it looks as if the sine terms lead to deterioration of particle confinement. To verify our prediction, we check the spatial distribution of lost protons in toroidal misalignment cases, as in Fig. 3.7.7-7. The result indicates that the distribution of lost protons changes significantly in a SA misalignment case.

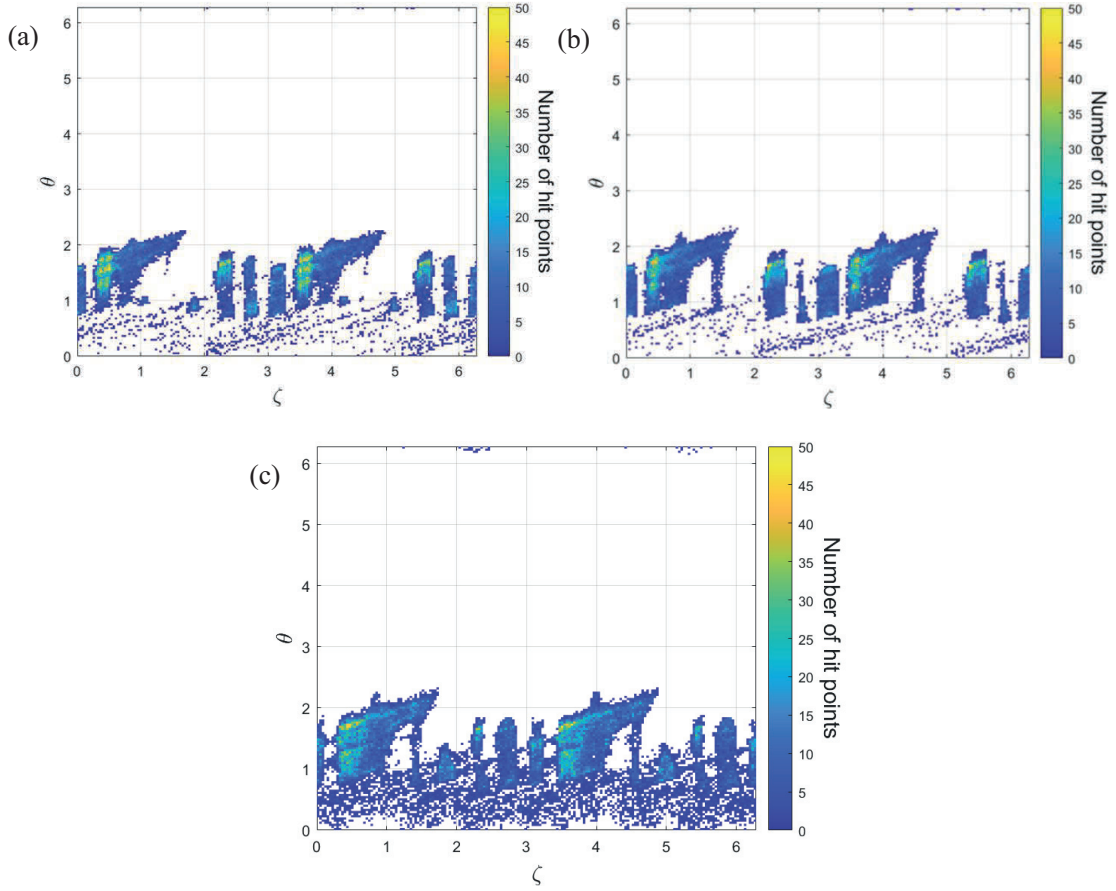


Fig. 3.7.7-7 Distribution of hit points of lost protons on last closed magnetic flux surface in different cases.

(a) Distribution of hit points of lost protons on last closed magnetic flux surface in standard case. (b) Distribution of hit points of lost protons on last closed magnetic flux surface in stellarator symmetry misalignment case with  $\delta\phi$  of 10 mm. (c) The distribution of hit points of lost protons on last closed magnetic flux surface in stellarator asymmetry misalignment case with  $\delta\phi$  of 10 mm.

To further study the difference between cases, comparisons are shown in Fig. 3.7.7-8. Fig. 3.7.7-8 (a) shows the difference of spatial distributions of lost protons on the LCFS between a standard case

and an SS misalignment one with 10 mm toroidal displacement. Fig. 3.7.7-8 (b) shows the difference of distribution of lost protons between a standard case and an SA misalignment one with 10 mm toroidal displacement. It is clearly seen that the number of lost protons decreases at positions where adjacent MCs are moved close to each other. On the contrary, at positions where adjacent MCs are moved away from each other, the number of lost protons increases. This phenomenon is due to the structure of TF ripple changed by the displacement of MCs. When distance between two neighboring ones decreases, the TF ripple between them also become shallower. As a result, particles tend not to be trapped between the two MCs. Similarly, when distance between them increases, the TF ripple well becomes deeper and particles tend to be trapped in it.

The most significant difference between the two cases, *i.e.*, the MCs' SS and SA misalignments, is that the number of lost protons increases in the outboard side (where  $\pi/4 > \theta > 0$ ) in the SA misalignment case. The protons are lost due to grad-**B** drift, strike points of them are mainly concentrated in the upper region of LCFS. This result can be understood by the grad-**B** drift. They are lost through the ripple banana diffusion or TF ripple trapping induced by the discreteness of the MCs. This denotes that the effect of SA misalignment of the MCs is different from that of an SS one. The existence of sine terms leads to a higher particle loss rate. The results also tell us of the necessity of discussing SA misalignment cases.

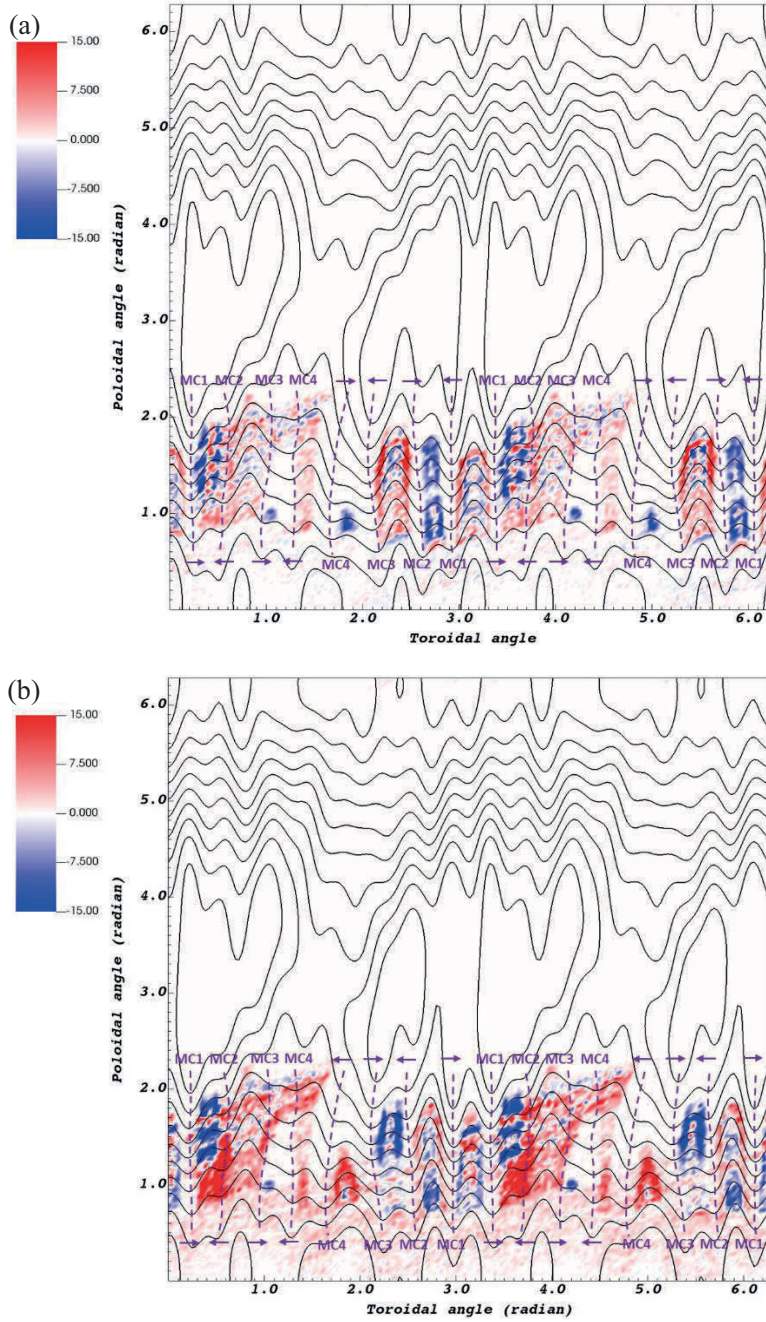


Fig. 3.7.7-8 Difference of distribution of hit points of lost protons at last closed magnetic flux surface on  $\theta$ - $\zeta$  plane. Purple dashed lines denote hill position of magnetic field strength, in other words, position beneath modular coils. Black lines represent contour of magnetic field strength on last closed magnetic flux surface. (a) Difference of distribution of lost protons between standard case and stellarator symmetry misalignment one with  $\delta\phi$  of 10 mm. (b) Difference of distribution of lost protons between standard case and stellarator asymmetry misalignment one with  $\delta\phi$  of 10 mm.

Our analyses tell us that the effect of MC misalignment is not very severe. By assuming a very large misalignment in MCs, *e.g.*, a 15 mm displacement case, the particle loss rate increases only by about 8 %. The increase of loss rate is not significant since in a standard case, more than 14 % protons are lost, due to combination of ripple banana diffusion and ripple trapping, resulting from discreteness of MCs. From an engineering point of view, such a large displacement would not be realistic because the minimal distance between the VV and the MCs is only about 10 mm. Therefore, we can reasonably mention that the CFQS magnetic field configuration is relatively robust against misalignment of MCs. Note that these results are not for defining an explicit tolerance for assembly work but provide a reference for engineers who will make a decision on this issue.

### 3.8 Divertor configuration

In designing the magnetic configuration of an experimental device, the first priority is placed on designing the configuration of the core confinement region. However, it is well known that without a proper design of magnetic configuration of the peripheral region the concept is not useful for the fusion reactor. This is called “divertor design” because the most important physics issue related to the peripheral magnetic configuration is particle and heat removal.

In tokamak research, the concept of divertor is almost established and all existing tokamak devices in the world have similar divertor configuration (single null divertor) with the direct extension to the tokamak demo design. There are still discussions for the new ideas of advanced configurations (double null divertor and snow flake divertor) but they have not been adopted in real experimental devices. In stellarator research, we do not have one established concept of divertor partly because we have varieties of stellarator configurations and divertor concept strongly depends on the magnetic configuration of core confinement region. In fact, for the two largest stellarator experiments, LHD and W7-X, these devices have different divertor structures. In LHD, the intrinsic helical divertor has divertor magnetic field lines connecting the ergodic boundary layer of the core confinement region and the divertor plates on the wall [3.8-1, 2, 3]. In W7-X, the island divertor provides a sophisticated divertor structure combined with small islands created near the boundary of the core confinement region [3.8-4, 5, 6, 7]. For the new stellarator CFQS in China, we are designing a new divertor configuration which provides a sufficiently long connection length of magnetic field lines between the plasma boundary and the wall [3.8-8].

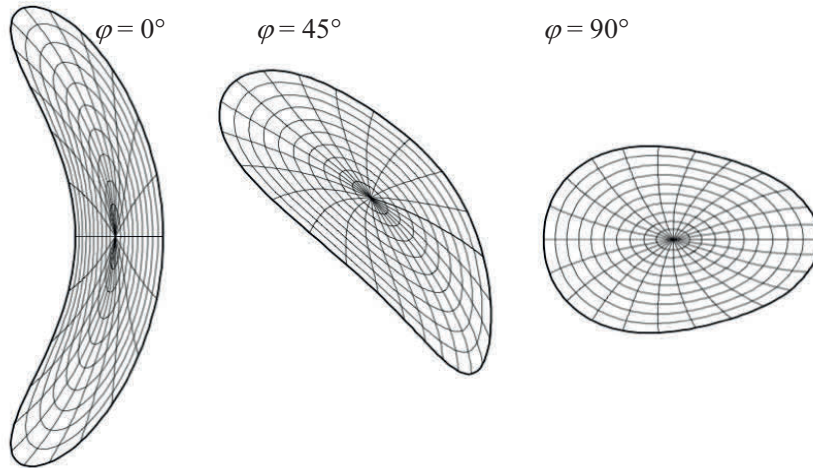


Fig. 3.8-1 LCFS for CFQS advanced stellarator design. Cross sections for three toroidal positions are shown. Here,  $\varphi$  means the toroidal angle.

Three poloidal cross sections of the LCFS of CFQS are shown in Fig. 3.8-1. These figures are VMEC output as a target configuration of the modular coil design. Modular coils were designed to



realize such a magnetic configuration with a choice of the number of coils around the torus as 16 [3.8-9, 10]. The success of this coil design was the most important contribution to the finding of a new divertor concept for CFQS.

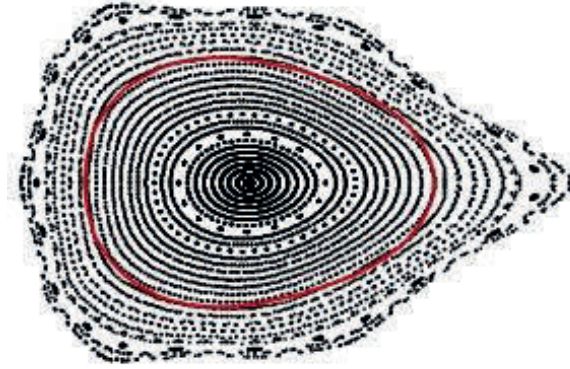


Fig. 3.8-2 Punctual plots of magnetic surfaces for CFQS configuration produced by 16 modular coils. Red line corresponds to the LCFS of the 3rd plot in Fig. 3.8-1.

Fig. 3.8-2 shows the punctual plots of the vacuum magnetic field lines (magnetic surfaces) produced with these modular coils (for the third cross section in Fig. 3.8-1). Red line shows the LCFS of the target configuration in the modular coil design. The magnetic field produced by the modular coils has many closed magnetic surfaces with a larger area beyond the target LCFS. The result of the magnetic structure outside of the VMEC-defined LCFS does not come from the target configuration. In fact, another modular coil design with 20 coils with the same target configuration gave similar magnetic surfaces inside LCFS but the boundary configuration is very different. It has a stochastic layer just outside of the LCFS with small islands ( $n = 2/m = 6$ ) surrounded by the stochastic layer. Fig. 3.8-3 shows the magnetic surfaces produced by 20 modular coils which was not adopted for the CFQS device design. Magnetic surfaces are formed within the LCFS depicted by red lines and the shape of the magnetic surface in the vicinity of the LCFS is very close to the target LCFS shape. The boundary region outside of the LCFS forms stochastic area with islands and the magnetic surface close to the LCFS works as a magnetic limiter of the plasma confinement region. On the other hand, Fig. 3.8-4 shows the magnetic surfaces produced by 16 modular coils, which is the present design of the CFQS device. Clear closed magnetic surfaces are formed in the peripheral region outside of the LCFS. The existence of clear magnetic surfaces in the peripheral region is essentially important for making the bundle divertor configuration for CFQS.



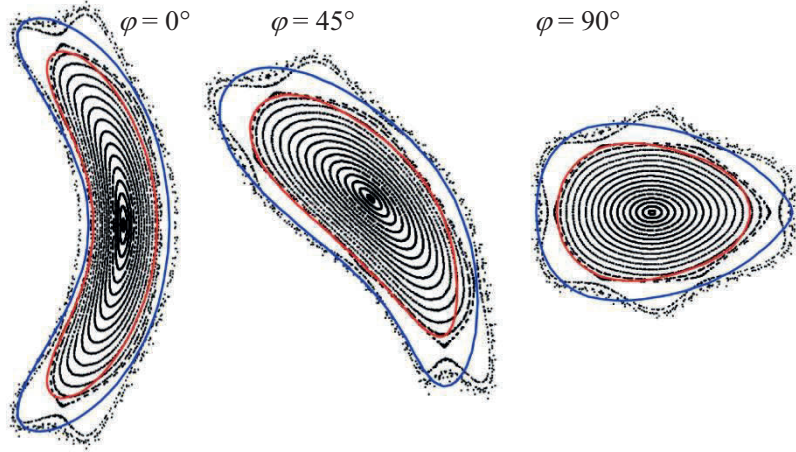


Fig. 3.8-3 Magnetic surfaces produced by 20 modular coils, which was not adopted as the CFQS device design. Magnetic surfaces in peripheral region outside of LCFS are stochastic.

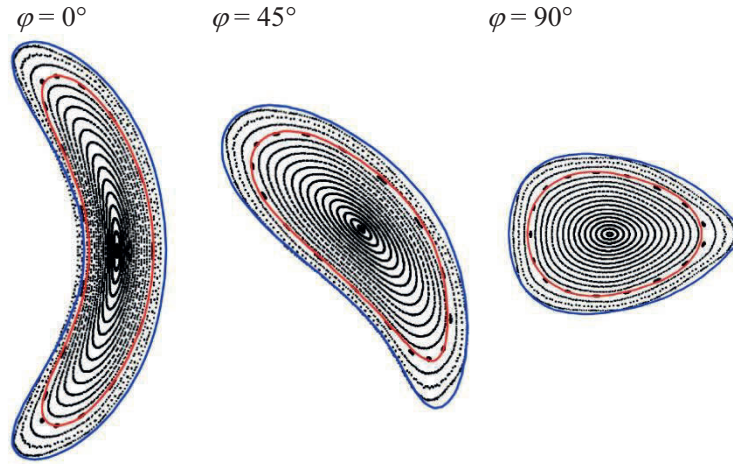


Fig. 3.8-4 Magnetic surfaces produced by 16 modular coils, which was used as the CFQS device design. Magnetic surfaces outside of LCFS are clearly formed.

The blue (lower) line in Fig. 3.8-5 shows the profile of the rotational transform of the vacuum magnetic configuration produced by the 16 modular coils. A very flat profile for the outer region is important for creating large islands for the divertor configuration. The rotational transform profile of W7-X is also flat, but not as flat as that of CFQS. The polarities of the weak shear of both devices are different, namely, the CFQS has a weak negative shear (in the stellarator terminology) at the boundary while W7-X has a positive shear. A black arrow shows the position of the averaged minor radius of the LCFS of the target configuration. Although we decided upon an aspect ratio of 4.0 for the CFQS device, it is technically possible to create a larger confinement region if we design the vacuum vessel with a sufficiently large size to provide space for such larger closed magnetic surfaces. A control of

plasma boundary with a movable limiter might be a possible choice for the plasma operation in experiments.

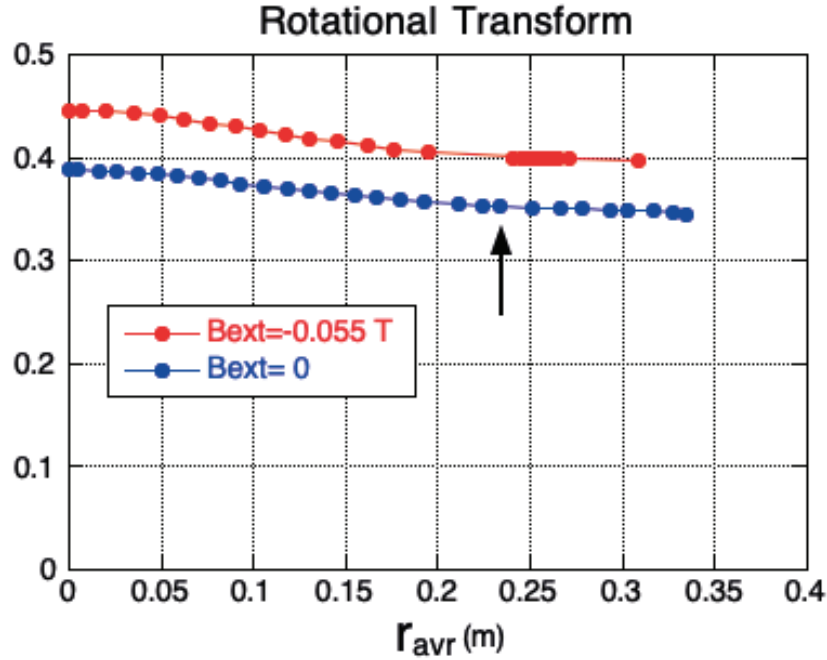


Fig. 3.8-5 Blue [lower] line: Rotational transform profile of vacuum field of CFQS. Arrow indicates the position of LCFS of target configuration. Red [upper] line: Rotational transform profile of island divertor configuration ( $n/m = 2/5$ ) with additional toroidal field.

When we introduce the auxiliary toroidal coils to provide additional toroidal field to the stellarator field produced with modular coils, the magnetic configuration is changed to include large islands at the boundary of the core confinement region shown in Fig. 3.8-6. The QA property is conserved with the additional toroidal field. The strength of the additional toroidal field is  $-0.055$  times averaged toroidal field produced by modular coils. The rotational transform is increased to change the boundary value to  $0.4$  (shown by red (upper) line in Fig. 3.8-5). This is a typical magnetic configuration for any type of stellarator that has a rational value of the rotational transform near the boundary. However, essential differences between the configurations shown in Fig. 3.8-5 from many other cases are 1) large size of islands and 2) the completeness of the island magnetic surfaces. It is shown in Fig. 3.8-6 that clearly formed island bundle flux surrounds the core confinement region with a clearly defined interface of the magnetic field separatrix. This is the reason why we call such a configuration as “island bundle divertor (IBD)”. The entire magnetic confinement area is clearly separated into two regions: hot plasma region in the core and cold plasma region in the periphery.

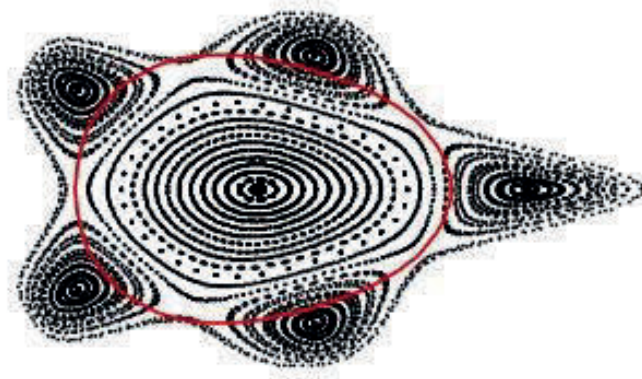


Fig. 3.8-6 Magnetic configuration of island bundle divertor.

Fig. 3.8-7 shows the divertor field line tracing, which is created in the following calculation procedures. We found first the LCFS of the core confinement region. Then we distributed many field line tracing starting points with a small deviation (5 mm for  $R = 1$  m torus) from the LCFS. Because the island magnetic surfaces are complete, there is no escaping field line in such a calculation. Fig. 3.8-7 shows blue line for one of the possible shapes of the vacuum vessel wall. If we install divertor plates at this wall position, the cold plasma in the island bundle flux can be absorbed at the divertor plates. Fig. 3.8-8 shows the divertor tracing with the wall target where the field line tracing is stopped. The pattern of the magnetic field line Poincaré plots is very similar to the tokamak divertor structure. In fact, the transport of the magnetic field lines is exactly the same as tokamak divertor, where the peripheral regions of the divertor are connected to the core confinement region with a clear magnetic separatrix, and magnetic field lines in divertor region have long connection length between the null point and the wall. Because the magnetic field lines go around through all five island bundle fluxes with very small incident angles to the wall, the distribution of the heat load on the divertor plates is determined by the precise geometric design of the shapes and the locations of divertor plates.

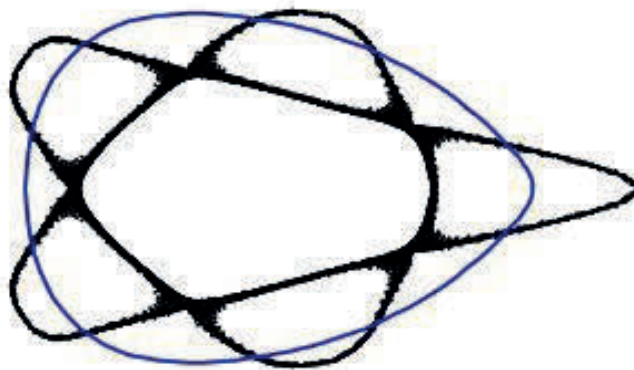


Fig. 3.8-7 Divertor field line tracing for island bundle divertor. Blue line shows one example of vacuum vessel wall position for locating divertor plates.

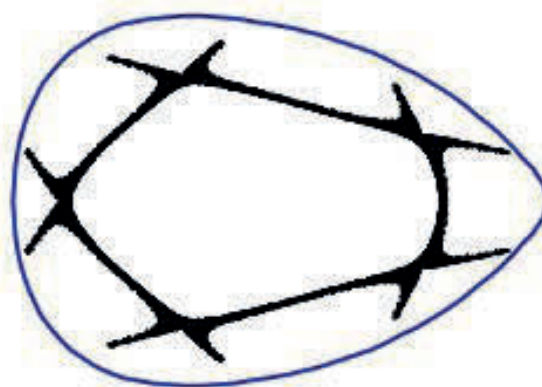


Fig. 3.8-8 Divertor field line tracing with assumed existence of divertor targets.

Fig. 3.8-9 shows the distribution of the connection lengths for magnetic field lines near the X point of inboard side at the toroidal angle  $\phi$  of  $90^\circ$ . The horizontal axis corresponds to the major radius of the calculation point in the poloidal cross section and the vertical axis to the vertical positions (a major radius of the device is 1 m). Calculation was made at 500 points for both horizontal and vertical directions. Three areas are clearly separated by a sharp separatrix created by the islands. A yellow area on the right of X point is the core confinement region, two violet areas above and yellow X point are inside islands and almost black area on the left of X point is outside of islands. In the magnetic island areas, the connection lengths of magnetic field lines are in the range of 500 to 1000 m and there is no exceptional field line with shorter length. This is because the island magnetic surfaces are very regular and there is only little ergodic region between the core confinement region and the island divertor flux. This is a clear difference from the LHD-type divertor structure where there are some field lines with shorter length between the core region and the divertor plate because of the ergodicity of the boundary layer of the core confinement region.

The magnetic field lines located on the separatrix lines (with red color) are parts of the field lines escaping from the core confinement region (yellow color) through the separatrix interface between core and island region. These field lines finally hit the wall (shown by the boundary of the black color area) at the left side of the figure. The position of this strike point moves as the position of the island changes. When the rotational transform value is shifted with the change of the current in the auxiliary toroidal field coils by 2 %, the position of the strike point moves about 1.5 cm along the wall. This sensitivity of the island position is within the controllability of the rotational transform with the auxiliary toroidal field coil.

Because the rotational transform of IBD region is 0.4, island bundles shown in Fig. 3.8-8 are connected together. In other words, this bundle flux is a single flux. Thus particles and heat flux transferred from the core confinement region to the IBD can be removed at any position in the torus.

Because the space between the plasma and the wall is very narrow in the toroidal position of the crescent shape of plasma (the leftmost LCFS in Fig. 3.8-1), we can avoid installing divertor structure at this region and take advantage of installing it where the space is larger. As shown in Fig. 3.8-8, the number of divertor feet is as many as ten. Thus it is possible to reduce the maximum heat load at the divertor compared with the tokamak case, where the number of feet is two (in the case of a single null). On the other hand, because the divertor fields are all connected into a single structure, it is not necessary to install as many as ten divertor plates.

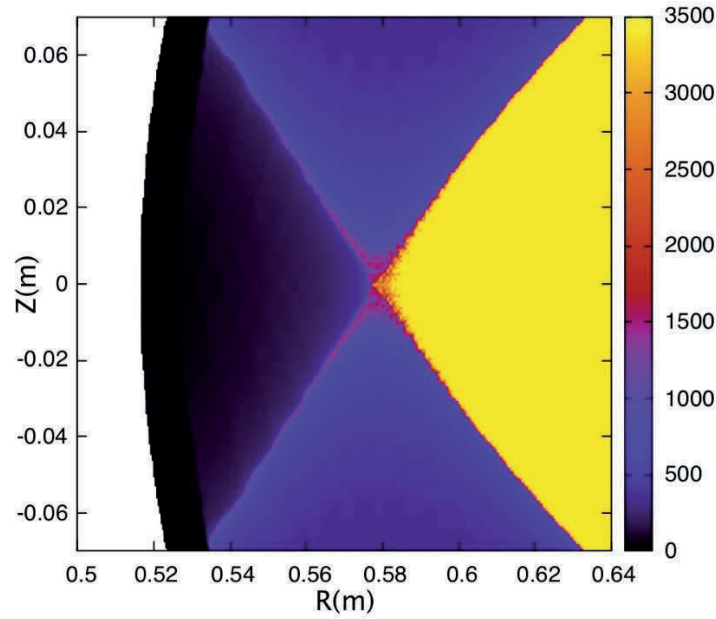


Fig. 3.8-9 Distribution of connection length near one of X-points in the island divertor of CFQS.

We have discussed so far the island divertor concept for CFQS based on the vacuum magnetic field produced by the external coils. Because the neoclassical bootstrap current is larger for the QA stellarator compared to other types of stellarator, it is necessary to find the operation scenario of the island divertor for the plasmas with finite beta. An example of the neoclassical bootstrap current calculation for CFQS is reported in the previous paper with planned experimental parameters [3.8-10]. Fig. 3.8-10 shows an example of the calculated profiles of the rotational transform in the operation with finite beta value. The calculation is based on the VMEC code which is widely used for the calculation of three dimensional equilibria with given plasma current profile. The black line shows the profile for the vacuum equilibrium with zero beta. It is equivalent to the blue line in Fig. 3.8-5 plotted from the magnetic field line tracing for the vacuum field. The red line shows the rotational transform profile with the averaged beta value of 0.35 %. The neoclassical bootstrap current is calculated using BOOTSJ code [3.8-11] for the pressure profile shown by the blue curve in the Pascal unit. This shape of the pressure profile is assumed based on the typical density and temperature profiles observed in many stellarator experiments [3.8-10]. When these codes are used for calculating the rotational

transform profile with neoclassical bootstrap current, the reliability of the profile data in the vicinity of the magnetic axis is not good. Therefore these line are shown by dots for that area. It passes the value of 0.4 ( $n/m = 2/5$ ) at the edge, which is expected to form islands. However, because the VMEC code assumes the existence of clear magnetic surfaces, the discussions of island structure need more advanced theoretical work using HINT, which is beyond the scope of this section.

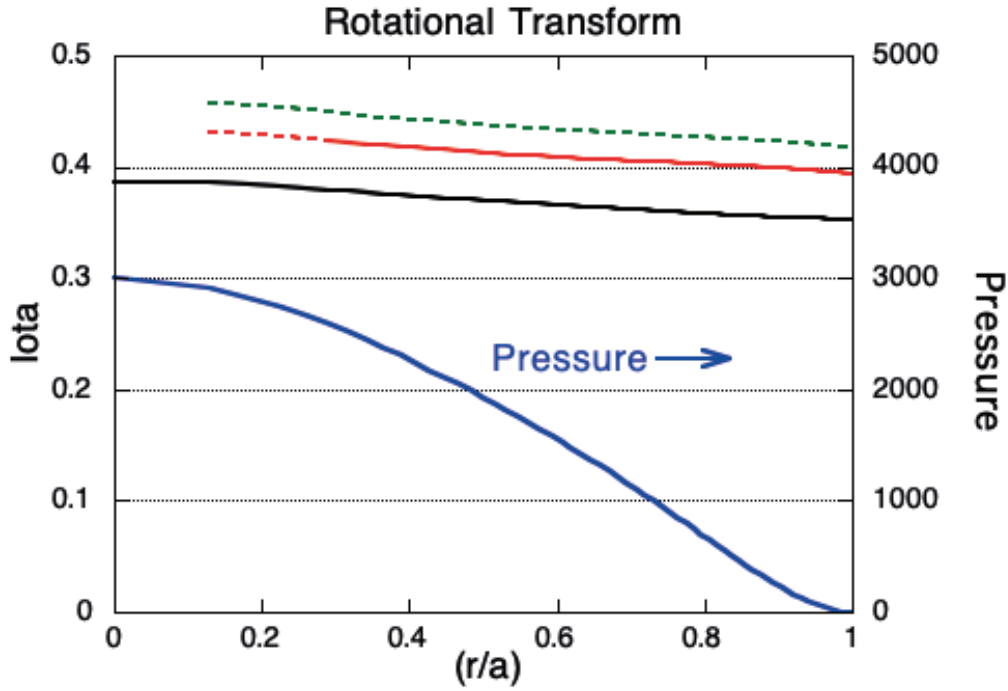


Fig. 3.8-10 Rotational transform profiles calculated by VMEC code. Black line shows the profile for the vacuum field (zero beta). Red line shows the profile with neoclassical bootstrap current calculated for beta value of 0.35 % and the pressure profile shown by blue curve. Green line shows an example of profile control using auxiliary toroidal field to shift up the red profile by reducing the toroidal field produced by modular coils.

The green dotted line shows an example of controllability for the rotational transform profile using auxiliary toroidal field coil. This profile is an example of applying the additional toroidal field to shift up the profile from the one with neoclassical bootstrap current. Actually the expected operation would be either shifting up or shifting down the rotational transform profile to match to the value of 0.4 in order to create island divertor configuration for the plasma with beta value different from 0.35 %.

For such finite beta plasmas, it is necessary to make two different controls in order to create good island divertor configuration. The first one is to adjust the rotational transform value near plasma edge at 0.4, which is resonant to the  $n/m = 2/5$  islands. This control is relatively easy using an adjustable power supply for the auxiliary toroidal field coils. The second one is to control plasma pressure profile for obtaining a suitable neoclassical bootstrap current profile, which produces the rotational transform



profile with very low negative shear. This control would be technically difficult but could be achievable with proper heating control, which will be an important research topic in the experiments. The duration of the plasma discharge planned in the CFQS program is 100 ms due to the limitation of the heating devices. The estimated rising time of the neoclassical bootstrap current is between 20 to 100 ms depending on the collisionality. Even if the fully developed equilibria with neoclassical bootstrap current is not possible for collisionless plasmas in the strict sense, the experimental analysis for this scientific topic will be possible.

Because theoretical analysis of the island divertor configuration needs the equilibrium calculation including island structure, the model calculation using HINT code [3.8-12] is now in progress and will be reported in the future. The equilibrium calculations using VMEC for the rotational transform profiles with auxiliary toroidal field coils were made for different volume-averaged beta values up to 1.5 %. For higher beta than 0.35 %, the auxiliary toroidal field must be positive (same polarity as the basic toroidal field) in order to decrease the rotational transform at the plasma edge down to 0.4.

Since the island structure is in general very sensitive to the control of the rotational transform, the control of neoclassical bootstrap current in the stellarator operation will be essential to keep the IBD concept stable. However, we know that any plasma parameters and engineering parameters must be controlled extremely accurately in the future fusion reactor. The control of neoclassical bootstrap current would be within available control knobs in the fusion reactors.

CFQS device design has included now the vacuum vessel structure [Section 4.3]. Fig. 3.8-11 shows the magnetic field configuration of the IBD of CFQS with the designed position (shape) of the vacuum chamber. Blue lines shows the toroidal cross sections of the 3-D designed vacuum vessel wall. In spite of the hard restrictions of the allowed space between the modular coils and the plasma boundary, we designed the vacuum chamber shape in order to make as large space as possible between in the periphery region of the plasma. As shown in Fig. 3.8-11, the IBD configuration will have a sufficiently long divertor legs and large space for installing necessary components of the gas pumping for suppressing the gas pressure in the divertor region. Because the IBD has as many as ten divertor leg around the plasma, the arrangement of the divertor targets will be the next important issues of the divertor design. The experimental results would help to select the best design of the IBD scenario.



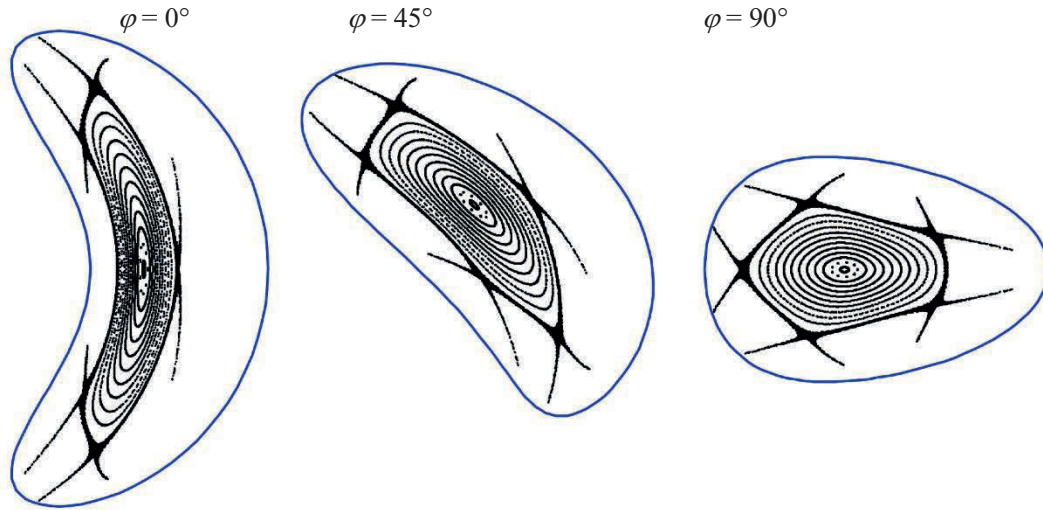


Fig. 3.8-11 Magnetic field configuration of island bundle divertor of CFQS. Blue curves shows the vacuum vessel positions of CFQS device design.

#### References

- [3.8-1] Y. Takeiri *et al.*, Nucl. Fusion **57** (2017) 102023.
- [3.8-2] S. Masuzaki *et al.*, Fusion Sci. Technol. **50** (2006) 361.
- [3.8-3] M. Kobayashi *et al.*, Fusion Sci. Technol. **58** (2010) 220.
- [3.8-4] R. C. Wolf *et al.*, Nucl. Fusion **47** (2017) 102020.
- [3.8-5] H. Renner *et al.*, Plasma Phys. Control. Fusion **44** (2002) 1005.
- [3.8-6] Y. Suzuki, J. Geiger, Plasma Phys. Control. Fusion **58** (2016) 064004.
- [3.8-7] Y. Feng *et al.*, Nucl. Fusion **56** (2016) 126001.
- [3.8-8] S. Okamura *et al.*, J. Plasma Phys. **86** (2020) 815860402.
- [3.8-9] H. Liu *et al.*, Plasma Fusion Res. **13** (2018) 3405067.
- [3.8-10] A. Shimizu *et al.*, Plasma Fusion Res. **13** (2018) 3403123.
- [3.8-11] K. C. Shaing *et al.*, Phys. Plasma **B1** (1989) 148.
- [3.8-12] Y. Suzuki *et al.*, Nucl. Fusion **46** (2006) L19.

### 3.9 Magnetic field control by TFC, PFC, and MC current ratio

#### 3.9.1 Background

The CFQS is optimized with 16 modular coils to generate a QA configuration with low shear and weak magnetic well. It is designed to allow the physical properties of the magnetic surface to be changed by adding the toroidal field coil (TFC) and the poloidal field coil (PFC). Furthermore, the magnetic surface can be controlled by the current ratio of four types of the MC. Taking advantage of this feature, we plan to experimentally investigate the effects of rotational transform and the characteristics of high-beta and the divertor configuration. In this chapter, the relationship between the coil current and the magnetic surface will be discussed.

Schematic of the coil system is shown in Fig 3.9.1-1. It shows 16 MCs (brown), 4 PFCs (yellow) and 12 TFCs (pink). In the PFCs, the smaller radius coil is called IV and the larger radius coil is called OV. The LCFS (beige) is also shown in the figure. A basic QA configuration can be produced by four types of 16 MCs. However, to allow flexible configuration, we will install the PFC to move the magnetic axis horizontally to compensate for the Shafranov shift during high beta experiment, and the TFC to change the rotational transform by adjusting the toroidal magnetic field. The MC is designed to lower the voltage and simplify the insulation by driving each type of the MC with a separate power supply. The coil currents are driven by a total of nine power supplies. The power supplies, the diagnostics and the heating apparatus are different in the experimental phase, but the coil system will be common. They will be designed under the rated operation conditions for the 1T.

The magnetic surface control is planned to be performed mainly by the PFC, then by the MC, and finally by the TFC. The maximum coil current was assumed to be 400 kAT for the IV, 200 kAT for the OV, 312.5 kAT for the MC, and 32 kAT for the TFC, which were designed from current density and temperature rise limitations in one shot. The PFC and MC are cooled by pure water. The TFC is a simple planar coil which will be made by winding a cable around a vacuum vessel without any cooling. It will take a long time to cool down with natural air and return the temperature to the value before discharge, so the pulse width of energization will be restricted less than 0.2s for one shot and number of shots in a day will be limited less than 10 to not raise the temperature. It may be difficult to obtain good results in experiments under these conditions.

At the beginning of the project, it was planned to control the rotation transform by changing the toroidal magnetic field by the TFC, but since the TFC has such engineering weaknesses, possibility of the rotation transform control by the PFC or the MC was also examined.

It is known that the so-called Island Bundle Divertor (IBD) can be achieved by creating the rational surfaces near the plasma boundary where the rotational transform is rational. We hope to study the divertor configuration by utilizing the rotation transform control.

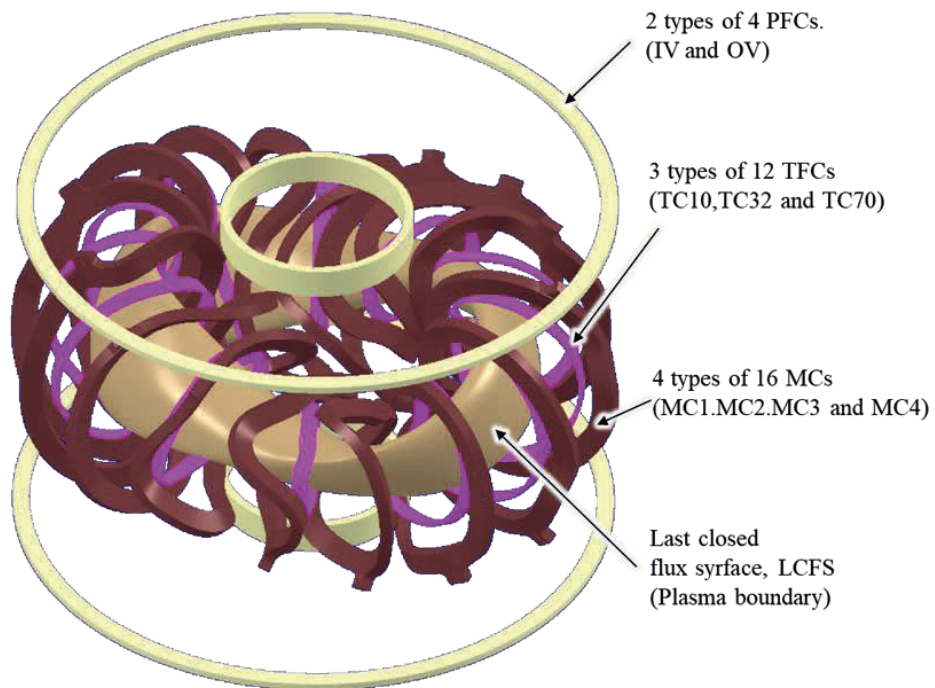


Fig 3.9.1-1 Schematic drawing of the three coil systems. The brown shows the modular coil (MC), the pink the toroidal field coil (TFC), and the yellow the poloidal field coil (PFC). The last closed flux surface (LCFS) is also shown in the picture. In the PFCs, the smaller radius coil is called IV and the larger radius coil is called OV. The PFC and the MC are cooled by pure water and the TFC is without any cooling.

### 3.9.2 Magnetic surface and physical parameters of a standard configuration

Fig 3.9.2-1 shows magnetic surfaces at different toroidal angles for a 2b40 configuration, which is name of a standard configuration without the PFC and the TFC in the CFQS. Blue points indicate closed magnetic surfaces in the vacuum vessel, orange points indicate open or intersecting magnetic lines of force with the vacuum vessel. The blue dashed lines show the inner wall of the vacuum vessel. They were obtained by the field line tracing in a vacuum with the Biot-Savart law and the Runge-Kutta method.

Fig 3.9.2-2 shows the rotational transform and the magnetic well depth for the 2b40, and Fig 3.9.2-3 the magnetic field spectrum in the Boozer coordinate. From Fig 3.9.2-2, the rotational transform does not pass through the rational number with  $2/5$  or  $2/6$  and a weak magnetic well is formed. They are one of the features of the CFQS. In Fig 3.9.2-3, the toroidal mode number  $n$  is that in the global coordinate system and one of the even numbers. The CFQS is also characterized by dominant  $B(0,0)$  and  $B(1,0)$  spectrums. It is also characterized by large mirror ripples of  $B(0,2)$  and  $B(0,16)$ , and large helical ripples of  $B(1,2)$  and  $B(1,-2)$  near the plasma boundary.

Reorganizing the above, the CFQS was optimized with the following expectations:

- **The  $B(0,0)$  and  $B(1,0)$  spectrums are dominant, which is similar to a tokamak. It is the most obvious reason we call the CFQS as a quasi-axisymmetric stellarator.**
- **The radial profile of rotational transform and magnetic wells are similar to those of a tokamak. It may be possible to stabilize the MHD instability by weak magnetic wells and to prevent deterioration of confinement due to magnetic islands.**
- **The magnetic field characteristics experienced by plasma particles may be resemble those of a tokamak.**
- **Ripple that causes degraded confinement is exceedingly small near the magnetic axis. It may be large near the plasma boundary. Investigation of the relation between the ripples and a plasma confinement is a future task.**

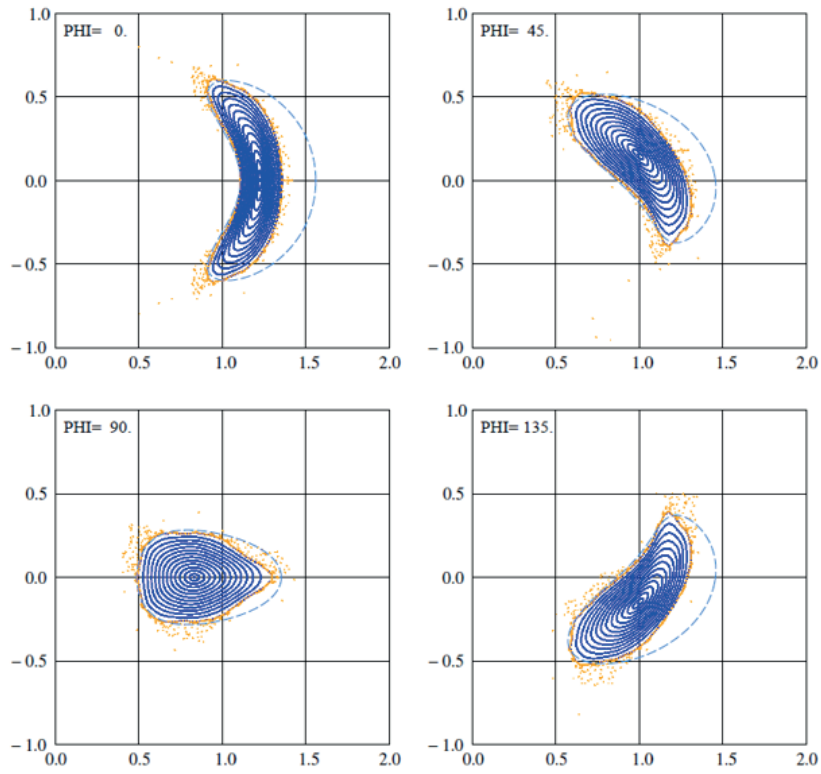


Fig 3.9.2-1 Magnetic surfaces at different toroidal angles with a standard configuration of 2b40. Blue points indicate closed magnetic surfaces in the vacuum vessel, orange points indicate open or intersecting magnetic lines of force with the vacuum vessel. The blue dashed lines show the inner wall of the vacuum vessel.

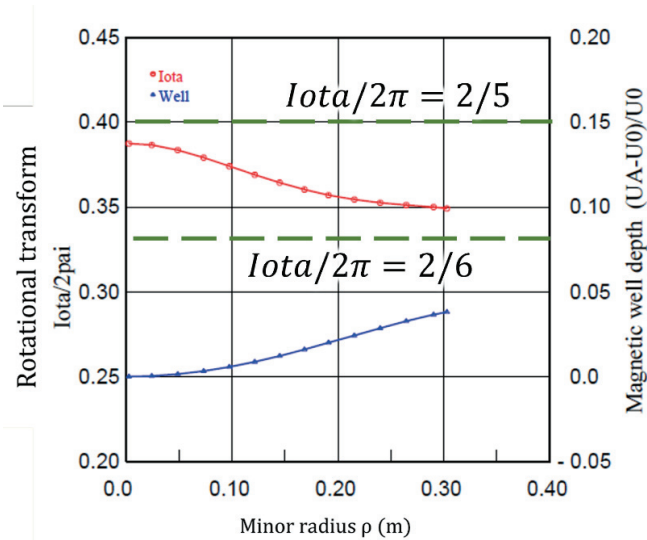


Fig 3.9.2-2 Radial profile of rotational transform and magnetic well depth with the standard configuration, which was obtained by the field line tracing. It can be seen that the rotational transform does not pass through the rational surface and a weak magnetic well is formed.

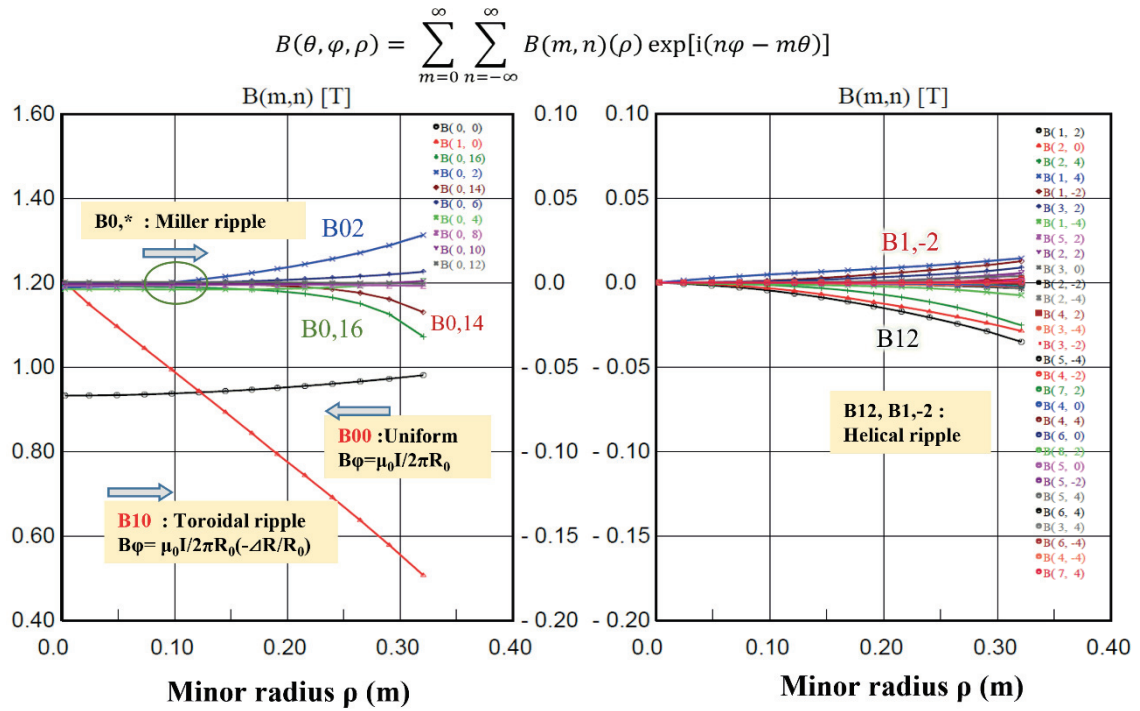


Fig 3.9.2-3 Magnetic field spectrum in the boozier coordinate with a standard configuration of 2b40, which was obtained by the field line tracing. The toroidal mode number  $n$  is that in the global coordinate system. It is one of the even numbers. The QA configuration is characterized by dominant  $B(0,0)$  and  $B(1,0)$  spectrums. Ripple that may cause degraded confinement is exceedingly small near the magnetic axis. It may be large near the plasma boundary.

### 3.9.3 Distribution of magnetic field strength

In Fig 3.9.3-1, distribution of magnetic field strength at different toroidal angles is shown, which was obtained by the Biot-Savart law in a vacuum. The upper figures show absolute value of the magnetic field. Here the green lines indicate magnetic surfaces, and the blue dashed lines the inner wall of the vacuum vessel. The lower figures show vertical magnetic field component. The polarity of the vertical field changes with the toroidal angle.

An upward field is generated at  $\varphi = 0$  degree, and a downward field is generated at  $\varphi = 90$  degrees. Such distributions are also one of the features of the QA configuration. The vertical magnetic field of the tokamak, which is created by PFC and plasma current, has a distribution in which the polarity is reversed on the inner and outer sides of the magnetic axis at all toroidal angles. The vertical magnetic field distribution at  $\varphi = 45$  of the CFQS is similar to that of tokamak.

The direction of rotational transform is aligned with the direction of the vertical magnetic field at  $\varphi = 45$  degrees. The vertical magnetic field of the CFQS has a distribution in which the direction is reversed depending on the toroidal angle. It is also one of the features of the QA configuration. It is



expected that the relation between the external coil current, such as the PFC and the TFC, and the plasma equilibrium may be also significantly different from the tokamak.

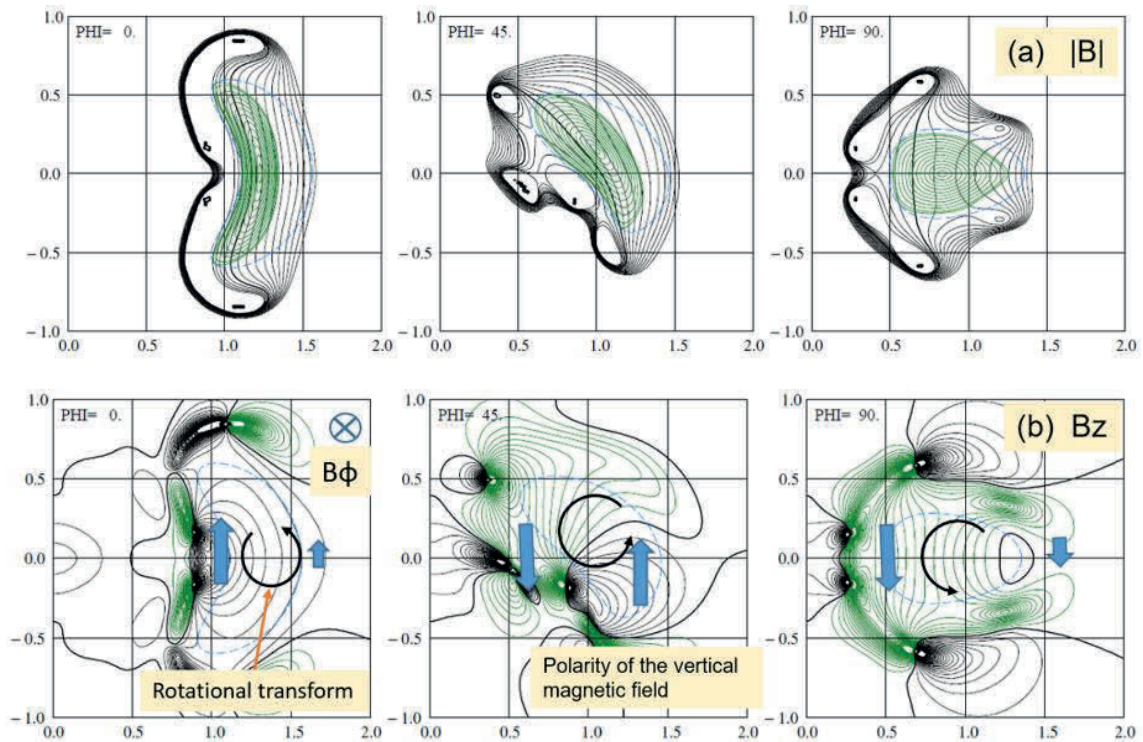


Fig 3.9.3-1 Contour plot of the magnetic field with the 2b40 configuration at different toroidal angles, which was obtained by the Biot-Savart law in a vacuum. The blue dashed lines show the inner wall of the vacuum vessel. The upper figures (a) show magnetic field strength (absolute value). Thick lines show 1T and the contour interval is 0.05T. Green lines indicate magnetic surfaces. The lower figures (b) show vertical magnetic field. Black lines show positive, green negative and the contour interval is 0.05T. The black arrows indicate the direction of rotational transform and blue arrows indicate the direction of the vertical magnetic field.



### 3.9.4 Rotational transform and type of boundary

The rotational transform of the torus fusion device is conceptually expressed by the ratio of the toroidal magnetic field and the poloidal magnetic field.

$$Iota/2\pi \cong R \langle B_\theta \rangle / \rho \langle B_\phi \rangle$$

where  $iota$  is the rotational transform angle,  $\langle B_\theta \rangle$  and  $\langle B_\phi \rangle$  are averaged poloidal and toroidal magnetic fields on the magnetic surface,  $R$  is a major radius, and  $\rho$  is a minor radius.

In the tokamak, the TFC generates  $\langle B_\phi \rangle$ , and the plasma currents generate  $\langle B_\theta \rangle$ . In the CFQS, both magnetic field components are generated by the modular coils,  $\langle B_\phi \rangle$  can be adjusted by the TFC, and  $\langle B_\theta \rangle$  can be adjusted by the PFC. The important point here is that the toroidal magnetic field changes at the same time when we try to control the rotational transform with the TFC. Since the CFQS does not have a current transformer, the plasma will be generated by the ECH. If we try to control the rotational transform by the TFC, the magnetic field will be changed at the same time, and plasma ignition may become difficult because the ECH resonance is broken.

Controlling the rotational transform is especially important to prevent deterioration of confinement and to form the local island bundle divertor (LIBD). Fig 3.9.4-1 shows the type of boundary. The plasma boundary can be classified into three types according to the positional relation between the vacuum vessel and a special magnetic surface call a separatrix which may be created with the magnetic islands. The CFQS can produce two types of separatrix, called a toroidal divertor (TD) or a local island bundle divertor (LIBD). The characteristics of each type are shown as conceptual diagrams. A metal limiter configuration (ML) without the separatrix may be created with the TFC current  $\leq 0$ , the toroidal divertor (TD) with the TFC current  $> 0$ , and the local island bundle divertor (LIBD) with the rotation transform near the boundary is rational. Here, it is assumed that the metal limiter is along the inner wall of the vacuum vessel. The TD is a specific configuration of the CFQS with TFC close to the vacuum vessel but is not produced in general fusion devices.

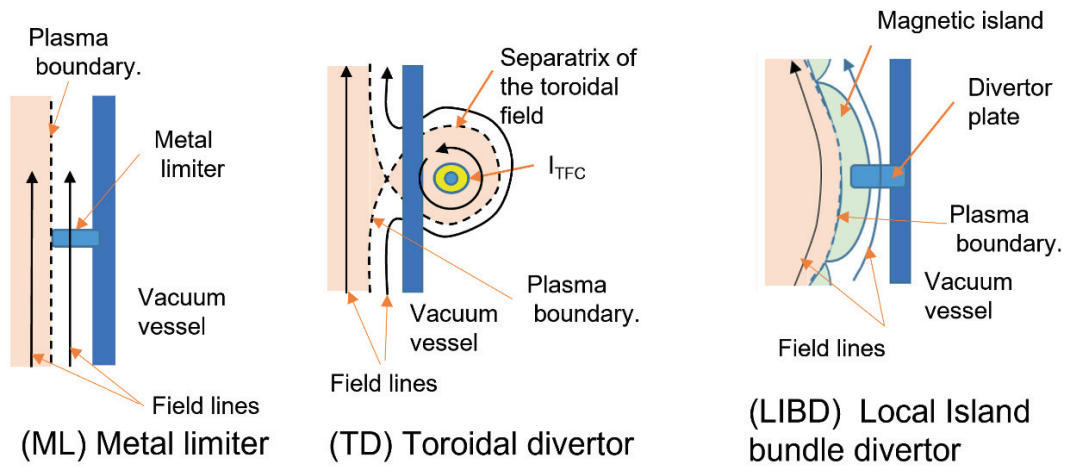


Fig 3.9.4-1 Type of plasma boundaries. The plasma boundary can be classified into three types according to the positional relation between the vacuum vessel as a metal limiter and a special magnetic surface call a separatrix which may be created with the magnetic islands or others. The characteristics of each type are shown as conceptual diagrams. The ML shows the metal limiter, the TD the toroidal divertor and the LIBD the local island bundle divertor. The ML may be created with the TFC current  $\leq 0$ , the TD with the TFC current  $> 0$ , and the LIBD with the rotation transform near the boundary is rational.

### 3.9.5 Magnetic surface control by the PFC

The PFC has engineering advantages such as easy cooling and simple shape. Originally, we planned to install a PFC system for major radius control to correct the Shafranov shift during high beta experiment. We had started to study expanding the use of the PFC. If the rotational transform can be controlled by the PFC, we believe that convenience of the CFQS will be greatly improved.

Fig 3.9.5-1 shows effects of the IV and OV currents on the physical quantity of the magnetic surface. The  $iota(0)$ ,  $R(0)$  and  $B_{00}(0)$  are the rotational transform, the major radius, and the averaged toroidal magnetic field on the magnetic axis. The  $iota(a)$  is the rotational transform at the LCFS. The  $R(0)$  falls to the right and the  $B_{00}(0)$  rises to the right with respect to IV and OV. Therefore, the  $B_{00}(0)$  and  $R(0)$  are almost inversely proportional to each other. The  $iota(a)$  rises to the right with respect to IV and falls to the right with respect to OV, that is, the direction of change is opposite. It suggests that the rotational transform of  $iota(a)$  can be independently controlled with the  $R(0)$  by combining IV and OV currents.

Fig 3.9.5-2 shows the effect of magnetic surface control by combining the IV and the OV currents and Fig 3.9.5-3 the shape of the magnetic surface at representative points, in which the shapes with toroidal angles of 0 and 90 degrees are drawn in a figure. The  $iota$  and the  $R$  are the rotational transform and the major radius respectively, where the  $(0)$  shows the value on the magnetic axis and the  $(a)$  the value on the last closed flux surface. Contour lines of the  $iota(0)$ ,  $iota(a)$  and  $R(0)$  are plotted in Fig 3.9.5-2. They were obtained from the calculation results with about 100 combinations of the IV and the OV currents. The figure also shows a region with few magnetic islands in the LCFS (white background,  $iota(a)/2\pi > 0.33$  and  $iota(0)/2\pi < 0.4$ ).

As shown at the points of (A), (S), and (B) in Fig 3.9.5-3, the  $R(0)$  can be controlled with a constant  $iota(a)$  under the condition of  $\Delta IV/\Delta OV = 2$ . As shown at the points of (L1), (L2), (S) and (C), it may be possible to control the  $iota(a)$  with a constant  $R(0)$  under the condition of  $\Delta OV/\Delta IV = -8$ . The standard QA configuration will be performed in the area of  $iota(a)/2\pi > 2/6$  and  $iota(0)/2\pi < 2/5$  with few magnetic islands as shown at (S), (L2) and (B). Under the condition at the point (A), higher mode islands with mode number  $n/m = 4/11$  ( $iota=0.364$ ) are visible due to the low shear as shown in Fig 3.9.5-3(A). The controllable range of the  $R(0)$  is about 0.15m, which is about 50 % of the minor radius at the LCFS. It may be enough to correct the Shafranov shift during high beta experiment. When the rotational transform becomes a rational number with  $iota(0)/2\pi > 2/5$  or  $iota(a)/2\pi < 2/6$ , a large magnetic island may be formed in the plasma as shown at the point (C), and the confinement will be deteriorated. By controlling the  $iota(a)$ , we may create the local island bundle divertor (LIBD) configuration with  $n/m = 2/7$  or  $n/m = 2/6$  as shown in (L1) and (L2). Although not shown in the figure, the LIBD with mode numbers of  $n/m = 2/5$  and  $n/m = 6/16$  may be also logically generated. However, since an excessive IV current of 800 kAT is required for the LIBD with  $n/m = 2/5$ , it may be difficult

to realize in actual experiments. The LIBD with  $n/m = 6/16$  is likely to have magnetic islands with  $n/m = 2/5$  in the plasma, so confinement may be deteriorated.

The results in this section are reorganized as follows.

- **The  $B_{\theta\theta}(0)$  and  $R(0)$  are almost inversely proportional to each other.**
- **The  $i(a)$  and  $R(0)$  can be independently controlled by combining IV and OV currents.**
- **The standard QA configuration will be performed in the area of  $i(a)/2\pi > 2/6$  and  $i(0)/2\pi < 2/5$  with few magnetic islands.**
- **The controllable range of the  $R(0)$  is about 0.15 m, which is about 50 % of the minor radius at the LCFS.**
- **By controlling the  $i(a)$ , we may create the local island bundle divertor (LIBD) configuration with  $n/m = 2/7$  or  $n/m = 2/6$ . The LIBD with  $n/m = 2/5$  may be difficult to realize due to the current limit of the PFC.**

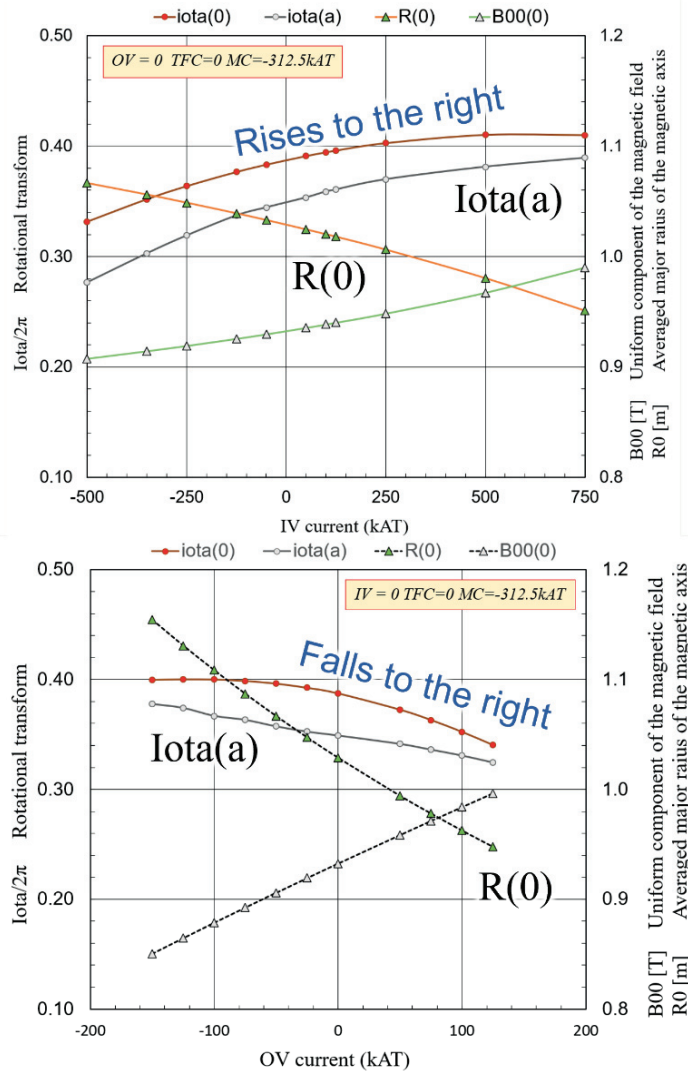


Fig 3.9.5-1 Effects of the IV or OV currents on the physical quantity of the magnetic surface. The major radius of  $R(0)$  falls to the right with respect to the IV or the OV. The rotational transform of  $iota(a)$  or  $iota(0)$  rises to the right with respect to the IV and falls to the right with respect to the OV. It suggests that the  $iota(a)$  or the  $iota(0)$  can be independently controlled with the  $R(0)$  by combining IV and OV currents.

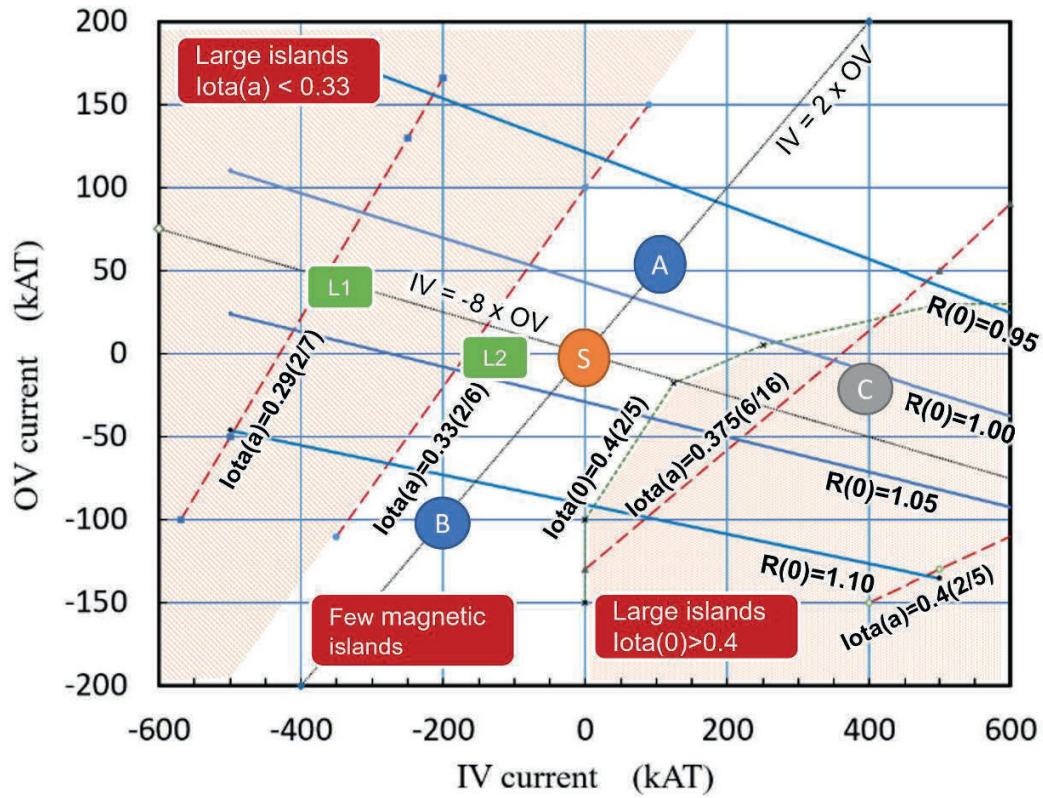


Fig 3.9.5-2 Effects of the IV and OV current combination on the physical quantity of the magnetic surface. Contour lines of the  $iota(0)$ ,  $iota(a)$  and  $R(0)$  are plotted in a figure. They were obtained from the calculation results with about 100 combinations of the IV and the OV currents. The  $R(0)$  can be controlled with a constant  $iota(a)$  under the condition of  $\Delta IV/\Delta OV = 2$ . It may be possible to control the  $iota(a)$  with a constant  $R(0)$  under the condition of  $\Delta OV/\Delta IV = -8$ . The figure also shows a region with few magnetic islands (white background,  $iota(a)/2\pi > 0.33$  and  $iota(0)/2\pi < 0.4$ ) and creating the bundle divertor at (L1) or (L2). The controllable range of the major radius  $R(0)$  is about 0.15m, which is about 50% of the minor radius at the LCFS. It may be enough to correct the Shafranov shift during high beta experiment.

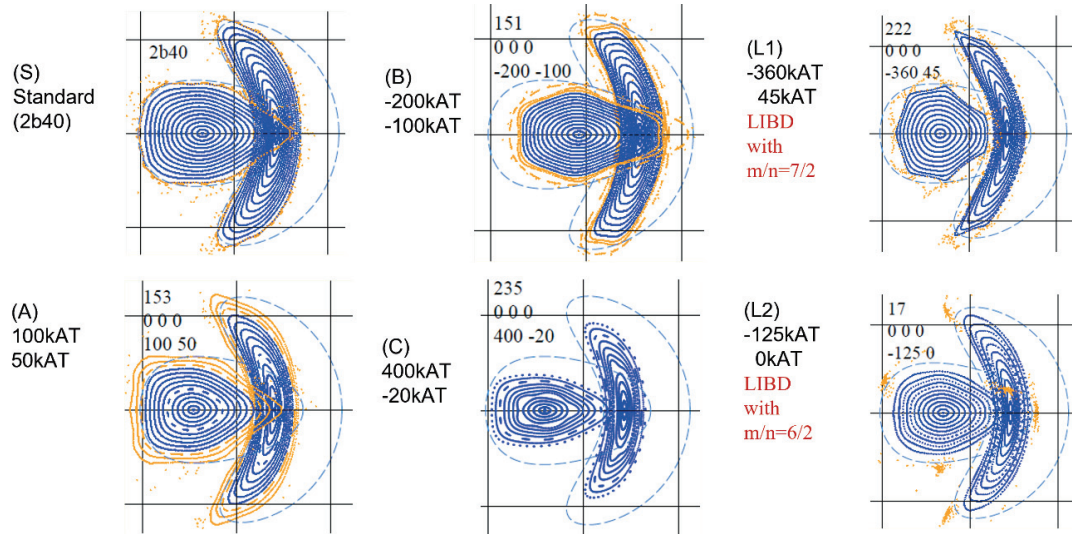


Fig 3.9.5-3 Magnetic surface with typical PFC currents. The symbols (S), (A), etc. correspond to the symbols in the previous figure. The figures show the shape of the magnetic surface at representative conditions, in which the shapes with toroidal angles of 0 and 90 degrees are drawn on one picture. The (S) and (B) show the typical metal limiter configuration with  $I_{\text{ota}}(0) < 0.4$  and  $I_{\text{ota}}(a) > 0.33$  where large magnetic islands cannot be formed. Experiments may be planned primarily in this area. The local island bundle divertor (LIBD) may be created at (L1) or (L2). Higher mode islands with  $n/m = 4/11$  or  $n/m = 2/5$  may be created in the plasma at (A) or (C).



### 3.9.6 Magnetic surface control by the TFC

It is expected that the rotational transform may be controlled by raising or lowering the average toroidal magnetic field by the TFC. We will discuss below how the rotational transform control by the TFC affects other parameters.

Fig 3.9.6-1 shows the relation between the TFC current and the physical quantity of the magnetic surface with all TFC current to be the same. The right side of the figure also shows the shape of the magnetic surface at the representative points. The rotational transform can be easily controlled by the TFC current without changing the plasma position, and the plasma shape and the arrangement of the magnetic islands change depending on whether the rotational transform becomes a rational number. The plasma boundary at the point of L3 is the type of LIBD, and at the point of D is the type of TD, which is explained in Fig 3.9.4-1. The configuration at the point D is presumed to have poor confinement because large magnetic islands are formed in the plasma. If the TFC current is further increased, the LIBD configuration of  $m/n = 5/2$  can be theoretically created under the condition of  $\text{iota}(a) = 0.4$ , but it is difficult to achieve due to the current limitation. When the TFC current is larger than 16 kA, the ECH resonance region disappears inside the LCFS. Plasma ignition with the ECH under these conditions may be difficult. The range where magnetic surface control is practically possible is between -32 kA and 16 kA for TFC current.

The CFQS is designed so that the TFC currents and the current direction can be changed for each type of the TFC. We examined what kind of experiments could be performed by the TFC current control. As an example, Fig 3.9.6-2 shows contour lines of the physical quantity of the magnetic surface with different combination of the TC10 and  $\text{TC32} = \text{TC70}$ . The figure also shows area where plasma generation is difficult because the ECH resonance region is disappeared inside the LCFS. It was found that if the current direction of the TC10 is reversed ( $\text{TC10} < 0$ ), only the mirror ripple component of  $B(0,2)$  can be independently controlled while keeping the  $B_{00}(0)$  and  $\text{iota}(0)$  constant. For an example, points E and F show different equilibria with similar plasma shapes and different polarities of mirror ripple components. The impact of mirror ripples on confinement is currently unclear. A study could be conducted in the CFQS to investigate that.

Fig 3.9.6-3 shows a comparison of ripple distributions at points E and F. Although the mirror ripples  $B(0,2)$  differ greatly under the two conditions, the values of the toroidal ripple  $B(1,0)$  and the helical ripples  $B(1, \pm 2)$  are almost the same. In this way, we may be able to investigate the relation between magnetic field components and plasma confinement by taking advantage of the ability to freely change the TFC current and polarity.

The results in this section are reorganized as follows.

- **The rotational transform control by the TFC is easy in a limited current range.**
- **Experiments to study the effect of the mirror ripple  $B(0,2)$  may be possible if the polarity of**

the TFC current is changed.

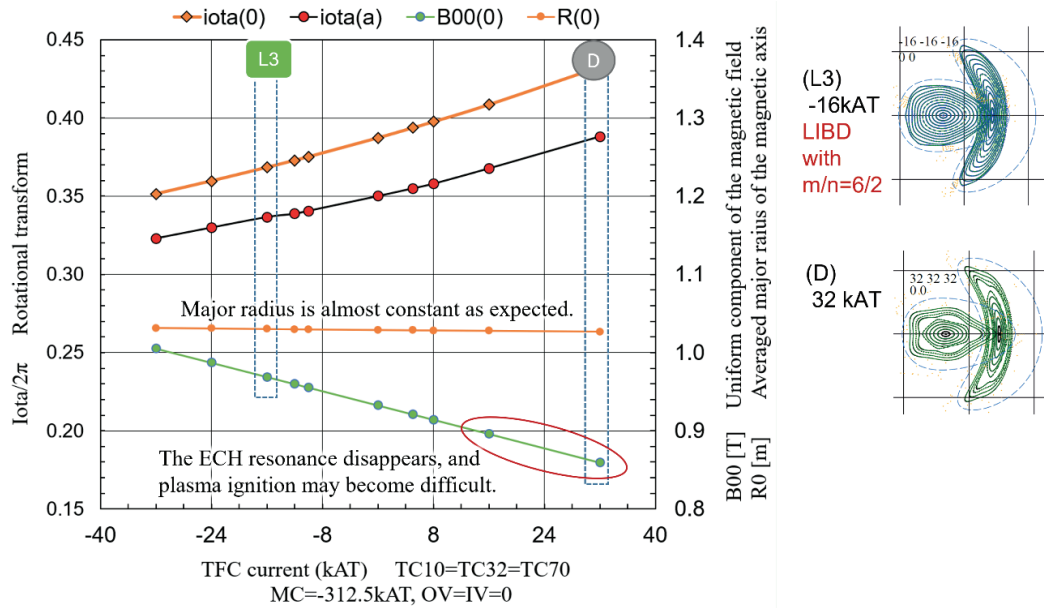


Fig 3.9.6-1 Relation between the TFC current and the physical quantity of the magnetic surface with all TFC current to be the same. The rotational transform  $\iota(0)$  or  $\iota(a)$  can be easily controlled by the TFC current without changing the plasma position. The right figures show the shape of the magnetic surface. The point L3 shows the so-called LIBD with  $m/n = 6/2$ . The point D shows a poorly confined configuration where large magnetic islands are formed in the plasma. The boundary at the point D is determined by the toroidal divertor (TD). When the TFC current is larger than 16 kA, the ECH resonance region disappears inside the LCFS. Plasma ignition with the ECH under these conditions may be difficult.

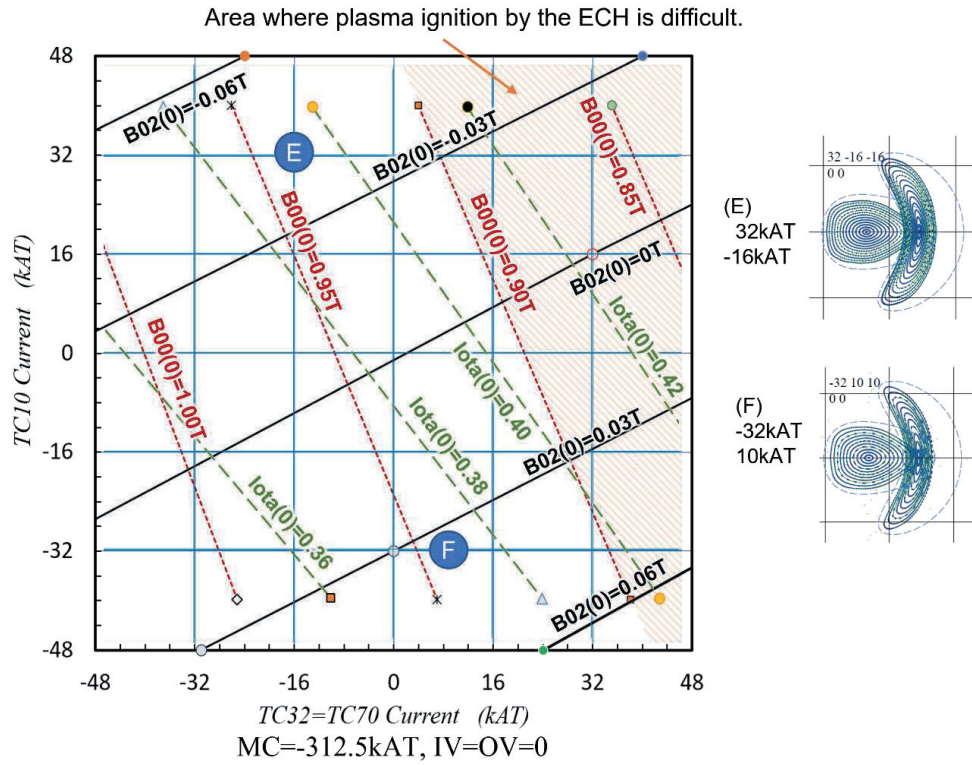


Fig 3.9.6-2 Contour lines of the physical quantity of the magnetic surface with different combination of the TC10 and TC32 = TC70. The  $B(0,0)(0)$  and mirror ripple component  $B(0,2)(0)$  can be independently controlled. The figure also shows area where plasma generation is difficult because the ECH resonance region disappears inside the LCFS. The right figures show the shape of the magnetic surface at representative points. Points E and F show different equilibria with similar plasma shapes and different polarities of mirror ripple components.

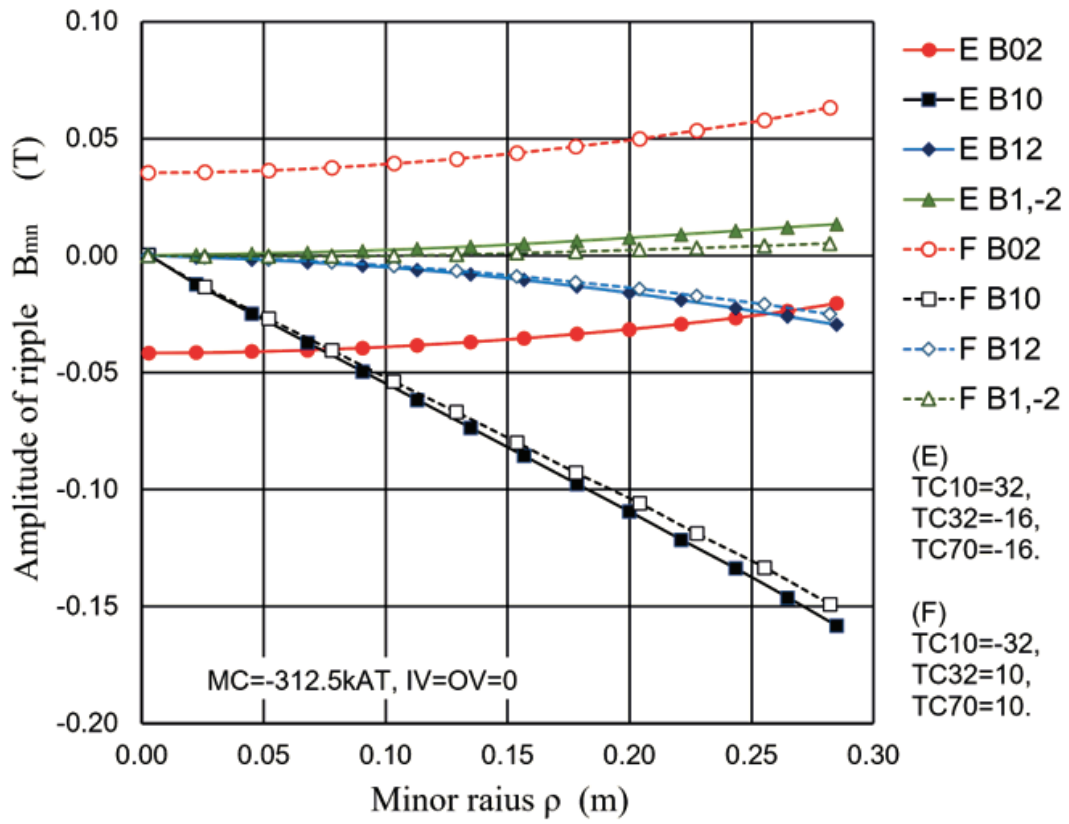


Fig 3.9.6-3 Comparison of ripple distributions with representative TFC currents at the points E and F. The TFC currents are TC10=32 kAT, TC32=TC70=-16 kAT at the point E and TC10=-32 kAT, TC32=TC70=10 kAT at the point F. Although the mirror ripples  $B(0,2)$  differ greatly under the two conditions, the values of the toroidal ripple  $B(1,0)$  and the helical ripples  $B(1, \pm 2)$  are almost the same.

### 3.9.7 LIBD control with $m/n=5/2$ by the PFC and TFC

As shown in Fig 3.9.5-2 and Fig 3.9.6-1, the LIBD with  $m/n = 6/2$  can be easily produced by the PFC or the TFC. The rotational transform  $iota(a)$  of the standard configuration 2b40 is about 0.35. When we can correct it to 0.333 using the PFC or the TFC, the LIBD with  $m/n = 6/2$  should be generated. Similarly, if we can modify the  $iota(a)$  from 0.35 to 0.4, then the LIBD with  $m/n = 5/2$  should also be produced. The LIBD with  $m/n$  of integer ( $6/2 = 3$ ) and half-integer ( $5/2 = 2.5$ ) may have significantly different plasma confinement, so comparative experiments between the two may be worthwhile. It is because the connection characteristics of the magnetic island are different between the two. The former requires at least two divertor plates to receive the thermal energy because the islands are divided into two. Since the latter separatrix are connected to each other, all the thermal energy can be received by one divertor plate. Such differences may affect plasma confinement or how it works as a divertor. Experimental research on it may also be a challenge in the CFQS.

As explained in the previous sections, making  $iota(a)=0.4$  with PFC or TFC alone is difficult due to engineering limitations because too much current is required. Therefore, we examined whether  $iota(a)=0.4$  can be made by combining both. The answer to that study was yes. However, the conditions that can be established in terms of engineering was limited and the experiment had to be conducted under certain constraint conditions.

Fig 3.9.7-1 shows the condition for obtaining the LIBD with  $m/n = 5/2$ . By combining the PFC and the TFC, the LIBD with  $m/n = 5/2$  can be theoretically generated under various conditions. However, only around the point H1 in an extremely limited range may be substantially effective within the engineering limitations. The vicinity of the point H1 may be optimal for the experiment of the LIBD with  $m/n = 5/2$ . Within the red square, required coil current exceeds the upper limit of the coil current. Within the green square, the ECH resonance is outside the LCFS. If plasma ignition can be realized with NBI or ECH with other frequencies, experiments may be also possible within the green square. In the CFQS project, a low-field experiment with 0.09 T is planned separately from the 1 T experiment. The experiment plans to generate a plasma with an ECH of 2.45 GHz. In that plan, the LIBD experiments with  $m/n = 5/2$  may be possible under various conditions, because there are less restrictions on the coil current.

Fig 3.9.7-2 shows the magnetic field strength under typical conditions to create the LIBD with  $m/n = 5/2$ . The current values of TC10, TC32, and TC70 are indicated in the legend in the figure. The ECH resonance ( $B=0.97$  T for 54.5 GHz ECH) exists near the vertically elongated sector with a condition of H1. At cross-sections away from that toroidal angle, the ECH resonance is outside the LCFS. So, the ECH antenna should be positioned near that toroidal angle. It is difficult to create ECH resonance in plasma with other condition due to the limitation of PFC current.

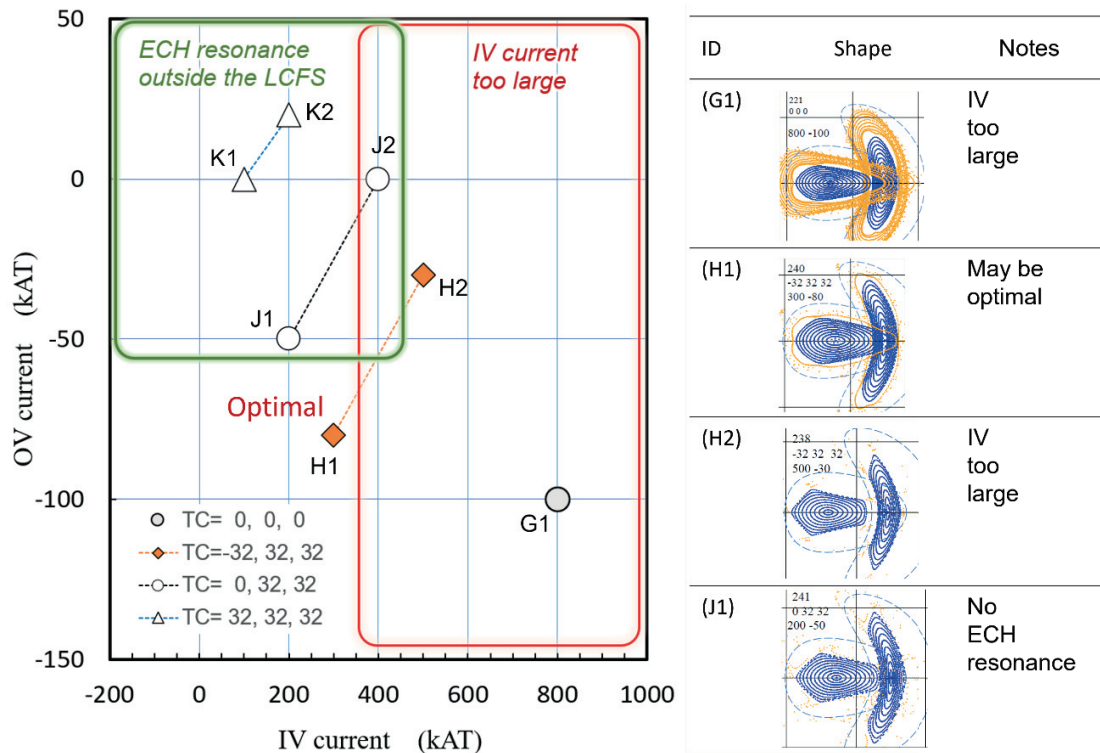


Fig 3.9.7-1 Optimal conditions for obtaining the LIBD with  $m/n = 5/2$ . The LIBD can be theoretically generated under various conditions. However, only the vicinity of the point H1 in an extremely limited range may be substantially effective due to the engineering limitations.

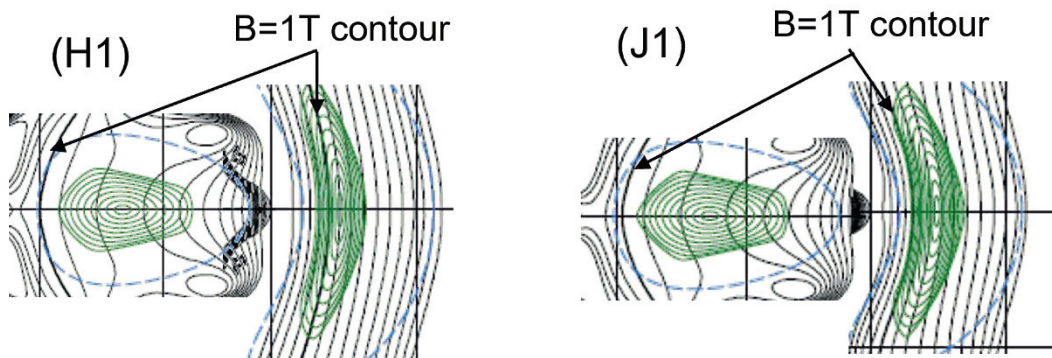


Fig 3.9.7-2 Magnetic field strength under typical conditions to create the LIBD with  $m/n = 5/2$ . Green lines indicate magnetic surfaces and black lines contours of the magnetic field strength. The ECH resonance ( $B = 0.97$  T for 54.5 GHz ECH) to ignite the plasma plotted by thick lines, which exists only near the vertically elongated sector with the conditions of (H1). It is difficult to create ECH resonance in plasma with other condition due to the limitation of PFC current.



### 3.9.8 Magnetic surface control by the MC

Since the MC is driven by a separate power supply for each type, different values of current can flow for each coil type. Taking advantage of this feature, it is possible to control the toroidal direction distribution of the toroidal magnetic field similar to the TFC.

Fig 3.9.8-1 shows the relation between the MC current and the physical quantity of the magnetic surface. The MC current on the horizontal axis indicates the coil current shown in the caption. All currents other than the coils described in the caption are 100 % (4.34 kA/turn).

The linear change in  $B(0,0)$  and  $B(0,2)$  when the current in each coil is controlled individually resembles the effect of TFC as shown in Fig 3.9.6-1. However, the effect on the rotation transform may be different from the TFC. The MC2 and MC3 do not affect the  $Iota(0)$ , and the MC1 does not affect the  $Iota(a)$ . The reason for this is presumed to be that the  $R(0)$  changes along with the MC current.

When the two coil currents are moved together under the condition of  $MC2 = MC3$  or  $MC1 = MC4$ , only the  $Iota(a)$  can be controlled with fixing the  $Iota(0)$ . Fig 3.9.8-2 shows the relation between the ratio of MC1 and MC2 currents and the physical quantity of the magnetic surface with  $MC2=MC3$  and  $MC1=MC4$  currents. When the MC2 current decrease under such control, the LIBD configurations with the rotational transform of  $2/6$  can be created. Since such equilibrium can be realized only by controlling the MC, we believe that it is advantageous from the viewpoint that the experiment is easy.

Under such control conditions, the magnetic shear, that is rate of change of the rotational transform, changes simultaneously with the  $Iota(a)$ . The effect seems to appear as an ergodic diverter configuration. As can be seen from the magnetic surface diagram shown in Fig 3.9.8-2, when the  $MC1/MC2$  is decreased, that is, when the magnetic shear is decreased, higher-order magnetic islands become visible near the plasma boundary. Such a characteristic shape is thought to be created by overlapping magnetic islands with different mode numbers. The characteristic structure in which the many magnetic islands overlap is called an ergodic island configuration. The ergodic island configuration is considered to occur easily with small magnetic shear.

Under such control, the change in the mirror ripple is also characteristic. The mirror ripple of  $B(0,2)$  is almost constant and the change in the mirror ripple of  $B(0,4)$  is large. If we pay close attention to this characteristic, it may be possible to conduct an experiment to extract the effect of mirror ripples.

The results of this section are summarized below.

- **Distribution control of the rotational transform is possible only by controlling the ratio of MC current.**
- **The effects on the  $B(0,0)$  and  $B(0,2)$  are similar to that of TFC, but the effect on the rotational transform profile is different.**
- **When the two coil currents are moved together under the condition of  $MC2 = MC3$  and  $MC1$**



= MC4, only the  $Iota(a)$  can be controlled with fixing the  $Iota(0)$ .

- The LIBD configurations with a rotational transform of  $2/6$  can be created only by controlling the MC current.
- The configuration with low magnetic shear and ergodic magnetic islands can be realized by controlling the MC current.
- The rotational transform can be controlled without increasing the mirror ripple of  $B(0,2)$ , but since the high-order mode of  $B(0,4)$  becomes large, it is important to consider the effect of this as well.

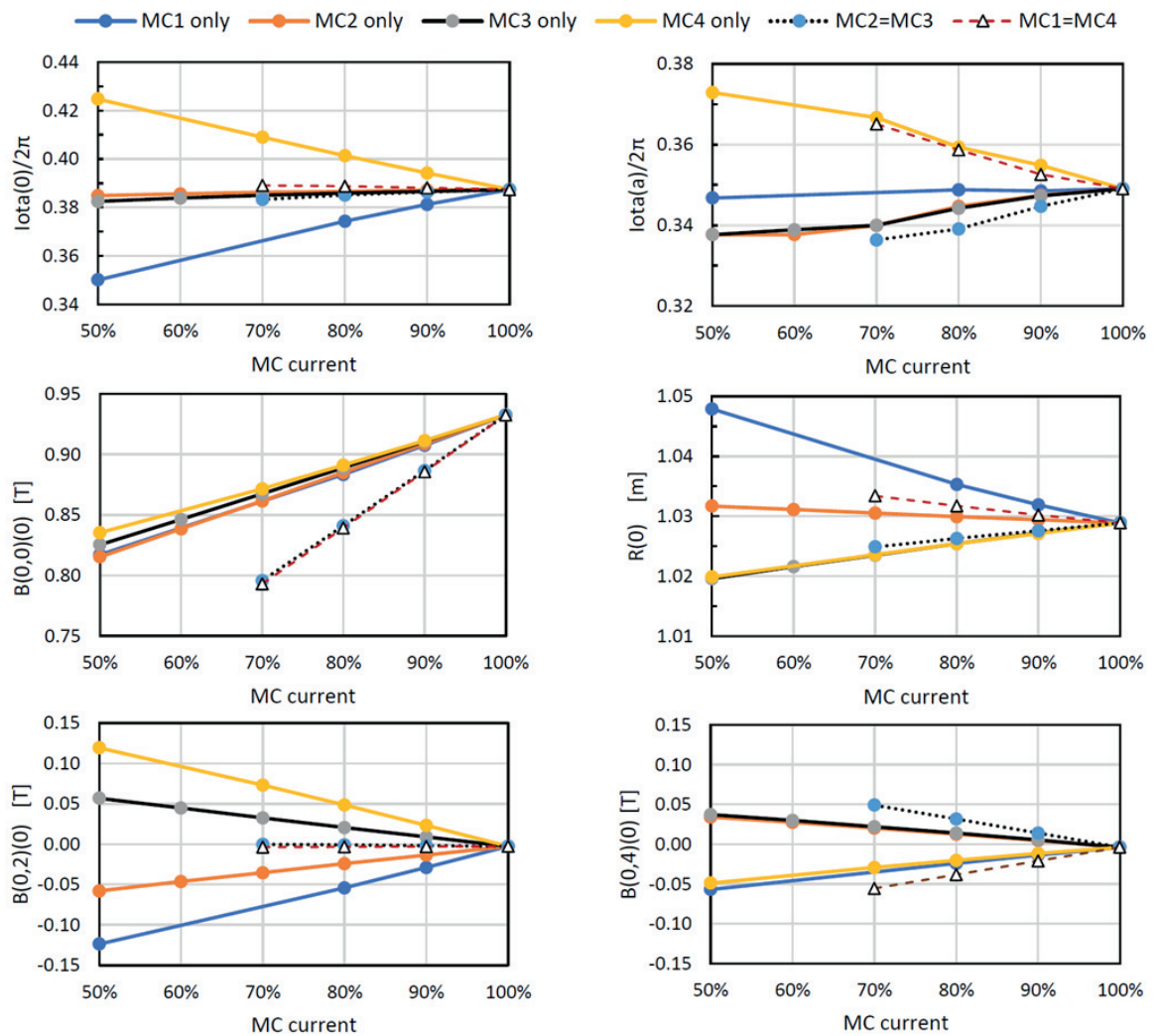


Fig 3.9.8-1 Magnetic surface control by the MC currents. The MC current on the horizontal axis indicates the coil current shown in the caption. Other currents are 100 % (4.34 kA/turn). When the two coil currents are moved together under the condition of  $MC2 = MC3$  or  $MC1 = MC4$ , it may be possible to control the  $Iota(a)$  with fixing the  $Iota(0)$ . At this time, the mirror ripple of

$B(0,2)$  is almost constant, but the  $B(0,4)$  increases.

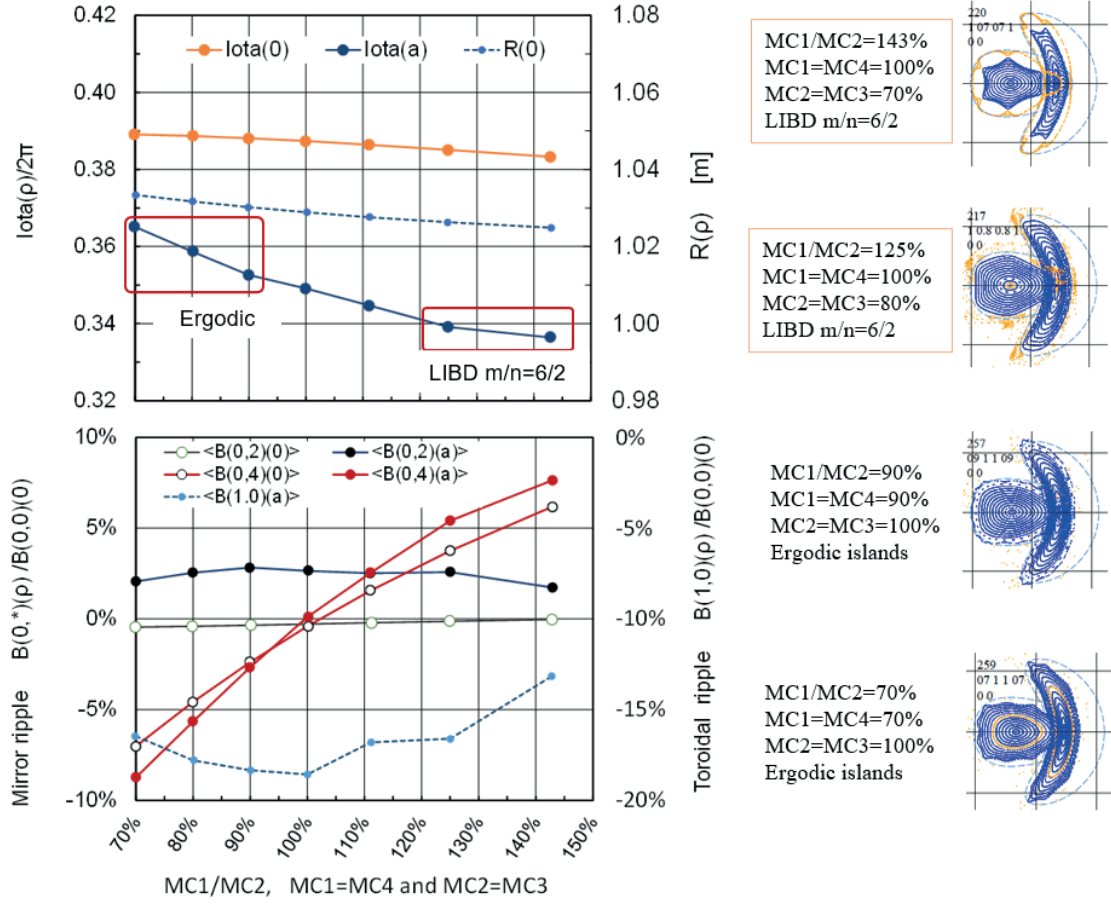


Fig 3.9.8-2 Magnetic surface control by the ratio of  $\text{MC1} = \text{MC4}$  and  $\text{MC} = \text{MC3}$  currents. When the  $\text{MC2}$  current decrease, the LIBD configurations with the rotational transform of  $2/6$  can be created, which can be realized only by controlling the MC. When the  $\text{MC1}$  current decreases, the ergodic islands may be created. Mirror ripple  $B(0,2)$  is almost constant. The change in mirror ripple  $B(0,4)$  is large.

### 3.9.9 Role of poloidal field for QAS equilibrium

For the toroidal magnetic confinement system, the largest component of the magnetic field is the toroidal magnetic field. In addition to this field component, the poloidal field in the toroidal magnetic confinement field geometry has a couple of different roles depending on the confinement scheme.

For tokamaks, the most important role of the poloidal field is to supply the inductive electric motive-force to drive the plasma current. The central solenoid coil, which is a bunch of many poloidal coils, produces a strong poloidal field (vertical magnetic field flux passing through the torus) and a time variation (a time swing) of this magnetic flux creates the electric field along the toroidal magnetic field that produces the plasma current. In addition to this basic role of the poloidal field in tokamaks, controlling detailed distribution of the poloidal field near the plasma boundary makes it possible to control the shape of the LCFS, which is called the plasma shape control. In contrast to the time swing of the magnetic flux in the central solenoid, poloidal field for the plasma shape control is applied in the time scale of the plasma discharge.

When we discuss about the plasma shape control, it is useful to decompose the distribution of the poloidal field into several terms of the multipole expression. If we define the poloidal flux  $\Psi(r, z)$  as a function of  $r$  and  $z$ , it gives the  $r$  and  $z$  components of the poloidal field as follows:

$$B_z = (1/r) d\Psi/dr, \quad B_r = -(1/r) d\Psi/dz$$

Let us decompose here the poloidal flux into three multipole terms (in general we can define as many multipole terms as we need): v denotes for ‘vertical’, q for ‘quadrupole’ and h for ‘hexapole’.

$$\Psi = C_v \Psi_v + C_q \Psi_q + C_h \Psi_h$$

These multipole terms of the poloidal flux are expressed as follows: [3.9.9-1]

$$\Psi_v = (1/2) (r^2 - R^2)$$

$$\Psi_q = (1/8) \{4 r^2 z^2 - (r^2 - R^2)^2\}$$

$$\Psi_h = (1/24) \{8 r^2 z^4 - 12 r^2 (r^2 - R^2) z^2 + (r^2 - R^2)^3\}$$

$R$  is a constant and we use a nominal radius of the configuration for  $R$  (for example, the radius of the magnetic axis).

For a given poloidal field distribution  $\Psi(r, z)$ , the decomposition to the multipole components are completed by calculating coefficients of  $C_v$ ,  $C_q$  and  $C_h$  by solving these three equations.

$$[\Psi \Psi_v] = C_v [\Psi_v \Psi_v] + C_q [\Psi_q \Psi_v] + C_h [\Psi_h \Psi_v]$$

$$[\Psi \Psi_q] = C_v [\Psi_v \Psi_q] + C_q [\Psi_q \Psi_q] + C_h [\Psi_h \Psi_q]$$

$$[\Psi \Psi_h] = C_v [\Psi_v \Psi_h] + C_q [\Psi_q \Psi_h] + C_h [\Psi_h \Psi_h]$$

Here the inner product of the bracket  $[\ ]$  means the following value:

$$[\Psi_a \Psi_b] = \text{Integral} [B_{z,a} B_{z,b} + B_{r,a} B_{r,b}]$$

(Integration area is within a circle around the  $R$ )

$$B_{z,a} = (1/r) d\Psi_a/dr, \quad B_{r,a} = -(1/r) d\Psi_a/dz$$

$$B_{z,b} = (1/r) d\Psi_b/dr, \quad B_{r,b} = -(1/r) d\Psi_b/dz$$

In tokamak discussions, three coefficients  $C_v$ ,  $C_q$ ,  $C_h$  have a close relation to the parameters of plasma position and shape, namely,  $C_v$  to the position of the plasma in the major radius,  $C_q$  to the ellipticity of the plasma shape and  $C_h$  to the triangularity.

For stellarators, because the magnetic configuration is 3-D, we can discuss the structure of the poloidal field in two categories of non-axisymmetric component and the axisymmetric component. For stellarators with no plasma current, the non-axisymmetric poloidal field is produced by helical coils or modular coils and this poloidal field produces the rotational transform without the plasma current. For Torsatron-type stellarators such as CHS and LHD, because two major helical coils have currents along the toroidal direction with the same polarity, similar level currents in poloidal coils (in the reversed polarity) are necessary for making the magnetic surfaces for the plasma confinement. In stellarators with modular coils, currents in poloidal coils are not necessary in order to make the magnetic configuration for the plasma confinement. The currents in modular coils are sufficient for producing all necessary magnetic field components including the toroidal field and the poloidal field required for constructing the toroidal magnetic field configuration.

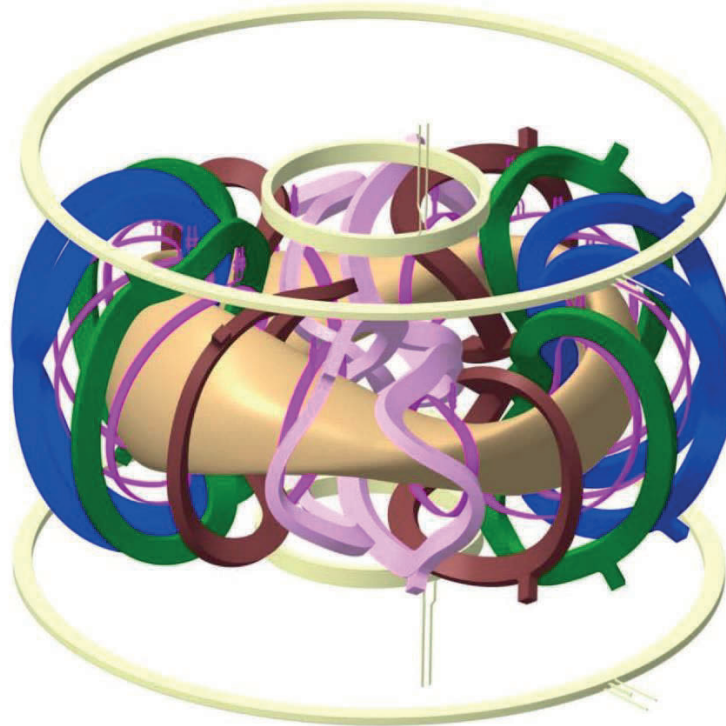


Fig. 3.9.9-1 Magnetic coils for CFQS device. 16 coils with four colors: blue, green, brown and light pink are modular coils. 12 coils with magenta color are auxiliary TFCs. 4 coils with light yellow color are PFCs.

However it is possible and actually useful for stellarators to introduce the plasma shape control with the use of poloidal field coil currents. For this purpose, we use axisymmetric poloidal field in the

similar way of tokamak operation. For CFQS device, in addition to the modular coils, which are sufficient for producing the confinement magnetic field by itself, 12 auxiliary TFCs and 4 auxiliary PFCs are equipped for the purpose of the flexible controls of fundamental characteristics of stellarator configuration. Shapes and installation of all 32 coils are shown in Fig. 3.9.9-1. In this section, the ellipticity control using poloidal coils is reported. 12 auxiliary TFCs are used for controlling the rotational transform, which is explained in detail in Section 3.8, 3.9.6.

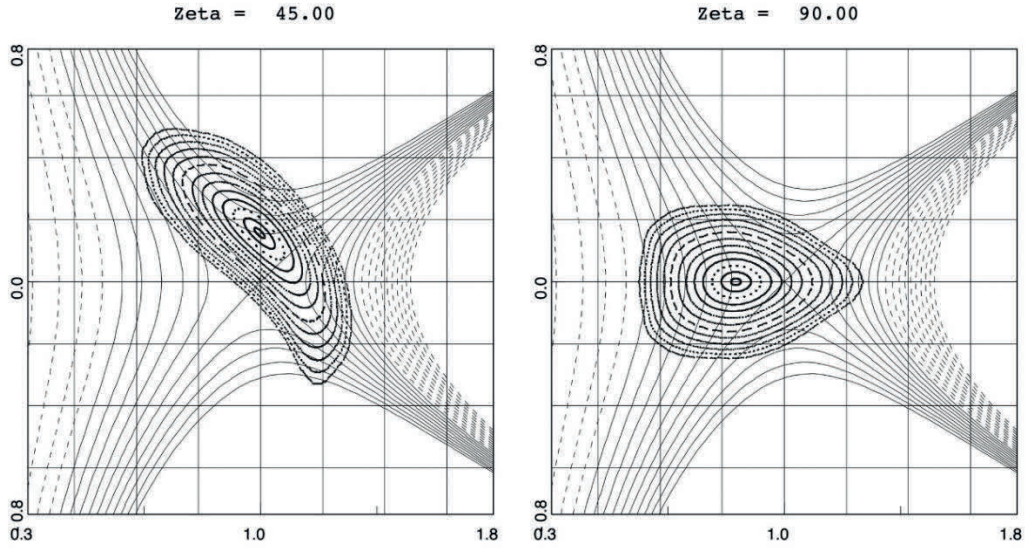


Fig. 3.9.9-2 Contour plots of poloidal flux of quadrupole field for two different toroidal cross section of CFQS magnetic surfaces. Pattern of magnetic field vector is along each contour line.

The field pattern of the vertical field  $\Psi_V$  is very simple. It has only  $B_z$  component and  $B_r$  is zero.  $B_z$  is uniform everywhere. The field pattern of the quadrupole field is complicated. The magnetic field at  $R$  (nominal radius of the configuration) is vanishing at  $z = 0$  and the field strength is linearly increasing when the measuring point is going away from this null point. Fig. 3.9.9-2 shows the contour map of the quadrupole poloidal flux  $\Psi_Q$ , where the magnetic field vector is aligned on these contour lines. Because the amplitude of quadrupole field cannot be expressed with the strength of magnetic field at the nominal point  $R$ , we use the magnetic field strength at 0.3 m away from  $R$  for expressing the quadrupole field amplitude.

When we excite PFCs of CFQS, the poloidal field with the combination of the vertical field term and the quadrupole field term appears. Because the component ratio of these two multipole field are different for two types of poloidal coils (IVF and OVF), it is possible to choose the different ratio of the multipole poloidal field components by adjusting the current ratio in two PFCs. The amplitudes of the multipole poloidal field terms for two types of the PFCs are shown in Table 3.9.9-1.



Table 3.9.9-1 Amplitude of multipole components of each poloidal field coil. Strength of multipole field components are shown for poloidal field coil current of 1 MA.

Poloidal Coil	Vertical Field Component	Quadrupole Field Component
IVF	0.04(T)	0.055 (T at 0.3m)
OVF	0.374(T)	0.053(T at 0.3m)

Taking into account the multipole poloidal field components of two types of PFCs, we selected the currents in poloidal coils: 200 kA for IVF coil and -24.6 kA for OVF coil for producing a horizontally elongated shape of the magnetic surfaces compared to the standard shape of CFQS plasma. Fig. 3.9.9-3 shows the magnetic surfaces for this configuration. Red line shows the VMEC target shape of the CFQS, for which the modular coil design was made. Blue line shows the present vacuum chamber wall position. Producing such a horizontally elongated configuration in the experimental conditions is possible using the present vacuum vessel design.

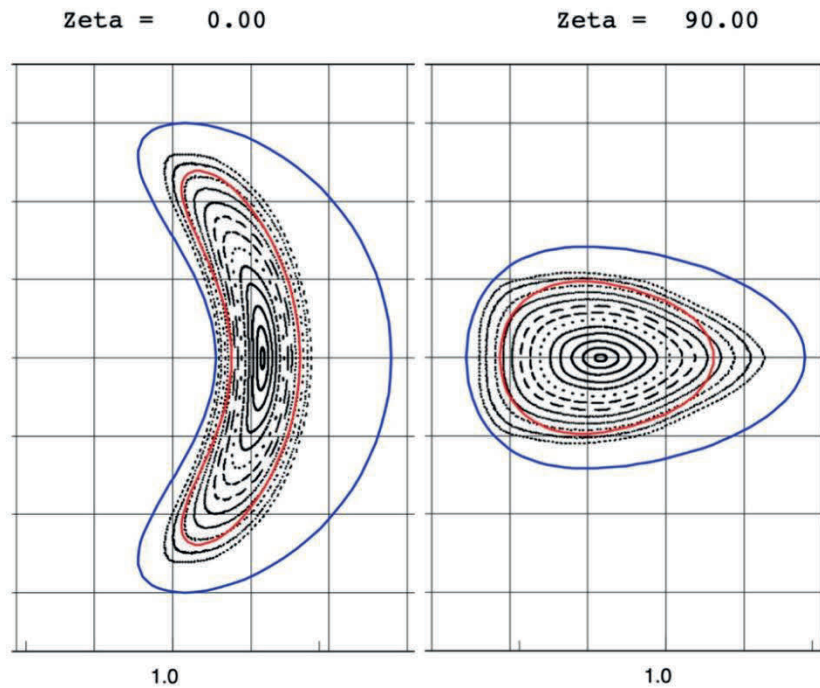


Fig. 3.9.9-3 Horizontally elongated magnetic surfaces with poloidal currents 200 kA for IVF and -24.6 kA for OVF PFCs. Red line shows shape of standard configuration. Blue line shows the vacuum vessel wall.

For creating the vertically elongated shape of the magnetic surfaces, we changed the polarity of the poloidal coil currents. The magnetic surfaces of this operation is shown in Fig. 3.9.9-4. Island of 2/6 mode appears because the rotational transform profile is shifted down. The application of the poloidal field has an effect of the rotational transform change in this case. In order to eliminate islands, we applied the auxiliary toroidal field of -0.045 T (toroidal field is decreased) for shifting up the rotational transform as shown in Fig. 3.9.9-5. A clear magnetic surfaces are created again with such a combination of the PFC currents and the auxiliary TFC currents.

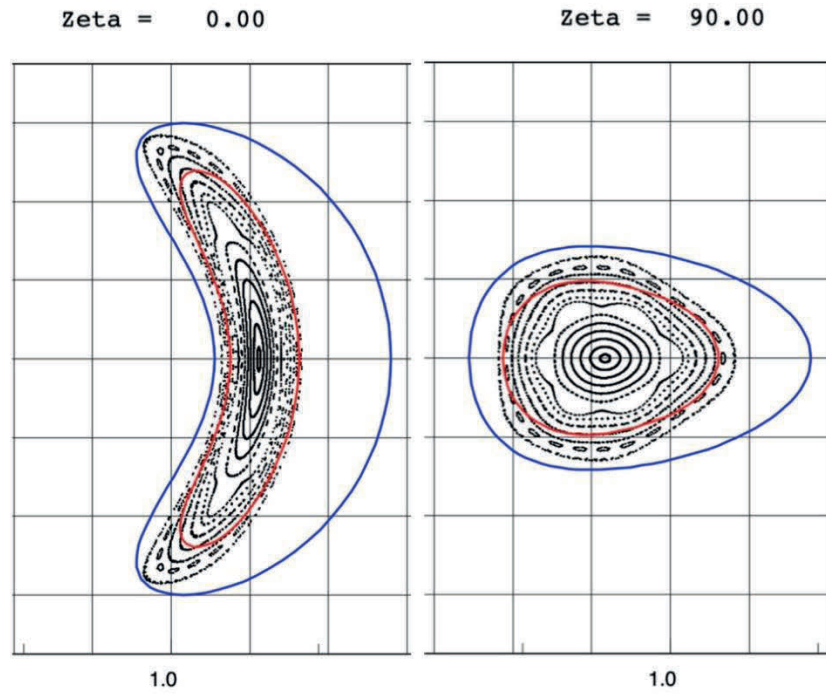


Fig. 3.9.9-4 Vertically elongated magnetic surfaces with poloidal currents -200 kA for IVF and 24.6 kA for OVF PFCs. Magnetic islands of 2/6 mode appears

The shape of magnetic surfaces are different at different toroidal angles of 3-D configuration. However it is possible to find a toroidally averaged shape of the full torus. Fig. 3.9.9-6 shows toroidally averaged cross sections of the LCFS for two cases of the quadrupole poloidal field controls of CFQS. Fig. 3.9.9-6(a) is the toroidally averaged cross section of the horizontally elongated configuration. The shape of the magnetic surfaces is shown in Fig. 3.9.9-3. Fig. 3.9.9-6(b) is the toroidally averaged cross section of the vertically elongated configuration (magnetic surfaces are shown in Fig. 3.9.9-5). Fig. 3.9.9-6(b) looks like a standard tokamak cross section. In fact, it has an ellipticity of  $\kappa = 1.7$  and the triangularity  $\delta = 0.33$ . In the standard operation of ITER, they designed the plasma shape with  $\kappa = 1.7$  and the triangularity  $\delta = 0.33$ , which are exactly the same values of the CFQS toroidally averaged cross section shape.



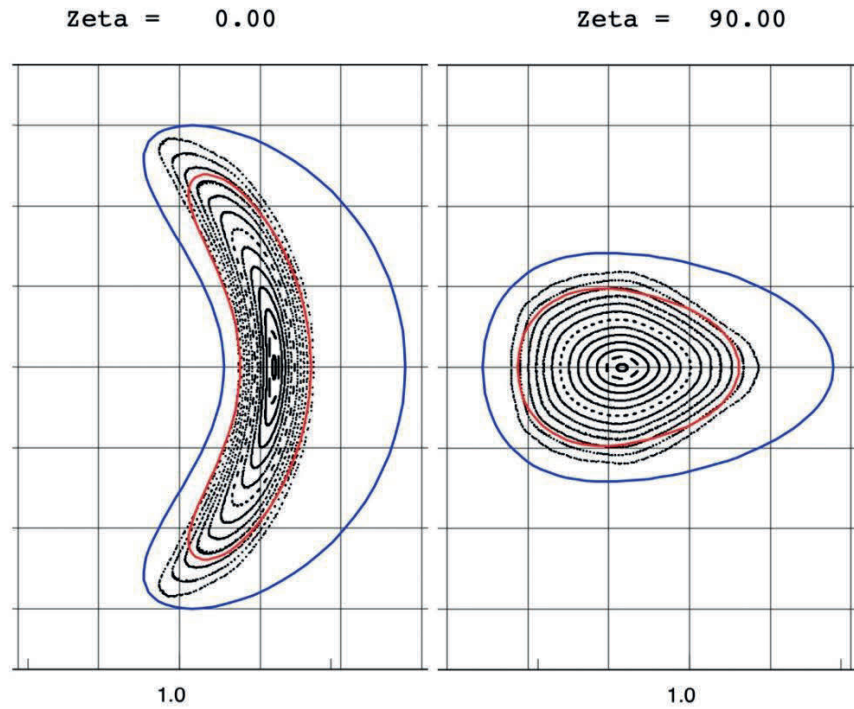


Fig. 3.9.9-5 Vertically elongated magnetic surfaces with poloidal currents -200 kA for IVF, 24.6 kA for OVF poloidal field coils and auxiliary toroidal field of -0.045 T. Magnetic islands are eliminated due the upper shift of the rotational transform with auxiliary toroidal field.

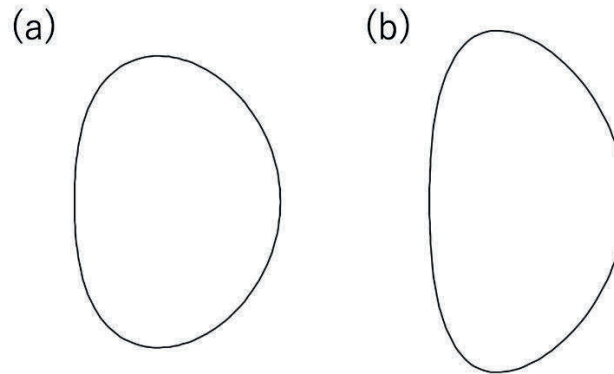


Fig. 3.9.9-6 Toroidally averaged cross sections of the LCFS for two cases of the quadrupole poloidal field controls. (a) is for the horizontally elongated configuration. (b) is for the vertically elongated configuration.

The Mercier stability conditions for three different configurations with quadrupole control is shown in Fig. 3.9.9-7. The equilibria are calculated with the volume-averaged plasma beta of 0.5 %. The equilibrium of horizontally elongated configuration is marginally stable. The stability of the plasma turbulence is now investigated using the GKV code [3.9.9-2]. Because these equilibria are produced

within available range of magnetic coil operations of CFQS device, the measurement in the experiment of plasma turbulence is very important for understanding the plasma transport in the advanced stellarators.

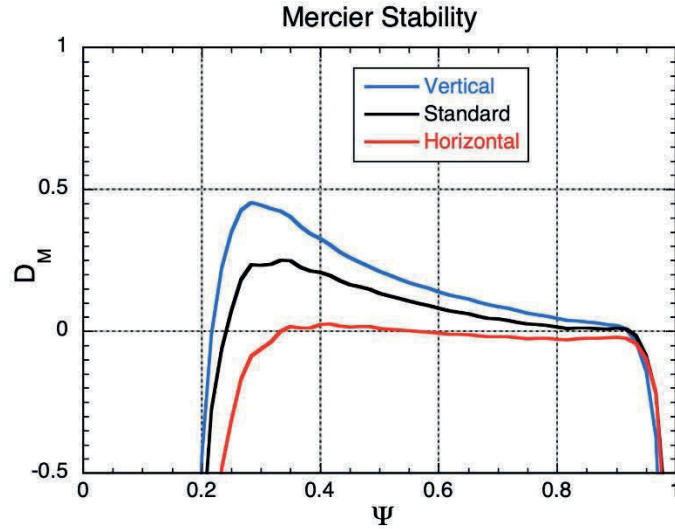


Fig. 3.9.9-7 Mercier stabilities for three configurations with different ellipticities. Plasma pressure is set for the volume-averaged beta of 0.5 % for all three cases.

## References

- [3.9.9-1] J. Todoroki, MAGN code (1986).
- [3.9.9-2] T. –H. Watanabe *et al.*, Nucl. Fusion **46** (2006) 24.

## 4 Engineering design

Only an overview of engineering design is given in this chapter. If you want to see the details, please refer to the appendix.

### 4.1 Whole assembly

#### 4.1.1 Specification for engineering design

The CFQS design is based on 2b32 CHS-qa configuration, and reduces the major radius, increases the aspect ratio, and reduces the magnetic field slightly to reduce costs and make it easier to manufacture. Table 4.1.1-1 shows physical main parameters of the CFQS. We can achieve low magnetic shear and a shallow well structure throughout the entire region as mentioned in the chapter

for the equilibrium. The dominant ripple is the toroidal mode  $B_{1,0}$ , which indicates a tokamak-like or QA configuration. The CFQS project aims to confirm the effectiveness of this equilibrium. The aspect ratio of CFQS is the smallest in helical devices and the coil shape is extremely complicated. They are the disadvantages that make engineering is relatively harder than other devices. For example, the work area in the central region is very narrow and special structural idea is necessary for assembling the CFQS. The electromagnetic force will be locally large although the magnetic field in the plasma is not so large and only 1T. Therefore, a strong reinforcement structure is required. They are engineering disadvantages for cost reduction. As described later, the direction of the electromagnetic force is unlike the tokamak. Distinctive design is required because vertical and toroidal components are generated in the electromagnetic force.

Table 4.1.1-2 gives technical data of the CFQS. A basic QA configuration can be produced by four types of modular coils (for total of 16). However, to allow flexible configuration, we will install four poloidal field coils (to move the magnetic axis horizontally) and twelve toroidal field coils (to change the rotational transform).

Table 4.1.1-1 Comparison of physical specifications for stellarator.

No	Parameter	CFQS	W7-X	HSX
1	Type	QA	QI	QH
2	Major Radius (m)	1.0	5.5	1.2
3	Minor radius (m)	0.25	0.5	0.15
4	Aspect ratio	4	11	8
5	Magnetic field (T)	1	3	1
6	Toroidal periodic number	2	5	4
7	Rotational transform	0.35-0.38	0.85-1.0	1.0-1.1
8	Magnetic well depth	0-0.025		

QA; Quasi-axisymmetric configuration

QI; Quasi-isodynamic configuration

QH; Quasi-helical symmetric configuration

Table 4.1.1-2 Facilities of the CFQS.

Facility	Parameter	Unit	Value			
Plasma	Pulse width (s)	s	0.1 s for short pulse, 120 s for long pulse			
	Magnetic field	T	1 T for short pulse, 0.09T for long pulse			
	Heating	kW	450 (54.5GHz ECH 0.1s pulse)			
			20 (2.45GHz RF)			
			1,000 (NBI 40kV 0.1s pulse)			
	Diagnostics		Thomson scattering, microwave interferometer, Langmuir probe, HIBP, CXRS et al.			
Coil	Name		MC	PFC(IV)	PFC(OV)	TFC
	Cross section	mm <sup>2</sup>	69 x 132	48 x 184.5	100.5 x 48	66 x 7
	Number of types		4	1	1	3
	Number of coils		16	2	2	12
	Number of turns per one coil		12 x 3 x 2	16 x 4	8 x 2 x 2	8 x 2
	Winding method		Pancake	Solenoid	Pancake	Solenoid
	Cross-sectional area	mm <sup>2</sup>	58.83	58.83	58.83	22
	Maximum current	kA	4.34	6.25	6.25	2.0
	Ground insulation	kV	2.4	2.4	2.4	0.6
	Test voltage against the ground	kV	5.8	5.8	5.8	2.2
	Layer insulation	kV	0.4	0.3	0.4	0.16
	Impulse test voltage	kV	1.0	1.0	1.0	0.4
	Heat resistance class		B	A		B
	Cooling method		Water cooling			Natural air
Short pulse PS	Total flat top power	MW	34.18	6.28	9.86	2.38
	Energy consumption	MJ	30.98	2.87	4.46	0.45
	Pulse width (RWET)	s	0.906	0.457	0.452	0.189
	Power source		A motor generator			
Long pulse PS	Total flat top power	MW	0.28	0.051	0.080	0.019
	Power source		Mobile energy storage stations			
Vacuum vessel	Cross-sectional shape		Bean shape			
	Load support		8 leaf spring type legs			
	Material		SUS316 with thickness of 6mm			
	Number of ports		Over 46			
	One turn break		Nothing			
	One turn resistance	mΩ	0.4 (By ANSYS/Maxwell)			
	Baking temperature		130 °C or less			
	Vacuum pumping		1500 ℓ/s TMP x 2			

#### 4.1.2 Overall Structure

Fig 4.1.2-1 shows schematics of the CFQS. The CFQS body is approximately 2800 mm high between a top frame and a bottom frame and has an outer diameter of 4300 mm. The electromagnetic force applied to the modular coils is supported by a cage-type support. These devices will be installed in a torus hall with power supplies, as shown in Fig 4.1.2-2. Fig 4.1.2-3 and Fig 4.1.2-4 indicate main dimension of the CFQS. To install various equipment's around the CFQS body, stages with a height of approximately 2.315m and a width of 10m will be installed. The center height of the body is planned to be 3.5m from the floor, and we are going to create large space under the device to install measuring instruments and related equipment.

The part list is shown in Table 4.1.2-1. The total weight is about 34 tons, and the heaviest part is the top and bottom frame.

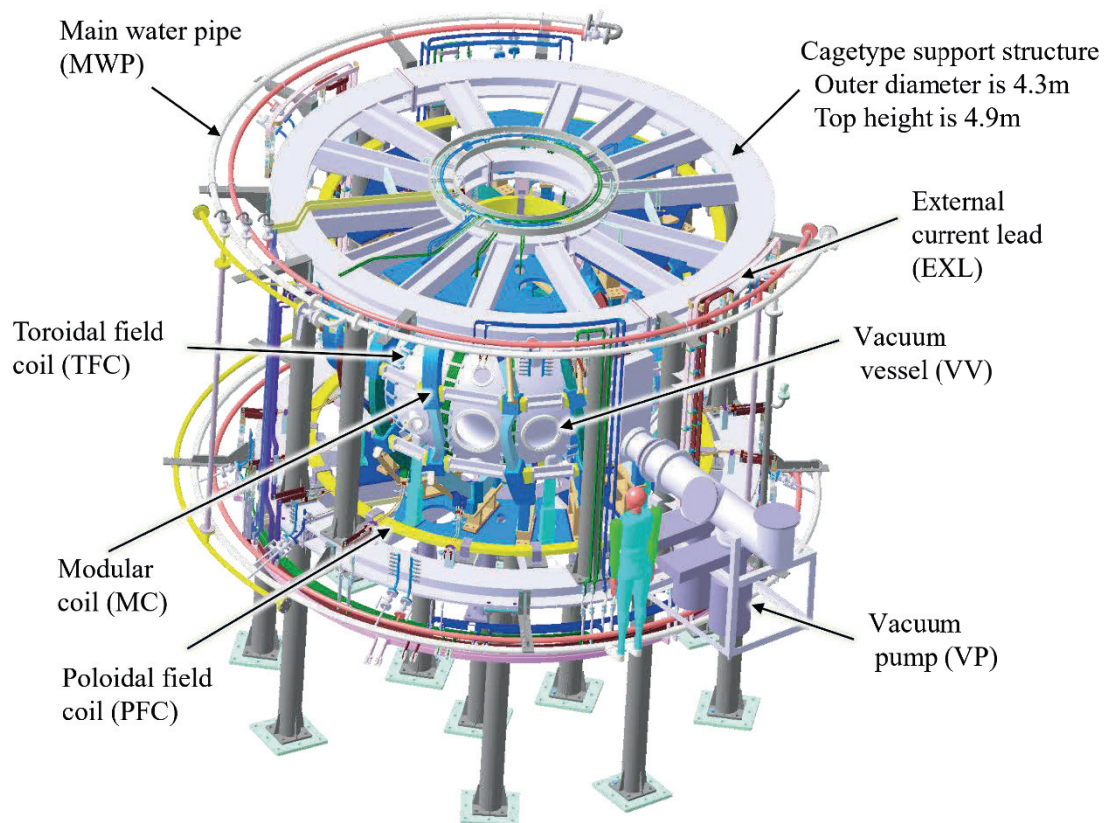


Fig 4.1.2-1 Schematic drawing of the CFQS. The top height and the outer diameter are approximately 4900 mm and 4300 mm respectively.

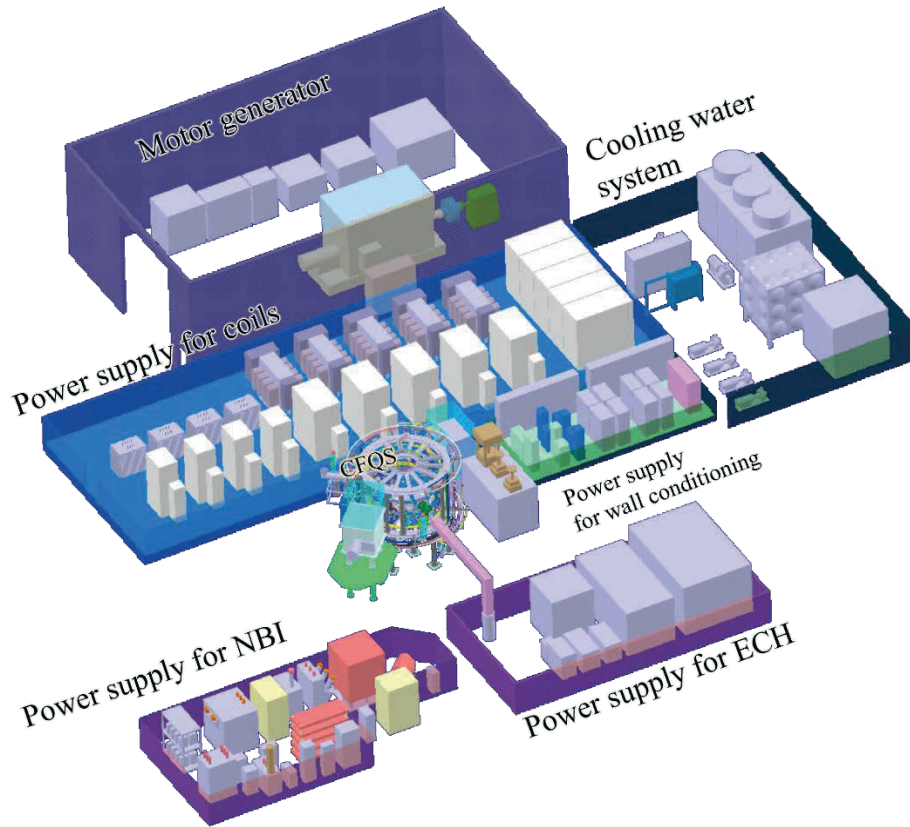


Fig 4.1.2-2 Layout of the research laboratory. The installation space for the power supply systems is much larger than that of the CFQS itself. A laboratory with about 60 m times 40 m that can store them is required. A new experimental building to store them will be built on another site separate from the 0.09 T experiment.



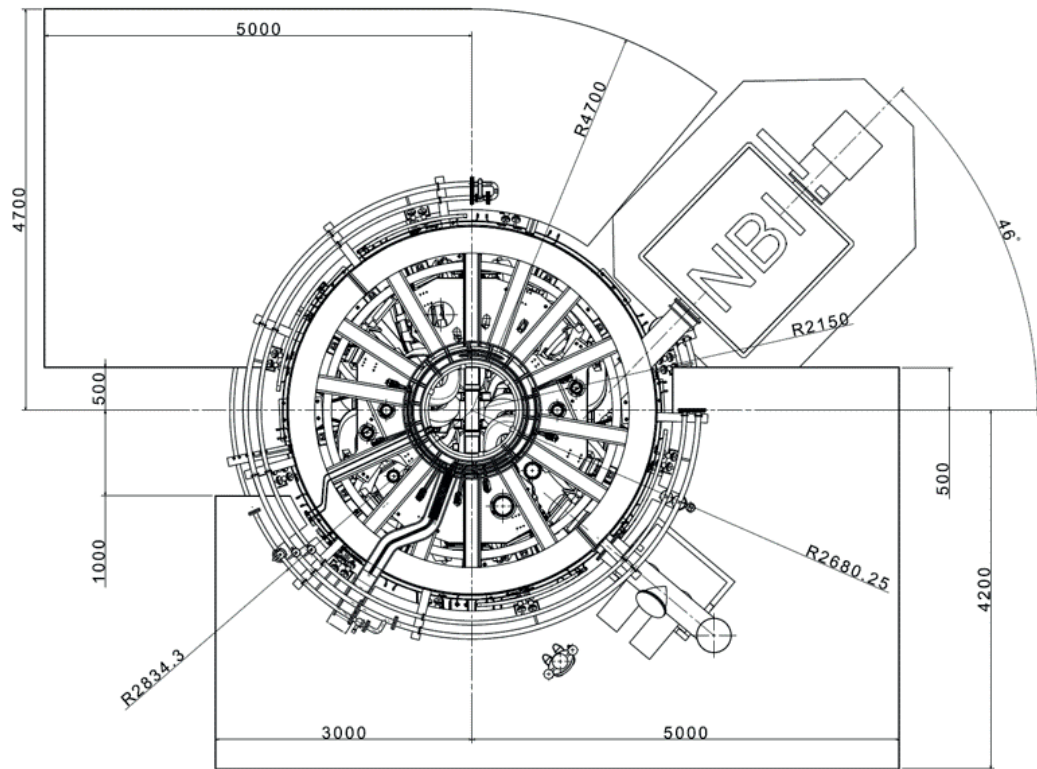


Fig 4.1.2-3 Top view of the CFQS. To install various equipment's around the CFQS body, the stages with a height of about 2.3 m and a width of about 10 m will be installed.

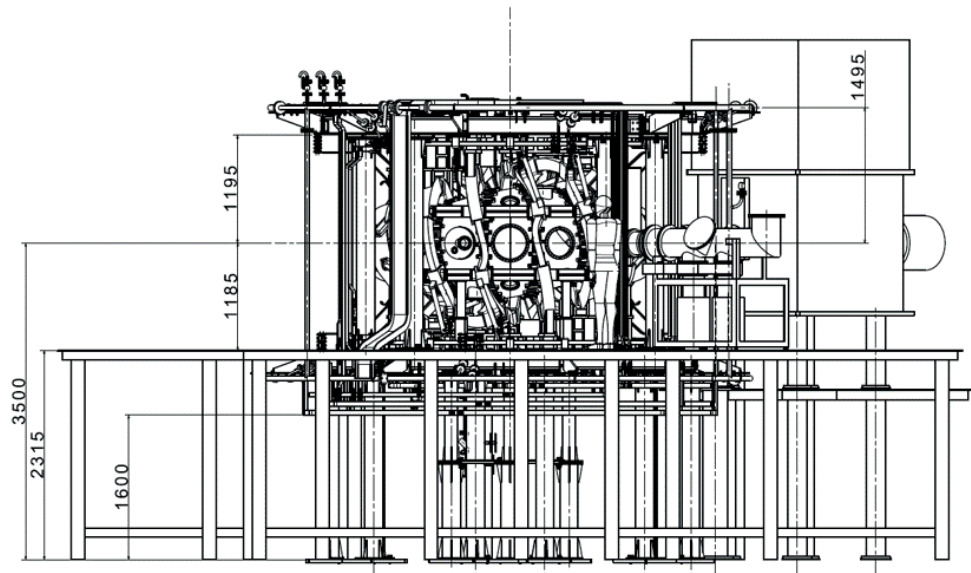





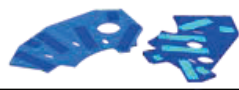


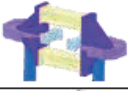


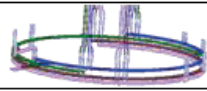


Fig 4.1.2-4 Front view of the CFQS. The center height of the CFQS body is planned to be 3.5 m from the floor to create large space under the CFQS body to install related equipment.

Table 4.1.2-1 Parts list of the CFQS.

The total weight is about 34 tons, and the heaviest is the bottom frame.

No	Product	Part	Mass(kg)	Quantity	Total(kg)	Picture
1	Vacuum vessel with TFC's and legs	Type A	400	2	2,160	
		Type B	680	2		
2	NBI port flange		60	2	120	
3	Modular coils (MC)	MC1	810	4	12,584	
		MC2	772	4		
		MC3	782	4		
		MC4	782	4		
4	Linked beam between MCs (LBB)	Long	16	28	480	
		Short	4	8		
5	Top and bottom frames (TPF and BTF)	Top	4100	1	8,300	
		Bottom	4200	1		
6	Intermediate base plate (IBP)	M1M2	300	4	2,080	
		M3M4	220	4		
7	Outer pillars (OP)	Pillar	140	8	1,120	
8	Leg of the CFQS (LOF)	out	140	8	1,600	
		in	120	4		
9	Center support structure (CSS)		400	1	400	
10	Main water pipes (MWP)		1500	1	1,500	
11	PFC (IO and OV)	IV	350	2	1,600	
		OV	450	2		
12	External current leads		400	1	400	
13	Others (extra)		1656	1	1656	
Sum					34,000	

## 4.2 Coil system

### 4.2.1 System configuration

Schematic of the coil system is shown in Fig 4.2.1-1. It shows 16 modular coils (brown), 4 poloidal field coils (yellow) and 12 toroidal field coils (pink). The last closed magnetic flux surface (LCFS) is shown in beige. A basic QA configuration can be produced by four types of modular coils (for total of 16). However, to allow flexible configuration, we will install four poloidal field coils (to move the magnetic axis horizontally) and twelve toroidal field coils (to change the rotational transform). Plasma equilibrium control is planned to be performed mainly by the PFC and secondarily by the TFC. A TFC is a simple planar coil which will be made by winding a cable around a vacuum vessel without any cooling. A PFC is a simple planar coil cooled by pure water, which will be made by the vacuum pressure impregnation (VPI). A MC is a complex shape coil cooled by pure water, which will be made by the vacuum pressure impregnation. The coil geometry (winding path) of the MC was numerically designed to produce the QA configuration.

The coil currents are driven by nine power supplies. The power supplies, the diagnostics and the heating apparatus are different in the experimental phase, but the coil system is common. It will be constructed under the rated operation conditions.

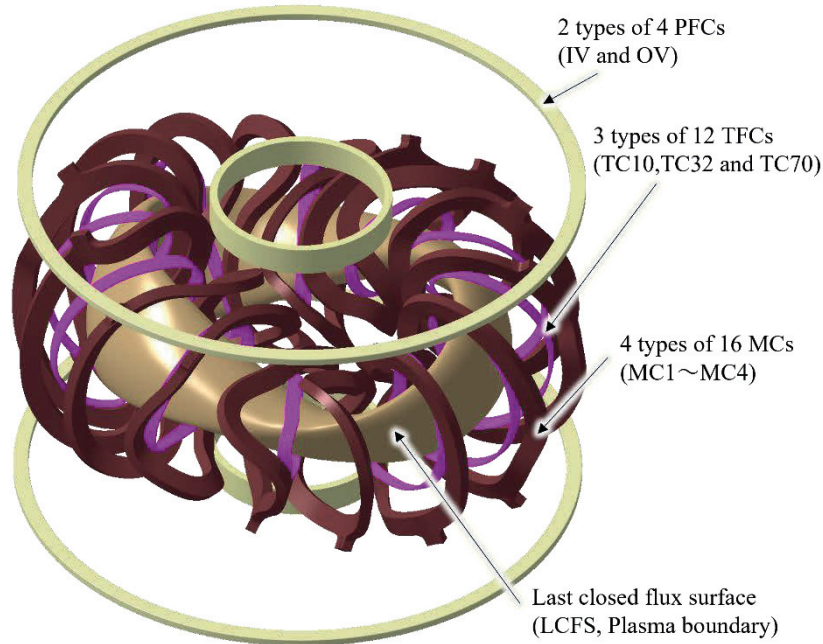


Fig 4.2.1-1 Schematic drawing of the three coil systems. the brown shows the modular coils, the pink the toroidal field coils, and the yellow the poloidal field coils. The LCFS is also shown in the picture. In the PFCs, the smaller radius coil is called IV and the larger radius coil is called OV.

#### 4.2.2 Modular coil system (MC)

Fig 4.2.2-1 shows the shape of the modular coil. Shape of the coil lead is not easy to decide properly in a desk study, because it is necessary to bend intricately considering interference with peripheral parts and fixing place. Therefore, the conductor shape will be adjusted according to the surrounding structure during installation. To prepare for this, leave 500 mm to 800 mm as an extra length and cut the conductor at an appropriate place during installation. After adjusting the length and bending them, the go and return conductors are wrapped with glass tape and fixed with a resin.

The cross section is shown in Fig 4.2.2-2. Since the current density is extremely high, the conductor temperature rises about 20 degrees per second of operation. To absorb this heat before next shot, the coils are cooled by pure water. Fig 4.2.2-3 shows joint of conductors. To reduce the number of power supplies, the three conductors are electrically connected in series outside the coil by the copper blocks of joint\_1 and the joint\_2. And in order not to increase the head loss of cooling water, the inlet and outlet of cooling water will be provided for each conductor. Therefore, the number of electric circuits is 1 per coil, and the number of cooling water flow paths is 3 per coil.

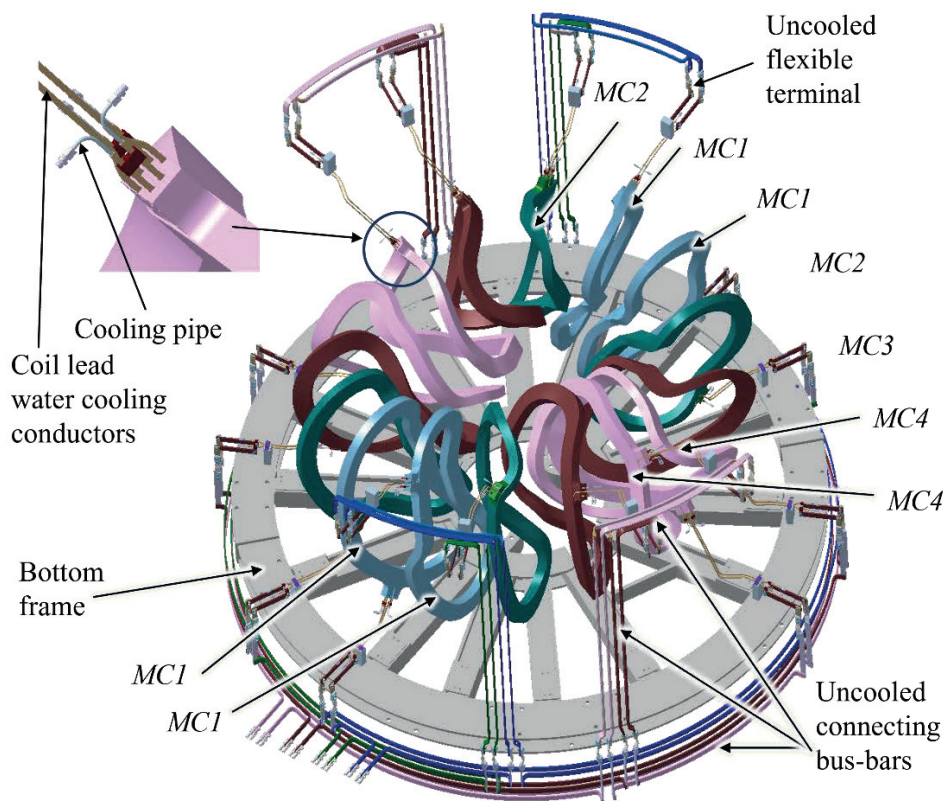


Fig 4.2.2-1 Modular coil system. Showing current leads, cooling pipes and connecting busbars. It consists of 16 modular coils with 4 types. The 2nd and 4th quadrant coils are installed upside down with the 1st and 3rd quadrant coils.



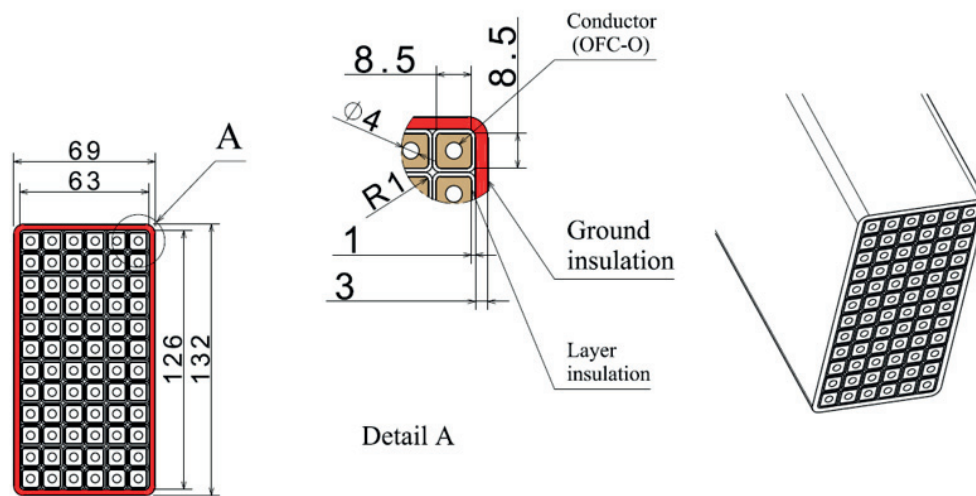


Fig 4.2.2-2 Cross section of the modular coil. The winding method is a double pancake with three simultaneous winding. The number of turns is 72 ( $6 \times 12$ ). The insulation process is vacuum pressure impregnation (VPI). The material of the conductor is hollow copper square tube of the Oxygen free copper annealed (OFC-O).

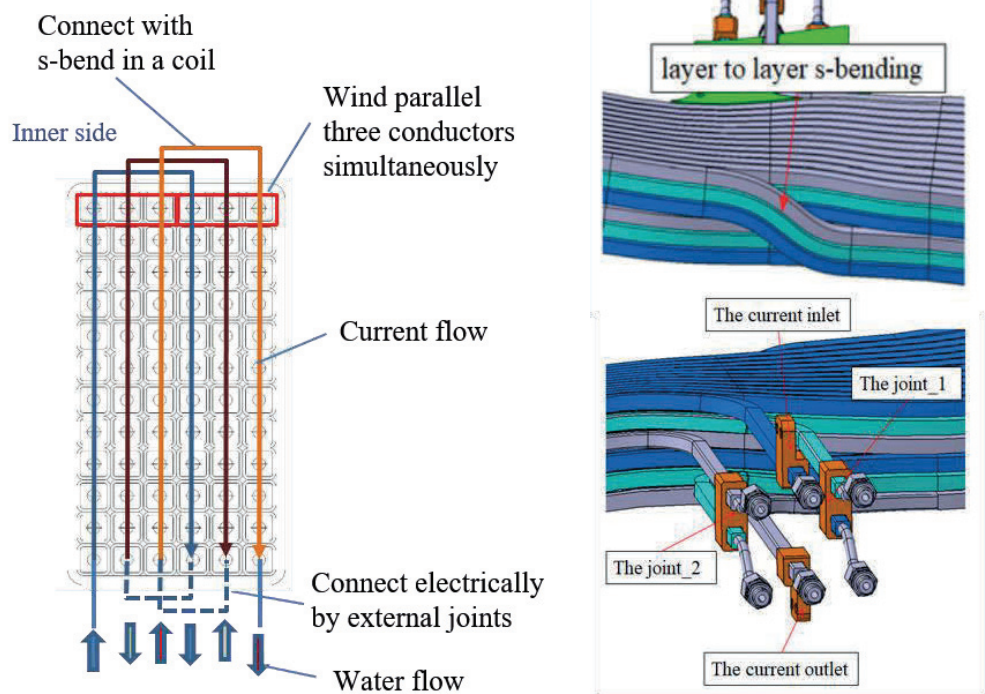


Fig 4.2.2-3 Joint and cooling pipes of the modular coil. Three double pancakes are electrically connect in series coutside the coil by the copper blocks. The inlet and outler of water is provided for each double pancake.

Exceptionally large magnetic forces are applied to the modular coils. The forces' magnitude and direction may be extremely complicated, and their characteristics are not easy to describe. They are like those of a tokamak's toroidal field coil, but the modular coils are more difficult to analyze and operated under more severe conditions because even the components that are negligible for tokamaks cannot be ignored. The strength of the coil conductor is not expected to be sufficient for large forces, the modular coil must be reinforced with the metal cases like the tokamak's toroidal field coil.

Fig 4.2.2-4 and Fig 4.2.2-5 show the coil support with the partial clamping type coil case. The shape of the clamp is roughly classified into 3 types of A, B and C. The type-A is the u-shaped clamp with one side open, the type-B is the u-shaped clamp made of flat plates, and the type-C is the u-shaped clamp with open inside. The two Type B clamps are connected by a connecting bar to prevent movement along the coil.

Pedestals for transmitting electromagnetic force to other support structure are welded on the coil case. It is necessary to strictly control the accuracy of the pedestal to contact other support structures, but it is difficult to secure that accuracy by assembly adjustment. Therefore, the policy is to manufacture pedestals with extra length left, assemble the coil and the case, and then machine to ensure the accuracy of the pedestal surface.

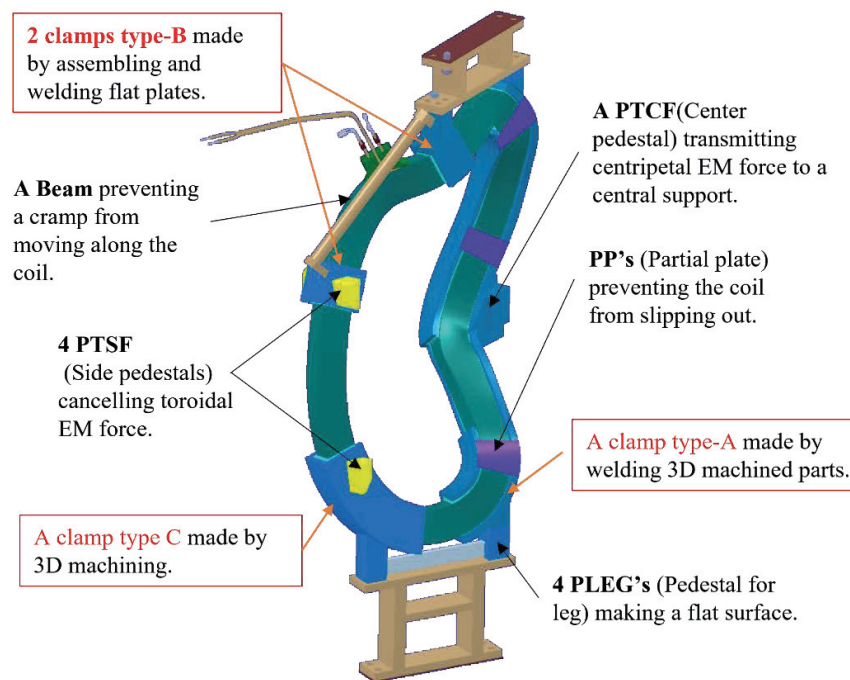


Fig 4.2.2-4 Modular coil with the partial clamping type coil case. In order to withstand a large electromagnetic force, reinforcement with a metal container is necessary. The figure shows a design example using a machined U-shaped clamps as a coil container. We will call it a partial large clamp type (PLCL).



Fig 4.2.2-5 Modular coil system with the PLCL, showing coils, legs, coil cases as a supporting structure, linked beams between the modular coils and the coil leads.



### 4.2.3 Poloidal field coil system (PFC)

Two pairs of PFCs will be installed in the CFQS. Main purpose of the poloidal field coil is to apply vertical field to change the position of magnetic axis. Layout and cross section of the PFC's are shown in Fig 4.2.3-1 and Fig 4.2.3-2.

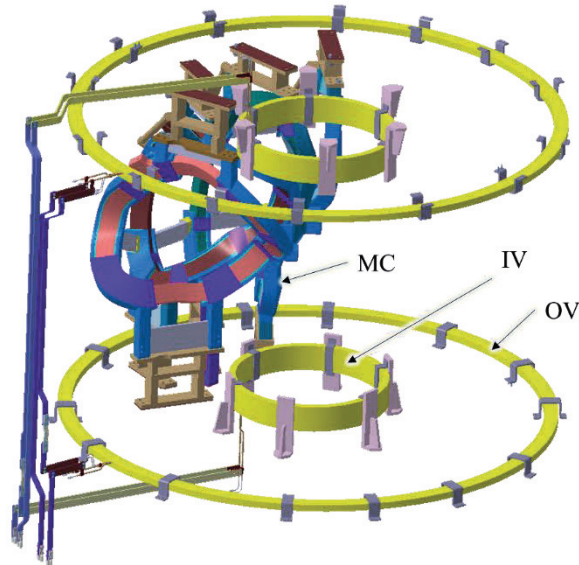


Fig 4.2.3-1 Layout of the poloidal field coil system. Showing the coils, the current leads, and the coil supports.

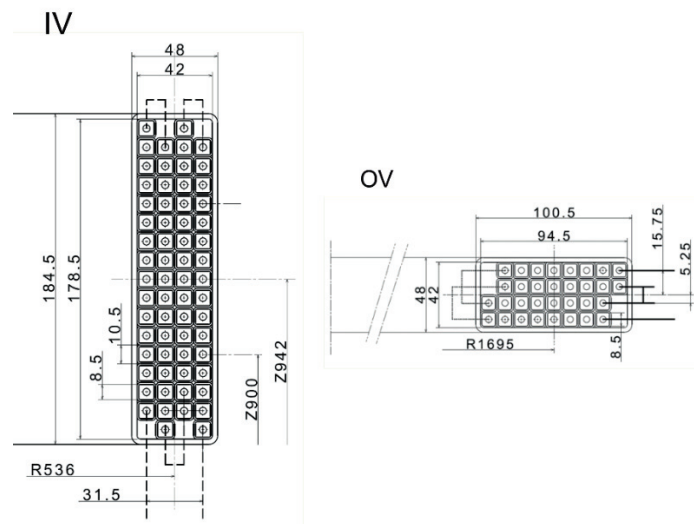


Fig 4.2.3-2 Cross section of the poloidal field coils. The winding method is a solenoid winding for the IV and a double pancake with two simultaneous winding for the OV. The number of turns is 64 for the IV and 32 for the OV. The insulation process is vacuum pressure impregnation (VPI). The material of the conductor is hollow copper square tube of the Oxygen free copper annealed (OFC-O).

#### 4.2.4 Toroidal field coil system (TFC)

The 12 toroidal field coils with three types will be installed in the CFQS. Main purpose of the toroidal field coil is to apply toroidal field to control the rotational transform. The shape of the coil are shown in Fig 4.2.4-1 and Fig 4.2.4-2.

It is obvious that the water-cooled coil is desirable to realize the low magnetic field long-time operation. For that purpose, it is necessary to increase the coil cross-sectional area, which makes winding difficult and there is a concern that the TFC may interfere with the MC. In addition, the development of a water-cooled current lead, which should be thin and flexible as in the current design, is not easy. Originally, the TFC is supposed to be an experiment with a short pulse, so it is judged that the experiment can be performed with natural air cooling. However, we want to expect cooling due to heat conduction.

The wiring path should be adjustable according to the actual product because it must pass through a complicated and narrow gap, and it is difficult to strictly design the route only by desk study. The conductor may be wound directly onto the vacuum vessel by the solenoid wind method. A cable with no cooling channel wrapped in insulator is clamped to the bobbin. First, a rectangular solid conductor was considered to reduce the occupied volume. A winding test was performed to confirm its validity, and it became clear that it was unrealistic to wind the rectangular conductor along the wall surface because the shape of the CFQS vacuum vessel was complicated very much. Therefore, although the occupied volume increases, priority is given to the ease of winding, and a cable with a circular cross section will be used as a conductor.

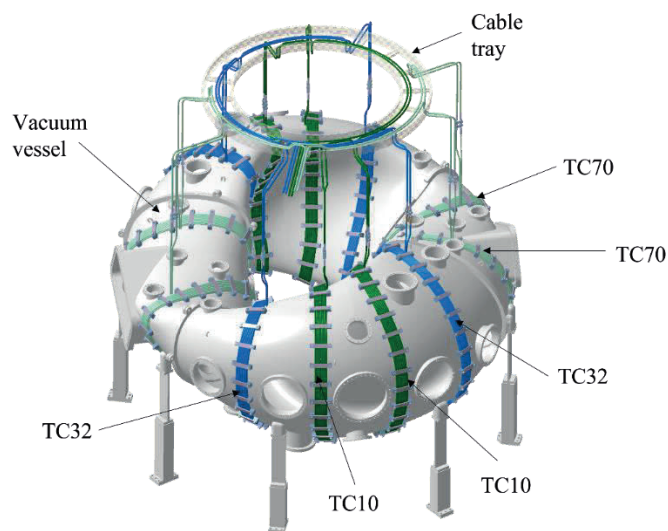


Fig 4.2.4-1 Schematic drawing of the TFC. Cables with insulation are directly wound on the vacuum vessel. The cables are cooled by natural air and heat conduction from the vacuum vessel.

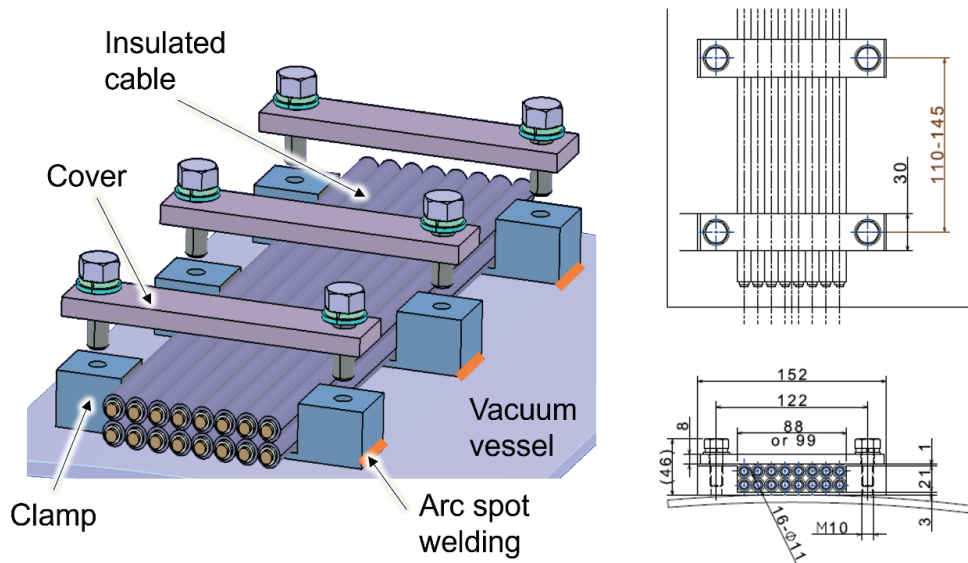


Fig 4.2.4-2 Cross section of the TFC. A conductor with no cooling channel coated by insulator is clamped to the bobbin on the vacuum vessel. The SUS bobbins are fixed on the vacuum vessel by the arc spot welding. Winding structure is two solenoids.

#### 4.2.5 Cage type support structure

The cage type support structure is shown in Fig 4.2.5-1 and Fig 4.2.5-2. Its main role is to prevent deformation of the modular coil. It also has, among other components, a vacuum vessel, other coils, and a diagnostic system attached on it.

Large tokamaks are typically designed with TFC wedges to support the centripetal forces. However, the CFQS cannot take this approach due to shape of constraints. Instead, a center support is designed to absorb such a large force, whose main components are central connection boards (CCB), some pedestals (PTCF) and central pillars (CP). The CPs are installed to support the PTCFs during assembly work. There is a big rectangular free area to access the inside port on the vacuum vessel.

Intermediate base plates (IBP) are flat on which the vacuum vessel and the modular coils are installed. Their upper surface becomes the installation reference for other parts, so it should be strictly controlled, such as improving flatness by machining and marking reference points for coil placement.

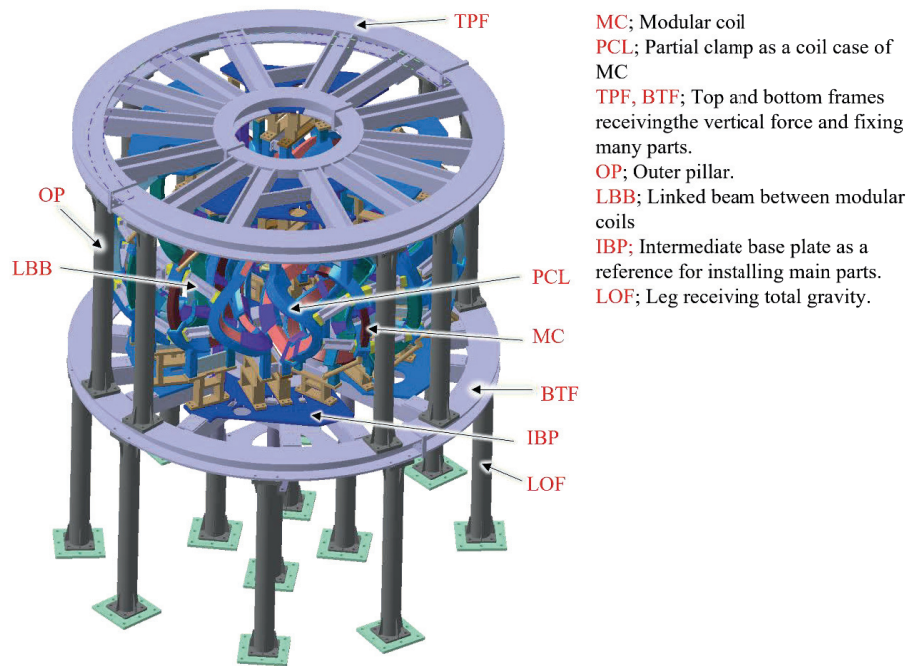


Fig 4.2.5-1 Cage type support structure with the PCL (Partial Large clamp). Even if the modular coil is reinforced with the coil case, the deformation of the coil cannot be reduced by itself. All modular coils must be strung together to cancel the EM force.

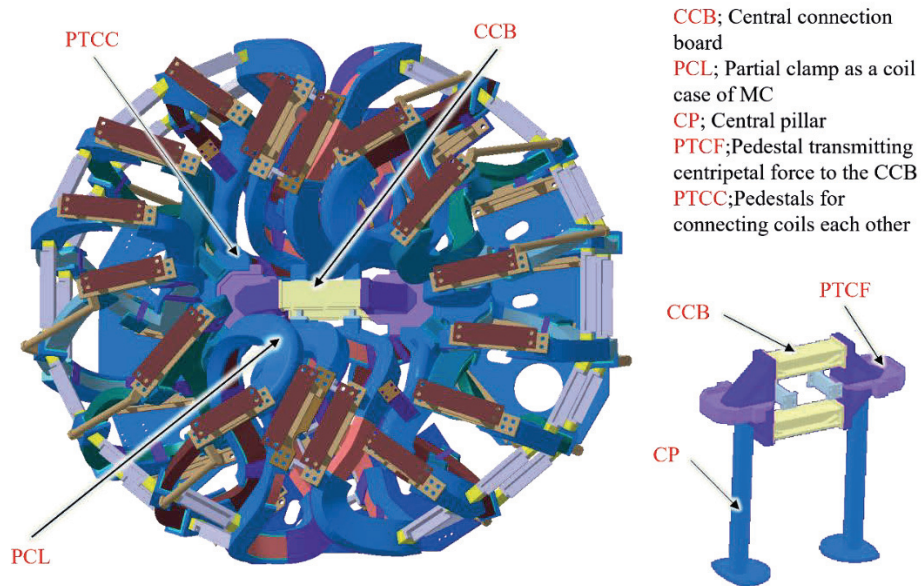


Fig 4.2.5-2 Cutaway view of the cage-type support structure. The electromagnetic force applied to the modular coils is supported by the support structure with the central connection board (CCB) to absorb the centripetal force. In order to cancel the centripetal force of each coil, it is necessary to connect the opposing coils. The CCB is a part for that purpose.

### 4.3 Vacuum vessel

#### 4.3.1 Structure of the main vessel

Fig 4.3.1-1 shows a schematic of the main vacuum vessel, which will be manufactured by welding together four sections of two types in the toroidal direction. The flanges used for welding are also shown in the figure. Since the electromagnetic forces on the vessel are expected to be small, it will be fabricated from SUS316L with relatively thin walls of 6 mm. As a result, the one-turn resistance is roughly  $0.3\text{ m}\Omega$  which we believe to be sufficiently large while not producing significant joule heating. The wall will be conditioned by baking them at  $130\text{--}150^\circ\text{C}$  via baking sheath heaters. The main vessel is fixed by eight leaf-type legs, added to allow for the vessel's thermal expansion during baking.

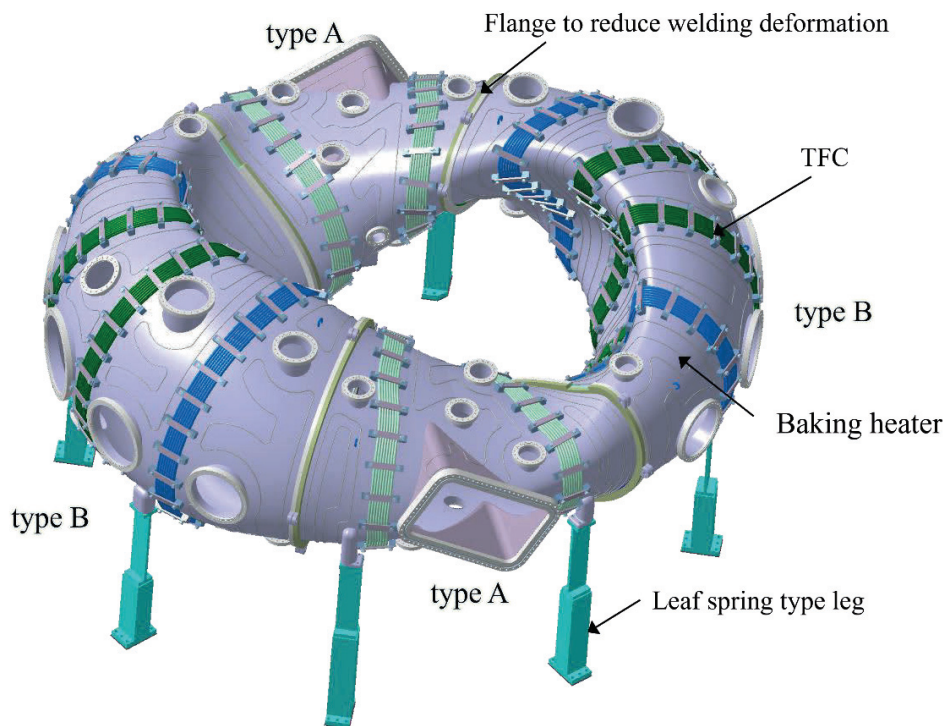


Fig 4.3.1-1 Schematic of the vacuum vessel. A torus-shaped vacuum vessel is made by joining four sectors with 2 types by welding. Each sector is assembled with modular coils, and a worker enters the vacuum vessel and welds them from the inside.



### 4.3.2 Cross-sectional shape of the main vessel

The shape of inner surface is shown in Fig 4.3.2-1. The shape of the inner wall of the vacuum vessel (VVIN) was defined by a plane moved out another 30 mm from the 2b32 surface on the inner side and an ellipse as large as possible without interfering with the MCs on the outer side. The cross section is much larger than the 2b40 standard configuration to work inside a vacuum vessel and to increase flexibility of various experiments. The metal limiters and the magnetic measurements are installed in the space with the minimum gap of 30 mm between the 2b32 plane and the inner surface of main vessel. The width and height of the inner surface are both at least 450 mm, which is sufficient for people to work inside. Using such a large vessel also helps to make the experiment more flexible.

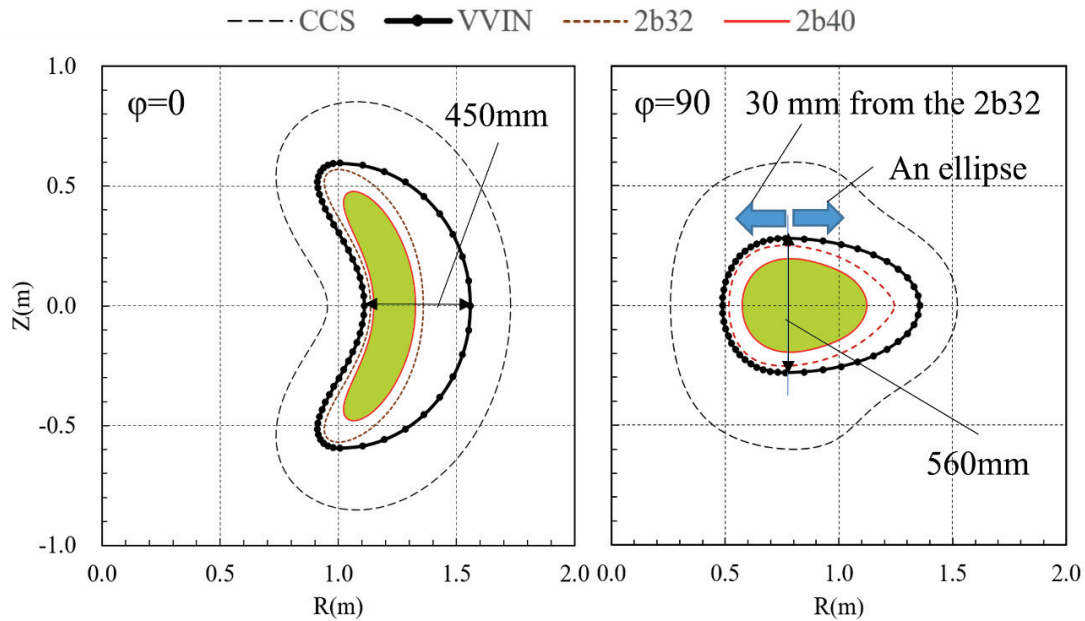


Fig 4.3.2-1 Cross section of the main vessel inner surface. The 2b40 shows a last closed magnetic surface of the standard equilibrium, The 2b32 a last closed magnetic surface of a reference configuration with the aspect ratio of 3.2, the CCS a current carrying surface on which the center of modular coil is placed, and the VVIN an inner surface of the vacuum vessel. The inner wall of the vacuum vessel is separated from the 2b32 by more than 30 mm. The metal limiters and the magnetic measurements are installed in that space. The cross-sectional size of the vacuum vessel is larger than 450 mm, and workers may move in that space.

## 4.4 Related equipment

### 4.4.1 Limiter system

As in other magnetically confined fusion devices, the plasma in the CFQS is confined within last closed magnetic flux surfaces and a boundary exists between plasmas and the machine-wall components. This boundary is called the scrape-off layer (SOL), which is determined by a solid surface (limiter) or topologically by magnetic field perturbations (divertor). In the SOL, the impurities originated from plasma-facing components may cause a lot of problems, such as huge radiative power loss and dilution of fuel particles.

The limiter configuration is to use a solid surface to define the edge of the plasma. Depending on the shape and the positioning of the solid diaphragm, the limiters are divided into (a) poloidal limiter; (b) rail limiter and (c) toroidal limiter, as depicted in Fig 4.4.1-1. In the CFQS, we intend to put four sets of the poloidal or rail limiter inside the vacuum vessel. These four limiters will be installed at two opposite toroidal locations of the torus. The limiter primarily serves to protect the wall from erosion by plasma heat loads. For withstanding heavy heat load, the limiter itself is usually made of a refractory material, such as carbon, tungsten, or molybdenum. Because the CFQS is free of major plasma disruptions, there is little thermal shock occurred during the operation. Thus, the sputtering and arcing rates from limiters are expected to be exceptionally low.

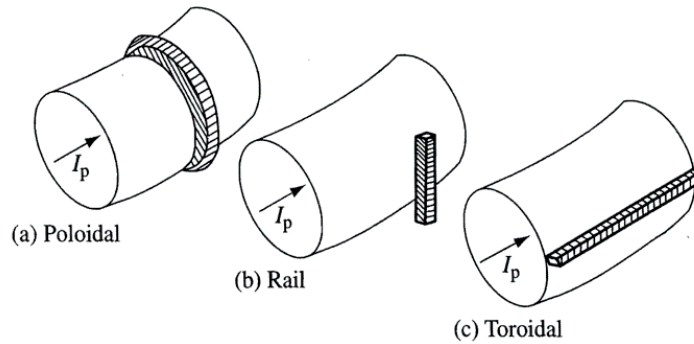


Fig 4.4.1-1 Schematic of several types of the limiter.



#### 4.4.2 Vacuum pumping system

The pumping system shown in Fig 4.4.2-1 will be installed for the CFQS.

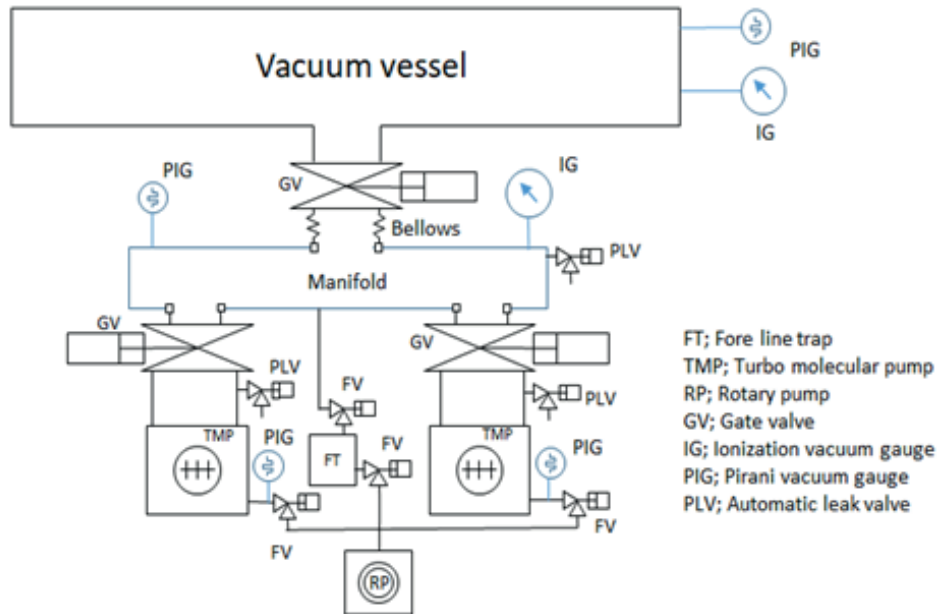


Fig 4.4.2-1 Vacuum pumping system. A rotary pump (RP) will be used in vacuum range of 20 to 30 Pa or more. Exhaust speed of two turbo molecular pumps (TMP) is 1500  $\ell/s$  each. The ultimate vacuum pressure will be  $1 \times 10^{-6}$  Pa.

#### 4.4.3 Wall conditioning system

Wall conditioning is important to produce plasma after the maintenance of vacuum vessel. Typical methods are glow discharge with helium or hydrogen, and titanium getter.

For other conditioning, the discharge cleaning with the ECH may be applied. The plasma may be created by 2.45 GHz microwave heating. The resonance magnetic field strength of this frequency is 0.0875 T, and steady state magnetic field is favorable for this purpose. Microwave will be generated by magnetron and transferred by a wave guide.

#### 4.4.4 Fuel gas supply system (Gas puff system)

Various kinds of gases will be injected for various purposes, it is likely that an equipment for performing them is required.

To generate plasma, it is necessary to control the supply amount of high purity gas. To do that, high-speed control valve system to adjust gas injection rate with gas purification function to remove impurities from the injected gas is required. The equipment that does them is commonly called a gas puff system.

Normally, hydrogen gas is injected for plasma generation, but noble gas such as helium or argon may be injected. Nitrogen gas may be injected to calibrate the measuring instrument. Argon gas may be used for magnetic surface measurements. In addition, a large amount of nitrogen gas or dry air may be injected to open the inside of the vacuum vessel to the atmosphere.

#### **4.4.5 Vacuum management system**

Vacuum management is important to produce high-performance plasma, and instruments for that purpose and protective functions in case of trouble are required.

Typical instrument is high speed ionization vacuum gauge, quadrupole mass spectrometer, helium leak detector, and so on. As a vacuum protection device, a gate valve system for interrupting the vacuum in an emergency is essential. Detail will be designed in the future.

#### **4.4.6 Shutter system to protect the glass window**

Glass windows may be attached for plasma measurements. The plasma may cause the glass window to be coated with some film, making it difficult for light to pass through. To prevent such a problem, it is preferable to add a movable shutter on the vacuum side of the glass window and close the shutter when the glass window is not used. Since there is a high possibility that the glass window will be coated at the time of the wall conditioning with titanium getter or glow discharge, the shutter should be closed in such a case.

#### **4.4.7 Vacuum test equipment**

As the experiment progresses, various equipment will be added to the vacuum vessel port. To reduce the risk of vacuum leaks causing damage to working equipment, it is essential to confirm that newly added equipment has no leak in a unit test. The vacuum vessel with a vacuum pumping unit should be prepared separately from the CFQS body for a unit leak test.

#### **4.4.8 Compressed air supply system**

Compressed air supply system is used to control the gate valve. Detail will be designed in the future.

#### **4.4.9 Liquid nitrogen supply system**

Liquid nitrogen is often used for various purposes in fusion devices. They are nitrogen trap for removing impurities, pre-cooling of superconducting device, cooling of heat shields and so on. If desired, liquid nitrogen can be purchased in a Dewar bottle, but when the amount used is large, there are many cases where a liquid nitrogen production device is prepared. The need for such equipment will be considered separately.

4.4.10 Pure water cooling system

Pure water-cooling system is required to cool magnetic coil system, heating system, diagnostic system, and pumping system. And industrial water system to cool the motor generator may be also required. The below figure shows preliminary layout of pure water cooling system.

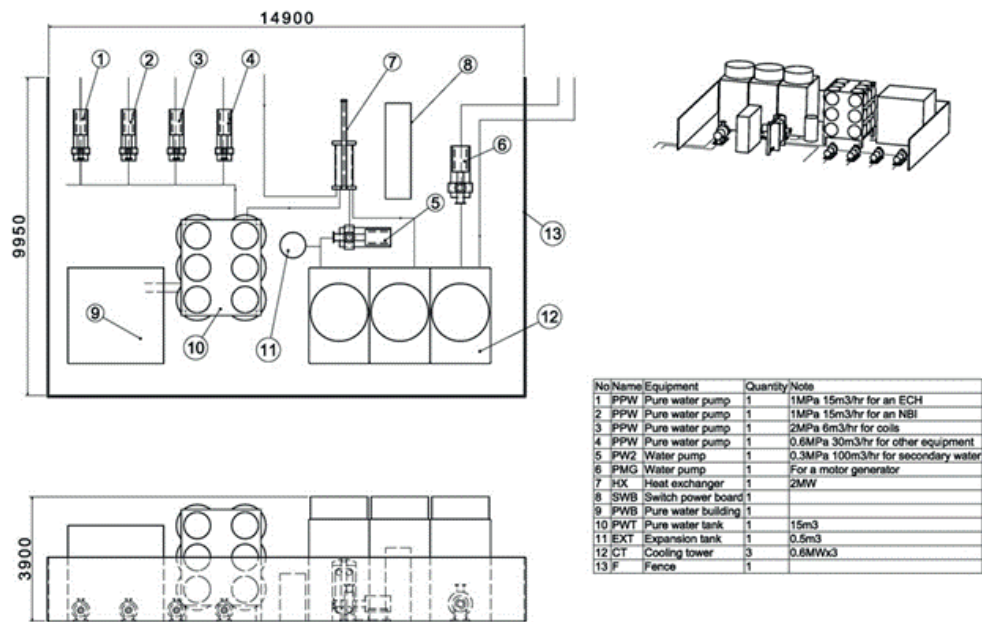


Fig 4.4.10-1 Preliminary layout of pure water cooling system

## 4.5 Power supply

### 4.5.1 Power supply system for the 1T operation

To apply large currents to the CFQS coils, a short pulse large capacity power supply of about 70 MVA and 1s of a pulse length is required. Since it is difficult to supply this power from the commercial power source, a current source with energy storage function is required. The power supply with an induction motor (IM) and a synchronous generator (SG) may be most suitable type for 1.0 T operation because it can store large amount of electrical energy and supply power with good controllability.

Fig 4.5.1-1 shows the preliminary one line diagram of power supply system with the generator with a flywheel type energy storage driven by the induction motor.

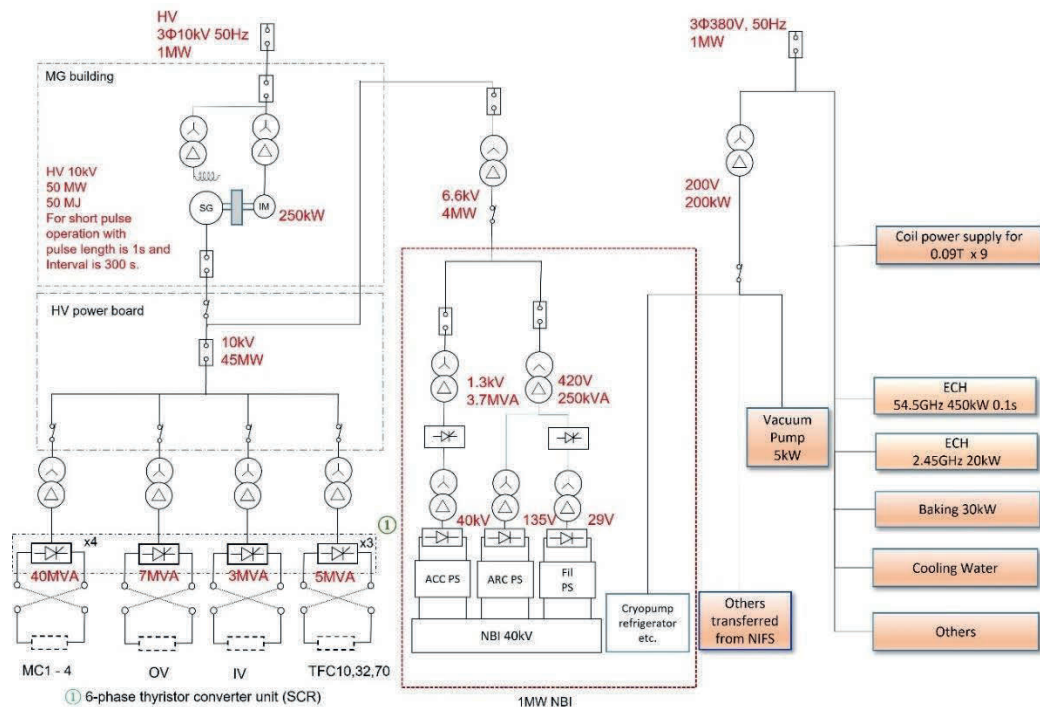


Fig 4.5.1-1 Power system with a flywheel type energy storage generator for the 1T operation.

## 4.6 Plasma heating system

### 4.6.1 Electron cyclotron resonance heating (ECRH) system

The main component of the electron cyclotron resonance heating (ECRH) system is gyrotron. The gyrotron system with an oscillation frequency of 54.5 GHz, a maximum output power of up to 450 kW and a maximum pulse length of 100ms will be installed. Fig 4.6.1-1 shows a preliminary layout of the ECRH system. It is necessary to secure a large area (100 m<sup>2</sup> for the power supply) near CFQS to install the ECRH system.

The EC-waves generated by the gyrotron effectively and locally heat the electrons at a position on the EC-wave beam path where the resonance condition ( $n \cdot \omega_{ce} = \omega - k_{\parallel} v_{\parallel}$  and  $\omega_{ce} \equiv eB/m_e$ ) is satisfied. Here, integer  $n$  denotes harmonic number,  $\omega_{ce}$  is electron cyclotron angular frequency,  $e$  is a unit charge of an electron,  $B$  is the strength of magnetic field,  $m_e$  is the mass of an electron with relativistic effect,  $\omega$  is angular frequency of EC-waves, and  $k_{\parallel}$  and  $v_{\parallel}$  are the components of wave number and electron velocity parallel to the magnetic field line, respectively. Applying the frequency of 54.5 GHz, the resonance condition for  $n = 2$  (second harmonic resonance) is satisfied with  $B = 0.97$  T.

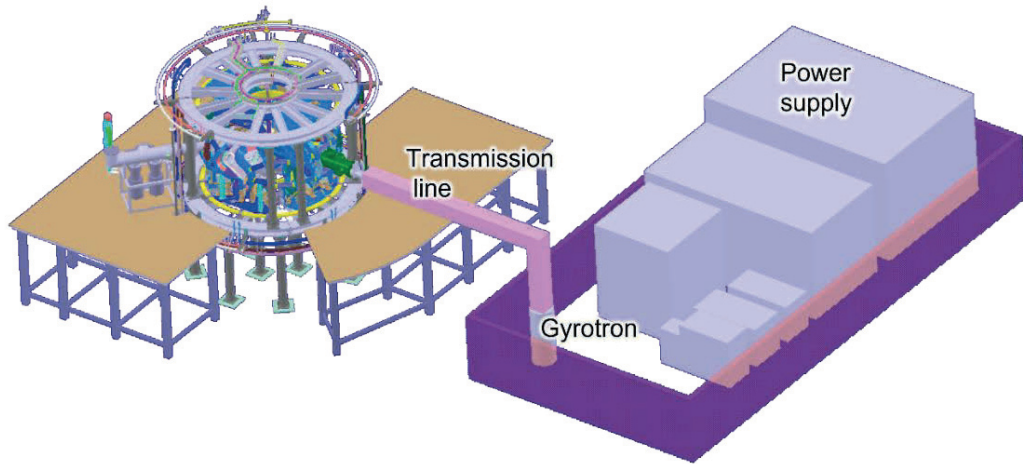


Fig 4.6.1-1 Preliminary layout of the ECRH system.

#### 4.6.2 Neutral beam injection (NBI) heating system

Neutral beam injection (NBI) is a powerful tool for plasma heating and drive of the plasma current and flow. To study energetic particle physics, tangential NBI is an inevitable device. Tangential port with diameter of 300 mm is recommended to install NBI. Fig 4.6.2-1 shows a preliminary layout of the NBI system for the CFQS. It is necessary to secure a large area (100 m<sup>2</sup> for the power supply and 10 m<sup>2</sup> for the ion source) near CFQS to install the NBI system.

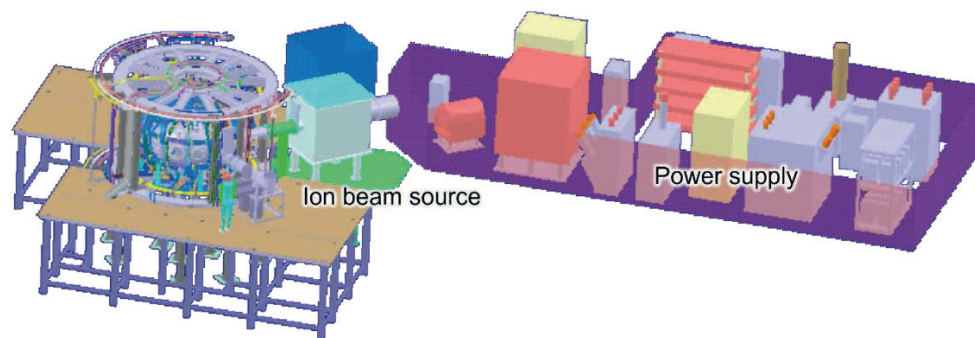


Fig 4.6.2-1 Preliminary layout of the NBI system.

## 4.7 Diagnostics system

### 4.7.1 Overview of diagnostic system

Diagnostics are indispensable for studying high temperature plasma physics in modern fusion research. There are interesting topics to be studied; transitions to improved confinement modes, formation of transport barriers, and their impact on plasma turbulence, etc. Roles of diagnostics are increasing in the studies on high temperature plasma properties, not only for fusion but also for basic physics.

CFQS is an innovatively designed device to achieve tokamak-like confinement properties and helical-like stability at the same time. Plasmas produced in the CFQS will become a good target for research which aim at achieving cost-effective stable burning plasmas. High-quality data based on detailed measurements should be obtained for comprehensive understanding of toroidal plasmas.

As mentioned above, anomalous transport and improved confinement modes are important issues for understanding toroidal plasmas. Based on the successful results of the advanced diagnostics in CHS and LHD, we will employ advanced diagnostic systems such as heavy ion beam probe (HIBP) and microwave reflectometry to study the spatio-temporal turbulence structure and the structures of electric field and plasma flow. After the installation of NBI in the future, we will consider developing charge exchange spectroscopy (CXs) for the measurement of radial electric field and plasma flow velocity to study the relation between toroidal rotation and momentum input.

Also, physics of density limit is important in helical devices because confinement property of helical systems is improved as the density increases following the scaling law. Therefore, higher priorities are given for the diagnostics of edge plasma, MHD and radiation power, including magnetic probe, bolometer, etc.

For basic diagnostics, microwave interferometer should be firstly developed to measure the electron density. Thomson scattering is also important to study the physics of transport barriers. Multi-dimensional measurement is useful for studying internal structure of basic plasma parameters. Therefore, the development of two-dimensional or three-dimensional measurements will be performed as far as possible. So that the structure and non-linear development of plasmas can be observed in detail.

Diagnostics planned in the CFQS are listed in Table 4.7.1-1 and

Table 4.7.1-2. Assignment of ports to these diagnostics is planned as shown in the section about the vacuum vessel. Some of the ports should be specifically designed for HIBP and Thomson scattering because these diagnostics require special geometries.



Table 4.7.1-1 Basic diagnostics.

<b>Diagnostics</b>	<b>Target</b>	<b>Remark</b>
Multichannel Thomson scattering	Electron temperature Electron density	
150 GHz $\mu$ -wave interferometer	Electron density	
Electron cyclotron emission	Electron temperature	
Soft x-ray detector	Bremsstrahlung	Motion of electrons
Hard x-ray detector	Runaway electron	
Fast neutral particle analyzer (NPA)	Ion temperature	
Visible light spectroscope	Ion temperature	
H $\alpha$ detector	Edge plasma	
Langmuir probe	Edge plasma	
Vacuum ultraviolet spectroscope	Impurities	
Pyroelectric detector	Radiation power	
Mirnov probe (Magnetic probe)	MHD instability	
Diamagnetic loop	Stored energy	
Rogowski coil	Plasma current	
CCD camera	Shape of plasma	

Table 4.7.1-2 Advanced diagnostics.

<b>Diagnostics</b>	<b>Target</b>	<b>Remark</b>
Beam fluorescence	Magnetic surface	Mapping
Far infrared interferometer	Electron density	High density
Multichannel resistive bolometer	Radiation power	
AXUV photodiode array	Radiation power	
Heavy ion beam probe (HIBP)	Electric potential	
	Turbulence	
	Plasma flow velocity	Rotation
Charge exchange spectroscopy (CXS)	Electric field	
	Plasma flow velocity	Rotation
	Ion temperature	
Motional stark effect (MSE)	Magnetic field	q-profile
Fast-ion loss diagnostics (FAST)	Beam ion loss	
Microwave reflectometer	Turbulence	

## 5 Research plan and schedule

The CFQS manages to offer available solutions to critical challenges for toroidal confinement fusion: it provides a steady-state, disruption-free reactor concept as well as neoclassically optimized

magnetic configurations. With respect to the magnetic configurations, the CFQS is designed and operated to achieve three types of advanced configurations, *i.e.*, QA, mirror linked, and divertor configurations. To guarantee the safety of the facility operation and accuracy of each magnetic configuration two steps are scheduled to operate CFQS, which are the low magnetic field operation and standard magnetic field operation.

## **5.1 Physics research plan**

### **5.1.1 Research plan for 0.1 T operation**

The research plan for the 0.1 T operation is as follows,

- i. Operate all the diagnostics and auxiliary systems, *e.g.*, electron gun, CCD camera, interferometer, probes, visible light, *etc.*
- ii. Achieve flexible magnetic configurations, *i.e.*, QA configuration, mirror linked configuration as well as divertor configuration; check the accuracy of magnetic field configurations in vacuum by mapping experiment.
- iii. Verify optimization of neoclassical transport and whether the tokamak-like fundamental transport properties are realized or not.

### 5.1.2 Research plan for 1.0 T operation

The research plan for the 1.0 T operation is as follows,

- i. Neoclassically optimized magnetic configurations.
- ii. Turbulence and transport research.
- iii. Island bundle divertor.
- iv. Plasma-materials interactions in 3-D systems.
- v. Energetic-particle confinement.
- vi. Equilibrium and stability at high- $\beta$ .
- vii. Impurity confinement and accumulation.
- viii. Optimize the coil system for the next generation stellarator.

## 5.2 Construction schedule

- Phase I; Physics design and main machine design
  - Configuration
  - Neoclassical transport
  - MHD
  - Modular coils
  - Vacuum vessel
  - Supporting structure *etc.*
- Phase II; Fabrication of CFQS, transfer essential heating, and diagnostic systems from NIFS to SWJTU
  - NBI
  - Gyrotron
  - Interferometer
  - X-ray diagnostic *etc.*
- Phase III; Commissioning, verify construction accuracy, and obtain first plasma.
- Phase IV; Magnetic configuration studies and heating experiments in 0.1 T operation.
- Phase V; Magnetic configuration studies and heating experiments in 1.0 T operation.

For the experimental phase of 0.1 T operation, experiment building in Jiuli campus in SWJTU was renovated as China-Japan collaboration laboratory during 2020-2021. Following pictures, Fig. 5.2-1

and Fig. 5.2-2, show entrance, torus hall, control room, and meeting room of China-Japan collaboration laboratory.



Fig. 5.2-1 China-Japan collaboration laboratory in Jiuli campus, left: entrance, right: torus hall.



Fig. 5.2-2 China-Japan collaboration laboratory in Jiuli campus, left: control room, right: meeting room.

During FY 2024, the first plasma of the CFQS will be achieved.

NIFS-SWJTU JOINT PROJECT FOR CFQS  
~PHYSICS AND ENGINEERING DESIGN~  
VER. 5.1  
2023. AUG.

APPENDIX -A1 (BD)

~BASIC DESIGN~

CFQS TEAM



*NIFS; National Institute for Fusion Science*

*SWJTU; Institute of Fusion Science, School of Physical Science and Technology, Southwest Jiaotong University*

*Hefei Keye; Hefei Keye Electrical Physical Equipment Manufacturing Co., Ltd*

## Table of Contents

<b>1</b>	<b>General information</b>	<b>4</b>
1.1	Abbreviation	4
<b>2</b>	<b>Coil system</b>	<b>6</b>
2.1	System configuration	6
2.2	Modular coil system (MC)	6
2.2.1	Shape of the modular coil	6
2.2.2	Trajectory of the center the cross section	11
2.2.3	Tilt angle of each modular coil	18
2.3	Poloidal field coil system (PFC)	28
2.4	Toroidal field coil system (TFC)	33
2.5	Resistance	40
2.6	Inductance matrix	41
2.7	Wiring of the coil system	43
2.8	Current wave form to estimate required power of coil power supply	46
2.9	Support structure	50
2.9.1	Coil case for the modular coil	50
2.9.2	Cage type support structure to prevent deformation of the modular coil	53
2.10	Water piping system to cool the MC and the PFC	56
2.10.1	Flow rate and pressure drop of the cooling water in each coil	56
2.10.2	Requirements of main water piping system	59
2.10.3	Design of main water piping system	60
<b>3</b>	<b>Validation of the coil design</b>	<b>63</b>
3.1	Validating the ANSYS/Maxwell result for inductance	63
3.2	Electromagnetic force of the modular coil (MC)	64
3.2.1	Coil system for the CFQS and analysis method	64
3.2.2	Magnetic field and EM force distribution on the modular coils	66
3.3	Eddy current on the modular coil case (MC)	73
3.4	Structural analysis of the cage type support structure and the MC for 1T	74
3.4.1	Model of the analysis	74
3.4.2	Result of the analysis	76
3.5	Structural analysis of the modular coils for 0.1T	81
3.5.1	Magnetic field distribution and EMF on the modular coil	81
3.5.2	Model of the structural analysis	81
3.5.3	Result of the structural analysis	82
3.6	Magnetic field distribution of the poloidal field coil (PFC)	84
3.7	Magnetic field distribution and electromagnetic force of the toroidal field coil (TFC)	87
3.7.1	Magnetic field distribution	87
3.7.2	Estimation of the magnitude and direction of the EM force	88
3.8	Deflection of the TFC	92
3.8.1	Concept to fix the TFC	92
3.8.2	Equivalent Young's modulus of the cable obtained by experiment	93
3.8.3	Clamp pitch required to reduce the deflection of the cable	95
3.8.4	Design of the clamp to fix the 16 conductors	97

<b>4</b>	<b>Vacuum vessel</b>	<b>99</b>
4.1	The design goal of the vacuum vessel.	99
4.2	Cross section of vacuum vessel	100
4.3	Shape of the vacuum vessel defined by the Fourie expansion	104
4.4	Port location and the cross-sectional shape of vacuum vessel at the port	105
4.5	Design of leaf-spring type leg	114
4.5.1	Design values	114
4.5.2	Buckling load and safety factor	115
4.5.3	Bending stress with the forced displacement	116
4.6	Eddy current analysis of vacuum vessel	117
4.6.1	Time constant of eddy current and its effect on plasma discharge.	117
4.6.2	EM force on the vacuum vessel	121
4.6.3	Inductive heating of the vacuum vessel	123
4.7	Structural analysis of vacuum vessel	125
4.7.1	Stress and displacement in various operating conditions	125
4.7.2	Effect of mesh size in the analysis for the vacuum vessel	131
4.8	Baking heater for vacuum vessel	133
4.9	Preliminary layout of magnetic measuring elements	134
4.10	Preliminary layout of the view ports	135
4.11	Preliminary layout of the limiters	136
<b>5</b>	<b>Production flow of the CFQS</b>	<b>137</b>
5.1	Pre-assembly procedure of modular coils and vacuum vessel on site	137
5.2	Overall production flow	139
<b>6</b>	<b>Power supply system</b>	<b>140</b>
6.1	Requirements for the power supply system	140
6.2	Trial design of coil power supply for 0.09 T operation	141
6.3	Trial design of coil power supply for 1 T operation	142
6.3.1	Designed circuit diagram and the layout of MG building	142
6.3.2	Specifications of SG, IM, and a flywheel	143
<b>7</b>	<b>Related equipment</b>	<b>145</b>
7.1	ECH power injection antenna	145
7.2	Baking power supply	147
7.3	Vacuum pumping system	148
7.4	HIBP system	149
7.5	Magnetic surface measurement system	153
7.6	Langmuir probe in CFQS	156
7.7	LIBP system	157



## 1 General information

### 1.1 Abbreviation

This document includes various abbreviations. The following table shows their meaning.

Table 1.1-1 Abbreviation

No	Abbreviation	Description
1	A / F	Arc and filament
2	ACB	Air circuit cabinet
3	ACC / ACL	Acceleration
4	ACR / AVR	Auto current / Auto voltage regulator
5	ACSW	Acceleration Thyristor switch
6	AP	AC power distribution cabinet
7	APR	AC power regulator
8	ARTP	Adiabatic rise of temperature in a pulse
9	AVP / VP / TMP	Auxiliary vacuum / Vacuum / Turbo molecular pumping system
11	AWTR	Average water temperature rise
12	AXUV / VUV	Absolute extreme / Vacuum ultraviolet
13	BLA	Beam line auxiliary control board
14	BMAG	Bending magnet
15	BQ/BV	Quadrupole /Vertical magnetic field
16	BTF	Bottom frame receiving vertical force
18	CB	Control board or Circuit breaker
19	CCB	Central connection board
20	CCSC	Continuous c-shaped case
21	COOL OIL	Cooling oil equipment
22	CP / OP	Inner / Outer pillar
23	CRYOP	Cryogenic pump
24	CP/CTRL	Control panel
25	CV	Cross-linked polyethylene insulated Vinyl sheath
26	CXS	Charge exchange spectroscopy
27	DCC	DC capacitor
28	DCFL	Dedicated clamp for fixing a coil
29	DCL	DC reactor, DC inductor or Deceleration
30	DCM	DC generator and motor
31	DS	Disconnecter
32	ECE/ECH	Electron cyclotron emission / heating
34	EM/EMF	Electromagnetic/ Electromagnetic force
36	EQ	Equipment
37	FAST	Fast ion loss diagnostics
38	Fb/Fn	Binormal / Normal component of force
39	FIR	Far infrared
41	GS	Grounding switch
42	GTO	Gate turnoff Thyristor
43	HIBP	Heavy ion beam probe
44	HSYG	Horizontal synchronous generator
46	HX / SX	Heat exchanger or Hard / Soft x-ray
48	IACS	Conductivity of international annealed copper standard
49	IBP	Intermediate base plate
50	IM	Induction motor
51	Iota(t)	Rotational transform angle
52	IS	Ion source

No	Abbreviation	Description
53	ISO	Isolation
54	IV / OV	Inner / Outer vertical coil
55	Keye	Hefei Keye Electro Physical Equipment Manufacturing Co.
56	LBB	Linked beam between coils
57	LCFS	Last closed flux surface, Outermost magnetic surface
58	LHe	Liquid helium
59	LN2	Liquid nitrogen
60	LOF	Leg receiving gravity
61	LV / HV	Low / High voltage
62	MC	Modular coil or magnet contactor
63	MCCB	Molded case circuit breaker
64	MG	Motor generator
65	MSE	Motional stark effect
66	NBI	Neutral beam injector
67	NIFS	National Institute for Fusion Science
68	NPA	Fast neutral particle analyzer
69	OFC	Oxygen free copper
70	OH	Ohmic heating
73	PFC	Poloidal field coil or Plasma facing component
74	PLCL	Partial large clamp
75	PLEG	Pedestal for leg
76	PP	Partial plate
77	PS	Power supply
78	PSC	Polarity switching circuit
79	PTCF	Pedestal transmitting centripetal force or Center pedestal
80	PTSF	Side pedestal transmitting toroidal force to the next
81	q	Safety factor
82	QA / QH / QI	Quai-axisymmetric / Quasi-helical symmetric / Quasi-isodynamic configuration
85	REFCR	Refrigerator for cryogenic pump
86	RF	Radio frequency wave
87	RP	Rotary pump
88	RWET	Rectangular wave equivalent time
89	SA	Surge absorber
90	SB	Surge blocker
91	SCR	Thyristor
92	SG	Synchronous generator
93	SHIM	Thin piece of material used for alignment or spacer seam
95	SIM	Self-excited induction generator and motor
96	SW/SWB	Switch, switch board or power board
97	SWJTU	Southwest Jiaotong university
99	TB	Table or Terminal box
100	TCB	Temperature converter board
101	TFC	Toroidal field coil
102	TIC	Temperature indication and controller
104	TPF	Top frame receiving vertical force
105	TRF/TR	Transformer
106	VCB	Vacuum circuit breaker
107	VD	Voltage divider
109	VSYG	Vertical synchronous generator
111	VV/VC	Vacuum vessel or Vacuum chamber

## 2 Coil system

### 2.1 System configuration

Schematic of the coil system is shown in Fig 2.1-1. It shows 4 poloidal field coils (yellow), 12 toroidal field coils (pink) and 16 modular coils. The modular coils are a major part of coil system, they have the most complicate shape and largest total current. The coil geometry (winding path) of the MC was numerically designed to produce the QA configuration. A basic QA configuration, whose name is the 2b40 we defined, can be produced by the modular coils. The shape of plasma boundary, which is controlled by the last closed flux surface, is also shown in the figure. However, to allow flexible configuration, we will install the poloidal field coils (PFC) and the toroidal field coils (TFC). Plasma shape (equilibrium) control is planned to be performed mainly by the PFC and secondarily by the TFC. A TFC is a simple planar coil which will be made by winding a cable around a vacuum vessel without any cooling. A PFC is a simple planar coil cooled by pure water, which will be made by the vacuum pressure impregnation (VPI).

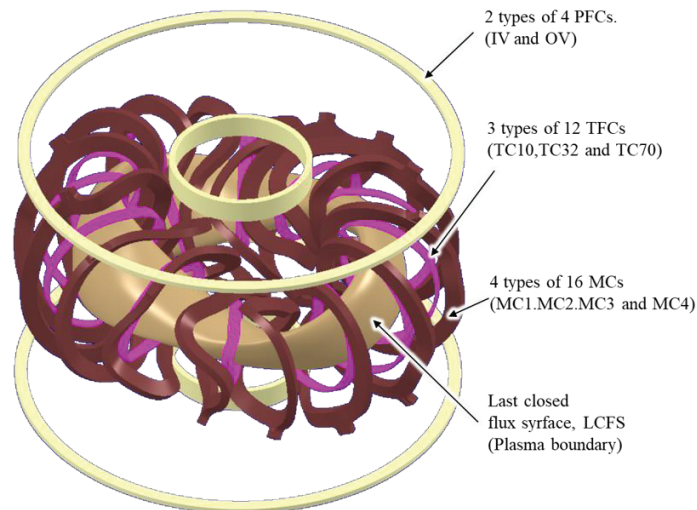


Fig 2.1-1 Schematic drawing of the three coil systems. the brown shows the modular coils, the pink the toroidal field coils, and the yellow the poloidal field coils. The last closed flux surface is also shown in the picture.

### 2.2 Modular coil system (MC)

#### 2.2.1 Shape of the modular coil

Fig 2.2-1 shows shape of the modular coil system. Shape of the coil lead is not easy to decide properly in a desk study, because it is necessary to bend intricately considering interference with peripheral parts and fixing place. Therefore, the conductor shape will be adjusted according to the surrounding structure during installation. To prepare for this, leave 500 mm to 800 mm as an extra length and cut the conductor at an appropriate place during installation. It will be wired in its final position after installing the modular coil in the CFQS body. After adjusting the length and bending them, the go and return conductors are wrapped with glass tape and fixed with a resin. The system consists of 4 types of 16 coils. In the figure, for example, four white MC1s have the same shape, but half of them are installed upside down. Table 2.2-1 shows the design parameters and Table 2.2-2 shows the

operation conditions.

The cross section of the coil is shown in Fig 2.2-2. The winding method is a double pancake with three simultaneous windings. The structure of the conductors at the beginning and end of winding is shown in Fig 2.2-3. The function of the S-bending filler block is to fill the gap of the S-bending area to provide a smooth surface for wrapping the 3 mm ground insulation. The function of the joint filler block is to fix all conductors together to resist electromagnetic force, and to fill the gap of the joint area for wrapping the ground insulation.

Since the current density is exceedingly high, the conductor temperature rises about 20 degrees per second of operation. To absorb this heat before next shot, the coils are cooled by pure water. Fig 2.2-4 shows current and cooling water flow, and conductor connection. To reduce the number of power supplies, the three double pancakes are electrically connected in series outside the coil. And in order not to increase the head loss of cooling water, the inlet and outlet of cooling water will be provided for each conductor.

Detail of joints are shown in Fig 2.2-5. Two types of copper block are designed to connect conductors. One of them is for connection between pancakes and other is for current lead. The copper blocks of joint\_1 and the joint\_2 electrically connects the conductors in series. Location the copper blocks must be far from the coil main body to avoid damage of the insulation by the high temperature of the brazing. Two square holes are designed on the copper block and the conductor can be inserted from one side. After inserting of the conductor, the copper block will be welded with the conductors by silver brazing. Therefore, the number of electric circuits is one per one coil, and the number of cooling water flow paths is three per one coil. A  $\Phi 6 \times \Phi 4$  pipe is designed for the water-cooling pipes as shown in the figure. The material of the pipes is stainless steel. The terminal of the conductors will be drilled a  $\Phi 6$  mm hole for inserting of the pipe. A standard water pipe joint is selected for the cooling water and the material is also stainless steel. The pipes will also be welded with the conductors by silver brazing.

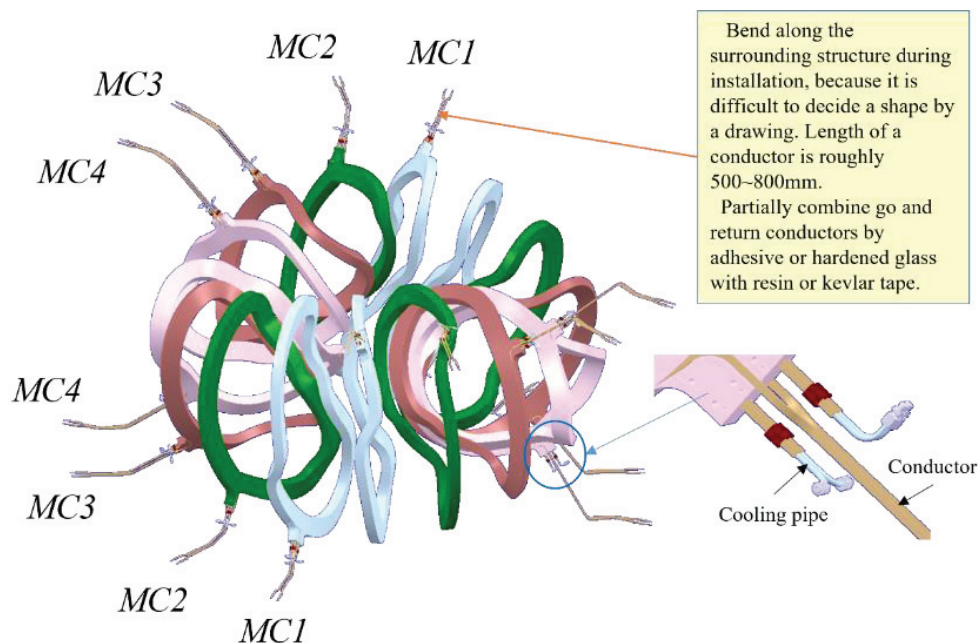


Fig 2.2-1 Modular coil system. Showing current leads and cooling pipes.

Table 2.2-1 Design parameters of the modular coil

Category	Parameter	Unit	Modular coil				Remarks
			MC1	MC2	MC3	MC4	
General	Width DW	mm	69	69	69	69	Include earth isolation and cooling hall
	Height DH	mm	132	132	132	132	
	Number of coils in series		4	4	4	4	
	Winding method		Pancake				
	Position		$\varphi=10.1^\circ$	$\varphi=30.9^\circ$	$\varphi=53.5^\circ$	$\varphi=76.9^\circ$	
	Cooling method		Water cooling				
	Heat resistance class		B [ < 130°C ]				
	Resistance(75°C)	$\Omega$	0.470	0.463	0.448	0.433	Note 1
	Inductance	H	0.083	0.081	0.079	0.076	Note 2
	Time constant	s	0.175	0.175	0.176	0.176	
Conductor	Type		OFC with a hole				
	CSA(Cross-sectional area)	mm <sup>2</sup>	58.83	58.83	58.83	58.83	
	Arc length of a conductor	m/turn	4.39	4.33	4.2	4.13	By CATIA
	Number of turns in a coil		72	72	72	72	
Insulation	Ground insulation	kV	2.4	2.4	2.4	2.4	
	Test voltage against the ground	kV	5.8	5.8	5.8	5.8	
	Layer insulation	kV	0.4	0.4	0.4	0.4	
	Impulse test voltage	kV	1.0	1.0	1.0	1.0	
Cooling	Number of cooling circuits	1/coil	3	3	3	3	
	Length of cooling pipe	m	105.4	103.9	100.8	99.1	
	Flow velocity	m/s	1.9	1.9	1.9	1.9	
	Flow rate	m <sup>3</sup> /s	2.39E-05	2.39E-05	2.39E-05	2.39E-05	
	Loss head	m	126	124	121	119	Note 3

Note 1 ; Added 5% margin to the calculated result

Note 2 ; Including the effect of mutual inductance and 5% margin.

Note 3 ; Hazen Williams' equation

Table 2.2-2 Operation condition of the modular coil

Category	Parameter	Unit	Modular coil				Remarks
			MC1	MC2	MC3	MC4	
Short pulse (1T)	Maximum current	kA	4.3	4.3	4.3	4.3	
	Total current in a coil	kAT	312.5	312.5	312.5	312.5	
	Maximum current density	A/mm <sup>2</sup>	73.8	73.8	73.8	73.8	Conductor only
	Discharge period	s	300	300	300	300	
	Current rise time	s	0.4	0.4	0.4	0.4	
	Flat top time	s	0.6	0.6	0.6	0.6	
	Pulse width in a pulse	s	0.906	0.906	0.906	0.906	RWET ; Note 4
	Temperature rise in a pulse	Kelvin	29	29	29	29	ARTP ; Note 5
	Water temperature	Kelvin	22	22	21	21	AWTR ; Note 6
	Stored magnetic energy	MJ	0.78	0.76	0.74	0.72	
	Time averaged current	kA	0.24	0.24	0.24	0.24	
	Start up voltage	kV	2.27	2.24	2.17	2.09	Maximum
	Flat top voltage	kV	2.04	2.01	1.95	1.88	
	Flat top power	MW	8.86	8.73	8.45	8.15	
	Energy consumption	MJ	8.03	7.91	7.66	7.39	
Long pulse (0.09T)	Maximum current	kA	0.3906	0.3906	0.3906	0.3906	
	Maximum current density	A/mm <sup>2</sup>	6.64	6.64	6.64	6.64	
	Discharge period	s	600	600	600	600	
	Water temperature	Kelvin	27	27	26	25	AWTR ; Note 6
	Pulse width in a pulse	s	269	269	269	269	Adiabatic rise <70 Kelvin
	Flat top voltage	kV	0.184	0.181	0.175	0.169	
	Flat top power	MW	0.072	0.071	0.068	0.066	

Note 4 ; RWET - Rectangular wave equivalent time or square wave conversion time.

Note 5 ; ARTP - Adiabatic rise of temperature in a pulse.

Note 6 ; AWTR - Average water temperature rise



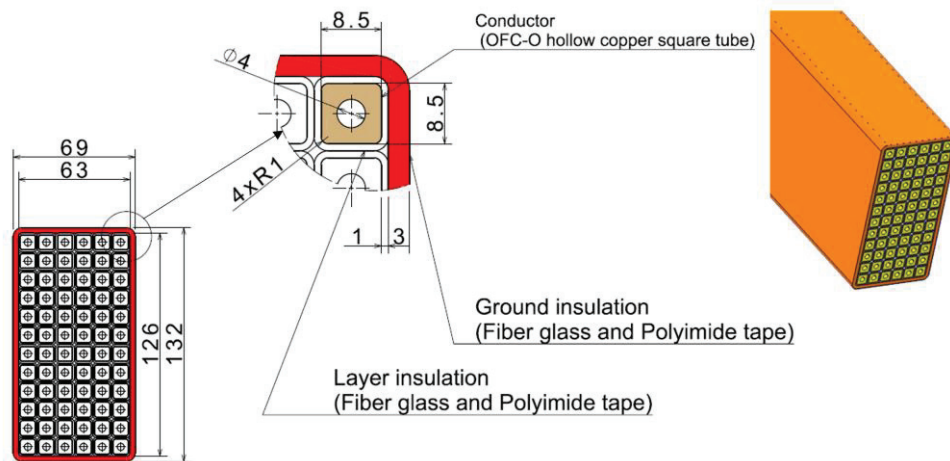


Fig 2.2-2 Cross section of the modular coil. The winding method is a double pancake with three simultaneous winding. The insulation process is vacuum pressure impregnation (VPI).

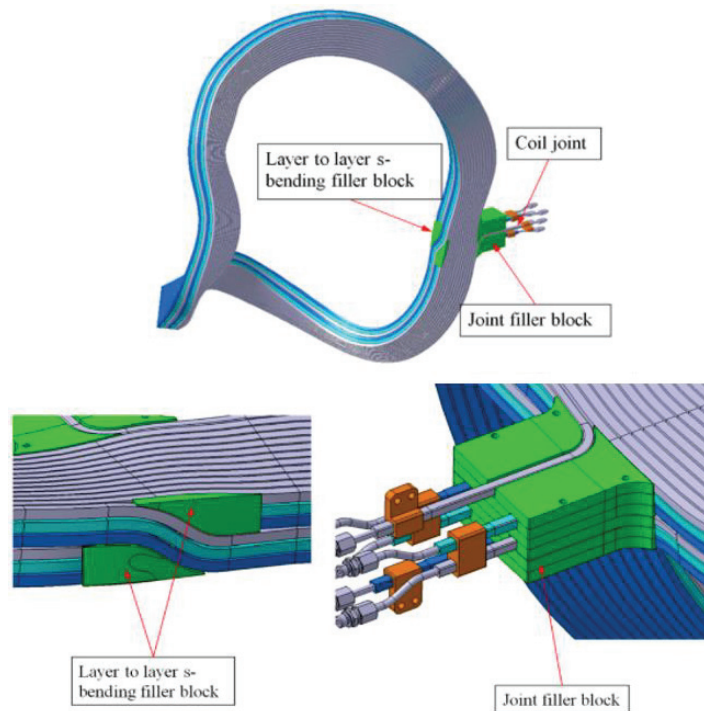


Fig 2.2-3 Structure of winding start and winding end. The winding start is the s-bending on the inner side of the coil, and the winding end is the terminal. At the beginning and end of winding, the filler blocks made of the FRP (Fiber Reinforced Plastics) are placed to fill the gap and fix conductors.

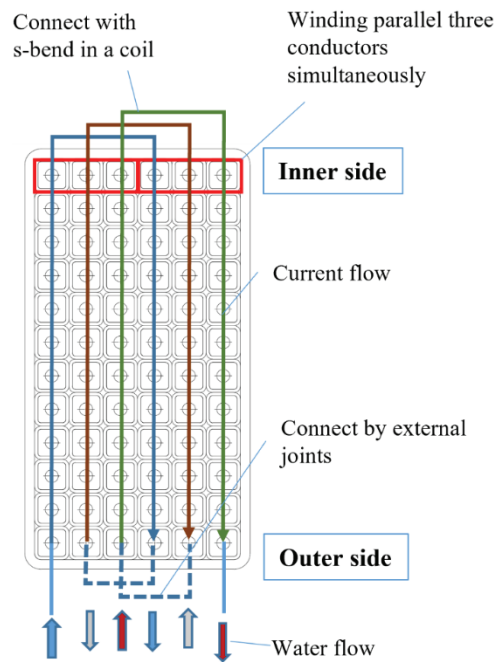


Fig 2.2-4 Current and cooling water flow. The three conductors are electrically connected in series outside the coil. The inlet and outlet of cooling water are provided for each conductor not to increase the head loss.

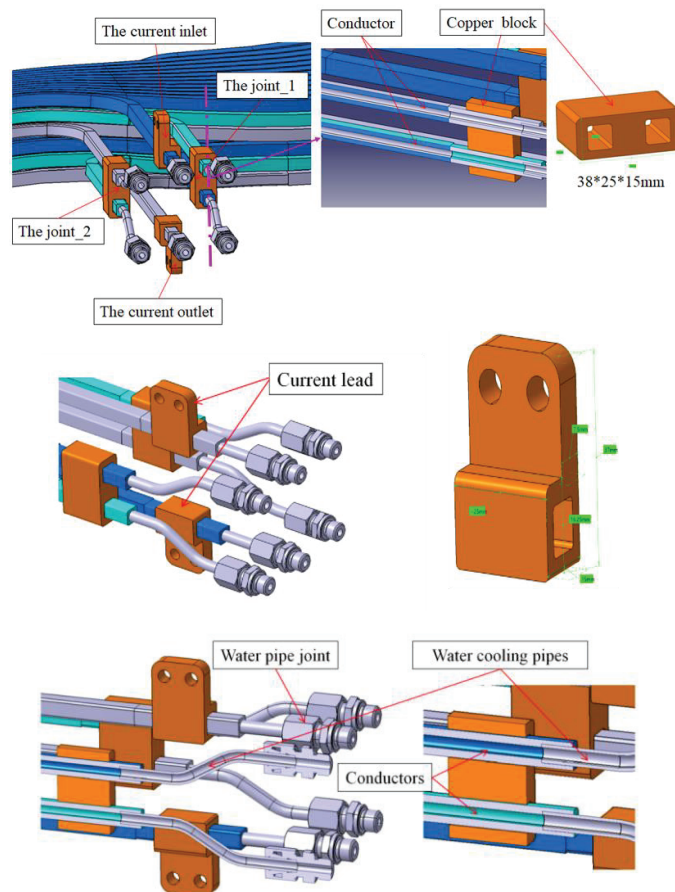


Fig 2.2-5 Detail of the conductor joint and the cooling water joint. Copper blocks of joint\_1 and joint\_2 are electrical connections. Insulated hoses are connected to the six water pipe joints (The tube fitting) at the ends of the cooling pipes.



### 2.2.2 Trajectory of the center the cross section

The current carrying surface (CCS), on which the coil current flows, will be defined by the optimization calculation. As a restriction condition of the optimization calculation, the area where the CCS can be arranged is defined.

$$\begin{aligned} R_{in}(\theta, \phi) &= \sum R_{in\ mn} \cos(m\theta - N_p n\phi) \\ Z_{in}(\theta, \phi) &= \sum Z_{in\ mn} \sin(m\theta - N_p n\phi) \\ R_{out}(\theta, \phi) &= \sum R_{out\ mn} \cos(m\theta - N_p n\phi) \\ Z_{out}(\theta, \phi) &= \sum Z_{out\ mn} \sin(m\theta - N_p n\phi) \end{aligned}$$

where  $\theta$  and  $\phi$  is the poloidal and the toroidal angle in the VMEC magnetic coordinate system,  $m$  and  $n$  is the poloidal and toroidal mode number. and  $N_p$  is the toroidal periodic number and equal 2 for the CFQS. Note that the angles in the magnetic coordinate system are normalized in one period. The toroidal angle of  $2\pi$  in the magnetic coordinate system corresponds to  $\pi$  in the real space.

$R_{in}(\theta, \phi)$  and  $Z_{in}(\theta, \phi)$  is the coordinate of the inner limit surface, and  $R_{out}(\theta, \phi)$  and  $Z_{out}(\theta, \phi)$  is the coordinate the outer limit surface.  $R_{in\ mn}$ ,  $Z_{in\ mn}$ ,  $R_{out\ mn}$  and  $Z_{out\ mn}$  are the Fourier series expansion coefficients of the position coordinates. The Fourier coefficients are shown in Table 2.2-3.

The designer considers the situation around the coil and defines these limit surfaces. In the CFQS design, a surface 0.2 m outside the last closed flux surface (LCFS) was defined as the inner limit surface, and a surface 0.4 m outside the LCFS was defined as the outer limit surface. The LCFS coordinates are calculated by the VMEC and are described in the MHD equilibrium chapter.

$$\begin{aligned} R_{LCFS}(\theta, \phi) &= \sum R_{mn} \cos(m\theta - N_p n\phi) \\ Z_{LCFS}(\theta, \phi) &= \sum Z_{mn} \sin(m\theta - N_p n\phi) \end{aligned}$$

The Fourier coefficients of the LCFS are shown in the MHD equilibrium chapter and the shape of the LCFS and the limit surfaces are shown in Fig 2.2-6.

The current carrying surface (CCS) and the trajectory of the cross sectional center were determined by the NESCOIL system. The trajectory is defined by the following equations.

$$\begin{aligned} \phi &= 2\pi \sum \{C_m \cos(m\omega) + D_m \sin(m\omega)\} \\ \theta &= \omega + 2\pi \sum \{E_m \cos(m\omega) + F_m \sin(m\omega)\} \\ \omega &= 0 \sim 2\pi \end{aligned}$$

where  $\theta$  and  $\phi$  is the magnetic coordinate of the point on the trajectory of the cross sectional center.  $\omega$  is the auxiliary variable. The angular coordinate  $(\theta, \phi)$  is calculated by the above equations for each variable  $\omega$  divided at equal intervals. Fig 2.2-7 shows the magnetic coordinates of the trajectory. The position of the trajectory is obtained by substituting them into the following equations.

$$R_{ccs}(\theta, \phi) = (1 - A)R_{in}(\theta, \phi) + A R_{out}(\theta, \phi)$$

$$Z_{ccs}(\theta, \phi) = (1 - A)Z_{in}(\theta, \phi) + A Z_{out}(\theta, \phi)$$

$$A = \frac{1}{2}(1 + \tanh\{F(\theta, \phi)\})$$

$$F(\theta, \phi) = \sum F_{mn} \cos(m\theta - N_p n\phi)$$

where  $F(\theta, \phi)$  is the function defining the CCS. The Fourier coefficients of  $C_m$ ,  $D_m$ ,  $E_m$ ,  $F_m$  and  $F_{mn}$  are optimized numerically by the NESCOIL system. The result is shown in Table 2.2-4 and Table 2.2-5 and shape of the CCS is shown in Fig 2.2-8. Fig 2.2-9 shows the trajectory of the cross sectional center and Table 2.2-6 shows the coordinate of the trajectory in the real space.

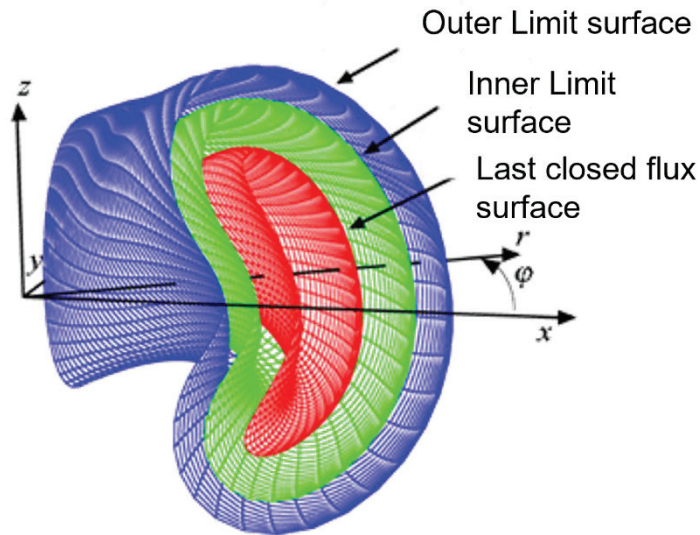


Fig 2.2-6 The last closed flux surface (LCFS) and the limit surfaces. By the optimaizaion calculation, the current carrying surface (CCS) will be placed between the inner limit surface and the outer limit surface.

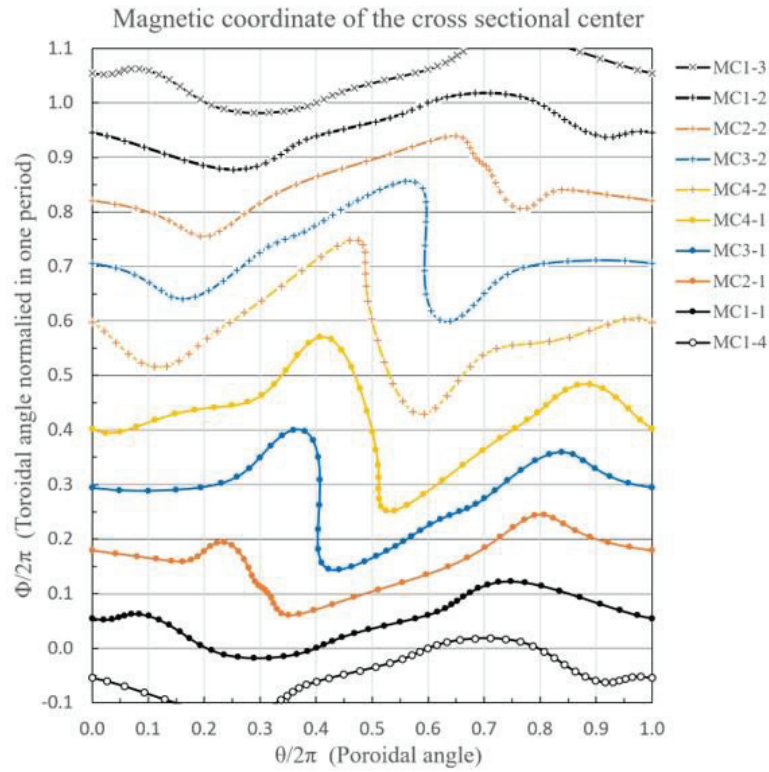


Fig 2.2-7 Cross sectional center of the modular coils in the magnetic coordinate system. The MC1-1, MC2-1, MC3-1, and MC4-1 show the reference trajectories, and others are parallel or inverted copies of them.

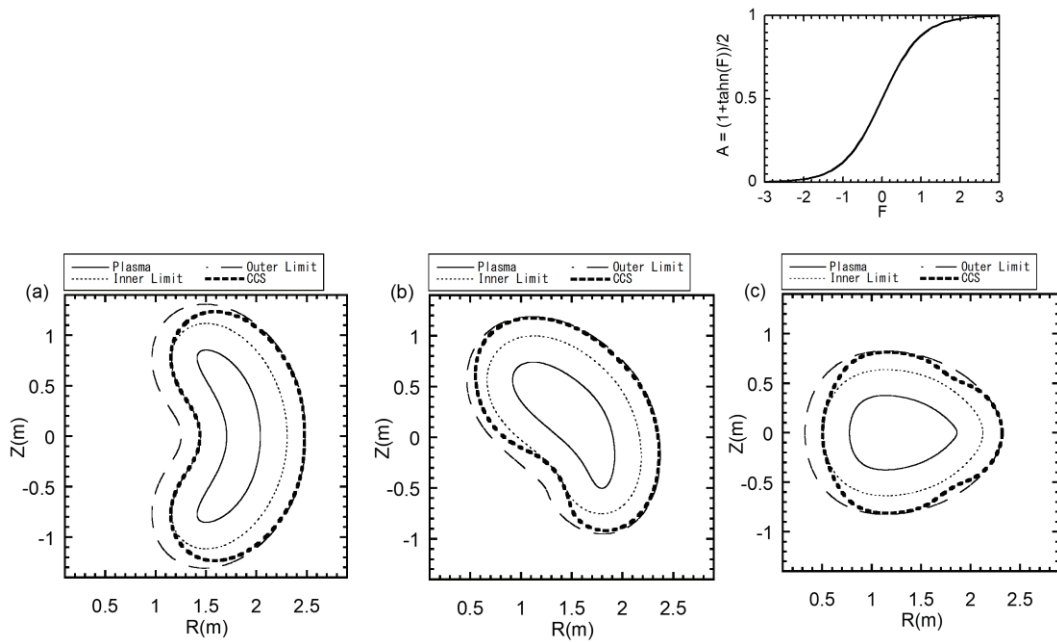


Fig 2.2-8 Current carrying surface for the CFQS on three toroidal angle planes in the real space coordinate system (Cartesian coordinate system). The LCFS of the CFQS-2b40, the inner limit surface and the outer limit surface are also shown in the figures.

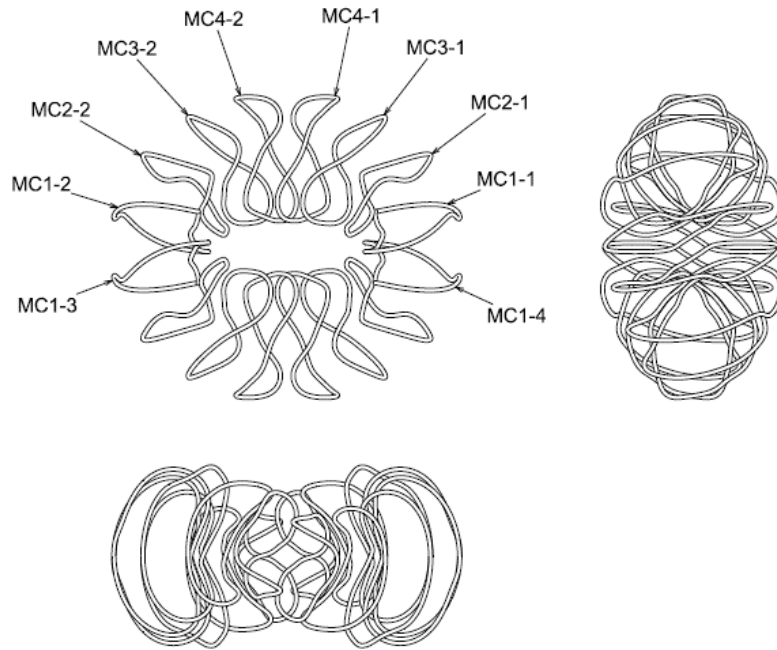


Fig 2.2-9 Center trajectory of the modular coil. The modular coil system consists of 16 coils of 4 types. For example, the MC1-3 is arranged 180 degrees rotational movement with respect to the z-axis, and the MC1-2 and the MC1-4 are arranged in reversal movement with respect to the x-axis and the y-axis.

Table 2.2-3 Fourier coefficients of inner and outer limit surfaces

NP=-2

No	m	n	$R_{in\ mn}$	$Z_{in\ mn}$	No	m	n	$R_{out\ mn}$	$Z_{out\ mn}$
1	0	-5	7.58893E-05	-1.23896E-04	1	0	-5	-7.24653E-05	-1.76900E-03
2	1	-5	5.88874E-04	-5.90320E-04	2	1	-5	-5.62472E-04	-2.38014E-03
3	2	-5	-9.93690E-04	-8.29019E-04	3	2	-5	-7.46116E-04	-1.05989E-03
4	3	-5	2.00471E-04	7.09052E-04	4	3	-5	-8.99424E-04	-1.27986E-03
5	4	-5	-2.89474E-05	-2.25925E-04	5	4	-5	5.36311E-04	-3.53406E-04
6	5	-5	4.60150E-04	9.86710E-05	6	5	-5	-1.10476E-04	-2.79005E-04
7	0	-4	-8.82758E-04	2.10849E-04	7	0	-4	-2.30944E-04	4.76685E-04
8	1	-4	-2.52390E-03	-3.72585E-03	8	1	-4	-7.99981E-04	1.07888E-04
9	2	-4	5.98392E-04	4.95277E-04	9	2	-4	4.06099E-04	6.04160E-04
10	3	-4	6.43471E-05	3.98781E-04	10	3	-4	1.01270E-03	1.78005E-03
11	4	-4	-9.14981E-04	-1.76857E-05	11	4	-4	-1.68382E-03	9.41983E-04
12	5	-4	6.60776E-04	-9.35607E-04	12	5	-4	1.77685E-03	-5.20256E-04
13	0	-3	2.67142E-04	1.64110E-03	13	0	-3	5.08546E-04	1.28775E-03
14	1	-3	9.69115E-04	1.66142E-03	14	1	-3	2.21033E-03	2.20875E-03
15	2	-3	3.78223E-04	6.89165E-04	15	2	-3	-2.62808E-03	8.16607E-04
16	3	-3	4.81043E-03	-1.90706E-03	16	3	-3	7.89832E-03	-2.00844E-03
17	4	-3	-4.01147E-03	-5.31294E-05	17	4	-3	-8.22716E-03	-7.76895E-04
18	5	-3	5.96518E-04	-1.75179E-04	18	5	-3	4.13703E-03	-1.20405E-03
19	0	-2	4.88553E-03	-4.54739E-03	19	0	-2	8.68554E-03	-4.60778E-03
20	1	-2	-1.91325E-02	7.90749E-03	20	1	-2	-2.33415E-02	-8.39923E-03
21	2	-2	1.53106E-02	7.38326E-03	21	2	-2	2.13368E-02	2.44986E-02
22	3	-2	-5.78966E-03	-2.13940E-02	22	3	-2	-8.84368E-03	-4.38617E-02

No	m	n	R <sub>in mn</sub>	Z <sub>in mn</sub>	No	m	n	R <sub>out mn</sub>	Z <sub>out mn</sub>
23	4	-2	-4.07759E-03	-3.21457E-03	23	4	-2	-9.87862E-03	-1.00593E-02
24	5	-2	2.16776E-03	1.15788E-03	24	5	-2	5.77898E-04	-6.75209E-05
25	0	-1	1.14085E-01	-8.90299E-02	25	0	-1	7.52536E-02	-7.12151E-02
26	1	-1	-6.07918E-02	8.64941E-02	26	1	-1	1.93247E-04	7.37886E-02
27	2	-1	7.79414E-02	6.66492E-02	27	2	-1	1.13775E-01	1.06531E-01
28	3	-1	-4.15514E-02	-4.57962E-02	28	3	-1	-7.67599E-02	-8.01721E-02
29	4	-1	-2.24503E-03	-2.67740E-03	29	4	-1	-4.55782E-03	-6.19579E-03
30	5	-1	9.10644E-04	4.07485E-04	30	5	-1	1.02690E-03	1.54877E-03
31	0	0	9.89838E-01	0.00000E+00	31	0	0	9.84164E-01	0.00000E+00
32	1	0	4.01667E-01	4.79762E-01	32	1	0	5.93841E-01	6.55724E-01
33	2	0	4.18809E-02	2.97421E-02	33	2	0	5.29714E-02	4.38610E-02
34	3	0	-5.06871E-03	-1.28982E-03	34	3	0	7.49001E-04	6.89802E-03
35	4	0	-2.59686E-03	-2.45049E-03	35	4	0	-7.30051E-03	-5.82146E-03
36	5	0	-1.61801E-04	-4.98495E-04	36	5	0	6.28137E-04	6.60517E-04
37	0	1	0.00000E+00	0.00000E+00	37	0	1	0.00000E+00	0.00000E+00
38	1	1	-2.71483E-03	1.53054E-03	38	1	1	-3.36202E-02	-3.42443E-02
39	2	1	1.21748E-02	1.21290E-02	39	2	1	2.11696E-02	2.46768E-02
40	3	1	4.50659E-03	3.18066E-03	40	3	1	3.58031E-03	7.14075E-04
41	4	1	-4.71928E-04	-1.01870E-03	41	4	1	2.52975E-03	6.92529E-04
42	5	1	4.39000E-04	6.64062E-04	42	5	1	-1.24835E-04	-2.82946E-04
43	0	2	0.00000E+00	0.00000E+00	43	0	2	0.00000E+00	0.00000E+00
44	1	2	5.64231E-03	3.45978E-03	44	1	2	1.13825E-02	1.31972E-02
45	2	2	1.92327E-03	-3.37713E-04	45	2	2	-4.92088E-05	-5.53134E-03
46	3	2	-1.49141E-04	-1.08491E-04	46	3	2	9.99323E-04	1.73881E-03
47	4	2	-3.95140E-04	-5.72319E-04	47	4	2	-1.97504E-03	-1.51006E-03
48	5	2	4.38081E-04	-3.16476E-04	48	5	2	1.04029E-06	1.35136E-04
49	0	3	0.00000E+00	0.00000E+00	49	0	3	0.00000E+00	0.00000E+00
50	1	3	-2.63734E-03	-2.40970E-03	50	1	3	-2.45286E-03	-4.84102E-03
51	2	3	2.90365E-04	2.60341E-04	51	2	3	-9.68455E-04	5.50127E-04
52	3	3	-3.45647E-04	-1.06698E-03	52	3	3	-8.91717E-04	-1.14382E-03
53	4	3	-4.72284E-04	-4.57068E-04	53	4	3	7.91674E-04	3.10660E-04
54	5	3	7.15537E-05	2.24636E-04	54	5	3	2.14578E-04	-1.45782E-04
55	0	4	0.00000E+00	0.00000E+00	55	0	4	0.00000E+00	0.00000E+00
56	1	4	3.06708E-03	3.10727E-03	56	1	4	5.64010E-04	9.25952E-04
57	2	4	5.33223E-04	6.82975E-04	57	2	4	6.44155E-04	-5.18989E-04
58	3	4	-2.25753E-04	-2.75855E-04	58	3	4	5.29607E-05	-6.69925E-05
59	4	4	-2.56868E-05	-2.83892E-04	59	4	4	-1.09624E-03	-1.03013E-03
60	5	4	1.34530E-04	3.80411E-05	60	5	4	-6.23919E-05	-5.44685E-06
61	0	5	0.00000E+00	0.00000E+00	61	0	5	0.00000E+00	0.00000E+00
62	1	5	-1.37126E-05	-4.32788E-04	62	1	5	9.03430E-04	1.13871E-03
63	2	5	4.49605E-04	2.83268E-04	63	2	5	1.01342E-03	6.98894E-04
64	3	5	-2.54177E-04	-2.30475E-04	64	3	5	2.43954E-04	8.65377E-05
65	4	5	-4.62391E-05	-1.40534E-04	65	4	5	8.72839E-05	-3.13013E-04
66	5	5	8.01961E-05	1.35227E-04	66	5	5	1.07874E-04	-7.81701E-05

Input for the NESCOIL system

Table 2.2-4 Fourier coefficients defining trajectory of cross-sectional center

No	Coil	m	C <sub>m</sub>	D <sub>m</sub>	E <sub>m</sub>	F <sub>m</sub>
1	MC1	0	5.08238063E-02	0.00000000E+00	-4.46786279E-02	0.00000000E+00
2	MC1	1	3.17161288E-02	-4.67121323E-02	3.57121610E-03	8.97025268E-03
3	MC1	2	-8.50878306E-03	5.97887485E-03	1.96052598E-02	9.68120583E-03
4	MC1	3	-1.42922019E-02	1.40667751E-03	1.77332574E-02	7.30683970E-04
5	MC1	4	-4.95305439E-03	-1.79961895E-04	-1.72787726E-03	-3.94294552E-03
6	MC1	5	-3.19256196E-04	-2.62164294E-05	5.49677186E-03	5.94815068E-04
7	MC2	0	1.54442039E-01	0.00000000E+00	-5.67830447E-02	0.00000000E+00
8	MC2	1	6.06780744E-02	-8.72720177E-03	8.41699345E-02	4.42984135E-02
9	MC2	2	-3.06081594E-02	-2.48111140E-02	-3.02522546E-02	6.18334659E-03
10	MC2	3	-9.97758074E-03	-3.92713621E-03	3.23212753E-03	2.39406697E-02
11	MC2	4	1.85804822E-03	-2.09923315E-03	2.06865760E-03	3.06592036E-03
12	MC2	5	2.94826018E-03	6.96195525E-03	-2.43542004E-03	3.69679871E-03
13	MC3	0	2.77245336E-01	0.00000000E+00	2.39217568E-02	0.00000000E+00
14	MC3	1	7.80796685E-02	1.48474079E-02	1.39028660E-02	8.33803903E-02
15	MC3	2	-5.23875821E-02	-1.48848340E-04	-1.80686429E-02	2.97898452E-02
16	MC3	3	-1.04369860E-02	-3.89659092E-02	-8.98503055E-03	-1.55357504E-03
17	MC3	4	6.83482331E-03	3.26077377E-03	-2.04836764E-03	8.17832166E-03
18	MC3	5	-5.18198119E-03	8.05588182E-03	-8.72258156E-03	4.19837022E-03
19	MC4	0	4.15911850E-01	0.00000000E+00	2.35306646E-02	0.00000000E+00
20	MC4	1	4.75027013E-02	6.33649000E-02	1.34852253E-03	6.12024715E-02
21	MC4	2	-4.95492054E-02	-7.43992241E-02	-2.23766903E-02	-2.09709873E-02
22	MC4	3	9.77380093E-03	3.10392796E-03	-6.16152784E-03	1.24809127E-02
23	MC4	4	-8.68311865E-03	4.77923986E-03	4.84051215E-03	-7.75099870E-03
24	MC4	5	-1.23679439E-02	-6.94790762E-03	-1.18148146E-03	-3.11969834E-03

Obtained by the NESCOIL system

Table 2.2-5 Fourier coefficients defining the CCS

Np=-2

No	m	n	F <sub>mn</sub>	No	m	n	F <sub>mn</sub>	No	m	n	F <sub>mn</sub>
1	0	-5	1.0451526E-02	22	2	-1	3.0167782E-02	43	4	-2	-3.0186636E-03
2	0	-4	-3.2246210E-02	23	2	0	1.1424471E-01	44	4	-1	-7.7384896E-03
3	0	-3	-5.5378747E-02	24	2	1	1.8902919E-01	45	4	0	5.3603370E-02
4	0	-2	-1.4575198E-01	25	2	2	-1.3637218E-01	46	4	1	-8.8244211E-03
5	0	-1	-4.2343833E-01	26	2	3	1.2191454E-01	47	4	2	2.8490246E-02
6	0	0	1.2111113E+00	27	2	4	-6.3524118E-03	48	4	3	5.1272386E-02
7	1	-5	2.1197255E-02	28	2	5	-2.8253809E-04	49	4	4	-4.0296114E-02
8	1	-4	4.7218044E-03	29	3	-5	2.9258881E-02	50	4	5	2.5810687E-02
9	1	-3	7.2852863E-02	30	3	-4	1.8245548E-02	51	5	-5	-4.8638491E-02
10	1	-2	-2.2770681E-01	31	3	-3	2.1531166E-02	52	5	-4	-4.8215517E-02
11	1	-1	1.5708038E+00	32	3	-2	4.5203975E-01	53	5	-3	-2.2685688E-02
12	1	0	1.3316260E+00	33	3	-1	-6.8609554E-01	54	5	-2	-1.1746071E-01
13	1	1	-1.3103095E-01	34	3	0	1.9339655E-01	55	5	-1	7.0528030E-04
14	1	2	-1.5026153E-01	35	3	1	-1.0553564E-01	56	5	0	9.1842103E-02
15	1	3	1.4170268E-02	36	3	2	1.5037399E-01	57	5	1	2.4884115E-02
16	1	4	2.6749029E-02	37	3	3	1.1815016E-01	58	5	2	1.4915268E-03



17	1	5	-2.3231334E-02	38	3	4	2.9072859E-03	59	5	3	-6.6864726E-03
18	2	-5	-3.2638846E-02	39	3	5	1.5208853E-02	60	5	4	-2.0354558E-03
19	2	-4	1.5357525E-02	40	4	-5	-2.2644707E-02	61	5	5	1.4333211E-02
20	2	-3	-2.8669915E-02	41	4	-4	-6.5898961E-03				
21	2	-2	-4.2796981E-01	42	4	-3	-1.1506971E-01				

Obtained by the NESCOIL system

Table 2.2-6 Coordinate of the cross-sectional center

No	M1-N0			M2-N0			M3-N0			M4-N0		
	X	Y	Z	X	Y	Z	X	Y	Z	X	Y	Z
1	1695.5	293.0	20.7	1411.2	891.5	9.7	962.8	1275.3	-56.4	463.9	1468.2	-68.1
2	1689.9	279.6	103.7	1394.8	848.1	205.8	955.7	1230.0	191.4	497.3	1455.5	23.2
3	1678.3	282.8	164.5	1364.2	799.0	344.1	905.6	1158.6	384.0	480.4	1433.6	130.6
4	1663.3	296.8	212.9	1327.8	750.3	450.3	841.7	1089.4	503.8	422.0	1388.8	239.4
5	1646.0	313.2	257.9	1282.9	705.7	541.7	765.1	1018.5	589.3	345.3	1316.6	330.2
6	1626.2	323.0	307.5	1231.7	672.5	615.1	675.2	943.7	656.4	281.4	1253.0	422.1
7	1602.8	318.8	368.3	1178.9	656.7	666.6	580.8	876.8	698.6	235.2	1183.2	509.8
8	1573.1	296.2	444.3	1125.5	657.4	700.3	487.7	823.7	716.4	202.3	1095.0	565.0
9	1532.1	254.8	535.6	1069.3	666.2	724.7	396.1	776.5	717.2	174.9	1004.7	600.0
10	1474.1	198.5	635.7	1010.1	670.7	747.8	309.0	721.6	707.5	141.1	915.1	620.9
11	1395.4	135.2	731.1	950.2	659.2	774.7	235.1	651.1	689.7	94.5	826.9	625.4
12	1295.2	74.0	806.4	893.2	624.7	806.3	183.8	567.3	664.3	37.3	740.4	609.9
13	1176.4	23.0	848.4	840.7	567.7	838.8	158.8	480.1	633.5	-20.7	653.2	572.9
14	1046.7	-12.9	848.3	792.5	495.8	864.5	157.1	402.3	602.0	-66.8	565.7	516.1
15	919.5	-33.4	801.9	748.9	421.0	876.0	173.6	341.5	571.1	-91.5	482.8	446.4
16	816.9	-41.9	706.7	711.8	354.7	870.7	203.9	297.0	540.6	-91.9	407.4	371.3
17	769.0	-44.0	573.3	682.4	303.2	852.4	245.4	264.6	509.8	-73.0	343.1	294.9
18	782.6	-43.3	438.0	658.7	267.0	827.6	301.0	245.3	467.0	-44.9	299.8	222.6
19	819.6	-38.6	331.5	637.6	242.4	800.2	367.5	235.7	409.3	-13.5	276.6	168.5
20	851.4	-29.0	255.5	618.0	224.8	770.8	431.3	232.2	339.0	19.8	264.6	135.7
21	873.8	-15.6	203.2	601.3	209.5	738.6	486.0	238.7	259.6	53.8	260.6	110.5
22	888.6	0.6	166.8	590.0	193.3	703.0	531.0	258.1	178.1	87.1	259.8	84.2
23	899.3	18.6	138.3	585.9	175.1	664.0	565.7	288.0	102.1	119.5	262.4	58.1
24	908.9	38.0	111.0	588.6	155.6	621.1	590.1	322.6	37.9	153.6	271.9	36.1
25	919.4	58.6	80.7	596.1	137.3	572.4	605.8	356.3	-11.4	190.9	286.3	20.2
26	930.1	80.1	46.9	607.1	124.0	514.6	614.8	386.3	-46.7	231.3	302.4	8.4
27	938.8	102.1	12.5	622.9	120.1	443.7	619.0	413.0	-71.5	274.3	319.4	-5.1
28	942.5	123.6	-20.2	649.8	129.4	357.8	619.4	438.5	-90.4	318.0	338.6	-26.4
29	939.4	143.6	-51.7	693.0	154.3	261.2	617.5	465.8	-106.1	357.7	362.3	-60.2
30	930.1	161.7	-84.6	745.3	193.1	162.9	615.0	496.5	-119.6	387.4	393.7	-107.8
31	917.7	178.1	-118.5	791.8	240.2	71.6	612.9	529.3	-131.7	402.6	436.5	-166.1
32	905.8	193.9	-150.3	823.8	289.0	-1.2	610.4	560.3	-144.8	402.9	493.8	-227.5
33	896.2	210.2	-176.9	838.6	334.9	-50.3	607.7	586.3	-159.9	389.6	564.7	-284.8
34	888.5	227.8	-198.6	834.8	376.0	-89.6	605.1	607.5	-176.1	363.4	641.0	-337.6
35	881.8	247.1	-218.2	815.5	414.0	-135.2	601.3	626.7	-192.8	330.8	717.6	-381.6
36	875.3	268.1	-239.4	792.5	456.0	-188.5	593.7	648.2	-211.0	299.7	794.8	-403.5
37	869.5	290.2	-265.4	773.0	506.9	-242.5	579.4	676.7	-232.1	271.5	867.6	-401.7
38	865.7	312.2	-298.9	757.3	565.0	-291.0	557.3	715.5	-256.9	243.8	930.1	-391.3



No	M1-N0			M2-N0			M3-N0			M4-N0		
	X	Y	Z	X	Y	Z	X	Y	Z	X	Y	Z
39	865.6	332.4	-342.4	743.5	622.7	-334.5	528.8	765.4	-284.3	213.4	984.1	-383.0
40	868.7	347.6	-401.2	733.4	671.2	-381.1	498.6	824.3	-312.8	177.2	1035.6	-377.8
41	867.2	351.7	-492.1	734.9	707.1	-439.6	474.7	889.6	-341.5	136.0	1090.2	-372.7
42	882.5	351.0	-630.8	758.6	734.0	-508.8	466.5	957.0	-370.7	95.4	1151.0	-363.3
43	991.3	373.0	-743.8	812.8	759.2	-574.2	482.5	1021.6	-406.2	67.1	1218.9	-346.8
44	1180.2	405.4	-767.0	900.0	787.5	-619.3	528.2	1081.5	-445.2	65.5	1297.1	-326.1
45	1392.4	422.3	-674.5	1017.6	822.2	-628.6	602.2	1133.6	-468.3	103.0	1380.9	-298.3
46	1560.4	407.5	-484.7	1156.7	863.3	-577.6	698.2	1180.9	-461.4	180.4	1441.0	-252.4
47	1652.7	367.8	-271.3	1291.7	900.1	-441.7	806.4	1229.0	-406.7	282.8	1468.1	-197.5
48	1688.3	324.4	-99.0	1383.5	912.8	-227.6	906.0	1269.5	-274.4	386.0	1474.0	-139.2

Obtained by the NESCOIL system

### 2.2.3 Tilt angle of each modular coil

The MHD equilibrium created by the modular coil is almost determined by the center trajectory and the total current, which are calculated with the NESCOIL system. The cross-sectional area is defined in consideration of the limit of current density.

It is also necessary to determine the direction of the coil cross section for winding. The NESCOIL system optimizes the center trajectory assuming the longer axis (the normal vector) is perpendicular to the current carrying surface (CCS) as shown in Fig 2.2-10, but it was found that the twisting angle ( $\theta$ ) has little effect on the equilibrium. Therefore, the twisting angle was adjusted from the viewpoint of manufacturability, the gap with other parts and curvature of the three-dimensional (3-D) surface.

The optimized result of the twisting angle is shown in Table 2.2-7 to Table 2.2-10 and Fig 2.2-11. For comparison, the orthogonal direction views after and before optimization are shown in Fig 2.2-12 and Fig 2.2-13. For comparison, the coil shapes before and after optimization are shown in Fig 2.2-14. It can be clearly seen that the twisting angle of the MC4 is changed significantly. The twisting angle was determined according to the following procedure.

- The angle was changed continuously so that the curvature and the torsion in the Frenet-Serret formular did not increase abruptly.
- The initial angle was selected so that they would not interfere when the coil was inserted into the case.
- The gap between the coils and the gap with the vacuum vessel were evaluated on 3-D CAD, and the solution with an appropriate size was manually selected.

Fig 2.2-12 shows that the coil dose not contact the case when the coil is inserted, and Fig 2.2-13 shows that it is difficult to pull out the coil from the coil case.

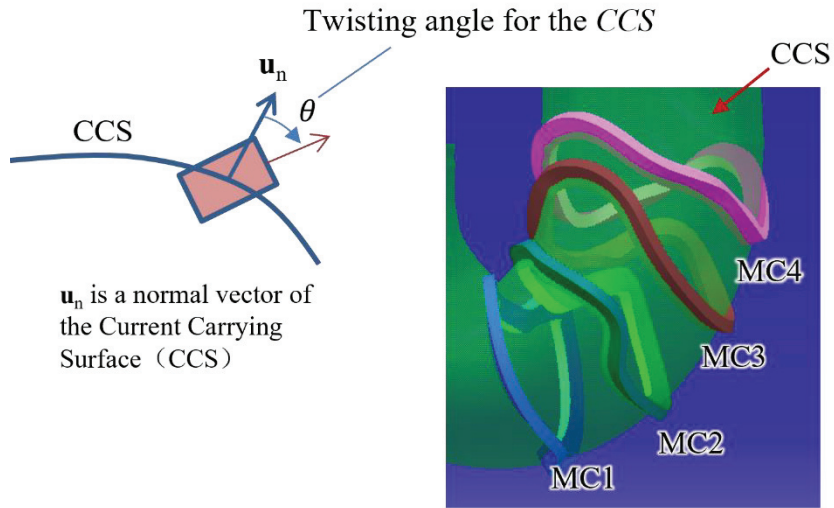


Fig 2.2-10 Normal direction of the rectangular cross section. The NESCOIL system gives us the optimized result with the long axis of the cross section orthogonal to the CCS ( $\theta=0$ ).

Table 2.2-7 Coordinate of 4 corners of the MC1 (SWJTU-Type X)

No	M1-N1			M1-N2			M1-N3			M1-N4			Angle twisted
	X	Y	Z	X	Y	Z	X	Y	Z	X	Y	Z	
1	1630.3	328.7	24.6	1762.2	325.4	28.0	1628.8	260.6	13.5	1760.8	257.3	16.9	15.00
2	1626.9	317.1	91.1	1756.8	310.8	113.4	1623.0	248.3	94.1	1753.0	242.0	116.3	15.97
3	1620.4	320.5	136.7	1746.0	311.4	176.2	1610.5	254.1	152.8	1736.1	245.1	192.4	18.20
4	1608.9	334.7	179.0	1730.9	324.1	228.3	1595.7	269.5	197.6	1717.7	259.0	246.9	20.07
5	1589.7	352.3	228.6	1711.9	341.7	277.6	1580.1	284.6	238.2	1702.2	274.1	287.1	20.16
6	1565.8	362.2	288.4	1689.8	352.4	332.6	1562.5	293.6	282.4	1686.5	283.8	326.6	20.20
7	1539.7	356.6	357.0	1664.5	347.2	398.8	1541.1	290.4	337.8	1665.9	281.0	379.7	20.95
8	1508.9	332.9	435.2	1632.7	323.0	480.2	1513.6	269.4	408.5	1637.3	259.5	453.5	21.64
9	1468.3	291.2	523.7	1588.2	279.9	577.7	1476.0	229.6	493.5	1595.9	218.3	547.6	21.62
10	1412.4	235.6	616.6	1524.2	222.1	685.5	1424.0	174.9	585.9	1535.8	161.4	654.7	20.50
11	1339.4	173.9	700.8	1435.5	157.4	789.8	1355.2	113.0	672.4	1451.3	96.5	761.4	17.66
12	1251.5	115.0	762.1	1320.0	95.5	873.3	1270.4	52.6	739.6	1338.8	33.0	850.7	12.19
13	1153.6	66.2	792.1	1181.2	44.9	919.4	1171.6	1.2	777.3	1199.2	-20.1	904.6	3.71
14	1049.8	30.9	788.1	1029.7	10.3	917.0	1063.7	-36.2	779.6	1043.6	-56.7	908.4	-6.12
15	949.3	9.0	748.4	880.1	-7.6	859.6	958.9	-59.2	744.2	889.7	-75.8	855.3	-16.13
16	871.7	-3.3	674.2	757.4	-11.6	739.7	876.4	-72.1	673.6	762.1	-80.4	739.1	-27.88
17	835.6	-10.8	572.8	703.7	-8.3	574.2	834.3	-79.8	572.3	702.4	-77.3	573.7	-38.09
18	847.6	-13.3	458.6	721.2	-4.6	421.5	844.1	-82.0	454.4	717.7	-73.4	417.3	-40.76
19	882.3	-9.5	359.3	759.0	0.6	313.3	880.3	-77.8	349.8	756.9	-67.7	303.8	-36.13
20	912.8	-0.6	286.6	789.2	9.4	241.3	913.6	-67.5	269.8	790.0	-57.5	224.5	-29.25
21	934.2	11.5	237.2	809.3	20.9	195.7	938.3	-52.1	210.7	813.3	-42.7	169.1	-25.47
22	948.8	25.8	202.7	822.3	34.4	166.0	955.0	-33.3	167.5	828.5	-24.7	130.9	-24.91
23	959.5	43.0	174.7	832.4	51.3	140.2	966.2	-14.1	136.5	839.0	-5.8	102.0	-25.31
24	969.2	62.7	147.0	842.2	71.1	112.1	975.6	4.9	109.9	848.6	13.2	75.0	-25.44
25	980.2	83.9	115.4	852.8	92.0	81.7	985.9	25.1	79.7	858.5	33.3	45.9	-25.42
26	992.3	105.8	79.0	863.5	113.0	51.1	996.8	47.2	42.8	868.0	54.5	14.9	-25.08
27	1003.2	128.4	39.0	872.2	133.6	23.7	1005.3	70.6	1.3	874.3	75.8	-14.0	-23.69
28	1009.6	151.8	-4.6	877.7	153.6	1.0	1007.2	93.5	-41.4	875.3	95.3	-35.8	-19.93
29	1006.9	175.1	-50.5	878.2	173.0	-21.2	1000.7	114.2	-82.3	872.0	112.1	-53.0	-14.44
30	996.1	195.3	-92.5	871.6	190.8	-49.0	988.7	132.5	-120.2	864.2	128.0	-76.6	-11.04
31	983.4	211.9	-128.2	860.3	206.8	-80.8	975.2	149.4	-156.3	852.1	144.3	-108.9	-9.97
32	972.5	226.3	-157.2	849.2	221.2	-110.3	962.4	166.5	-190.2	839.2	161.5	-143.3	-10.17
33	964.4	240.1	-179.9	840.8	235.1	-133.9	951.7	185.3	-219.9	828.1	180.3	-173.8	-11.34

No	M1-N1			M1-N2			M1-N3			M1-N4			Angle twisted
	X	Y	Z	X	Y	Z	X	Y	Z	X	Y	Z	
34	957.7	255.4	-198.7	833.7	250.7	-153.7	943.3	204.9	-243.5	819.4	200.2	-198.4	-13.14
35	951.1	274.2	-216.1	825.8	270.1	-174.7	937.7	224.1	-261.7	812.4	220.0	-220.2	-14.69
36	944.2	296.1	-234.8	816.6	293.3	-201.1	934.0	242.9	-277.6	806.4	240.1	-244.0	-15.52
37	937.5	319.5	-257.7	807.4	318.6	-235.8	931.6	261.7	-295.0	801.5	260.9	-273.1	-15.64
38	932.8	342.7	-288.1	801.0	344.2	-280.7	930.4	280.1	-317.1	798.6	281.7	-309.7	-15.03
39	932.0	363.9	-331.0	800.2	367.5	-336.4	930.9	297.2	-348.4	799.1	300.8	-353.8	-13.72
40	935.5	380.3	-397.2	803.7	383.9	-402.1	933.8	311.4	-400.2	801.9	314.9	-405.2	-12.42
41	933.7	385.2	-494.6	801.8	387.2	-489.8	932.6	316.2	-494.4	800.7	318.2	-489.6	-10.44
42	943.3	379.4	-598.6	822.0	390.2	-649.5	942.9	311.8	-612.2	821.6	322.6	-663.0	-5.15
43	1014.3	396.1	-676.8	958.8	416.5	-794.8	1023.7	329.6	-692.7	968.2	350.0	-810.7	1.69
44	1165.7	428.9	-697.8	1185.3	449.5	-826.7	1175.1	361.2	-707.2	1194.8	381.8	-836.1	6.98
45	1351.1	448.9	-618.5	1430.8	464.2	-722.6	1354.0	380.4	-626.3	1433.7	395.7	-730.5	10.73
46	1504.5	437.2	-445.5	1618.1	445.7	-512.1	1502.6	369.3	-457.3	1616.3	377.8	-523.9	12.75
47	1590.7	399.7	-245.0	1717.6	403.0	-281.3	1587.8	332.7	-261.3	1714.6	336.0	-297.6	13.83
48	1623.8	357.9	-82.7	1754.9	357.6	-97.9	1621.7	291.1	-100.1	1752.8	290.9	-115.2	14.56

Table 2.2-8 Coordinate of 4 corners of the MC2 (SWJTU-Type X)

No	M2-N1			M2-N2			M2-N3			M2-N4			Angle twisted
	X	Y	Z	X	Y	Z	X	Y	Z	X	Y	Z	
1	1336.8	895.0	10.5	1456.6	949.6	20.2	1365.8	833.4	-0.8	1485.6	888.0	9.0	15.00
2	1321.2	853.7	196.3	1438.8	902.9	230.2	1350.8	793.2	181.3	1468.4	842.4	215.3	16.18
3	1292.1	806.7	326.8	1405.5	850.7	378.2	1322.8	747.2	310.1	1436.2	791.2	361.4	16.96
4	1258.6	761.1	424.7	1366.4	799.8	490.3	1289.1	700.9	410.3	1396.9	739.6	475.9	17.68
5	1218.9	720.6	506.6	1319.3	753.5	585.8	1246.5	658.0	497.6	1346.9	690.9	576.7	18.72
6	1177.5	693.2	568.4	1266.7	718.1	662.5	1196.7	627.0	567.8	1285.9	651.8	661.8	20.52
7	1141.3	684.1	608.5	1213.3	698.0	718.2	1144.6	615.5	615.1	1216.6	629.4	724.8	24.28
8	1102.1	689.6	637.3	1156.9	693.5	757.3	1094.0	621.3	643.3	1148.8	625.3	763.3	28.80
9	1046.4	699.9	662.4	1096.5	701.3	784.5	1042.1	631.1	664.9	1092.3	632.5	787.0	29.65
10	976.1	702.3	689.5	1032.2	707.0	808.9	987.9	634.4	686.7	1044.0	639.1	806.0	28.14
11	903.3	685.1	723.1	967.0	694.1	838.3	933.5	624.2	711.1	997.2	633.2	826.4	28.01
12	838.6	644.6	759.7	905.5	655.4	873.1	881.0	594.0	739.6	947.9	604.9	852.9	29.49
13	784.6	584.4	792.7	847.3	592.8	908.6	834.1	542.7	768.9	896.8	551.1	884.8	30.48
14	740.1	512.9	814.3	789.8	514.0	936.6	795.1	477.5	792.3	844.8	478.6	914.6	29.16
15	705.9	442.4	819.1	732.6	431.5	947.9	765.2	410.4	804.1	791.9	399.5	932.9	24.64
16	684.2	384.2	808.1	679.1	358.3	937.5	744.6	351.1	803.9	739.5	325.2	933.2	16.90
17	673.3	343.0	790.1	635.3	303.3	910.1	729.5	303.2	794.7	691.5	263.5	914.7	7.81
18	665.5	315.6	771.6	603.3	267.0	877.4	714.1	266.9	777.8	651.9	218.4	883.6	0.41
19	655.1	296.2	751.7	577.7	242.9	844.5	697.5	242.0	756.0	620.2	188.7	848.7	-4.77
20	642.2	280.8	728.1	553.6	224.5	808.1	682.5	225.1	733.6	593.9	168.8	813.6	-8.91
21	630.8	266.1	700.2	531.6	207.6	764.9	671.0	211.3	712.3	571.8	152.9	777.0	-12.87
22	625.2	249.8	669.6	516.7	190.4	715.5	663.4	196.3	690.6	554.8	136.8	736.4	-16.80
23	626.6	231.6	637.5	511.5	172.6	663.9	660.3	177.6	664.1	545.2	118.7	690.5	-19.91
24	632.8	212.7	602.8	514.5	155.1	613.4	662.6	156.1	628.7	544.3	98.5	639.3	-21.28
25	642.0	195.3	563.8	522.4	139.4	561.9	669.8	135.1	582.9	550.3	79.2	581.0	-21.42
26	653.5	182.2	517.5	533.8	128.6	502.3	680.4	119.4	527.0	560.7	65.8	511.7	-21.94
27	668.7	176.7	459.5	550.8	127.2	426.6	695.1	113.0	460.8	577.2	63.5	428.0	-23.78
28	693.0	183.0	386.4	580.1	139.4	333.7	719.6	119.4	381.9	606.6	75.9	329.2	-27.07
29	732.6	204.6	299.2	625.2	166.2	232.8	760.8	142.3	289.6	653.4	103.9	223.2	-31.74
30	783.1	241.9	204.6	676.7	204.2	136.2	814.0	182.1	189.5	707.6	144.4	121.1	-35.68
31	829.0	287.7	115.3	720.9	248.6	50.4	862.7	231.8	92.8	754.6	192.8	27.8	-36.09
32	860.7	333.4	45.9	750.6	292.5	-14.5	897.0	285.5	12.0	786.9	244.6	-48.3	-34.44
33	879.6	378.0	-5.4	764.2	331.9	-50.0	913.0	338.0	-50.5	797.7	291.8	-95.1	-32.58
34	883.4	426.3	-63.9	763.7	370.8	-68.1	906.0	381.2	-111.1	786.3	325.7	-115.2	-21.89
35	865.2	467.1	-119.2	747.4	409.1	-105.3	883.5	418.9	-165.1	765.7	361.0	-151.2	-15.43
36	842.2	506.7	-165.9	723.1	449.9	-162.1	861.9	462.2	-214.8	742.8	405.4	-211.1	-15.59

No	M2-N1			M2-N2			M2-N3			M2-N4			Angle twisted
	X	Y	Z	X	Y	Z	X	Y	Z	X	Y	Z	
37	821.6	553.0	-209.8	701.8	498.9	-222.3	844.3	514.9	-262.7	724.5	460.8	-275.2	-16.94
38	803.9	608.0	-251.9	684.8	556.4	-276.3	829.8	573.6	-305.8	710.7	522.0	-330.2	-17.77
39	788.8	668.5	-297.1	670.0	617.4	-323.7	817.0	628.0	-345.4	698.2	576.9	-371.9	-16.11
40	777.6	723.2	-351.1	659.0	672.5	-379.3	807.9	670.0	-382.9	689.3	619.3	-411.2	-12.24
41	777.8	760.6	-410.8	662.3	714.4	-454.9	807.4	699.8	-424.4	691.9	653.5	-468.5	-7.09
42	797.9	783.8	-469.8	694.4	748.5	-543.7	822.8	719.6	-473.9	719.2	684.3	-547.7	0.49
43	840.9	800.2	-518.8	765.3	784.2	-625.8	860.3	734.2	-522.6	784.7	718.1	-629.6	7.40
44	908.0	817.0	-551.5	873.1	823.7	-678.6	926.8	751.2	-560.1	891.9	757.9	-687.2	10.95
45	1000.0	839.6	-558.4	1011.9	868.6	-686.6	1023.3	775.8	-570.6	1035.2	804.8	-698.9	12.40
46	1112.6	870.3	-518.0	1172.3	918.0	-625.7	1141.1	808.6	-529.6	1200.7	856.3	-637.2	12.85
47	1228.4	901.8	-402.5	1324.8	959.7	-471.5	1258.6	840.4	-411.8	1355.0	898.4	-480.8	13.20
48	1311.0	914.1	-210.4	1426.4	973.1	-235.9	1340.6	852.4	-219.3	1455.9	911.4	-244.9	13.88

Table 2.2-9 Coordinate of 4 corners of the MC3 (SWJTU-Type H)

No	M3-N1			M3-N2			M3-N3			M3-N4			Angle twisted
	X	Y	Z	X	Y	Z	X	Y	Z	X	Y	Z	
1	909.1	1223.8	-58.1	951.2	1348.8	-52.5	974.4	1201.8	-60.3	1016.6	1326.8	-54.6	-10.00
2	906.2	1179.7	167.4	940.0	1301.2	206.2	971.3	1158.7	176.6	1005.1	1280.3	215.3	-12.68
3	862.8	1113.4	343.1	886.6	1227.3	405.4	924.6	1089.8	362.5	948.5	1203.7	424.8	-13.89
4	808.0	1050.8	449.7	818.6	1155.3	529.6	864.8	1023.5	477.9	875.3	1128.0	557.8	-15.94
5	740.6	985.2	527.4	738.3	1082.4	616.6	791.9	954.6	562.0	789.6	1051.9	651.3	-17.26
6	660.3	915.2	589.3	646.9	1007.3	682.9	703.4	880.0	630.0	690.1	972.1	723.6	-17.60
7	576.7	853.0	628.2	553.0	941.2	723.4	608.6	812.3	673.8	584.9	900.5	769.1	-18.70
8	493.8	803.2	645.0	458.5	888.1	739.7	516.9	759.3	693.0	481.6	844.2	787.7	-21.30
9	411.3	758.3	646.6	359.4	837.7	738.4	432.9	715.3	696.0	381.0	794.6	787.8	-25.20
10	333.8	707.0	638.7	259.8	774.8	724.5	358.2	668.3	690.4	284.3	736.1	776.2	-29.86
11	270.4	644.0	624.4	173.2	691.1	700.4	297.1	611.2	678.9	199.9	658.2	754.9	-34.05
12	227.8	571.3	604.3	113.3	591.1	667.0	254.3	543.4	661.5	139.9	563.2	724.3	-36.07
13	207.7	496.4	579.8	85.0	488.4	627.7	232.5	471.8	639.3	109.8	463.8	687.2	-36.02
14	207.3	432.2	556.0	84.2	396.9	587.7	229.9	407.6	616.3	106.8	372.3	648.1	-36.41
15	219.9	387.9	535.8	106.1	321.8	546.3	241.0	361.2	595.8	127.2	295.1	606.4	-38.04
16	243.0	355.2	515.5	144.1	268.2	506.9	263.7	325.8	574.4	164.9	238.8	565.7	-35.25
17	272.9	332.4	496.3	190.2	232.6	471.3	300.5	296.5	548.3	217.9	196.7	523.3	-32.41
18	316.3	318.2	465.7	251.7	211.4	422.6	350.2	279.2	511.4	285.7	172.4	468.3	-32.22
19	379.2	309.1	414.1	315.9	203.6	366.2	419.1	267.9	452.4	355.8	162.4	404.5	-29.50
20	441.1	305.3	349.3	375.4	201.8	300.4	487.3	262.6	377.6	421.6	159.1	328.7	-24.74
21	492.9	310.6	277.9	427.9	209.5	223.4	544.1	267.9	295.9	479.1	166.8	241.4	-21.64
22	535.7	327.4	205.0	471.7	230.3	142.6	590.2	286.0	213.6	526.2	188.9	151.2	-21.51
23	569.3	353.9	136.7	505.4	261.6	67.3	625.9	314.5	137.0	562.0	222.1	67.6	-23.23
24	593.7	384.6	79.0	528.8	297.6	3.9	651.5	347.6	72.0	586.5	260.5	-3.1	-25.96
25	609.8	413.9	35.6	543.4	332.7	-44.5	668.2	379.9	21.7	601.7	298.7	-58.4	-29.50
26	619.7	438.5	6.2	551.3	363.3	-78.0	678.4	409.3	-15.3	610.0	334.1	-99.6	-33.75
27	625.3	459.3	-13.6	554.5	389.2	-100.1	683.5	436.7	-42.9	612.7	366.6	-129.5	-38.76
28	627.9	478.7	-28.3	554.0	414.9	-117.0	684.8	462.2	-63.8	610.8	398.4	-152.5	-44.56
29	628.7	499.2	-40.5	550.9	445.4	-132.5	684.0	486.3	-79.7	606.2	432.5	-171.8	-50.54
30	628.8	524.9	-52.2	547.3	479.8	-145.7	682.7	513.2	-93.6	601.2	468.1	-187.1	-55.01
31	628.7	559.5	-65.6	544.2	512.8	-155.6	681.5	545.8	-107.9	597.0	499.1	-197.9	-55.79
32	628.0	598.1	-83.1	541.2	541.4	-164.7	679.6	579.3	-124.8	592.8	522.5	-206.5	-51.19
33	626.8	631.7	-104.0	538.0	565.4	-175.8	677.4	607.3	-144.1	588.6	541.0	-215.8	-43.10
34	625.8	657.2	-124.7	535.3	583.8	-186.7	674.9	631.2	-165.6	584.4	557.8	-227.6	-36.34
35	623.7	677.7	-143.4	532.7	598.0	-196.2	670.0	655.3	-189.5	579.0	575.6	-242.3	-32.64
36	618.2	698.5	-161.9	527.0	615.1	-208.3	660.4	681.2	-213.7	569.1	597.8	-260.1	-32.18
37	606.8	725.4	-182.9	513.9	641.9	-225.6	644.9	711.4	-238.7	552.0	628.0	-281.4	-35.09
38	588.0	761.9	-207.4	491.8	681.2	-248.1	622.8	749.8	-265.7	526.7	669.1	-306.4	-40.71
39	563.1	808.7	-234.3	461.9	734.1	-274.7	595.7	796.6	-293.9	494.6	722.0	-334.2	-47.22

No	M3-N1			M3-N2			M3-N3			M3-N4			Angle twisted
	X	Y	Z	X	Y	Z	X	Y	Z	X	Y	Z	
40	536.8	862.3	-261.4	428.4	800.7	-304.7	568.8	847.9	-320.9	460.4	786.2	-364.2	-50.91
41	516.3	919.2	-287.3	400.8	880.9	-338.5	548.6	898.3	-344.6	433.1	860.0	-395.8	-48.47
42	507.9	978.9	-312.8	393.6	970.4	-378.3	539.3	943.6	-363.1	425.0	935.0	-428.5	-40.86
43	519.5	1035.7	-343.2	419.3	1055.3	-426.8	545.6	988.0	-385.6	445.4	1007.6	-469.3	-34.02
44	551.7	1082.1	-374.5	481.8	1131.5	-475.1	574.6	1031.4	-415.4	504.8	1080.9	-515.9	-28.24
45	605.1	1119.6	-395.2	572.9	1195.0	-498.6	631.6	1072.3	-437.9	599.3	1147.6	-541.3	-20.89
46	678.5	1152.5	-395.4	679.4	1248.7	-485.8	717.0	1113.1	-437.0	717.9	1209.3	-527.3	-13.92
47	765.1	1186.3	-361.8	793.8	1301.2	-420.1	818.9	1156.8	-393.3	847.7	1271.7	-451.6	-9.86
48	854.1	1218.2	-259.4	894.5	1343.1	-273.6	917.4	1195.9	-275.3	957.9	1320.8	-289.5	-10.00

Table 2.2-10 Coordinate of 4 corners of the MC4(SWJTU-Type G)

No	M4-N1			M4-N2			M4-N3			M4-N4			Angle twisted
	X	Y	Z	X	Y	Z	X	Y	Z	X	Y	Z	
1	423.9	1406.5	-56.4	439.8	1537.5	-55.4	487.9	1398.9	-80.9	503.9	1529.9	-79.8	-5.00
2	454.1	1396.3	10.0	472.9	1525.7	28.1	521.7	1385.3	18.3	540.5	1514.7	36.5	-4.80
3	442.6	1378.6	97.5	456.4	1503.8	137.0	504.3	1363.3	124.3	518.1	1488.5	163.8	-5.20
4	395.3	1341.7	188.2	391.3	1454.4	256.8	452.7	1323.2	221.9	448.6	1435.9	290.5	-4.80
5	322.1	1271.1	276.1	308.8	1377.3	353.3	381.8	1255.9	307.2	368.6	1362.2	384.4	0.17
6	253.6	1201.3	376.2	245.7	1315.0	442.9	317.0	1191.0	401.3	309.1	1304.7	468.0	5.88
7	215.8	1143.0	450.3	190.8	1231.8	544.6	279.7	1134.6	475.1	254.6	1223.5	569.4	-2.48
8	189.0	1068.3	496.8	152.4	1130.8	607.1	252.2	1059.2	522.9	215.6	1121.7	633.2	-8.61
9	165.7	987.7	528.0	123.6	1037.6	642.7	226.2	971.8	557.2	184.0	1021.6	671.9	-9.26
10	137.5	908.9	546.8	90.0	948.7	663.3	192.3	881.5	578.5	144.8	921.3	695.0	-9.29
11	98.1	832.0	551.2	42.5	859.5	667.7	146.4	794.4	583.1	90.8	821.9	699.6	-10.05
12	49.1	755.9	538.0	-18.8	767.6	650.6	93.4	713.2	569.2	25.5	724.9	681.8	-12.10
13	-1.1	678.7	505.7	-83.7	671.1	608.4	42.2	635.3	537.3	-40.3	627.7	640.1	-15.19
14	-40.9	601.0	455.9	-136.2	571.9	542.5	2.6	559.5	489.8	-92.7	530.4	576.4	-18.21
15	-61.8	527.1	394.4	-164.3	476.5	460.3	-18.6	489.0	432.4	-121.1	438.4	498.3	-19.82
16	-61.3	460.0	328.4	-164.6	391.2	373.4	-19.3	423.7	369.3	-122.5	354.9	414.3	-19.80
17	-44.3	404.0	263.0	-143.6	320.6	287.7	-2.4	365.7	302.2	-101.6	282.3	326.9	-20.44
18	-20.6	367.6	203.9	-109.9	270.5	201.0	20.1	329.0	244.1	-69.3	231.9	241.2	-23.03
19	7.3	347.5	158.4	-67.9	242.5	130.8	41.0	310.7	206.2	-34.2	205.8	178.5	-22.45
20	32.8	337.9	134.5	-24.9	228.6	88.3	64.5	300.6	183.1	6.8	191.3	136.9	-24.36
21	60.1	334.6	115.5	12.3	224.8	60.0	95.2	296.4	161.0	47.4	186.6	105.5	-26.09
22	92.0	333.8	91.7	44.7	225.0	33.8	129.5	294.7	134.5	82.2	185.9	76.6	-26.23
23	117.1	335.4	72.7	83.9	229.2	1.8	155.1	295.7	114.5	121.8	189.4	43.6	-30.58
24	140.6	341.6	58.7	132.2	243.7	-29.4	175.0	300.0	101.7	166.5	202.1	13.5	-35.07
25	172.6	353.6	46.2	178.9	262.9	-49.5	203.0	309.6	89.9	209.2	218.9	-5.8	-35.66
26	212.8	369.2	35.5	218.9	279.9	-61.6	243.7	324.8	78.3	249.9	235.5	-18.8	-34.59
27	257.7	386.5	22.6	253.2	294.6	-72.0	295.5	344.3	61.9	291.0	252.3	-32.7	-32.89
28	302.6	405.7	1.9	284.5	308.9	-85.9	351.5	368.3	33.1	333.3	271.4	-54.8	-30.69
29	341.5	428.1	-29.4	314.1	326.2	-108.7	401.3	398.4	-11.8	373.8	296.4	-91.1	-28.64
30	369.3	456.0	-71.3	339.5	351.7	-146.5	435.2	435.6	-69.1	405.4	331.3	-144.3	-28.17
31	383.5	492.1	-120.5	354.3	392.1	-201.5	450.8	480.8	-130.7	421.6	380.8	-211.7	-31.47
32	385.0	539.6	-171.6	354.6	450.9	-264.5	451.3	536.7	-190.5	420.8	448.0	-283.5	-41.69
33	374.1	603.3	-223.0	341.0	521.6	-321.3	438.1	607.7	-248.3	405.0	526.1	-346.6	-57.37
34	350.7	675.0	-272.5	314.5	597.7	-373.2	412.4	684.4	-301.9	376.2	607.0	-402.6	-70.53
35	324.8	738.4	-310.4	277.9	682.3	-420.3	383.8	753.0	-343.0	336.9	696.9	-452.9	-79.38
36	302.1	797.2	-329.1	241.8	770.1	-443.4	357.5	819.5	-363.6	297.3	792.4	-477.9	-83.52
37	278.3	861.5	-327.8	212.4	844.8	-441.0	330.5	890.3	-362.5	264.7	873.7	-475.6	-81.76
38	251.0	926.0	-317.3	187.4	901.0	-430.2	300.3	959.2	-352.3	236.7	934.3	-465.3	-76.55
39	219.4	984.1	-308.7	160.8	947.9	-421.3	265.9	1020.4	-344.6	207.3	984.1	-457.2	-71.59
40	183.8	1036.7	-303.6	125.7	997.1	-415.3	228.8	1074.1	-340.3	170.7	1034.4	-452.0	-68.18
41	146.2	1088.2	-299.0	80.5	1056.2	-408.9	191.5	1124.2	-336.6	125.8	1092.2	-446.5	-64.70
42	111.6	1141.5	-291.3	31.4	1130.8	-395.6	159.5	1171.2	-331.1	79.3	1160.5	-435.4	-58.18

No	M4-N1			M4-N2			M4-N3			M4-N4			Angle twisted
	X	Y	Z	X	Y	Z	X	Y	Z	X	Y	Z	
43	87.4	1200.6	-277.5	-3.4	1224.1	-370.4	137.5	1213.7	-323.2	46.7	1237.2	-416.1	-47.97
44	85.7	1270.3	-259.6	-0.8	1327.5	-341.4	131.7	1266.7	-310.8	45.3	1323.9	-392.6	-38.48
45	114.1	1337.1	-239.1	51.5	1434.6	-302.3	154.4	1327.2	-294.3	91.9	1424.8	-357.4	-29.98
46	175.3	1385.1	-203.4	150.9	1508.7	-242.8	209.8	1373.3	-261.9	185.4	1496.8	-301.4	-19.19
47	266.5	1408.9	-155.3	265.1	1538.5	-180.6	300.5	1397.8	-214.4	299.0	1527.3	-239.6	-11.24
48	356.1	1414.0	-106.7	370.2	1544.5	-121.1	401.7	1403.5	-157.4	415.8	1534.0	-171.8	-5.00

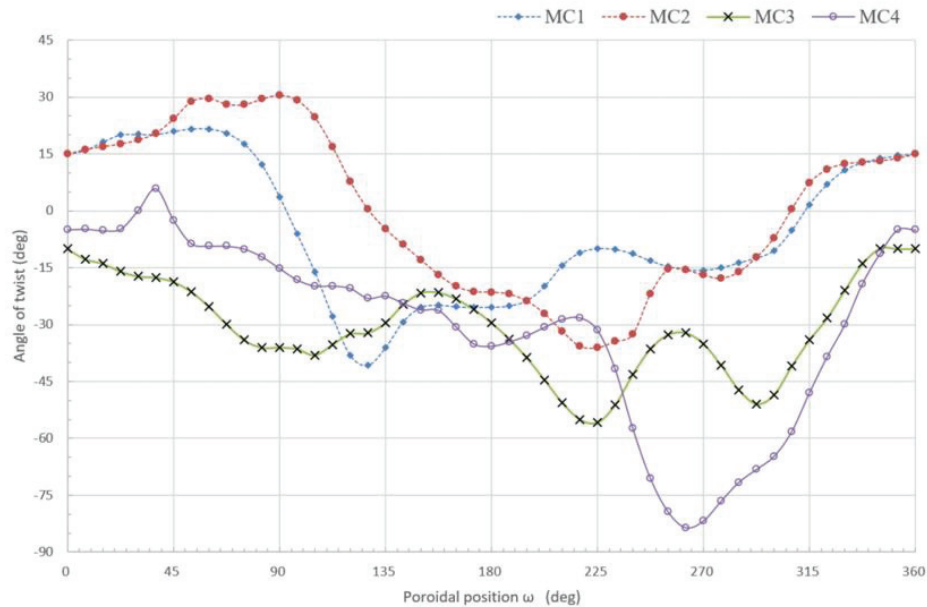
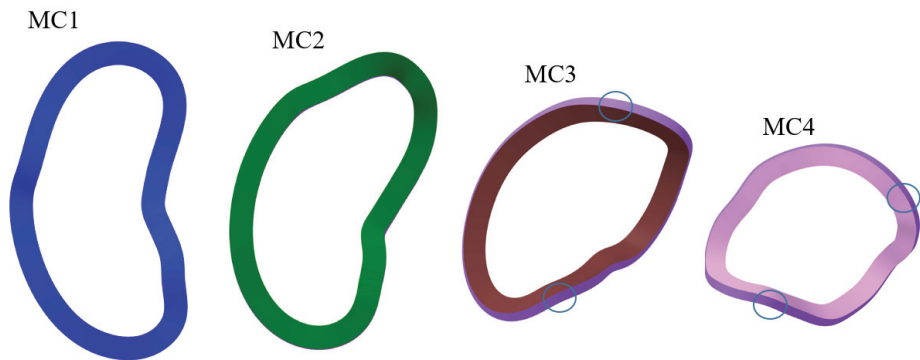


Fig 2.2-11 Optimized twisting angle of each modular coil. The angle of twist of 0 degree indicates that the long axis of the cross section is orthogonal to the CCS.



The inner and outer walls are not visible because they are parallel to view direction.

Only the outer walls (purple parts) are visible because they are open faces.

It shows that the coil does not contact the case when the coil is inserted.

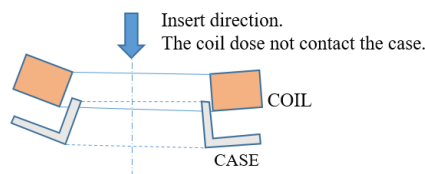
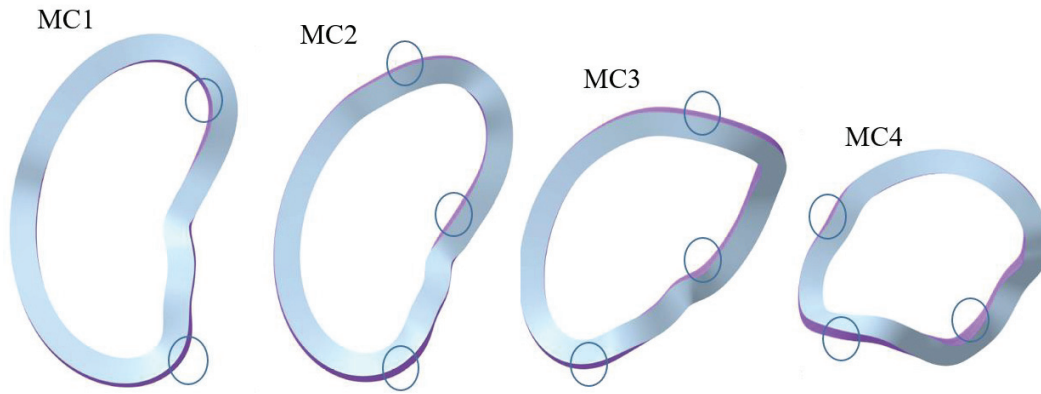


Fig 2.2-12 Orthogonal direction view of the optimized coils. All inner surface of the coil is behind the coil itself (invisible or parallel to the view)





The inner and outer walls (purple parts) are visible. It shows that the coil contacts the case when the coil is inserted.

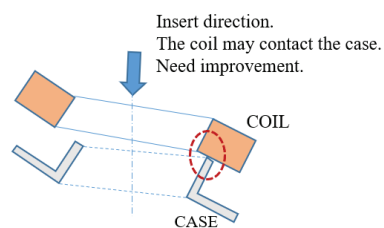
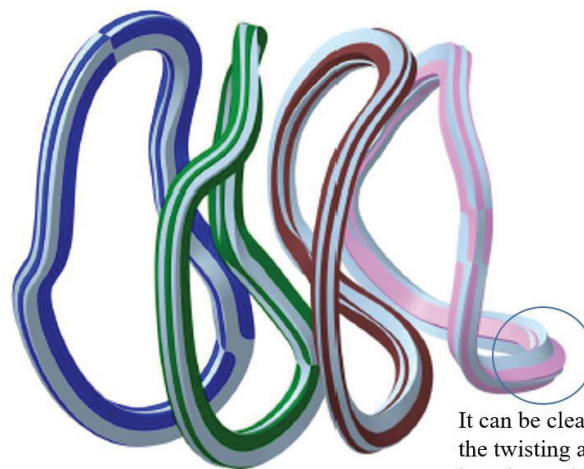


Fig 2.2-13 Orthogonal direction view of the unoptimized coils. Part of the inner surface of the coil is visible in the view.



It can be clearly seen that the twisting angle of MC4 has changed about 90 degrees from before optimization.

Fig 2.2-14 Comparison of coil shapes. The gray coils show the shape before optimization and others show shape after optimization.

The 3-D surface curvature on the ground insulation are shown in Table 2.1 5 and Table 2.1 6. The definition of the surface curvature is as follows by the differential geometry.

Gaussian curvature  $\sqrt{k} = \sqrt{k_1 k_2}$ ,

Mean curvature  $H = (k_1 + k_2)/2$ ,

Maximum curvature  $\text{Max}(k_1, k_2)$ ,

where,  $k_1$  and  $k_2$  are principal curvatures.  $\text{Max}(k_1, k_2) \gg \text{Min}(k_1, k_2)$  indicates near cylindrical bending (single dimensional bending), and  $\text{Max}(k_1, k_2) = \text{Min}(k_1, k_2)$  indicates bowl or saddle bending (two dimensional bending).



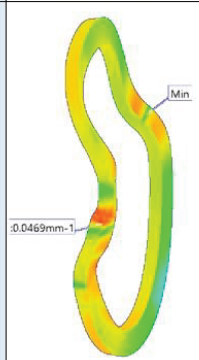
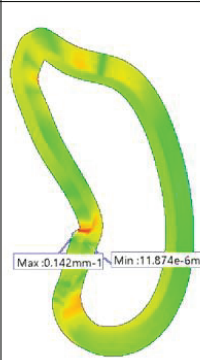
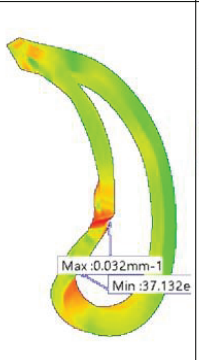
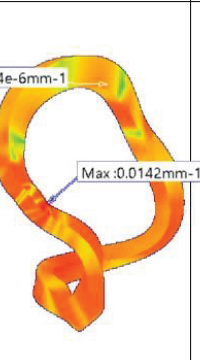
It is better that the minimum curvature radius of  $1/\text{Max}(k_1, k_2)$  is as large as possible, and it is desirable that it is 5 times or more the conductor diameter to prevent the conductor cross section from being deformed during winding.

Table 2.2-11 shows the coil without the optimization has small radius curvature, which indicates that winding is difficult, and Table 2.2-12 shows the coil after the optimization has larger curvature radius. In this way, the ease or difficulty of winding changes, so the twisting angle was optimized in consideration of these factors.

By changing the twist angle, the distance between the coil surface and the coil surface and the distance between the coil surface and the vacuum vessel change. Originally, the NESCOIL system determined the trajectory of the centerline on the condition that the coil cross section was orthogonal to a continuous plane called CCS, so it was unlikely that the coil would interfere with other coils or vacuum vessels. However, since the twist angle was corrected from the viewpoint of manufacturability, there was a concern that the coil would interfere with others. Therefore, the gap between the coil surface and others was also taken into consideration when considering optimization, and the design that made the gap extremely small was excluded. Table 2.2-13 and Table 2.2-14 show a comparison of the gaps. It was found that the change in the gap was not so large, and the gap became smaller after the twisting angle optimization in places.

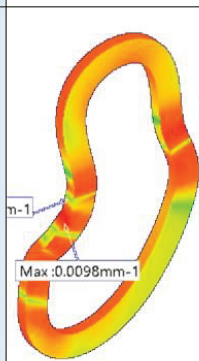
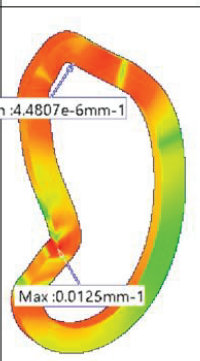
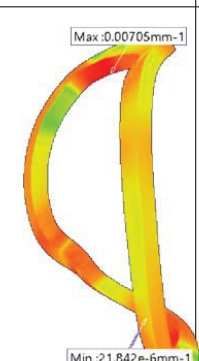
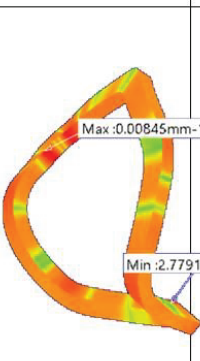
The optimized result may not be a logical optimum solution, but it is considered that the selection is an appropriate choice that is problem-free as can be seen by comparing with before optimization.

Table 2.2-11 3D surface curvature before optimizing the twist angle.

Name of coil		MC1 (TypeB)	MC2 (TypeB)	MC3 (TypeB)	MC4 (TypeB)	Design Criterion
Feature		Normal vector orthogonal to the CCS				
Maximum curvature on the 3D surface of ground insulation (1/m)	√Gaussian	37.2 NG	15.8	9.6	5.1	Should be less than 23.5 1/m. (r>42.5mm)
	Mean	38.2 NG	72 NG	16.8	7.5	
	Max(k <sub>1</sub> ,k <sub>2</sub> )	46.9 NG	142 NG	32 NG	14.2	
Profile of curvature Max (k <sub>1</sub> ,k <sub>2</sub> )						



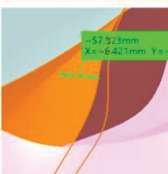
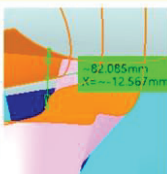

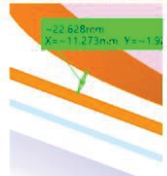
The curvature partially exceeds the design standard. Since the radius of curvature = 7 mm (curvature = 142 1 / m) is smaller than the conductor diameter of 8.5 mm, winding is considered very difficult.

Table 2.2-12 3D surface curvature after optimizing the twist angle.

Name of coil		MC1 (TypeX)	MC2 (TypeX)	MC3 (TypeH)	MC4 (TypeG)	Design Criterion
Feature		Twisted to an angle where the inner wall can be seen				
Maximum curvature on the 3D surface of ground insulation (1/m)	√Gaussian	4.8	9.5	2.6	1.4	Should be less than 23.5 1/m. (r>42.5mm)
	Mean	5.2	9.7	3.6	4.3	
	Max(k <sub>1</sub> ,k <sub>2</sub> )	9.8	12.5	7.1	8.5	
Profile of curvature Max (k <sub>1</sub> ,k <sub>2</sub> )						

All curvatures are below the design criteria. Since the radius of curvature is more than 9 times the conductor diameter, there is no problem with winding.

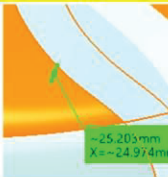
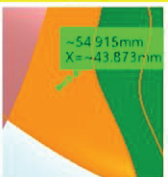
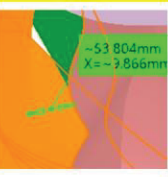
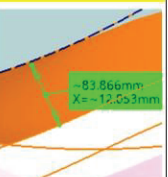


Table 2.2-13 Minimum gap before optimizing the twist angle.

Name of coil		MC1 (TypeB)	MC2 (TypeB)	MC3 (TypeB)	MC4 (TypeB)	Design guide
Feature		Normal vector orthogonal to the CCS				
Minimum gap between coils without case (mm)	MC1-MC1	64.1				Should be larger than 50mm.
	MC1-MC2	55.7				
	MC2-MC3		60			
	MC3-MC4			73.1		
	MC4-MC4				150.9	
Minimum gap between the coil without case and the vacuum vessel (mm)	With inner surface of the shell	27.7 	57.5 	57.8 	82.1 	Should be larger than 25mm.
	With a port	50(CF420) 			22.6 (Rectangle OP) 	

The gap is expected to be maximized because the twist angle orthogonal to the reference plane (CCS) is selected.

It is estimated that the problem of interference will not occur even if it is assumed that a coil case of about 10 mm will be added.

Table 2.2-14 Minimum gap after optimizing the twist angle.

Name of coil		MC1 (TypeX)	MC2 (TypeX)	MC3 (TypeH)	MC4 (TypeG)	Design guide
Feature		Twisted to an angle where the inner wall can be seen				
Minimum gap between the coils without case (mm)	MC1-MC1	106.7				Should be larger than 50mm.
	MC1-MC2	76.9				
	MC2-MC3		84.3			
	MC3-MC4			67.3		
	MC4-MC4				107.3	
Minimum gap between the coil without case and the vacuum vessel (mm)	With inner surface of the shell	25.2 	54.9 	53.8 	83.9 	Should be larger than 25mm.
	With a port	55.7(CF420) 			43.6 (Rectangle OP) 	

Since it is not orthogonal to the reference plane (CCS), there was a concern that the gap would become smaller.

However, as a result of searching for an angle that does not cause this, it was designed so that the problem of interference does not occur.

### 2.3 Poloidal field coil system (PFC)

Two pairs of PFCs will be installed in the CFQS as shown in Fig 2.3-1. Main purpose of the PFC is to apply vertical field to change the position of the magnetic axis. However, it may also be used to control rotational transform.

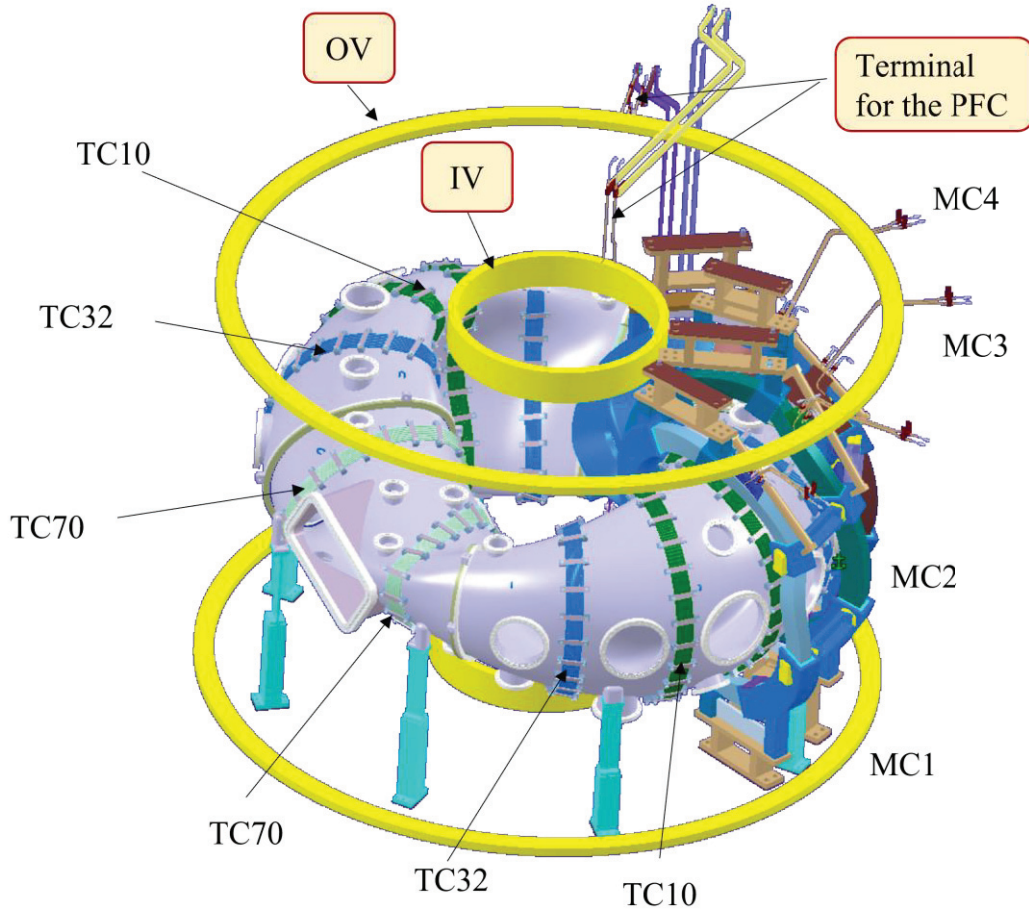


Fig 2.3-1 CFQS with the PFC

Table 2.3-1 shows the design parameters and Table 2.3-2 shows the operation condition. Fig 2.3-2 shows the cross-sectional shape of the PFC. The winding method is a solenoid winding for the IV and a double pancake with two simultaneous winding for the OV. The number of turns is 64 with 16 turns and 4 layers for the IV and 32 with 8 turns and 4 layers for the OV. The insulation process is vacuum pressure impregnation (VPI). The material of the conductor is hollow copper square tube of the Oxygen free copper annealed (OFC-O).

The layout of the PFCs and the connection bars are shown in Fig 2.3-3 to Fig 2.3-6. A pair of the IVs and a pair of the OVs will be connected in series with solid bus bars around the CFQS body, and cables connected between the two pairs of coils and two power supplies. The solenoid winding was selected for the IV to provide lead-outs on the top and bottom, and the pancake winding was selected for the OV to provide lead-outs on the outer side.

Table 2.3-1 Design parameters of the PFC

Category	Parameter	Unit	PFC		Remarks
			IV	OV	
General	Width DW	mm	48	100.5	Include earth isolation and cooling hall
	Height DH	mm	184.5	48	
	Number of coils in series		2	2	
	Winding method		Solenoid	Pancake	
	Position		R=536 Z=±942	R=1695 Z=±1100	
	Cooling method		Water cooling		
	Heat resistance class		A [ < 105°C ]		
	Resistance(75°C)	Ω	0.161	0.251	Note 1
	Inductance	H	0.019	0.020	Note 2
	Time constant	s	0.115	0.078	
Conductor	Type		OFC with a hole		
	CSA(Cross-sectional area)	mm <sup>2</sup>	58.83	58.83	
	Arc length of a conductor	m/turn	3.37	10.65	By CATIA
	Number of turns in a coil		64	32	
Insulation	Ground insulation	kV	2.4	2.4	
	Test voltage against the ground	kV	5.8	5.8	
	Layer insulation	kV	0.3	0.4	
	Impulse test voltage	kV	1.0	1.0	
Cooling	Number of cooling circuits	1/coil	1	2	
	Length of cooling pipe	m	215.6	170.4	
	Flow velocity	m/s	1.3	1.5	
	Flow rate	m <sup>3</sup> /s	1.63E-05	1.88E-05	
	Loss head	m	128	132	Note 3

Note 1 ; Added 5% margin to the calculated result

Note 2 ; Including the effect of mutual inductance and 5% margin.

Note 3 ; Hazen Williams' equation



Table 2.3-2 Operation condition of the PFC

Category	Parameter	Unit	PFC		Remarks
			IV	OV	
Short pulse (1T)	Maximum current	kA	6.3	6.3	
	Total current in a coil	kAT	400.0	200.0	
	Maximum current density	A/mm <sup>2</sup>	106.2	106.2	Conductor only
	Discharge period	s	600	600	
	Current rise time	s	0.2	0.2	
	Flat top time	s	0.3	0.3	
	Pulse width in a pulse	s	0.457	0.453	RWET ; Note 4
	Temperature rise in a pulse	Kelvin	30	30	ARTP ; Note 5
	Water temperature	Kelvin	35	24	AWTR ; Note 6
	Stored magnetic energy	MJ	0.36	0.38	
	Time averaged current	kA	0.17	0.17	
	Start up voltage	kV	1.22	1.70	Maximum
	Flat top voltage	kV	1.01	1.57	
	Flat top power	MW	6.30	9.82	
	Energy consumption	MJ	2.88	4.45	
Long pulse (0.09T)	Maximum current	kA	0.5625	0.5625	
	Maximum current density	A/mm <sup>2</sup>	9.56	9.56	
	Discharge period	s	1800	1800	
	Water temperature	Kelvin	27	18	AWTR ; Note 6
	Pulse width in a pulse	s	130	130	Adiabatic rise <70 Kelvin
	Flat top voltage	kV	0.091	0.141	
	Flat top power	MW	0.051	0.080	

Note 4 ; RWET - Rectangular wave equivalent time or square wave conversion time.

Note 5 ; ARTP - Adiabatic rise of temperature in a pulse.

Note 6 ; AWTR - Average water temperature rise

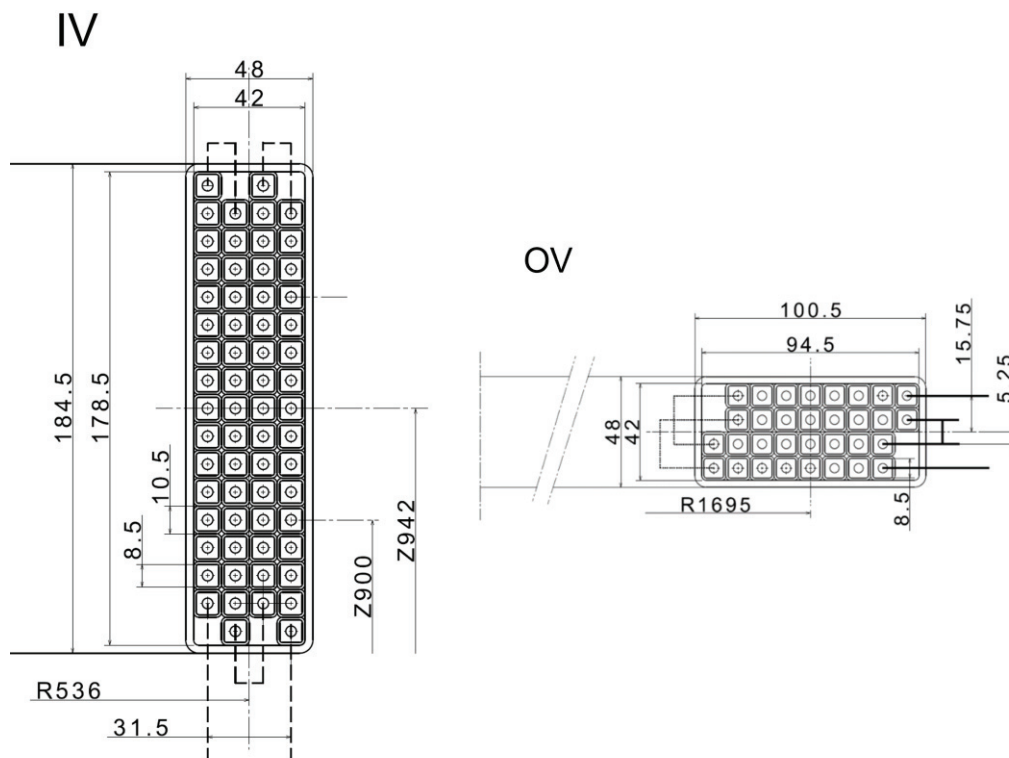


Fig 2.3-2 Cross section of PFC

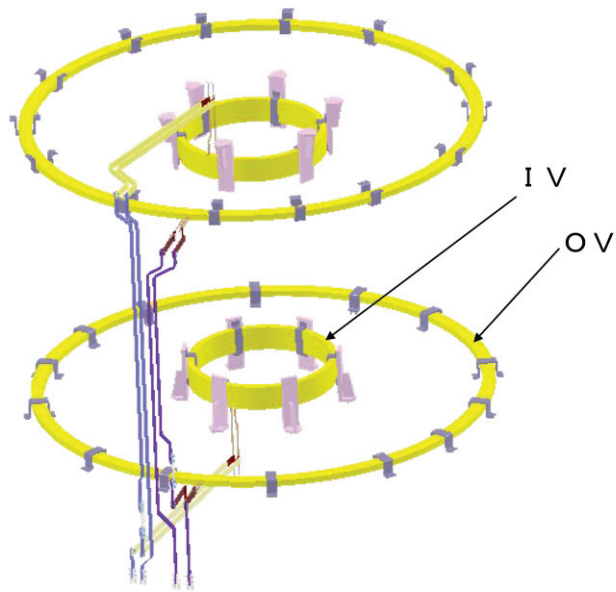


Fig 2.3-3 Layout of the PFC and connection bars

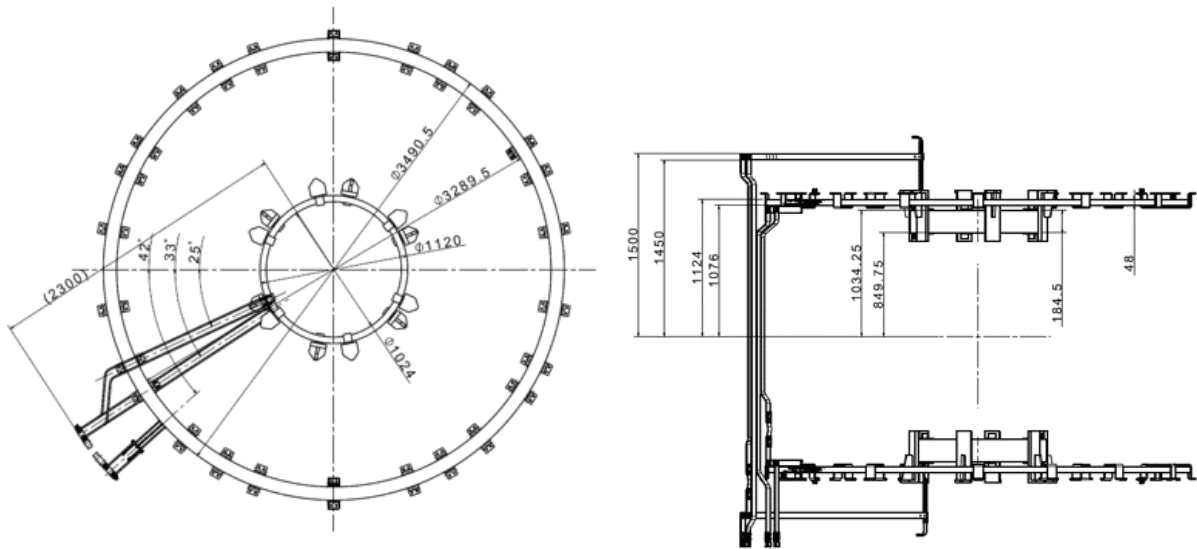


Fig 2.3-4 Installation position of the connection bars



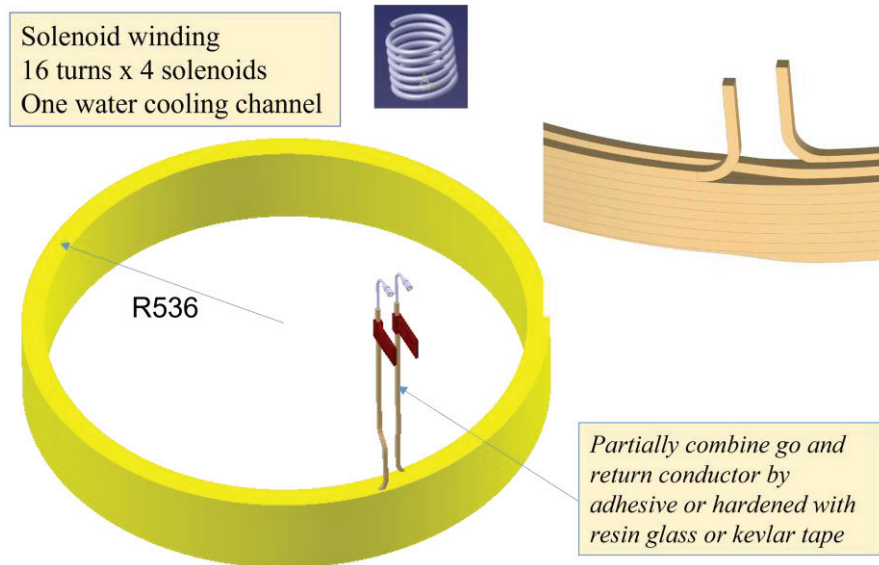


Fig 2.3-5 Structure of start and end of winding for the IV coil

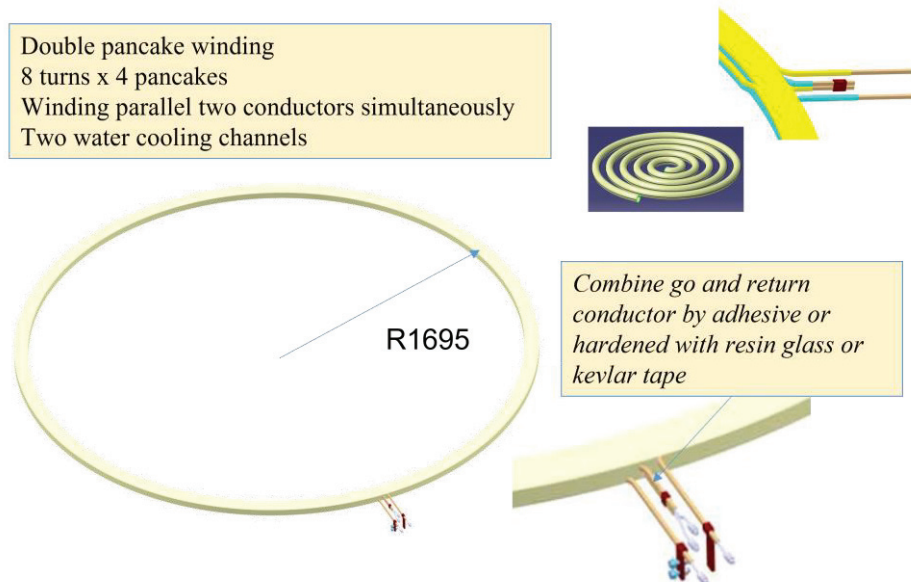


Fig 2.3-6 Structure of start and end of winding for the OV coil

## 2.4 Toroidal field coil system (TFC)

Layout of the toroidal field coil system is shown in Fig 2.4-1. The TFC will be installed in the CFQS to control the rotational transform. Each TFCs will be manufactured by winding an insulated cable around the vacuum vessel.

The cable is cooled by natural air flow. It is obvious that the water cooled coil is desirable to realize long time operation. In order to install it, it is necessary to increase the cross-sectional area of the coil, which makes winding difficult, and we are worried about interference of the TFC and the modular coil. In addition, development of a water cooled current lead, which should be thin and flexible, is not easy.

It is clear that a conductor with a rectangular cross-section may be preferable in order to reduce the installation space. A winding test was conducted to confirm the effect, and it was found that there were places where it was difficult to bring the conductor surface into close contact with the vacuum vessel due to the large torsion. It was also found that if the surface is hit with a strong force in order to twist the conductor, there is a concern that the work may damage the insulation coating. Based on the above test results, we gave up on applying rectangular conductor and decided to use circular cable that does not require twisting.

We had no choice but to reduce the cross-sectional area with a circular air-cooled cable. However, although it is difficult to evaluate by calculation, we also expect a cooling effect due to heat conduction.

Table 2.4-1 shows the design parameters and Table 2.4-2 shows the operation condition. We have designed total of 12 TFCs with three types.

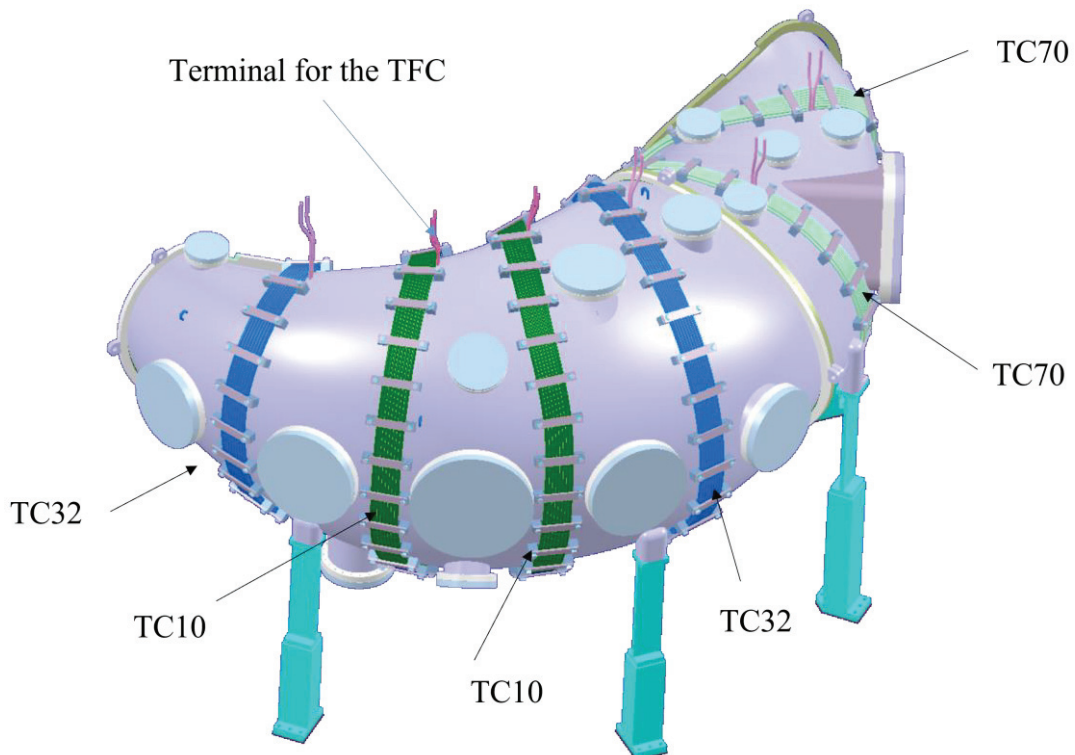


Fig 2.4-1 CFQS with the TFC

Table 2.4-1 Design parameters of the TFC

Category	Parameter	Unit	TFC			Remarks
			TC10	TC32	TC70	
General	Width DW	mm	88	88	88	Include earth isolation
	Height DH	mm	22	22	22	
	Number of coils in series		4	4	4	
	Winding method		Solenoid			
	Position		$\varphi=10^\circ$ on VV	$\varphi=32^\circ$ on VV	$\varphi=70^\circ$ on VV	
	Cooling method		Natural air flow			
	Heat resistance class		B [ < 130°C ]			
	Resistance(75°C)	$\Omega$	0.221	0.205	0.168	Note 1
	Inductance	H	0.003	0.003	0.002	Note 2
	Time constant	s	0.014	0.013	0.013	
Conductor	Type		CV cable			
	CSA(Cross-sectional area)	mm <sup>2</sup>	22.0	22.0	22.0	
	Arc length of a conductor	m/turn	3.33	3.09	2.53	By CATIA
	Number of turns in a coil		16	16	16	
Insulation	Ground insulation	kV	0.6	0.6	0.6	
	Test voltage against the ground	kV	2.2	2.2	2.2	
	Layer insulation	kV	0.16	0.16	0.16	
	Impulse test voltage	kV	0.4	0.4	0.4	
Cooling	Number of cooling circuits	1/coil	0	0	0	
	Length of cooling pipe	m				
	Flow velocity	m/s				
	Flow rate	m <sup>3</sup> /s				
	Loss head	m				

Note 1 ; Added 5% margin to the calculated result

Note 2 ; Including the effect of mutual inductance and 5% margin.

Table 2.4-2 Operation condition of the TFC

Category	Parameter	Unit	TFC			Remarks
			TC10	TC32	TC70	
Short pulse (1T)	Maximum current	kA	2.0	2.0	2.0	
	Total current in a coil	kAT	32.0	32.0	32.0	
	Maximum current density	A/mm <sup>2</sup>	90.9	90.9	90.9	Conductor only
	Discharge period	s	600	600	600	
	Current rise time	s	0.05	0.05	0.05	
	Flat top time	s	0.15	0.15	0.15	
	Pulse width in a pulse	s	0.190	0.189	0.189	RWET ; Note 4
	Temperature rise in a pulse	Kelvin	9.2	9.2	9.2	ARTP ; Note 5
	Water temperature	Kelvin				
	Stored magnetic energy	MJ	0.006	0.005	0.004	
	Time averaged current	kA	0.035	0.035	0.035	
	Start up voltage	kV	0.45	0.42	0.34	Maximum
	Flat top voltage	kV	0.44	0.41	0.34	
	Flat top power	MW	0.89	0.82	0.67	
	Energy consumption	MJ	0.17	0.16	0.13	
Long pulse (0.09T)	Maximum current	kA	0.180	0.180	0.180	
	Maximum current density	A/mm <sup>2</sup>	8.18	8.18	8.18	
	Discharge period	s	3600	3600	3600	
	Water temperature	Kelvin				
	Pulse width in a pulse	s	177	177	177	Note 7
	Flat top voltage	kV	0.0399	0.0369	0.0303	
	Flat top power	MW	0.0072	0.0066	0.0054	

Note 4 ; RWET - Rectangular wave equivalent time or square wave conversion time.

Note 5 ; ARTP - Adiabatic rise of temperature in a pulse.

Note 7 ; Thermal upper limit. Adiabatic rise <70 Kelvin.

Table 2.4-3 Coordinate of the cross-sectional center of the TFC for the field calculation

Name	No	x(mm)	Y(mm)	Z(mm)	$\Phi$ (deg)	R(mm)	$\theta$ (deg)	Ave-R(mm)	s(mm)
TC10-1	1	1542.3	271.9	-119.2	10.0	1566.1	-18.4	1206.7	0.0
TC10-1	2	1553.8	274.0	6.7	10.0	1577.7	1.0		126.4
TC10-1	3	1539.0	271.4	132.2	10.0	1562.8	20.4		252.9
TC10-1	4	1498.8	264.3	251.9	10.0	1521.9	38.6		379.3
TC10-1	5	1435.4	253.1	360.7	10.0	1457.5	55.2		505.7
TC10-1	6	1352.3	238.5	454.9	10.0	1373.2	69.9		632.2
TC10-1	7	1253.6	221.0	532.1	10.0	1273.0	82.9		758.7
TC10-1	8	1143.1	201.6	590.5	10.0	1160.7	94.5		885.2
TC10-1	9	1023.9	180.5	627.1	10.0	1039.7	104.9		1011.6
TC10-1	10	899.9	158.7	631.5	10.0	913.8	114.9		1137.7
TC10-1	11	804.8	141.9	560.3	10.0	817.2	124.8		1257.6
TC10-1	12	825.6	145.6	438.3	10.0	838.3	130.0		1381.4
TC10-1	13	889.2	156.8	329.5	10.0	902.9	132.7		1508.0
TC10-1	14	957.6	168.8	223.6	10.0	972.4	136.3		1634.6
TC10-1	15	1017.5	179.4	112.6	10.0	1033.2	147.0		1761.2
TC10-1	16	1054.6	186.0	-8.0	10.0	1070.9	-176.6		1887.5
TC10-1	17	1055.0	186.0	-134.1	10.0	1071.3	-135.3		2013.6
TC10-1	18	1022.3	180.3	-256.1	10.0	1038.1	-123.4		2140.1
TC10-1	19	976.0	172.1	-373.7	10.0	991.0	-120.0		2266.7
TC10-1	20	948.9	167.3	-496.3	10.0	963.5	-116.1		2392.4
TC10-1	21	1026.2	180.9	-583.1	10.0	1042.0	-105.8		2509.5
TC10-1	22	1149.3	202.7	-573.0	10.0	1167.1	-94.0		2634.9
TC10-1	23	1262.9	222.7	-521.6	10.0	1282.4	-81.7		2761.2
TC10-1	24	1362.3	240.2	-445.4	10.0	1383.3	-68.4		2887.6
TC10-1	25	1444.2	254.6	-350.2	10.0	1466.5	-53.4		3014.1
TC10-1	26	1505.1	265.4	-239.9	10.0	1528.3	-36.7		3140.5
TC10-1	27	1542.3	271.9	-119.2	10.0	1566.1	-18.4		3266.9
TC32-1	1	1286.1	803.6	39.6	32.0	1516.5	5.8	1129.6	0.0
TC32-1	2	1258.5	786.4	151.5	32.0	1484.0	23.1		116.5
TC32-1	3	1213.4	758.2	255.2	32.0	1430.8	40.3		233.1
TC32-1	4	1153.6	720.8	348.0	32.0	1360.2	56.5		349.6
TC32-1	5	1081.8	676.0	428.1	32.0	1275.6	71.2		466.2
TC32-1	6	1000.5	625.2	494.5	32.0	1179.7	84.2		582.8
TC32-1	7	911.8	569.7	546.0	32.0	1075.1	95.7		699.4
TC32-1	8	817.5	510.9	581.4	32.0	964.0	105.9		816.0
TC32-1	9	719.6	449.7	597.2	32.0	848.6	115.2		932.5
TC32-1	10	621.9	388.6	582.9	32.0	733.4	124.2		1048.6
TC32-1	11	550.1	343.8	508.3	32.0	648.7	133.4		1161.4
TC32-1	12	557.2	348.2	394.7	32.0	657.0	140.1		1275.3
TC32-1	13	608.3	380.1	295.1	32.0	717.3	144.4		1391.7
TC32-1	14	671.6	419.7	205.5	32.0	792.0	148.7		1508.4
TC32-1	15	737.5	460.8	118.4	32.0	869.6	155.5		1625.1
TC32-1	16	799.9	499.8	27.8	32.0	943.2	171.5		1741.8
TC32-1	17	851.6	532.1	-71.5	32.0	1004.2	-150.3		1858.3
TC32-1	18	883.7	552.2	-181.6	32.0	1042.1	-115.7		1974.7
TC32-1	19	895.1	559.3	-297.4	32.0	1055.5	-104.0		2091.3
TC32-1	20	911.7	569.7	-411.7	32.0	1075.0	-97.6		2207.3
TC32-1	21	990.5	618.9	-472.3	32.0	1167.9	-85.4		2318.2
TC32-1	22	1086.2	678.7	-447.4	32.0	1280.8	-71.3		2433.9

Name	No	x(mm)	Y(mm)	Z(mm)	$\Phi$ (deg)	R(mm)	$\theta$ (deg)	Ave-R(mm)	s(mm)
TC32-1	23	1169.1	730.5	-384.3	32.0	1378.5	-57.1	945.8	2550.1
TC32-1	24	1233.8	771.0	-296.6	32.0	1454.9	-42.4		2666.5
TC32-1	25	1275.8	797.2	-191.3	32.0	1504.4	-27.0		2782.8
TC32-1	26	1292.8	807.8	-76.6	32.0	1524.4	-11.0		2899.2
TC32-1	27	1286.1	803.6	39.6	32.0	1516.5	5.8		3015.7
TC70-1	1	478.0	1313.2	-98.8	70.0	1397.5	-12.3	945.8	0.0
TC70-1	2	475.9	1307.6	-4.0	70.0	1391.6	-0.5		95.0
TC70-1	3	463.1	1272.5	84.0	70.0	1354.1	11.6		190.6
TC70-1	4	444.4	1221.1	162.6	70.0	1299.5	24.7		286.3
TC70-1	5	421.5	1158.1	230.9	70.0	1232.4	38.9		382.1
TC70-1	6	395.2	1085.9	288.1	70.0	1155.6	53.9		477.8
TC70-1	7	366.4	1006.7	333.6	70.0	1071.3	69.4		573.6
TC70-1	8	335.7	922.4	367.4	70.0	981.6	84.4		669.4
TC70-1	9	303.9	834.9	389.6	70.0	888.4	98.4		765.2
TC70-1	10	271.3	745.3	399.6	70.0	793.2	110.9		861.0
TC70-1	11	238.6	655.5	395.2	70.0	697.5	122.1		956.8
TC70-1	12	206.9	568.6	371.0	70.0	605.0	132.6		1052.4
TC70-1	13	179.7	493.8	318.8	70.0	525.4	142.8		1147.6
TC70-1	14	163.4	448.8	236.8	70.0	477.6	153.2		1242.4
TC70-1	15	161.0	442.2	141.9	70.0	470.6	163.4		1337.7
TC70-1	16	169.3	465.2	49.5	70.0	495.0	173.7		1433.2
TC70-1	17	185.6	509.9	-33.4	70.0	542.6	-175.3		1528.8
TC70-1	18	208.5	572.8	-101.7	70.0	609.6	-163.2		1624.4
TC70-1	19	236.4	649.6	-151.4	70.0	691.3	-149.3		1720.1
TC70-1	20	267.3	734.4	-183.4	70.0	781.5	-131.9		1815.8
TC70-1	21	299.4	822.6	-202.4	70.0	875.4	-109.2		1911.6
TC70-1	22	332.0	912.1	-213.4	70.0	970.6	-83.4		2007.5
TC70-1	23	364.7	1002.0	-219.2	70.0	1066.3	-61.2		2103.3
TC70-1	24	397.5	1092.1	-220.1	70.0	1162.1	-45.5		2199.2
TC70-1	25	430.1	1181.7	-211.3	70.0	1257.5	-34.1		2294.9
TC70-1	26	460.4	1265.0	-177.1	70.0	1346.2	-23.9		2390.0
TC70-1	27	478.0	1313.2	-98.8	70.0	1397.5	-12.3		2483.6

Obtained by the 3D cad system (CATIA)

Fig 2.4-2 shows the location of the TFC and Table 2.4-3 shows the coordinate for the field calculation. In order to avoid interference with the vacuum vessel port, the real TFC is partially displaced in the torus direction, it was approximated that the coil was on a plane with a constant  $\Phi$  when calculating the magnetic field.

Twelve bean-shaped coils will be placed at even intervals. Fig 2.4-3 shows the position of its terminal. All cables (power leads) that supply current to the TFC are designed to be pulled out from the opening of the top frame. There are 12 TFC bodies of 3 types, but half of them are installed upside down. There are 6 types including the terminal as shown in Fig 2.4-4. The coil and power supply are connected by a 2-core CV cable (CV-2C) (cross-linked polyethylene insulated vinyl sheath cable) that is easy to adjust the wiring route as shown in Fig 2.4-5. The wiring path must be adjustable according to the actual product because it must be pass through a complicated and narrow space, and it is not easy to strictly design by desk study only. The heat resistance class of the insulation is F for TFC body that touches the vacuum vessel to be baked, and A for the CV cable to be wired in the air.

Cross section of each TFC is shown in Fig 2.4-6. An insulated cable with no cooling channel is fixed by the



clamps on the vacuum vessel, the clamp covers, and the bolts. The winding structure is the solenoid. The clamps are welded by the arc spot welding.

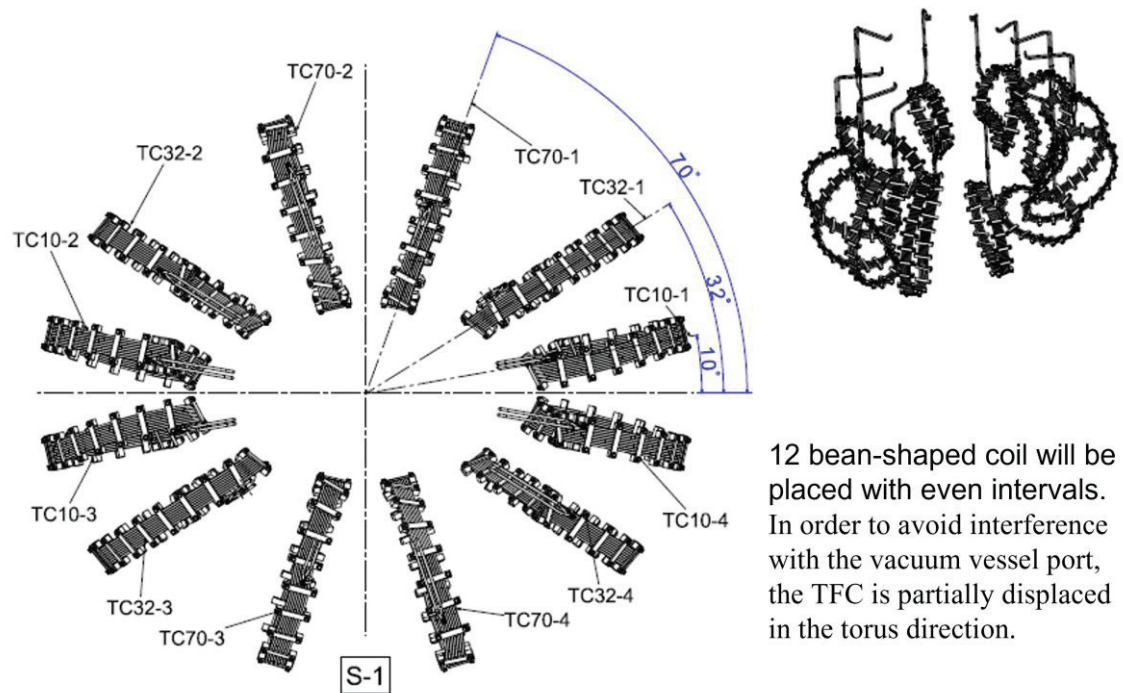


Fig 2.4-2 Location of each toroidal field coil

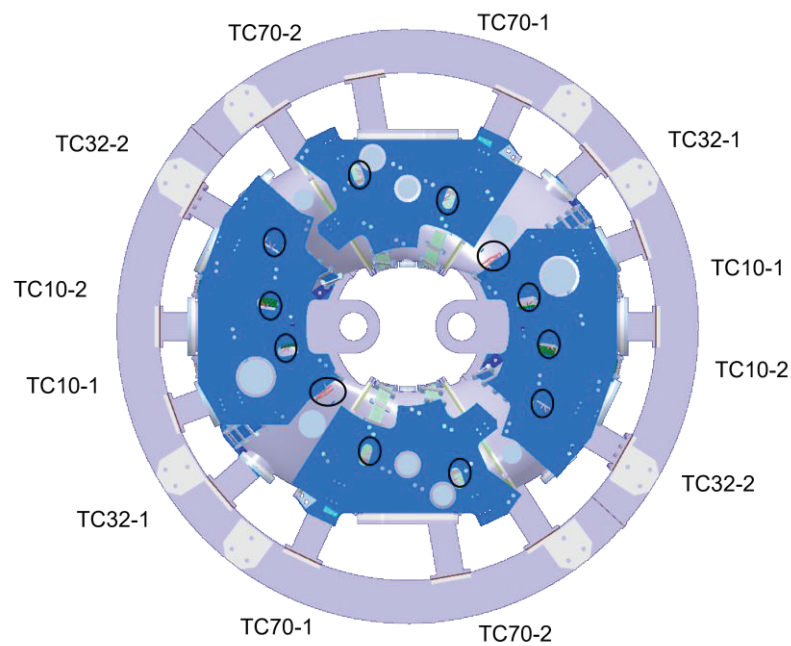


Fig 2.4-3 Position of current leads. Each current leads for the TFC will be pulled out through the gaps in the top frame.

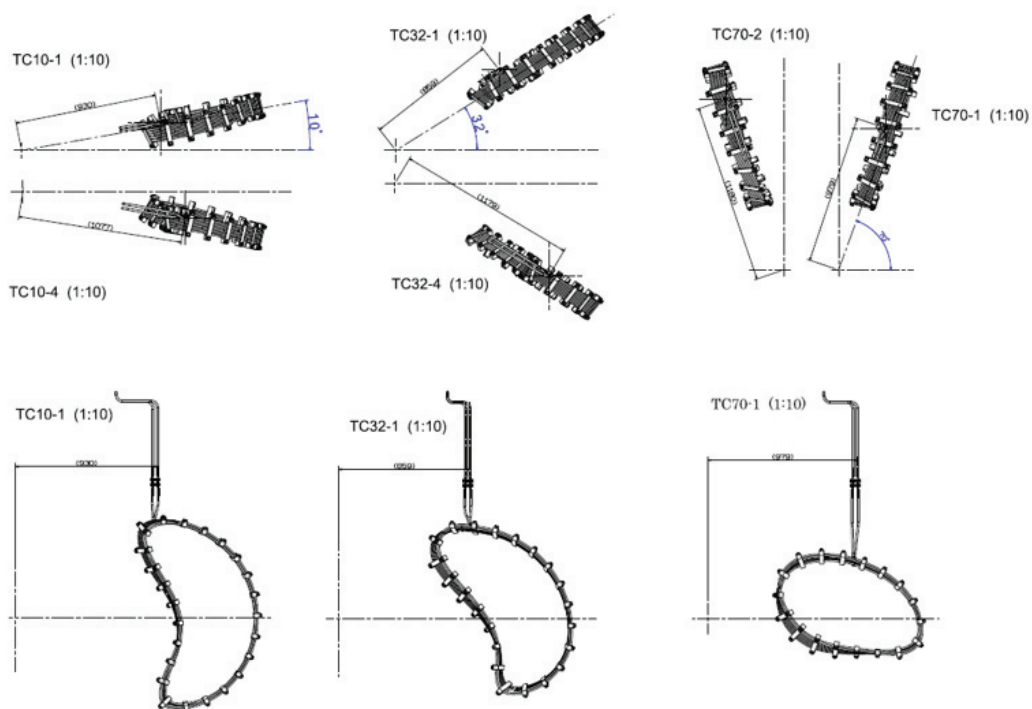


Fig 2.4-4 The coil body and the terminal of each TFC. The bodys of TC10-1 and TC10-4, TC32-1 and TC32-4, and TC70-1 and TC70-2 have the same shape and placed upside down. All terminals are placed on the top.

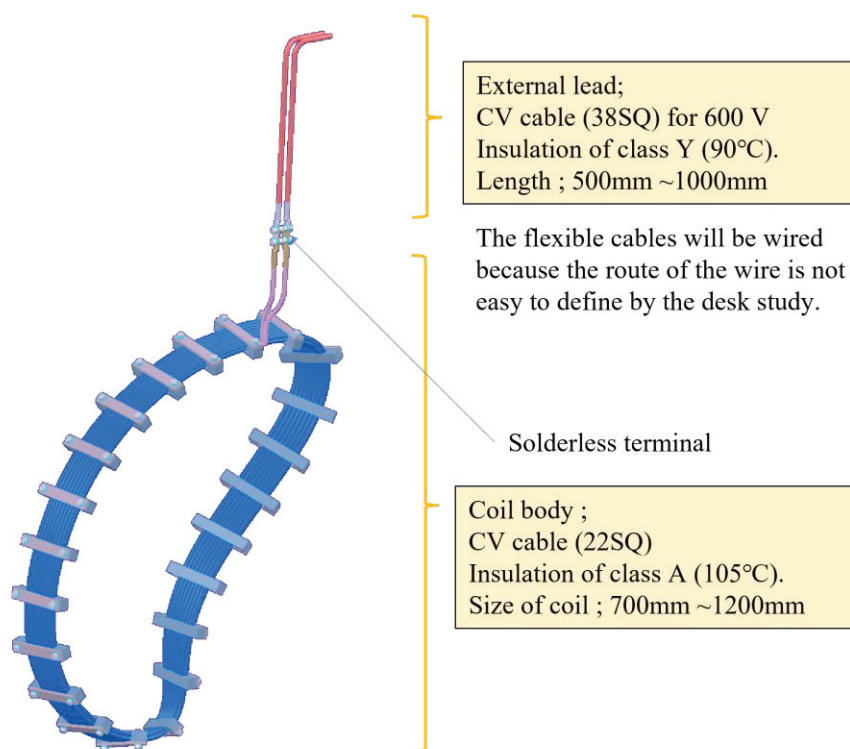


Fig 2.4-5 Example of current lead for the TFC



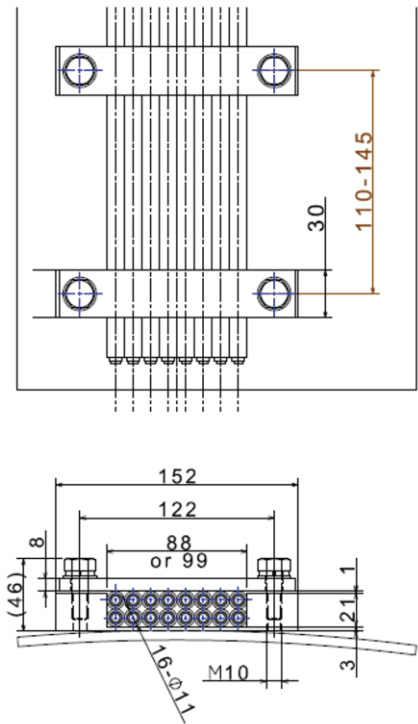
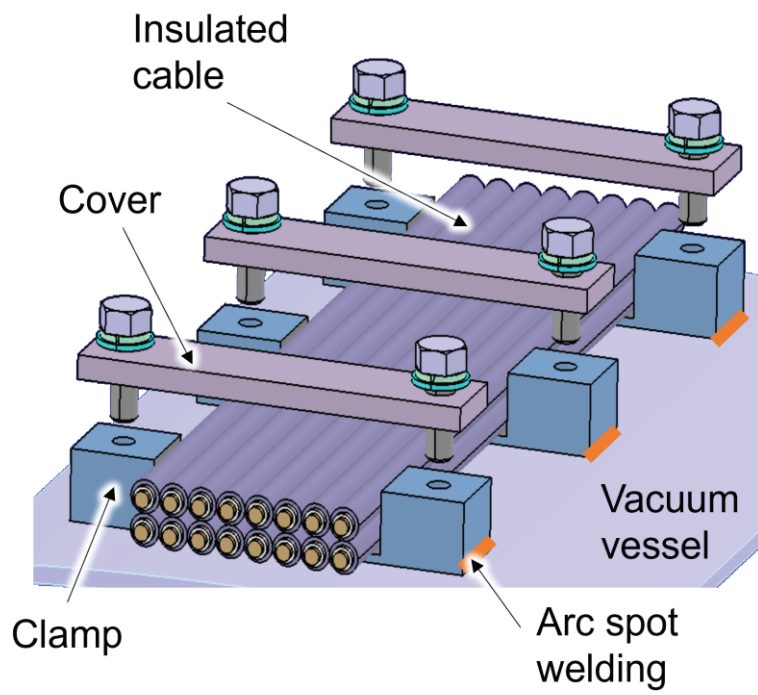


Fig 2.4-6 Cross section of each TFC

## 2.5 Resistance

Resistance of the MC was obtained by the ANSYS/Maxwell system. Resistance of the modular coil was calculated from the ohmic loss obtained by ANSYS/Maxwell with the condition of the cross section of 132 mm × 69 mm that was an average value including isolator and cooling hole. Since the actual conductor cross-section is smaller, the resistance was evaluated by correcting the difference in cross-sectional area. Specifically, the above result shows the value obtained by multiplying the Maxwell result by 126.5/58.825=2.15.

Resistance of the PFC and the TFC was obtained by the simple formula which is the resistivity times the conductor length times the cross section of a conductor.

Table 2.5-1 shows the calculation result in which a margin shown in the tables is added for correction of calculation errors. The resistivity of copper vary greatly with temperature. It is particularly important in design. Please see the appendix of A4(ST).

Table 2.5-1 Resistance of each coil

Name	MC1	MC2	MC3	MC4	IV	OV	TC10	TC32	TC70
Arc length of one turn L (m)	4.39	4.33	4.20	4.13	3.368	10.65	3.334	3.085	2.531
Number of turns N	72	72	72	72	64	32	16	16	16
Cross section S (mm <sup>2</sup> )	58.83	58.83	58.83	58.83	58.83	58.83	22	22	22
Margin (%)	5	5	5	5	5	5	10	10	10
Resistance R(mΩ)	0°C	89.1	87.7	84.9	82.0	60.5	95.7	42.0	38.8
	20°C	96.7	95.2	92.2	89.0	65.7	103.8	45.5	42.1
	22.5°C	97.6	96.2	93.1	89.9	66.3	104.9	46.0	42.5
101%IACS	75°C	117.6	115.8	112.1	108.3	79.9	126.3	55.4	51.2
Obtained by	ANSYS/Maxwell				Formula ( ρNL/S)				

IACS; Conductivity of international annealed copper standard;  $\rho(T) = \rho_{20} [1 + \alpha_{20} (T - 20)]$

101 %IACS(OFC);  $\alpha_{20}=0.00393$ ,  $\rho_{20}=1.707 \times 10^{-8} \Omega\text{m}$

## 2.6 Inductance matrix

The ANSYS/Maxwell obtained the inductance matrix. Table 2.6-1 and Table 2.6-2 show the result.

Table 2.6-1 Inductance matrix for each coil group.

Name	MC1	MC2	MC3	MC4	IV	OV	TC10	TC32	TC70
Number of coils	4	4	4	4	2	2	4	4	4
Number of turns in a coil	72	72	72	72	32	32	16	16	16
MC1	58.87	14.15	5.77	3.72	0.07	0.85	-5.16	-1.73	-0.43
MC2	14.15	49.45	11.69	5.82	0.27	0.21	-2.00	-3.68	-0.72
MC3	5.77	11.69	47.41	13.86	-0.27	-0.48	-0.74	-1.68	-1.89
MC4	3.72	5.82	13.86	52.57	-0.60	-0.66	-0.45	-0.76	-3.32
IV	0.07	0.27	-0.27	-0.60	4.28	0.72	0.00	0.00	0.00
OV	0.85	0.21	-0.48	-0.66	0.72	18.13	0.00	0.00	0.00
TC10	-5.16	-2.00	-0.74	-0.45	0.00	0.00	2.683	0.262	0.057
TC32	-1.73	-3.68	-1.68	-0.76	0.00	0.00	0.262	2.335	0.108
TC70	-0.43	-0.72	-1.89	-3.32	0.00	0.00	0.057	0.108	1.996

Obtained at May 2019 by NIFS after the design change of reducing the maximum curvature and tilting the normal direction to the current carrying surface. ANSYS/Maxwell obtained them. Each value includes margin of 5 %. Unit of inductance is mH.

Table 2.6-2 Inductance matrix for each coil

	MC1-1	MC1-2	MC1-3	MC1-4	MC2-1	MC2-2	MC2-3	MC2-4	MC3-1	MC3-2	MC3-3	MC3-4	MC4-1	MC4-2	MC4-3	MC4-4
MC1-1	2215	14	13	461												
MC1-2	14	2216	461	13												
MC1-3	13	461	2215	14												
MC1-4	461	13	14	2215												
MC2-1	462	15	14	160	2166	19	13	73								
MC2-2	15	462	160	14	19	2166	73	13								
MC2-3	14	160	462	15	13	73	2166	19								
MC2-4	160	14	15	462	73	13	19	2166								
MC3-1	157	21	17	71	451	31	14	41	2079	60	11	28				
MC3-2	21	157	71	17	31	451	41	14	60	2079	28	11				
MC3-3	17	71	157	21	14	41	451	31	11	28	2079	60				
MC3-4	71	17	21	157	41	14	31	451	28	11	60	2079				
MC4-1	70	36	26	39	158	62	21	27	463	140	16	18	1988	399	15	14
MC4-2	36	70	39	26	62	158	27	21	140	462	18	16	399	1986	14	15
MC4-3	25	39	70	36	21	27	158	62	16	18	462	140	15	14	1985	399
MC4-4	39	26	36	70	27	21	62	158	18	16	140	462	14	15	399	1987
IV-L	-1	8	-1	8	-8	35	-8	35	-17	-11	-17	-11	-27	-34	-27	-34
IV-U	8	-1	8	-1	35	-8	35	-8	-11	-17	-11	-17	-34	-27	-34	-27
OV-L	34	54	34	54	15	7	15	7	-7	-43	-7	-43	-24	-44	-24	-44
OV-U	54	34	54	34	7	15	7	15	-43	-7	-43	-7	-44	-24	-43	-24
T32-1	-254	-9	-9	-85	-702	-11	-9	-38	-301	-17	-9	-20	-95	-36	-12	-14
T32-2	-9	-254	-85	-9	-11	-702	-38	-9	-17	-301	-20	-9	-36	-95	-14	-12
T32-3	-9	-85	-254	-9	-9	-38	-702	-11	-9	-20	-301	-17	-12	-14	-95	-36
T32-4	-85	-9	-9	-254	-38	-9	-11	-702	-20	-9	-17	-301	-14	-12	-35	-95
T70-1	-41	-15	-11	-22	-100	-25	-10	-14	-313	-56	-9	-11	-502	-162	-11	-11
T70-2	-15	-41	-22	-11	-25	-100	-14	-10	-56	-313	-11	-9	-162	-502	-11	-11
T70-3	-11	-22	-41	-15	-10	-14	-100	-25	-9	-11	-313	-56	-11	-11	-502	-161
T70-4	-22	-11	-15	-41	-14	-10	-25	-100	-11	-9	-56	-313	-11	-11	-161	-502
T10-1	-754	-8	-8	-295	-300	-9	-8	-95	-92	-12	-10	-39	-37	-19	-14	-21
T10-2	-8	-754	-295	-8	-9	-300	-95	-8	-12	-92	-39	-10	-19	-37	-21	-14
T10-3	-8	-295	-754	-8	-8	-95	-300	-9	-10	-39	-92	-12	-14	-21	-37	-19
T10-4	-295	-8	-8	-754	-95	-8	-9	-300	-39	-10	-12	-92	-21	-14	-19	-37

	IV-L	IV-U	OV-L	OV-U	T32-1	T32-2	T32-3	T32-4	T70-1	T70-2	T70-3	T70-4	T10-1	T10-2	T10-3	T10-4
IV-L	1971	19														
IV-U	19	1971														
OV-L	275	59	8124	306												
OV-U	59	275	306	8125												
T32-1	0	0	0	0	2138	7	5	22								
T32-2	0	0	0	0	7	2138	22	5								
T32-3	0	0	0	0	5	22	2138	7								
T32-4	0	0	0	0	22	5	7	2137								
T70-1	0	0	0	0	69	16	6	9	1766	77	6	7				
T70-2	0	0	0	0	16	69	9	6	77	1766	7	6				
T70-3	0	0	0	0	6	9	69	16	6	7	1766	77				
T70-4	0	0	0	0	9	6	16	69	7	6	77	1767				
T10-1	0	0	0	0	180	5	5	53	24	9	7	13	2280	5	5	207
T10-2	0	0	0	0	5	180	53	5	9	24	13	7	5	2279	207	5
T10-3	0	0	0	0	5	53	180	5	7	13	24	9	5	207	2279	5
T10-4	0	0	0	0	53	5	5	180	13	7	9	24	207	5	5	2279

Obtained by the ANSYS/Maxwell. Each coil is composed of one turn and unit of inductance is nH.

## 2.7 Wiring of the coil system

The 32 coils are installed in the CFQS, but it is not realistic to wire all those current leads to a control power supply room because large space is necessary. We think that it is preferable to connect the coils with copper bus bar near the CFQS body to minimize space of the wiring and to reduce cost. The busbar system saves space but is difficult to design because it is inflexible.

Fig 2.7-1 shows the CFQS with external current leads. The water-cooling coils of PFC and MC are connected by copper busbars and flat braid flexible terminals which may absorb thermal displacement and assembly error. The TFCs with complicated wiring routes are connected by flexible cables.

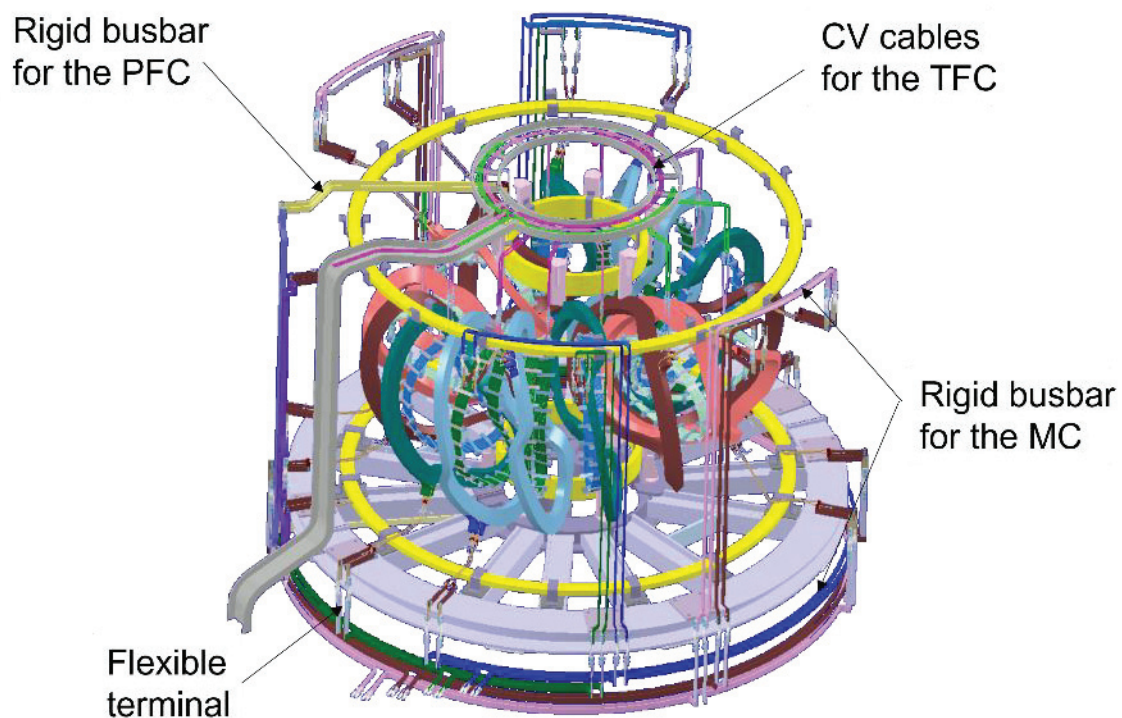


Fig 2.7-1 CFQS with external current leads

Table 2.7-1 summarizes the requirement of the solid bus bar and cable. The wiring plan for each coil system are shown in Fig 2.7-2 to Fig 2.7-4.

Table 2.7-1 Requirement for solid bus bar and cable.

Part	Item	Requirement	Criteria	Notes	Target
Solid Bus bar	Rigidity	Rigid	Does not easily deform		All
	Dis- placement and stress	Within allowable range for the repulsive force between returning conductors	Stress <20 MPa	No breakdown	
			Deflection<2 mm	No interference	
			Natural frequency >20 Hz	Stiffness evaluation	
	Cross section	No excessive temperature rise	ARTP<5 Kelvin	For short pulse	
			$J < 2A/mm^2$	For long pulse	
	Fastening	Multiple bolts	Size $\geq M10$		
			Number $\geq 2$	For one place	
	Insulation	Class A.	$\geq 90\text{ }^{\circ}\text{C}$		
Cable and flexible terminal	Cross section	Current in long pulse operation is below the capacity except in special cases	$S \geq 200\text{ mm}^2$	390A	MC
			$S \geq 200\text{ mm}^2$	560A	PFC
			$S \geq 60\text{ mm}^2$	180A	TFC
	Fastening	Multiple bolts	Size $\geq M10$		All
			Number $\geq 2$	For one place	
	Allowable voltage	Above the operating voltage	$\geq 6000\text{V}$	2300V	MC
			$\geq 6000\text{V}$	1700V	PFC
			$\geq 600\text{V}$	600V	TFC
	Insulation	Class A.	$\geq 90\text{ }^{\circ}\text{C}$		All

ARTP; Adiabatic rise of temperature in a pulse

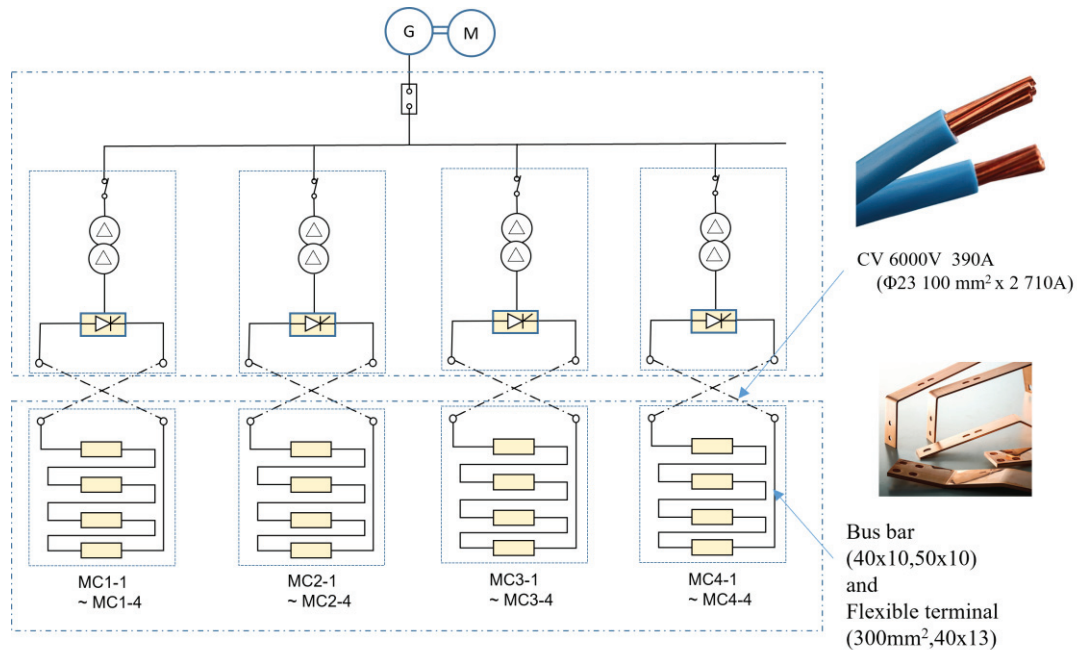


Fig 2.7-2 Wiring plan for the modular coil.



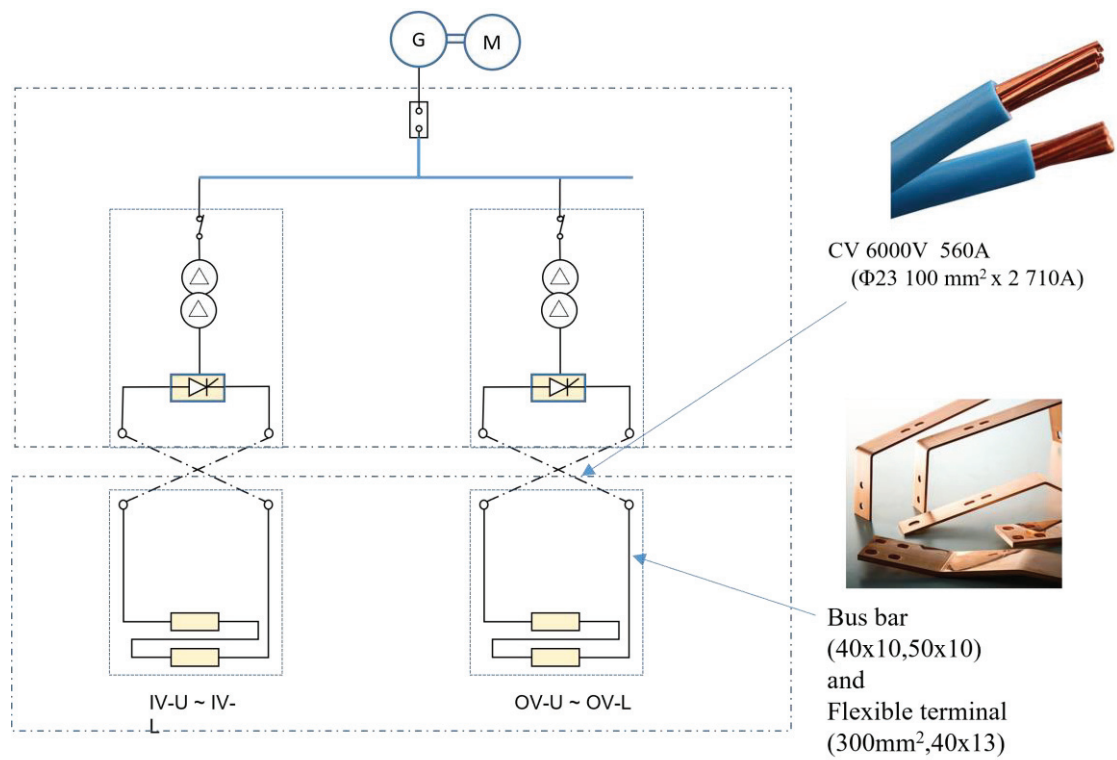


Fig 2.7-3 Wiring plan for the PFC

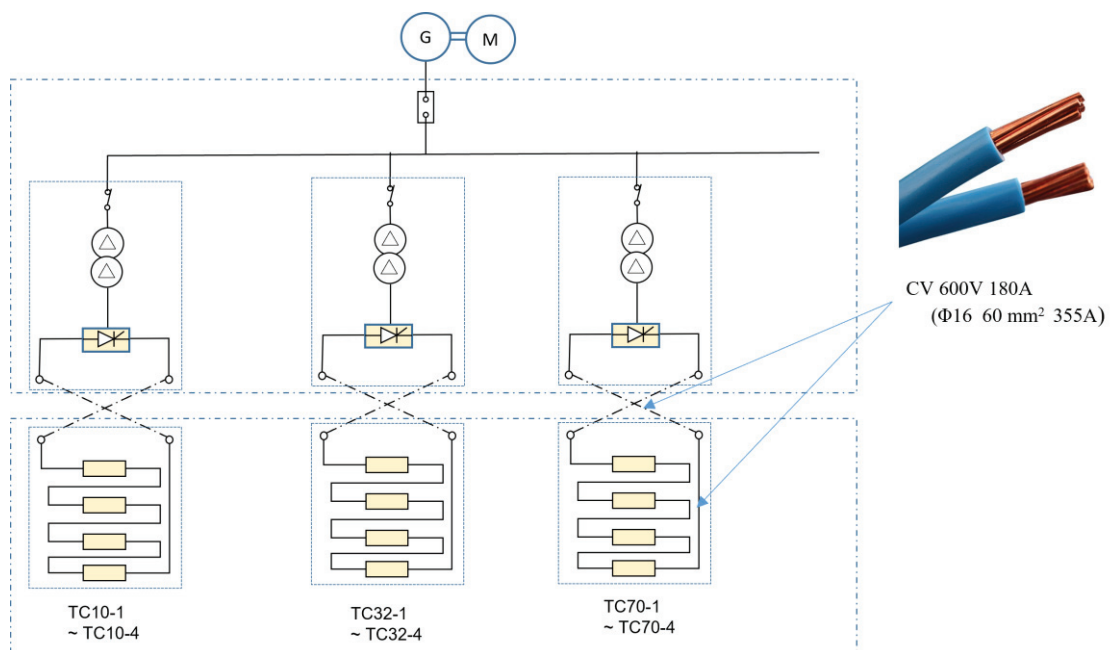


Fig 2.7-4 Wiring plan for the TFC



## 2.8 Current wave form to estimate required power of coil power supply

To study the specifications of the coil power supply, the current waveform of each coil was defined. Fig 2.8-1 shows an equivalent circuit of the coil power supply and assumed current and voltage waveform. In the actual operation, the coil power supply with current feedback control (ACR; Auto Current Regulator) will be desirable, but here, for simplicity, the coil power supply with pre-programmed voltage control (AVR; Auto Voltage Regulator) is defined for which an analytical solution exists.

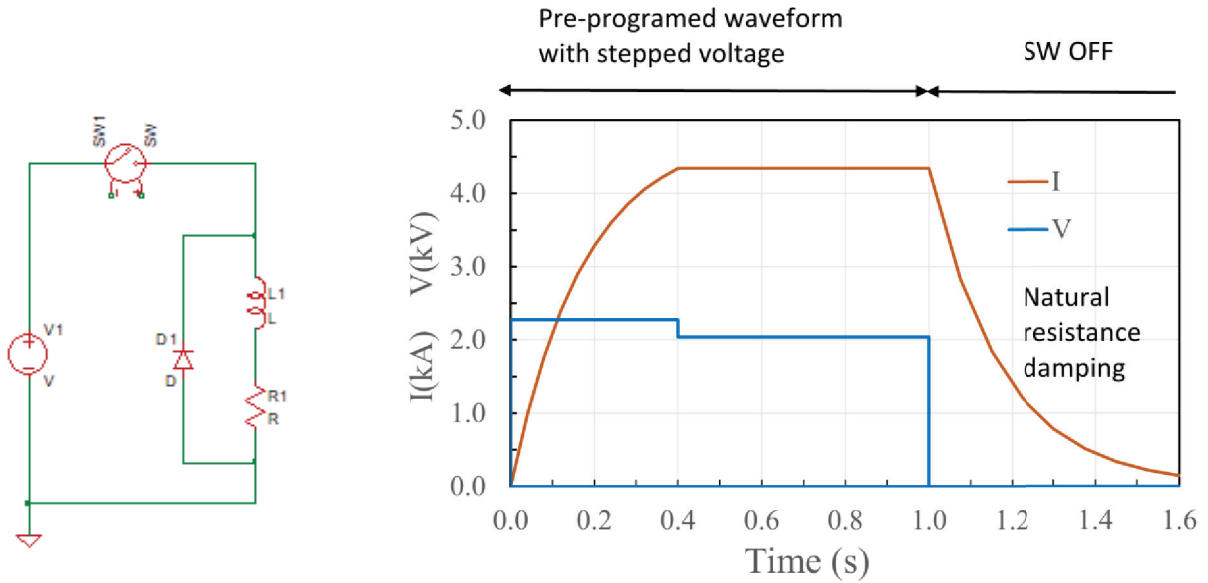


Fig 2.8-1 Equivalent circuit and voltage / current waveform.

The current waveform is represented by a combination of exponential functions.

- Current ramp up ( $0 < t - t_{start} < dt_{up}$ )

$$I(t) = \frac{V_{up}}{R} \left\{ 1 - \exp\left(-\frac{t - t_{start}}{\tau}\right) \right\}$$

$$V_{up} = V_{flat} / \left\{ 1 - \exp\left(-\frac{dt_{up}}{\tau}\right) \right\}$$

$$\tau = L/R$$

- Flat top ( $0 < t - t_1 < dt_{flat}$ )

$$I(t) = V_{flat}/R$$

$$t_1 = t_{start} + dt_{up}$$

- Current decay ( $0 < t - t_2$ )

$$I(t) = I(t_2) \exp\left(-\frac{t - t_2}{\tau}\right)$$

$$t_2 = t_{start} + dt_{up} + dt_{flat}$$

Where  $R$  is a resistance,  $L$  is an inductance,  $\tau$  is a time constant and  $V_{flat}$  is a voltage at the flat top.  $t_{start}$  is an energization start time,  $dt_{up}$  is a current ramp up duration and  $dt_{flat}$  is a flat top duration. Table 2.8-1 shows parameters to define waveform for each type of coil and Fig 2.8-2 shows typical example of current waveform. Fig 2.8-3 to Fig 2.8-4 show current and voltage waveform for each coil.

Table 2.8-1 Parameters that define the waveform.

Item	Symbol	Unit	MC	IV	OV	TFC	Plasma
Start time	$t_{start}$	s	0	0.4	0.4	0.65	0.73
Current ramp up duration	$dt_{up}$	s	0.4	0.2	0.2	0.05	0
Flat top duration	$dt_{flat}$	s	0.6	0.3	0.3	0.15	0.1
Flat top (maximum) current	$I_{flat}$	kA	4.34	6.25	6.25	2	-
Time constant of coil	$\tau$	s	0.175~0.176	0.115	0.078	0.012~0.013	-
Voltage at the flat top	$V_{flat}$	kV	1.9~2.0	1.008	1.571	0.36~0.48	-

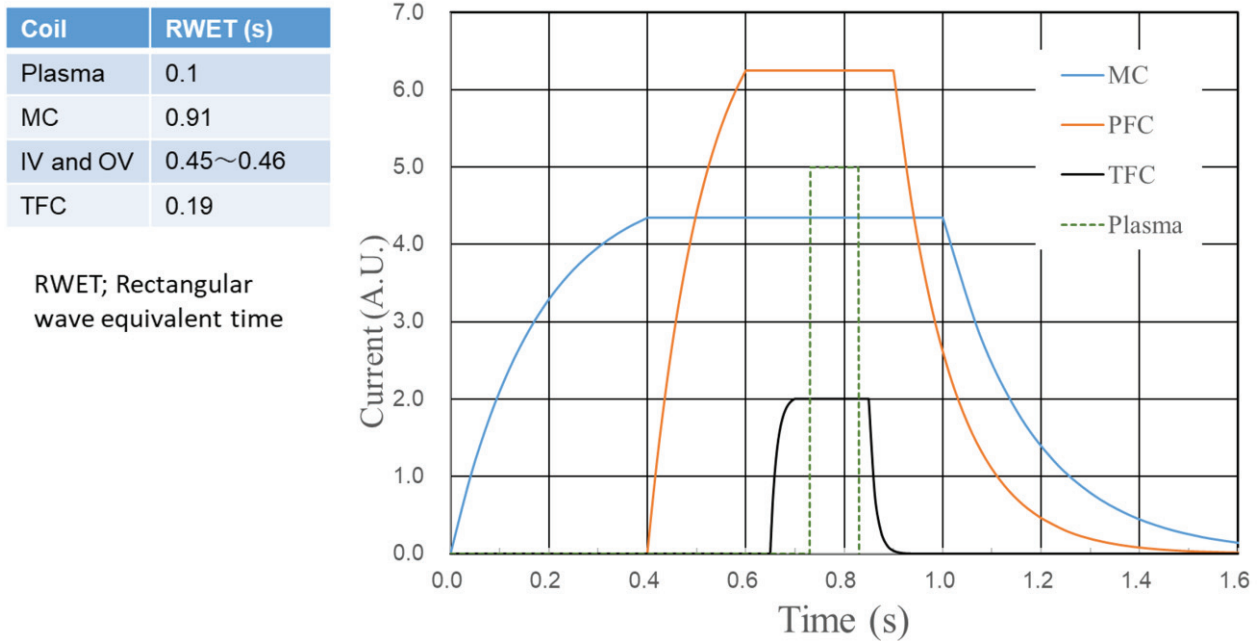


Fig 2.8-2 Typical example of the current waveform. Exponential function waveforms are assumed for ease of calculations

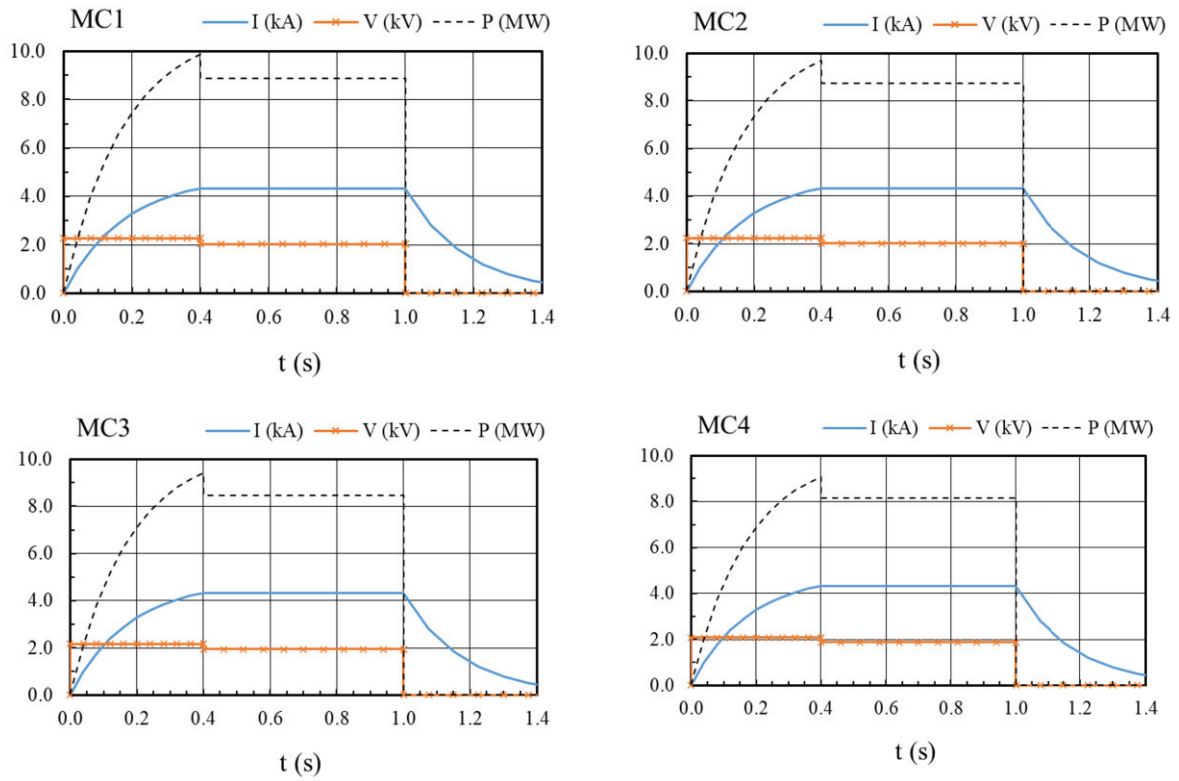


Fig 2.8-3 Current and voltage waveform for the MC

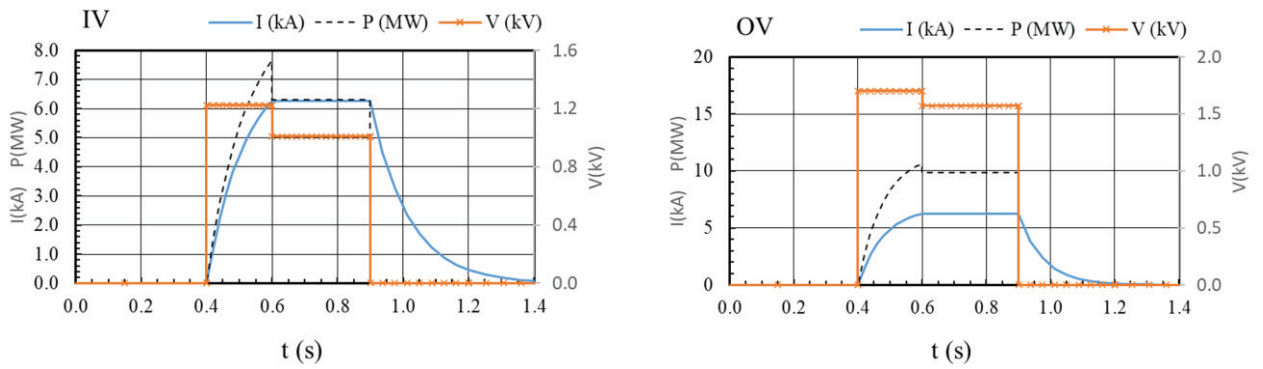


Fig 2.8-4 Current and voltage waveform for the PFC

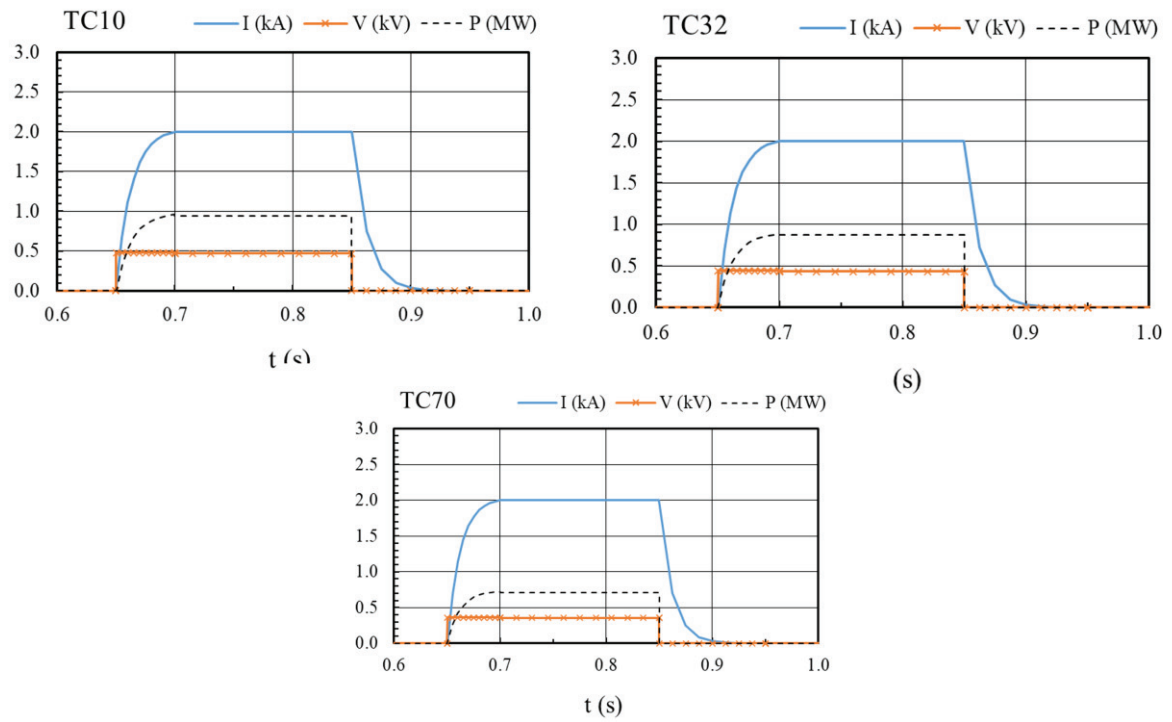


Fig 2.8-5 Current and voltage waveform for the TFC

## 2.9 Support structure

### 2.9.1 Coil case for the modular coil

As for magnetic confinement fusion device, the electromagnetic (EM) force is a main load on coil system. The hoop force is applied to the circular coil like the PFC, and the stress is the tensile component. Since the only way to reduce such a stress component is to increase the cross-sectional area to lower the current density, a structure without reinforcement such as a coil case is standard. Coils with straight sections, such as the D-shaped TFCs of tokamak are subject to bending stress components. Since it is difficult for the stiffness of the coil conductor and the insulation to withstand the bending stress, the body of the coil is often surrounded by a metal case so that the stiffness of the metal can withstand the stress. For the modular coils of the CFQS, when the current density increases to extent, reinforcement with a metal case is considered essential. Three types of structures shown in Fig 2.9-1, Fig 2.9-2 and Fig 2.9-4 were examined for reinforcement of modular coils.

Fig 2.9-1 shows a continuous c-shaped case (CCSC) applied to large tokamaks. This structure can be said to be reliable because deformation is prevented by the rigidity only of the coil case. Although it is most advantageous in terms of strength, there is technical difficulty in the case of a complicated form. The CCSC can be made by pressing thick plates of 10mm, but we are worried about the production cost of the press die and plate thickness may be limited to thin due to press working. In addition, there is concern about whether the coil can be inserted into the coil case. It is surely feasible with structure in a procedure to weld the coil case divided finely after inserting a coil. In that case, there is the worry that the coil is damaged when the coil case is finished by welding.

Fig 2.9-2 shows partial large clamps (PLCL) type manufactured by cutting out the forged material in the same way as the CCSC. Fig 2.9-3 shows the cross sectional shape of the clamp. Each clamp (coil case) is designed to be 20-30 mm thick so that it can be easily manufactured with existing machining technology. A thickness of 5-10mm seems to be sufficient for design clamp strength, but machining may become difficult. The clamp A is completed by welding the split clamps after inserting the coil, so the problem of coil damage during welding remains. However, it is more advantageous than the CCSC because the number of divisions is reduced. Since the clamp is made by machining, there is also the advantage that there is no limit on the plate thickness. Regarding the clamps B and C, it seems that there are no technical issues other than cost. From the viewpoint of deformation prevention, the rigidity of the coil itself is also expected, so it seems that the reliability is inferior to that of the CCSC.

Fig 2.9-4 shows dedicated clamps type for fixing a coil (DCFL). This structure limits the range of EM forces that can be applied, as the coil's own stiffness reduces deformation. The range of EM force that this structure can withstand was investigated by FEM analysis, and it was found that it can be used for low magnetic field experiments of 0.09T.

As a result of examination of various technical feasibility, cost, and production period, we decided that the CFQS was manufactured as the DCFL at first, and then modified to the PLCL after investigating the QA configuration with the 0.09T weak magnetic field experiment. In order to realize this strategy, the coil body and the upper and lower legs are designed so that they can be used without modification.

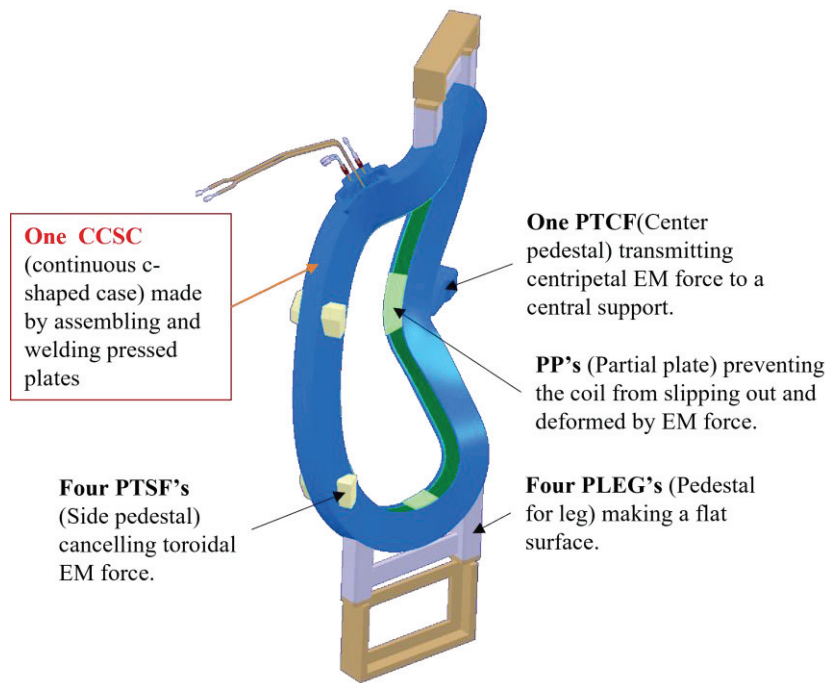


Fig 2.9-1 Continuous c-shaped case (CCSC) for the MC2

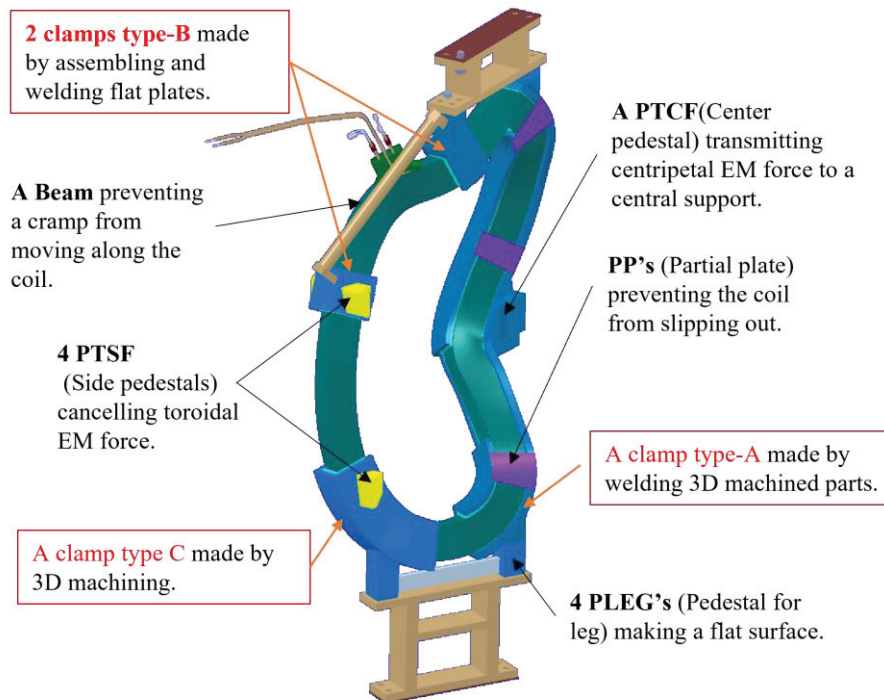


Fig 2.9-2 Partial large clamps (PLCL) for the MC2

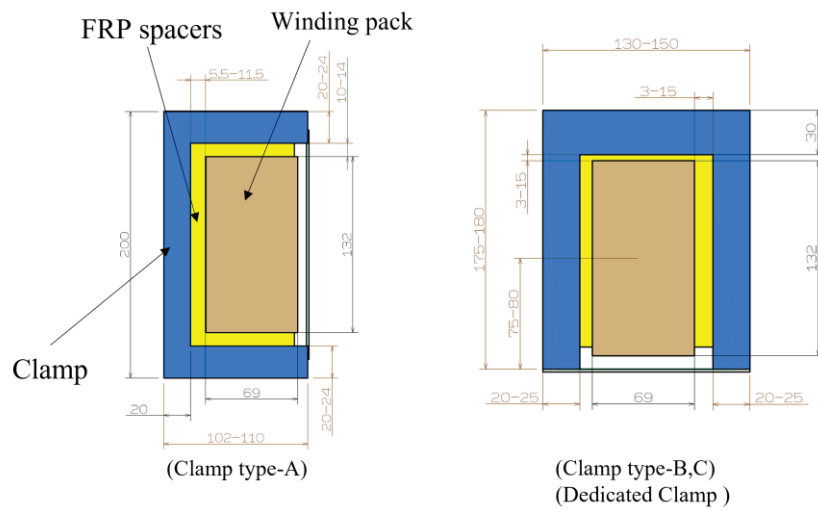


Fig 2.9-3      Cross sectional shape of the clamp for the PLCL

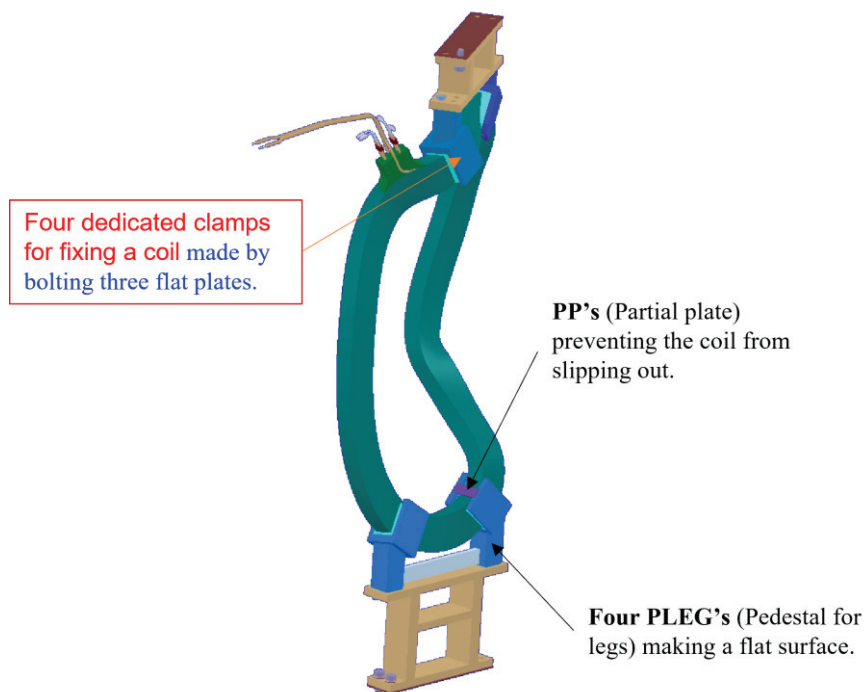


Fig 2.9-4      Dedicated clamps for fixing a coil (DCFL) for the MC2



## **2.9.2 Cage type support structure to prevent deformation of the modular coil**

Even if it is reinforced with the coil case, the deformation of the coil cannot be reduced by itself. The 16 modular coils must be strung together to cancel out the EM forces of the coil system as a whole.

Fig 2.9-5 and Fig 2.9-6 show the cage type support structure with the partial large clamps (PLCL). The large tokamak are typically designed with TFC wedges to support huge centripetal force. The CFQS also needs a structure to support centripetal force, but it cannot take this approach due to shape of constraints. Instead, a central support was designed to absorb such a large force with the CCBs, the PTCFs and the CPs. The CP is installed to support the PTCF during assembly work. There is a big rectangular free area to access the inside port on the vacuum vessel.

The main role of the LBB is to cancel the toroidal forces of the modular coil. Since the TFC of the tokamak is pulled by the same force from the adjacent coils, the toroidal load is negligibly small. However, since the coils on both sides of the modular coil have different shapes, the forces that are pulled from them are different. The modular coils must be connected to support their asymmetrical loads. The LBB fulfills this function.

The IBP are references for installing main parts. The main parts such as the vacuum vessels and the modular coils must be placed in the designed position with high accuracy. In order to achieve this, we need surfaces to refer to during assembly. The IBP is placed for that purpose.

Fig 2.9-7 shows the cage type support structure with the dedicated clamps for fixing a coil (DCFL). Since this structure is only for smaller EM force, we believe that no central support or beam between coils is required.

Table 2.9-1 shows the minimum gap in the support structure with the PLCL. In it, the gaps between the modular coils and between the modular coil and the vacuum vessel are shown. It is considered that the minimum gap of 13 mm between the coil and the vacuum vessel is within the adjustable range.

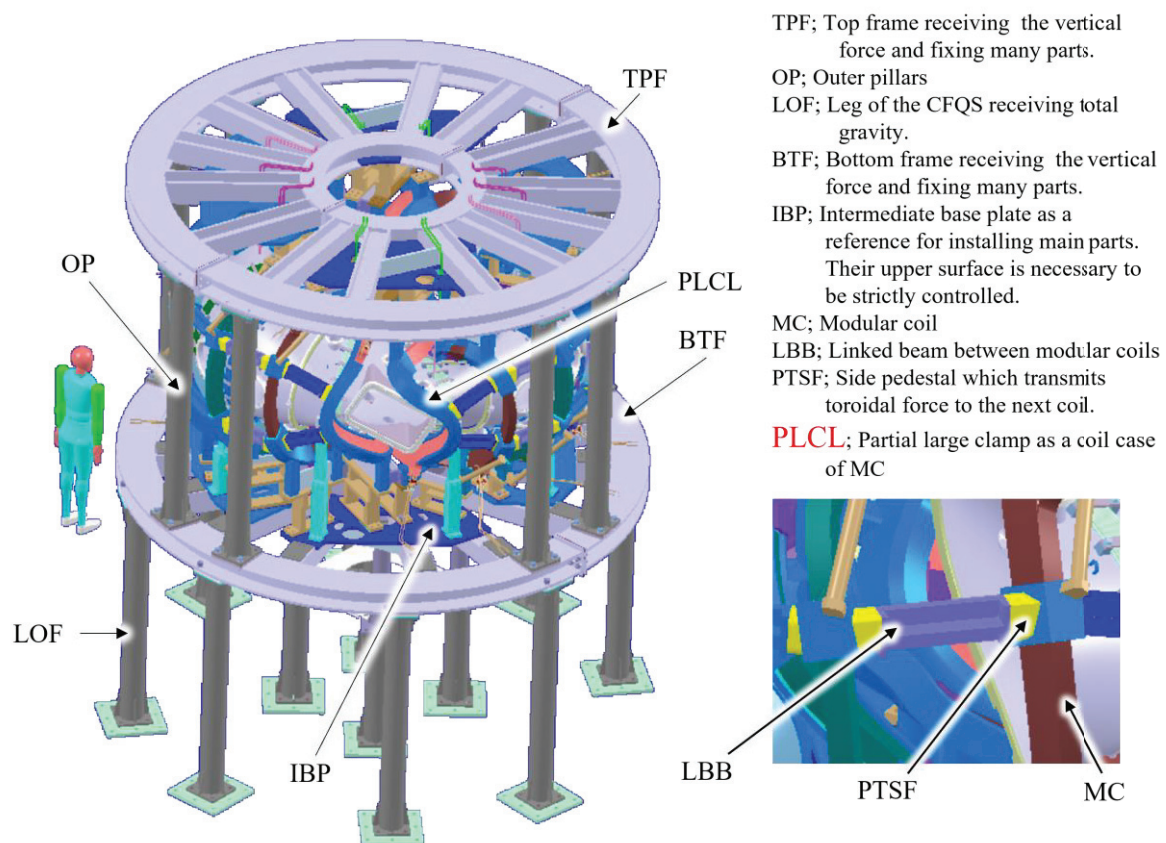


Fig 2.9-5 Top view of the cage type support structure with the PLCL

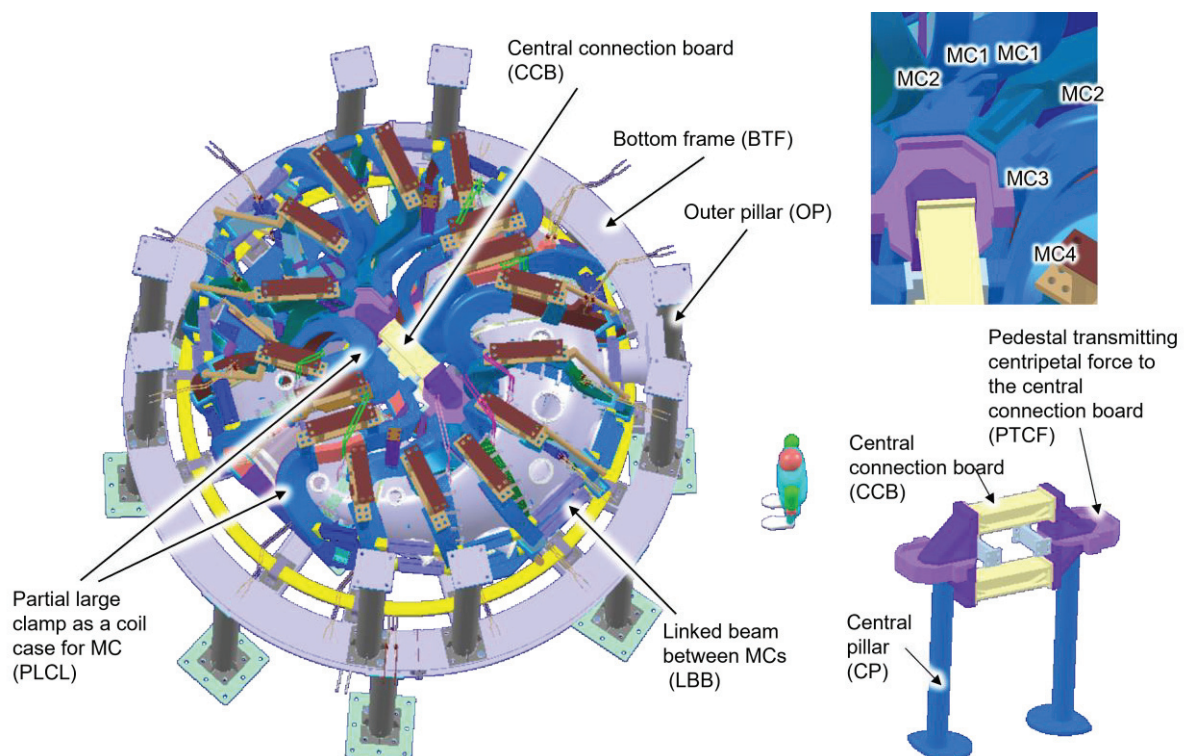


Fig 2.9-6 Cutaway view of the cage type support structure with the PLCL

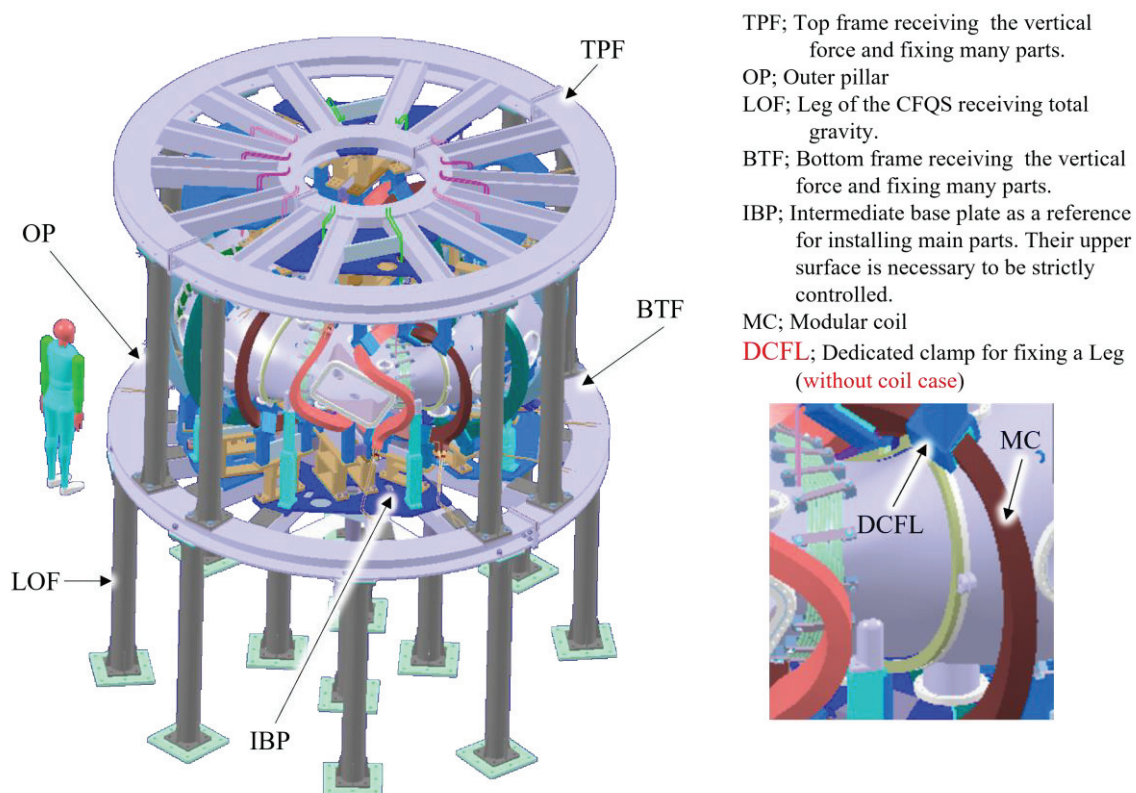

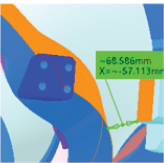
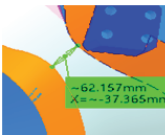
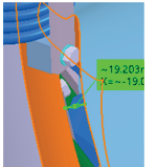
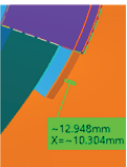
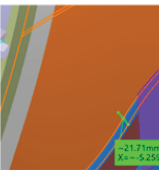
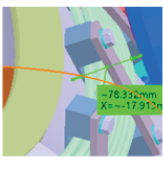


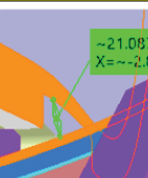
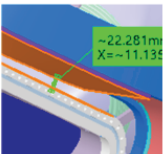


Fig 2.9-7 Top view of the cage type support structure with the DCFL

Table 2.9-1 Minimum gap in the structure with the PLCL

Name of coil		MC1 (TypeX)	MC2 (TypeX)	MC3 (TypeH)	MC4 (TypeG)	Design guide
Minimum gap between coils (mm)	MC1-MC1	Inboard pedestals touch each other				The gap should be larger than 20 mm except between inboard pedestals.
	MC1-MC2					
	MC2-MC3					
	MC3-MC4	68.6(Case MC4-PEDE MC3)				
	MC4-MC4	62.2 (case-case)				
						
Minimum gap between coil with case and others (mm)	With inner surface of the shell	19.2 (coil)	13 (case)	21.7(case)	78.3 (case)	Requires 5mm, which is a tolerance of the vacuum vessel.
						
	With others	55.7(CF420)	36.5(TC32)	21.1 (Split F)	22.3 (Rectangle OP)	It should be larger than 10 mm with the margin.
						

## 2.10 Water piping system to cool the MC and the PFC

### 2.10.1 Flow rate and pressure drop of the cooling water in each coil

A pure water cooling system will be installed to cool the modular coils and the poloidal field coils. Flow rate and pressure drop of the water in the coil were evaluated. Table 2.10-1, Table 2.10-2 and Fig 2.10-1 show the design value of the cooling water, in which the pressure loss (loss head) was calculated by the Hazen Williams' equation below.

$$h_f = 10.67 \cdot L \frac{(Q/C)^{1.85}}{D^{4.87}}$$

$$\Delta P = \rho \times g \times h_f$$

$$Q = Au = u \times \frac{(\pi D^2)}{4}$$

Where  $h_f$  is the loss head (m),  $L$  is the length of one cooling tube (m),  $Q$  is the flow rate in a tube (m<sup>3</sup>/s),  $C$  is the roughness coefficient (Hazen-Williams-coefficient), and  $D$  is the inside tube diameter (m).  $g$  is the gravitational acceleration (=9.8m/s<sup>2</sup>),  $\rho$  is the density of water(=996kg/m<sup>3</sup>),  $\Delta P$  is the pressure drop ( $P_a$ ),  $A$  is the cross section of cooling hole (m<sup>2</sup>), and  $u$  is the flow velocity(m/s). Here the Hazen Williams coefficient  $C$  of 160 was adjusted according to the experimental data in the appendix A2(RD).

From Table 2.10-1, the flow velocity may exceed the expected value of 2m/s, but it is considered to be within the allowable range.

Table 2.10-3 and Fig 2.10-2 show the measurement results with the actual coil. Since the pressure loss of the actual coil is 5 to 10 % larger than the approximation formula, we will prepare a cooling water system that takes this into consideration.

Table 2.10-1 Design value of the cooling channel for each coil

Name of coil				MC1	MC2	MC3	MC4	IV	OV
Nominal	Pressure drop	$\Delta P$	MPa	1.17	1.17	1.17	1.17	1.64	1.28
	Flow rate for a coil	$Q$	m <sup>3</sup> /s	7.17E-05	7.17E-05	7.17E-05	7.17E-05	1.88E-05	3.77E-05
			l/min	4.30	4.30	4.30	4.30	1.13	2.26
	Flow velocity	$v$	m/s	1.9	1.9	1.9	1.9	1.5	1.5
Maximum	Pressure drop	$\Delta P$	MPa	2.00	2.00	2.00	2.00	2.00	2.00
	Flow rate for a coil	$Q$	m <sup>3</sup> /s	9.30E-05	9.37E-05	9.54E-05	9.63E-05	2.10E-05	4.80E-05
			l/min	5.58	5.62	5.72	5.78	1.26	2.88
	Flow velocity	$v$	m/s	2.5	2.5	2.5	2.6	1.7	1.9
Average arc length of one turn				$L_{one}$	m	4.4	4.34	4.2	4.13
Number of turns for a cooling channel				NT		24	24	24	24
Cooling hole length				L	m	105.6	104.2	100.8	99.2
Number of cooling channels				NC		3	3	3	3
Diameter of a cooling hole				d	m	0.004	0.004	0.004	0.004
Restrictions				Pressure drop $\Delta P$ must be less than 2MP to avoid cost increases. Flow velocity $v$ should be less than 2m/s to avoid vibration.					



Table 2.10-2 Pressure loss of cooling water.

Flow velocity $v(\text{m/s})$	Flow rate per one channel $Q(\text{m}^3/\text{s})$	Pressure loss $\Delta P(\text{MPa})$					
		MC1	MC2	MC3	MC4	IV	OV
0	0.00E+00	0.000	0.000	0.000	0.000	0.000	0.000
0.5	6.28E-06	0.104	0.103	0.100	0.098	0.215	0.168
1	1.26E-05	0.376	0.371	0.359	0.353	0.775	0.604
1.1	1.38E-05	0.449	0.442	0.428	0.421	0.924	0.720
1.2	1.51E-05	0.527	0.520	0.503	0.494	1.086	0.846
1.3	1.63E-05	0.611	0.603	0.583	0.573	1.259	0.981
1.4	1.76E-05	0.701	0.691	0.669	0.657	1.444	1.125
1.5	1.88E-05	0.796	0.785	0.760	0.747	1.640	1.279
1.6	2.01E-05	0.897	0.885	0.856	0.841	1.848	1.441
1.7	2.14E-05	1.004	0.990	0.958	0.941	2.068	1.612
1.8	2.26E-05	1.115	1.100	1.065	1.046	2.299	1.791
1.9	2.39E-05	1.233	1.216	1.177	1.156	2.540	1.980
2	2.51E-05	1.356	1.337	1.294	1.271	2.793	2.177
2.1	2.64E-05	1.484	1.463	1.416	1.391	3.057	2.383
2.2	2.76E-05	1.617	1.595	1.543	1.516	3.332	2.597
2.3	2.89E-05	1.755	1.732	1.676	1.646	3.617	2.819
2.4	3.02E-05	1.899	1.873	1.813	1.781	3.914	3.050
2.5	3.14E-05	2.048	2.020	1.955	1.921	4.221	3.290
2.6	3.27E-05	2.202	2.172	2.102	2.065	4.538	3.537
2.7	3.39E-05	2.362	2.329	2.254	2.215	4.866	3.793

They were estimated by the Hazen Williams equation with  $C=160$

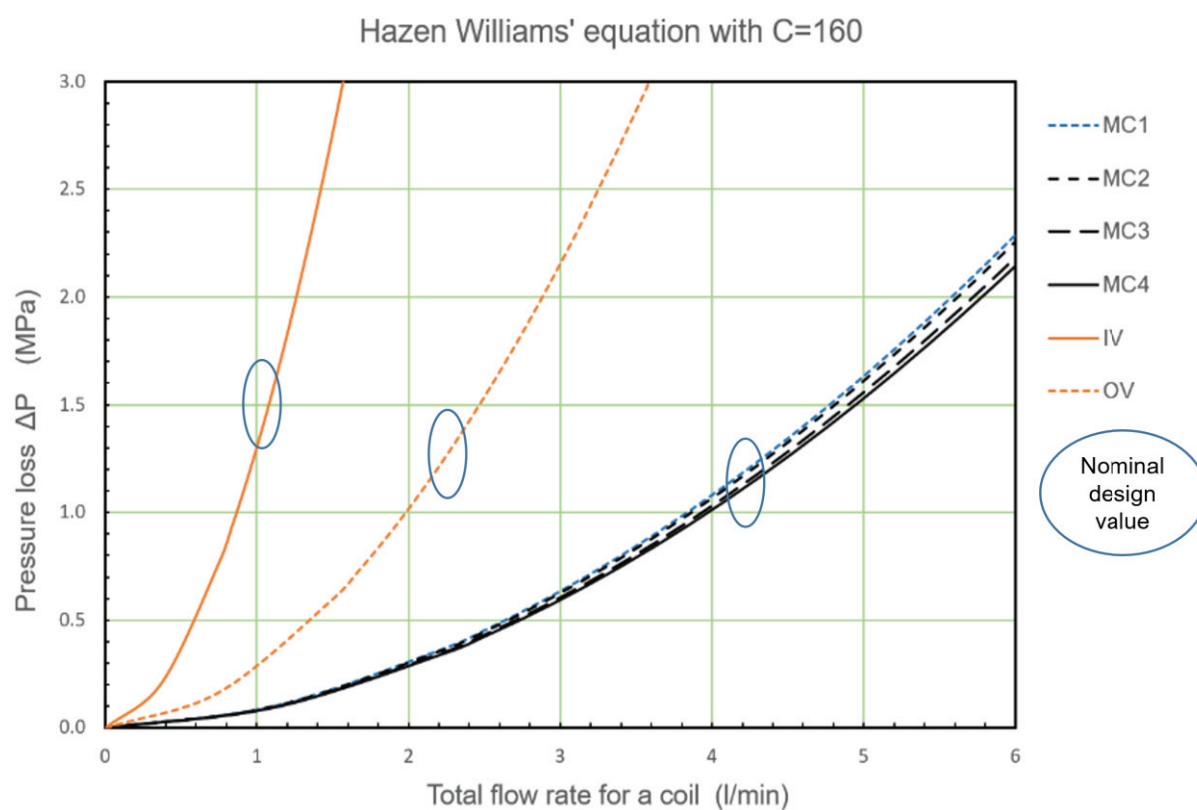


Fig 2.10-1 Flow rate dependence of the pressure loss

Table 2.10-3 Experimental result of the pressure drop

Unit Q(l/min) $\Delta P$ (MPa)						Unit Q(l/min) $\Delta P$ (MPa)	
MC1-1		MC1-2		MC1-4		MC2-1	
Q	$\Delta P$	Q	$\Delta P$	Q	$\Delta P$	Q	$\Delta P$
2.42	0.550	2.40	0.460	2.41	0.500	2.42	0.500
3.21	0.870	3.20	0.710	3.29	0.870	3.31	0.870
3.81	1.190	3.81	0.980	3.92	1.180	3.91	1.180
4.01	1.330	4.21	1.180	4.19	1.330	4.20	1.340

Unit Q(l/min) $\Delta P$ (MPa)					
MC3-1		MC3-2		MC3-3	
Q	$\Delta P$	Q	$\Delta P$	Q	$\Delta P$
2.41	0.460	2.40	0.480	2.29	0.396
3.30	0.810	3.27	0.830	3.30	0.758
3.90	1.090	3.93	1.150	3.88	1.054
4.42	1.370	4.29	1.350	4.55	1.340

Unit Q(l/min) $\Delta P$ (MPa)									
MC4-mockup		MC4-1		MC4-2		MC4-3		MC4-4	
Q	$\Delta P$	Q	$\Delta P$	Q	$\Delta P$	Q	$\Delta P$	Q	$\Delta P$
1.500	0.187	2.34	0.425	2.34	0.430	2.41	0.450	2.40	0.460
2.400	0.394	3.25	0.731	3.21	0.540	3.20	0.770	3.30	0.780
3.300	0.698	3.80	0.759	3.88	0.980	3.82	1.050	3.90	1.120
3.900	0.943	4.30	1.261	4.21	1.230	4.21	1.240	4.25	1.320

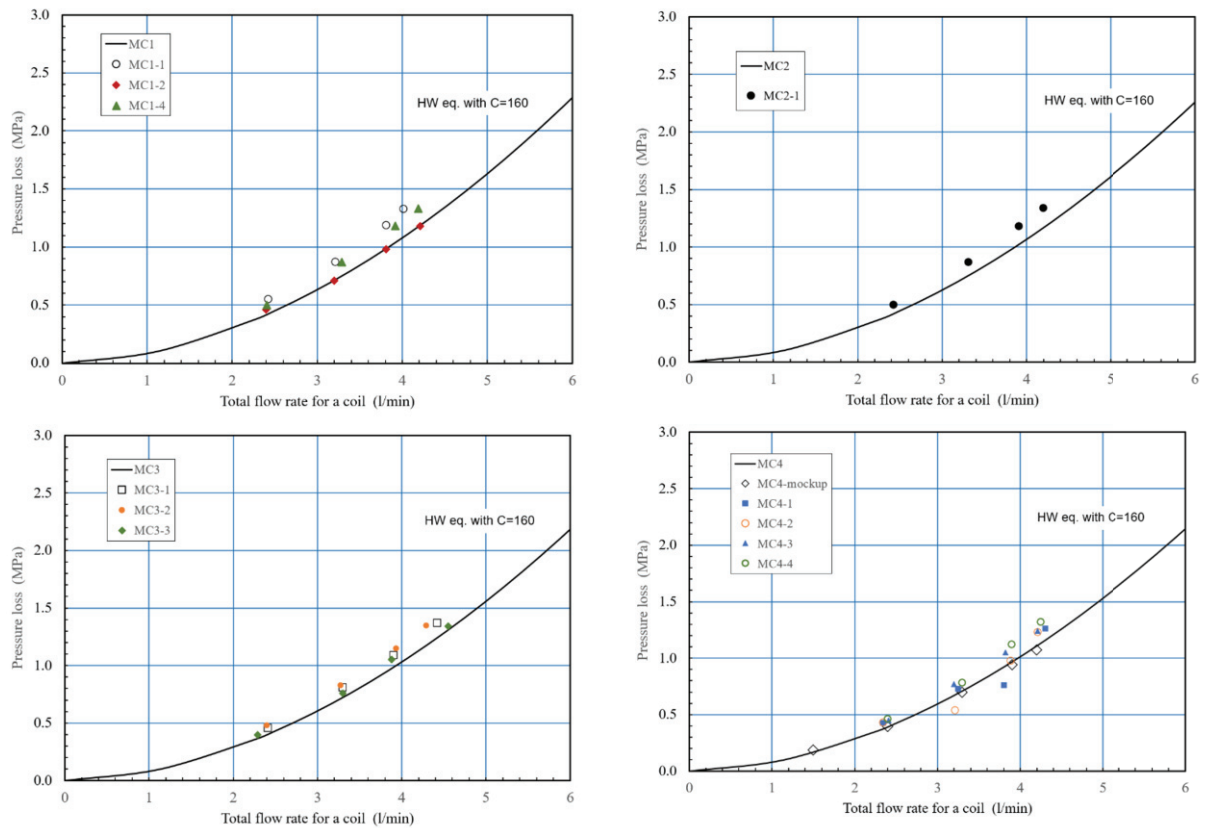


Fig 2.10-2 Experimental result of the pressure drop

## 2.10.2 Requirements of main water piping system

Fig 2.10-3 shows the CFQS with main water piping system, which consists of thick pipes with some instruments that branch the water from the cooling water supply and supply it to 96 pipes for the MC and 12 pipes for the PFC. Requirements of the main water piping system were obtained by calculation and are summarized in Table 2.10-4.

Flow rate in a main pipe is about  $6 \text{ m}^3/\text{hr}$ . In order to evenly distribute the water, the main pipe pressure drop should be much less than the coil pressure drop. Since the pressure loss of this design is about 3% of the pressure loss of the coil, it is considered appropriate.

Since the pressure loss of 48 (3x16) channels of MC is almost constant, it is thought that the flow control valve for each channel is unnecessary. The flow rate in each channel will be measured by a portable ultrasonic flow meter, and the flow balance between channels will be adjusted by inserting an orifice.

Since the flow rate of the PFC is approximately one order of magnitude smaller than the MC, if one pump is used to supply cooling water to both, more water will flow to the PFC, which has less pressure drop, and there is concern that sufficient water will not be supplied to the MC. In order to eliminate this concern, two flow control valves will be required in the main pipe for the MC and the PFC.

Similarly, the IV flow rate is about half that of the OV, so we have a concern that more water will flow into the IV than necessary and not enough into the OV. However, the difference between IV and OV is not as large as the difference between MC and PFC, so overwatering the IV may not be a problem. If desired, additional flow control valves may be added in the IV circuit.

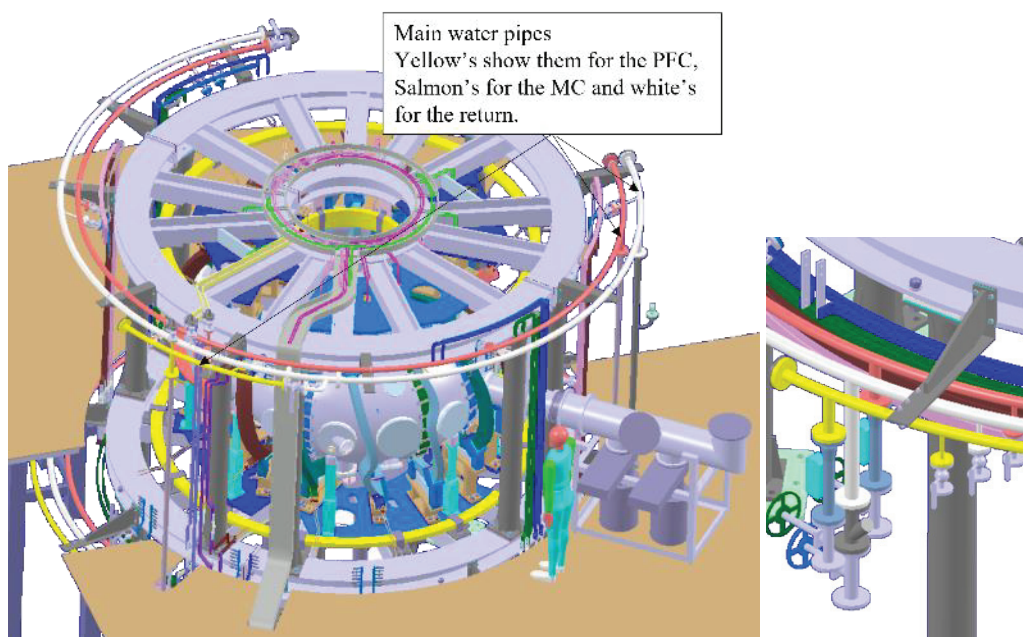


Fig 2.10-3 Main water piping system



**Table 2.10-4 Requirements of the water piping system**

Name of coil			MC1	MC2	MC3	MC4	IV	OV	ALL
Number of coils	NCL		4	4	4	4	2	2	
Pressure drop for a coil	$\Delta P$ CL	MPa	2.00	2.00	2.00	2.00	2.00	2.00	
Flow rate for a coil	Q CL	m <sup>3</sup> /s	9.3E-05	9.4E-05	9.5E-05	9.6E-05	2.1E-05	4.8E-05	
Name of main pipe			Inlet 1				Inlet 2		Outlet
Type of main pipe			40A SCH20				40A SCH20		50A SCH20
Diameter of a cooling hole	d	mm	42.6				42.6		53.5
Cooling hole length (Preliminary)	L	m	200				200		200
Total flow rate	Q	m <sup>3</sup> /s	1.51E-03				1.38E-04		1.65E-03
		m <sup>3</sup> /hr	5.45				0.50		5.95
Flow velocity	v	m/s	0.27				0.02		0.29
Pressure drop	$\Delta P$	MPa	0.0500				0.0006		0.0194
Restrictions			Pressure drop in a main pipe must be much less than that in each coil for even distribution of water.						
			Flow velocity should be less than 2m/s to avoid vibration.						

### 2.10.3 Design of main water piping system

Fig 2.10-4 shows layout of the main water piping system, which is consist of six c-shaped main pipes and three straight main pipes and others. The system supplies pure water to the 16 MC's and 4 PFC's and will include equipment as shown in the right table. There are two water supply systems, one of which is for the MC and other is for the PFC. The drainage system is common. In the figure, salmon shows the main pipe for the MC, yellow for the PFC, and white for the return or drainage.

The main pipes will be made of the 40A(1-1/2B) or the 50A(2B) pipe and welding flange with gasket seal to improve reliability. The screw-in flange (or threaded flange) should not be applicable as much as possible. They will be fixed to the upper and lower frames by 16 piping supports.

Half of the coils have inlets and outlets for cooling water at the top of the CFQS. Cooling water will be supplied to the c-shaped lower main pipes from the bottom of the device, but half of the water must rise to the upper main pipes. To achieve this, three straight pipes connect the upper and lower main pipes. Fig 2.10-5 shows the installation location of the straight main pipes to connect the upper and lower c-shaped main pipes and water supply pipes. One y-strainer to remove debris in the water, two flow meters, and three flow control valves will be installed near the water supply pipes under the device. Fig 2.10-6 shows cooling water flow direction. The pure water will be supplied from below the CFQS body and drained to the bottom.

Fig 2.10-7 shows how the MC and the main pipe are connected. They will be connected with insulated nylon or PFA hoses. Applying metal reinforced hose may be prohibited because high voltage is applied to the coil. Hose length will be determined during the overall assembly on site. The function of connecting both ends of the hose will be accomplished with Swagelok fittings.

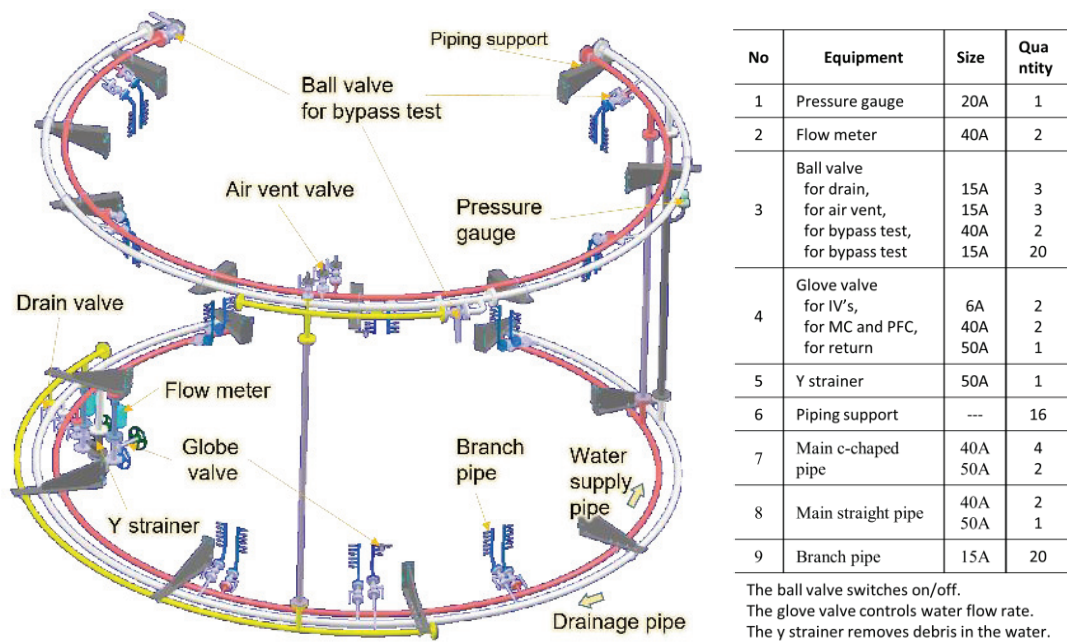


Fig 2.10-4 Layout of the main water piping system

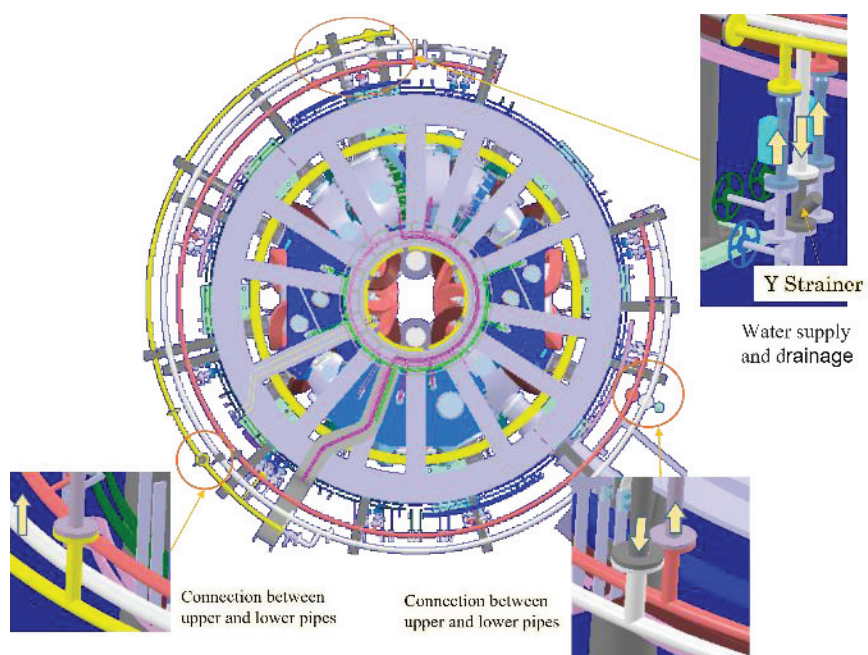


Fig 2.10-5 installation location of the straight main pipes and water supply pipes.

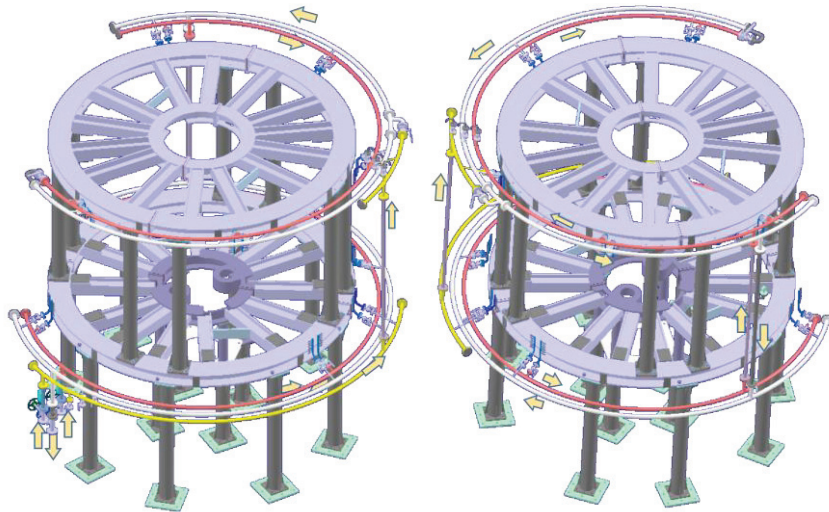


Fig 2.10-6 Cooling water flow direction.

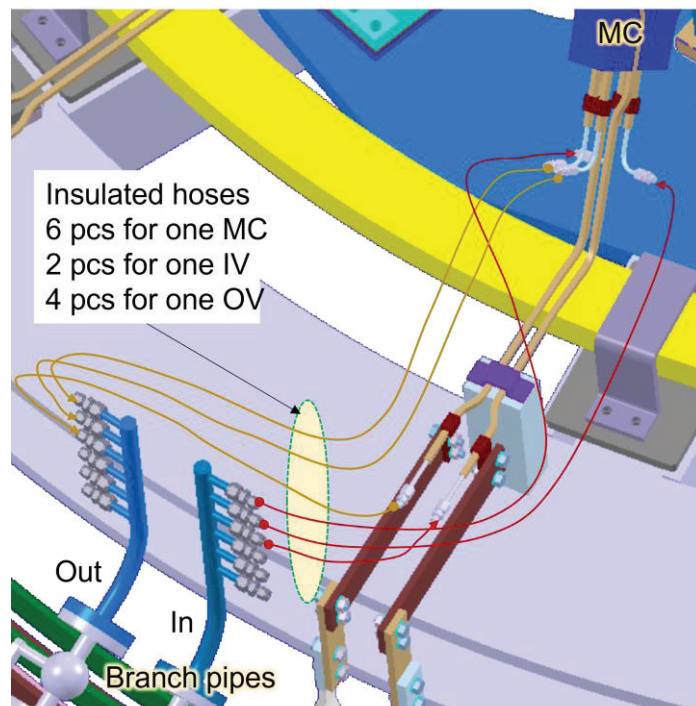


Fig 2.10-7 How the MC and the main pipe are connected

### 3 Validation of the coil design

#### 3.1 Validating the ANSYS/Maxwell result for inductance

The inductance can be analytically estimated by the solenoid formula with the Nagaoka coefficient.

$$L = K \times 4\pi \times 10^{-7} \times \mu_r \times N^2 \times S / L_{length}$$

where  $K$  is a Nagaoka coefficient,  $\mu_r$  is a relative permeability,  $N$  is the number of turns,  $S$  is a cross section of inside area of coil and  $L_{length}$  is a coil width.

##### □ MC1

$$S = \pi \times 0.92 \times \frac{1.62}{4} = 1.17$$

$$L_{length} = 0.069$$

$$\frac{D}{L_{length}} \sim \frac{0.61}{0.07} = 9$$

$$K = 0.2$$

$$L = \frac{0.2 \times 4\pi \times 10^{-7} \times 72^2 \times 1.17}{0.07} = 0.021[H]$$

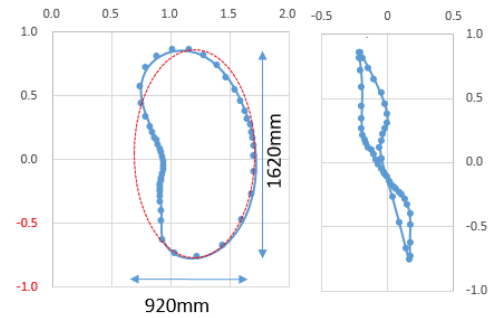
Obtained by the formula

$$L = 2216 \times 10^{-9} \times 72^2 = 0.0115[H]$$

Obtained by the ANSYS/Maxwell

69

132



##### □ MC4

$$S = \pi \times 1.03 \times \frac{1.16}{4} = 0.94$$

$$L_{length} = 0.069$$

$$\frac{D}{L_{length}} \sim \frac{0.55}{0.07} = 7.9$$

$$K = 0.2$$

$$L = \frac{0.2 \times 4\pi \times 10^{-7} \times 72^2 \times 0.94}{0.07} = 0.017[H]$$

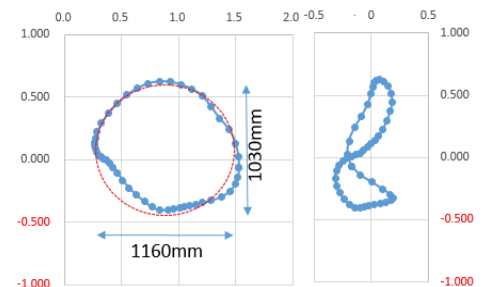
Obtained by the formula

$$L = 1985 \times 10^{-9} \times 72^2 = 0.0103[H]$$

Obtained by the ANSYS/Maxwell

69

132



The results of the ANSYS/Maxwell are considered reasonable, which shows a value slightly larger than the estimated value.

### 3.2 Electromagnetic force of the modular coil (MC)

A strong support structure is necessary for keeping device in a safety state when operating it. As for magnetic confinement fusion device, the electromagnetic force is the main load on coil system, which is the key component of whole device. Therefore, we need to understand the electromagnetic force on coil system and then design a reliable support structure.

#### 3.2.1 Coil system for the CFQS and analysis method

Each coil name in the modular coil system is shown in Fig 3.2-1. In our analysis, the ANSYS Maxwell system was used to get the magnetic field distribution in the 3D space and the electric magnetic force (EMF) on the coil.

To make it easy for predicting the behavior of coils, the EM forces on MCs are divided into centripetal (radial), toroidal, and vertical components based on a cylindrical coordinate system of Fig 3.2-2. The characteristics of each component are as follows.

- The centripetal force ; It is a component that tends to move the coil toward the center of the device. The torus device has a strong magnetic field on the center side. The centripetal force is mainly generated by the difference in hoop force between the center side and the outer side. In the TFC design of a tokamak, the supporting structure that withstands this component is most important.
- The toroidal force ; Sum of toroidal components that is a vertically symmetry component. It is caused by the coil being pulled from the neighbor. The tokamak does not generate this component because the TFC is pulled with the same force from the left and right.
- The vertical force ; This is sum of vertical components that is a vertically asymmetry component. Since the normal tokamak TFC is designed to have a vertically symmetrical shape, this component is small. Since the CFQS uses vertically asymmetric modular coils, it is necessary to design it in consideration of supporting this component.
- Overturning force ; A component that turns (rotates) the coil in the toroidal direction. It is mainly caused by the interaction of the TFC current and the PFC field in the tokamak. Since this force does not disappear even when the total force of the TFC is added, a large rotational moment is generated. In the TFC design of a tokamak, the supporting structure that withstands this component is very important. It is caused by vertical asymmetry of the coil shape in the CFQS. There is this component when we look at each coil, but the whole is canceled, and the rotational moment is lost.



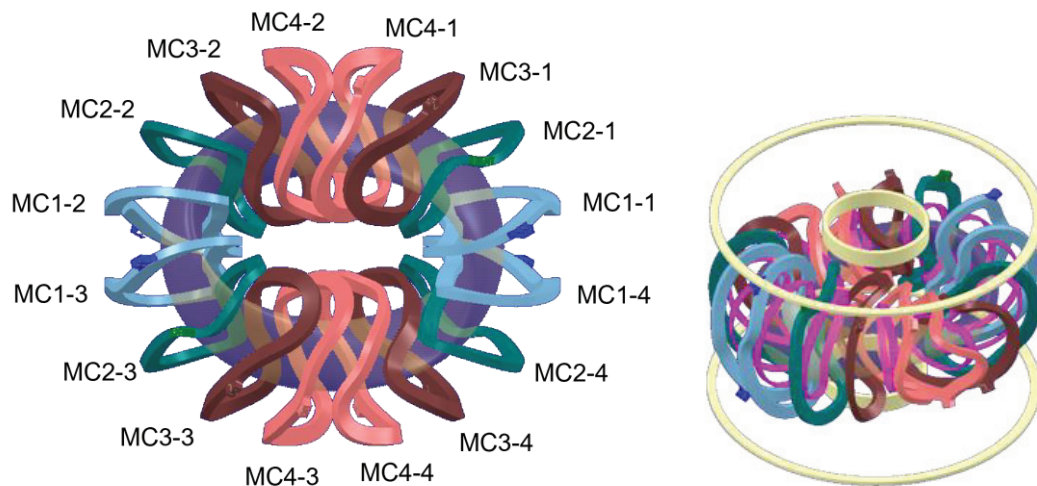


Fig 3.2-1 Top view of the modular coil system. The modular coil system consists of four types of coils, which are displayed with different colors.

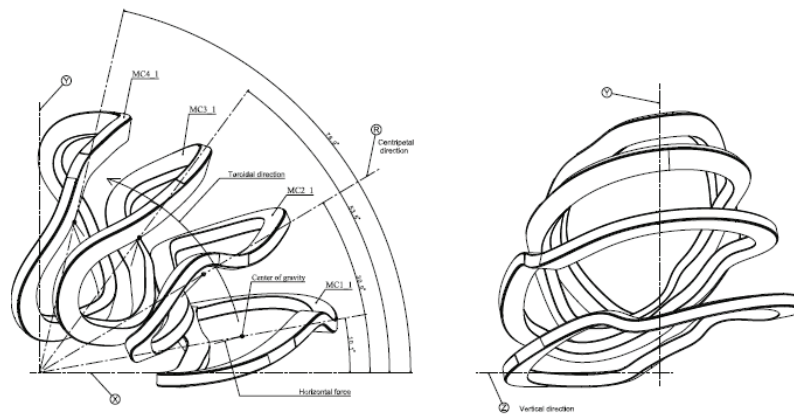


Fig 3.2-2 Definition of coordinate system.

### 3.2.2 Magnetic field and EM force distribution on the modular coils

Fig 3.2-3 shows the magnetic field and the EM force distribution on each coil. Here, the EM force is displayed as a vector graph of body force.

The magnetic field on each coil is not uniform, and the magnetic field strength on the inboard side is larger than on the outboard side. The maximum magnetic strength reaches about 2.2 T, which is located on the inboard side of the MC4.

It is clearly seen by the magnetic field distribution that the EM force will be irregular on MCs during the machine operation. The EM force are larger on the high-field side of the MCs as we expected, but it is difficult to grasp their characteristics such as the direction of the force that deforms the coil. In a tokamak, supporting the centripetal force and the overturning force generated by the interaction of TFC, PFC and plasma current is an important issue. Although the CFQS also generates an overturning force which is generated by the vertical asymmetry, it is not as conspicuous as that in the tokamak. The centripetal support is as important in the CFQS as it is in tokamak. The different force components on the different type of coil are shown in Fig 3.2-4 to Fig 3.2-7. We can see that the main components are different for each coil.

A comparison of the total values of the EM force is shown in Table 3.2-1 and Table 3.2-2. From the tables, we can understand the EM force applied each coil and it will be helpful for us to design and improve our support structure. As we all know, the CFQS is a tokamak-like device, but has its own characteristics. The MC1 and the MC2 are like the TFC of tokamak and the centripetal support is particularly important. The MC3 and the MC4 are special coils with large vertical and toroidal forces. The diagonal force of the MC3 is big enough not to ignore, which requests the strong support resists it. The EM force to the MC4 is smaller than others, but it is estimated that it will be difficult to install support due to the large vacuum port. The vertical force and the overturning component in the toroidal force are applied due to the vertical asymmetry. They are features not found in tokamak. Since they can be easily canceled by connecting the coils, they may not pose big problems.



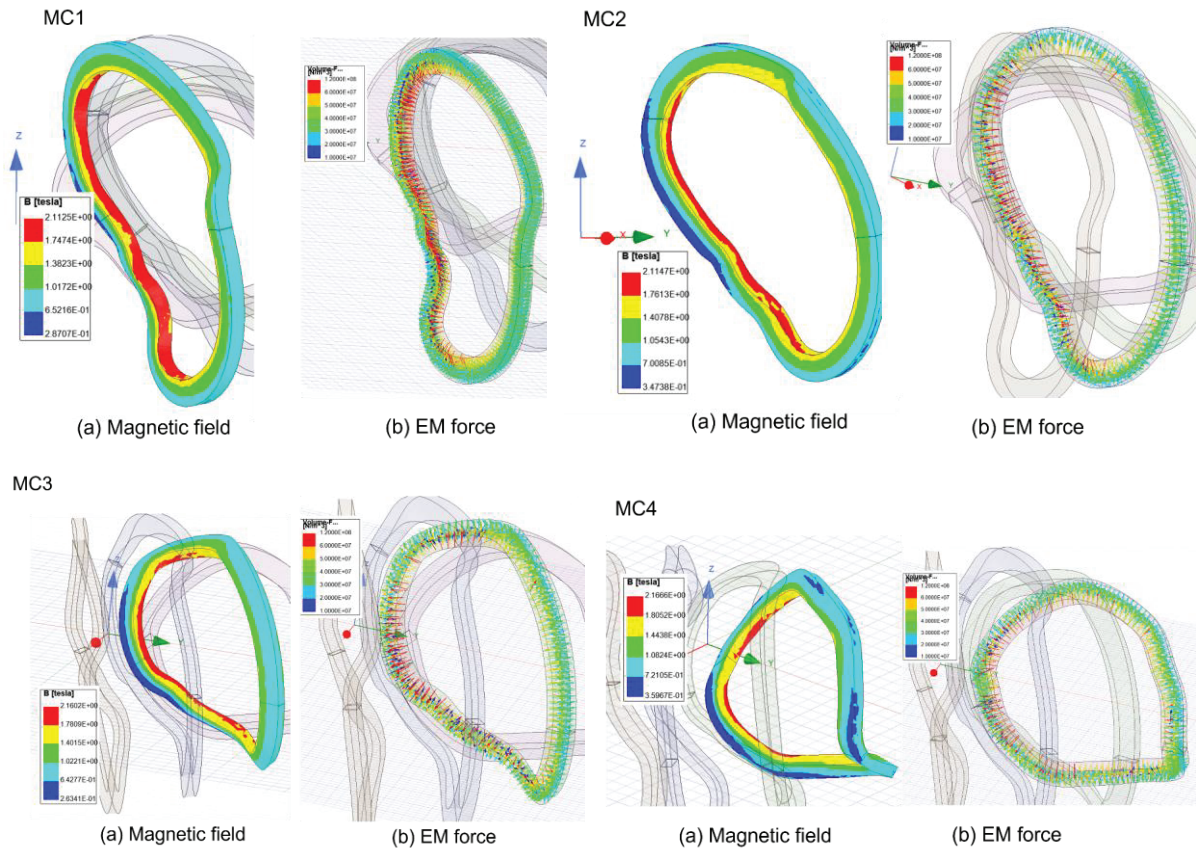
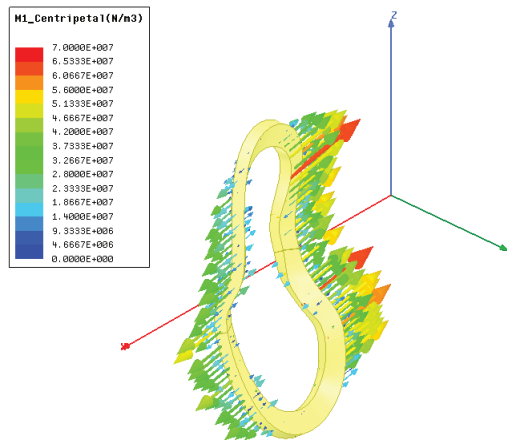
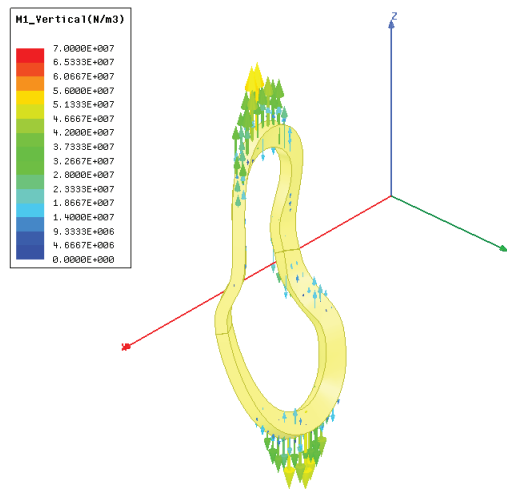


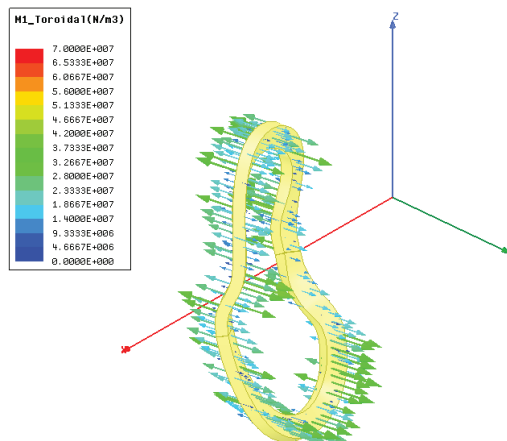
Fig 3.2-3 Distribution of the magnetic field and the EM force on the modular coils. The maximum field reaches about 2.2T, where is located on the inboard side of the MC4.



(a) Centripetal component.

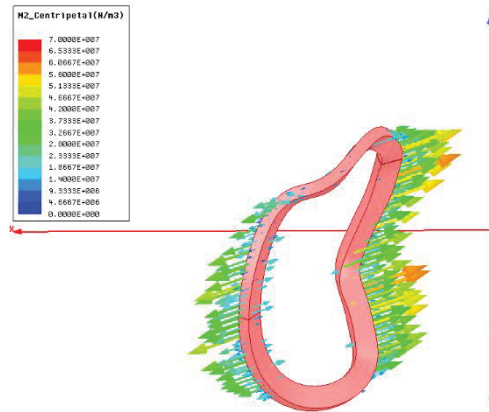


(b) Vertical component.

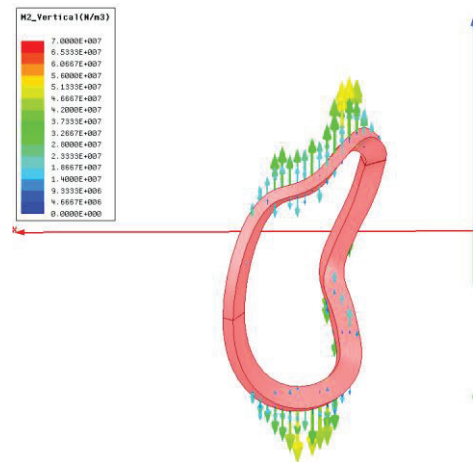


(c) Toroidal component.

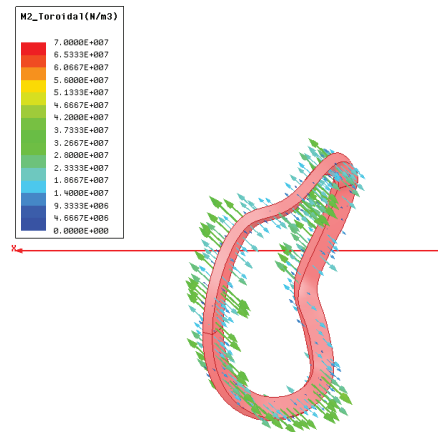
Fig 3.2-4 EM force on the MC1. The centripetal component (a) is dominant.



(a) Centripetal component.

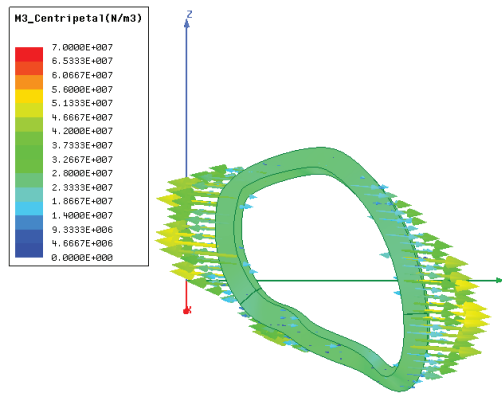


(b) Vertical component.

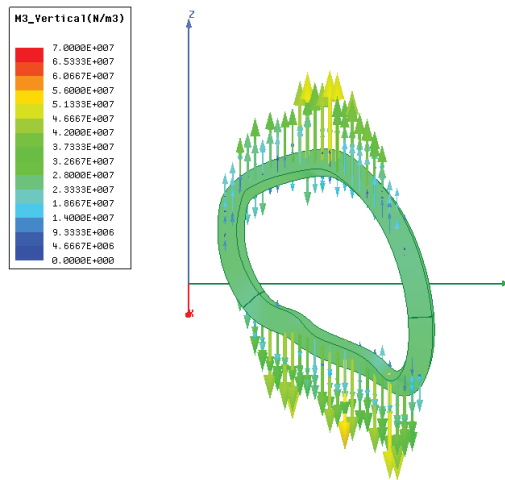


(c) Toroidal component.

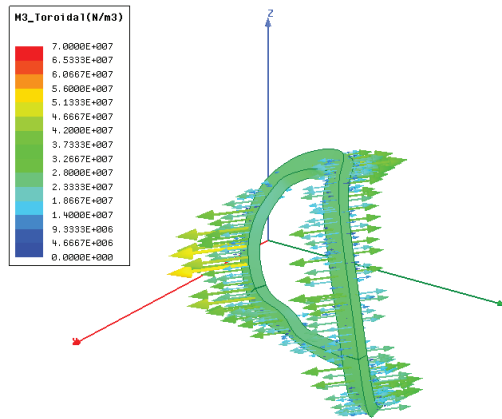
Fig 3.2-5 EM force on the MC2. The centripetal component (a) is dominant.



(a) Centripetal component.

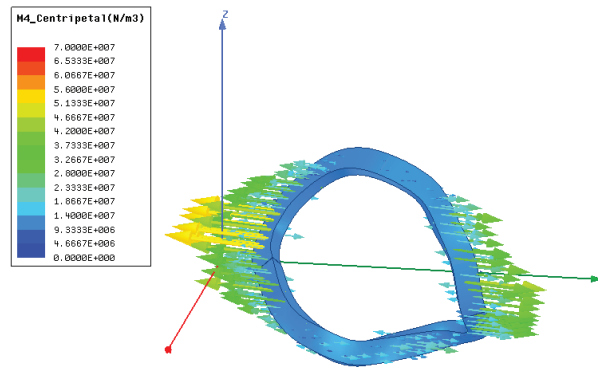


(b) Vertical component.

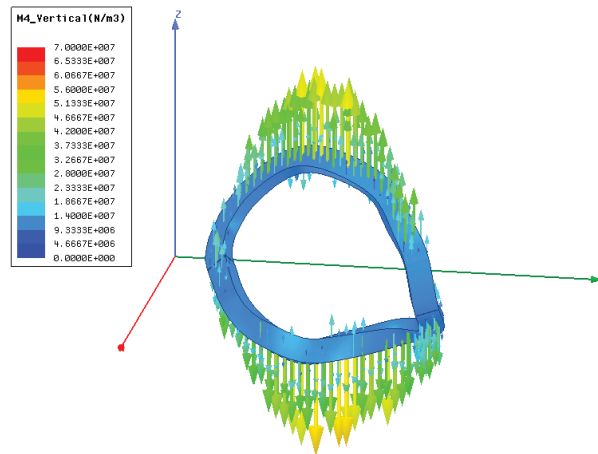


(c) Toroidal component.

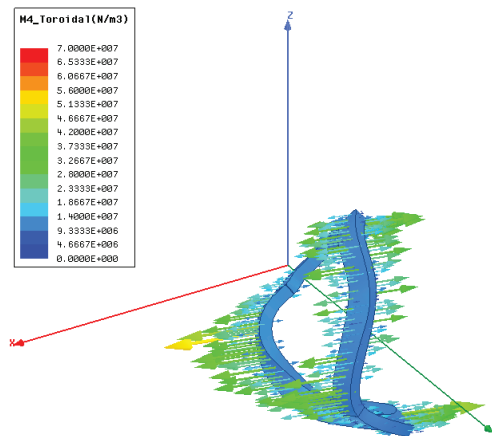
Fig 3.2-6 EM force on the MC3. The vertical component (b) is dominant.



(a) Centripetal component.



(b) Vertical component.



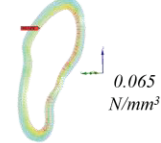
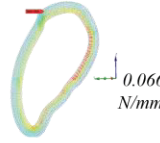
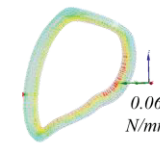
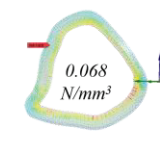
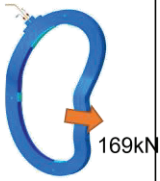
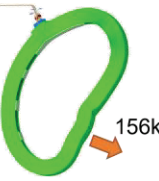
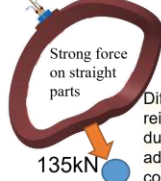
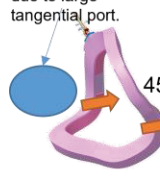
(c) Toroidal component.

Fig 3.2-7 EM force on the MC4. The toroidal component (c) is dominant.

Table 3.2-1 Total EM force on the modular coil.

Coil name			MC1_1	MC2_1	MC3_1	MC4_1	Note
Coil position	Cartesian coordinate	x(mm)	1202.9	973.4	593.3	207.0	
		y(mm)	215.1	582.5	801.3	891.5	
Center of gravity		z(mm)	52.5	146.1	165.5	75.9	
	Major radius	R(mm)	1222.0	1134.4	997.0	915.2	
	Toroidal angle	$\varphi$ (degrees)	10.1	30.9	53.5	76.9	
Total load		$F_x$	-162.46	-103.65	-29.39	34.56	
		$F_y$	-43.47	-106.26	-99.97	-49.27	
	Vertical	$F_z$	-18.70	-60.86	-93.46	-39.20	
	Horizontal	$F_h$	168.17	148.44	104.20	60.18	$\sqrt{F_x^2+F_y^2}$
	Centripetal	$F_R$	-167.57	-143.51	-97.84	-40.18	$F_x \cos(\varphi) + F_y \sin(\varphi)$
	Toroidal	$F_T$	-14.19	-37.95	-35.86	-44.81	$F_y \cos(\varphi) - F_x \sin(\varphi)$
	Total	F	169.21	160.43	139.97	71.83	$\sqrt{F_x^2+F_y^2+F_z^2}$
Proportion (%)	Vertical	$P_z$	11.1	37.9	66.8	54.6	$\text{abs}(F_z/F)$
	Centripetal	$P_R$	99.0	89.5	69.9	55.9	$\text{abs}(F_R/F)$
	Toroidal	$P_T$	8.4	23.7	25.6	62.4	$\text{abs}(F_T/F)$

Table 3.2-2 Characteristics of the EM force on the MCs.

		MC1	MC2	MC3	MC4
Maximum physical strength density					
Total load	Absolute	169.2kN	160.1kN	140.0kN	71.8kN
	Vertical	18.7kN	60.9kN	93.5kN	39.2kN
	Centripetal	167.6kN	143.5kN	97.8kN	40.2kN
	Toroidal	14.2kN	38.0kN	35.9kN	44.8kN
Features		<p>Similar to D-type TFC Great centripetal force</p> 	<p>Similar to D-type TFC Great centripetal force</p> 	<p>Large diagonal force</p> 	<p>Large toroidal force Difficult to reinforce due to large tangential port.</p> 
		<p>Vertical force is applied due to the vertical asymmetry. Overturning component in the toroidal force is also applied due to the vertical asymmetry. However, since they can be canceled by connecting the coils, they do not pose a big problem.</p>			

### 3.3 Eddy current on the modular coil case (MC)

A time constant of an eddy current on a modular coil case was obtained. This analysis was performed preliminary for the design of continuous coil case. The time constant of the latest clamp type case is much shorter than the result of this analysis, so we would like to mention that it does not matter.

Fig 3.3-1 shows the MC4 for the eddy current analysis and its coil case. Thickness of the coil case is 13 mm and the material stainless steel. A current is applied in a cross section of the coil according to a waveform shown in Fig 3.3-2. The eddy current is obtained by integrating over a cross section. As a result, a time constant of the eddy current on coil case is estimated to be 2.5 ms, that is much shorter than the flat top length of the coil current. So, the effect of the coil case on the magnetic field is negligible.

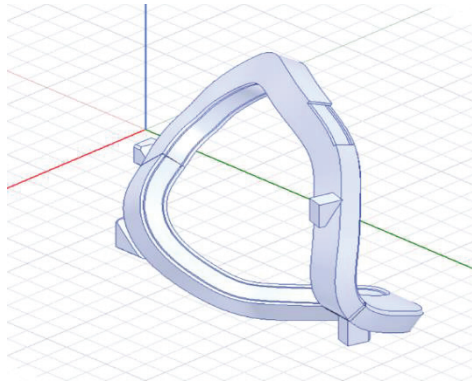


Fig 3.3-1 MC4 and its coil case. It is a C-type continuous shape of the coil case. Please note that this design is preliminary and is different from the latest design.

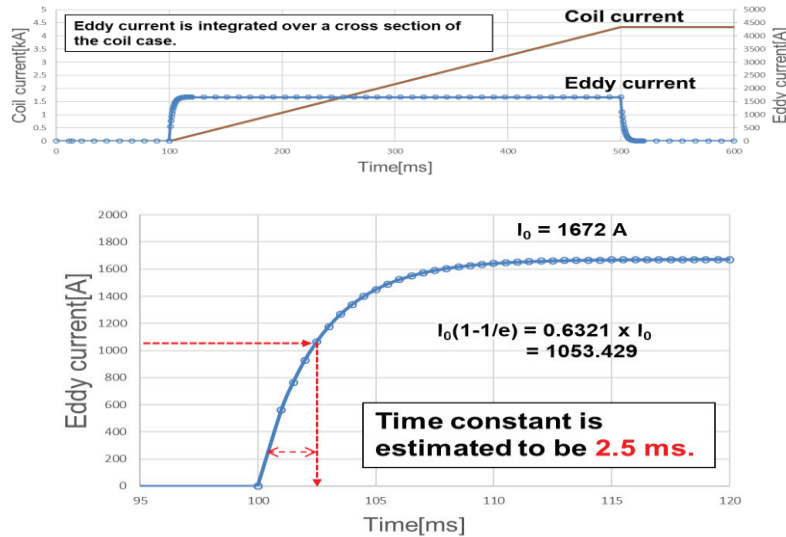


Fig 3.3-2 Time evolution of eddy current on the coil case. The time constant of 2.5 ms is much shorter than the flat top length of the coil current. The effect of the coil case on the magnetic field may be negligible.



### 3.4 Structural analysis of the cage type support structure and the MC for 1T

A strong support structure is necessary for keeping device in a safety state when operating it. As for magnetic confinement fusion device, the electromagnetic force is the main load on coil system, which is the key component of whole device. Therefore, we need to understand the electromagnetic force on coil system and then design a reliable support structure. There are three types of coils in CFQS, modular coil, poloidal field coil and toroidal field coil. The modular coil is a major part of coil system. It has the most complicate shape and largest total current, so our analysis focuses on them.

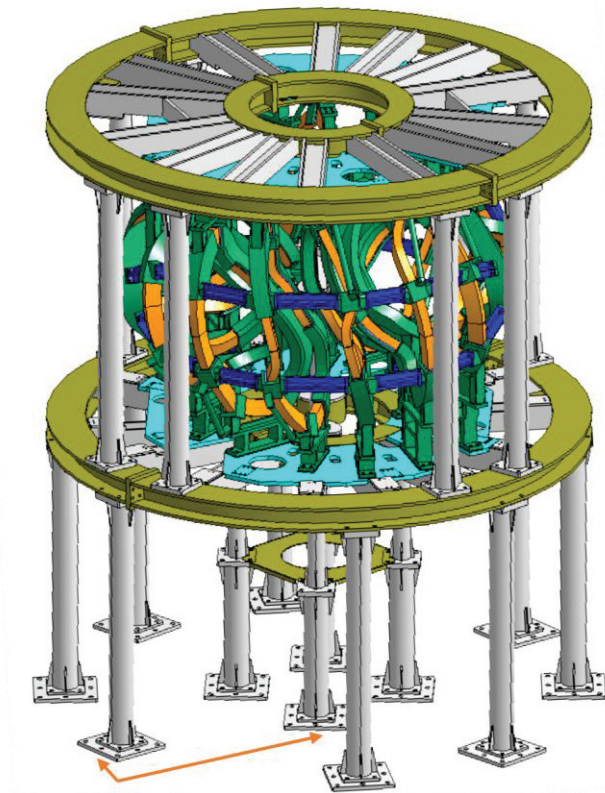
The finite element analysis has been widely used for structural analysis in fusion devices. Usually, the analysis result is considered as a reference to estimate the quality of the supporting structure design and help designers to make optimization. Here, previous result of electromagnetic force analysis by the ANSYS/Maxwell was coupled into ANSYS mechanical, and deformation and von-Mises stress were evaluated. As a result, we have confirmed the design validity of the modular coil system with a mechanical support.

#### 3.4.1 Model of the analysis

Fig 3.4-1 shows the model of the cage type support structure with the partial large clamp (PLCL). The main points of modeling are shown below.

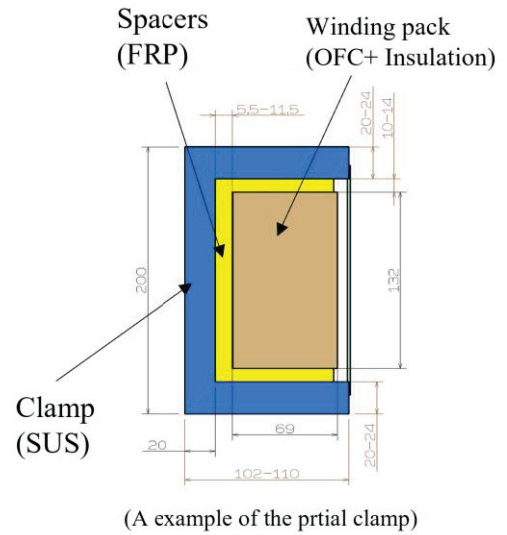
- The vacuum vessel is not included.
- The bottom surface of twelve legs is set as fixed boundary.
- All parts are bonded together.
- Actually, the FRP spacer will be bonded to the clamp with resin, but it may peel off due to aging deterioration and slip. In the real situation, the FRP spacer will be divided into small pieces and inserted, but in our simulation, the FPR spacers have to be a simplified continuous model. Since the continuous spacer may have higher rigidity than the splited spacers, the Young's modulus should be reduced so that a large displacement could be obtained. In order to simulate these states, the Young's modulus of the spacer is set softly 1 GPa, which is extremely smaller than the actual value of 100 GPa.
- The Young's modulus of the winding packs is 110 GPa(OFC with isolation).
- The Young's modulus of others is 193 GPa (SUS).

We divided whole structure into three major parts, a) support frame, b) center support, c) modular coil with support. Fig 3.4-2 shows the three major parts. According to previous result of electromagnetic force analysis, these three parts support different force components. The support frame is used for supporting vertical force and whole device. The center support resists the large centripetal force. The coil support resists the toroidal force, overturning force, and coil's bending.



Fixed boundary

(a) Simplified global model



(A example of the prtial clamp)

(b) Cross section of the modular coil

Fig 3.4-1 Model of the modular coil with supporting for the stress analysis. A bottom surface of twelve base legs is set as fixed boundary. Contact surface of all parts is set as the contact condition with the bonded. The Young's modulus of the spacer is set softly 1 GPa, which is extremely smaller than the actual value of 100 GPa.

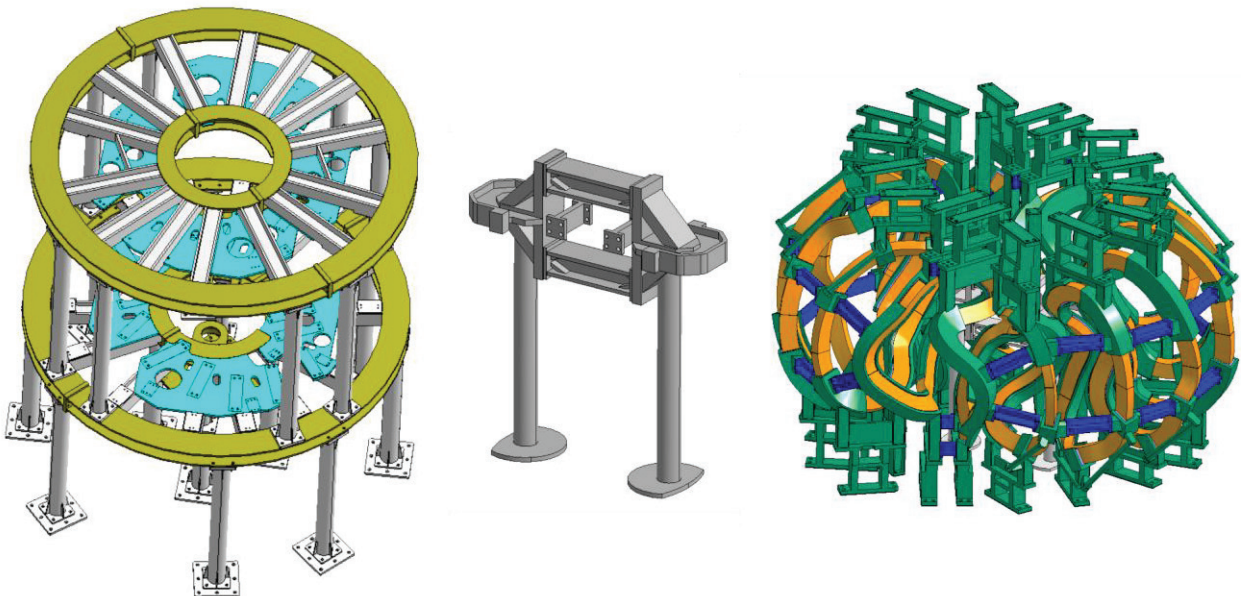


Fig 3.4-2 Three major parts of the supporting structure.

Fig 3.4-3 shows the EM load distribution on the modular coils. It is the same as that of Fig 3.2-3. Fig 3.4-4 shows the mesh diagram for the FEM analysis. Number of nodes is about 2 million, number of contact elements is about 400 thousand, and number of solid elements is about 1 million. Depending on the size, thickness and shape of the target part, the element has a side length of 10 to 80 mm. The elements were created using ANSYS' automatic meshing technique.

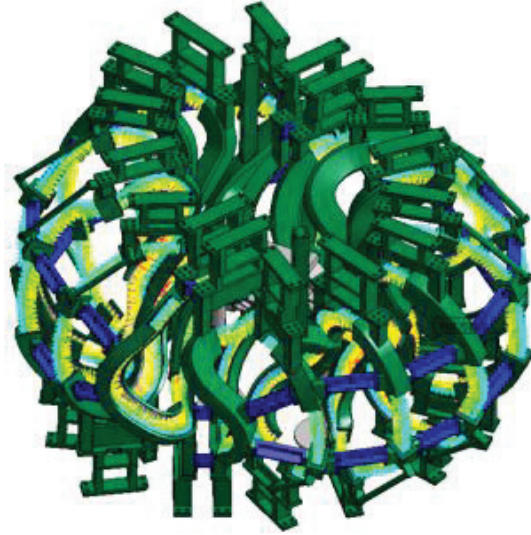


Fig 3.4-3 Electro magnetic (EM) load distribution

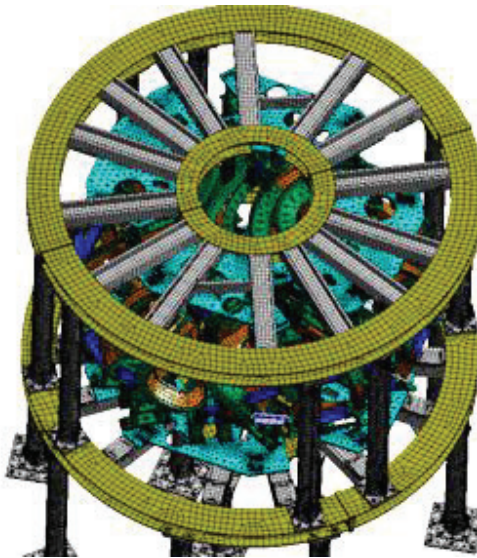


Fig 3.4-4 Mesh diagram of the FEM analysis. Number of nodes is 2,375,760, number of contact elements is 440,434, number of solid elements is 1,026,418 and size of elements is 10 mm to 80 mm.

### 3.4.2 Result of the analysis

The two contour plots in Fig 3.4-5 and Fig 3.4-6 show the displacement distribution. The maximum displacement is about 0.83 mm on the clamp for the MC2. It is in the acceptable range. The design target is less than 1 mm. The direction of displacement is mainly vertical as shown in Fig 3.4-6. About 50 % of this



displacement is due to deformation of the upper support frame. Since it is only fixed by the pillars on the outermost periphery, we think that this degree of deformation is unavoidable. Actually, we would like to fix the innermost periphery as well, but we cannot stand a pillar there because of the modular coil. As there are legs in the inner periphery of the bottom frame, the displacement for the lower half is smaller. The deformation of coil oneself or the clamp is about 0.4mm that it is hard to detect. We think that we do not have to worry about the deformation of that level.

If a coil is bent by EM force, strain occurs in coil. The copper conductor is very flexible and does not break in a short time even beyond the yield strain. However, if the large strain is repeated, there may be a risk of cracks in the insulation. So, the coil should be designed so that strain does not increase. Here, instead of strain, the stress distribution of the coil is used to confirm the validity of the design. In linear FEM analysis, the stress and the strain are proportional ( $\sigma=E \cdot \epsilon$ ). So, the results are the same regardless of whether the strain or the stress is evaluated.

Fig 3.4-7 shows the Von-Mises stress distribution on the winding pack. Maximum of the stress is 46 MPa at the MC2. The allowable strain, or stress, of the coil is not clear, because it is also expected to depend on the conditions of repeated loading and the insulation method. Originally, it should be investigated experimentally, but it is practically difficult. Although several tens of MPa is sometimes selected in the design of electric power equipment, it is not a good idea because the number of repetitions is extremely small in nuclear fusion devices. Here, 60 MPa is assumed as the upper limit. Since this is close to the design stress of copper, it is considered not an unreasonable value. The MC2 stress of 46 MPa is below the acceptable value of 60 MPa, so it is considered appropriate.

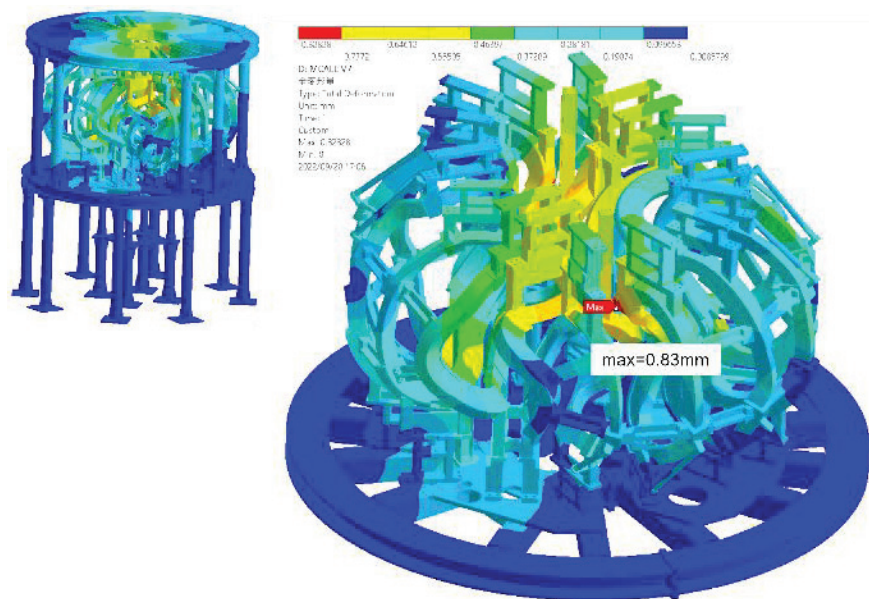


Fig 3.4-5 Displacement distribution of the cage type support structure with PLCL. The displacement of 0.83 mm is maximum at the MC2, which is in the acceptable range. The design target is less than 1 mm.

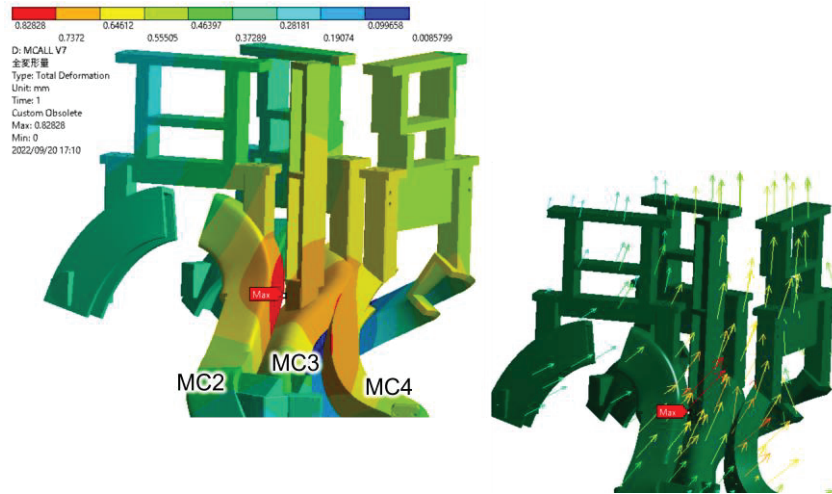


Fig 3.4-6 Displacement direction near the place where displacement is the largest

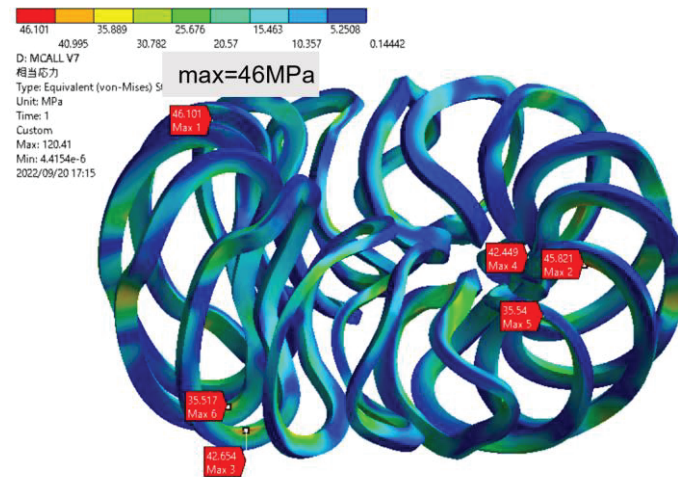


Fig 3.4-7 Von-Mises stress distribution on the winding pack. The stress of 46 MPa is maximum at the MC2, which is in the acceptable range. The design target is less than 60 MPa.

To check the support structure reliability, we need to check the stress of the device. Fig 3.4-8 to Fig 3.4-10 show the stress distribution on the support structure. It is obvious that the maximum stress on the supporting structure is 105 MPa at root of the linked beam as shown in Fig 3.4-8 and at the center support as shown in Fig 3.4-9. The stress at a root of the center pedestal as shown in Fig 3.4-10. These stresses are within the allowable range, so there is no problem with this structure, but the stress is maximum at the base of the pedestal, in other words, the discontinuous connection of the parts. If the weld length is not sufficient at such places, the stress on the weld bead will be extremely large, and there is concern that the weld will break. It is necessary to increase the penetration amount of welding, where full penetration is preferred, or eliminate the need for welding by cutting out from a metal block.

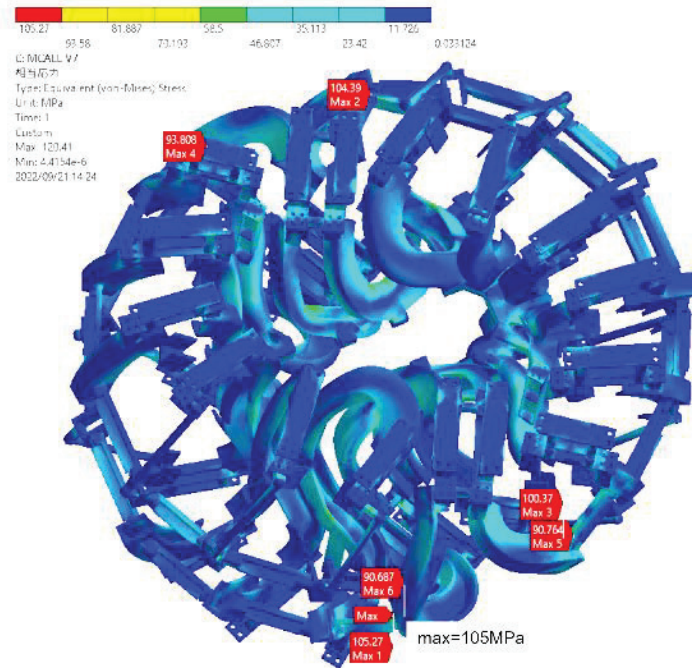


Fig 3.4-8 Von-Mises stress distribution on the clamp and the linked beam. The stress of 105 MPa is maximum at root of the linked beam for MC4 and it is in the acceptable range. The design target is less than 137 MPa.

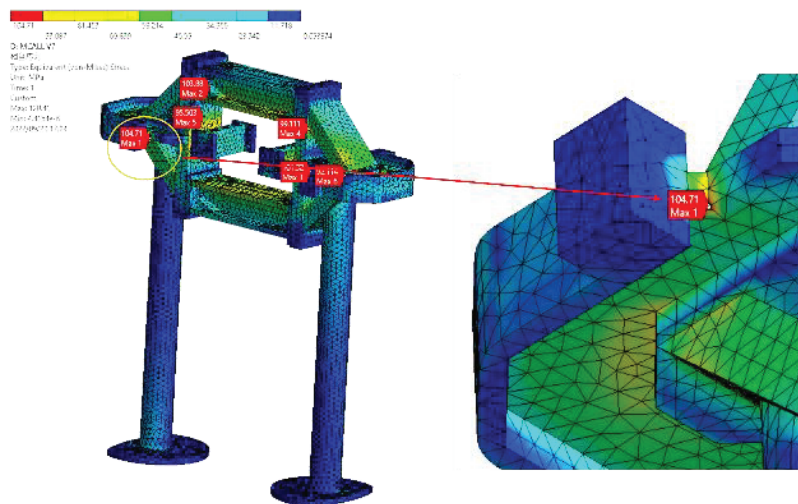


Fig 3.4-9 Von-Mises stress distribution on the center support. The maximum of the stress is 105 MPa, which is in the acceptable range. The design target is less than 137 MPa.

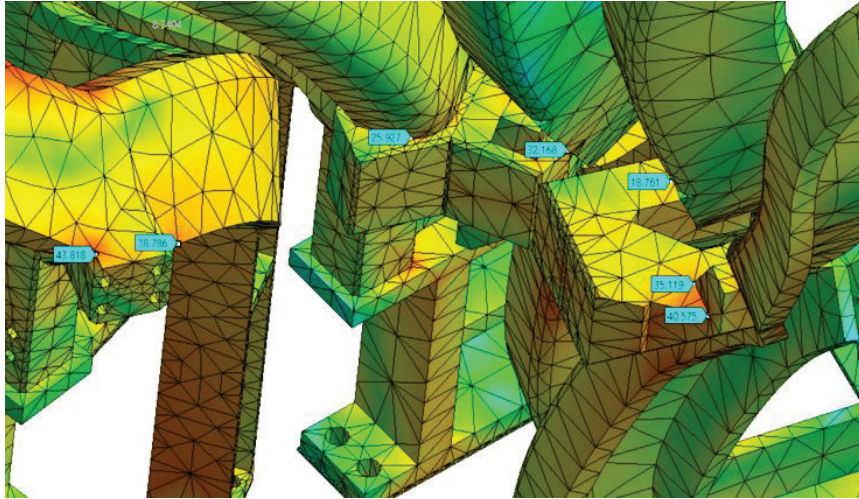


Fig 3.4-10 Von-Mises stress distribution on the center pedestal. The maximum of the stress is 44 MPa, which is in the acceptable range. The design target is less than 137 MPa.



### 3.5 Structural analysis of the modular coils for 0.1T

Simplified coil cases are used during 0.09 T experiment. It is necessary to investigate stresses and deformations of the simplified coil case with EM force. The experiment will be scheduled with 0.09 T to match the ECH resonance frequency of 2.45 GHz, but when confirming the structural validity, the numerical value will be rounded and evaluated at 0.1 T.

#### 3.5.1 Magnetic field distribution and EMF on the modular coil

At first, EM force on the coils with a magnetic field of 0.1 T was calculated using ANSYS/Maxwell. Coil current is set to 1/10 of that used in the analysis of 1 T. As shown in Fig 3.5-1, magnetic field strength was confirmed to be about 0.1 T at a main radius of 1m. Furthermore, EM force was confirmed to be about 1 % of that for the 1 T operation as shown in Table 3.5-1, where x, y and z represent the components of the global coordinate system. Here, the result for 1 T operation is the same as that in Table 3.2-1.

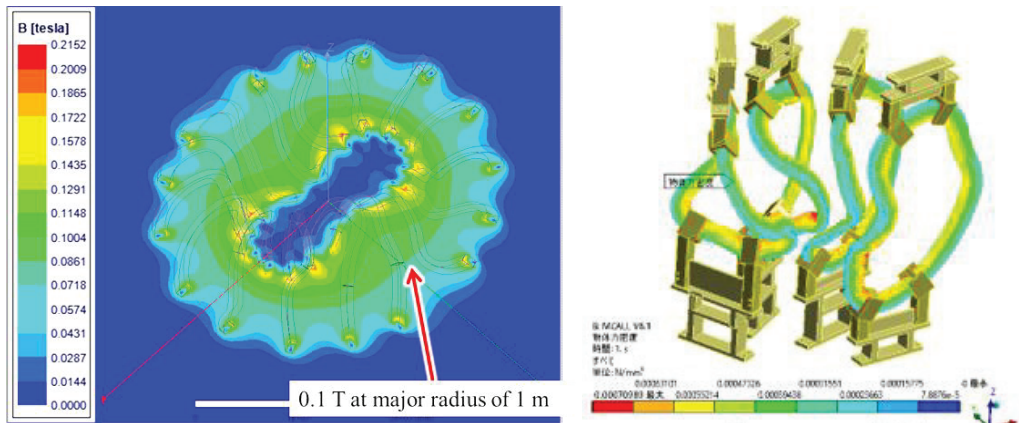


Fig 3.5-1 Magnetic field on equatorial plane and EMF vectors with the 0.1 T operation.

Table 3.5-1 Comparison of total electromagnetic forces (EMF)

Operation condition	Component	Total load EMF (kN)			
		MC1	MC2	MC3	MC4
1T (4.3kA)	Fx	-162.46	-103.65	-29.39	34.56
	Fy	-43.47	-106.26	-99.97	-49.27
	Fz	-18.7	-60.86	-93.46	-39.2
0.1T (430A)	Fx	-1.613	-1.024	-0.281	0.364
	Fy	-0.419	-1.048	-0.993	-0.486
	Fz	-0.194	-0.598	-0.929	-0.383

#### 3.5.2 Model of the structural analysis

Fig 3.6-9 shows analysis model for a structural analysis. Each coil is supported on the upper and lower sides with a simplified support structure. Only 4 coils and their support structures were analyzed for the structural analysis since these 4 coils are used as 1 unit and repeated 4 times to form CFQS modular coil system with 16 coils. Fig 3.6-9 also shows boundary condition for structural analysis. The upper and lower surface of each leg are fixed

and not deformed, i.e., “fixed boundary” is applied. The contact surfaces between coil conductor/FRP spacer and FRP spacer/clamp of coil support are completely bonded to each other, i.e., "bonded surface". Table 3.6-2 shows the material and properties of components. Clamps and legs are stainless steel, spacers are FRP, and conductors are copper. Their physical properties comply with the analysis of a 1 T experiment (see 3.6.2).

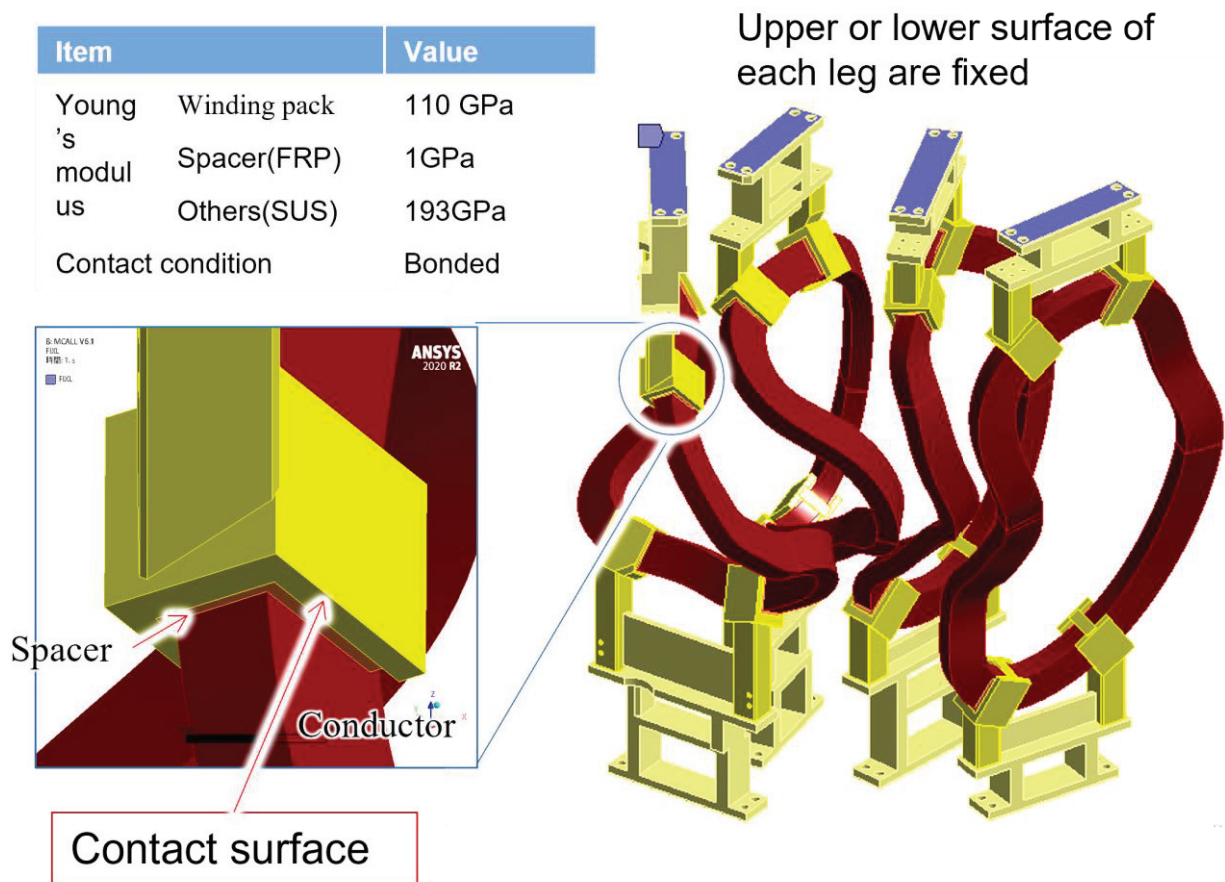


Fig 3.5-2 Models and boundary conditions for stress analysis.

### 3.5.3 Result of the structural analysis

The contour plot in Fig 3.5-3 shows the displacement distribution. The maximum displacement is 0.12 mm, which is too small to be detected. Fig 3.5-4 shows the Von-mises stress distribution. The maximum stress of 6.9 MPa and 3.9 MPa are within an acceptable range, as we expected. It becomes clear that simplified support structure satisfied our design guideline.

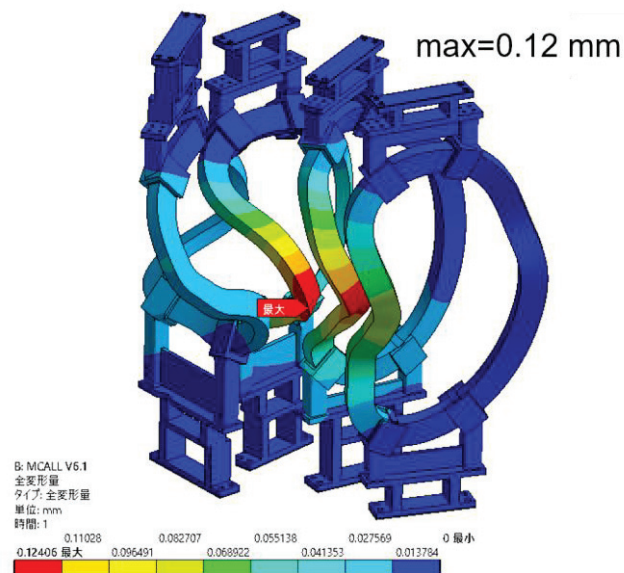


Fig 3.5-3 Displacement distribution of the modular coils with the 0.1 T operation. The displacement of 0.12 mm at the MC3, which is in the acceptable range. The design target is less than 1 mm

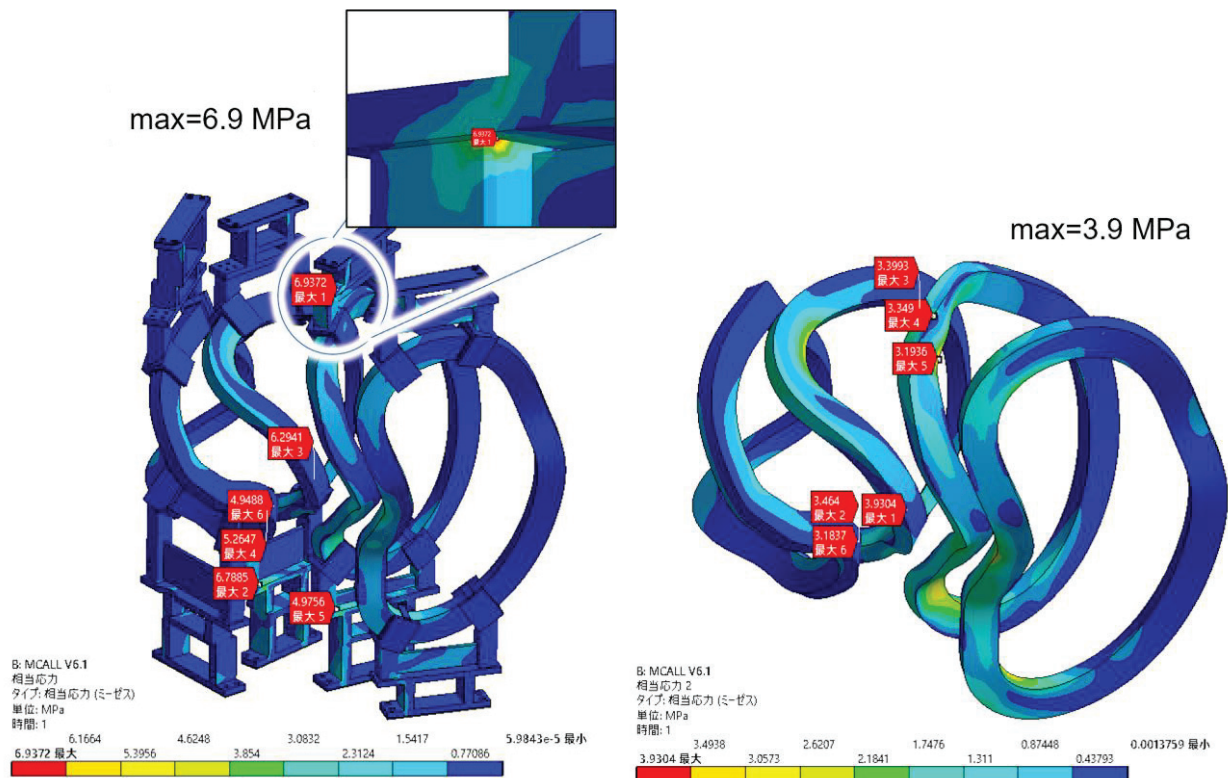


Fig 3.5-4 Von-Mises stress on the modular coils with the 0.1 T operation. The stress of 6.9 MPa at the MC2 is maximum on the support and leg, 3.9 MPa at the MC3 is maximum on the winding pack. They are in the acceptable range. The design target is less than 60 MPa for the windinff pack, and 137 MPa for others.

### 3.6 Magnetic field distribution of the poloidal field coil (PFC)

The distribution of vertical magnetic field generated by PFC was calculated by filament current approximation by Biot-Savart law. The results are shown in Fig 3.6-3 and Fig 3.6-2. The magnetic field generated by the IV coil is small in areas with larger major radius, and changes linearly in areas with a major radius of smaller than 1 m.

In the research of tokamak devices, the spatial distribution of the PFC magnetic field is represented by a set of typical magnetic field components called the functional magnetic fields, which often explains the effectiveness of equilibrium control. For example, the position of the magnetic axis is controlled by the uniform vertical magnetic field component  $B_V$ , and the ellipse of the plasma cross section is controlled by the quadrupole vertical magnetic field component  $B_Q$ . In addition, if the induced voltage is calculated from the time change of the interlinkage flux  $\partial\psi/\partial t$ , the influence on the plasma current can be evaluated. The relationship between the functional magnetic field component of the PFC and the equilibrium of the modular coil device is not clear in theory, but it may be possible to expect the same effect as the tokamak device.

The distribution of the magnetic field created by the IV coil has characteristics close to a so-called quadrupole magnetic field  $B_Q$ . The change in the magnetic field generated by the OV coil is small and has characteristics close to the so-called uniform vertical magnetic field component  $B_V$ . Therefore, it is presumed that IV may control the plasma ellipticity and OV may control the magnetic axis position.

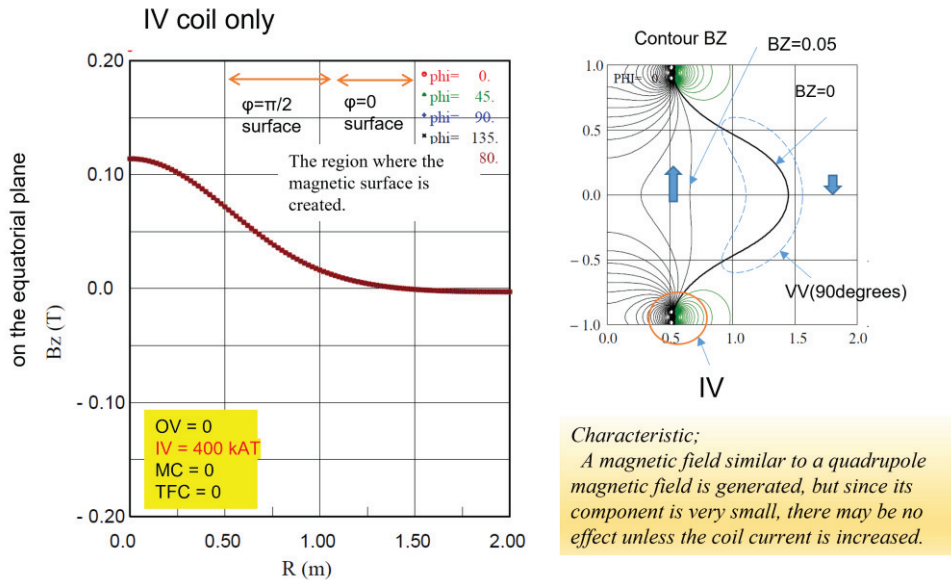


Fig 3.6-1 Vertical magnetic field generated by the IV coil



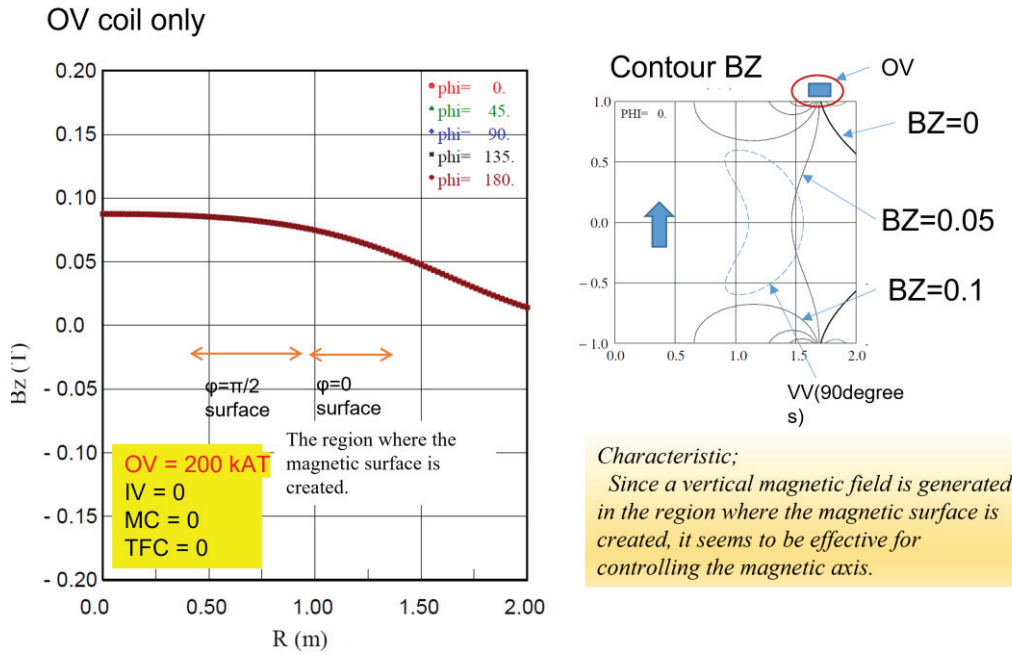


Fig 3.6-2 Vertical magnetic field generated by the OV coil

The magnetic field distribution was also calculated with the ANSYS/Maxwell volume current model. In this calculation, the flux linkage was also obtained in addition to the vertical magnetic field. The results are shown in Fig 3.6-3 and Fig 3.6-4. The magnetic field created by each coil varies from place to place. The results of the filament current model and the volume current model show the same distribution, and it can be seen that the difference between the two is small.

With a current of about 140 kA, the IV generates about 3 % (0.03 T) of the MC field and the OV 6 % (0.06 T) of the MC field at the position where the major radius is 0.5 m that is near the plasma surface. Originally, the toroidal ripple component ( $B_{0,1}$  mode) which is the lowest order mode of the MC is up to 15 % of the toroidal magnetic field, and the other higher components are up to 3 %. Since the PFC can generate a magnetic field of the same magnitude as the higher-order mode, it is expected to be effective for deformation of the equilibrium magnetic surface.

Fig 3.6-4 shows the distribution of the magnetic flux. Plasma current may be induced by electromagnetic induction when the flux linkage changes with the PFC current. It can be seen from Fig 3.6-4 that even if the PFC current is changed with a high speed of 1.4 MA/s, the induced voltage is 0.1 V to 0.4 V. The current change that can be realized with the PFC power supply is a maximum of 200 kA/0.2 s (1 MA/s).

The effect of this voltage depends on the plasma temperature. It is difficult to evaluate the effect of the PFC on the plasma current when the rate of current change and the plasma temperature are not clear, but it cannot be ignored. There is a mode in the tokamak that changes only the magnetic flux without the  $B_v$  and  $B_Q$  components (called OH mode), but the CFQS cannot control this component. Although the  $B_Q$  mode has a magnetic field distribution like that of the OH mode, the one-turn voltage may be small, so it is difficult to positively control the plasma current by the PFC.

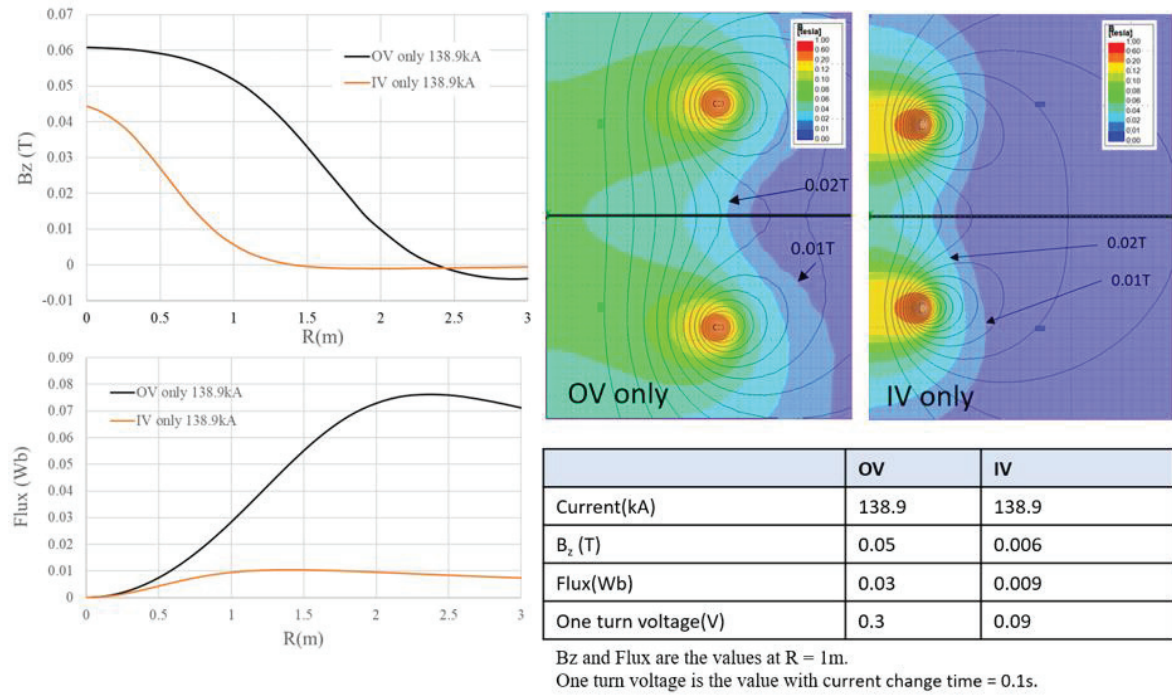


Fig 3.6-3 Magnetic field distribution of the IV and OV coil by the Maxwell.

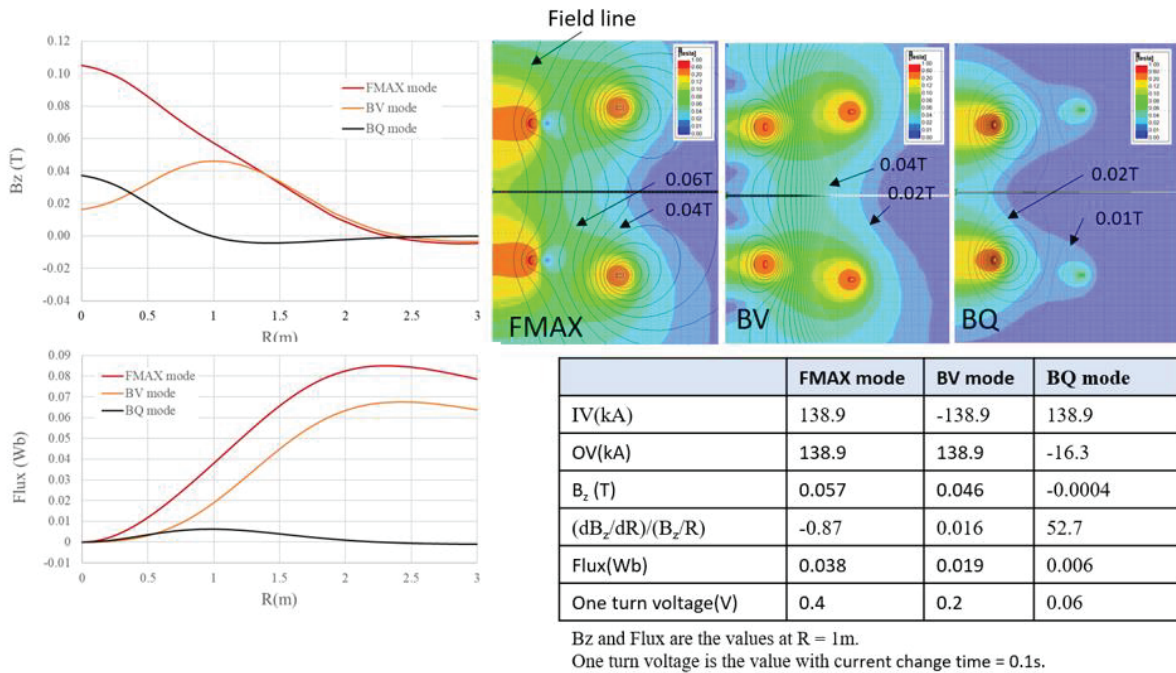


Fig 3.6-4 Magnetic field distribution of the control function produced by the PFC. FMAX is the mode with maximum magnetic flux, BV is the mode with the uniform vertical magnetic field, and BQ is the mode with a large quadrupole component.



### 3.7 Magnetic field distribution and electromagnetic force of the toroidal field coil (TFC)

#### 3.7.1 Magnetic field distribution

The distribution of the magnetic field generated by TFC was calculated by the ANSYS/Maxwell. The results is shown in Fig 3.7-1. The magnetic field created by each coil varies from place to place. The TFC system generates a magnetic field of about 10% (0.1T) of the modular coil magnetic field in the region where the equilibrium magnetic surface exists (about 0.5m around the magnetic axis  $R = 1\text{m}$ ).

Name	Current (kAT)
TC10	32
TC32	48
TC70	48

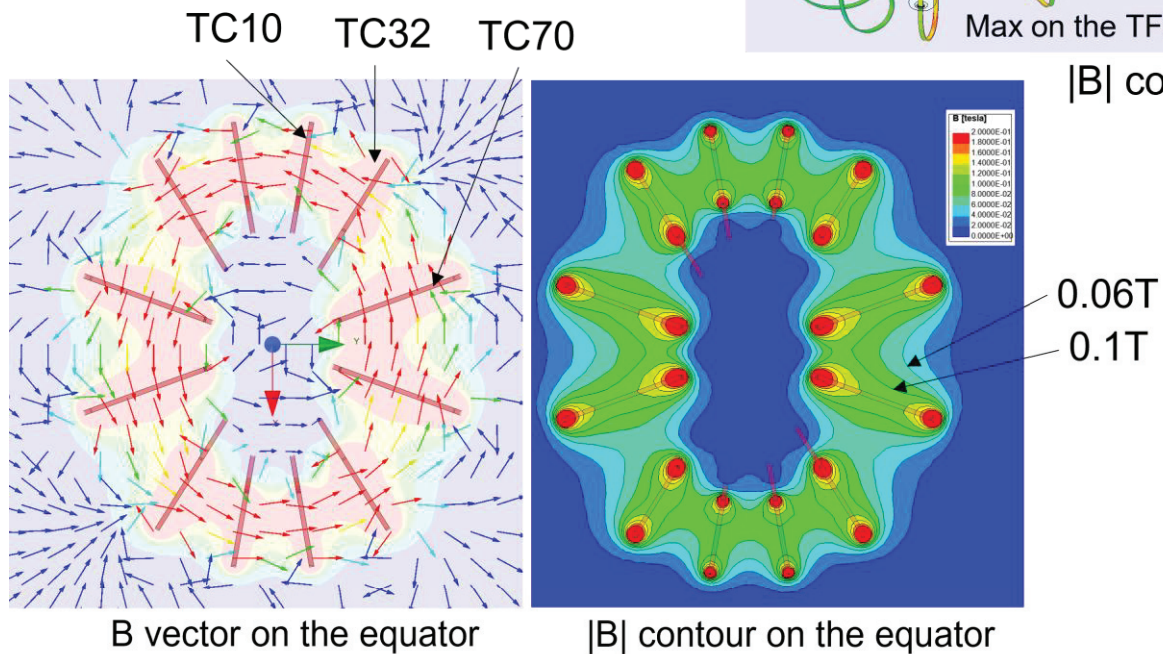
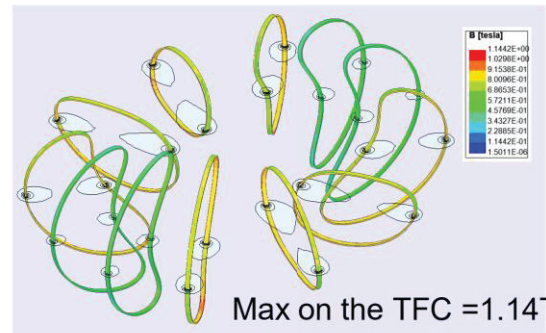


Fig 3.7-1 Magnetic field distribution of the TFC

### 3.7.2 Estimation of the magnitude and direction of the EM force

The ANSYS/Maxwell obtained the electromagnetic force distribution of the toroidal filed coil system. It calculates the body force vector, which are created by the automatic meshing function. Fig 3.7-2 shows the body force vectors as an example. Usually, the number of elements exceeds 10,000. By adding the body force vectors to the mesh element of structural analysis, it becomes possible to grasp the effect on the coil as a structure. However, since the body force vector has various directions and magnitudes for each small element, results with too many meshes do not help the designer.

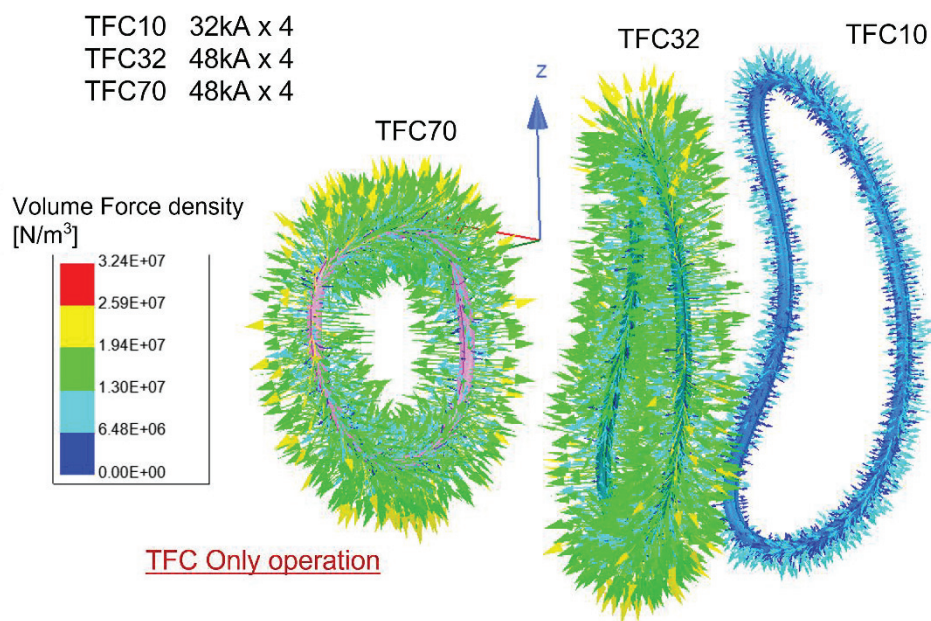


Fig 3.7-2 The body force vectors as an example. Since the body force vector has various directions and magnitudes for each small element, results with too many meshes do not help the designer.

Distribution of the force integrated over the coil cross section is required to derive the support requirements. Unfortunately, the ANSYS/Maxwell does not have the ability to integrate 3D vectors over a complex surface. Therefore, the coil was divided into suitable large parts, and the force was volume-integrated for each part. The shape of the model in which each TFC was divided into 10 parts are shown in Fig 3.7-3. The coordinates of the nodes dividing the TFC are shown in Table 3.7-1. These models were simplified to understand the characteristics of electromagnetic force distribution. The shape of the coil cross section was approximated by a circle with a diameter of 40 mm. The center line of a coil was a similar curve shifted by 20 mm from the vacuum vessel outer surface.

The number of divisions is 10 each, and the cross section of the coil is represented by a circle with a diameter of 40 mm. The center line of the coil cross section is a similar curve shifted by 26 mm from the inner surface of the vacuum vessel. The  $n$  is the normal vector which corresponds to the hoop force, and the  $b$  is the binormal vector which corresponds to the toroidal force. The  $N1 \sim N10$  is the name of the nodes and  $P1 \sim P10$  is the name of the

elements by dividing the TFC

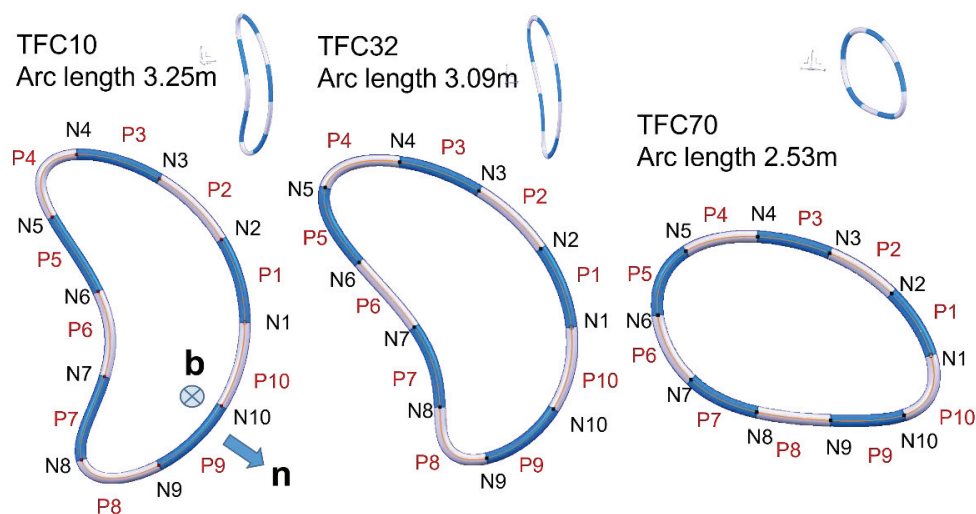


Fig 3.7-3 The shape of the model in which each TFC is divided into parts with appropriate size. The shape of the coil cross section was approximated by a circle with a diameter of 40 mm. The center line of the cross section was evaluated using a series approximation formula of the VV. The arc length was obtained assuming 26 mm offset from the inner surface of VV. The  $n$  is the normal vector which corresponds to the hoop force, and the  $b$  is the binormal vector which corresponds to the toroidal force. The N1~N10 is the name of the nodes and P1~P10 is the name of the elements.

Table 3.7-1 Coordinate of the nodes dividing the TFC.

Coil name	Node name	Coordinate (mm)			Node name	Coordinate (mm)		
		X	Y	Z		X	Y	Z
TC10	N1	1559.8	275.0	0.0	N6	1008.6	177.9	118.6
	N2	1471.5	259.5	316.9	N7	1033.5	182.2	-205.3
	N3	1239.5	218.6	548.1	N8	946.9	167.0	-522.2
	N4	928.6	163.7	641.0	N9	1236.9	218.1	-543.4
	N5	837.3	147.6	402.7	N10	1472.6	259.7	-317.1
TC32	N1	1296.0	809.8	0.0	N6	643.6	402.1	234.8
	N2	1202.7	751.5	284.8	N7	812.7	507.9	-0.3
	N3	1012.3	632.6	493.3	N8	891.7	557.2	-289.4
	N4	768.3	480.1	598.7	N9	1035.6	647.1	-474.9
	N5	540.0	337.4	505.3	N10	1240.9	775.4	-295.7
TC70	N1	477.6	1312.2	0.0	N6	158.9	436.5	136.8
	N2	431.5	1185.6	211.3	N7	197.9	543.8	-83.7
	N3	359.5	987.6	348.7	N8	274.6	754.5	-194.4
	N4	275.5	756.8	404.9	N9	360.5	990.5	-223.3
	N5	191.9	527.3	355.1	N10	446.4	1226.5	-204.6

The results of the EM force analysis are shown in Table 3.7-2, Table 3.7-3, Fig 3.7-4 and Fig 3.7-5. Here, the total force vector was obtained by the volume integral function of the ANSYS/Maxwell. The surface force density was calculated by the coordinate transformation. The  $f_n$  shows the normal component and the  $f_b$  shows the

binormal component. The normal component is the hoop force of the planer coil and the binormal component is difference in force pulled from the left and right coils.

Table 3.7-2 and Fig 3.7-4 show the EMF distribution with operation of the TFC alone for the heat run test etc. The normal force of  $f_n$  may be applied to the coil. It has a component in the direction of expanding the coil and is a self-load. As can be seen from Fig 3.7-3, the outboard side of TC10 and the TC32 and the entire TC70 has convex surface similar to general circular coils. The normal load applied to convex surface may be easily supported only by the tensile stiffness of conductor. The inboard side of TC10 and the TC32 has concave surface. Since the stiffness of the conductor may not be effective for this surface, it is necessary to hold the conductor against the vacuum vessel with clamps. In addition, since the maximum load of 2200N/m is not so large, it is expected that deformation can be easily reduced with the conductor's stiffness or fixing the coil with clamps.

Table 3.7-3 and Fig 3.7-5 show the EMF distribution with operation in which the TFC and the MC current flows at the same time. The polarity of the TFC current is in the direction of increasing the rotational transform of the MC ( $B_{\Phi TC}/B_{\Phi MC} < 0$ ). At this time, the direction of the normal force component is negative, that is, the coil will be pressed against the vacuum vessel. In addition, since the maximum load of 37,000 N/m is not so small, the coils may be displaced in the toroidal and the normal direction to the vacuum vessel. A reinforcing structure is important to reduce the deformation of the coil.

Table 3.7-2 EMF distribution of the TFC in the TFC only operation for the heat run test

Arc length	EM force (N/m)								
	$f_b$ -TC10	$f_n$ -TC10	$ f $ -TC10	$f_b$ -TC32	$f_n$ -TC32	$ f $ -TC32	$f_b$ -TC70	$f_n$ -TC70	$ f $ -TC70
5%	22.1	1381.5	1381.7	-96.1	1186.6	1190.5	21.2	1359.4	1359.6
15%	52.7	1449.2	1450.2	-68.4	1199.2	1201.1	5.3	1252.7	1252.8
25%	194.3	1678.1	1689.3	-49.7	1287.8	1288.8	80.7	1319.1	1321.6
35%	32.5	2119.3	2119.6	-25.4	1711.3	1711.5	64.1	1543.7	1545.0
45%	-157.9	2028.0	2034.1	-226.3	1722.7	1737.5	39.7	1700.4	1700.9
55%	-73.7	1504.2	1506.0	-264.5	1114.4	1145.3	-62.7	1668.5	1669.7
65%	-8.1	2149.6	2149.6	-199.9	838.2	861.7	-74.6	1573.9	1575.7
75%	-53.8	2065.5	2066.2	-104.1	1764.2	1767.3	-49.5	1255.9	1256.8
85%	-47.3	1567.9	1568.6	-82.2	1528.1	1530.3	-36.2	1361.3	1361.8
95%	-12.3	1445.6	1445.6	-89.7	1299.2	1302.3	8.1	1808.1	1808.1
Max(abs)	194.3	2149.6	2149.6	264.5	1764.2	1767.3	80.7	1808.1	1808.1

The TFC currents are -32kAT each without and the MC currents.

The center position of the TFC was evaluated using a series approximation formula of the VV.

The arc length was obtained assuming 26 mm offset from the inner surface of VV.



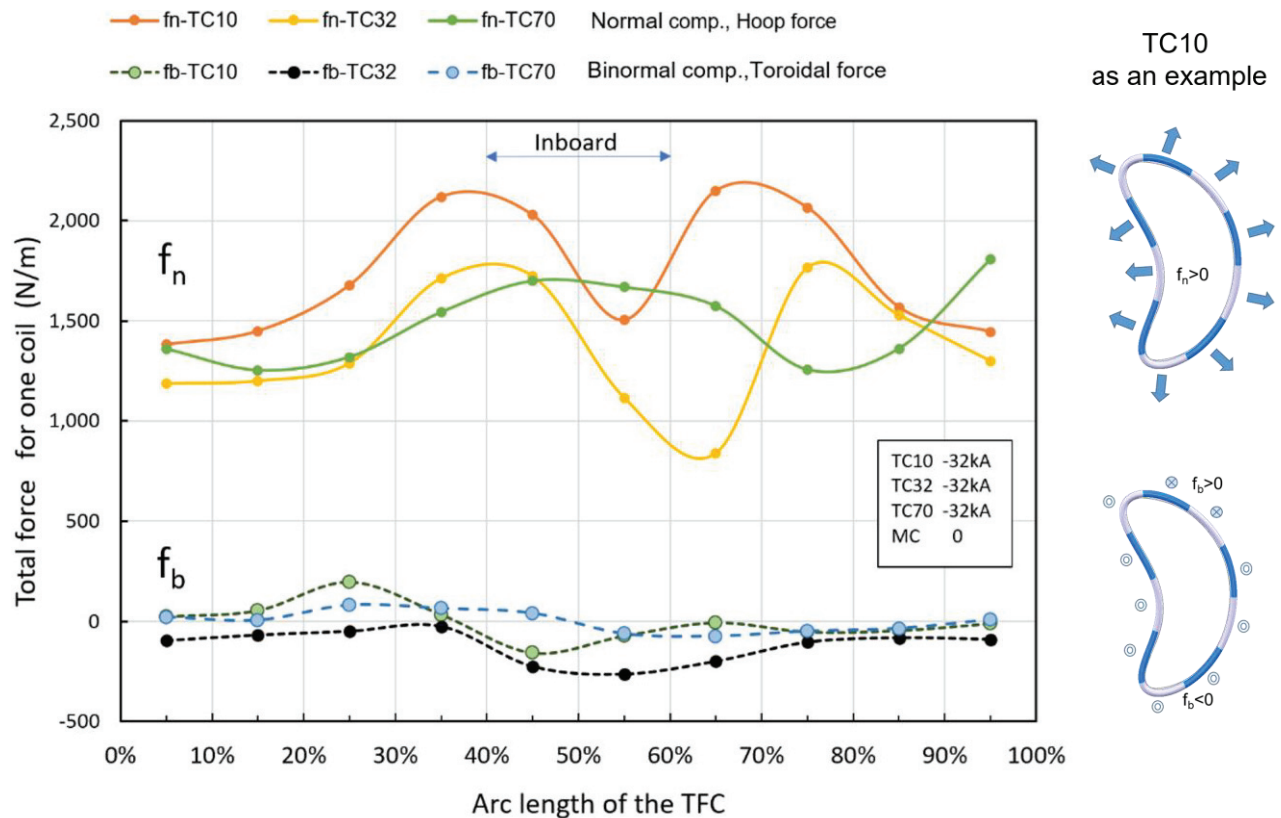


Fig 3.7-4 EMF distribution of the TFC in the TFC only. The polarity of  $f_n$  is positive, that is, the coil tries to expand.

Table 3.7-3 EMF distribution of the TFC with the MC field.

Arc length	EM force (N/m)								
	$f_b$ -TC10	$f_n$ -TC10	$ f $ -TC10	$f_b$ -TC32	$f_n$ -TC32	$ f $ -TC32	$f_b$ -TC70	$f_n$ -TC70	$ f $ -TC70
5%	-1600.7	-27455.4	27502.0	593.2	-26603.2	26609.8	-1037.6	-26168.0	26188.6
15%	-889.0	-24639.0	24655.0	842.9	-24184.0	24198.7	-5808.3	-23947.1	24641.4
25%	1880.5	-23303.5	23379.3	-5808.5	-24482.4	25162.0	-8300.8	-26909.7	28160.9
35%	13021.5	-21744.1	25345.0	-835.9	-22872.6	22887.9	-13446.0	-27470.2	30584.4
45%	13761.9	-32302.3	35111.6	21299.5	-26551.1	34038.6	-5457.1	-25057.5	25644.8
55%	4562.1	-35806.7	36096.2	19056.3	-31316.7	36658.9	18079.7	-25545.6	31296.2
65%	-8766.0	-30788.1	32011.7	6973.1	-33653.5	34368.3	20633.5	-25433.0	32750.3
75%	-7148.5	-22386.9	23500.5	-10576.1	-20277.0	22869.4	7060.1	-30681.7	31483.5
85%	-4476.2	-21906.9	22359.5	-7091.5	-24223.9	25240.6	-5004.5	-24461.2	24967.9
95%	-3793.1	-24761.7	25050.5	-3910.1	-26764.0	27048.1	-4200.7	-19016.8	19475.2
Max(abs)	13761.9	35806.7	36096.2	21299.5	33653.5	36658.9	20633.5	30681.7	32750.3

The TFC currents are -32kAT each, and the MC currents 312.5 kAT each, which generates 1T. The polarity of the TFC current is in the direction of increasing the rotational transform of the MC. The center position of the TFC was evaluated using a series approximation formula of the VV. The arc length was obtained assuming 26 mm offset from the inner surface of VV.

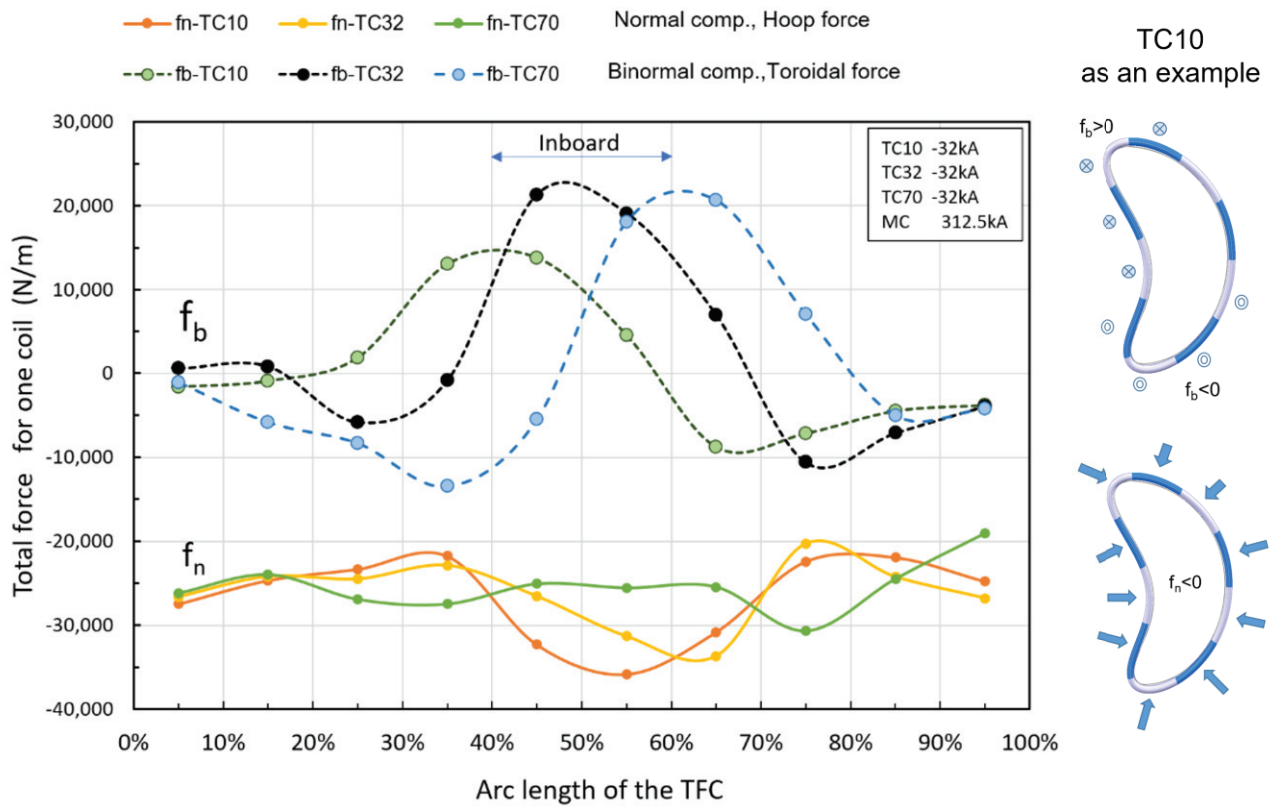


Fig 3.7-5 EMF distribution of the TFC with the MC magnetic field. The polarity of the TFC current is in the direction of increasing the rotational transform of the MC ( $B_{\phi_{TC}}/B_{\phi_{MC}} < 0$ ). The polarity of  $f_n$  is negative, that is, the coils will be pressed against the vacuum vessel. Reversing the direction of the TC current may also result in  $f_n > 0$ , i.e. a force directed away from the vacuum vessel.

### 3.8 Deflection of the TFC

The maximum electromagnetic force of 37,000 N/m may be applied to the TFC as shown in the previous chapter. It is concerned that it will be difficult to withstand the deformation of the coil due to this force with only the rigidity of the coil conductor. A function to fix the coil conductor to the vacuum vessel may be required. We will evaluate the deflection of the conductor when the coil is fixed on the vacuum vessel.

#### 3.8.1 Concept to fix the TFC

Fig 3.8-1 shows the concept to fix the TFC on the vacuum vessel. The electromagnetic force vector  $\mathbf{F}$  has all four components, which are two components of the normal vector  $\mathbf{n}$  (outward and inward) and two components of binormal vector  $\mathbf{b}$  (left and right) with respect to the vacuum vessel. It is unclear which of the four components is the most dangerous, as it varies with driving conditions, type of coil and location. However, we believe that a structure that is effective for all components is necessary in order to conduct various experiments.

We think that the only possibility of having such a function is to fix the 16 cables with clamps on the vacuum vessel. The cable must be clamped on the vacuum vessel with appropriate intervals to suppress the deflection. The clamp pitch for keeping the deflection below the proper value will be determined.



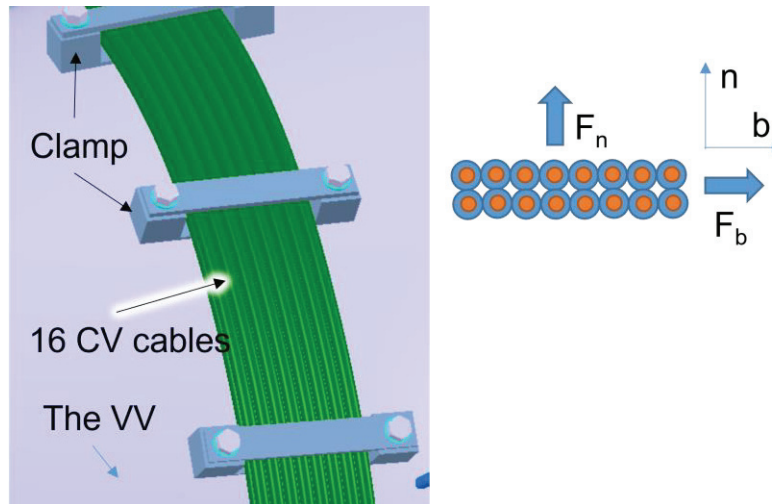


Fig 3.8-1 Concept to fix the TFC. The TFC will be manufactured by winding CV cable with insulator on the vacuum vessel. The cables will be clamped to the vacuum vessel with appropriate intervals to suppress the displacement due to the electromagnetic force. The clamp pitch for keeping the displacement of the conductor below the proper value will be determined.

### 3.8.2 Equivalent Young's modulus of the cable obtained by experiment

The Young's modulus of a cable is required to evaluate the deflection of the cable. However, there is no such data because the cable is a composite of different materials (copper twisted wire, insulation, sheath) and there is no formula to calculate the physical properties for such a complex configuration.

A commercially available standard cable was procured, and the equivalent Young's modulus was experimentally obtained from the relation between load and deflection. Fig 3.8-2 shows the stranded CV cable for the TFC. The CV is an abbreviation for the cross-linked polyethylene insulated poly-Vinyl-chloride sheathed. The CV cable is commonly used in various places as a power cable. Since it bends easily by hand, it is expected that it can be easily wound. In order to measure the relation between the cable deflection and load, we developed a simple instrument as shown in Fig 3.8-3. Using this instrument, we investigated the relation between the deflection, the load and the length of the cable.

Measurement results of the deflection are shown in Fig 3.8-4. The slope of linear equation  $\delta/W$  was approximated in the small  $\delta$  range. The cable may actually be used in the range where the deflection is less than 1 mm. From the slope of linear equation, the Young's modulus was estimated to be 1 GPa by beam model with fixed concentrated load at both ends.

We tried to reproduce the experimental data of 1 GPa with the flexural rigidity of the composite material, but it failed. It seems that the bending rigidity of the stranded wire cannot be expressed by such a simple formula.

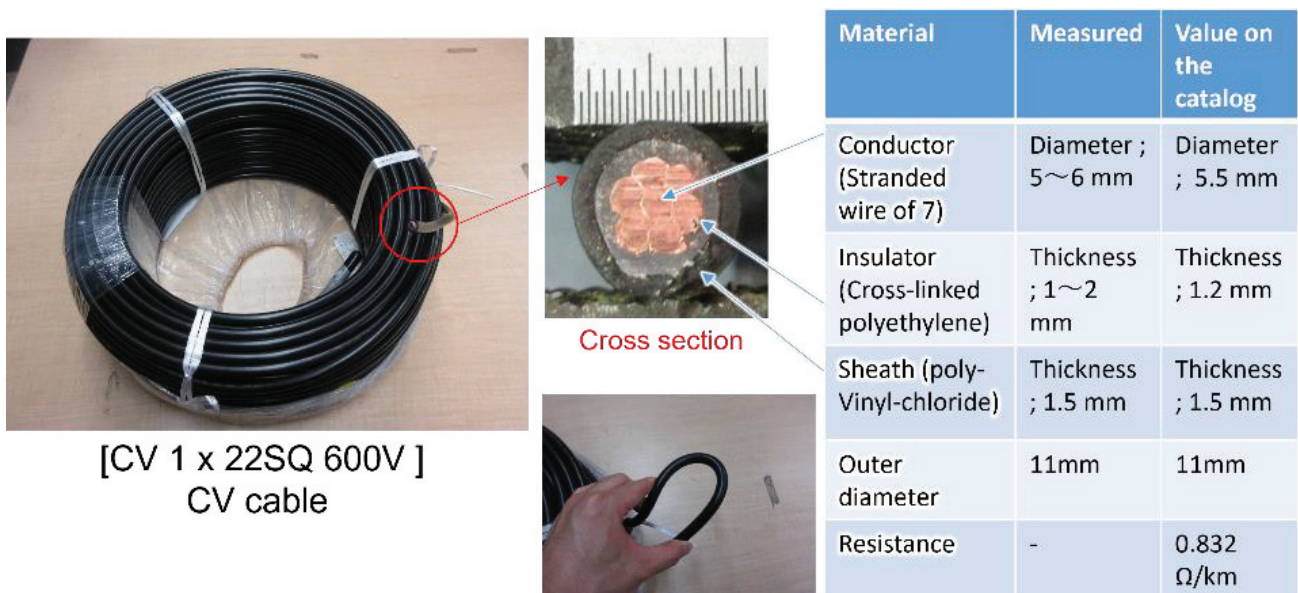


Fig 3.8-2 Stranded CV cable for the TFC. The “CV” is an abbreviation for “Cross-linked polyethylene insulated poly-Vinyl-chloride sheathed”. The CV cable is commonly used in various places as a power cable. Since it bends easily by hand, it is expected that it can be easily wound.

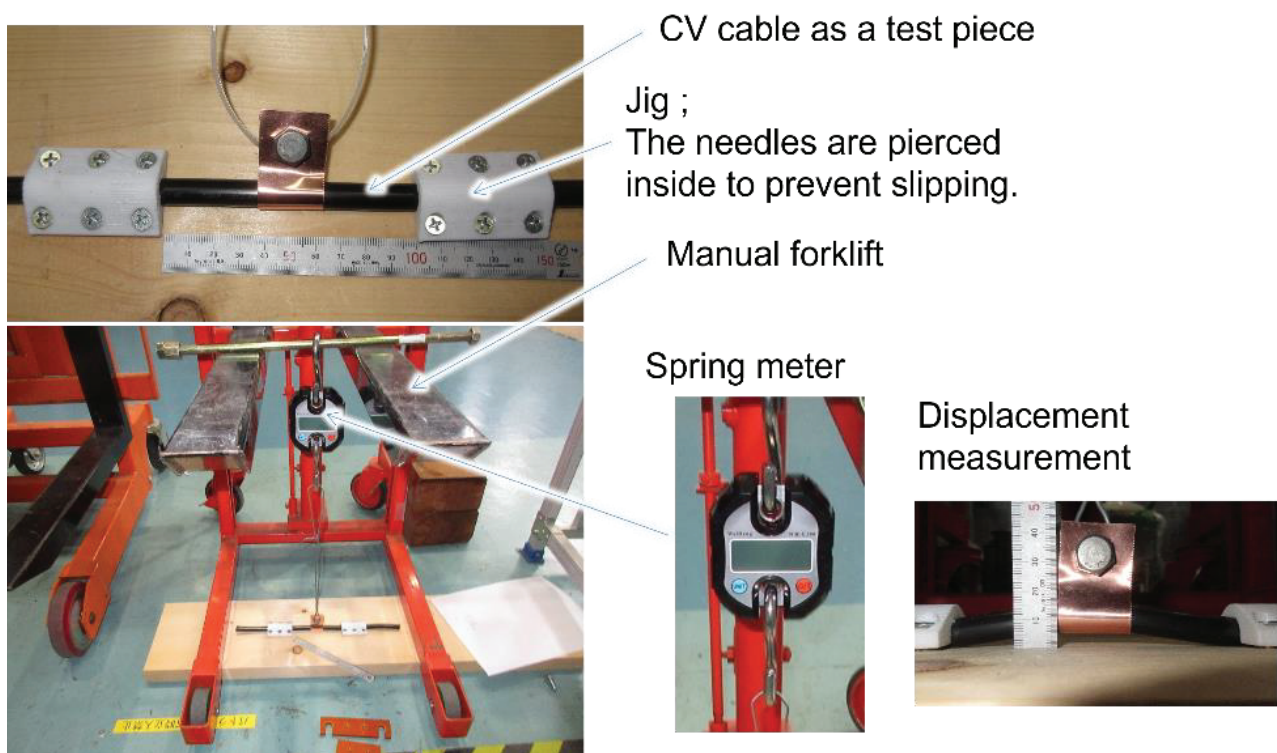


Fig 3.8-3 How to measure the cable deflection. Both ends of the cable were fixed with the jig, and the relation between the deflection (by a ruler), the load (by a spring meter) and the length of the cable (by a ruler) was investigated.

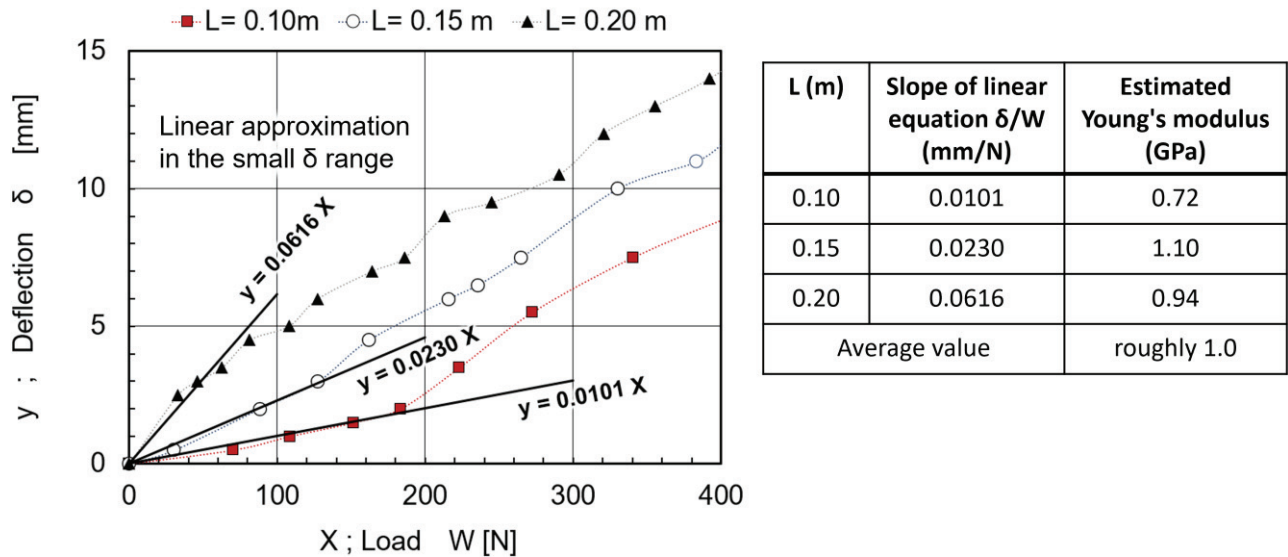


Fig 3.8-4 Measurement results of the deflection and estimated Young's Modulus. The slope of linear equation  $\delta/W$  was approximated in the small  $\delta$  range. The cable may actually be used in the range where the deflection is less than 1 mm. Estimated Young's modulus was obtained by beam model with fixed concentrated load at both ends. We tried to reproduce the experimental data of 1GPa with the flexural rigidity of the composite material, but it failed. It seems that the bending rigidity of the stranded wire cannot be expressed by such a simple formula.

### 3.8.3 Clamp pitch required to reduce the deflection of the cable

The FEM analysis was used to evaluate the relation between electromagnetic force and deflection of the cable. Fig 3.8-5 is an FEM model. The equivalent Young's modular was assumed 1 GPa for the cable and 200GPa for the clamp. We evaluated the relation between the clamp pitch and deflection.

Fig 3.8-6 shows examples of the analysis results. Although the TFC is a collection of 16 cross-section conductors, the contact conditions between the conductors may change the results. Two types of contact conditions between conductors were assumed, and the analysis results were compared. One was the type of AB (All Bonded), where adjacent cables were integrated on the surface and there is no relative displacement. The other was the type of NS (No Separation), where the adjacent cables were in contact, but they may slip with no friction. As the whole coil, the former has a larger rigidity and deformation due to a load may be smaller. The contact condition of the real coil may be estimated to be between the NS and the AB. Fig 3.8-6 shows the deformation with the contact condition of the NS. Results with the contact condition of the AB are not shown. If we change the contact condition, the amount of displacement will change but the shape after deformation is similar. Please understand that the difference will not be identified from displacement diagrams shown in Fig 3.8-6.

Fig 3.8-7 shows the relation between the clamp pitch and the deflection. Calculations were made assuming each of two electromagnetic force components. One was the  $F_n = 2300$  N/m and the other was  $F_b = 1300$  N/m. NS and AB indicate the difference in contact conditions with between adjacent cables. From the figure, it can be seen that the amount of deflection changes about three times depending on the contact conditions. Since the real coil has

large friction between conductors, it is expected to be close to the AB.

The design specification has been defined that the deflection should be less than 1.0 mm in the best case (AB) with a load of the normal component of electromagnetic force  $F_n=2300$  N/m per cable, which is 1/16 of the maximum EM force for the TC32. To satisfy this condition, the clamp pitch must be less than 160 mm, which is equivalent to a clamp separation of 130 mm.

Based on this result, we defined the design value of the clamp pitch as shown in Table 3.8-1. The clamp pitch of 140 mm was designed to satisfy the requirements. The deflection of the cable was estimated between 0.6 mm and 2. mm with  $F_n=2300$  N/m. A worst-case deflection of 2 mm is estimated, but since there is more dimensional margin between the vacuum vessel and the modular coil, it is thought that the TFC will not come in contact with the modular coil.

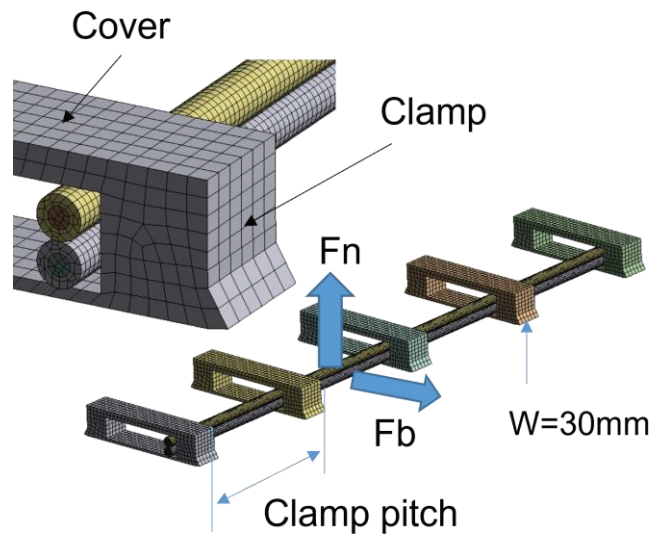


Fig 3.8-5 FEM model to evaluate the cable deflection. The equivalent Young's modular was assumed 1GPa for the cable and 200GPa for the clamp. We evaluated the relation between the clamp pitch and deflection.  $F_n=2300\text{N/m}$  is the maximum load for a cable in the normal direction and  $F_b=1300\text{N/m}$  is the maximum load for a cable in the binormal direction.

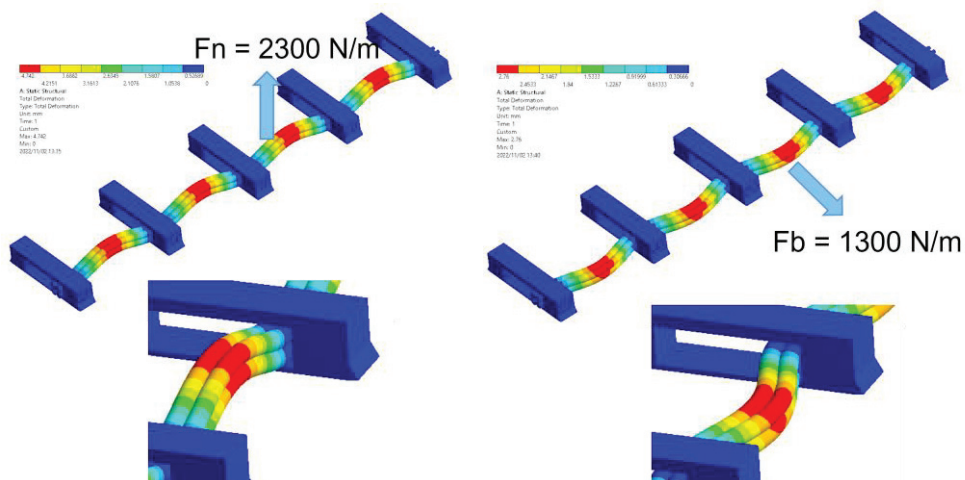


Fig 3.8-6 Deflection of conductor with the clamp pitch = 170mm, the contact condition with conductor is NS, and the electromagnetic force of the  $F_n$  or the  $F_b$  applied.



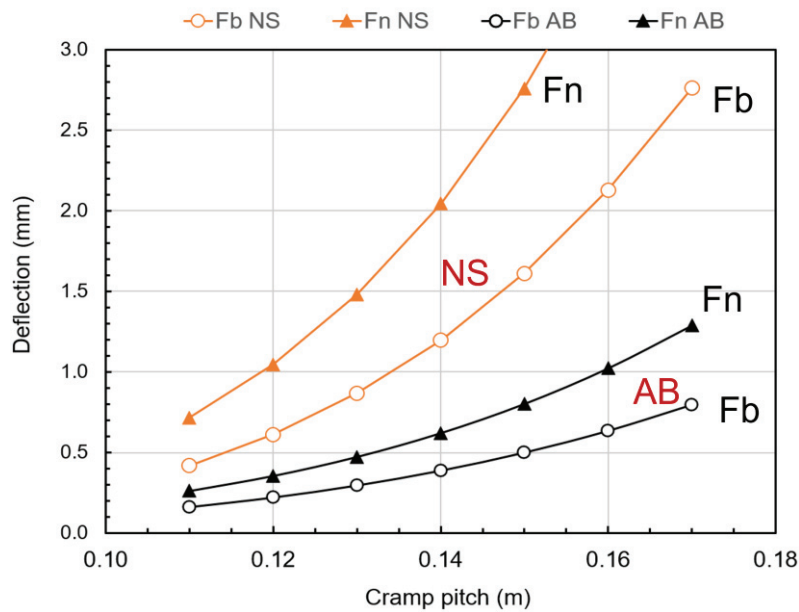


Fig 3.8-7 Relation between the clamp pitch and the deflection. Calculations were made assuming each of two electromagnetic force components. One was the  $F_n = 2300 \text{ N/m}$  and the other was  $F_b = 1300 \text{ N/m}$ . NS and AB indicate the difference in contact conditions with between adjacent cables. The AB is an abbreviation to show “All Bonded” and the NS to show “No Separation”. The deflection of the actual device is estimated to be between the NS and the AB. Since the friction between cables is large, it seems to be close to the AB. The design specification has been defined that the deflection should be less than 1.0 mm in the best case (AB) with the load of  $F_n=2300 \text{ N/m}$  per cable, which is 1/16 of the maximum EM force for the TC32. To satisfy this condition, the clamp pitch must be less than 160 mm, which is equivalent to a clamp separation of 130 mm.

Table 3.8-1 Number of clamps for each TFC

Coil name	Arc length of the TFC (mm)	Clamp pitch designed (mm)	Clamp pitch required(mm)	Number of clamps
TC10	3334	140	< 160	24
TC32	3085	140	< 160	22
TC70	2531	140	< 160	18

The clamp pitch of 140 mm was designed to satisfy the requirements.

The deflection of the cable was estimated between 0.6 mm and 2 mm with  $F_n=2300 \text{ N/m}$ .

A worst-case deflection of 2 mm is estimated, but since there is more dimensional margin between the vacuum vessel and the modular coil, it is thought that the TFC will not come in contact with the modular coil.

### 3.8.4 Design of the clamp to fix the 16 conductors

The design and validation of clamps that secure the 16 conductors should be performed. Especially clamp cover and fillet weld stresses may be excessive. FEM analysis was performed to confirm the validity of their design. Fig 3.8-8 shows the analysis model. The width and height of the clamp groove were required to arrange 16 conductors. Real coils may require extra width near the terminal for conductor transitions, but it was ignored in the

analysis. In order to simulate the stress in the fillet weld, a triangular protrusion was provided at the end of the clamp, which was used as a fixed point in the FEM analysis.

The results of FEM analysis are shown in Fig 3.8-9. The maximum stress on the clamp cover is 87MPa when the normal component of electromagnetic force  $F_n$  is applied. The maximum stress on the fillet welding is 50 MPa when the binormal component of electromagnetic force  $F_b$  is applied. These stresses are reasonable because they are below the design guideline of 137MPa. To satisfy this condition, a thickness of 8 mm for the clamp cover and a fillet weld leg length of 5 mm are required.

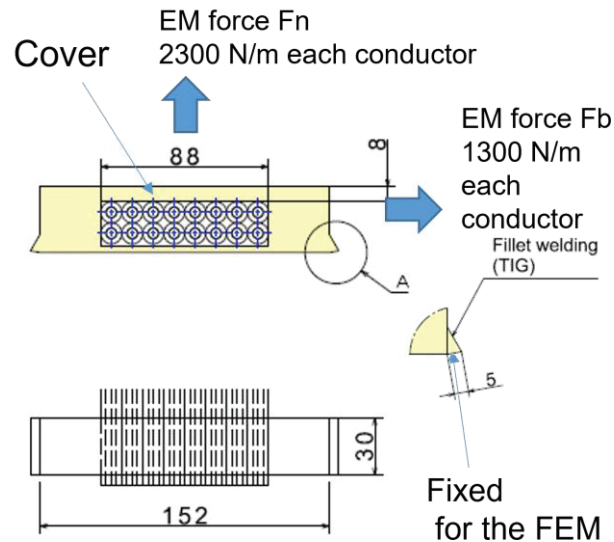


Fig 3.8-8 Structure of the clamp for the analysis. The width and height of the clamp groove are required to hold the conductors side by side. Real coils may require extra width near the terminal for conductor transitions, but it was ignored in the analysis. A large force may be applied to the clamp to stop the conductor from moving due to electromagnetic forces. In particular, the stress on the clamp cover and the fillet weld tends to increase, so their validity evaluation should be done.

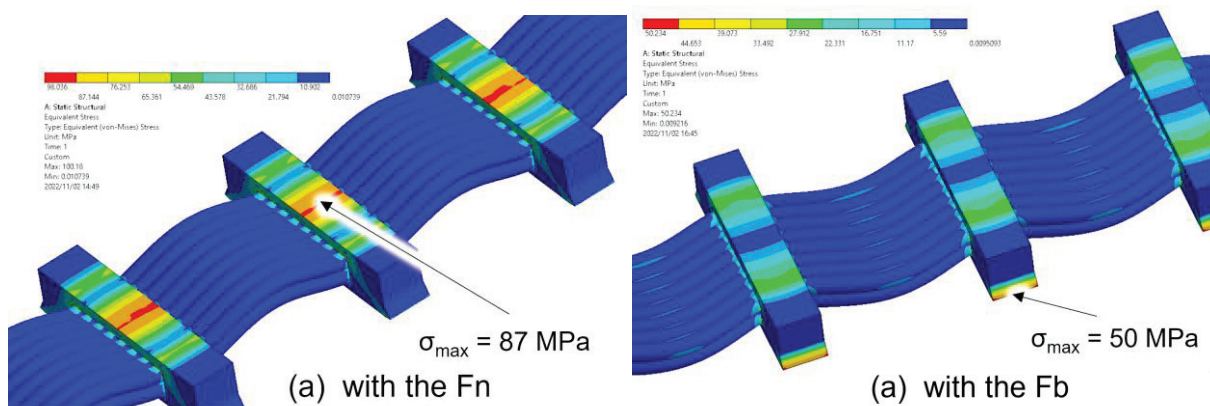


Fig 3.8-9 Von Mises stress on the clamp with the clamp pitch = 140mm. A thickness of 8 mm for the clamp cover is required so that the stress is below the design standard. A fillet weld leg length of 5 mm is required to stop the clamp from trying to move along the vacuum vessel.



## 4 Vacuum vessel

### 4.1 The design goal of the vacuum vessel.

Fig 4.1-1 shows a schematic view of the vacuum vessel. There are various possibilities depending on what is given priority in designing the vacuum vessel. In designing the CFQS, we prioritized the flexibility of the experiments and set the following goals.

1. Reuse as many CHS assets as possible.
2. The tangential NBI of the CHS can be installed for high beta experiment.
3. Provide as many large ports as possible to enhance plasma measurement.
4. Simplify the structure without one turn break since there will be no plasma current.
5. Widen the internal space to increase the freedom in the experiment and allow people to work inside the vacuum vessel. In the future, the following will be done in the vacuum vessel, because it is difficult to access from the outside because mainly modular coils are installed nearby.
  - Welding together split places in the vacuum vessel.
  - Installing measurement equipment like magnetic probes.
  - Installing plates to protect vacuum vessel from heat.
6. Provide inspection process in the middle of the production to reduce the risk of backtracking work.
7. Assemble the main parts in a factory and make sure there will be no interferences or vacuum leaks to minimize field work on the laboratory for cost saving and reduce lead time. If a defect will be found during on-site work, it will take a lot of time and cost to deal with it. Repairing defects found on the site may be exceedingly difficult and will take a lot of time.

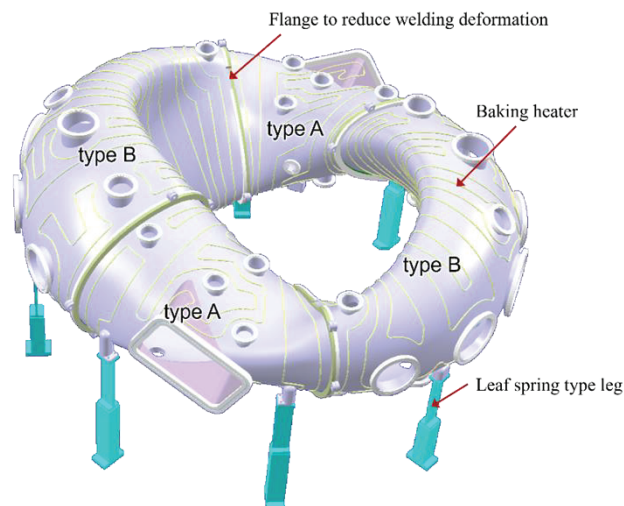


Fig 4.1-1 Schematic of the vacuum vessel

## 4.2 Cross section of vacuum vessel

The shape of inner surface is shown at different toroidal angle in this chapter. Fig 4.2-1 shows how to define the shape. In the figure, symbols have the following meanings.

- a) CFQS-2b40 shows a last closed magnetic surface of the standard equilibrium,
- b) CFQS-2b32 shows a reference surface of the IBD configuration (aspect ratio =3.2),
- c) CCS shows the current carrying surface on which the center of modular coil is placed,
- d) VVIN shows the inner surface of the vacuum vessel.

The other figures show cross sectional shape at different angles. The cross sectional area is larger than that of the cfqs-2b32 reference surface that is the last closed magnetic surface with the aspect ratio of 3.2. It will cover the bundle divertor configuration. The width and the height of the inner surface are both at least 450mm, which is sufficient for people to work inside.

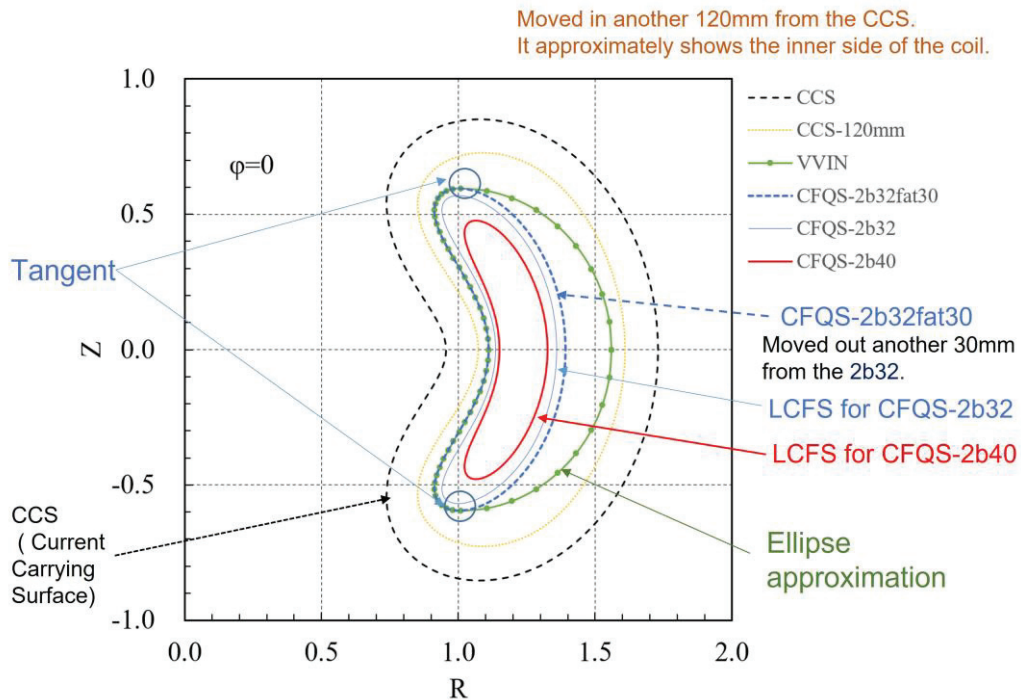


Fig 4.2-1 Drawing with showing how to define the shape of the vacuum vessel.

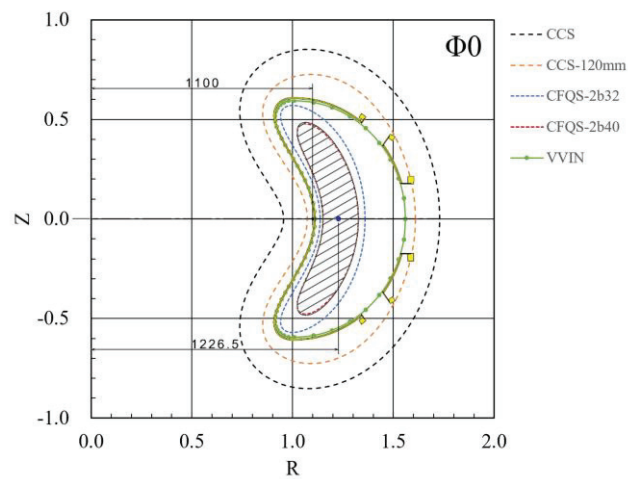


Fig 4.2-2 Shape of main vessel at 0 degrees.

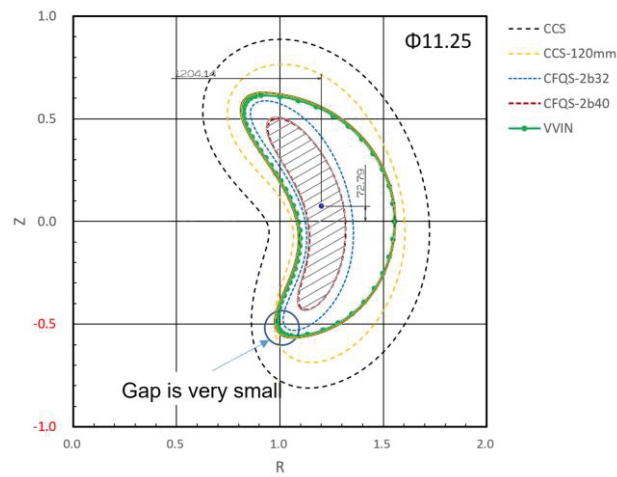


Fig 4.2-3 Shape of main vessel at 11.25 ( $1/8 \times 90$ ) degrees.

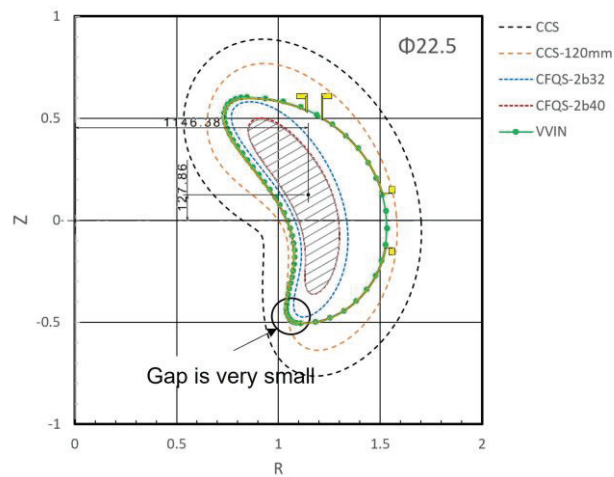


Fig 4.2-4 Shape of main vessel at 22.5 ( $2/8 \times 90$ ) degrees.

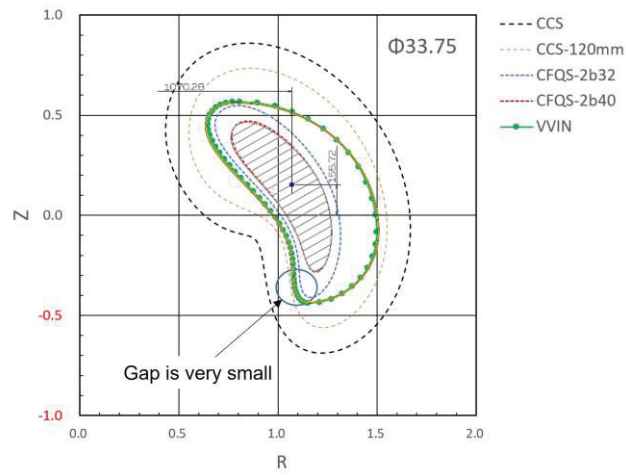


Fig 4.2-5 Shape of main vessel at 33.75 ( $3/8 \times 90$ ) degrees.

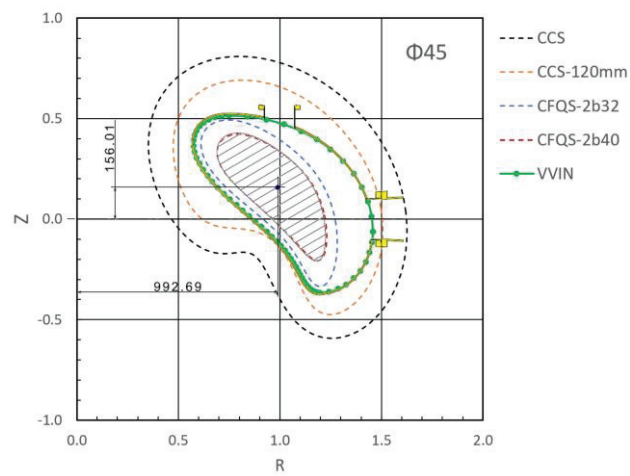


Fig 4.2-6 Shape of main vessel at 45 ( $4/8 \times 90$ ) degrees.

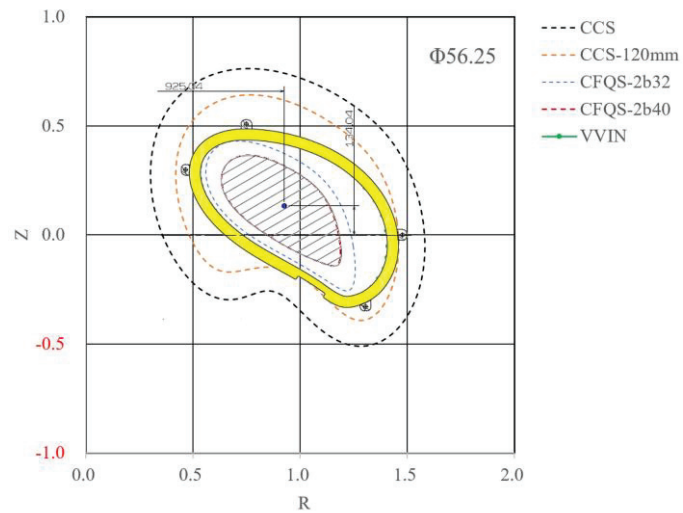


Fig 4.2-7 Shape of main vessel at 56.25 ( $5/8 \times 90$ ) degrees.

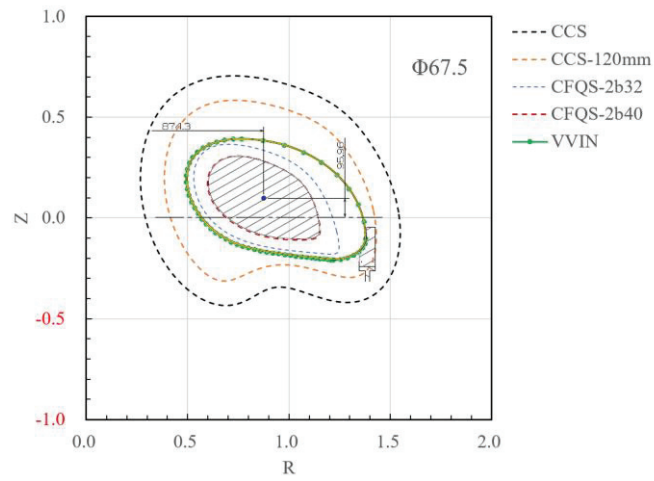


Fig 4.2-8 Shape of main vessel at 67.5 ( $6/8 \times 90$ ) degrees.

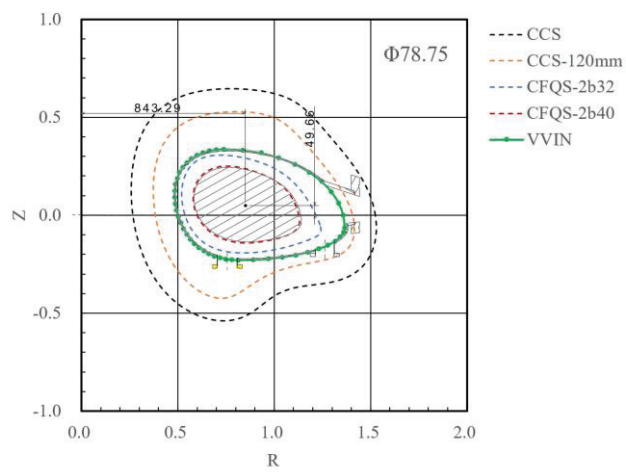


Fig 4.2-9 Shape of main vessel at 78.75 ( $7/8 \times 90$ ) degrees.

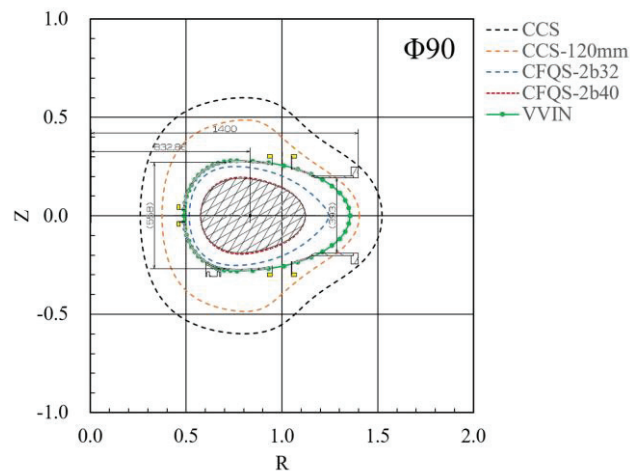


Fig 4.2-10 Shape of main vessel at 90 degrees.

### 4.3 Shape of the vacuum vessel defined by the Fourier expansion

The shape of the vacuum vessel was defined by the nine planes with a 11.25 degree pitch described in the previous section. Since the shape in the middle of the definition plane is required for the design of the measuring device, the coordinates of the vacuum vessel was expressed by the Fourier series of the following equation with the toroidal periodic number of  $N_p=2$ .

$$R_{VV}(\theta, \phi) = \sum R_{VVmn} \cos(m\theta - N_p n\phi)$$

$$Z_{VV}(\theta, \phi) = \sum Z_{VVmn} \sin(m\theta - N_p n\phi)$$

The Fourier coefficients of the vacuum vessel were obtained by the fitting technique. The shape of the inner wall of the vacuum vessel expressed in Fourier series is shown in Fig 4.3-1, and the Fourier coefficient is shown in Table 4.3-1.

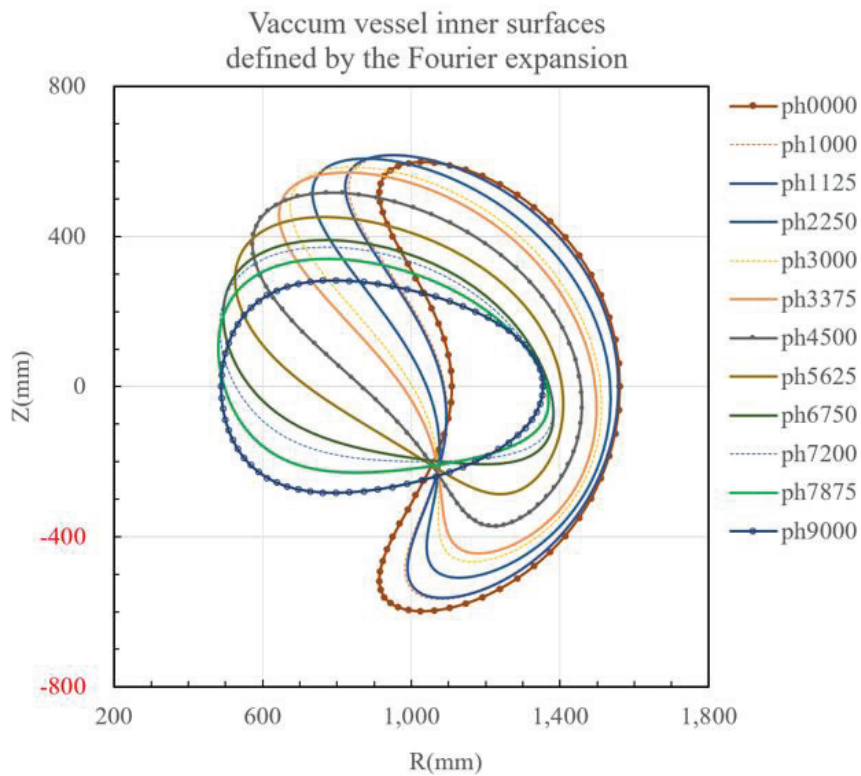


Fig 4.3-1 Inner surface of the vacuum vessel defined by the Fourier expansion of CFQS-VVIN. The ph0000 to ph9000 are the toroidal angles.



Table 4.3-1 Fourier coefficients of  $R_{vv}$ ,  $Z_{vv}$  for the vacuum vessel with  $N_p=2$ .

No	m	n	$R_{vvmn}$	$Z_{vvmn}$	No	m	n	$R_{vvmn}$	$Z_{vvmn}$
1	0	0	1.0288E+00	0.0000E+00	31	3	-3	-2.0327E-04	-3.5711E-04
2	0	1	1.2320E-01	-8.0194E-02	32	3	-2	3.7360E-04	6.7231E-04
3	0	2	-5.9446E-03	1.1979E-02	33	3	-1	5.9290E-04	9.6489E-05
4	0	3	1.7701E-03	-2.9656E-03	34	3	0	-3.0117E-03	2.3752E-03
5	0	4	4.4606E-04	-4.2998E-03	35	3	1	-5.0933E-03	-1.8885E-03
6	0	5	1.4088E-03	-7.5785E-05	36	3	2	-7.1247E-03	4.1531E-03
7	1	-5	3.3737E-03	2.4269E-03	37	3	3	8.3291E-04	5.4984E-04
8	1	-4	-6.0060E-03	-3.0923E-03	38	3	4	1.5480E-03	-2.6492E-03
9	1	-3	7.7172E-03	2.9200E-03	39	3	5	-1.5080E-03	6.0208E-04
10	1	-2	-2.5688E-02	-1.9217E-02	40	4	-5	-2.6041E-05	5.6711E-05
11	1	-1	6.1708E-02	6.2221E-02	41	4	-4	-7.6778E-05	9.0399E-05
12	1	0	3.4249E-01	4.3172E-01	42	4	-3	-5.4953E-05	2.7751E-05
13	1	1	-1.5301E-01	1.0227E-01	43	4	-2	3.6087E-05	-6.5205E-05
14	1	2	1.9211E-02	2.2323E-02	44	4	-1	-1.8630E-04	-9.8974E-05
15	1	3	-9.6336E-03	-1.1164E-02	45	4	0	-5.8879E-04	3.7630E-04
16	1	4	7.6113E-03	6.7501E-03	46	4	1	-8.6959E-05	8.3362E-04
17	1	5	-6.9114E-03	-5.2297E-03	47	4	2	8.3636E-04	-1.6512E-05
18	2	-5	2.6371E-04	7.4712E-04	48	4	3	4.7682E-04	-7.8666E-04
19	2	-4	1.1591E-03	3.9776E-03	49	4	4	-3.2043E-04	3.7849E-04
20	2	-3	-3.0637E-03	-1.7396E-03	50	4	5	8.7689E-05	1.9705E-04
21	2	-2	-5.2165E-03	-1.9762E-03	51	5	-5	-6.6178E-06	6.5772E-06
22	2	-1	1.5203E-02	8.5773E-03	52	5	-4	-5.9262E-06	6.3467E-06
23	2	0	7.9277E-02	2.6113E-02	53	5	-3	-2.5895E-05	7.9294E-06
24	2	1	7.7361E-02	2.2256E-02	54	5	-2	2.7150E-05	-2.0119E-06
25	2	2	2.6689E-02	-7.1380E-03	55	5	-1	1.3339E-05	-3.6589E-05
26	2	3	-9.9115E-03	8.3411E-03	56	5	0	-3.5848E-05	6.2538E-05
27	2	4	3.1837E-03	-3.5510E-03	57	5	1	2.3349E-05	6.4511E-05
28	2	5	1.8954E-04	1.1027E-03	58	5	2	-1.8096E-04	-1.9627E-04
29	3	-5	-1.2095E-03	4.6626E-05	59	5	3	-9.3961E-05	2.0521E-04
30	3	-4	4.0349E-04	4.2148E-04	60	5	4	4.2087E-05	5.7100E-05
					61	5	5	-1.2199E-05	-9.9056E-05

Name of the data is CFQS-VVIN

#### 4.4 Port location and the cross-sectional shape of vacuum vessel at the port

More than 46 large ports with a diameter of at least 114 mm, are provided for heating and measurement. Two of them are large rectangular ports both for a worker to enter and for use in NBI and Thomson scattering.

We examined the location and size of the ports to get large ports. However, small ports with a diameter of 70 or less may not be considered and may be increased further if it will be necessary for the experiment. Table 4.4-1 and Fig 4.4-1 show the purpose and location of the port.

The location of each port and the shape of the vacuum vessel near the port are shown in this section, from Fig 4.4-2 to Fig 4.4-11, for convenience in considering the use of each port.

Table 4.4-1 Port list

No	name	Flange Size	Center Position				Use
			$\Phi$	Height (Z)	Radius (R)	Section	
1	I-090	$\Phi 114$	90	0	450	S05-I	150GHz interferometer
2	I-270	$\Phi 114$	270	0	450	S13-I	Beam dump for Thomson scattering
3	O-000U	$\Phi 203$	0	(55°)	((1424))	S01-U	A spectroscope observing visible light
4	O-000	$\Phi 420$	0	0	1600	S01-O	FIR with mirror
5	O-000L	$\Phi 203$	0	(-55°)	((1424))	S01-L	Mirnov-TA S2,S16
6	O-026	$\Phi 356$	26(150)	0	1570	S02-O	NPA, Tangential view port with CCD camera
7	O-050	$\Phi 305$	50(200)	0	1500	S03-O	Main vacuum pump
8	O-090S	440x680	90	0	1400	S05-O	150GHz interferometer, CCD and NBI
9	O-130	$\Phi 305$	130(200)	0	1500	S07-O	FILD(Sci-type)
10	O-154	$\Phi 356$	154(150)	0	1570	S08-O	Movable limiter
11	O-180U	$\Phi 203$	180	(55°)	((1424))	S09-U	Ti-getter
12	O-180	$\Phi 420$	180	0	1600	S09-O	54.5GHz ECH
13	O-180L	$\Phi 203$	180	(-55°)	((1424))	S09-L	Mirnov-TA S8,S10
14	O-206	$\Phi 356$	206(150)	0	1570	S10-O	2.45GHz ECH
15	O-230	$\Phi 305$	230(200)	0	1500	S11-O	HIBP
16	O-270S	440x680	270	0	1400	S13-O	Thomson,Fluorescent mesh for mapping
17	O-310	$\Phi 305$	310(200)	0	1500	S15-O	VUV, $\mu$ -wave reflectometer, camera for mapping
18	O-334	$\Phi 356$	334(150)	0	1570	S16-O	Tangential view port with CCD camera, Ti-getter
19	U-018	$\Phi 253$	18	630	1180	S02-U	Langmuir probe(Center)
20	U-045	$\Phi 203$	45	560	1000	S03-U	CXS & MSE
21	U-063	$\Phi 152$	63	440	1000	S04-U	
22	U-090	$\Phi 152$	90	320	1000	S05-U	
23	U-102IN	$\Phi 152$	102	280	750	S05-U	Ti-getter
24	U-102	$\Phi 152$	102	220	1250	S06-U	FILD(Sci-type)
25	U-130	$\Phi 152$	130	390	1200	S07-U	FILD(Sci-type)
26	U-198	$\Phi 253$	198	630	1180	S10-U	Langmuir probe(Center)
27	U-225	$\Phi 203$	225	560	1000	S11-U	HIBP
28	U-243	$\Phi 152$	243	440	1000	S12-U	FILD(Foil-type)
29	U-270	$\Phi 152$	270	320	1000	S13-U	
30	U-282IN	$\Phi 152$	282	280	750	S13-U	Ti-getter
31	U-282	$\Phi 152$	282	220	1250	S14-U	Nude and B-A ionization vacuum gauge
32	U-310	$\Phi 152$	310	390	1200	S15-U	Langmuir probe(Edge)
33	L-050	$\Phi 152$	50	-390	1200	S03-L	Visible light (Edge)
34	L-078	$\Phi 152$	78	-220	1250	S04-L	Grow discharge electrode
35	L-078IN	$\Phi 152$	78	-280	750	S05-L	Mirnov-TA (S4,S6)
36	L-090	$\Phi 152$	90	-320	1000	S05-L	Movable limiter
37	L-117	$\Phi 152$	117	-440	1000	S06-L	Gas puff
38	L-135	$\Phi 203$	135	-560	1000	S07-L	CXRS(ref)
39	L-162	$\Phi 253$	162	-630	1180	S08-L	Radiation detectors.E-gun for mapping exp.
40	L-230	$\Phi 152$	230	-390	1200	S11-L	Mirnov-PA
41	L-258	$\Phi 152$	258	-220	1250	S12-L	
42	L-258IN	$\Phi 152$	258	-280	750	S13-L	Mirnov-TA (S12,S14)
43	L-270	$\Phi 152$	270	-320	1000	S13-L	Gas puff
44	L-297	$\Phi 152$	297	-440	1000	S14-L	Rogowski, Diamagnetic
45	L-315	$\Phi 203$	315	-560	1000	S15-L	$\mu$ -wave reflectometer
46	L-342	$\Phi 253$	342	-630	1180	S16-L	SX and ECE

In parentheses in the  $\Phi$  column ; Movement from the center

FILD;Fast Ion Loss Detector

ECE;Electron Cyclotron Emission

Mirnov-TA;Toroidal Array of Mirnov probes

Mirnov-PA;Poloidal Array of Mirnov probes

E-gun;Electron gun

CXS;Charge exchange spectroscopy

MSE;Motional stark effect

HIBP;Heavy Ion Beam Probe

NPA;Neutral particle analyzer

SX;Soft X-ray detector

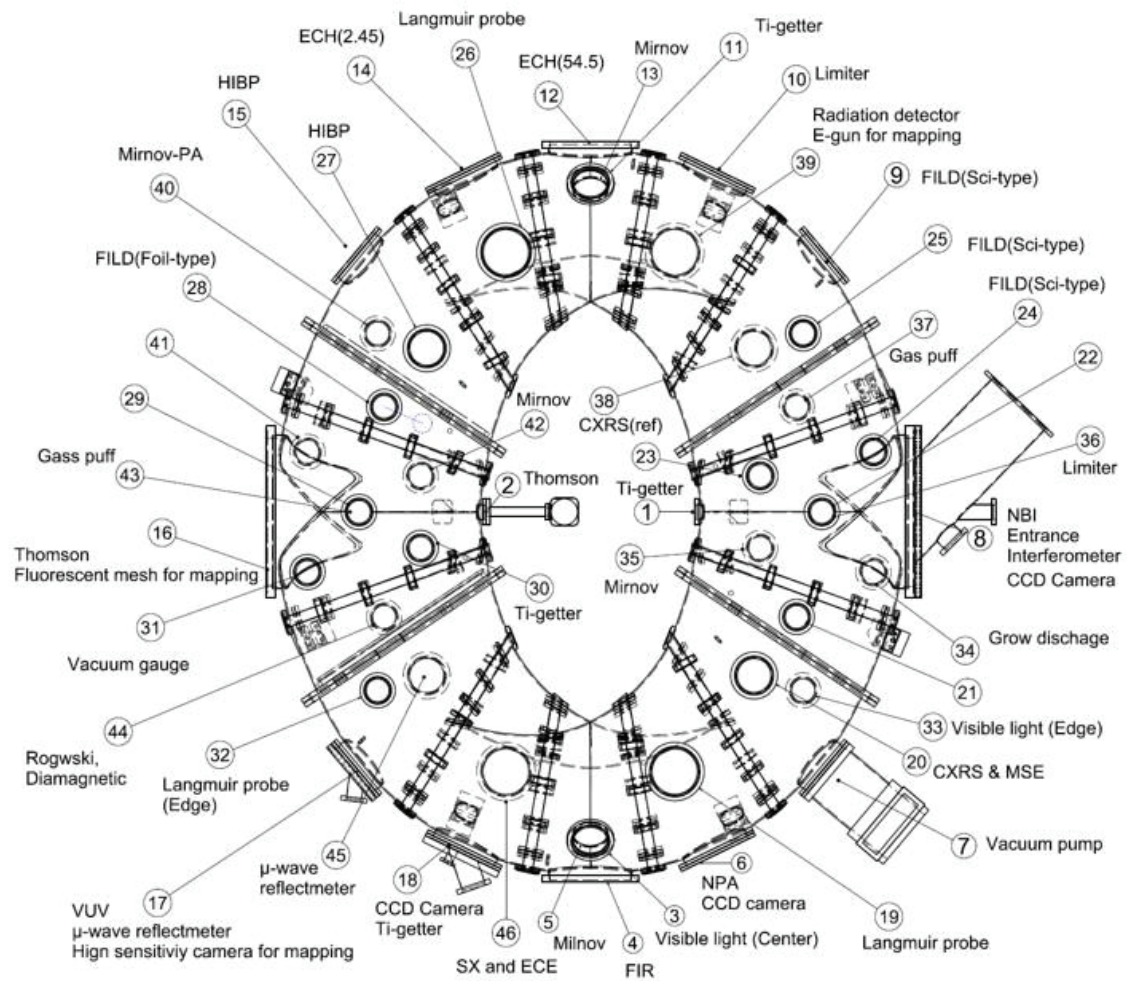


Fig 4.4-1 Port arrangement, it shows the usage of each port.



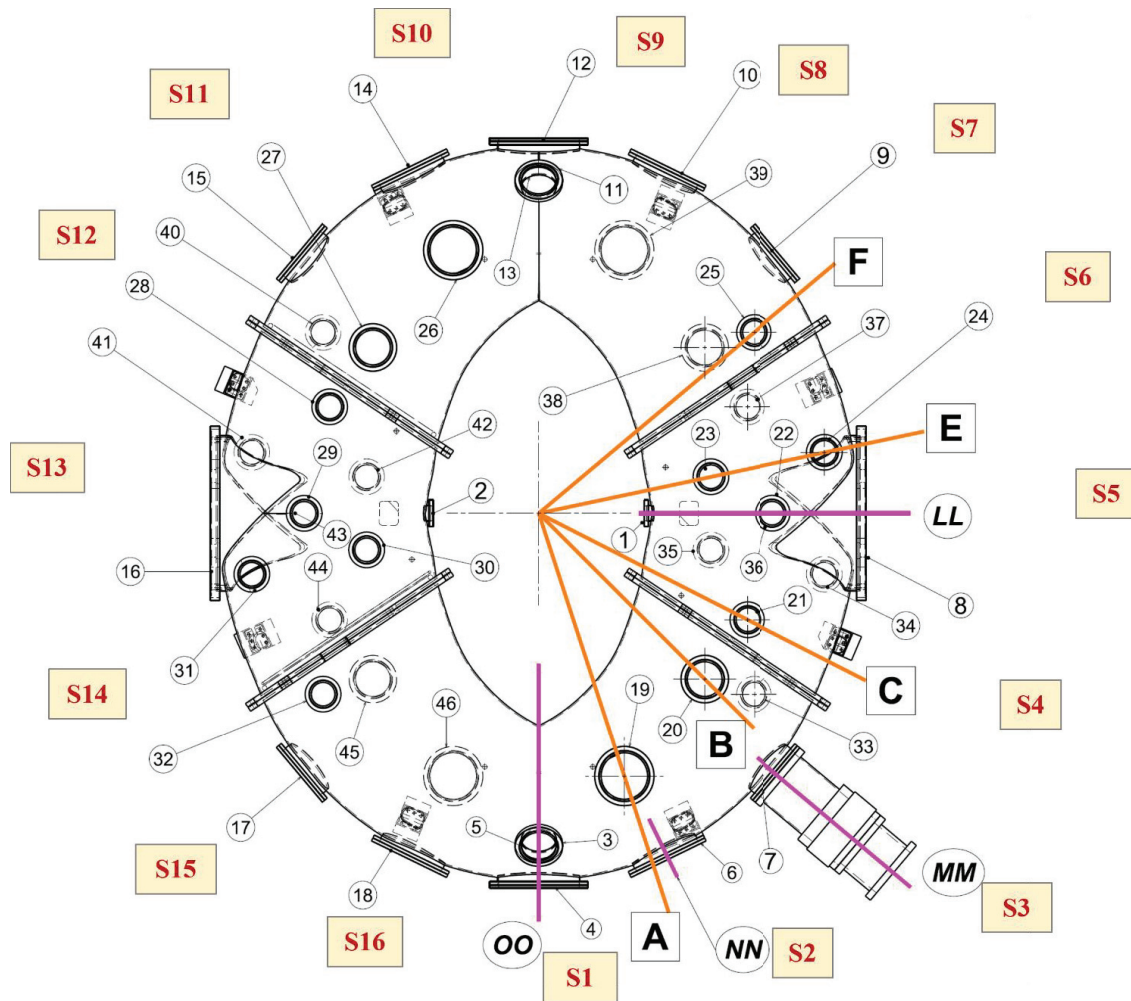


Fig 4.4-2 Position of the cut surface indicating the port arrangement. The S1 to S16 show the section numbers and the (1) to (46) show the port numbers.

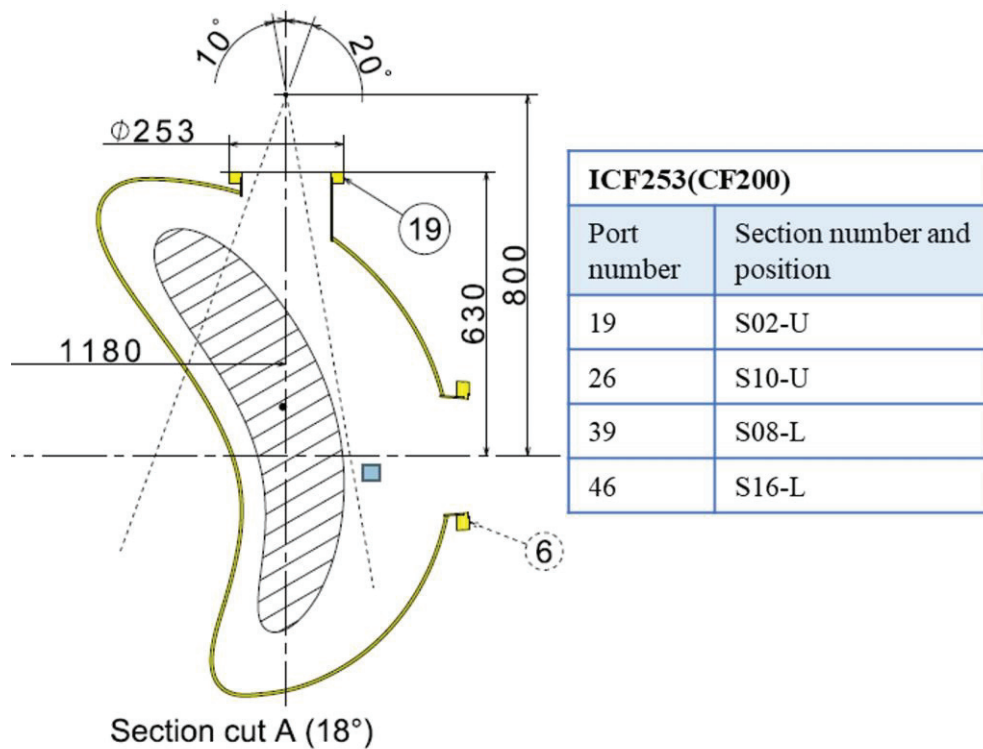


Fig 4.4-3 Port arrangement near the cut surface A. There are 4 ports in the table with the same arrangement. The position of U shows the upper port, L the lower port and O the outside port.

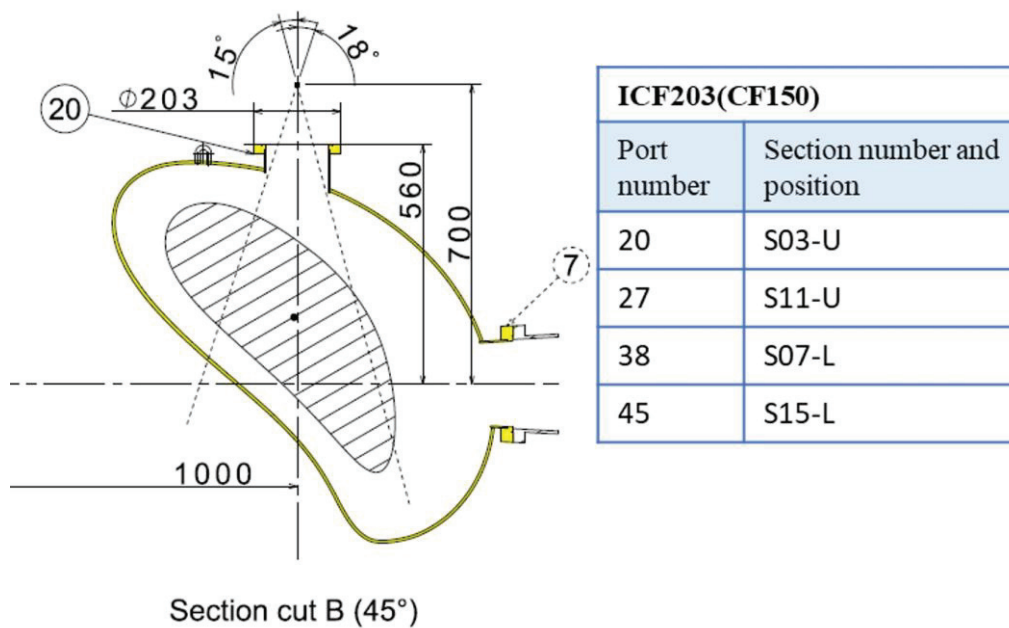


Fig 4.4-4 Port arrangement near the cut surface B. There are 4 ports in the table with the same arrangement. The position of U shows the upper port, L the lower port and O the outside port.

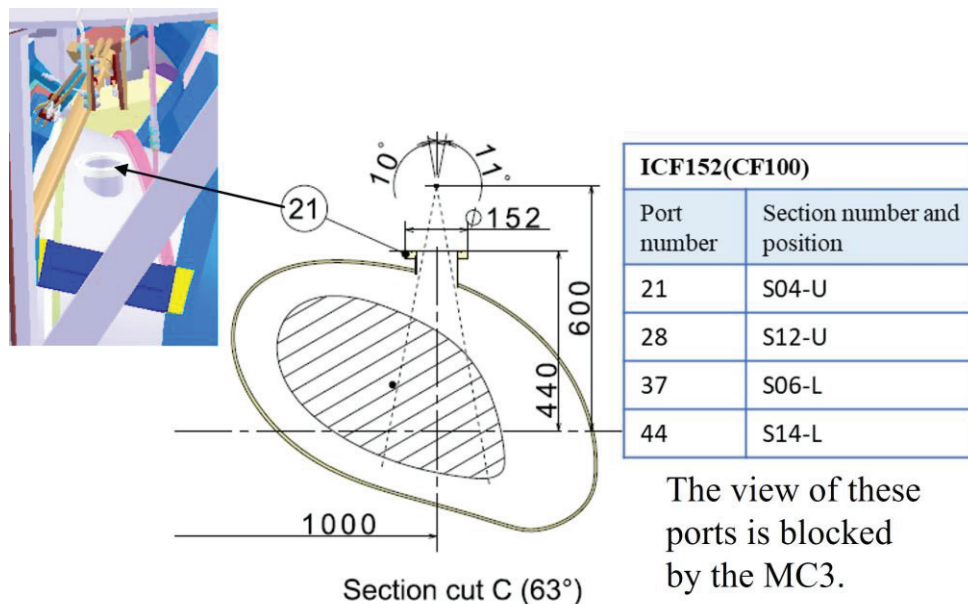


Fig 4.4-5 Port arrangement near the cut surface C. There are 4 ports in the table with the same arrangement. The position of U shows the upper port and L the lower port.

The view of ports 23~42 is blocked by the MC4.

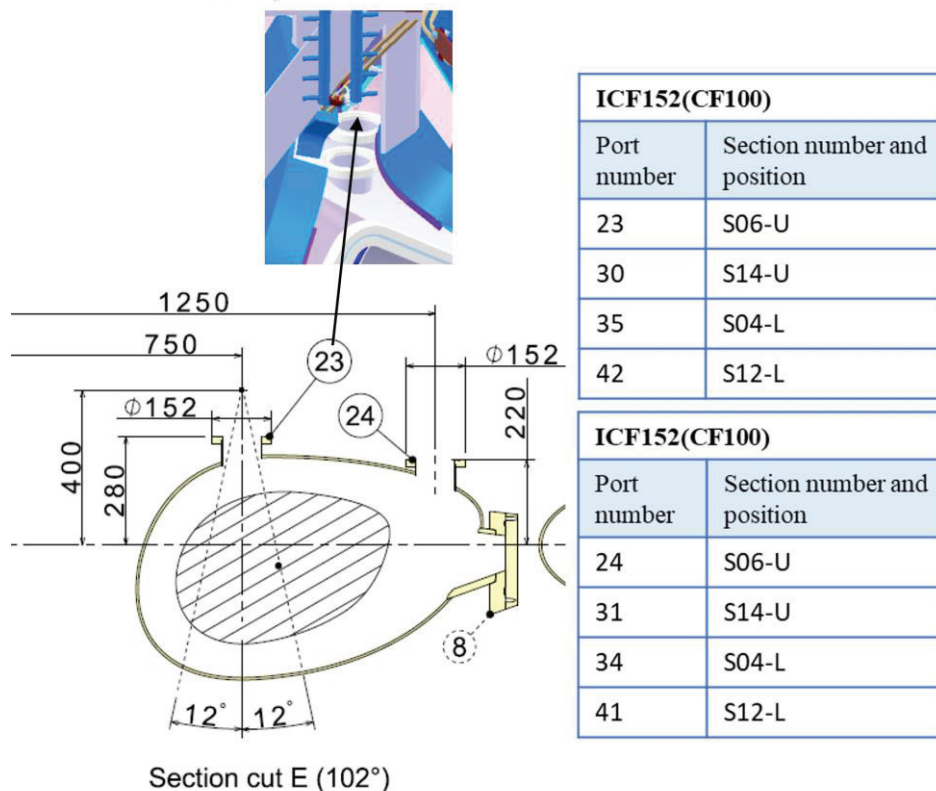


Fig 4.4-6 Port arrangement near the cut surface E. There are 4 ports or 2 ports in the table with the same arrangement. The position of U shows the upper port, L the lower port and O the outside port.



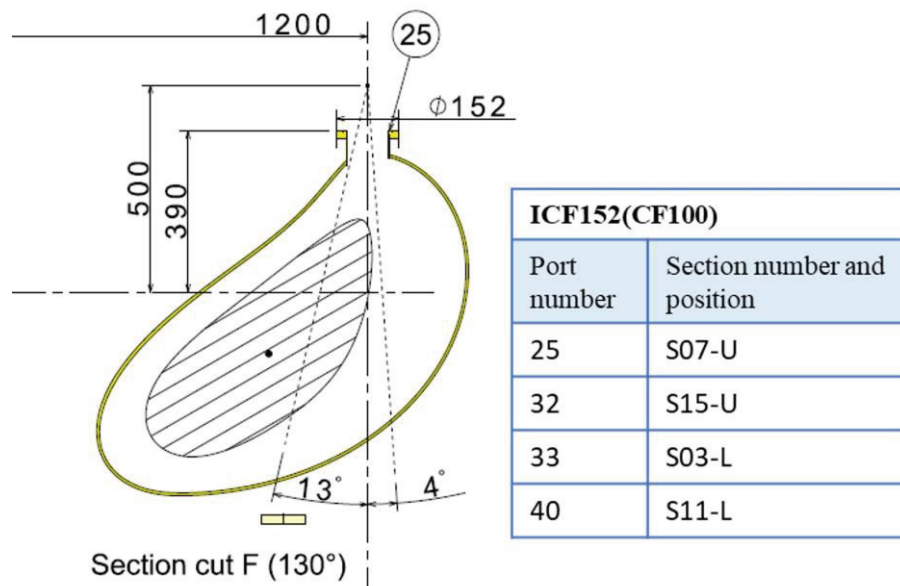


Fig 4.4-7 Port arrangement near the cut surface F. There are 4 ports in the table with the same arrangement. The position of U shows the upper port and L the lower port.

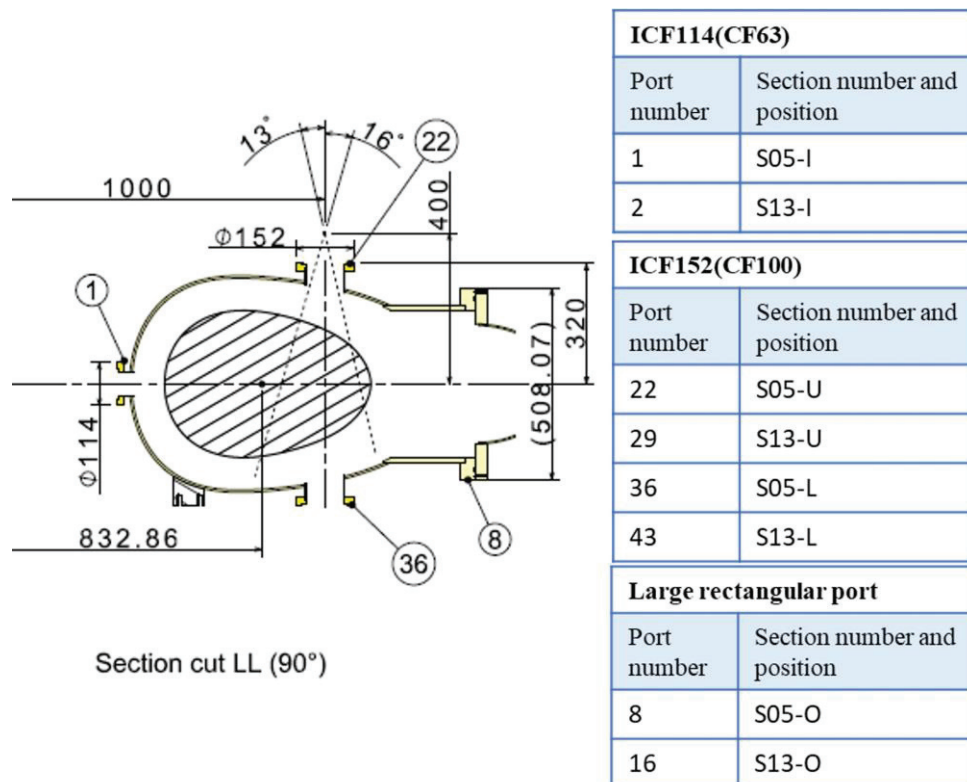


Fig 4.4-8 Port arrangement near the cut surface LL. There are 4 or 2 ports in the table with the same arrangement. The position of U shows the upper port, L the lower port, I the inside port and O the outside port.

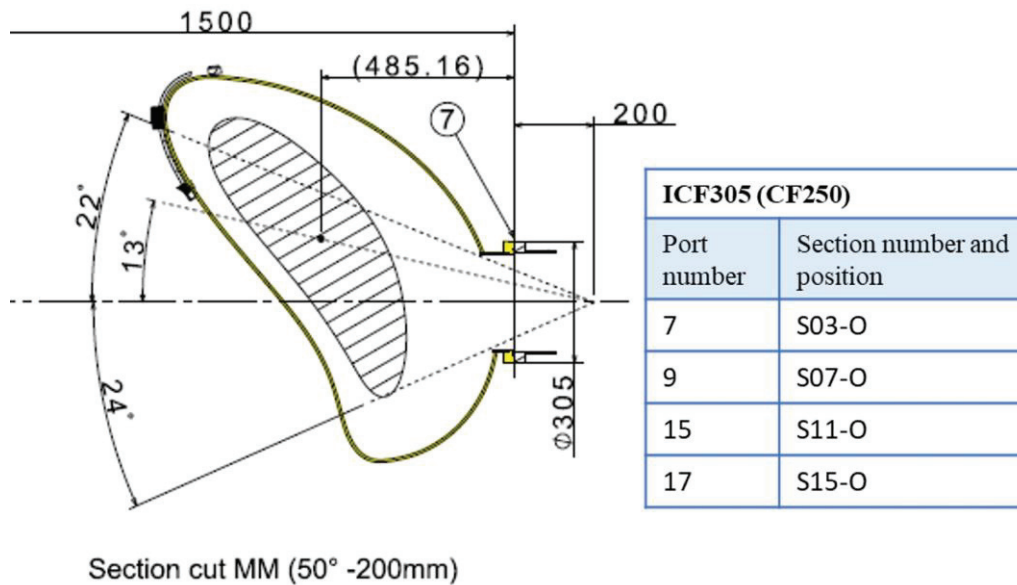


Fig 4.4-9 Port arrangement near the cut surface MM. There are 4 ports in the table with the same arrangement. The position of O shows the outside port.

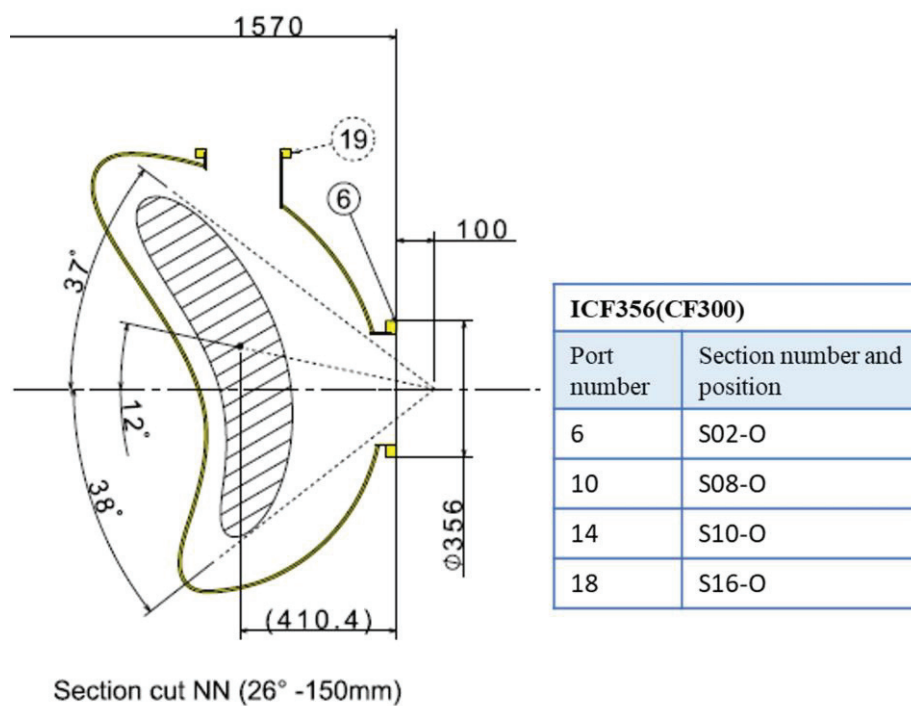


Fig 4.4-10 Port arrangement near the cut surface NN. There are 4 ports in the table with the same arrangement. The position of U shows the upper port, L the lower port and O the outside port.

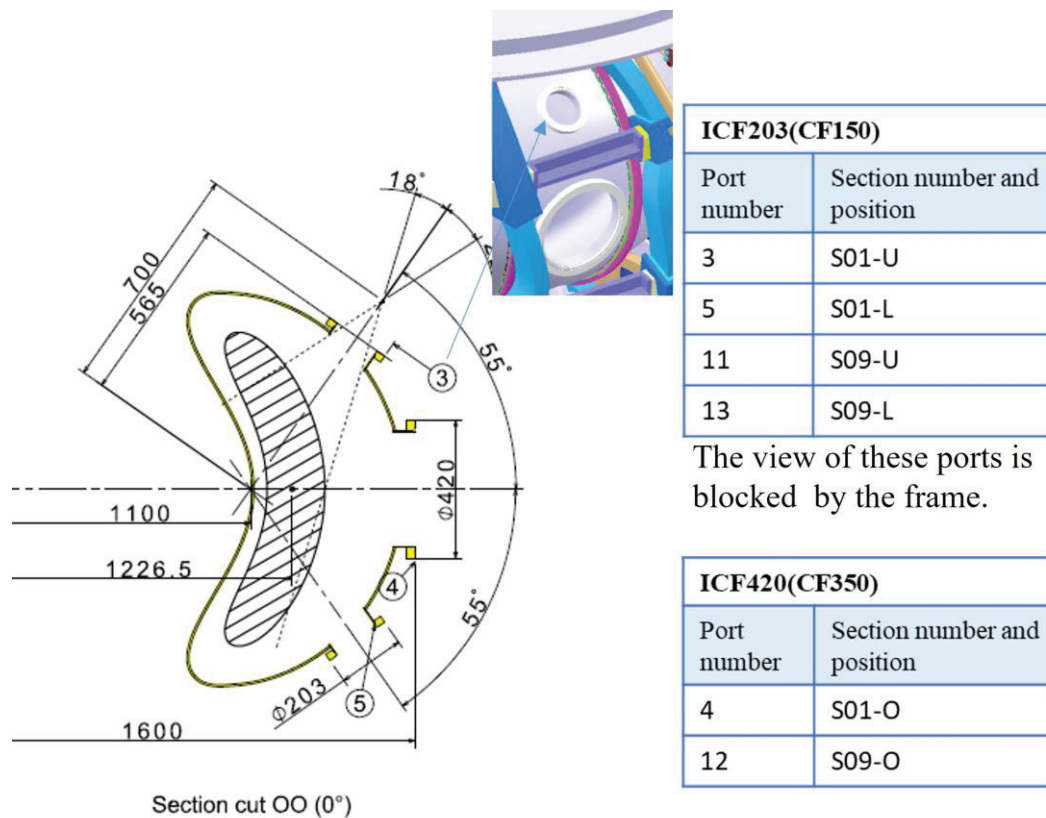


Fig 4.4-11 Port arrangement near the cut surface OO. There are 4 or 2 ports in the table with the same arrangement. The position of U shows the upper port, L the lower port and O the outside port.

#### 4.5 Design of leaf-spring type leg

To absorb the heat expansion deformation by the baking, the vacuum vessel is supported by eight leaf spring type legs. Since the leaf spring type leg will receive a compressive load, it is necessary to evaluate its buckling and bending stress. This chapter introduces the results of analysis and evaluation by hand calculation.

##### 4.5.1 Design values

Design values of the leaf spring are as follows.

Fig 4.5-1 shows the shape of the leaf spring type leg and Table 4.5-1 shows the design value of it. Since the weight of the vacuum vessel is about 4000 kg with extra 1400 kg of additional devices, it is assumed that one leg shares  $F=500\text{ kg}$ . The thermal expansion of the stainless steel is  $1.73 \times 10^{-5}/\text{degree}$ . The major radius increases by an average of 0.17 % ( $=1.73 \times 10^{-5} \times 100$ ) when the temperature of the vacuum vessel rises 100 degrees during baking. Since the major radius of the CFQS is 1 m, the amount of forced displacement is assumed to be  $\delta=2\text{ mm}$ .

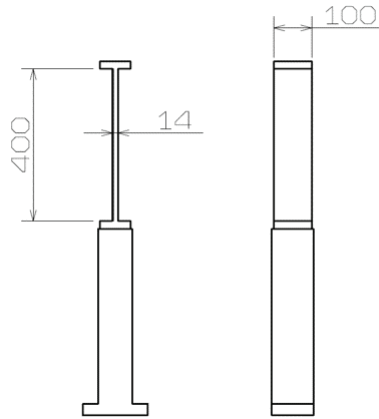


Fig 4.5-1 Design dimension of the leg

Table 4.5-1 Design values of the leaf spring type leg

Item	Symbol	Unit	Value
Beam thickness	$H$	mm	14
Beam width	$B$	mm	100
Beam length	$L$	mm	400
Number of legs			8
Material			SUS316L
Design temperature		Degrees C	150
Young's modulus	$E$	GPa	193
Design allowable stress		MPa	115
Yield stress (150°C)	$\sigma_y$	MPa	173
Support load	$F_s$	N	4903 (500kg)
Forced displacement		mm	2

#### 4.5.2 Buckling load and safety factor

The buckling load is calculated as follows by the formula of the beam fixed at two ends.

$$P_{cr} = \pi^2 EI / (KL)^2$$

$$\sigma_{cr} = \frac{P_{cr}}{A} = \pi^2 E / (KL/r)^2 < \sigma_y$$

where  $P_{cr}$  is the Euler's critical load (longitudinal compression load on column) and  $\sigma_{cr}$  is the critical buckling stress.  $E$  is the modulus of elasticity of column material (Young's modulus), and  $I$  is the minimum area moment of inertia of the cross section of the column,  $L$  is the unsupported length of column.  $K$  is the column effective length factor and  $K = 0.5$  is for the beam fixed at two ends. The value of  $K$  may change in the range of 0.5 to 2 at fixed conditions at both ends. In the worst case, the critical load will be 1/16 times, so it is necessary for the design to have a sufficient margin.  $A$  is the area cross section and  $r$  is the radius of gyration ( $r = \sqrt{I/A}$ ).

Substituting the design values will give us the results in Table 4.5-2. Here, the safety factor 222 is large enough.

Table 4.5-2 Buckling calculation

Item	Symbol	Unit	Value
Cross section	$A$	m <sup>2</sup>	0.014 x 0.1 = 0.0014
Moment of inertia of area	$I$	m <sup>4</sup>	$I = BH^3/12 = 2.29 \times 10^{-8}$ ,
Radius of gyration of area	$r$	m	$r = \sqrt{2.29 \times 10^{-8}/0.0014} = 0.00404$
Effective length factor	$K$		0.5, (Beam fixed on both ends)
Slenderness ratio	$KL/r$		$KL/r = (0.5 \times 0.4)/0.00404 = 49.5$
Critical buckling stress	$\sigma_{cr}$	Pa	$\sigma_{cr} = \pi^2 \times 193 \times 10^9 / 49.5^2 = 777 \times 10^6$
Buckling load	$P_{cr}$	N	$P_{cr} = 777 \times 10^6 \times 0.0014 = 1.089 \times 10^6$
Safety factor	$Safe$		$Safe = P_{cr}/F_s = 1.089 \times 10^6 / 4903 = 222$

### 4.5.3 Bending stress with the forced displacement

The bending stress of beam fixed at two ends can be obtained by expanding the model fixed at one end.

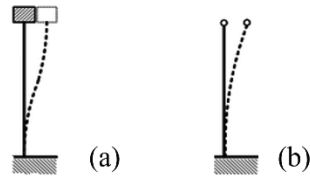


Fig 4.5-2 Bended shape of a beam. (a) a beam fixed at two ends and (b) fixed at one end and other free.

The deflection at the unsupported end of the model (b) in Fig 4.5-2 is calculated as follows.

$$y = \frac{WX^3}{3EI}$$

$$\sigma_b = \frac{M}{Z}$$

$$M = WX$$

where  $y$  is the Displacement at the top of the model (b).  $\sigma_b$  is the bending stress at the fixed end of the model (b).  $W$  is the load at unsupported end of the model (b).  $X$  is the beam length of the model (b),  $E$  is the young's modulus,  $I$  is the moment of inertia,  $M$  is the bending moment at the fixed end of the model (b).  $Z$  is the section modulus of the beam  $= I/(H/2)$ , and  $H$  is the thickness of the beam.

The bending stress of the model (a) is equal to a result with

$$y = 0.5 \times \text{the displacement at the top of the model (b),}$$

$$X = 0.5 \times \text{the beam length of the model (b).}$$

Substituting the design values will give us the results in the table. Here, the safety factor 1.65 is large enough.

Table 4.5-3 Bending stress calculation

Item	Symbol	Unit	Value
Fixed condition			Beam fixed on both ends
Equivalent displacement	$y$	m	$0.002/2 = 0.001$
Equivalent beam length	$x$	m	$0.4/2 = 0.2$
Section modulus	$Z$	$\text{m}^3$	$I/(H/2) = 2.29 \times 10^{-8}/0.007 = 3.27 \times 10^{-6}$
Load at unsupported end	$W$	N	$3 \times E \times I \times y / x^3 = 1655$
Bending moment	$M$	Nm	$W \times x = 331$
Bending stress	$\sigma_b$	Pa	$M/Z = 331/3.27 \times 10^{-6} = 1.013 \times 10^8$
Compressive membrane stress	$\sigma_m$	Pa	$F_s/A = 4903/0.0014 = 3.502 \times 10^6$
Bending plus membrane stress	$\sigma_b + \sigma_m$	Pa	$1.048 \times 10^8$
Safety factor			$\sigma_y / (\sigma_b + \sigma_m) = 1.65$



## 4.6 Eddy current analysis of vacuum vessel

In the CFQS using normal conducting coils, since the energization time of magnetic field coils is limited by the balance between heat generation and cooling performance of coils, the plasma discharge duration is also limited. Hence, the influence of the eddy current generated on the vacuum vessel may be exerted during the plasma discharge.

### 4.6.1 Time constant of eddy current and its effect on plasma discharge.

The eddy current on the vacuum vessel is induced by the current change of the external coil, such as the modular coil, the toroidal field coil, and the poloidal coil. A vacuum vessel in which eddy currents do not flow is preferable because eddy currents disturb the target magnetic field distribution of the external coil, but it is difficult in practice. Therefore, the strategy is to delay the generation of plasma until the induced eddy current decays and its effect can be ignored. To judge whether the strategy is appropriate, the time constant of the eddy current was evaluated by eddy current analysis.

Fig 4.6-1 shows example of the external coil current and the eddy current on the vacuum vessel. The figure below shows the eddy currents when three types of coil current change as the external coil.

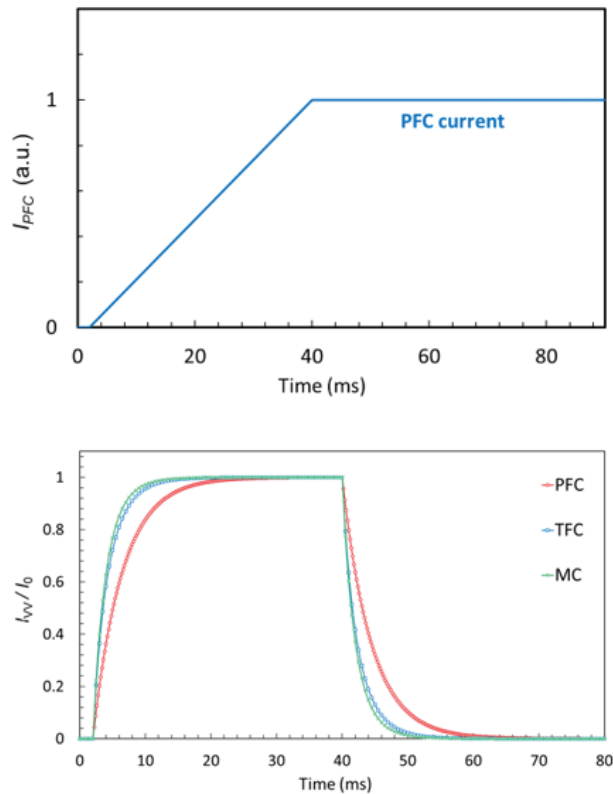


Fig 4.6-1 Example of time-varying waveform of external coil current and total eddy current.

Eddy current is induced on the VV by the current change of the external coils. This relationship can be expressed by the following equivalent circuit equation.

$$L \frac{dI_{VV}}{dt} + RI_{VV} = V = M \frac{dI_{EXT}}{dt} .$$

Where  $I_{VV}$  is a total eddy current induced on the VV,  $I_{EXT}$  is a current flowing in external coil like the modular coil, the poloidal field coil and the toroidal field coil.  $L$  and  $R$  are the inductance and resistance of the VV, respectively, and  $M$  is the mutual inductance between the external coil and the VV. Here, when the right-hand side of the equation is constant, that is, when the external coil current increases / decreases at a constant rate, the equation can be analytically solved, and the eddy current is given by the following equation.

$$I_{VV} = I_0 \left( 1 - e^{-\frac{t}{\tau}} \right) .$$

Where,  $I_0$  is the maximum value of the eddy current, and  $\tau$  is the time constant of the eddy current determined by  $L/R$ .

Note that the time constant  $\tau$  does not depend on the current value of the external coil and can be a useful method for evaluating the time to reach flattop or the remaining time of the eddy current. As shown in Fig 4.6-2, when  $t = \tau$ , the value of the eddy current is approximately 63 % of the maximum value and when  $t = 5\tau$ , the eddy current is approximately 99 % of the maximum value. Therefore, if the plasma discharge is performed at a time of  $5\tau$  or more after the rise of the external coil current, we can consider that the influence of the eddy current is almost eliminated.

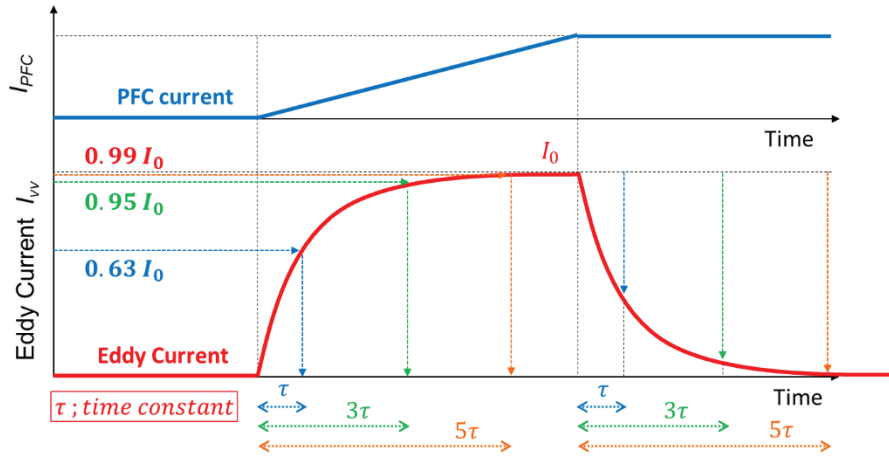


Fig 4.6-2 A time evolution of eddy current due to PFC.

The eddy current induced on the VV by the PFC was calculated by the ANSYS/Maxwell system. The PFC current was set to increase linearly from the time of 2 ms to 40 ms, and then was set to be constant as shown in Fig 4.6-1. Fig 4.6-3 shows the calculation meshes used in the eddy current analysis, in which the transient analysis is required to calculate the eddy current. To accurately evaluate the change in the eddy current, it is necessary to make the time step fine. The time step  $\Delta t$  was set to 0.2 ms in this analysis. A rectangular computational domain was designed to enclose the CFQS VV and the external coils. Also, on its boundaries, the Neumann condition ( $\partial H / \partial n = 0$ ) was applied. To detect the eddy current, fine meshes were arranged in the model. The average element size in the entire model is 36.14mm (minimum element size is 0.03mm). The number of elements is 267,454 for the vacuum vessel, and 501,532 for all elements with the computational domain.

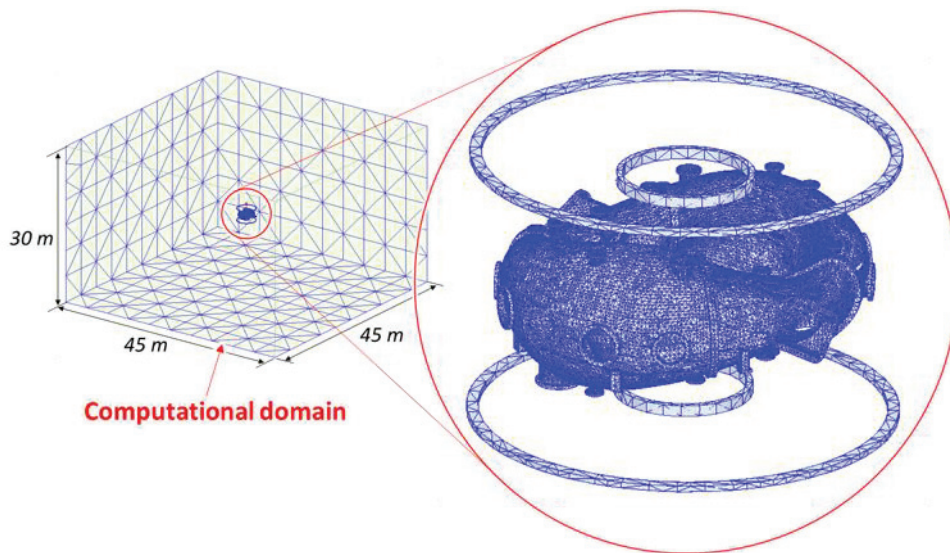


Fig 4.6-3 Computational meshes and computational domain.

Fig 4.6-4 shows a result of the eddy current density distribution at the time of 40 ms with the PFC current change as an example. The eddy current flows counterclockwise as seen from the top, and a high current density appears near diagnostics ports. This result is consistent with the theoretically expected trend. Similar calculations were performed with the TFC and the MC current change, and the results are shown in Fig 4.6-1 which shows the time evolution of the total eddy current on the vacuum vessel.

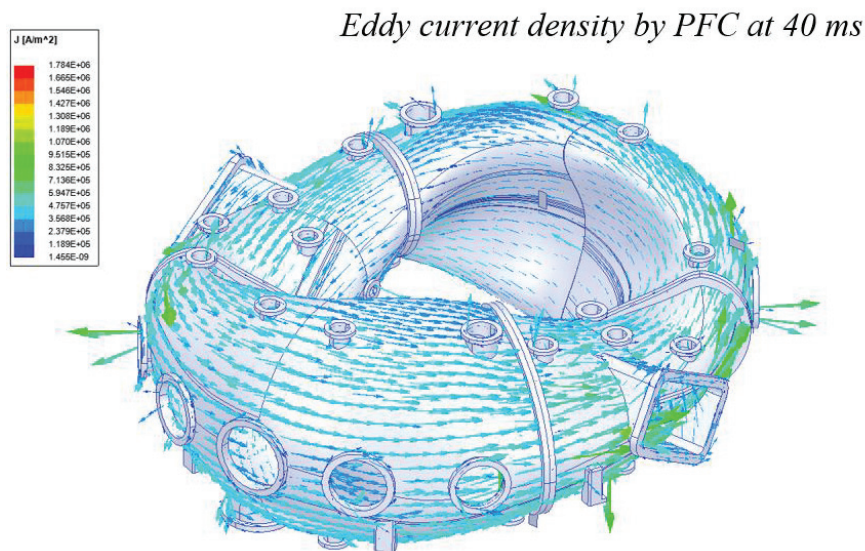


Fig 4.6-4 Distribution of eddy current density on the vacuum vessel with the PFC current change.

To calculate the total eddy current induced on the VV, it is necessary to integrate the current density in a cross-section perpendicular to the direction in which the eddy current flows. Fig 4.6-5 shows integral cross sections for calculating the total eddy current.

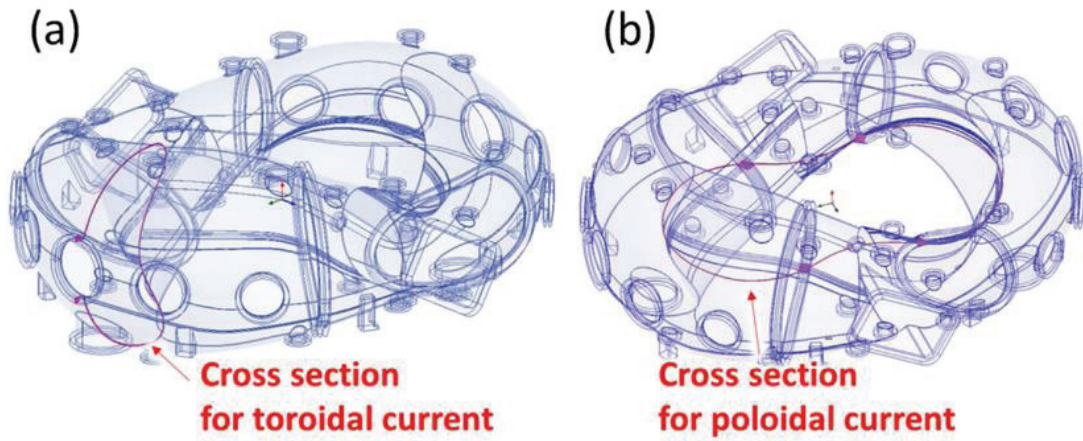
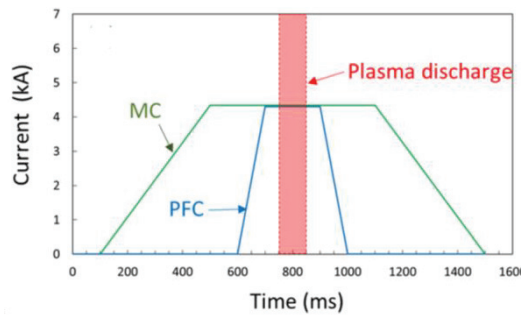
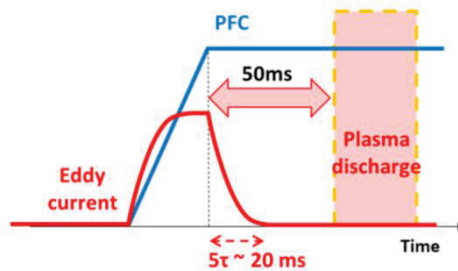


Fig 4.6-5 Cross section to obtain total eddy current. To obtain the total eddy current at each time, the current density was surface-integrated with the cross section indicated by the red line. (a) is for getting the toroidal eddy current induced by the PFC current change, (b) is for getting the poloidal eddy current induced by the TFC or the MC current change

From the current waveform, the time constant  $\tau$  is approximately 4 ms for the PFC and 2 ms for the MC and the TFC, respectively. Fig 4.6-6 shows a typical current scenario of the MC current and the PFC current in the CFQS experiment. The plasma discharge begins to start 50 ms after the PFC current reaches the flat top. The impact on the plasma discharge is expected to be negligibly small, because the eddy current ( $5\tau \sim 20$  ms) is small enough to ignore at the start of plasma discharge.



(a) Coil current waveform



(b) Relationship of the eddy current and the plasma discharge

Fig 4.6-6 Typical scenario of plasma experiment.

Further, the resistance  $R$  and the inductance  $L$  of the VV are obtained by using the time constant and stored magnetic energy from the result. To obtain a resistance of the VV in the toroidal direction, which is called the one-turn resistance, simple electrical circuit equation is used. Here, the magnetic energy  $U_M$  is given by the equation,

$$U_M = \frac{1}{2} L I_{vv}^2 = \frac{1}{2} \int \mathbf{B} \cdot \mathbf{H} dV,$$

where, B and H are integrated over the entire analysis region in ANSYS/Maxwell. Since  $I_{vv}$ ,  $U_M$ , and  $\tau$  are known, the resistance R and the inductance L can be calculated by the following equations.

$$L = 2U_M / I_{vv}^2,$$

$$R = L / \tau.$$

The resistance and inductance of the CFQS VV in the toroidal direction can be estimated to be 0.4 m $\Omega$  and 1.8 $\mu$ H, respectively, from the eddy current analysis with the PFC current. And those in the poloidal direction are 0.058 m $\Omega$  and 0.14  $\mu$ H, respectively, from the eddy current analysis with the MC current.

In a medium-sized tokamak, a Joule heating is required during experiment. In general, a one-turn voltage of the VV is applied to be about 10V for the Joule heating. If the one-turn resistance is 0.4 m $\Omega$ , current over 10 kA may flow. In this case, a one-turn break, or a bellow is required to increase the resistance. However, since we do not conduct the Joule heating in the CFQS, there is no need to consider the one-turn break or bellows. This result will contribute to the reduction on the VV construction costs.

#### 4.6.2 EM force on the vacuum vessel

Electromagnetic (EM) force is generated on the VV by the interaction of the eddy current and the magnetic field. The effect of the EM force is evaluated by structural analysis. Major component of the eddy current can be classified into a poloidal current and a toroidal current. The MC induces the former and the PFC the latter. The TFC current also induces a poloidal eddy current, but since its magnetomotive force is smaller than that of MC, it will be ignored below.

The typical current scenario of the PFC and the MC as shown in Fig 4.6-6 was assumed in this analysis. The current change rates of the MC and the PFC are 10.75 kA/s and 43 kA/s, respectively. The maximum current of the MC is 4.3 kA with 72 turns. Regarding the PFC, the maximum current is 4.3 kA with 32 turns. The EM force under this current scenario were investigated by using ANSYS Maxwell. The time step  $\Delta t$  was set to 1ms in this analysis.

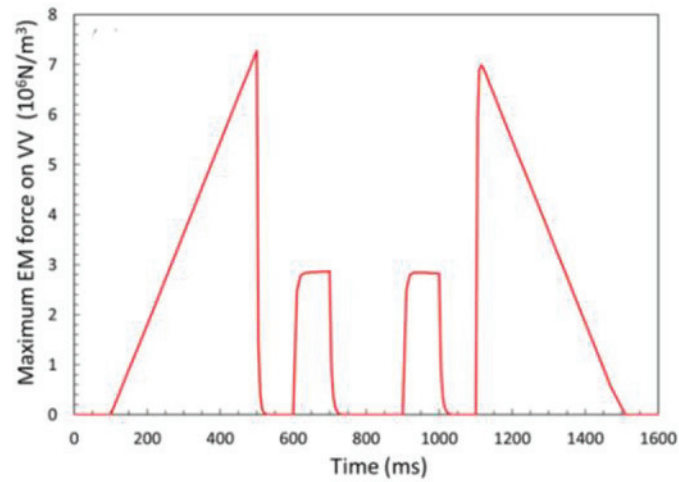
Fig 4.6-7(a) shows the time evolution of the maximum EM force per volume (N/m<sup>3</sup>) on the VV under the typical current scenario mentioned above. The EM force increases linearly with the rise of the MC current and decreases linearly with the fall of the MC current, since the eddy current induced by the MC is almost constant. We find two peaks of the EM force at 500 ms and 1,100 ms. We also found that the directions of the EM force at two peaks are opposite as shown in Fig 4.6-7(b) and (c), at 500 ms is more dangerous since the direction of force the same as the direction of vacuum pressure.

The EM force is generated again with the rise of the PFC current. We find that the EM force by the PFC is smaller than that of the MC.

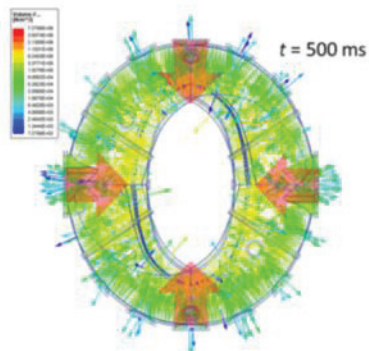
The force in this analysis can be converted into the EM pressure on the VV. The EM pressure is about 0.4 atm



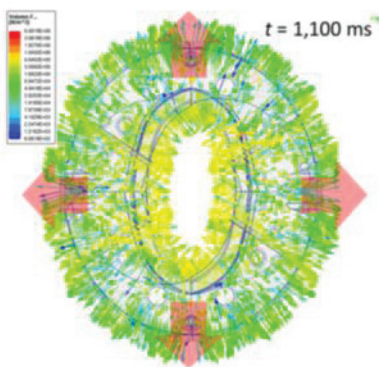
in consideration of the thickness of the stainless-steel plate of 6 mm. Although the EM pressure is lower than the atmospheric pressure (1 atm), it is not a negligible value.



(a) Time evolution of maximum EM force



(b) EM force distribution at 500 ms



(c) EM force distribution at 1100 ms

Fig 4.6-7 Time evolution of EM force on the VV under the typical scenario.



### 4.6.3 Inductive heating of the vacuum vessel

Gases such as nitrogen, oxygen, hydrogen, water vapor, and carbon dioxide are adsorbed on the inner wall of a VV under the atmospheric pressure, and these adsorbed gases are released as outgas from a VV inner wall during the vacuum pumping. Since these outgases hinder the high vacuum pumping process, it is necessary to heat up the entire VV by heaters such as tape-shaped heaters around the outer wall of the VV in general, and to release the adsorbed gas attached to the inner wall. Regarding a baking method for the CFQS VV, usage of an induction heating with an eddy current generated in the VV has been proposed. 16 MCs are connected in a series and an AC is applied to the MC to generate heat by resistance loss of eddy current generated in the VV. We must check the feasibility of adopting the induction heating in the CFQS from the engineering point of view.

In this analysis, the AC analysis is required to calculate the heat generation of the CFQS VV by the induction current induced by the MCs. In general, when an AC flows through a conductor, a skin effect appears in which the current density is high at the surface of the conductor and gradually decreases with distance from the surface. If the skin depth  $\delta$  is smaller than the thickness of the VV (6 mm), it can be considered that the eddy current concentrates on the VV surface. In this case, since a layered thin and fine mesh is required on the surface of the VV even in the FEA, the skin depth must be considered in advance. Here, skin depth  $\delta$  can be calculated by the following equation,

$$\delta = \sqrt{\frac{2}{2\pi f \mu_r \mu_0 \sigma}} \quad ,$$

where  $f$  is the AC frequency,  $\mu_r$  is the relative magnetic permeability,  $\mu_0$  is the vacuum magnetic permeability, and  $\sigma$  is the electric conductivity of the VV. When the skin depth is calculated using this equation, for example in the case of  $f = 2$  kHz, the skin depth  $\delta$  is approximately 9 mm. Therefore, since the skin depth is larger than the plate thickness of the VV, we considered that the current concentration due to the skin effect does not occur on the CFQS VV surface.

Fig 4.6-8 shows the heat generation of the CFQS VV with the current value and AC frequency of MC changing was investigated by using ANSYS Maxwell. The Root Mean Square (RMS) value  $I_{AC}$  of input current in a conductor was changed from about 7 A to 21 A, and the AC frequency was investigated at 500 Hz, 1 kHz, 1.5 kHz, and 2 kHz. Fig 4.6-9 shows an example of the heat distribution of the VV obtained by this analysis in the case of  $f = 1$  kHz and  $I_{AC} = 7$  A.

The heat generation is more strongly dependent on the current value than the AC frequency. Here, the heat generation required for baking in the CFQS VV is 25 kW. This value is determined based on the actual value of VV baking system of CHS which has a similar size to the CFQS. In this case, the current required for the CFQS VV baking can be obtained to be about 18 A. The voltage applied in the MC is obtained by this current value  $I_{AC}$  and AC resistance  $\omega L$  as follows.

$$V_{MC} = I_{AC} \cdot \omega L,$$

where  $\omega$  is the angular frequency represented as  $2\pi f$ . The inductance  $L$  of the MCs connected in series was calculated to be about 0.3 H by using ANSYS Maxwell. Substituting  $I_{AC} = 18$  A, and  $f = 1$  kHz, the applied voltage on the MC is obtained to be about 34 kV.

As a result, this voltage value exceeds the operation voltage of DC 2.4 kV. Therefore, we found that the

induction heating method could not be adopted in the CFQS. An alternative method should be considered as a next option, for example, the sheathed heater system.

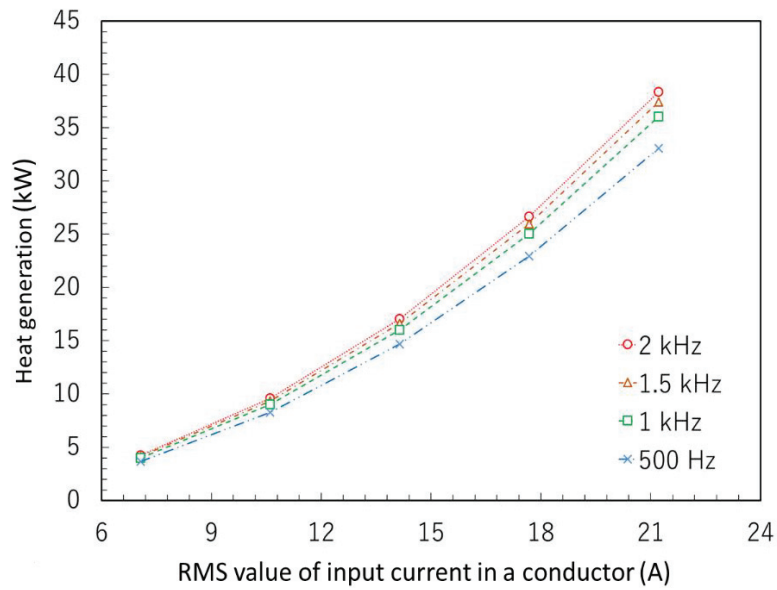


Fig 4.6-8 Heat generation with changing RMS value of input current. Number of MC and turns are 16 and 72, respectively.

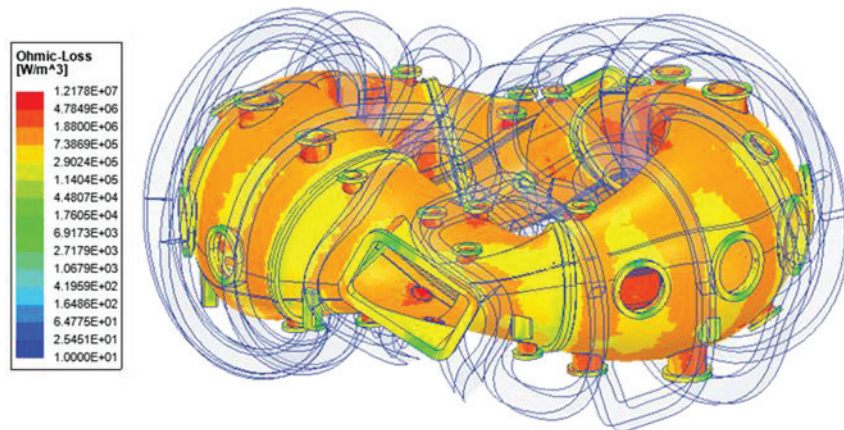


Fig 4.6-9 Distribution of the heat generation.  $I_{AC}=7$  A,  $f=1$  kHz. The maximum heat generation in VV is about  $1.2 \times 10^7$  W/m<sup>3</sup>.

## 4.7 Structural analysis of vacuum vessel

### 4.7.1 Stress and displacement in various operating conditions

On plasma operation, the vacuum vessel (VV) is exposed to loads, such as an atmospheric pressure, a thermal stress, and electromagnetic forces of eddy current. The most important of these is the vacuum force, and it is necessary to confirm that the deformation and stress due to that force are within a reasonable range. Due to its complexity of shape, it is hard to predict the mechanical behavior of the VV. Therefore, we have performed structural analyses to validate the reliability of VV with use of the ANSYS/Mechanical.

In the analysis, we had chosen 2 models as shown in Table 4.7-1. The results are summarized in Table 4.7-2. Here, the model for the case 1-0 and 1-1 was created according to the latest design of the vacuum vessel, and the model for the case 2-0 and 2-1 was created in the preliminary simplified design to reduce the computer load during eddy current analysis since the coupled analysis of eddy current and stress requires a huge amount of calculation time. Fig 4.7-1 shows the mesh of the vacuum vessel and Fig 4.7-2 shows the boundary condition and the load for the stress analysis. The vacuum pressure (atmospheric pressure 0.1 MPa) was applied on the outer surface as shown in the blue arrows. The bottom surfaces of eight legs was fixed for constraint condition. Furthermore, gravitational acceleration is applied on the entire vacuum vessel as a self-weight.

By comparing the case 1-0 and 2-0, it was found that there was a variation of 10 % in the result depending on the model. In the following, we will discuss the validity of the design on the assumption that there is an error of about 10 %.

The stress due to vacuum pressure is up to 96 MPa in case 1-0 of Fig 4.7-5 and up to 100 MPa in case 2-0 of Fig 4.7-8. These values are much less than the design stress of 137 MPa. The location with the maximum stress is near the root of the upper and lower diagnostic port. In this analysis, it was assumed that the port was connected to the vacuum vessel body by full welding. Incomplete welding is likely to be applied for the purpose of cost reduction, so the effects of this will be considered separately.

The deformation due to vacuum pressure up to 0.98 mm in case 1-0 of Fig 4.7-4 and up to 1.22 mm in case 2-0 of Fig 4.7-7. Since the distance between the vacuum vessel and the peripheral equipment is over 5 mm, it is presumed that this deformation is not a problem.

To evaluate thermal deformation during baking, the temperature distribution obtained by the heat transfer analysis in advance, whose result was shown in Fig 4.7-3. For simplicity, the vacuum vessel and bottom surfaces of legs were fixed to 130 °C and 22 °C, respectively.

Fig 4.7-4 and Fig 4.7-5 show comparisons of the stress analysis with and without the baking. As shown in Fig 4.7-5(b), the maximum stress was increased up to 109 MPa, which is acceptable. The location at the maximum was near the base of the leaf spring type legs. The maximum displacement of 3.3 mm in Fig 4.7-4(b) was caused by the increase in the major radius due to the temperature rise during baking. This deformation will be unavoidable because it is determined by the thermal expansion coefficient and temperature of the vacuum vessel.

By the coupled analysis function of the ANSYS/Maxwell and the ANSYS/Mechanical, the EM force due to the eddy current at 500 ms as shown in Fig 4.7-6 was applied to the stress analysis model as a distributed load. The body force distribution is locally up to 0.015 N / mm<sup>3</sup>, but in most places less than 0.002 N / mm<sup>3</sup>, which is 0.012 MPa (0.02 × 6 mm) in terms of surface pressure. Since the 0.012 MPa is only 10 % of atmospheric pressure, it is

estimated that the effect of the eddy current is exceedingly small.

Fig 4.7-7 and Fig 4.7-8 show comparisons of the stress analysis with and without the EM force. As shown in these figures, the differences of the stress and the deformation are small, and the effect of the EM force can be ignored.

Therefore, it was confirmed that the maximum stress is within an elastic deformation range, and there is also no possibility that the vacuum vessel will break due to repeated stress fluctuations.

Table 4.7-1 Condition of the stress analysis.

Name	Model	Main purpose	External pressure and self-weight	Thermal deformation	Distributed load (External)
Case 1-0 (VP)	Latest design with the legs	Validation under the vacuum pressure	0.1 MPa 1G	-	-
Case 1-1 (TD)		Validation at the time of baking	0.1 MPa 1G	108 Degrees (130-22 °C)	-
Case 2-0 (VP)	Preliminary simplified design without the legs and the close flange.	Validation of the model.	0.1 MPa 1G	-	-
Case 2-1 (EM)		Validation with EM force	0.1 MPa 1G	-	0.01 MPa equivalent

Table 4.7-2 Result of the stress analysis.

Name	Equivalent (Mises) stress (MPa)		Maximum deformation (mm)	Notes
	Maximum	Allowed		
Case 1-0 (VP)	100	137 (Sm at 30 °C)	0.98	Large stress and deformation near the base of the port.
Case 1-1 (TD)	109	150 (1.5Sm at 150 °C)	3.3	Thermal stress concentrates on the base of the leg.
Case 2-0 (VP)	96	137 (Sm at 30 °C)	1.22	There is a deviation of about 5 % from the case 1-0 due to the influence of the mesh or the leg.
Case 2-1 (EM)	97	137 (Sm at 30 °C)	1.23	The effect of EM force can be ignored.

The Sm is a design stress of SUS316L.

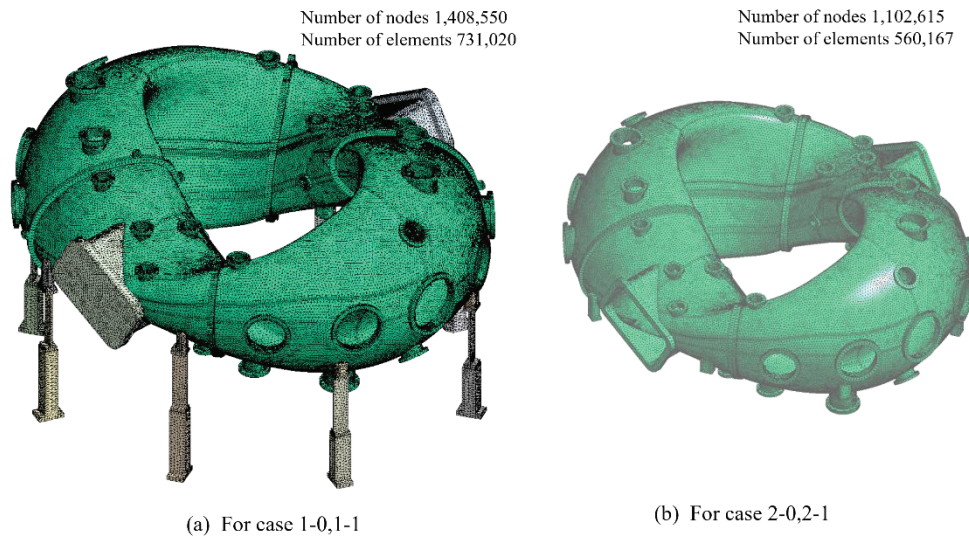


Fig 4.7-1 Mesh of the vacuum vessel for the stress analysis. Since the coupled analysis of eddy current and stress requires a huge amount of calculation time, a preliminary simplified model was used for the case 2-1. There are differences such as ignoring the legs and the rectangular close flange and the thickness of the large flanges at split location is different.

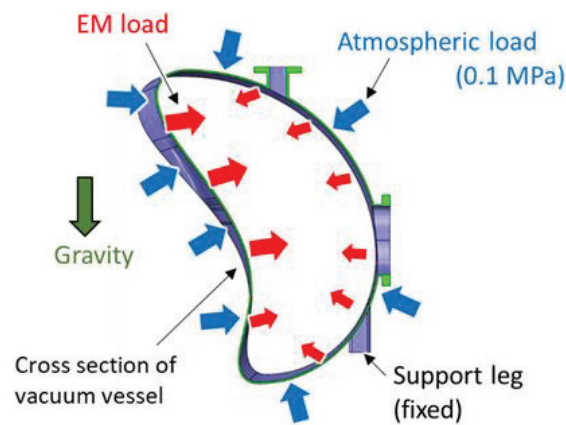


Fig 4.7-2 Boundary conditions for the stress analysis with the EM load and vacuum pressure. The EM load is applied by the eddy current.



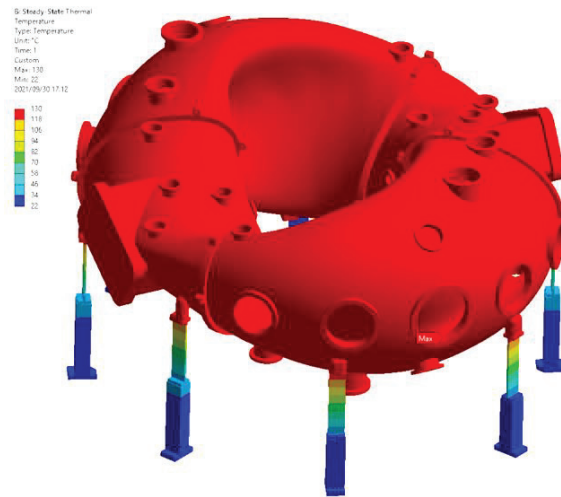
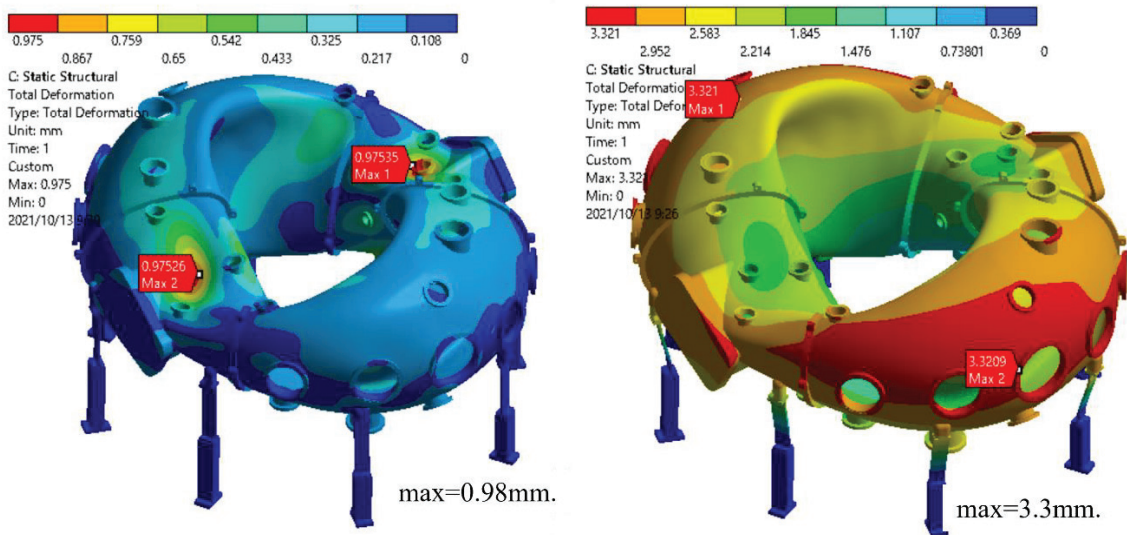


Fig 4.7-3 Temperature distribution that causes thermal deformation for the case 1-1. It was obtained by heat conduction analysis. It is 22 °C at the base of the legs, and 130 °C on the thin plates of the vacuum vessel.

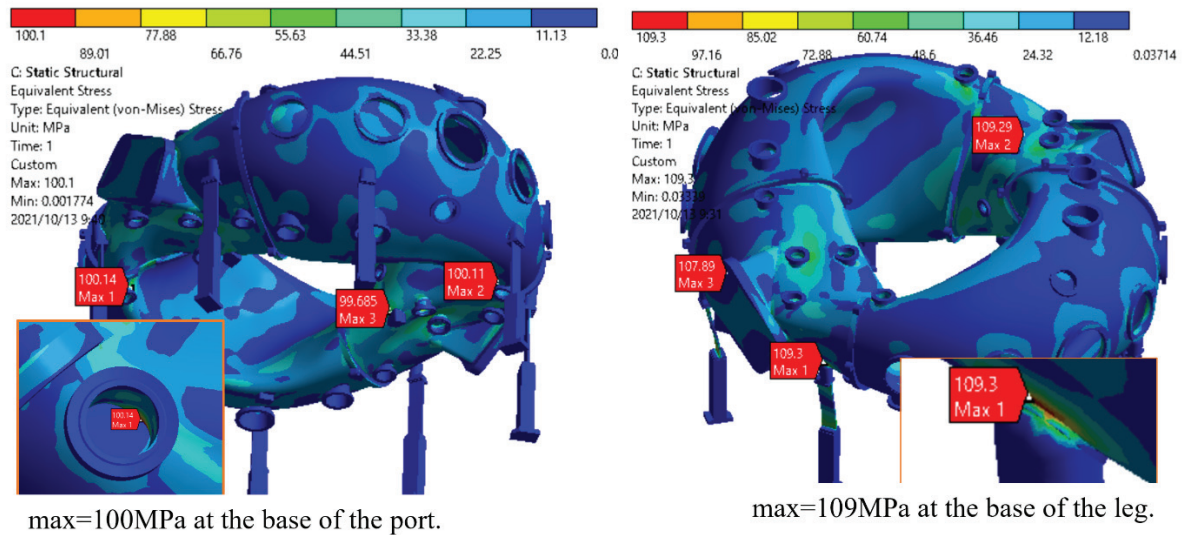


(a) Case 1-0, without the thermal deformation.

(b) Case 1-1, with the thermal deformation.

Fig 4.7-4 Changes in the deformation due to the baking.





(a) Case 1-0, without the thermal deformation.

(b) Case 1-1, with the thermal deformation.

Fig 4.7-5 Changes in the equivalent stress distribution due to the baking. The stress due to the deformation of the thin plate due to vacuum pressure is the largest without the baking, and the stress at the base of the leg due to thermal deformation is the largest with the baking.

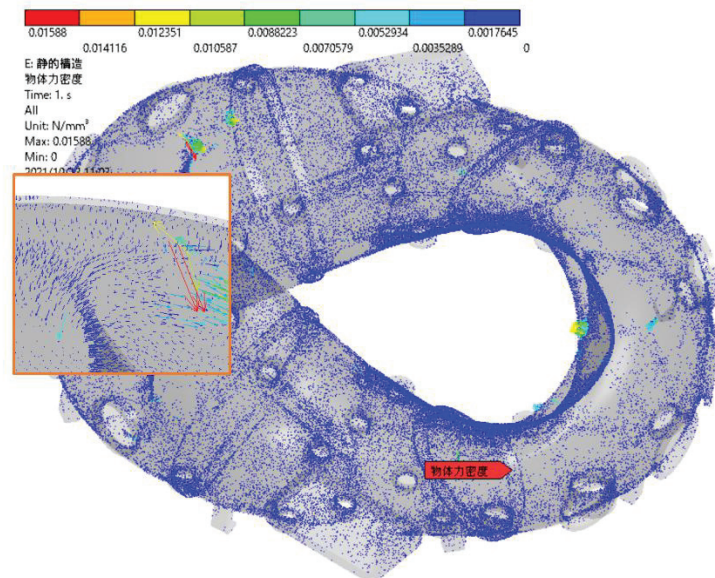
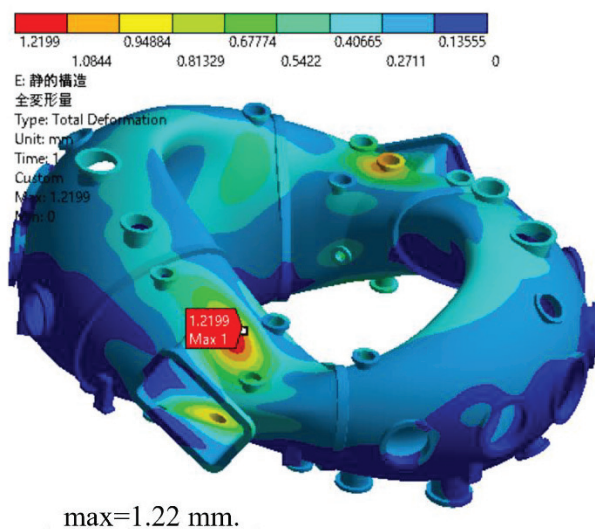
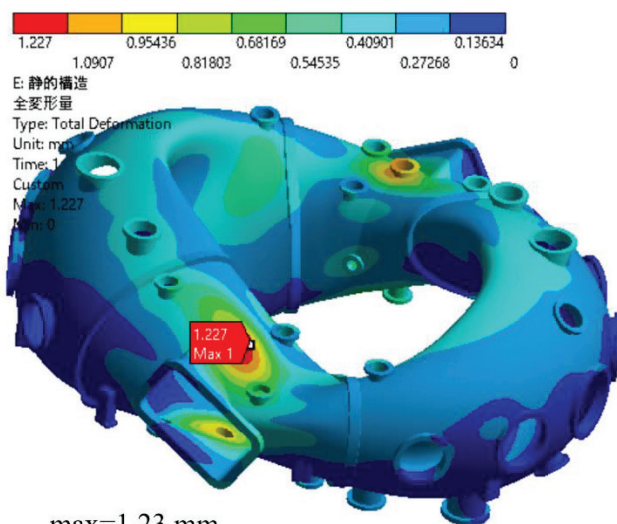


Fig 4.7-6 EM distribution by the eddy current at 500 ms.



max=1.22 mm.

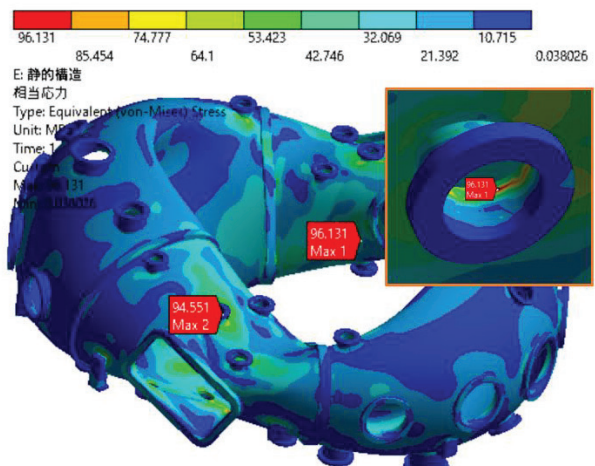
(a) Case 2-0, without the EM force



max=1.23 mm.

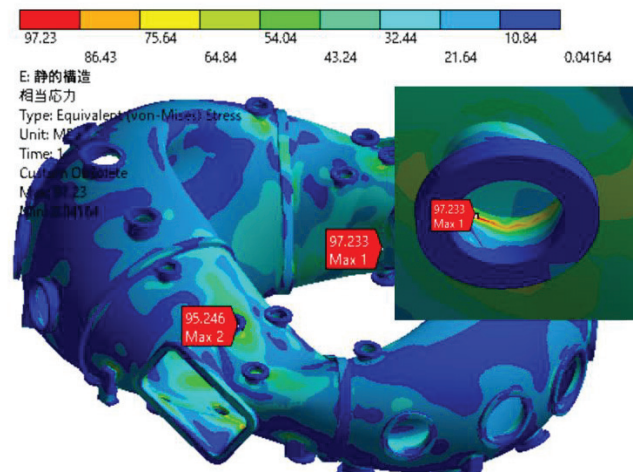
(b) Case 2-1, with the EM force

Fig 4.7-7 Changes in the deformation due to the EM force.



max=96MPa at the base of the port.

(a) Case 2-0, without the EM force



max=97MPa at the base of the port.

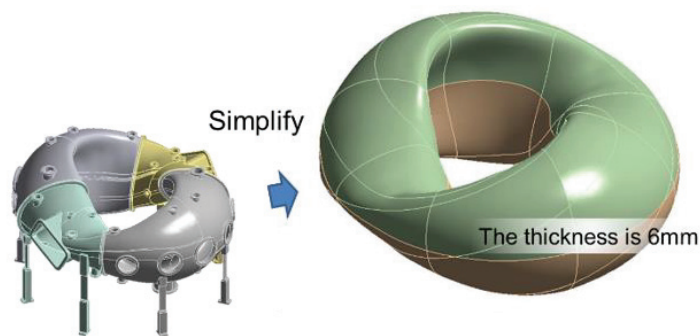
(b) Case 2-1, with the EM force

Fig 4.7-8 Changes in the equivalent stress distribution due to the EM force. The stress is the largest at the base of the port, which is mainly caused by the deformation of the thin plate due to the vacuum pressure. The effect of the EM force is very small.

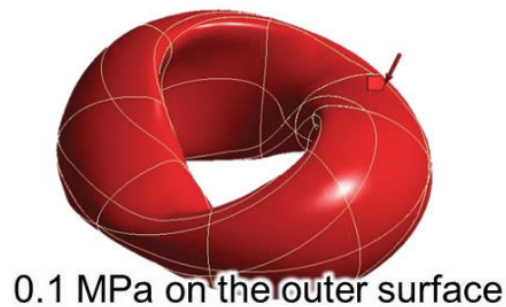
#### 4.7.2 Effect of mesh size in the analysis for the vacuum vessel

A mesh size is one of the most important factors in the FEM since a result of the FEM depends on mesh size significantly. Therefore, we have conducted preliminary analysis with a simplified model and estimated reasonable mesh size for the analysis of the CFQS vacuum vessel (VV). Fig 4.7-9 shows the model and analysis condition. We have investigated how the result changes with mesh refinement.

The results are summarized in Fig 4.7-10. The vertical lines show the maximum deformation and stress, and the horizontal one the number of elements. According to this figure, as the mesh size decreases, the result of solid element shown as red circle seems to converge, and in case of less than 25 mm, it agrees with the result of shell element. From this result, we can assume that the mesh size should be less than 25 mm in the analysis of the VV for the CFQS.



(a) Simplified model



(b) Simplified load condition

Fig 4.7-9 Simplified model and the load condition for the vacuum vessel.

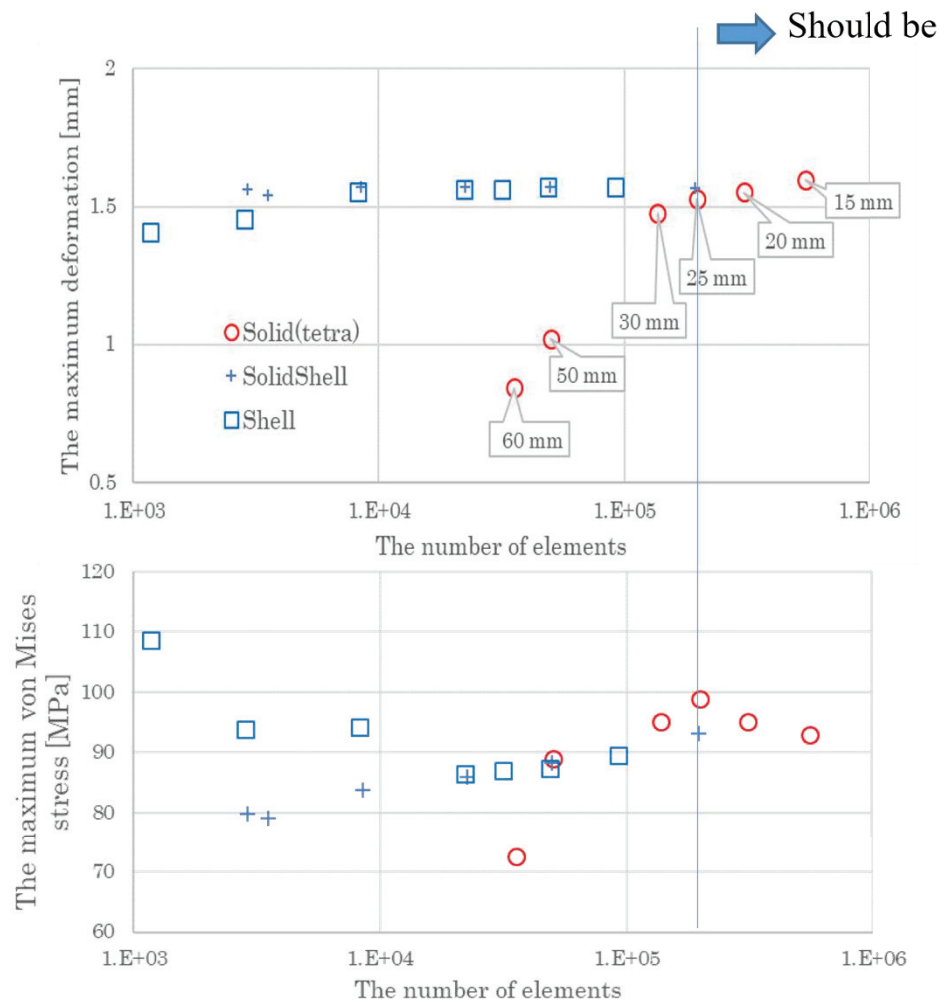


Fig 4.7-10 Relationship between FEM analysis and number of meshes. The results show that the mesh size should be less than 25 mm in the analysis.



#### 4.8 Baking heater for vacuum vessel

For baking of the vacuum vessel, we will wind sheath heaters on the vacuum vessel surface. Total required baking power is estimated about 25kW, which is referred by CHS baking system since the volume of the CFQS is almost equivalent to that of CHS. Baking regions are distinguished  $8 \times 2$  sections based on 12 Toroidal field coils (TFC) and 4 flanges to connect 4 sections as shown in Fig 4.8-1. Each heater is wound separately so as not to leap over them and has its own power system to make it easier to control the temperature. Each baking heater winding route is arranged as shown in the figure.

The heating capacity of each section was set so that the amount of heat per unit mass was almost constant. Diameter of each sheath heater is 4.8mm and its resistance is 1.55  $\Omega$ /m. The heater length was estimated from the 3D-CAD model. It is mounted on the surface of vacuum vessel with an interval of about 100mm. Table 4.8-1 shows the specification of the baking heaters, such as heater length, required capacity and voltage.

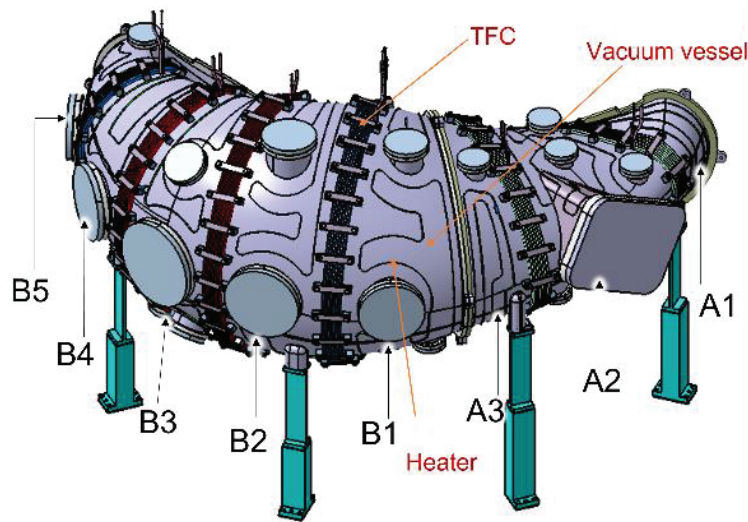


Fig 4.8-1 Baking heater on the vacuum vessel.

Table 4.8-1 Specification of baking heaters.

Region	Required capacity [kW]	Heater length [m]	Resistance [ $\Omega$ ]	Maximum voltage [V]	Maximum current [A]	Heating capacity [kW]
A1	0.98	5.1	7.6	110	14.4	1.6
A2	2.42	9.3	13.9	220	15.8	3.5
A3	1.05	5.0	7.5	110	14.6	1.6
B1	1.67	8.9	13.3	220	16.6	3.6
B2	1.63	10.3	15.5	220	14.2	3.1
B3	1.46	9.0	13.5	220	16.3	3.6
B4	1.62	10.0	14.9	220	14.7	3.2
B5	1.67	8.9	13.3	220	16.6	3.6
Sum	12.5	66.4				23.9

Diameter of each sheath heater is 4.8mm and its resistance is 1.55  $\Omega$ /m.

#### 4.9 Preliminary layout of magnetic measuring elements

In the future, four types of magnetic measuring instruments will be installed in the vacuum vessel to measure instability and energy in the plasma. We designed the installation location and wiring route of the magnetic measuring instrument so that those locations would not be used for other purposes. Fig 4.9-1 shows layout example of the magnetic measuring instruments.

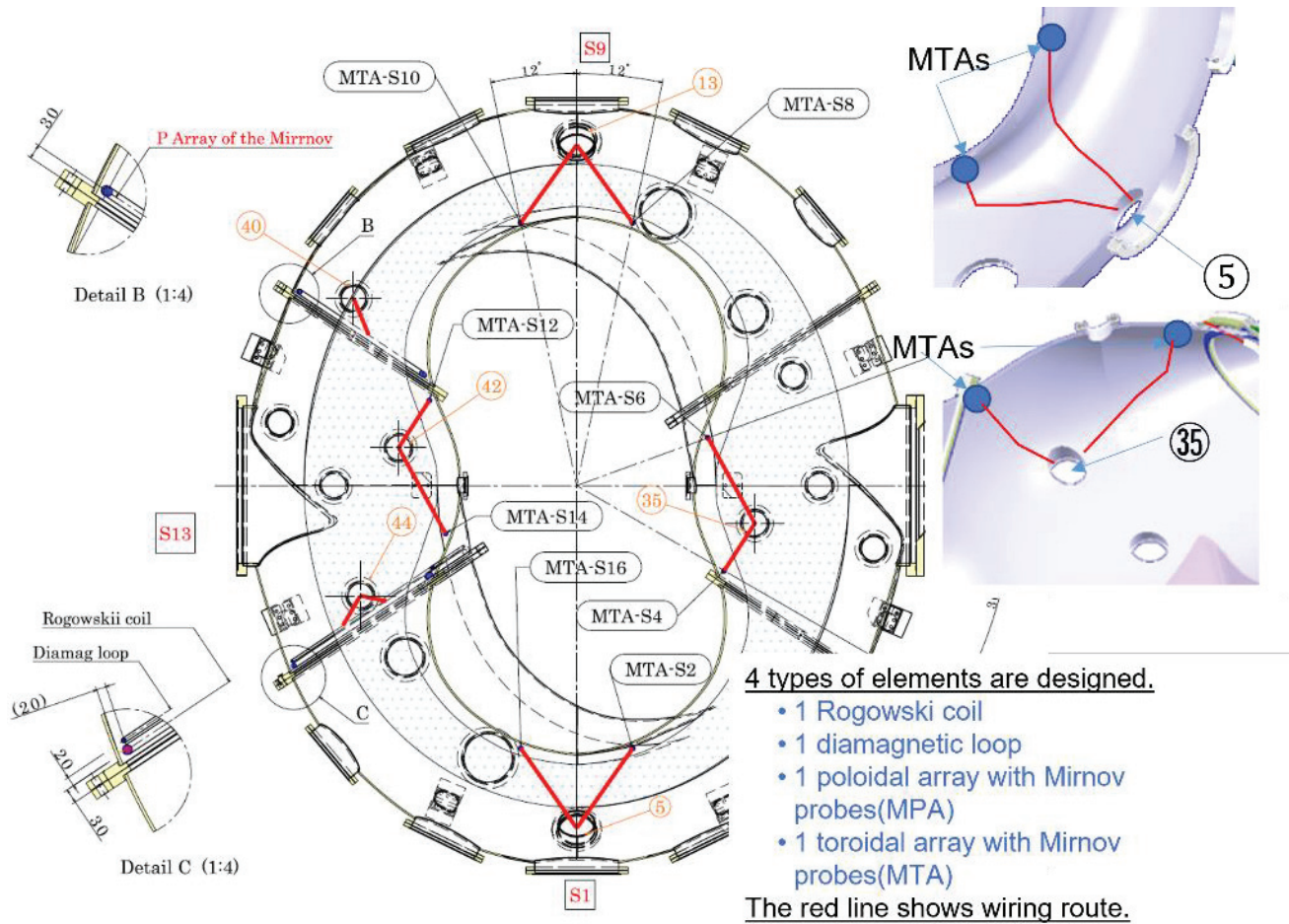


Fig 4.9-1 Magnetic measuring elements



#### 4.10 Preliminary layout of the view ports

To observe the shape and behavior of the plasma, we will provide view ports for seeing the plasma in the tangential direction in the vacuum vessel. However, since the shape of the vacuum vessel is complicated, it is not easy to secure a field of view in which the plasma can be seen in the tangential direction. Therefore, we searched for a port that could be used as a tangent port by 3D CAD. The results are shown in Fig 4.10-1. The plasma can be observed from ports # 8, 17 and 18, but the wall of the vacuum vessel may be in the way and the entire plasma cross section cannot be observed. Depending on which part of the plasma we want to observe, we need to adjust the position, tilt, or size of the flange.

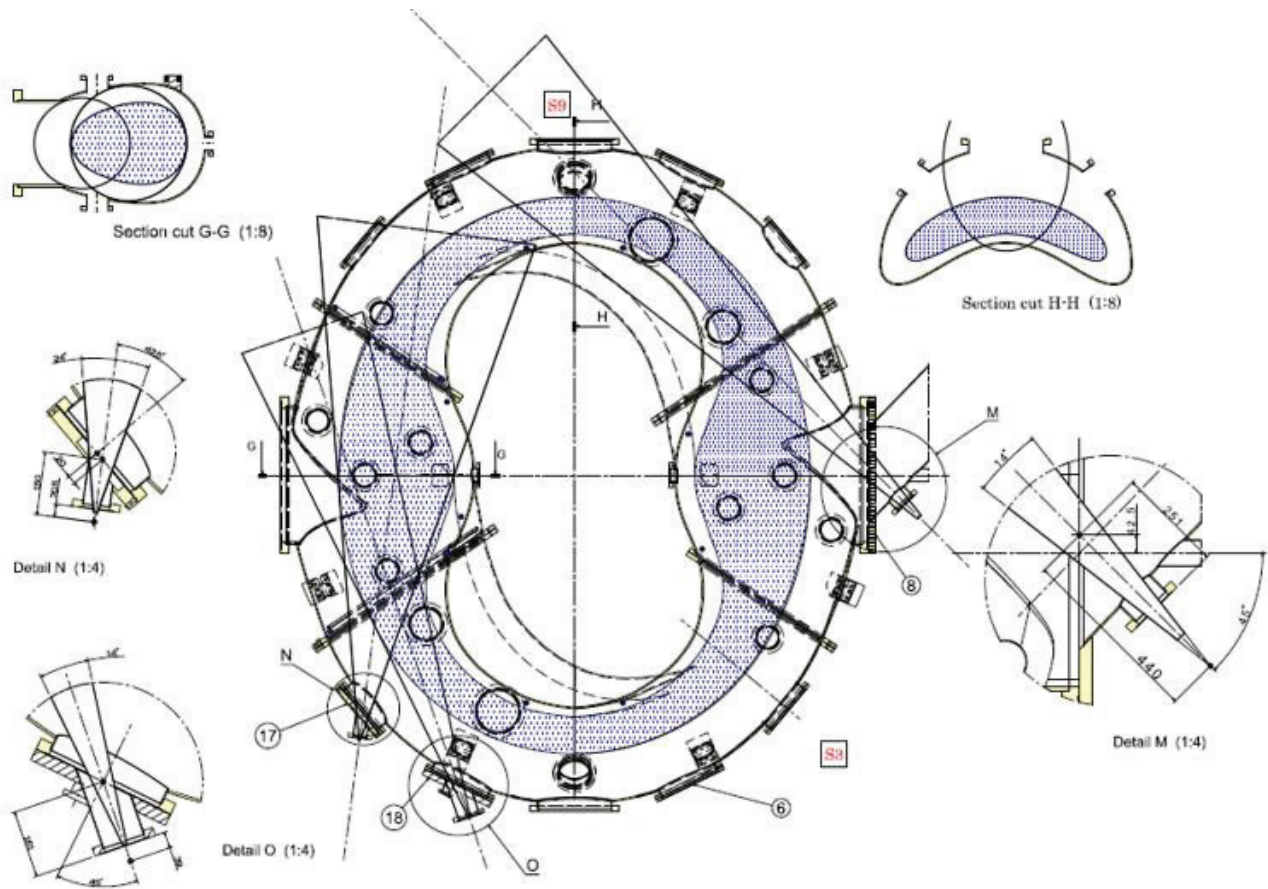


Fig 4.10-1 Tangential view ports

#### 4.11 Preliminary layout of the limiters

we intend to put four sets of the poloidal or rail limiter inside the vacuum vessel for defining the plasma and protecting the wall. Two of them are fixed limiters which will be installed primarily to protect the walls. Others are movable limiters which will be installed for defining the plasma and changing the size of plasma. Fig 4.11-1 shows the layout of the limiters and their conceptual shape.

Although detailed examination is required, it seems possible to install limiters with an outer diameter of about 30 mm x 30 mm in cross section.

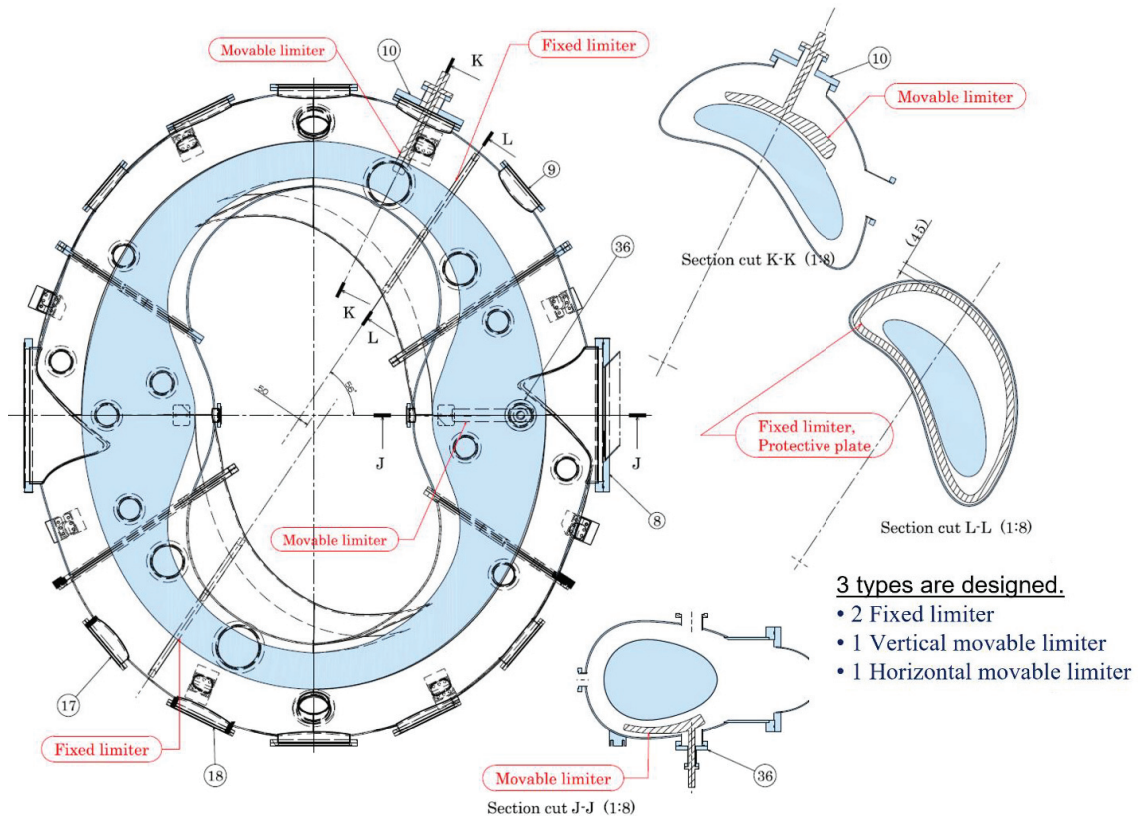


Fig 4.11-1 Limiters

## **5 Production flow of the CFQS**

### **5.1 Pre-assembly procedure of modular coils and vacuum vessel on site**

Before installing the modular coils and the vacuum vessel, it is necessary to pass the vacuum vessel through the coils. The work is planned to be done in a location different from the installation position in the same building. Although this work can be performed in the factory, it is difficult to safely carry the assembled parts together. Therefore, it is planned to transport each part and reassemble them in the laboratory after the defects in the temporary assembly are extracted in the factory. Since this pre-assembly work is complicated and delicate, confirmation of work steps and work training should be conducted in the factory.

Fig 5.1-1 shows the pre-assembly process of the modular coils and the vacuum vessel. In step 1, the vacuum vessel part is fixed with appropriate jigs on the workbench desirable to be composed of a surface plate which is a flat plate used as the main horizontal reference plane for precision inspection. The coil is inserted while rotating it in steps 2, 3, 4 and 5, but since the vacuum vessel has a complicated twisted shape, delicate adjustment work is required to move the coil. It is possible to develop a special transport machine for that work, but to reduce costs, it is also possible to work with an overhead crane and the manual hoist as shown in the figures. Since it is necessary to frequently attach and detach the legs of the vacuum vessel to pass the coil, a jig such as a hydraulic jack will be prepared to facilitate the work. In step 6, the whole is fixed to the upper temporary base and suspended by an overhead crane.

It is considered that the vacuum vessel and the coils can be suspended integrally by assembling in such a procedure. Steps 7 and 8 show a state in which two types of vacuum vessels and coils are suspended.





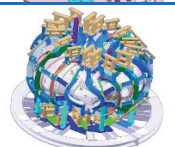

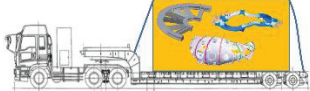
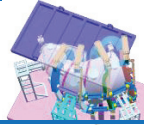
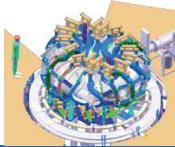

Fig 5.1-1 Pre-assembly process of the modular coil and vacuum vessel.



## 5.2 Overall production flow

The table below shows the overall production flow of the CFQS. Although it depends on the installation location and road conditions along the way, it is considered difficult to transport about 30 tons all at once. After verifying the quality of individual parts in the factory, it is planned to disassemble and transport the individual parts and reassemble them in the laboratory.

Fig 5.2-1 Rough production flow

STEP	Contents	Illustration
1	Purchase materials and standard products.	
2	Product parts and sub-assemblies in a factory.	
3	Pre-assemble the modular coil and vacuum vessel in a factory.	
4	Assemble the main parts, evaluate them, and verify quality of each sub assembly in a factory, such as the vacuum vessel, the coil, and the bottom frame.	
5	Disassemble it for the transportation.	
6	Transport sub assembling products and parts in a research laboratory.	
7	Pre-assemble the modular coils and vacuum vessel in the laboratory.	
8	Assemble major products, such as the bottom frame, vacuum vessel, modular coil, and lower PFC.	
9	Individually evaluate the major products on the way, such as the vacuum leak test and accuracy measurement of the coil position.	
10	Assemble other parts.	
11	Validate the CFQS by overall operation test.	

## 6 Power supply system

### 6.1 Requirements for the power supply system

Chinese power environment is different from Japan as shown in Table 6.1-1. To relocate equipment's of the CHS for CFQS experiments, it is reasonable to prepare converters, transformers, for solving the difference in voltage. Table 6.1-2 shows summary of required power with the low voltage power board for the CFQS.

Required capacity for the coil power supply system is shown in Table 6.1-3. They were estimated with the defined current waveform and the impedance of each coil.

Table 6.1-1 Comparison of power environment

	Frequency	High voltage	Low Voltage 1 $\phi$	Low Voltage 3 $\phi$
Japan	60 Hz (West)	6.6 kV	100 V	200 V
China	50 Hz	10 kV	220 V	380 V

Table 6.1-2 Total electric power required

No	Power board	Voltage	Phase	Total capacity	Usage
1	High voltage	10 kV	3 $\phi$	5 MVA	MG, NBI
2	Low Voltage	380 V	3 $\phi$	1 MVA	ECH, baking, cooling etc.
3	Low Voltage	220 V	1 $\phi$	Unknown	Diagnostic, control etc.
4	Low Voltage	200 V	3 $\phi$	Unknown	For equipment from Japan
5	Low Voltage	100 V	1 $\phi$	Unknown	For equipment from Japan

Table 6.1-3 Required capacity for the coil power supply system

Coil Name	0.09T					1T							
	Operation condition		Specification of power supply			Operation condition				Specification of power supply			
	I <sub>max</sub> (A)	V <sub>max</sub> (V)	I <sub>max</sub> (A)	V <sub>max</sub> (V)	kVA	I <sub>max</sub> (kA)	V <sub>max</sub> (kV)	Pulse (s)	MJ	I <sub>max</sub> (kA)	V <sub>max</sub> (kV)	MVA	MJ
MC1	391	184	420	230	107	4.34	2.27	0.91	8.0	4.5	2.3	11.5	8.5
MC2	391	181	420	230	107	4.34	2.24	0.91	7.9	4.5	2.3	11.5	8.5
MC3	391	175	420	230	107	4.34	2.17	0.91	7.7	4.5	2.3	11.5	8.5
MC4	391	169	420	230	107	4.34	2.09	0.91	7.4	4.5	2.3	11.5	8.5
IV	563	91	600	110	73	6.25	1.22	0.46	2.9	7	1.4	10.9	3.0
OV	563	141	600	180	120	6.25	1.7	0.45	4.5	7	1.9	14.8	4.5
TC10	180	42	200	55	12	2	0.48	0.19	0.18	2.2	0.52	1.3	0.20
TC32	180	39	200	55	12	2	0.44	0.19	0.17	2.2	0.52	1.3	0.20
TC70	180	32	200	55	12	2	0.36	0.19	0.14	2.2	0.52	1.3	0.20
Sum	659					39				75			



## 6.2 Trial design of coil power supply for 0.09 T operation

Initially, it was planned to execute a 0.09 T experiment using part of the 1.0 T power supplies. However, the experimental plan was changed to a plan to perform 0.09 T operation first to understand the characteristics of the generated magnetic surface. The power supply system for 1.0 T operation has not been determined yet due to its complicated configurations. On the other hands, the design of the power supply system for the 0.09 T operation needs to be determined immediately. Therefore, we decided that the power supply system for the 0.09 T and the 1 T are completely separated. It means that both systems do not share any electrical components.

Fig 6.2-1 shows the preliminary designed circuit diagram of the power supply system for 0.09 T. It consists of four 12-phase thyristor controlled unit which may be combined with two 6-phase thyristor controlled units and five 6-phase thyristor controlled units. The formers will supply current to the MC and the others will supply current to the PFC and the TFC. An energy storage stations with 2.1 MWh will be installed to supply these with a large amount of power equivalent to 700 kW during the experiment. The charging power will be reduced to 250 kW, and the charging time will be 10 hours per one day at night.

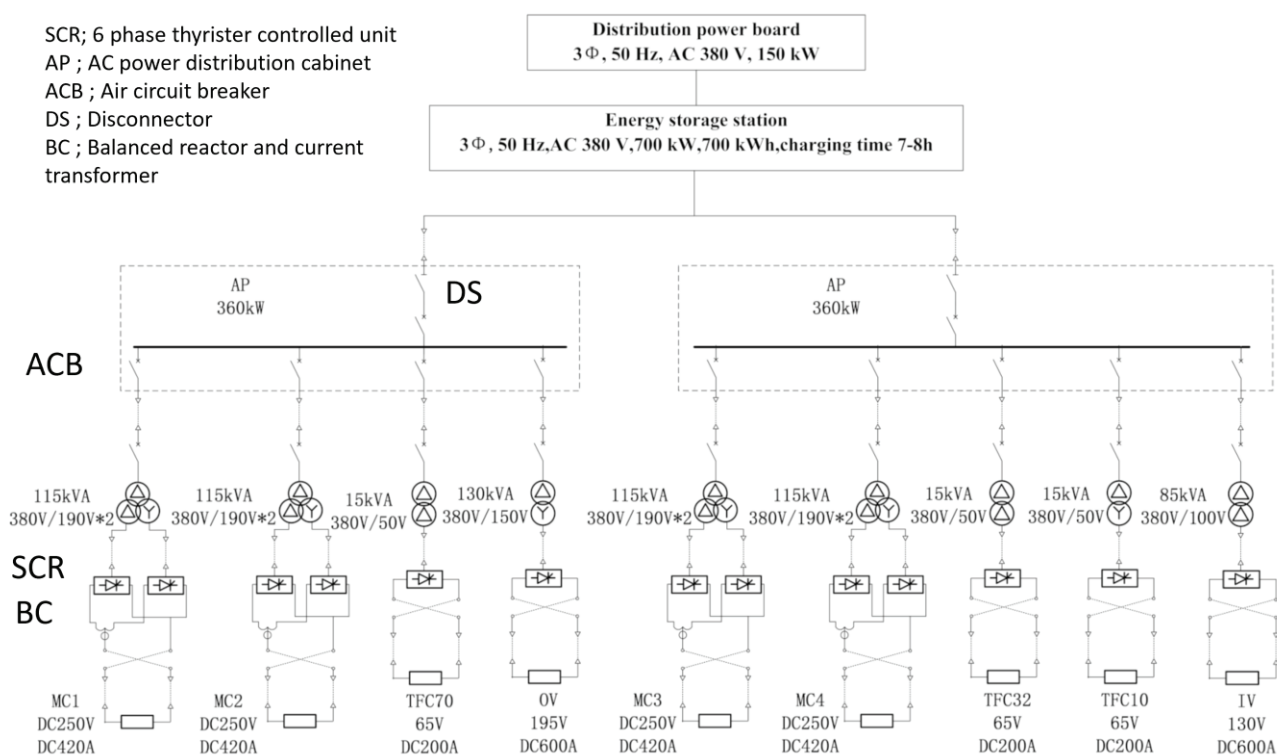


Fig 6.2-1 Circuit diagram of the power supply system for 0.09 T.

## 6.3 Trial design of coil power supply for 1 T operation

### 6.3.1 Designed circuit diagram and the layout of MG building

Based on rough estimation, we designed circuit diagram of the power supply system with IM and SG as represented in Fig 6.3-1. The circuit consists of IM, SG, the inverter for IM and SG revolution control, the excitation system for SG, six phase thyristor-control units, and polarity switching circuits. Typical SG with two pole, 50 Hz, 70 MVA rated output, 10 kV of operation voltage is selected by a manufacturer catalog. The static exciting system consisting of an exciting transformer (EXT), an automatic voltage regulator (AVR), and SCR is adopted for SG excitation control. The excitation system has rapid responsiveness for SG voltage control.

Based on the circuit diagram, the layout of power supply system including the MG for 1 T was estimated. The result is shown in Fig 6.3-2. In this plan, the system is divided into two parts. One is a MG system with a synchronous generator and an induction motor, and other is a system with thyristor-controlled transducers and transformers. The space for the system with thyristor-controlled transducers is as 30,000×10,000×3,500H, where it is better to be as close as possible to the CFQS. The space for the MG system is as 20,000×12,000×5,000H. Here, it is presumed that the MG system vibrates the building and generates a large amount of noise. Therefore, it should be installed in a building with noise barriers built on a sturdy foundation, preferably a building different from the CFQS laboratory. The design is based on the data of products with similar specifications published in the commercial catalog. Re-evaluation according to the specific product design is necessary. More details of designs should be proceeded with a manufacturer.

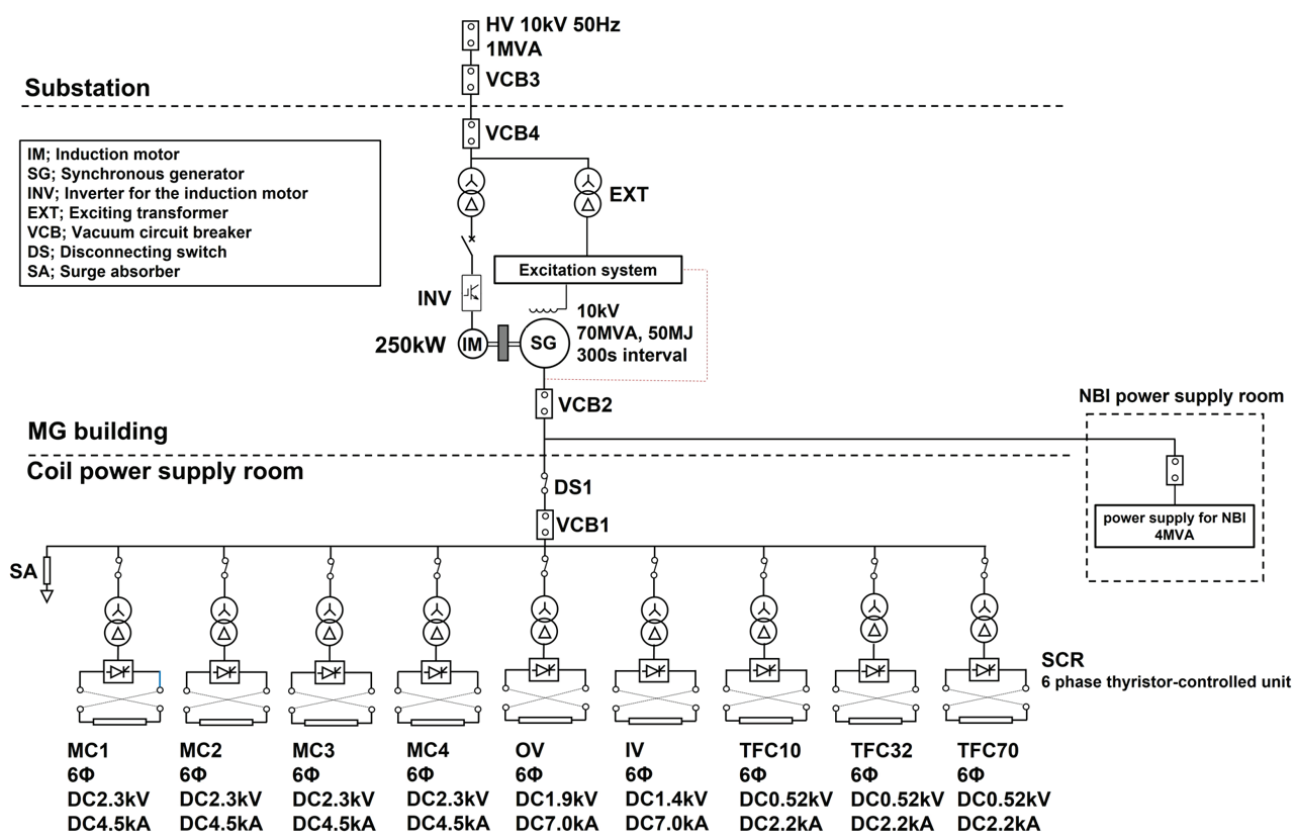


Fig 6.3-1 Designed circuit diagram of power supply system with IM and SG.

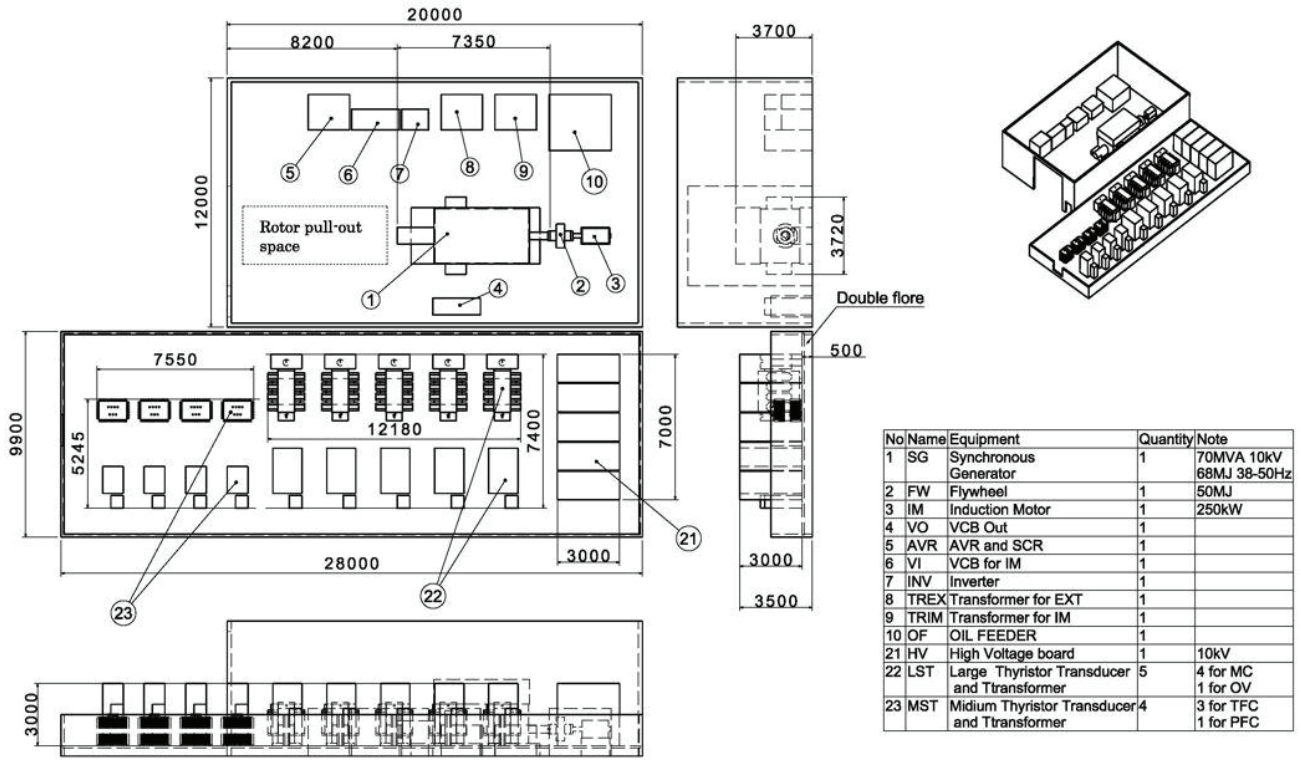


Fig 6.3-2 Layout of the power supply for 1T

### 6.3.2 Specifications of SG, IM, and a flywheel

Estimation results of specifications of IM, SG and a flywheel are summarized in Table 6.3-1. We have estimated stored energy in SG for CFQS by calculating of inertia moment of SG equipped in NIFS (250 MVA). The formula of inertia moment is followed:

$$J_x = \frac{1}{8} m \cdot D^2 = \frac{\pi}{32} \rho \cdot L \cdot D^4 [kg \cdot m^2], \quad (1)$$

where  $J_x$ ,  $m$ ,  $D$ ,  $\rho$  are inertia moment, mass of a rotor, diameter of a rotor and volume density of a rotor made of iron (8000 kg/m<sup>3</sup>) respectively. The calculated value of  $J_x$  of NIFS SG is 289,540 kg m<sup>2</sup>. Based on the calculation result, we estimated the  $J_x$  value of CFQS SG by calculating the ratio of rotor size and mass between NIFS SG and CFQS SG. Then, stored energy  $K_s$  of CFQS SG is calculated from the following formula:

$$K_s = \frac{1}{2} \times J_{CFQS} \times (2\pi f)^2 [J], \quad (2)$$

where  $f$  is frequency with 50 Hz (3000 rpm).  $J_{CFQS}$  is inertia moment of CFQS SG with 1386.8 kg m<sup>2</sup>. The calculated value of stored energy for CFQS SG is 68.4 MJ. Given 38 Hz of CFQS SG frequency after kinetic energy transfer to electrical power, only 28.9 MJ which cannot cover the required total energy for coils (40 MJ) is obtained. Therefore, the flywheel compensating stored energy for coil energization should be adopted. Required stored energy of the flywheel at 50 Hz (3000 rpm) is 49.9 MJ. Inertia moment of the flywheel  $J_{FLY}$  is  $J_{FLY} = 1013.3$  kg m<sup>2</sup> obtained by Eq. (1). We designed the size of flywheel made of iron with 1150 mm diameter and 750 mm thickness (~6229 kg, 1029.7 kg m<sup>2</sup>).

We also estimated required operation power for the IM. Given 300 s acceleration time (shot to shot) for

number of revolutions of SG rotor and the flywheel from 2280 rpm to 3000 rpm, required torque for the IM is obtained as following formula:

$$T_{IM} = \frac{2\pi \times (J_{CFQS} + J_{FLY})}{60} \times \frac{N_2 - N_1}{600} [N \cdot m], \quad (3)$$

where  $N_1$  and  $N_2$  show number of revolutions [rpm]. In this case,  $N_2$  is 3000 rpm and  $N_1$  is 2280 rpm. Calculated value of required torque for IM between 2280 rpm to 3000 rpm is 602.9 Nm. On the other side, if SG rotor and the flywheel are accelerated from 0 rpm to 3000 rpm in 1800 s, required torque for IM is 148.7 Nm. Consequently, required maximum mechanical output of IM is 189.5 kW. The value is calculated by

$$P_m = \frac{T_{IM} \times N}{9.545}, \quad (4)$$

where  $N$  is number of revolutions. Required input power for IM is estimated around 250 kW because loss factors such as copper loss, iron loss and windage need to be considered.

Table 6.3-1 Estimation of the IM and SG design values

Component	Parameter	Unit	Value
Generator	Number		1
	Capacity	MVA	70
	Voltage	kV	10
	Power factor	%	90%
	Frequency	Hz	38-50
	Revolution	rpm	2250-3000
	Number of poles	p	2
	Stored energy (Rotor)	MJ	68.4
Motor	Number		1
	Capacity	kW	250
	Voltage	kV	0.44
	Number of poles	p	2
Flywheel	Density	kg/m <sup>3</sup>	8000
	Diameter	m	1.15
	Height	m	0.75
	Weight	kg	6,229
	Stored energy	MJ	49.9
	Release energy (Rotor + Flywheel)	MJ	50.0
Accelerating torque	Accelerating time (Shot to Shot)	s	300
	Accelerating time (Start-up)	s	1800
	Torque (Shot to Shot)	Nm	602.8
	Torque (Start-up)	Nm	418.7
	Mechanical output from a Motor (Shot to Shot)	kW	189.5
	Mechanical output from a Motor (Start-up)	kW	131.6

## 7 Related equipment

### 7.1 ECH power injection antenna

The requirements for the ECH power injection system from the viewpoint of plasma experiment are to realize local and narrow power deposition and wide beam aiming area. Narrower power deposition by narrower beam at resonance layer requires larger mirrors. However, the power injection system should avoid interference with surrounding structures in CFQS (see Fig 7.1-1), that is, the system should be compact. Thus, the beam waist size and mirror size should be optimized simultaneously. The assigned port for ECH power injection system is O-180 port which has a ConFlat flange of the CF350. The inner diameter of the CF350 flange opening is 350 mm. As a result of design adjustment and optimization, the circular Gaussian beam parameters, the beam waist size, and beam waist position are determined as 30 mm and  $R = 1185$  mm, respectively. Here,  $R$  denotes major radial coordinate. Compared with the long radius of  $\sim 450$  mm of the bean-shape plasma at this toroidal position, the beam radius of 30 mm is narrow enough for localized power deposition, while the mirror antenna system can be contained in a mirror vacuum vessel with the CF350 dimension.

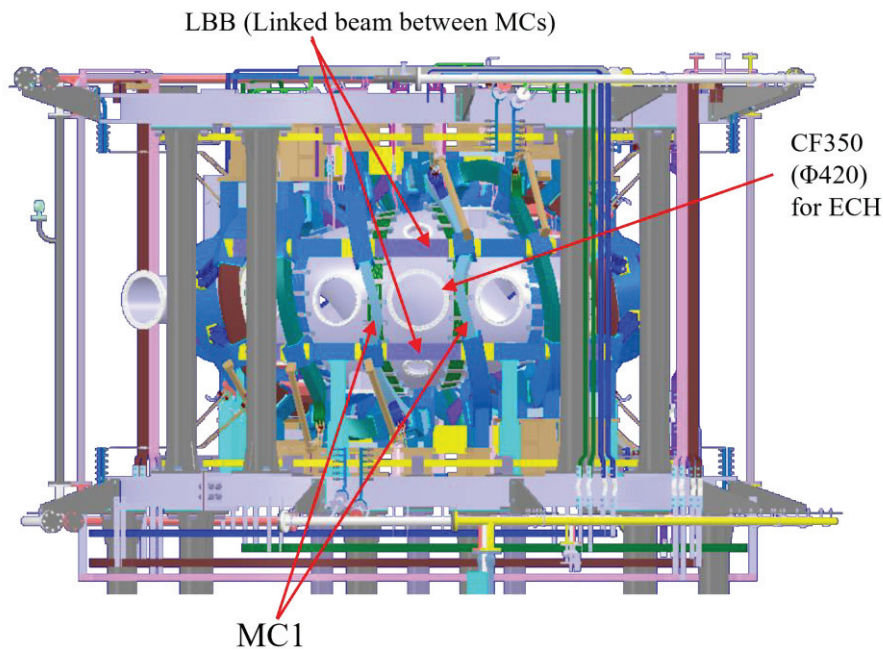


Fig 7.1-1 ECH port and surrounding structures.

A cross-sectional view of the ECH antenna and plasma are shown in Fig 7.1-2. The mirror system consists of 4 mirrors: 2 focusing mirrors and 2 plane mirrors. Counting from the plasma side, the mirrors are named M1, M2, M3, and M4. M1 and M3 are plane mirrors. M1 is steerable mirror for beam direction control, and M2, M3, M4 are fixed. The blue lines represent the Gaussian beam radius which denotes  $1/e$  radius of electric field. The red lines show the width of 1.5 times the Gaussian beam radius, and within the red lines, 98.9% of total power is contained. The mirror corners near the mirror vacuum vessel should be cut to avoid interference with the mirror vacuum vessel as shown in Fig 7.1-3. Beam aiming range of  $-450 \text{ mm} < Z < +100 \text{ mm}$  and  $-200 \text{ mm} < T < +200 \text{ mm}$  at  $R = 1185 \text{ mm}$  is obtained, which is sufficient for electron cyclotron current drive (ECCD) and off-axis



heating.  $Z$  and  $T$  denote vertical and toroidal coordinates, respectively.

As a future work, supporting structure of the mirrors M2, M3, M4 and the steering mechanism of the plane mirror M1 should be designed. Also, supporting structure of mirror vacuum vessel should be designed.

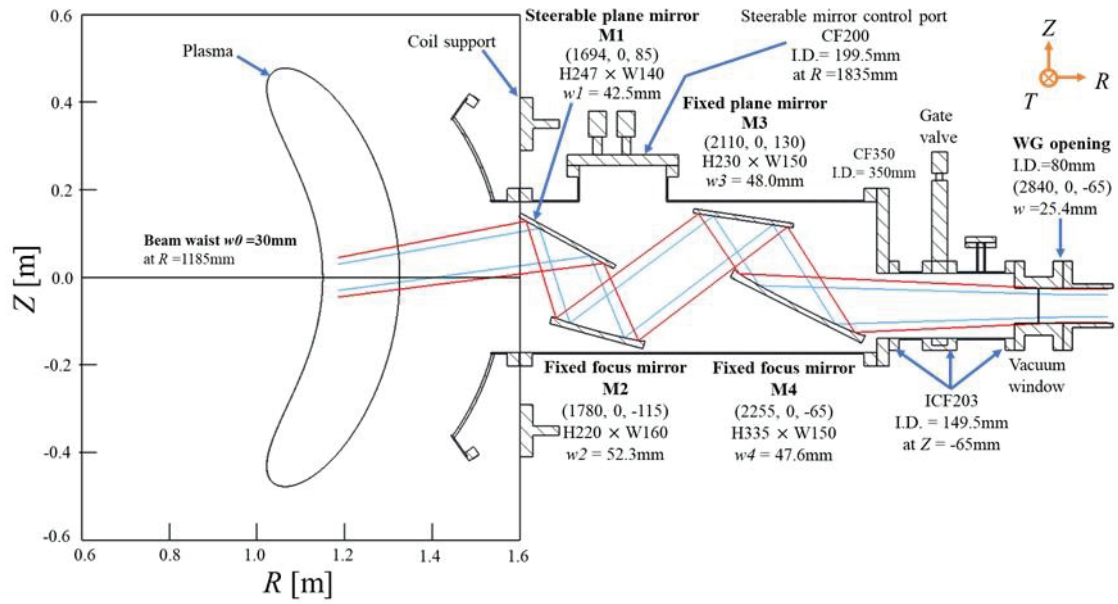


Fig 7.1-2 Design of ECH power injection antenna.

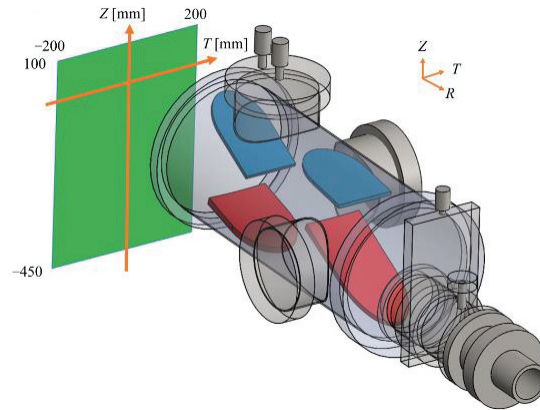


Fig 7.1-3 Beam aiming area and the mirror shapes.



## 7.2 Baking power supply

Total required baking power for CFQS vacuum vessel (VV) is estimated 25kW. We designed the power supply satisfying the electrical conditions for baking as represented in the below figure. Here, A1 to A3 and B1 to B5 are the names of the baking sections in which the vacuum vessel is divided in the toroidal direction. The heaters on A1 and A3 section are connected in series because these volumes of the A1 and A3 section are relatively small compared with other sections.

The baking power supply consists of AC power regulators (APR) which can change the applied voltage and applied power (up to AC220V, 3.6kW) for each baking heater, a magnet contactor (MC) for emergency shutdown to prevent overheating, molded case circuit breakers (MCCB) for each baking switching and transformer (TR) for insulation. The APR output is controlled by a temperature indication controller (TIC) which monitors surface temperature of VV. Surface temperature is monitored by not only TIC but also the other temperature monitoring system with over 64 measurement spots. The details of the other monitoring system will be designed later. MC is operated to stop baking when any surface temperature of VV exceeds critical value.

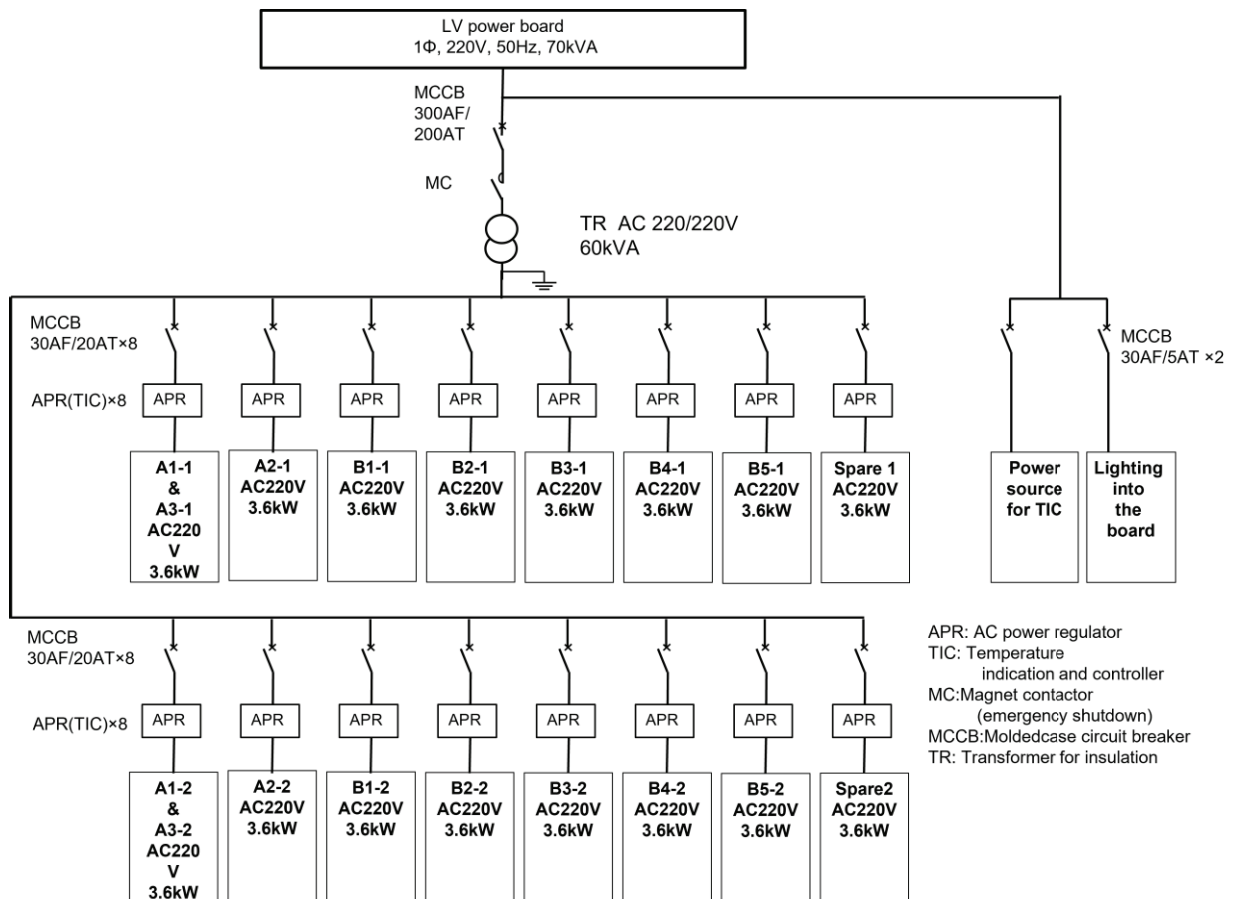


Fig 7.2-1 Circuit diagram of the baking system.

### 7.3 Vacuum pumping system

The pumping system for the CHS shown in Fig 7.3-1 will be transferred to the CFQS.

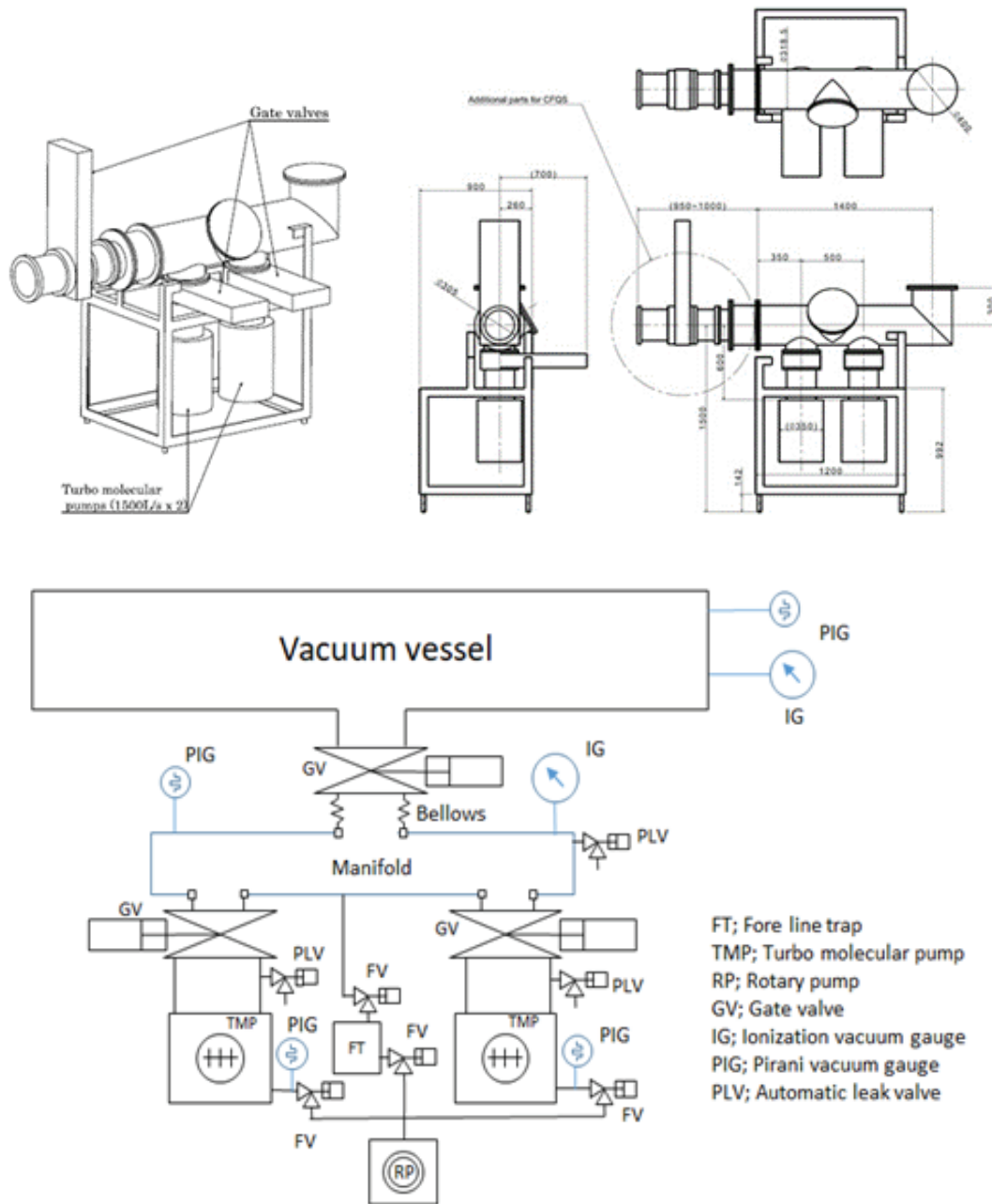


Fig 7.3-1 Vacuum pumping system. A rotary pump (RP) will be used in vacuum range of 20 to 30 Pa or more. Exhaust speed of two turbo molecular pumps (TMP) is 1500 l/s each. The ultimate vacuum pressure will be  $1 \times 10^{-6}$  Pa.

## 7.4 HIBP system

Heavy ion beam probe (HIBP) [1] is a powerful diagnostic tool to study the physics related to  $E_r$ , because it can measure the potential, the density, the magnetic field, and their fluctuations in magnetically confined high temperature plasmas, with good temporal and spatial resolutions, without giving any disturbances to plasma. Up to now, utilizing these superior features, HIBPs have been used to investigate many fascinating phenomena related to  $E_r$  and flow in plasmas. To study these attractive physics in CFQS with HIBP, HIBP will be installed. In this section, the feasibility study of this diagnostic is reported.

The vacuum vessel design of CFQS is shown in Fig 7.4-1, which has many ports for heating and diagnostic systems. We consider using two ports for HIBP, the top port with ICF203(CF150) size for probe beam injector, and the side port with ICF305(CF250) for energy analyzer and detector.

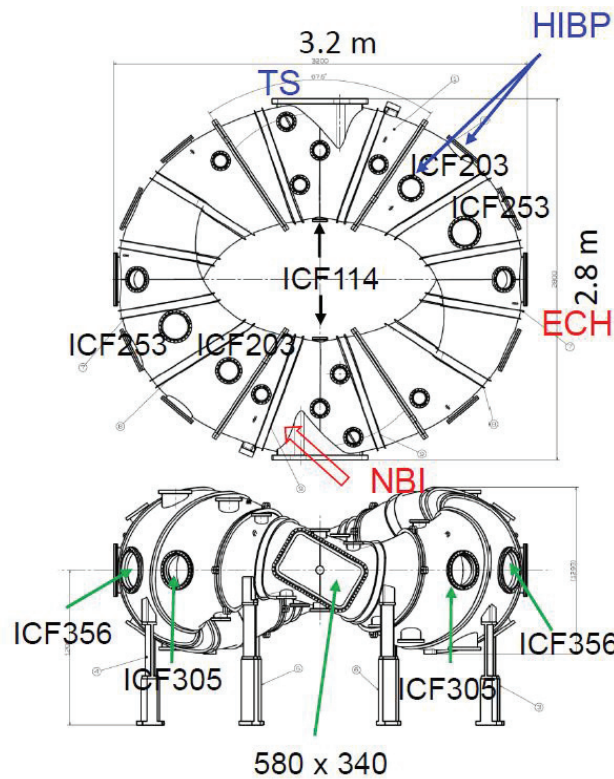


Fig 7.4-1 Vacuum vessel design and port arrangement for HIBP.

For a probe beam of HIBP, the Larmor radius of beam particle should be larger than the averaged radius of plasma to inject the beam into the plasma center. The Larmor radii as a function of beam energy is shown in Fig 7.4-2. Here, as beam particles, Li (7), Na (23), K (39), Rb (85), and Cs (133) with single charge are considered. Number means mass number of beam particles. Since, averaged minor radius of CFQS plasma is 0.25 m, at least the energy of 25 keV for Cs is required, however for Li the energy of 475 keV are required. We would like to reuse the high voltage power supply ( $< 200$  kV) of HIBP in CHS [2,3], therefore, K, Rb, Cs are acceptable from the point of probe beam energy, however, Li and Na, the beam energy is too large. In the orbit calculation, Cs particles are assumed in this section, but we can transform the required energy for other species easily by multiplying the mass ratio between Cs and considered beam species.

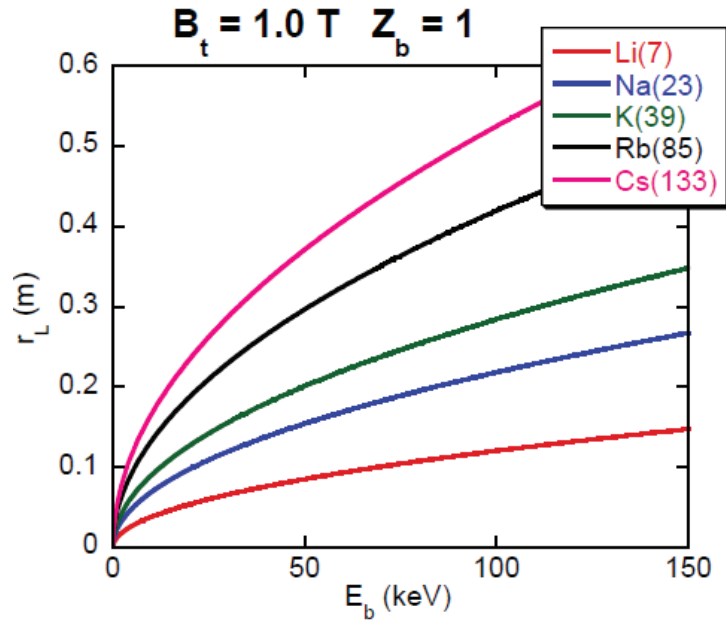


Fig 7.4-2 Larmor radius,  $r_L$ , of various ion as a function of beam energy,  $E_b$ .

In the orbit calculation, the detailed structure of HIBP system, e.g., 8 pole electrostatic deflector and energy analyzer, is not included, however, results shown here are utilized to determine actual arrangement of those components. Injection/ejection point of probe beam are chosen to be the center of top (injection)/side (ejection) port, for simplicity of initial and boundary condition. To optimize the probe beam orbit so that the beam injected from the center of injection port should reach to the ejection point at the center of side port, injection angle in the toroidal and poloidal direction is scanned and determined. A typical obtained orbit with the beam energy of 40 keV is shown in Fig 7.4-3. Projections of the orbit on top view plane (a) and on the poloidal cross section plane at the toroidal angle of 45 deg (b) are shown. In this case, primary beam are changed to be secondary beam near plasma center, so this means that observed region is plasma center.

By scanning the beam energy and the injection angle,  $E_b$ - $\theta$  grid map of observation region were calculated as shown in Fig 7.4-4. For Cs, the beam energy of 30 ~ 50 keV are useful for HIBP, which corresponds to the energy of Li: 570 ~ 950 keV, Na: 173 ~ 289 KeV, K: 102 ~ 171 KeV, and Rb: 47 ~ 78 keV.

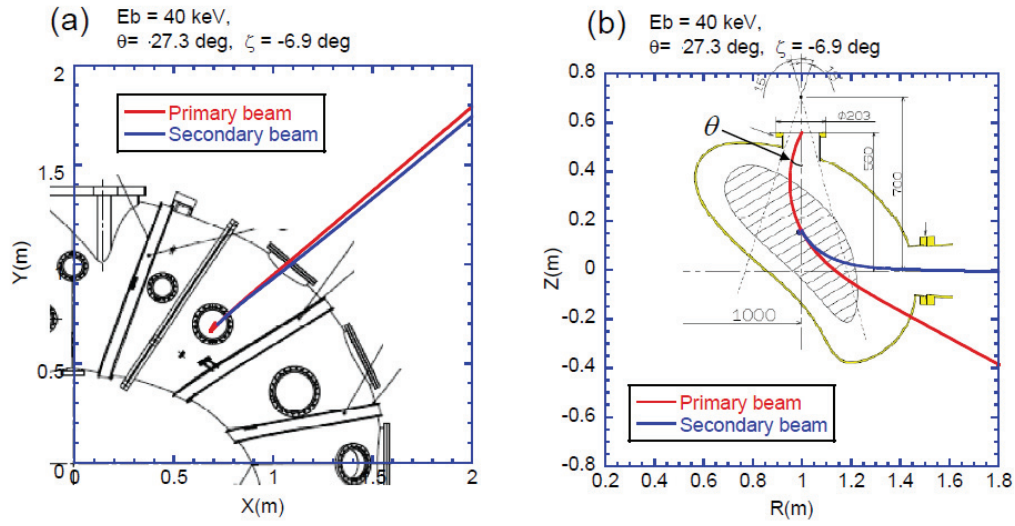


Fig 7.4-3 Typical example of probe beam orbit. Projection on (a) top view and (b) poloidal cross section plane. Cs of which beam energy of 40 keV is assumed in this orbit calculation.

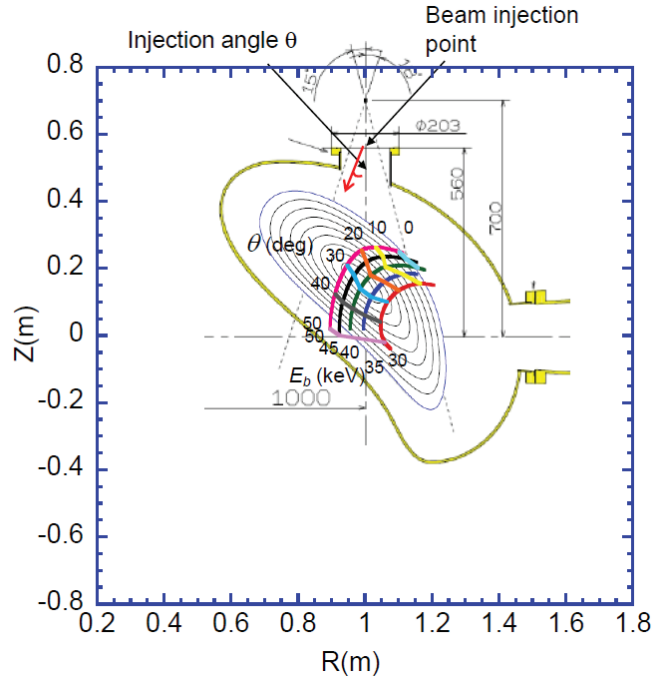


Fig 7.4-4  $E_b$ - $q$  grid map of observation region for HIBP are shown. Cs beam is assumed.

For HIBP, probe beam attenuation by the collision with plasma is an important factor to consider the appropriate density range in measurements. The probe beam is attenuated mainly by collisions with electrons. The detected beam current of the secondary beam at the detector can be expressed as,

$$I_D = 2I_0 n_e \langle \sigma_1 v_e \rangle w / v_B \times \exp[-\int n_e \langle \sigma_1 v_e \rangle / v_B d\ell - \int n_e \langle \sigma_2 v_e \rangle / v_B d\ell]. \quad (1)$$

Here,  $I_0$  is the injected current as the primary beam,  $I_D$  the detected current as the secondary beam,  $\langle \sigma_1 v_e \rangle$  rate coefficient of  $A^+ \rightarrow A^{2+}$  with electron impact,  $\langle \sigma_2 v_e \rangle$  rate coefficient of  $A^{2+} \rightarrow A^{3+}$  with electron impact,  $n_e$  the electron density,  $w$  the sample volume length,  $v_B$  the beam velocity, and  $d\ell$  the path integral along beam orbit. The

beam energy of 40 KeV for Cs, and orbit shown in Fig 7.4-3, are chosen to estimate  $I_D$ . We use the rate coefficient from the Lotz's empirical formula [4]. Temperature and density profiles of plasma are assumed as,  $T_{e0} (1 - \rho^2)$  and  $n_{e0} (1 - 0.8 \rho^2 + 1.3 \rho^4 - 1.5 \rho^6)$ , and  $T_{e0} = 1$  keV. In this case, estimated value of  $I_D/I_0$  as a function of the line averaged electron density,  $\bar{n}_e$ , is shown for Cs, Rb, K, Na in Fig 7.4-5. When  $\bar{n}_e < 1.0 \times 10^{19} \text{ m}^{-3}$ , Cs is the best in these species, while in the range of  $\bar{n}_e > 1.0 \times 10^{19} \text{ m}^{-3}$ , Rb is a better choice. For much larger density, K is another possible choice. From CHS experiments, when  $I_D$  is larger than a few hundreds of nA, large signal to noise ratio can be expected to measure turbulence, zonal flow etc. in plasma.  $I_D/I_0$  is  $10^{-3} \sim 10^{-2}$ , therefore, the primary beam current  $I_0$  of a few hundreds of  $\mu\text{A}$  is required. This range of current is not difficult to achieve by zeolite ion source [5], therefore, HIBP in CFQS will provide good opportunity to study attractive physics related to  $E_r$ .

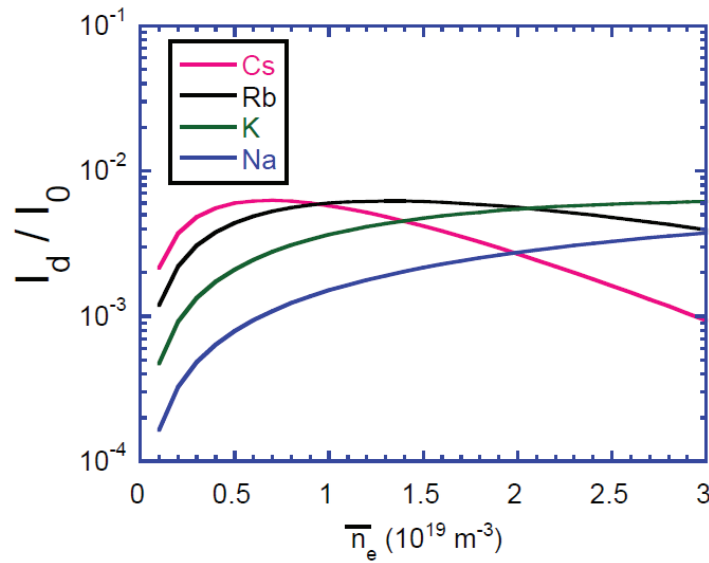


Fig 7.4-5 The beam attenuation of  $I_D/I_0$  as a function of line averaged electron density.

## References

- [1] F. C. Jobes *et al.*, Nucl. Fusion **10** (1970) 195.
- [2] A. Fujisawa *et al.*, Phys. Rev. Lett. **82** (1999) 2669.
- [3] A. Fujisawa *et al.*, Rev. Sci. Instrum. **67** (1996) 3099.
- [4] W. Lotz, Astrophys. J. Suppl. **14** (1967) 207.
- [5] S. Ohshima *et al.*, Rev. Sci. Instrum. **77** (2006) 03B704.



## 7.5 Magnetic surface measurement system

The presence of the magnetic surfaces in the plasma confinement region is indispensable to guarantee high-performance plasma discharge operation. The magnetic coil system in CFQS consists of modular coils (MCs), poloidal field coils (PFCs), and toroidal field coils (TFCs). After the construction of CFQS has been completed, an experiment for measuring magnetic surfaces by a fluorescent method using an electron beam and a fluorescent mesh is planned. Fig 7.5-1 shows the top view of the experimental setup for the measurement which consists of three apparatuses: movable electron guns, a fluorescent mesh, and high-sensitive cameras. An electron beam, which is extracted from the electron gun, toroidally circulates along the magnetic field line in the plasma confinement region inside the vacuum vessel. The electrons interact with the wires on the fluorescent mesh on which zinc oxide (ZnO) powders are sprayed, which emits luminescent light at the interaction points. The mesh is installed in the vacuum vessel at a toroidal angle where the shape of the magnetic surfaces is horizontally elongated. The distribution of the luminescent light on the mesh is observed with the high-sensitive cameras, providing a poloidal cross-section of the magnetic surfaces. The measurements are performed with the change of the radial position of the electron gun to obtain the magnetic surfaces at different radial positions. The fluorescent mesh is horizontally moved by about a few cm for the exposure time of the high-sensitive camera (about 2 minutes) to get the image of the magnetic surfaces at the positions between the mesh wires. These three apparatuses are installed so as not to disturb the measurement of the luminescent light by stray light emitted from the aperture of the electron gun. Fig 7.5-2(a) gives a perspective view of the vacuum vessel of CFQS for presenting the position of the apparatuses for the magnetic surface measurements. Fig 7.5-2(b) illustrates the field of view from the two candidate viewports for installing the high-sensitive cameras, which shows that most of the area on the mesh can be observed. The experiment for the magnetic surface measurements will be performed in a low magnetic field of 0.1 Tesla because the magnetic field has to be sustained for up to 2 minutes for the measurement. Calculations by magnetic field line tracing have revealed that the effect of the earth magnetism at the construction site (Chengdu in China) on the magnetic surfaces is negligible in the low magnetic field.

It has been already found that the magnetic surfaces are not significantly affected by the error magnetic fields caused by the displacement of the modular coils (MCs) in the standard magnetic configuration in which only the MCs are electrically excited. While this property is advantageous for maintaining magnetic surfaces in the plasma confinement region, it prevents the detection of the error fields. For this reason, a special magnetic configuration for detecting the error fields was proposed. In this magnetic configuration, the rotational transform crosses  $1/3$  in the middle of the plasma confinement region by optimizing the electric current of the poloidal field coils (PFCs). Fig 7.5-3 displays the calculations of the poloidal cross-section of the magnetic surfaces at the toroidal angle where the fluorescent mesh is installed. The magnetic field lines are traced from the position of an electron gun with the change of the vertical position by 5 mm. Here, the radial displacement of one MC is considered as one of the possible error field sources. Fig 7.5-3(a) and (b) show the calculations in the standard magnetic configuration without and with the error fields induced by a radial displacement of 10 mm, respectively. The calculations demonstrate that the magnetic surfaces in the standard configuration are not affected by the coil displacement. Fig 7.5-4(a) and (b) indicate the poloidal cross-section of the calculated magnetic surfaces in the special magnetic configuration without and with the radial displacement of the coil, respectively. In this configuration, magnetic islands are formed in the middle of the plasma confinement region. In the case of no coil displacement, up-down

symmetric magnetic islands are formed as shown in Fig 7.5-4(a). However, up-down asymmetric magnetic islands are produced in the case with the coil displacement as presented in Fig 7.5-4 (b). The calculations prove that the special magnetic configuration is advantageous for detecting the error fields induced by the coil displacement.

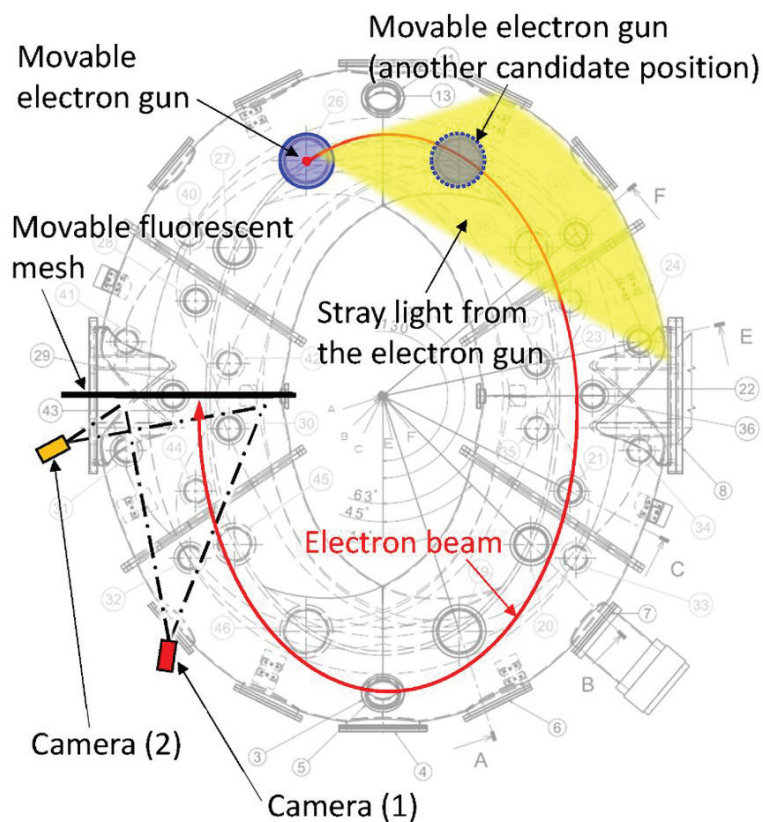


Fig 7.5-1 Top view of the experimental setup for the magnetic surface measurement in CFQS.

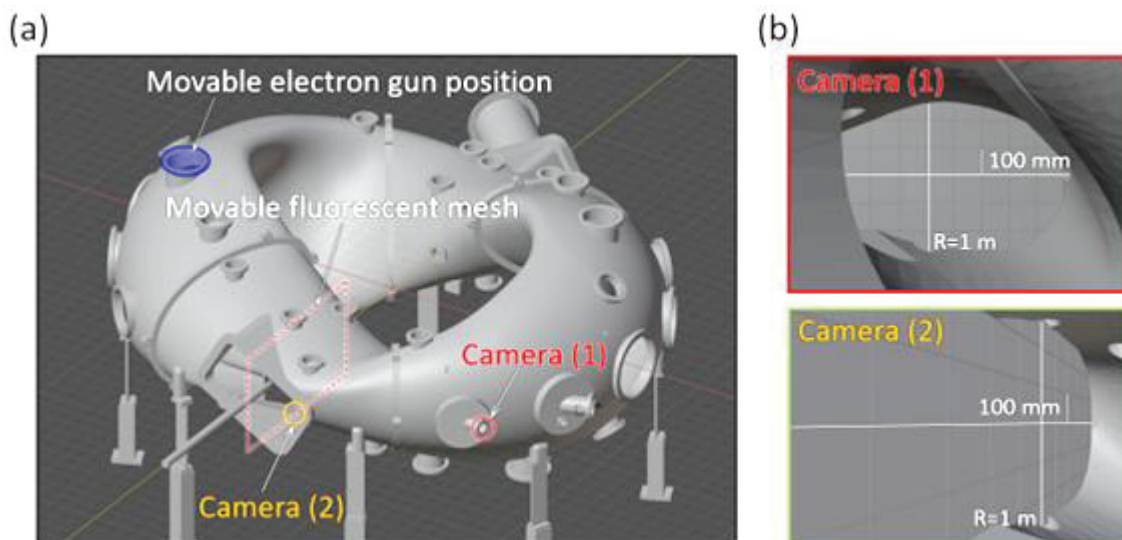


Fig 7.5-2 (a) A perspective view of the vacuum vessel of CFQS. (b) The field of view from the viewports for the high-sensitive cameras.

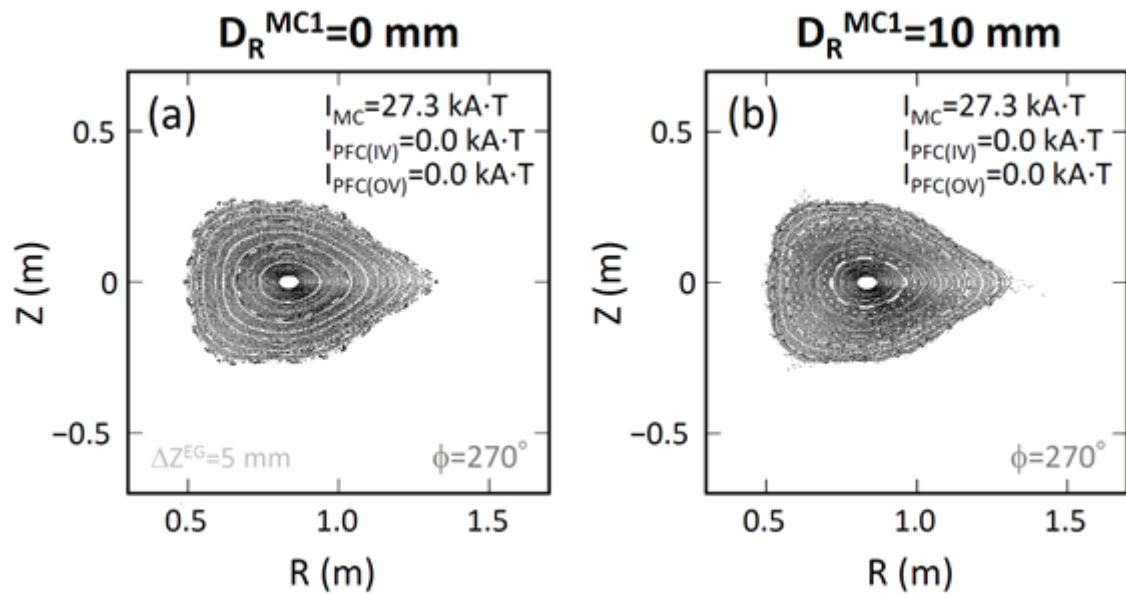


Fig 7.5-3 The calculation of the poloidal cross-section of the magnetic surfaces in the standard magnetic configuration without (a) and with (b) a radial displacement of one MC by 10 mm.

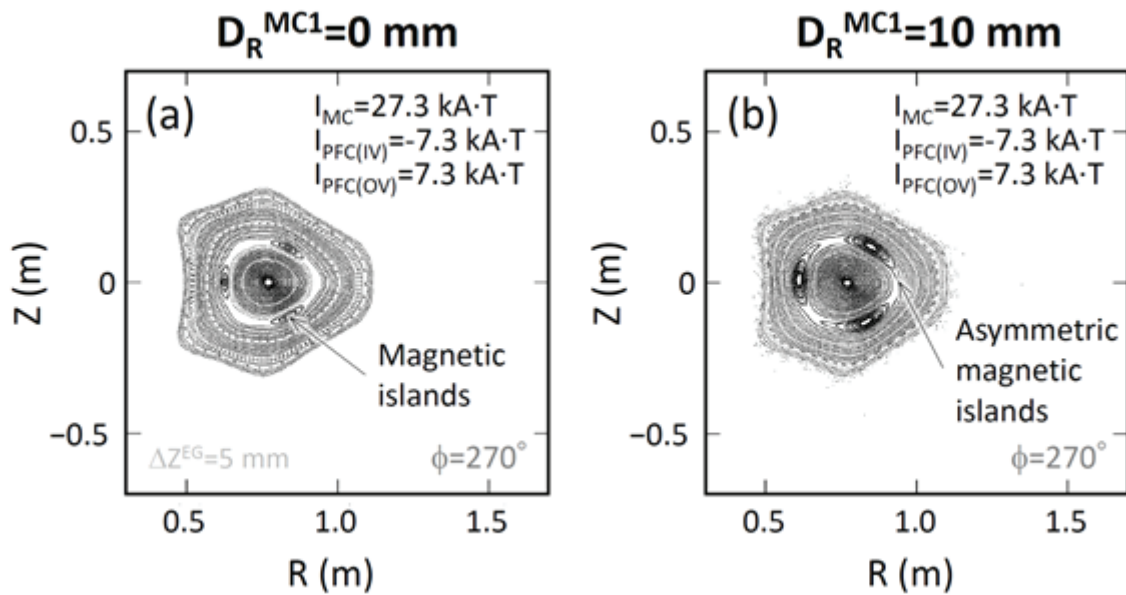


Fig 7.5-4 The calculation of the poloidal cross-section of the magnetic surfaces in a special magnetic configuration for the magnetic surface measurement without (a) and with (b) a radial displacement of one MC by 10 mm

## 7.6 Langmuir probe in CFQS

Reciprocating Probe System (RPS) has been designed to measure the equilibrium and fluctuating parameters involved plasma density, electron temperature, potential, radial electric field, etc. in CFQS for 0.1 T operation. The designed spatial and time resolution of RPS could reach 2 mm and 1  $\mu$ s, respectively. Plotted in Fig 7.6-1 (a) is the bird's view of CFQS. The equilibrium magnetic configuration of CFQS at port 16 together with the radial trajectory of RPS is sketched in Fig 7.6-1 (b). The RPS is fully driven by servo motor, which has the slow and fast motion phases as shown in Fig 7.6-1 (c). Before the discharge, the Langmuir probe installed at RPS could be carried inward by the servo motor with a rather slow motion (from A to B) and then keeps stationary at a pre-set radial position, e.g. B. Once the RPS receives the external trigger signal, the RPS rapidly moves inward from point B to point C with a roughly radial velocity 1~3 m/s (fast motion), and then RPS stays at point C for a sustainable measurement, here the staying time could be set from a few milliseconds to hundreds of milliseconds. Finally, the RPS returns back to the initial measurement position, e.g., point B. In general, the measured point B to point C could be flexibly adjusted via the servo control system according to the experimental requirements.

The diagram of RPS is sketched in Fig 7.6-2, which mainly contains the servo driving system, transmission shaft, vacuum pre-pumping, viewing window and optical grating measurement. The servo motor has advantages of fast response and high spatial-accuracy control. It could drive the transmission shaft to move inward or outward via the angular force produced by the permanent magnet (negligible effect by the toroidal magnetic field). The optical grating is designed to record the displacement signal of RPS motion with accuracy of 0.1 mm. The viewing window with diameter 200 mm is generally used to change the probe structure according to the experimental requirements. The vacuum pumping is mostly employed for pre-pumping after changing the probe structure. The detailed design on the probe structure involved the material and wire will be given in the next step.

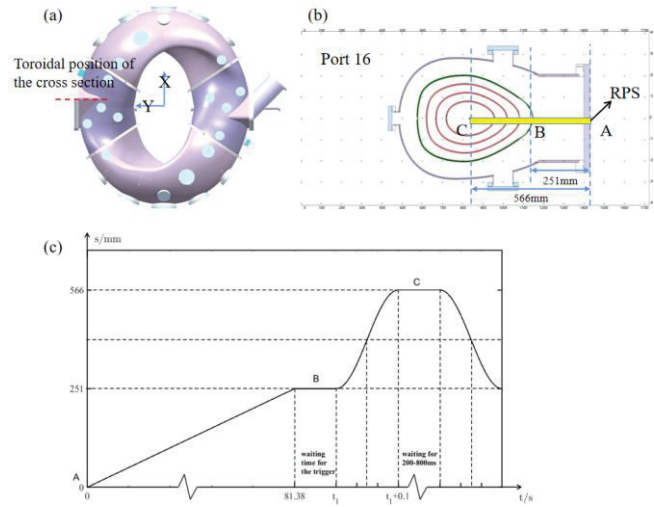


Fig 7.6-1 (a) The bird's view of CFQS, (b) the magnetic configuration at Port 16 and (c) the time trace of RPS displacement with slow (A-B) and fast (B-C) motion.

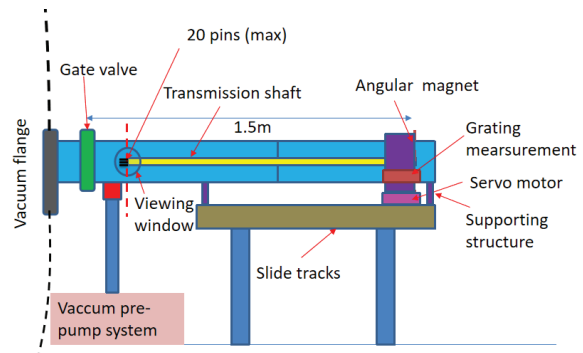


Fig 7.6-2 Schematic diagram of the RPS in CFQS



## 7.7 LIBP system

In the first phase of the CFQS operation program with 0.1 T, we cannot expect a normal operational scenario of the HIBP diagnostic system. The electron temperature is supposed to be extremely low (less than 10 eV) and the ionization rate from the single ionized state to the second ionized state of the heavy ion species will not be sufficiently large for the detection of the secondary ionized ion beam. However, in order to make progresses in the preparation of the HIBP system for the future 1.0 T operation of CFQS, we will perform the ion beam injection experiment without expecting the second ionization of the ion beam in the plasmas. Due to extremely low magnetic field strength, we choose the ion beam species of light mass for obtaining measurable trajectory of the charged beam. Thus, it is called light ion beam probe (LIBP).

What we learn from this LIBP experiment are

- Improving the ion beam detection method against the noises caused by the radiation from plasmas.
- Improving the precise control of the launching angle of ion beam using the bias control of steering electrodes.
- Learn the ion source development technique for getting a large beam current.

Li (mass number is 7) and Na (mass number is 23) with a single charge are considered to be the candidates. In order to satisfy the basic condition that the Larmor radius of the beam ion should be larger than the averaged radius of plasma [1], the minimum beam energies for Li and Na are 4.8 keV and 1.4 keV, respectively. We decided to select Na as beam species because the required operating temperature is low, and it is less corrosive. The primary beam current  $I_D$  is a few hundreds of  $\mu\text{A}$ . These required energies and current of the ion source can be easily obtained from high intensity alkali ion sources. Fig 7.7-1 shows an example of the Na primary beam orbits with energy of 1~10 keV and the injection angles of zero.

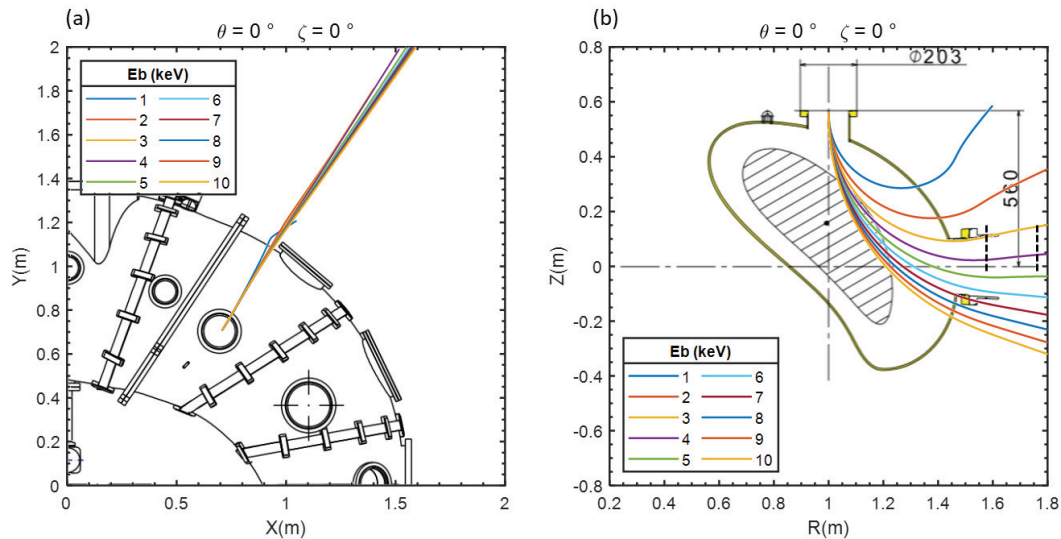


Fig 7.7-1 Example of primary beam orbits under 0.1 T. Projection on (a) top view and (b) poloidal cross section plane for Na beam orbits with energy of 1~10 keV and injection angles of zero.

Accordingly, we will develop a new ion beam source with energy varying from 1 to 10 keV and make the beam detection in the test stand. In Fig 7.7-2, a schematic of the beam injector is depicted. The beam is extracted

from the surface of the ion source by a Pierce-type electrode and focused by cylindrical electrostatic lenses. Two pairs of electrostatic plates are arranged to control the beam position in the radial direction, and a movable Faraday cup is used for the beam intensity measurements. Fig 7.7-3 shows an example of the Na beam divergence simulation with energy of 8 keV. After the buildup of the ion beam source, a model coil under the 0.1 T magnetic field will be constructed to calibrate the primary beam orbit.

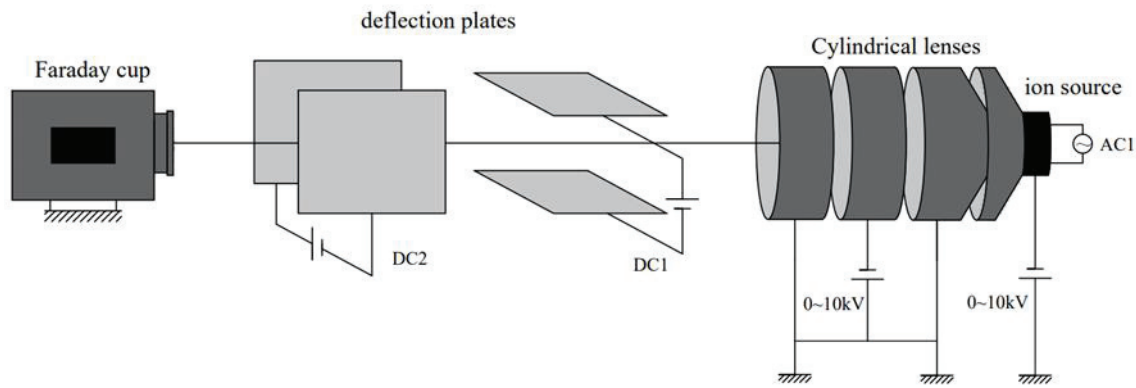


Fig 7.7-2 Schematic drawing of the Na beam injector.

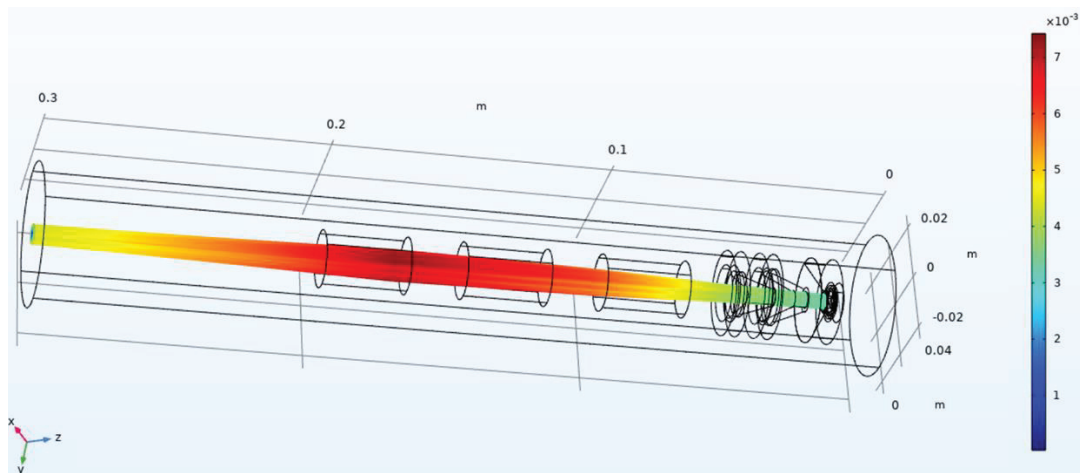


Fig 7.7-3 Simulation of the beam divergence with energy of 8 keV. The diameter of the beam is illustrated with various colors.

After the operation of the CFQS, we will firstly detect the beam trajectories without plasma discharge in the device. In order to monitor the ion beam location, which is deflected by the magnetic field, a primary beam detector will be installed inside the port at the right side of Fig 7.7-1(b). For LIBP, the secondary beam production is negligible because the plasma density at 0.1 T is extremely low, and consequently, the current is too small to measure.

## References

- [1] I. S. Bondarenko *et al.*, Rev. Sci. Instrum. **75** (2004)1826



NIFS-SWJTU JOINT PROJECT FOR CFQS  
~PHYSICS AND ENGINEERING DESIGN~

VER. 5.1

2023. AUG.

APPENDIX-A2 (RD)

~RESERCH AND DEVELOPMENT~

CFQS Team



*NIFS; National Institute for Fusion Science*

*SWJTU; Institute of Fusion Science, School of Physical Science and Technology, Southwest Jiaotong University*

*Hefei Keye; Hefei Keye Electrical Physical Equipment Manufacturing Co., Ltd.*

## Table of Contents

1	Production and test of a mockup modular coil for the MC4.....	3
1.1	Summary .....	3
1.2	Conductor and insulation material .....	3
1.3	Winding manufacture line.....	5
1.4	Design of winding mold.....	5
1.5	Production process of the MC4 mockup coil.....	7
1.6	Deformation measurement of the MC4 coil by a laser tracker .....	10
1.6.1	Winding mold before the VPI .....	10
1.6.2	Coil on the winding mold after the VPI .....	10
1.6.3	Coil without restraint after the heat run test .....	11
1.7	Impulse test .....	13
1.8	Resistance and inductance measurement of the MC4.....	16
1.9	Withstand voltage test for the ground insulation .....	19
1.10	Airtightness test with nitrogen gas.....	20
1.11	Flow rate dependence of the pressure drop.....	20
1.12	Heat run test.....	22
1.12.1	Summary .....	22
1.12.2	Test result of 1 kA/38 s without cooling water .....	23
1.12.3	Test result of 1 kA/38 s with cooling water .....	24
1.12.4	Test result of 500 A/120 s without cooling water .....	25
1.12.5	Test result of 500 A/120 s with cooling water .....	26
1.13	Overvoltage test .....	27
2	Production of a vacuum vessel.....	28
2.1	Summary .....	28
2.2	Design of the mold for pressing and welding .....	29
2.3	Method of dividing parts.....	30
2.4	Production process of the vacuum vessel.....	32
2.5	Deformation measurement by a laser tracker.....	38
3	Plastic model developed by 3-D printer.....	41
3.1	Plasma.....	41
3.2	Vacuum vessel .....	42
3.2.1	Examination of production.....	42
3.2.2	Real scale model of the vacuum vessel.....	43
3.2.3	Check of the baking heater.....	44
3.3	Modular coil.....	47
4	Actual size wooden model of the vacuum vessel.....	49
4.1	Wooden model of the vacuum vessel for trial winding of TFC.....	49
4.1.1	Wooden model of the vacuum vessel.....	49
4.1.2	Trial of winding a square solid conductor as a TFC .....	53
4.1.3	Trial of winding a cable as a TFC .....	56
4.2	Wooden model of the vacuum vessel for examining the installation of parts in a vacuum vessel .....	59

## 1 Production and test of a mockup modular coil for the MC4

### 1.1 Summary

The total number of the CFQS modular coil is 16. The number of MC4 coil is 4, and the MC4 is the most complex coil. So, the M4C mockup coil was manufactured firstly, the manufacturability and the validity of the design were confirmed. Fig 1.1-1 shows the mockup coil and the mold for the VPI process.

An electric current was applied to the coil and the change in coil temperature was measured. Since the experimental results are consistent with the theoretically estimated characteristics, it was confirmed that the coil fabrication was appropriate.

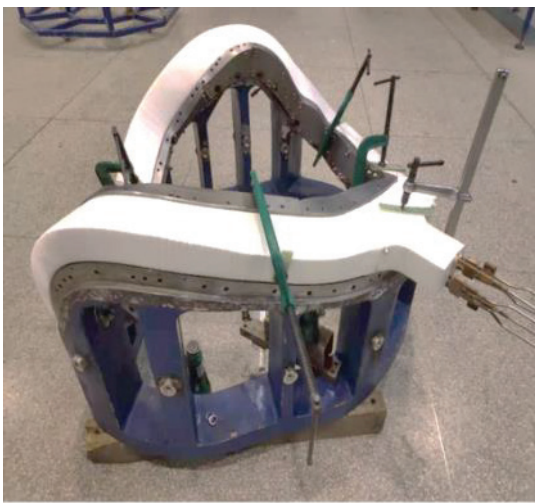
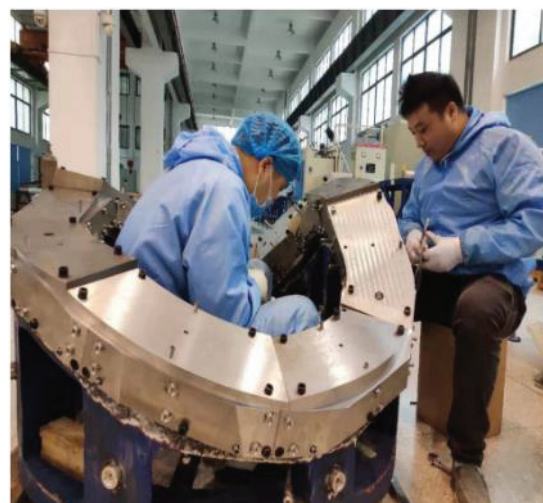


Fig 1.1-1



Picture of the mockup coil.

The test results are summarized below.

- (a) The manufacture and test of the MC4 mockup coil was finished.
- (b) The final dimension deviation of the mockup coil was about 3 mm.
- (c) The impulse test results showed that the layer-to-layer insulation was qualified.
- (d) The heat run test showed that the characteristics of temperature changes was as expected theoretically.
- (e) When operating for a long time for discharge cleaning, it is better to increase the flow rate of cooling water to improve the cooling performance. For that purpose, it is necessary to increase the pressure of the cooling water device.
- (f) The withstand voltage of layer insulation was DC10 kV or more. Since it can withstand the operating voltage by itself, it is possible to simplify the ground insulation.
- (g) The withstand voltage of ground insulation was DC 20 kV or more. So, the ground insulation ability is enough and if can be simplified if necessary.

### 1.2 Conductor and insulation material

The conductor dimension used for the mockup coil is  $8.5 \times 8.5 \times \Phi 4$  mm, the layer insulation thickness is 1 mm, and

the ground insulation is 3 mm. Eight units Cu conductors have been purchased for the mock-up coil; each unit length is about 100 m. The material of the conductor for the mockup coil is oxygen-free copper and the chemical composition is shown in Table 1.2-1. The Cu content is 99.97 % and oxygen content is 0.0008 %. The mechanical performance of the conductor is shown in Table 1.2-2. The tensile strength is 239 MPa, and elongation is 45 %. The dimension tolerance of the conductor is  $8.5 \times 8.5 \times \Phi 4 + 0.08$  mm. Fig 1.2-1 shows the cross section of the conductor.

Table 1.2-1      Chemical composition of the Cu conductor.

化学成分 (%) Chemical Composition	Cu	O							
标准值 Standard Requirement	≥99.97	≤0.002							
实测值 Test	99.97	0.0008							
180829									



Fig 1.2-1      Conductor for the mockup coil.

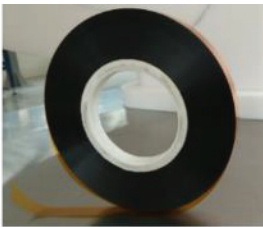
The main material for the insulation is fiber glass tape and polyimide (Kapton) as shown in Fig 1.2-2. The width and thickness of the fiber glass tape and the Kapton are 16 mm × 0.2 mm and 10 mm × 0.05 mm respectively for the mockup coil.

Table 1.2-2      Mechanical performance of the Cu conductor.

试验项目 Test	外观·尺寸 Visual & Dimension	抗拉强度 Rm(Mpa) Tensile Strength	延伸率 A(%) Elongation	导电率(%) Electrical	气压 Pneumatic Pressure	耐击穿电压	钢珠通试
标准值 Standard Requirement		≥205	≥35	≥100	合格		通过
实测值 Test	合格	239	45	100	合格		通过
180829							
检验员签章 Inspector:	技术条件 Technical Conditions:		备注 Remark :		上海上大众科技发展有限公司 SHANGHAI STARKING SCIENCE AND TECHNOLOGY CO., LTD 质保部 Quality Department		



(a) Fiber glass tape  
16mm x 0.2mm x 50m  
Tensile strength 1920N/25mm



(b) Polyimide (Kapton) tape  
10mm x 0.05mm x 2000m  
Tensile strength 115MPa

Fig 1.2-2      Insulation materials for the mock-up coil.

### 1.3 Winding manufacture line

The conceptual design of the coil winding manufacture line for the mockup coil is shown in Fig 1.3-1. It includes rotating platform, winding mold, and clamping, copper conductors, insulation wrapping, and conductor straightening.

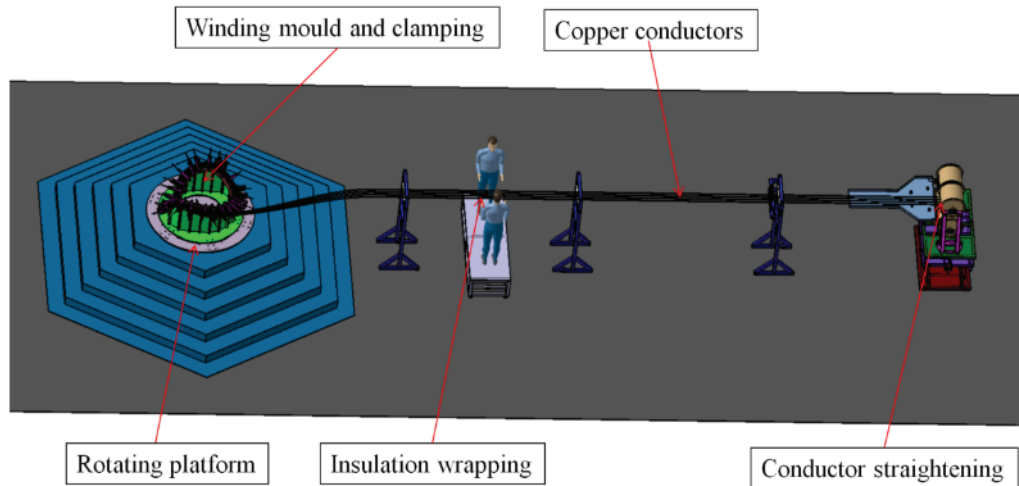


Fig 1.3-1 Conceptual design of the coil winding manufacture line.

### 1.4 Design of winding mold

The winding mold has been designed based on the MC4 coil profile shape as shown in Fig 1.4-1 and Fig 1.4-2. it consists of a bottom mold, inner plate, outer plate, and top cover plate. Each of the inner plate, outer plate and top cover plate is divided into around ten blocks and can be disassembled and assembled according to the progress.

The usage of the winding mold is divided into 5 stages.

- 1<sup>st</sup> stage: The bottom mold and inner plate are used for the coil winding with the layer insulation.
- 2<sup>nd</sup> stage: All blocks are used for the 1<sup>st</sup> VPI with the the layer insulation.
- 3<sup>rd</sup> stage: The surface of the all blocks facing the coil is scraped by 3 mm for the ground insulation.
- 4<sup>th</sup> stage: The coil is wrapped with 3 mm ground insulation without the winding mold.
- 5<sup>th</sup> stage; All blocks are used for the 2<sup>nd</sup> VPI with the the ground insulation.

(Attention)

In the production of the mockup coil, the second stage was omitted, and work of the ground insulation was proceeded without VPI, but it was exceedingly difficult to insert the coil into the mold for the fifth stage. Reflecting on that, we plan to add a second stage in the actual production.

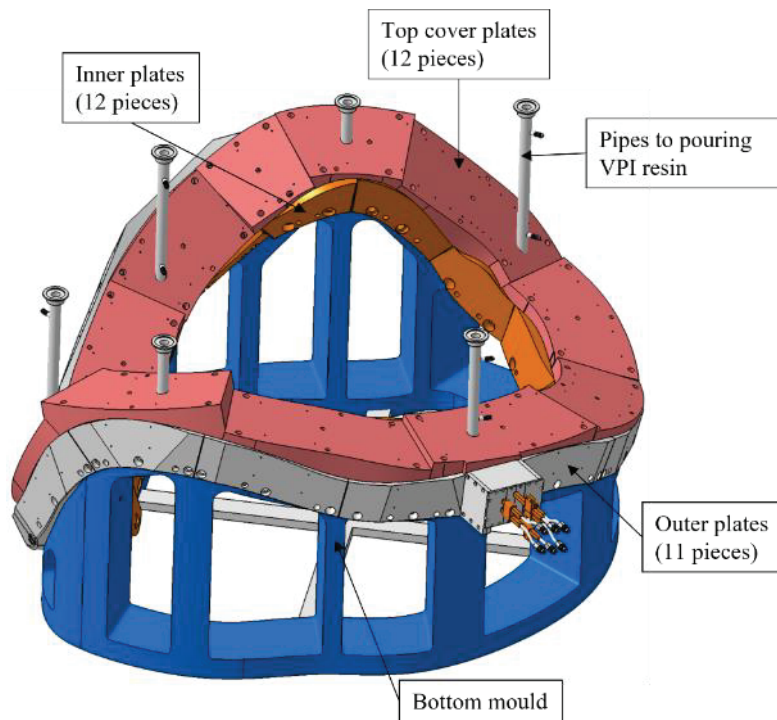


Fig 1.4-1 Winding mold for the MC4 mockup coil with a tank function of the VPI.

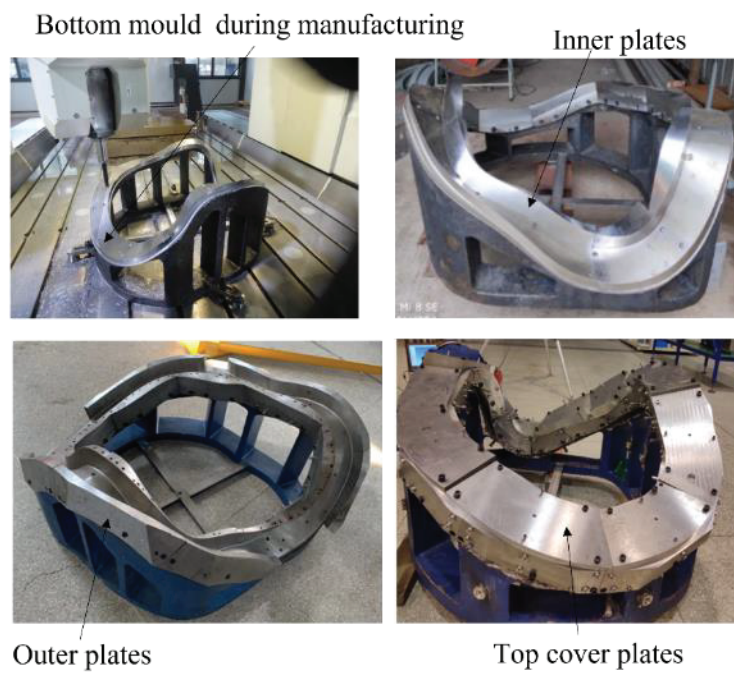


Fig 1.4-2 Pictures of the winding mold.



1.5 Production process of the MC4 mockup coil

The production process of the MC4 mockup coil is shown in Fig 1.5-1, and the main manufacture points is shown in Fig 1.5-2. The typical scenes in each work are summarized in Table 1.5-1.

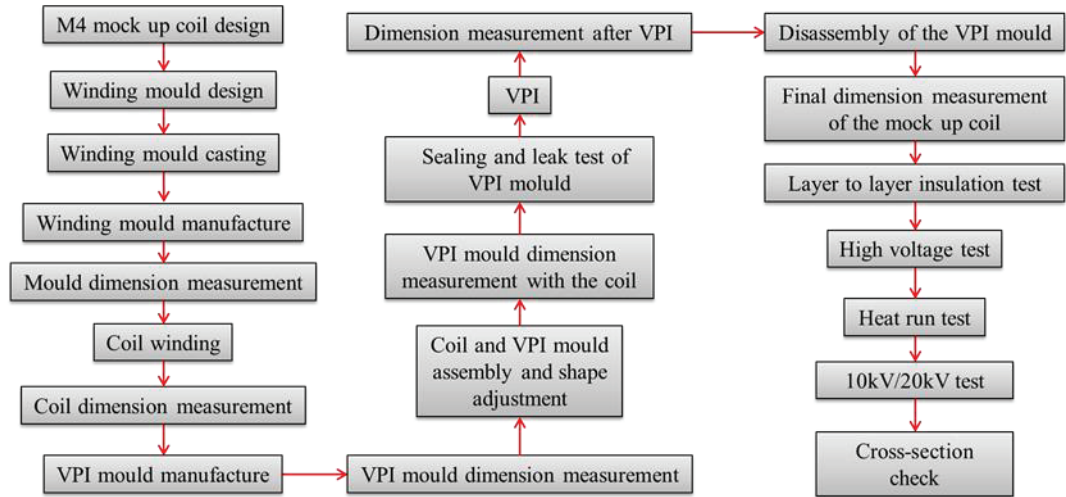







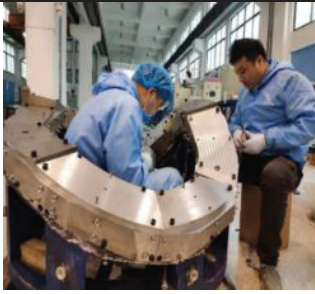
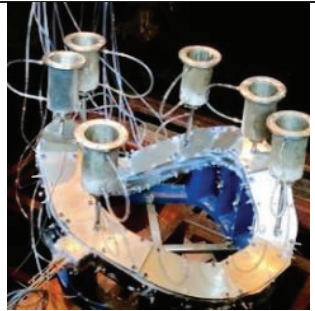




Fig 1.5-1 The production process of the MC4 mockup coil.



Fig 1.5-2 The main production points of the MC4 mockup coil.

Table 1.5-1 Production process of the MC4 mockup coil.

Step	work	Picture
1	Winding preparation. Half of conductor was wound around the cylindrical winding frame.	
2	Bending of a conductor on the mold. The conductor was bent along the winding mold by clamping and hammering.	
3	In the middle of winding work. The conductor was clamped to the winding mold.	
4	In actual production, a VPI dedicated to layer insulation will be added here.	---
5	Ground insulation. The conductor was removed from the winding mold and the ground insulating tape was wrapped.	
6	Reinstall the coil with ground insulation into the mold.	

Step	work	Picture
7	Close the winding mold. The coil was returned in the winding mold and the winding frame was closed with the top cover plates.	
8	The gap between the blocks was filled with glue to prevent the resin from leaking.	
9	VPI preparation. Resin tanks and hoses for injecting resin were added.	
10	VPI. All units were installed in a vacuum heating tank and the VPI process was conducted.	
11	Take the mold out of the VPI tank and open the top cover plate.	
12	Take out the top cover plates, inner plates, and outer plates. And clean up the coil by removing hardened excess resin.	
13	Disassemble the coil from the mold. The coil was removed from the winding mold and moved to the test stage.	



## 1.6 Deformation measurement of the MC4 coil by a laser tracker

### 1.6.1 Winding mold before the VPI

Deformation of the winding mold was measured before the VPI. The result is shown in Fig 1.6-1. The deviation was 0.05~0.52 mm.

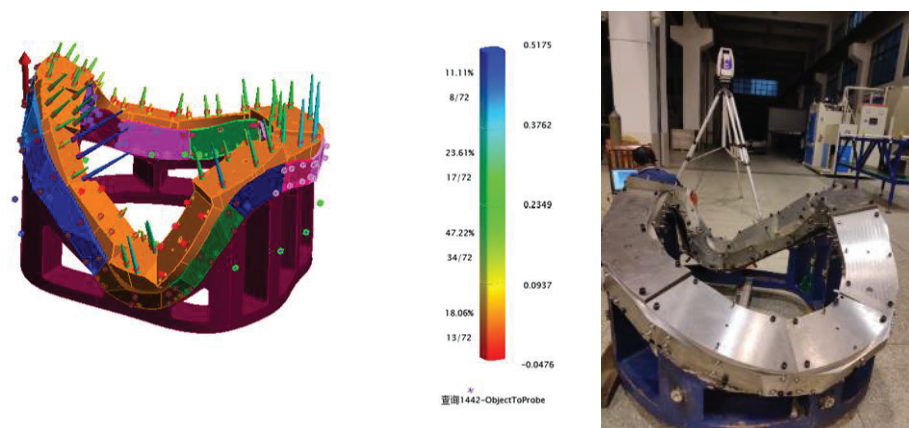


Fig 1.6-1 Deformation measurement result of the winding mold. On the upper surface. Before the VPI at 2019/10/24. The deviation was -0.05 to 0.52 mm.

### 1.6.2 Coil on the winding mold after the VPI

Deformation of the MC4 mockup coil was measured on the winding mold after the VPI with ground insulation. Example of the result is shown in Fig 1.6-2. The deviation was as follows:

- -0.39~0.77 mm on the upper surface,
- -0.13~-0.98 mm on the outer surface,
- 0.19~-0.66 mm on the inner surface.

The maximum deviation was about 1 mm which may include a measurement error, and it was found that the coil can be controlled with the mold accuracy.

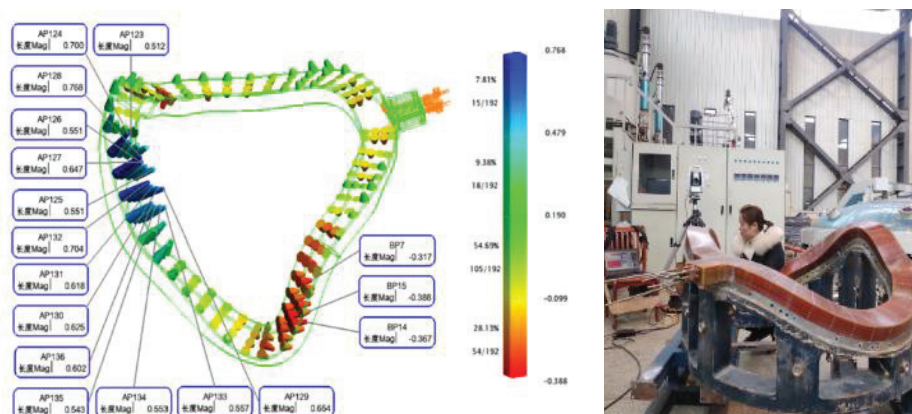


Fig 1.6-2 An example of the deformation measurement result of the MC4. Upper surface with ground insulation on the winding mold. After the VPI at 2019/12/24. The deviation was -0.39 to 0.77 mm.

### 1.6.3 Coil without restraint after the heat run test

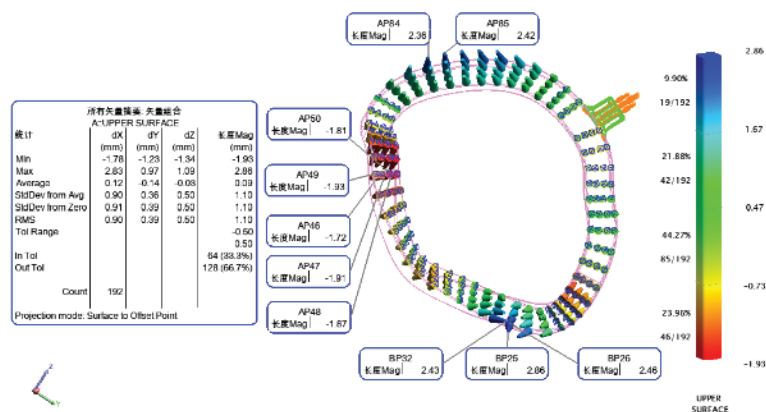
Deformation of the MC4 mockup coil was measured without restraint after heat run test as a final record. The result is shown in Fig 1.6-3 and Fig 1.6-4. The deviation was as follows:

- -1.93~2.86 mm on the upper surface,
- -0.72~3.21 mm on the outer surface,
- -3.26~0.69 mm on the inner surface.

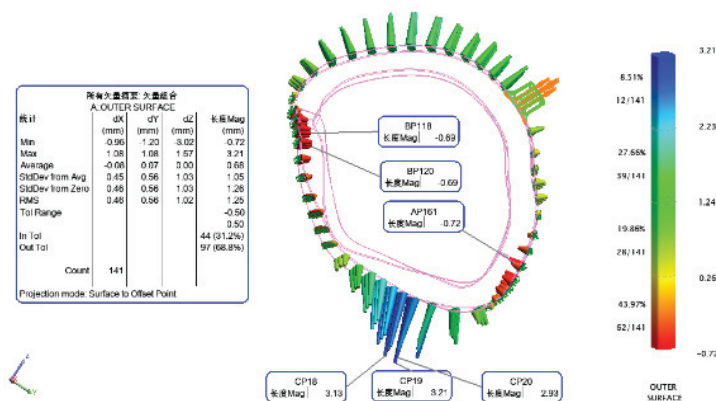
Compare with the result after the VPI, the deformation was about 3 times larger. The reason is not clear, but it is said that it may be the effect of deformation due to removal from the winding mold or the measurement error. In any case, it should be considered that there is a high possibility that a deviation of about 3 mm will occur. Since the standard tolerance of tolerance grades V (very coarse) or C (coarse) is a few mm, the deviation of 3 mm is considered reasonable.



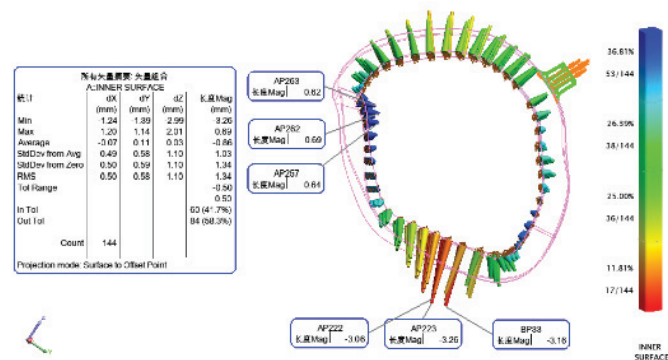
Fig 1.6-3 Scene of the deformation measurement without constraint.



(a) Upper surface, the deviation is -1.93~2.86 mm.



(b) Outer surface, the deviation is -0.72~3.21 mm.



(c) Inner surface, the deviation is -3.26~0.69 mm.

Fig 1.6-4 Deformation measurement result of the MC4. Without restraint. After the heat run test at 2020/07/20. As a final record.

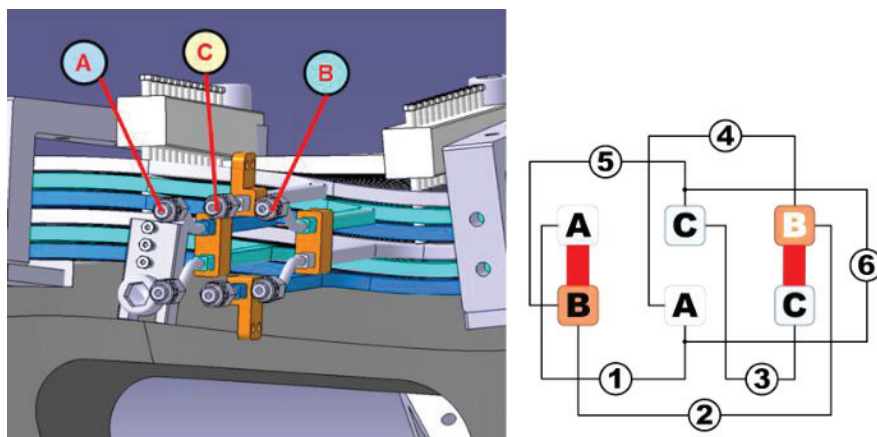


## 1.7 Impulse test

To inspect the turn-to-turn insulation, the impulse tests were performed as shown in Fig 1.7-1 to Fig 1.7-8. The connecting schematic diagram for the impulse test and example of the waveform are shown in Fig 1.7-1 and Fig 1.7-2. The test process as follow,

- Cut the series connection of the mockup coil, and perform the test of 1, 2, and 3,
- Connect the A and B to perform the test of 4,
- Connect the B and C to perform the test of 5,
- Connect the A, B, and C to perform the test of 6.

In the figure for the waveform of the impulse test, the X axis shows number of sampling time and Y shows voltage. The sampling frequency is 3.12 MSA/s ( $0.32 \mu\text{s}/\text{sample}$ ) and the number of time points displayed is 6000, which corresponds to 1.92 ms. Time between grids is 0.32 ms. The test results are shown in Fig 1.7-3 to Fig 1.7-8. The waveforms show that the oscillation attenuation trend of all test waveforms are same, so the turn-to-turn insulation is qualified.



A mark of ① to ⑥ indicates the name of a test, and a mark of A to B the name of a conductor.

TEST1 is the test of conductor A,  
TEST2 is of conductor B,  
TEST3 is of conductor C,  
TEST4 is of conductor A+B,  
TEST5 is of conductor B+C,  
and TEST6 is of conductor A+B+C.

Fig 1.7-1 The connecting schematic diagram for the impulse test.

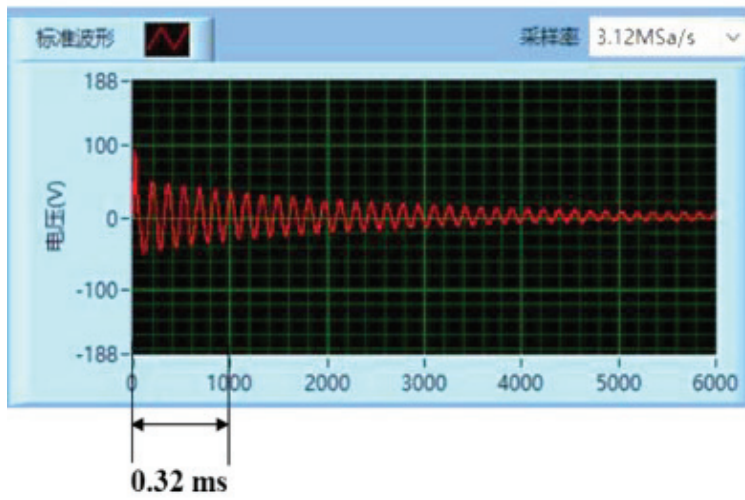


Fig 1.7-2 Scene of the impulse test and example of the waveform. The equipment used is the pulse coil tester of TH2883-1.

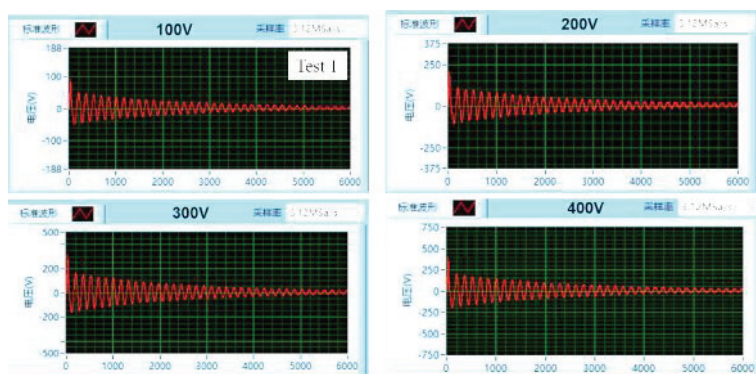


Fig 1.7-3 Test result of the TEST1 (Conductor-A).

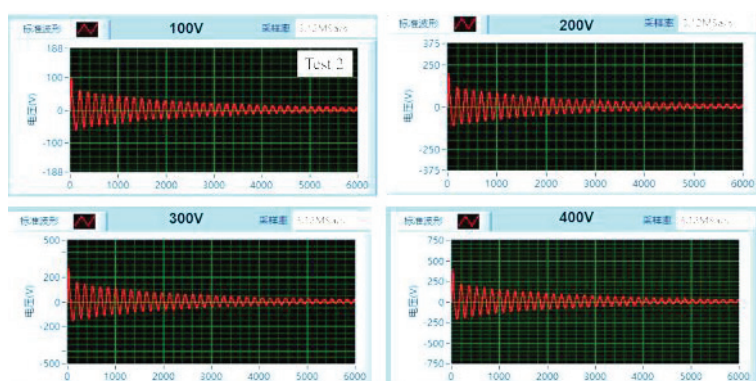


Fig 1.7-4 Impulse test result of the TEST2 (Conductor-B).

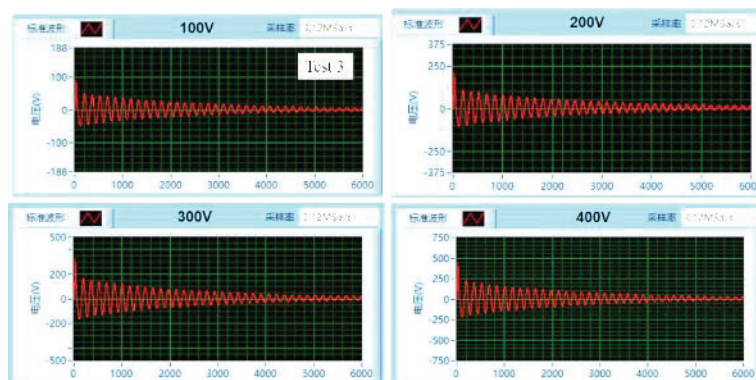


Fig 1.7-5 Impulse test result of the TEST3 (Conductor-C).

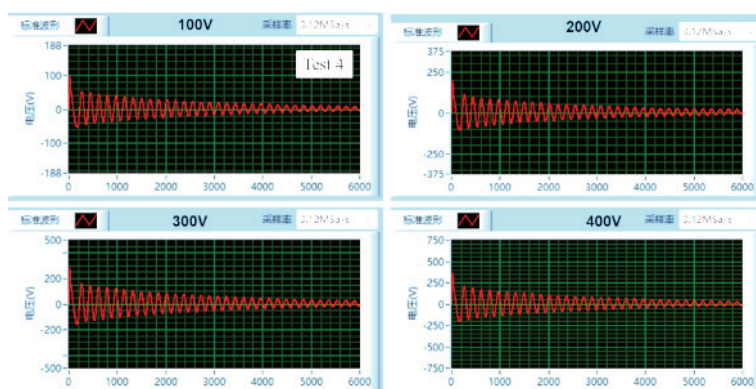


Fig 1.7-6 Impulse test result of the TEST4 (Conductor A+B).

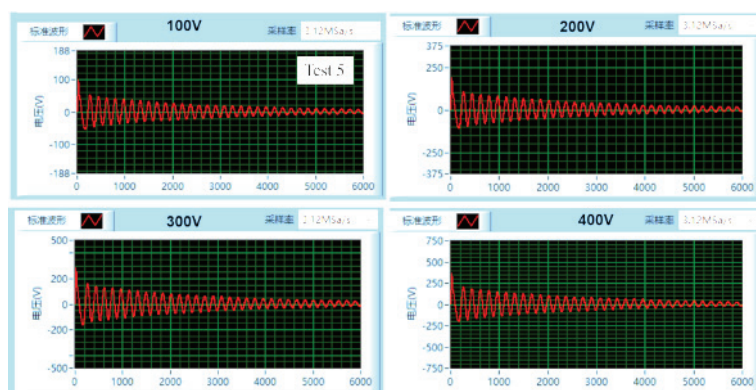


Fig 1.7-7 Impulse test result of the TEST5 (Conductor B+C).

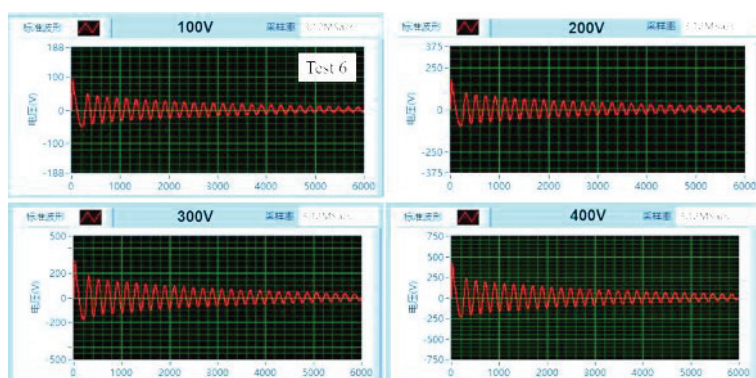


Fig 1.7-8 Impulse test result of the TEST6 (Conductor A+B+C).

## 1.8 Resistance and inductance measurement of the MC4

To inspect the winding, the resistance and inductance were measured as shown in this chapter. The structure of the measurement points is shown in Fig 1.8-1 and the scene of the inductance measurement is shown in Fig 1.8-2. For measurement, the electrical terminals of the coil and the instrument were connected by measuring wires with a clip. The measurement results are shown in Table 1.8-1, Table 1.8-2, Fig 1.8-3 and Fig 1.8-4. The measured values of this product meet the acceptance criteria.



Table 1.8-1 Result of resistance measurement.

Measurement point	Measured value (mΩ)		Converted value at 20 °C(mΩ)		
	Before the VPI	After the VPI	Before the VPI	After the VPI	Design value
Pancake 1	28.41	27.61	29.34	29.16	28.5
Pancake 2	29.39	27.86	29.32	29.42	28.5
Pancake 3	28.57	28.04	29.51	29.61	28.5
Sum all (1+2+3)	85.43	83.76	88.24	88.45	85.6
Acceptance	81.32~89.88 (±5%)				
Day and environment	2019/11/25 11.9℃ 55%	2020/1/15 6.5℃ 59%			
Measured current	100 A				
Equipment	DC tester (GD240-100A)				

Table 1.8-2 Result of inductance measurement.

Test frequency (kHz)	Measured value (mH)		Design value (mH)
	Before the VPI	After the VPI	
0.02	10.70	10.71	10.3
0.05	10.70	10.73	10.3
0.3	10.44	10.45	10.3
1.0	10.10	10.10	10.3
Acceptance	9.27 ~ 11.33 (±10%)		
Measurement point	Sum all (1+2+3)		
Day and environment	2019/11/25 11.9°C 55%	2020/1/15 6.5°C 59%	
Equipment	RCL Meter (LCR 8105G)		

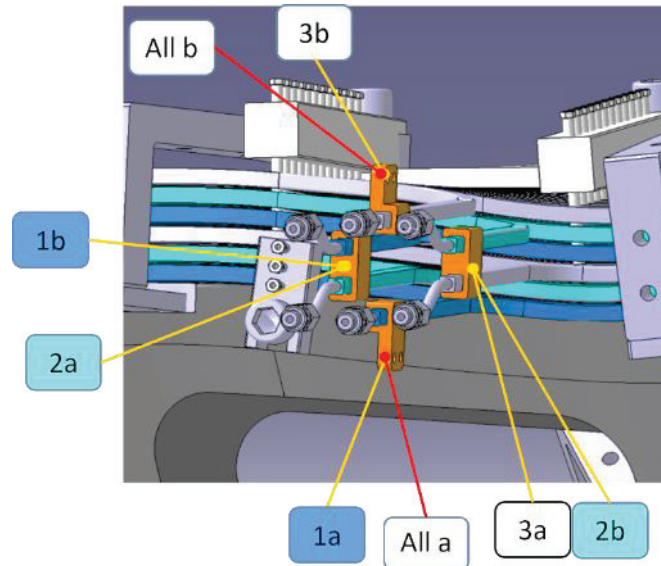


Fig 1.8-1 Schematic diagram of the resistance and inductance measurement.



Fig 1.8-2 Scene of the inductance measurement. To reduce the influence of the magnetic material under the floor, the whole was floated and measured.

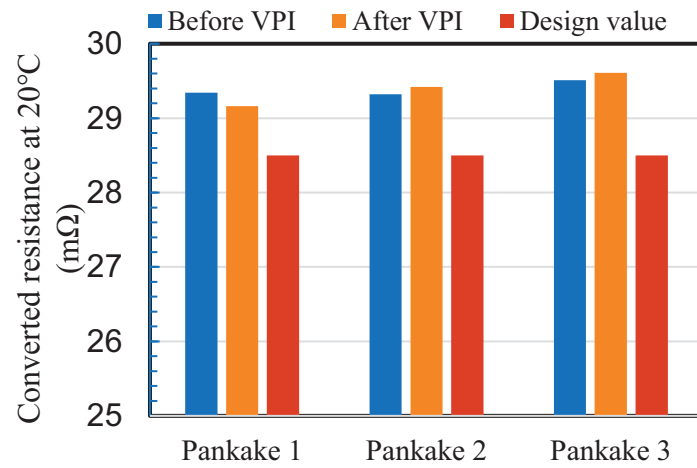


Fig 1.8-3 Result of resistance measurement.

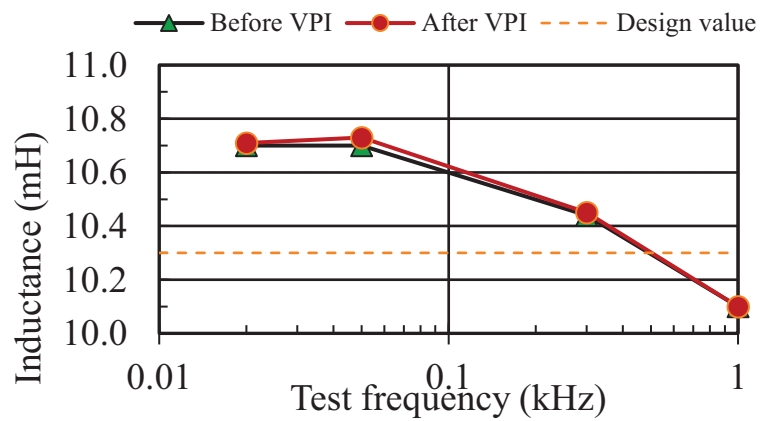


Fig 1.8-4 Result of inductance measurement.



## 1.9 Withstand voltage test for the ground insulation

To confirm the validity of coil insulation, a test was conducted in which a voltage more than twice the operating voltage was applied between the ground insulation surface and the conductor. The scene of the test is shown in Fig 1.9-1. The test procedure is as follows.

- Wrapping the outer insulation with aluminum foils.
- The high voltage terminal of the equipment is connected to any one of the coil terminals.
- The other ground terminal is connected with the aluminum foil.
- The test voltage is applied for 1 minute.
- The leakage current is measured.

The measurement results are shown in Table 1.9-1. All leakage currents were below the detection sensitivity, and no flashover and breakdown phenomenon were observed. The test result showed that the insulation performance met the required specifications.

Table 1.9-1 Result of the withstand voltage test after the VPI.

Test voltage (DC kV 1min)	Leakage Current (mA)
1.0	0.0
2.0	0.0
2.6	0.0
4.0	0.0
5.0	0.0
7.0	0.0
Acceptance	Less than 0.1 without flashover and breakdown.

Day and environment	2020/1/15 6.5°C 59%
Equipment	High Voltage DC Generator (DHV-100kV/5mA)



Fig 1.9-1 Scene of the withstand voltage test.

### 1.10 Airtightness test with nitrogen gas

The 2.5 MPa pressure was applied in the cooling water channels by nitrogen gas and kept the pressure about 1 hour. There was not any leak of the cooling water channels. The scene of the airtightness test is shown in Fig 1.10-1.



Fig 1.10-1 Scene of the airtightness test at 2020/06/13.

### 1.11 Flow rate dependence of the pressure drop

The pressure drop (loss head) of the cooling channel was measured as shown in this chapter.

Table 1.11-1 Test results of the pressure loss of the MC4.

Cooling channel	Flow rate (l/min)	Pressure (MPa)		
		Inlet	outlet	pressure loss
1	0.5	0.192	0.003	0.189
	0.8	0.375	0.006	0.369
	1.1	0.694	0.01	0.684
	1.3	0.96	0.013	0.947
2	0.5	0.188	0.003	0.185
	0.8	0.392	0.006	0.386
	1.1	0.642	0.009	0.633
	1.3	0.932	0.013	0.919
3	0.5	0.19	0.003	0.187
	0.8	0.39	0.006	0.384
	1.1	0.692	0.01	0.682
	1.3	0.918	0.013	0.905
All Parallel	1.5	0.204	0.017	0.187
	2.4	0.432	0.038	0.394
	3.3	0.764	0.066	0.698
	3.9	1.042	0.099	0.943
	4.2	1.185	0.113	1.072

2020/04/15 at Keye Co.

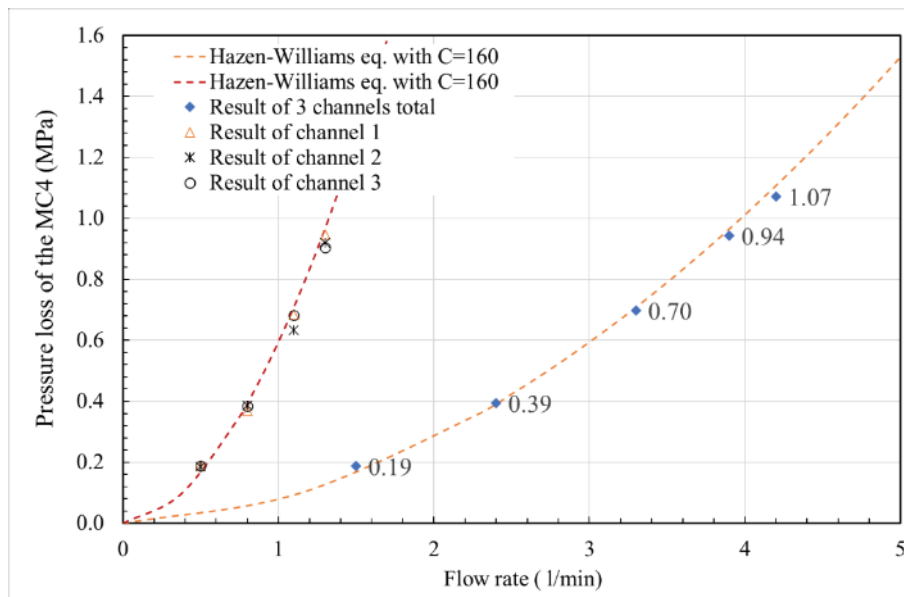


Fig 1.11-1 Flow rate dependence of the pressure loss of the MC4 at 2020/04/15. The broken line indicates a fitted approximation with the Hazen-Williams equation.

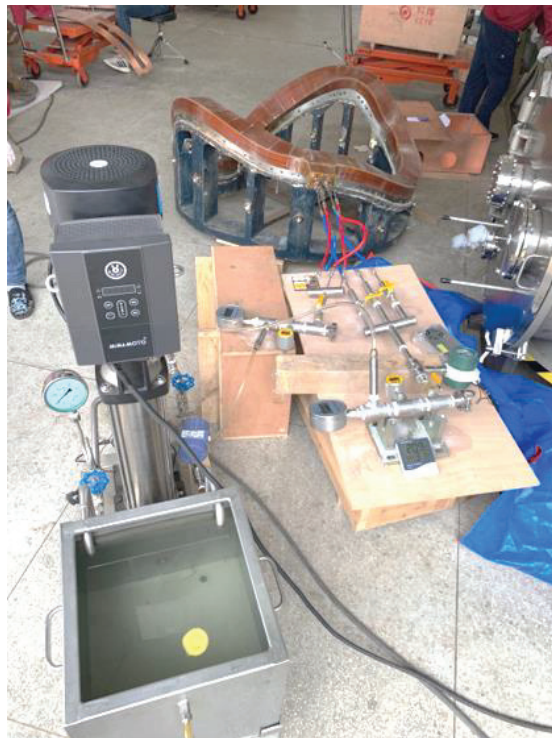


Fig 1.11-2 Scene of the pressure loss measurement.

1.12 Heat run test

1.12.1 Summary

To verify the cooling design, the heat run test was performed, the sketch of the heat run test system is shown in Fig 1.12-1 and Fig 1.12-2. The test was performed under 4 kinds of conditions.

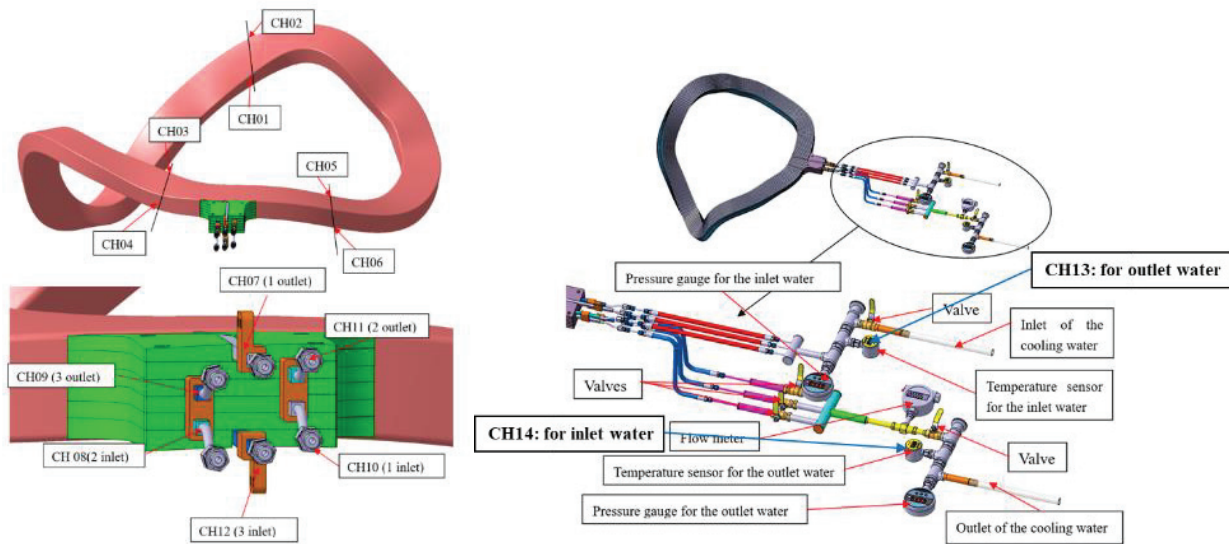


Fig 1.12-1 Sketch of the coil test system and the temperature sensor distribution.

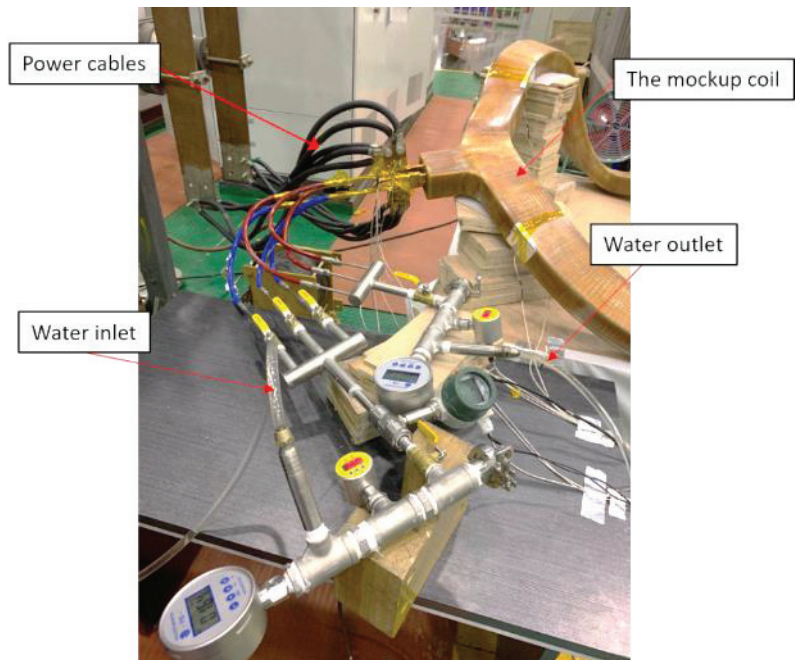


Fig 1.12-2 Heat run test of the MC4 mockup coil.

### 1.12.2 Test result of 1 kA/38 s without cooling water

- Heat generation of the 1 kA/38s is equivalent to that for the 1.0 T operation (4.34 kA and 2 s).
- Maximum of temperature rise on the insulation surface was 38 °C.
- The temperature on the insulation surface reached its maximum about 2 minutes, which was the time after the current is sut off.
- The temperature drop rate without cooling water was very slow (15 °C /hour).
- It took about half a day to recover and it may be unacceptable.

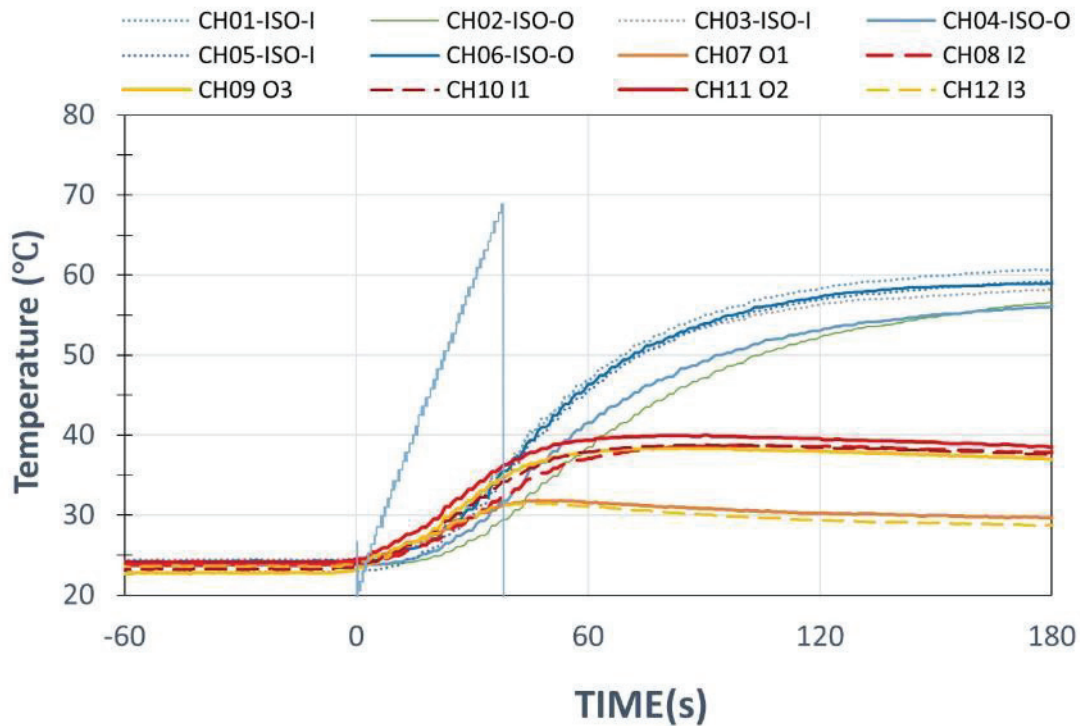
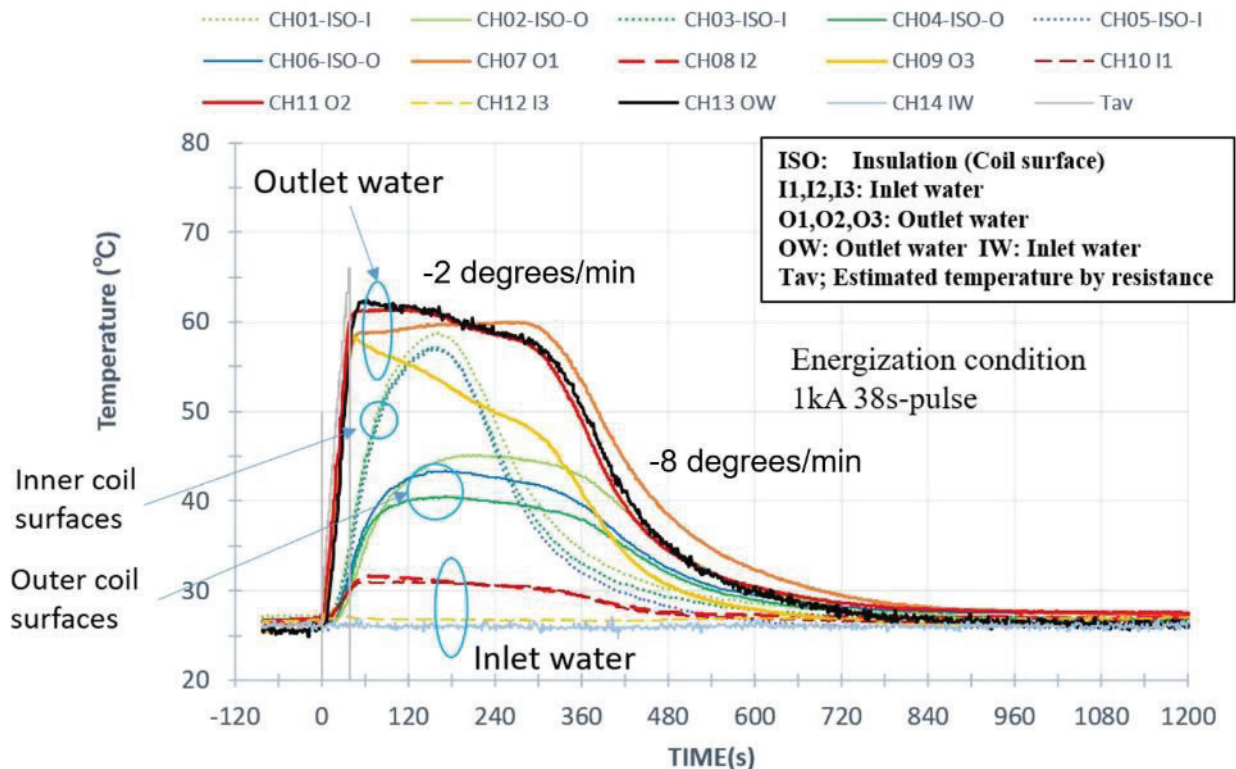


Fig 1.12-3 Temperature rise curve of 1kA/38s without cooling water.



### 1.12.3 Test result of 1 kA/38 s with cooling water

- Heat generation of the 1 kA/38s is equivalent to that for the 1.0 T operation (4.34 kA and 2 s).
- Maximum temperature rise on the insulation surface was 35 °C. It showed that the temperature rise did not depend on the presence or absence of cooling water.
- The required cooling time was greatly reduces by the water cooling.
- It took about 15 minutes to recover and it may be acceptable.



Note; The temperature change of the cooling water can be classified into two stages of -2 degrees/min and -8 degrees/min. It appears to be related to the time it takes for the water to circulate (a few minutes) and the time delay associated with heating the insulation. Greatly reduces the cooling time with water. It takes about 15 minutes to recover.

Fig 1.12-4 Temperature rise with current of 1 kA/38 s and water cooling of 3.9 L/min.



#### 1.12.4 Test result of 500 A/120 s without cooling water

- The 500 A/120s corresponds to the steady operation condition (434 A).
- Maximum of temperature rise on the insulation surface was 28 °C.
- It took about 3 hours to recover and it may be unacceptable.

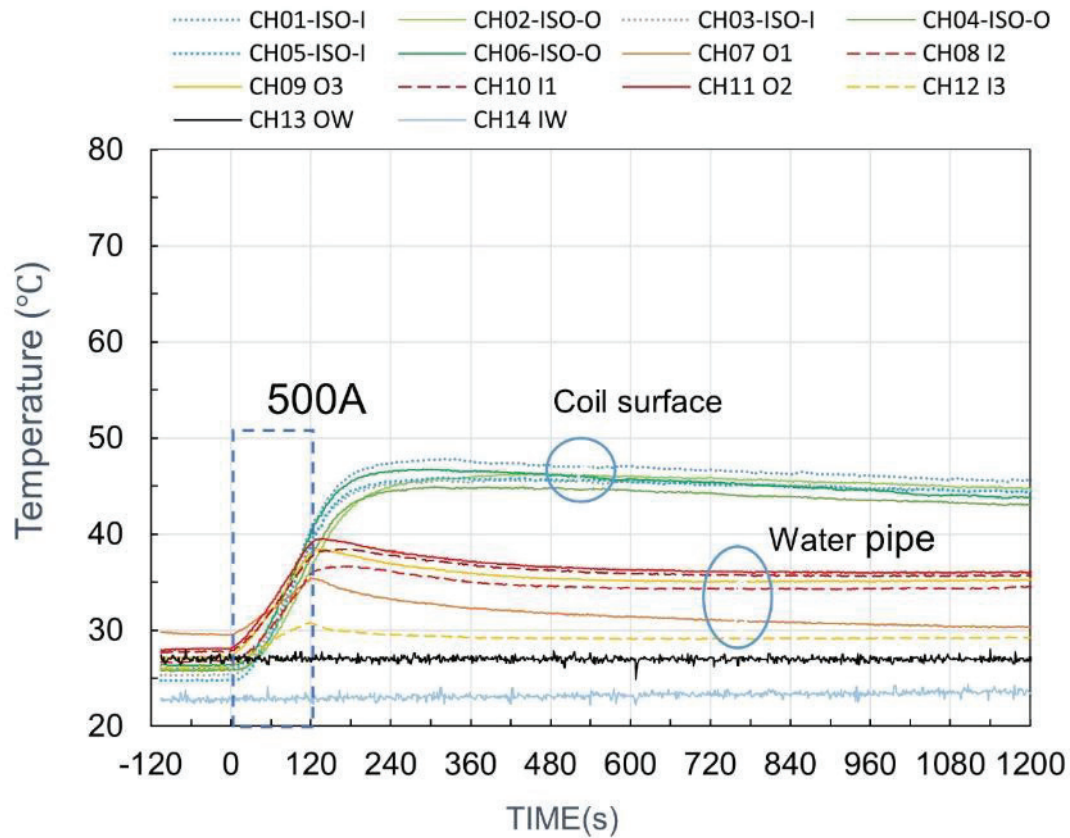


Fig 1.12-5 Temperature rise curve of 500 A/120 s without cooling water.

### 1.12.5 Test result of 500 A/120 s with cooling water

- The 500A/120s corresponds to the steady operation condition (434 A).
- Maximum of temperature rise on the insulation surface was 28 °C.
- It took about 8 minutes to recover and it may be acceptable.
- The temperature continues to rise after 2 minutes of operation, and it is estimated that the allowable temperature will be reached in about 5 minutes. For continuous operation for 30 minutes or more for discharge cleaning, the cooling water should be increased to saturate at an appropriate temperature.
- It suggests that to improve the cooling effect, the pressure of the cooling water system in the real coil should be increased from 1 MPa to 2 MPa.

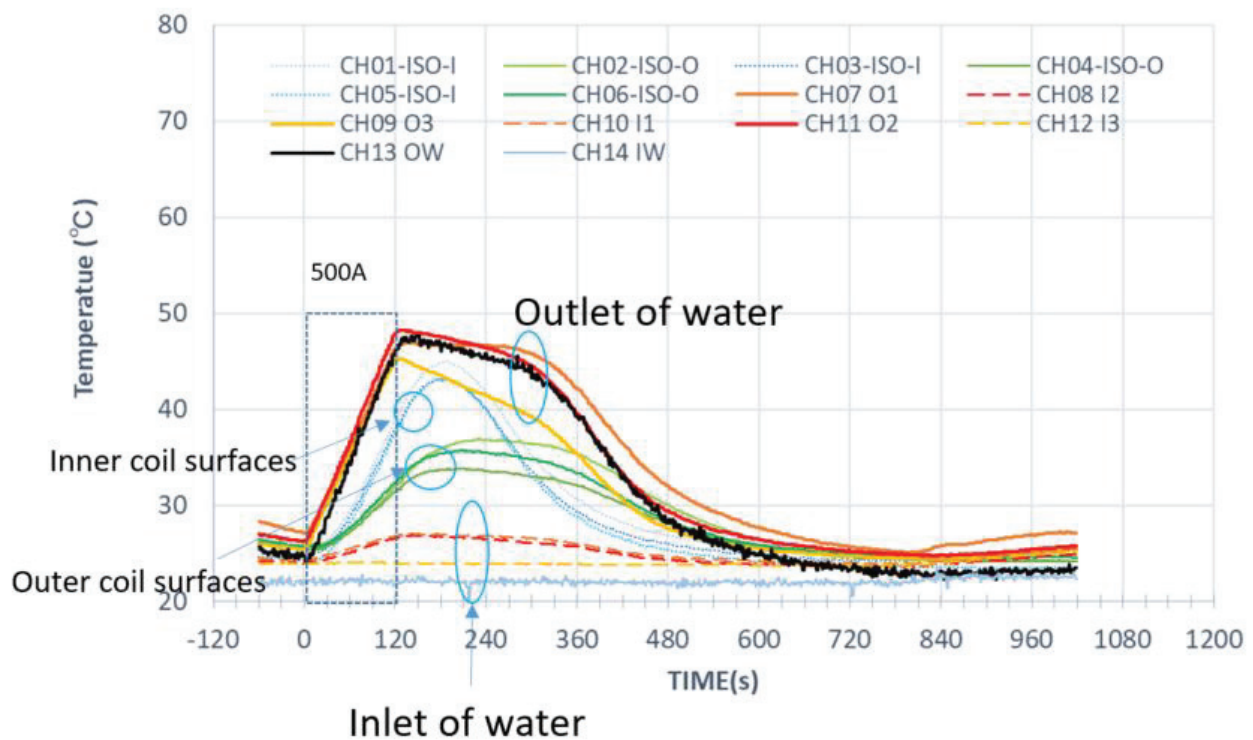


Fig 1.12-6 Temperature rise curve of 500A/120s with 4.2 L/min. cooling water.

### 1.13 Overvoltage test

To understand the insulation ability, a voltage higher than necessary was applied at the end of a series of tests, and it was confirmed that there was sufficient margin in insulation capacity. Fig 1.13-1 shows the scenes of the test. From this test, it was confirmed that this insulation system has a sufficient margin in the layer and layer insulation capacity.

- Layer to layer insulation test with DC 10 kV

The ground test voltage to confirm the validity of this coil is DC 5.8 kV. If the same insulation performance can be ensured only by the layer insulation, the ground insulation may be simplified more. To confirm that possibility, we planned a test in which a voltage of DC 10 kV was applied between adjacent conductors.

We cut series connection of 3 parallel conductor in the current lead area and apply DC 10 kV between each two conductors of 3 parallel. A high voltage DC generator (DHV-100 kV/5 mA) was used for the DC 10 kV test. Three types of tests were conducted, and it was confirmed whether the leakage current at DC 10 kV was less than 17  $\mu$ A (17  $\mu$ A between the A and the B, 1  $\mu$ A between the B and the C, or the A and the C).

- Ground insulation test with DC 20 kV

If there is sufficient margin, it may be possible to simplify ground insulation. To confirm that possibility, we planned a test in which a voltage of DC 20 kV, which was 3.4 times the required test voltage, was applied between the conductor and the ground. The leakage current at DC 20 kV was not observed.

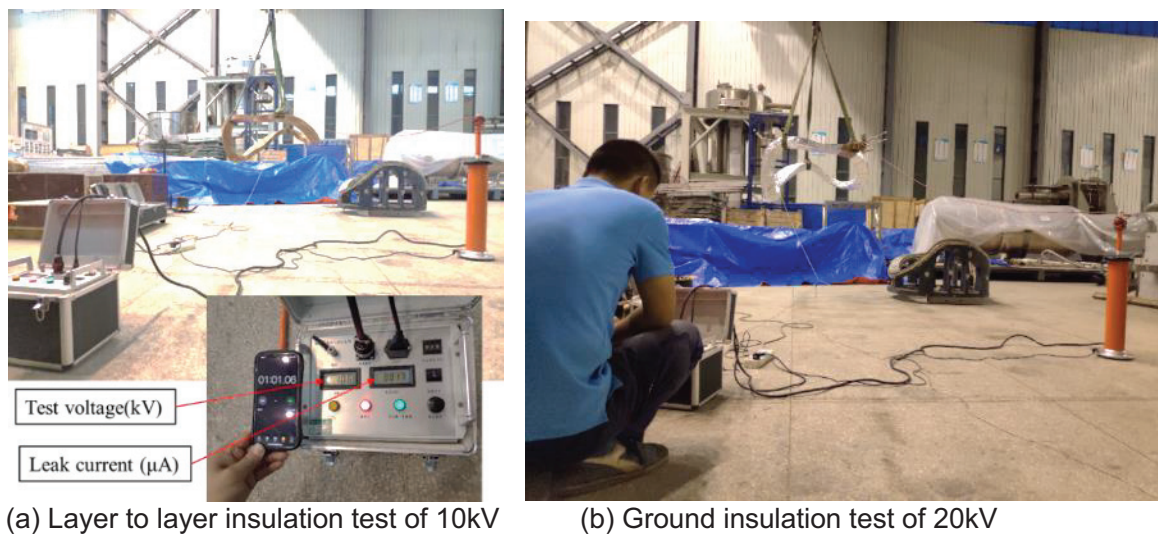


Fig 1.13-1 Scene of the overvoltage test.

## 2 Production of a vacuum vessel

### 2.1 Summary

The vacuum vessel will be manufactured by welding together four sections of two types in the toroidal direction. A type-A vacuum vessel section was manufactured as a trial production and the manufacturability, and the validity of the design were confirmed. Fig 2.1-1 shows the vacuum vessel type-A section and the assembly work of the ports.

We measured the displacement of the vacuum vessel with a laser tracker and confirmed that it could be manufactured with an accuracy of about 5 mm against the design value. It is consistent with the design goal, and it was confirmed that the fabrication was appropriate.



Fig 2.1-1 Picture of the vacuum vessel type-A section.

This trial production has revealed the following.

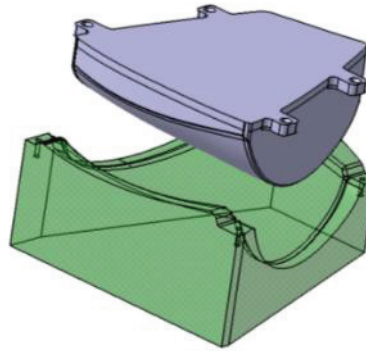
- (a) The final dimension deviation will be about 5 mm. The direction of deformation is the vacuum side.
- (b) At first, we tried to bend the plate by cold pressing, but found that the spring back was too large to keep the target tolerances. The spring back for partial region was larger than 50mm. Therefore, we changed to hot pressing to reduce the spring back.
- (c) This accuracy is insufficient for welding between sections of the vacuum vessel after coil assembly.
- (d) Therefore, it is necessary to leave an extra length in the weld between the sections and improve the accuracy by machining after each section is completed. Since it was estimated that an extra length would be necessary for improving accuracy, the design is such that an extra length of 5 mm is left. Therefore, there is no problem with the current design.
- (e) An error of about 5 mm is also assumed for the port position. If the flange surface of each port is used as a reference as it is, the position accuracy of plasma measurement is not good. Therefore, after the device is completed, the position of each flange surface should be measured, and markers should be added to the reference position for plasma measurement.
- (f) Since the direction of displacement of the vacuum vessel is the vacuum side, there seems to be no problem of interference with the coil. There is concern that the dimensional margin on the vacuum side will decrease, but since the vacuum vessel is designed with a large dimensional margin (10 mm or more) in advance, there does not seem to be a problem



## 2.2 Design of the mold for pressing and welding

Two types of molds are required to manufacture the vacuum vessel. A press die for pressing a thin plate with a thickness of 6 mm and a welding die for placing them. Their 3D CAD model and the manufactured molds are shown in Fig 2.2-1 and Fig 2.2-2. The molds were made by CNC machining the material made by forging.

(a) 3D CAD model



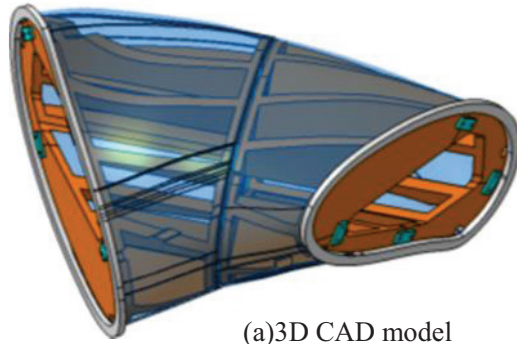
(b) Forging material



(c) Completed molds



Fig 2.2-1 Pressing die made by the CNC machine.



(a)3D CAD model



(b)Forging material



(c)A completed mold

Fig 2.2-2 Mold for thin plats assembly and welding by the CNC machining.

### 2.3 Method of dividing parts

We drew up a dividing proposal to conduct producing the vacuum vessel. As shown in Fig 2.3-1 and Fig 2.3-2, the type A and the type b sections of the vacuum vessel are manufactured by welding two large end flanges to prevent welding deformation, several curved thin plates made by the hot press working, etc. Fig 2.3-3 shows the example of the divided pieces for the type A section.





**Vacuum vessel of the type A ; Toroidal angle = 67.5 degree**

No	Name	Quantity	Production method
1	Curved thin plate	4 types of 8	Hot press molding.
2	End flange	2	Machining
3	Rectangular port	1	Machining, bending and welding
4	Circular port	2 types of 9	Machining and welding
5	Pedestal	3 types of 3	Machining

Fig 2.3-1 Material pieces divided plan for vacuum vessel type A. It will be reviewed in the detailed design.



**Vacuum vessel of the type B ; Toroidal angle ; 112.5 degree**

No	Name	Quantity	Production method
1	Curved thin plate	3 types of 6	Hot press molding.
2	End flange	2	Machining
4	Circular port	5 types of 13	Machining and welding
5	Pedestal	2 types of 2	Machining

Fig 2.3-2 Material pieces divided plan for vacuum vessel type B. It will be reviewed in the detailed design.

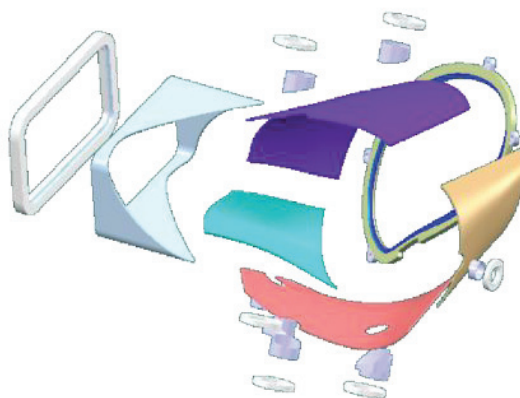


Fig 2.3-3 Half of the divided pieces for the vacuum vessel type A. It will be manufactured by welding 33 pieces in total.

## 2.4 Production process of the vacuum vessel

Fig 2.4-1 shows the procedure to product one section of the vacuum vessel. The position accuracy of the flange of the measuring port is the most important factor in the quality of the vacuum vessel. To achieve that goal, machining steps will be inserted in the middle of the production process. Except for the flange surface, large errors will be allowed within the range that does not interfere with other parts in the overall assembly.

The main manufacturing points is shown in Fig 2.4-2 and the typical scenes in each work are summarized in Table 2.4-1.

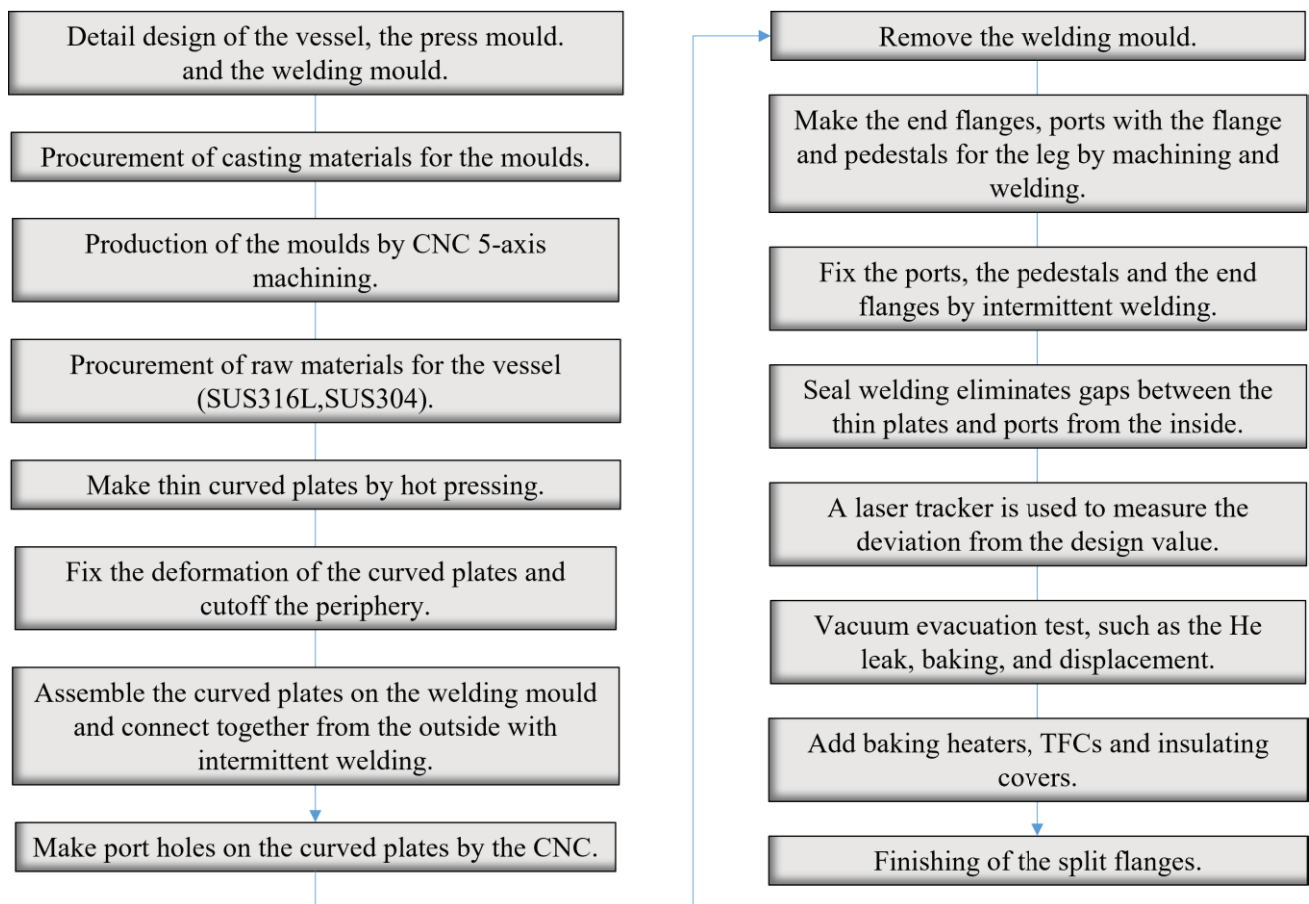

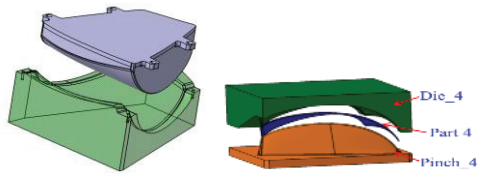
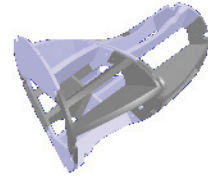





Fig 2.4-1 Procedure to product one section of the vacuum vessel.









Deformation measurement by the laser tracker	2022.08			
Remove the welding mould and welding split flanges and the ports. Seal weld from the inside by the TIG	2022.07			
Open holes by the CNC	2022.03			
Assemble and weld parts on the welding mould	2021.11			
Production of the welding moulds.	2021.10			
Hot pressing and edge removal	2021.09			
Production of the press moulds.	2021.02			
Procurement of casting material for the moulds.	2020.03~ 2020.11			



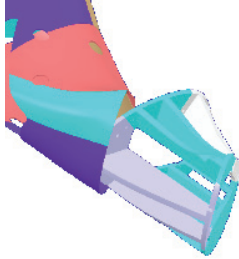

Fig 2.4-2 The main production record to make a type-A section.

Table 2.4-1 Production process of the type-A vacuum vessel.





Step	Work	Picture
1	Detail design of the vacuum vessel section.	
2	Detail design of the several press molds.	
3	Detail design of the welding mold.	
4	Procurement of casting materials for the molds. For press molds and welding molds.	
5	Make the press molds (7 or 8 mold sets) and the molds for welding. They were produced by the CNC machining.	
6	Make the welding mold. It were produced by the CNC machining, welding, and assembling about ten parts.	



Step	Work	Picture
7	Procurement of raw materials for the vessel.	
8	<p>Make the thin curved plates by hot press.</p> <ol style="list-style-type: none"> <li>1) Heat the raw material thin plates in the heating furnace.</li> <li>2) Press forming with the press mold and the 500T press machine.</li> <li>3) Hold the press pressure for 24 hours.</li> </ol> <p>Apply hot press forming (2020.11.10).</p> <p>At first, we tried to bend the plate by cold pressing, but found that the spring back was too large to keep the target tolerances. The spring back for partial region was larger than 50mm.</p> <p>Therefore, we procured the heating furnace and added heating process to reduce the spring back. As a result, the amount of spring back was reduced to 10mm.</p>	   
9	Cutoff the edge extra by the CNC machine and fitting the edge for the welding with the help of the welding mold. (2021.10.28)	  

Step	Work	Picture
10	<p>Assemble the curved plates and intermittent welding between thin plates on the mold.</p> <ol style="list-style-type: none"> <li>1) Correct the deformation of the thin plates based on the mold.</li> <li>2) Assemble the curved plates on the welding mold.</li> <li>3) Connect the thin plates by intermittent welding of the outer surface.</li> <li>4) Correct the deformation of the thin plates based on the mold by the point heat quenching or hammering.</li> </ol>	
11	Open holes by the CNC machine	
12	Remove the mold	
13	Make required parts by the CNC machine and the welding. The end flanges, ports with the flange and pedestals for the leg.	



Step	Work	Picture
14	Fix the ports, the pedestals, and the end flanges by intermittent welding.	
15	Seal welding eliminates gaps between the thin plates and ports from the inside.	
16	A laser tracker is used to measure the deviation from the design value.	
17	Preparation for the He leak test.	

2.5 Deformation measurement by a laser tracker.

Dimension of the vacuum vessel was measured by a laser tracker after the seal welding. The result is shown in Fig 2.5-1 to Fig 2.5-4Fig 2.5-3. The displacement perpendicular to the thin plate of the vacuum vessel was as follows.

- -4.66 ~ 4.06 mm on the 6mm thin plate surface. (Fig 2.5-1)
- -4.3 ~ -0.46 mm on the large rectangular flange. (Fig 2.5-2)
- -4.63 ~ -3.54 mm on the circular port flange. (Fig 2.5-3)
- -4.3 ~ 2.0 mm on the split flange. (Fig 2.5-4)

The deformation is large everywhere in the vacuum direction. There seems to be no problem of interference with the coil. There is concern that the dimensional margin on the vacuum side will decrease, but since the vacuum vessel is designed with a large dimensional margin (10 mm or more) in advance, there does not seem to be a problem

In any case, it should be considered that there is a high possibility that a deviation of about 5 mm will occur on the port center position in all directions. If the flange surface of each port is used as a reference as it is, the position accuracy of plasma measurement is not good. Therefore, after the device is completed, the position of each flange surface should be measured, and markers should be added to the reference position for plasma measurement.

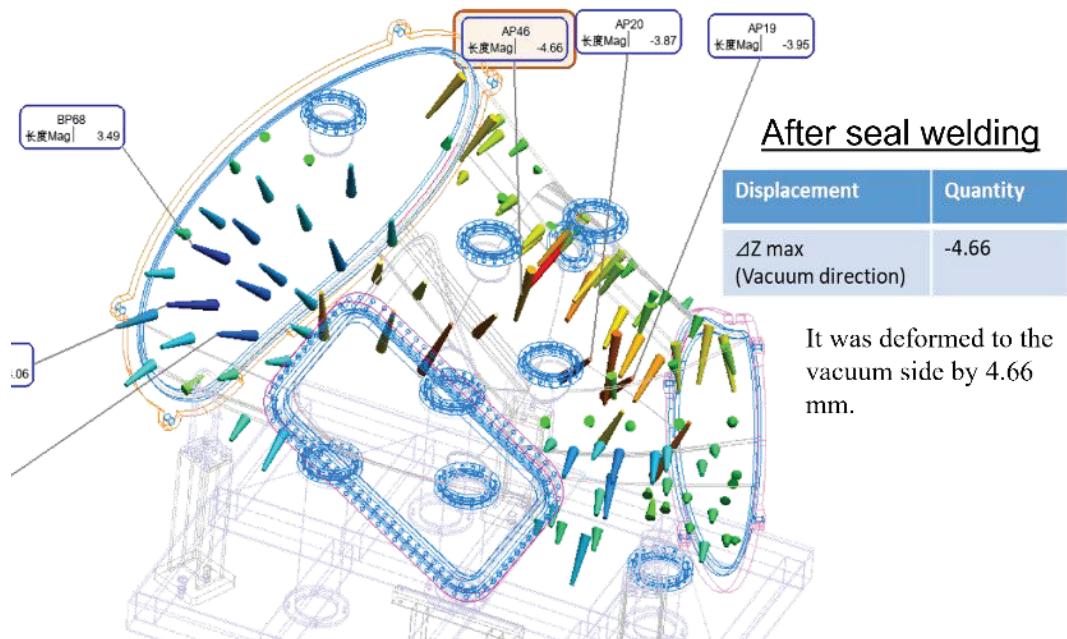


Fig 2.5-1 Deformation of vacuum vessel (Thin plate with thickness of 6mm).

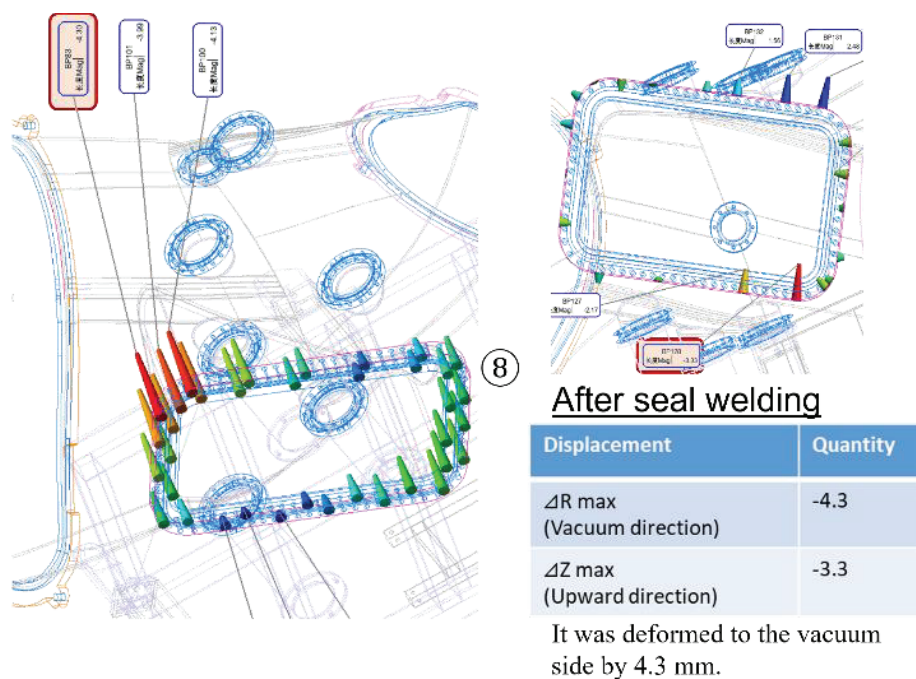


Fig 2.5-2 Deformation of vacuum vessel (⑧Rectangular port O-090S).

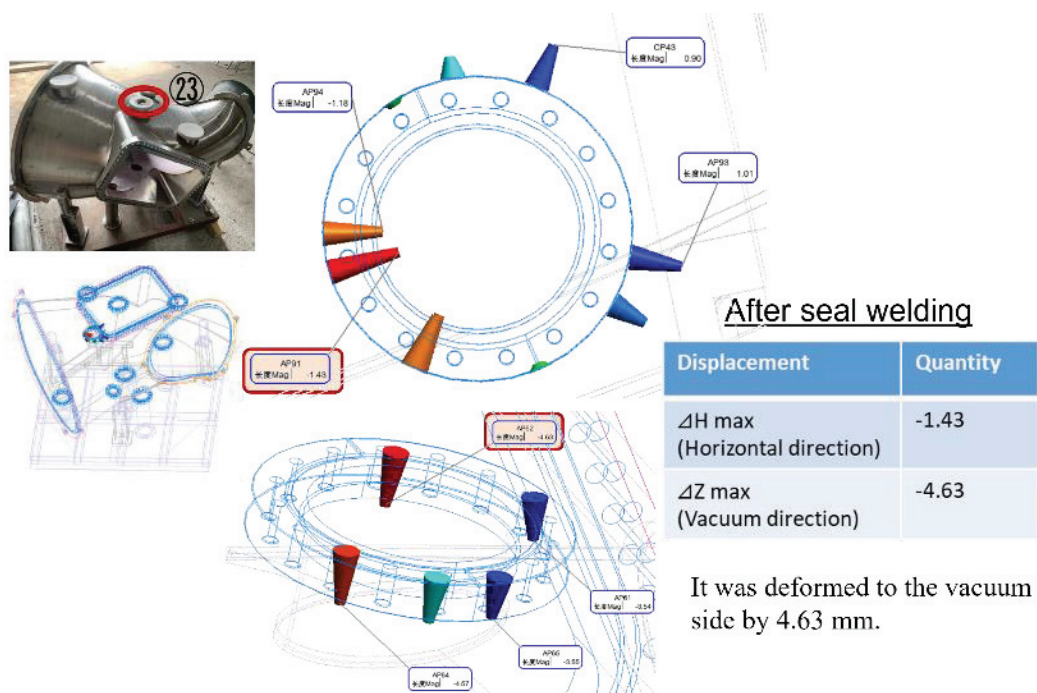
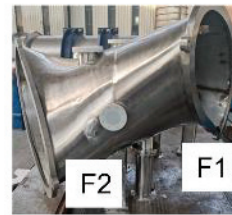
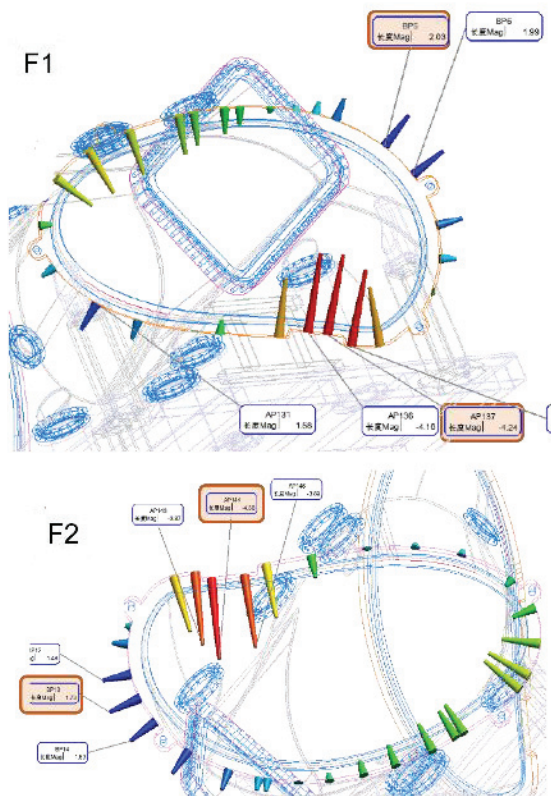


Fig 2.5-3 Deformation of vacuum vessel (㉓Upper port U-102IN).



### After seal welding

Displacement	Quantity
$\Delta r$ max (F1) (Vacuum and vertical direction)	-4.24
$\Delta r$ max (F1) (Air and outer direction)	2.03
$\Delta r$ max (F2) (Vacuum and vertical direction)	-4.30
$\Delta r$ max (F2) (Air and outer direction)	1.73

They were deformed to the vacuum side by 4.3 mm. The deformation mode is similar on the left(F2) and right(F1).

Fig 2.5-4 Deformation of vacuum vessel (Sprit flange).



### 3 Plastic model developed by 3-D printer

Various reduced models were developed on the 3-D printer to validate the device fabrication and assembly procedures.

#### 3.1 Plasma



Fig 3.1-1 Last closed surface of the equilibrium.



Fig 3.1-2 Data sharing in the project.

## 3.2 Vacuum vessel

### 3.2.1 Examination of production

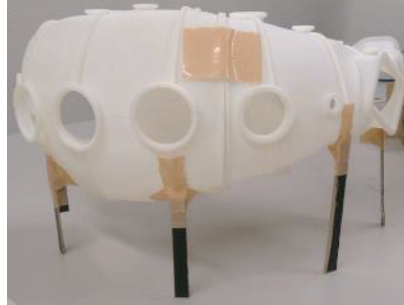


Fig 3.2-1 Examination of support legs.

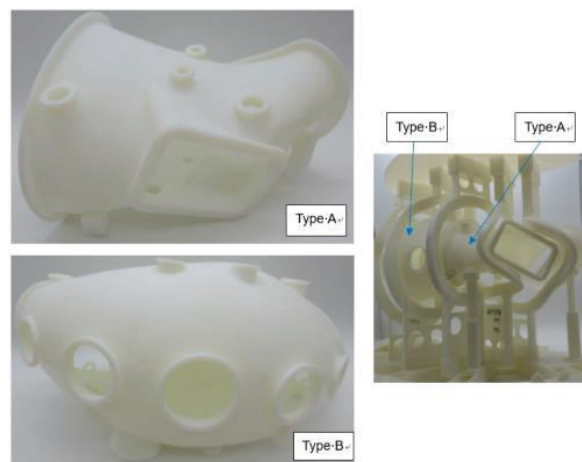


Fig 3.2-2 Examination of the shape and assembly problems.

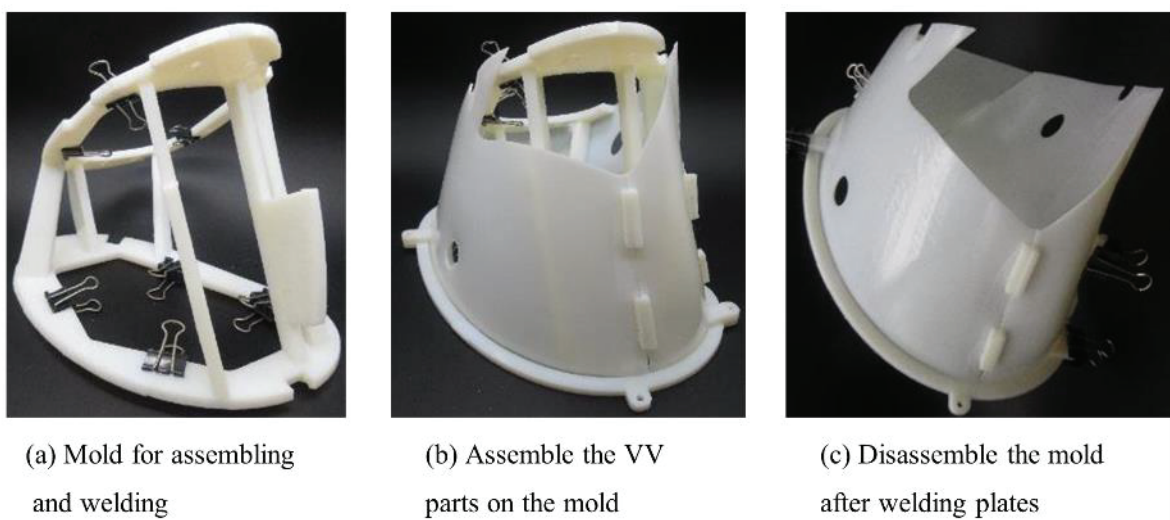


Fig 3.2-3 Simulation of production flow for the vacuum vessel.



### 3.2.2 Real scale model of the vacuum vessel

3D printer has manufactured real scale model of vacuum vessel type A. Since the size of the vacuum vessel is large, it cannot be made all at once. Therefore, the type A vacuum vessel has been cut into 16 pieces to print by 3D printer. Each of 16 pieces has been made by 3D printer in Keye company. These 16 pieces are being assembled.

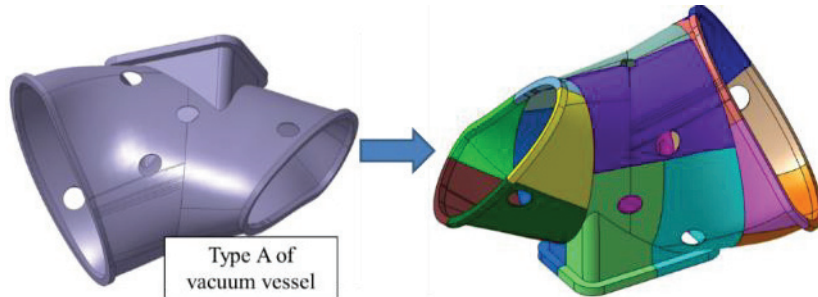


Fig 3.2-4 Type A of vacuum vessel is cut into 16 pieces to print by 3D printer.



Fig 3.2-5 3D printer to fabricate real scale vacuum vessel model.

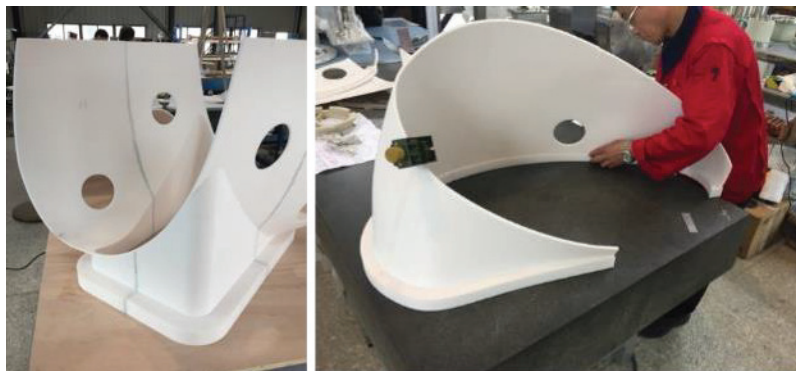


Fig 3.2-6 Pictures of assembled real scale 3D model.

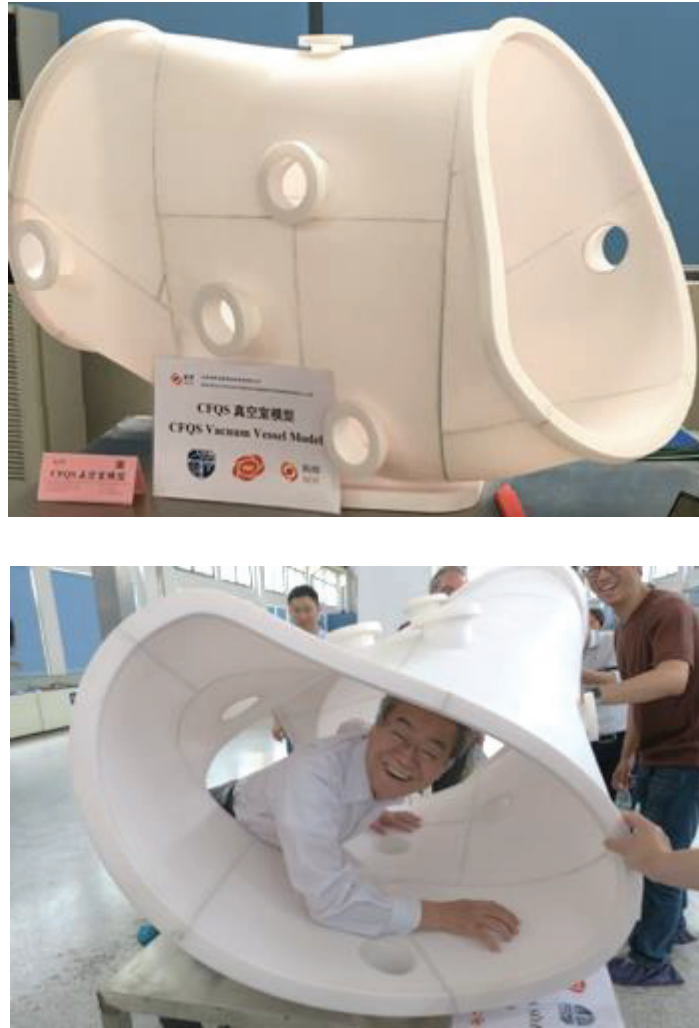


Fig 3.2-7 Type A of vacuum vessel model produced by the 3D printer. It was confirmed that a worker can enter the inside of the vacuum vessel.

### 3.2.3 Check of the baking heater

Since the baking heater for vacuum vessel is outsourced by specifying the length, it is necessary to evaluate the required length in advance. However, since the shape of the vacuum vessel is complicated and the wiring path of the heater is not simple, it is not easy to evaluate the required length.

It was a little tough to estimate a length of the baking heater. We know creating 3-D model is the best way to estimate the length however it usually takes long time and efforts to create complicated 3-D path in a CAD. In the early stage, we used strings and 3-D printed model to consider a suitable winding route and to estimate the length of baking heater. Following pictures in Fig 3.2-8 show 1/10 scale 3-D printer models with wound strings instead of heaters.

After determining the approximate winding policy using 3-D printer models, the heater route was determined on 3-D CAD. Table 3.2-1 shows a comparison between the heater length estimated by the 3-D printer model with strings and that estimated in 3-D CAD. As you can see from this table, there is no significant difference except for B2. In this region, heater path is modified to extent.

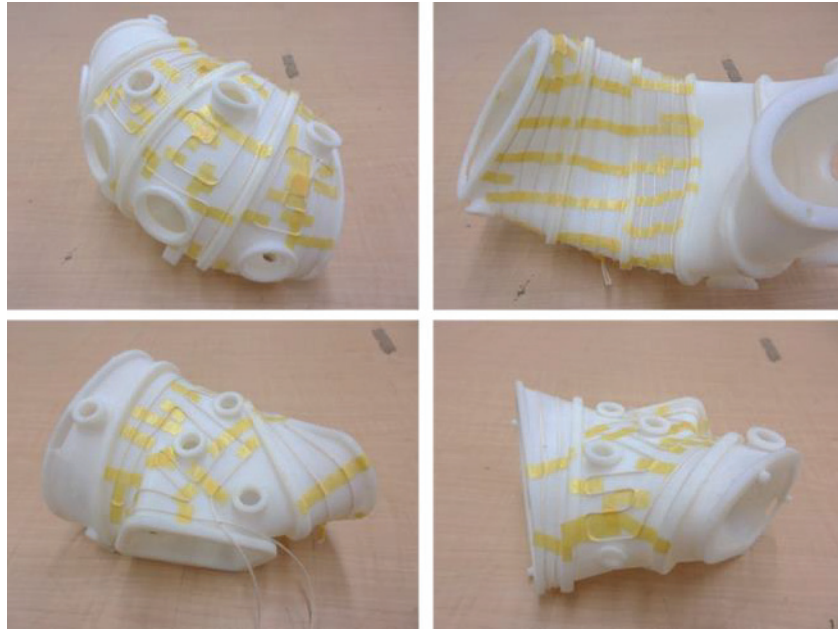


Fig 3.2-8 VV and baking heater (2021/09)

Table 3.2-1 Comparison of the heater length estimated.

Region	Heater length [mm]		Difference
	3-D printer model	3-D CAD	
A1	4,750	4,788	-0.8 %
A2	12,000	11,325	6.0 %
A3	-	4,752	-
B1	10,750	10,105	6.4 %
B2	12,200	10,746	13.5 %
B3	12,200	11,621	5.0 %
B4	-	10,883	-
B5	-	10,105	-





Fig 3.2-9 VV, TFC and baking heater (2022/11)

3.3 Modular coil

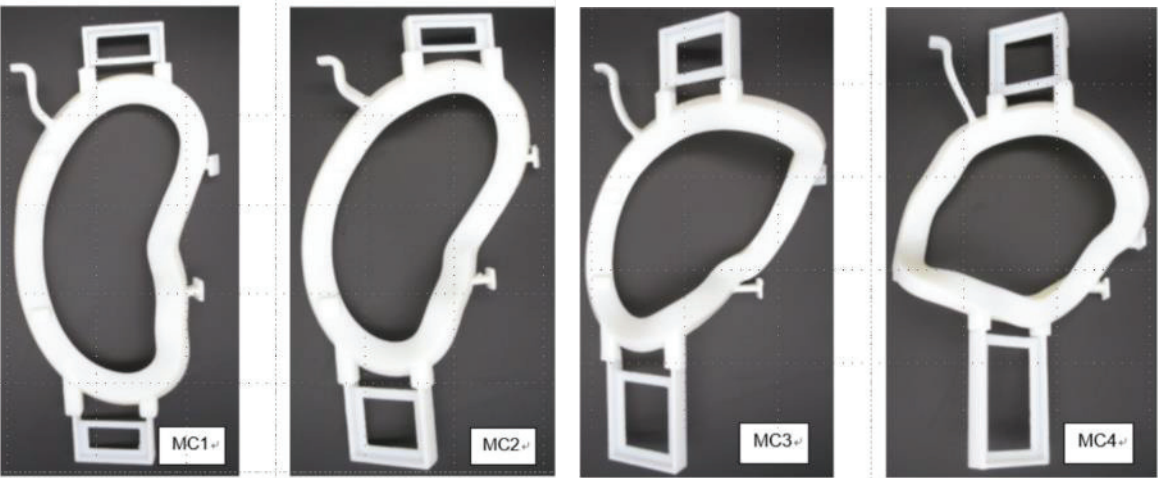


Fig 3.3-1 Examination of preliminary coil case with a continuouse c-shaped case (CCSC).

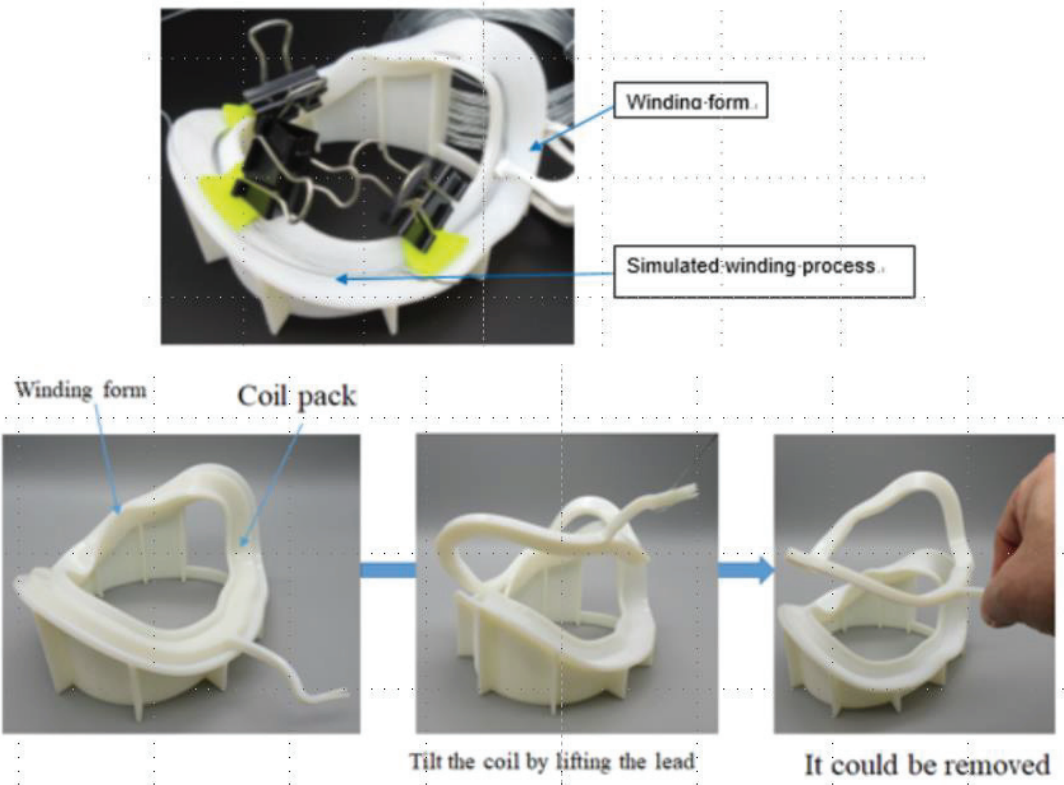


Fig 3.3-2 Simulation of removing the coil pack from the winding mold.



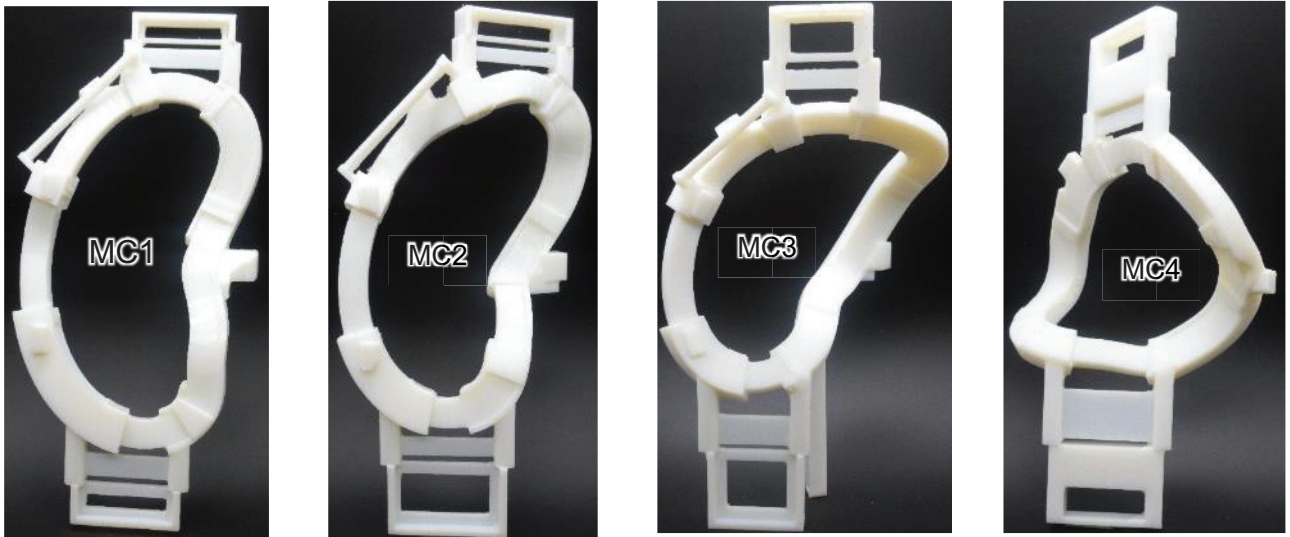


Fig 3.3-3 Examination of the coil case with partial large clamps (PLCL).

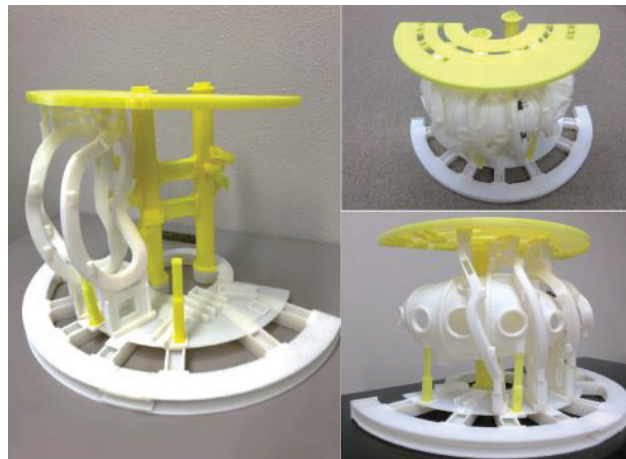


Fig 3.3-4 Assembly of the modular coil and the vacuum vessel.



Fig 3.3-5 Discussion of the structure and the assembly in a meeting.



## **4 Actual size wooden model of the vacuum vessel**

### **4.1 Wooden model of the vacuum vessel for trial winding of TFC**

#### **4.1.1 Wooden model of the vacuum vessel**

12 TFCs will be installed in the CFQS. They will be wound on the vacuum vessel (VV) directly. Because of complicated twisted shape of the VV, we may have trouble with a winding of the TFC. To understand the difficulties and problems in winding, we developed the actual size wooden model of the vacuum vessel and tried winding of the TFC.

Schematic view of the wooden model is shown in Fig 4.1-1. TC32 was selected from 3 types of the TFC, because it seemed to be the most difficult to wind. The wooden model was manufactured only in a width of about 108 mm, which is close to the TC32. The model consists of 5 wood boards with thickness of 12 mm. Each board is cut to follow the outer shape of VV and piled up one by one, with spacers in between. Grooves are made around the edge of the wood boards. Fig 4.1-2 shows how to install a clamp in the model. Please refer to the explanation in the figure caption for the procedure to fix the clamp.

Fig 4.1-3 shows pictures of the actual wooden model. The TC32 of the same shape can be flipped upside down and attached to a different location. Since the terminal positions are all upward, there are two types of TC32 coils with different winding start positions. The model and support legs are designed to test both.

Fig 4.1-4 shows the inserted flexible plates between conductor and the wooden boards. We inserted flexible plates (made of ABS resin) where there is no clamp before the winding to eliminate the step between the wooden boards. Since there is no step on the actual vacuum vessel, these plates will be unnecessary.

Fig 4.1-5, Fig 4.1-6 and Table 4.1-1 show the design of the clamp.

Fig 4.1-5 shows the clamp for a solid conductor. Size of the conductor is 7.3 mm x 3.3 mm. If the purpose of the clamp is only to stop the horizontal movement of the conductors,  $H=6.6$  mm is sufficient. The  $H$  was increased to create the thread (screw) depth for fixing the cover. A spacer is added to compensate for the higher clamp. Insulation protection sheet may be necessary for an actual coil, but it was omitted in the trial winding because we did not care about the damage in the test.

Fig 4.1-5 shows the clamp for a cable. Size of the cable is 11 mm in diameter. The actual coil requires a width of  $W1 = 8 \times 11 = 88$  mm. In the trial winding, the clamp for the solid conductor with  $W1=66$  was diverted for cost reduction. The number of the winding was reduced from  $8 \times 2$  to  $6 \times 2$  because the width of the clamp was not enough.

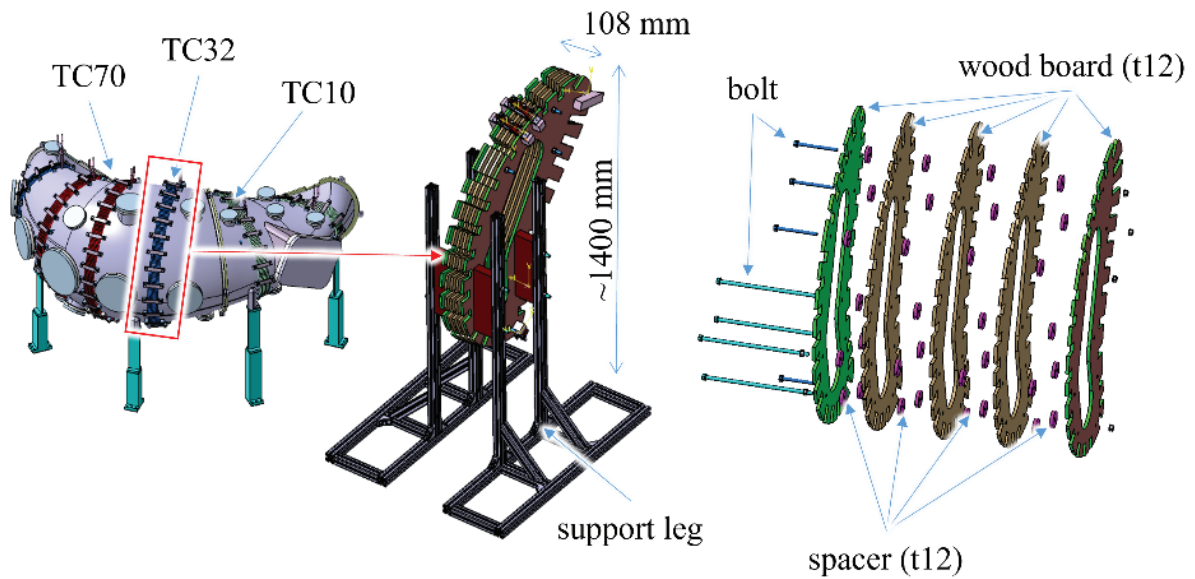


Fig 4.1-1 Schematic view of the wooden model for TFC winding test

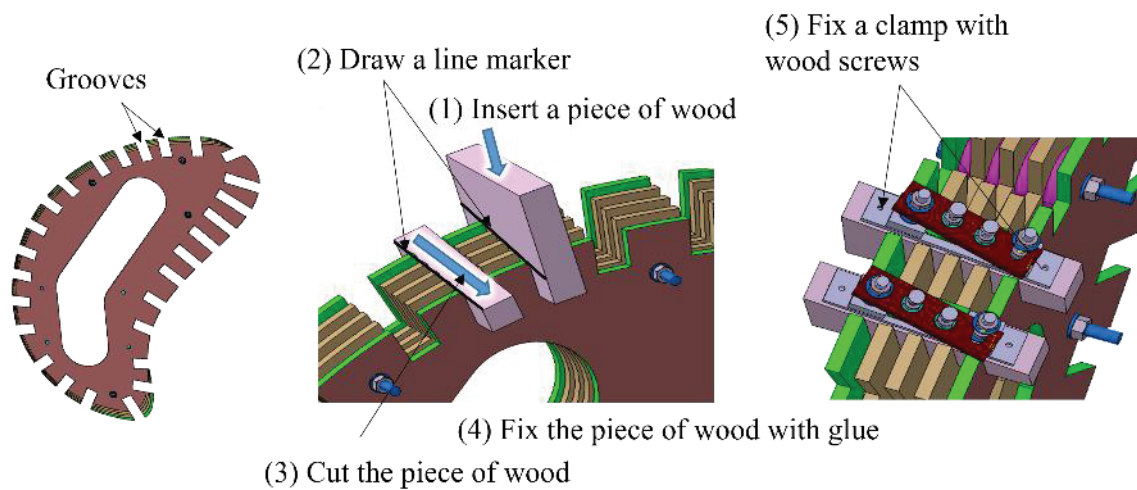


Fig 4.1-2 How to install a clamp in the wooden model. (1) insert a piece of wood into the groove, (2) draw a line as a marker on the side of it that matches the outer edge of the wooden board, (3) cut the piece of wood along the line, (4) fix it with glue, and (5) fix a clamp on the piece of wood with wood screws.

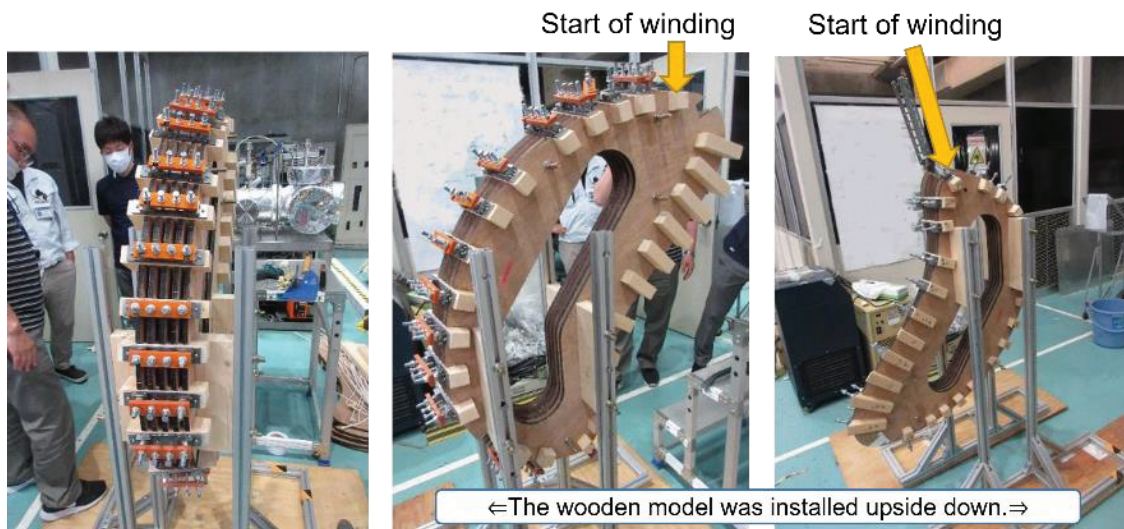


Fig 4.1-3 Pictures of the wooden model of the vacuum vessel. Two types of winding tests can be performed with different winding starts by turning the model upside down.

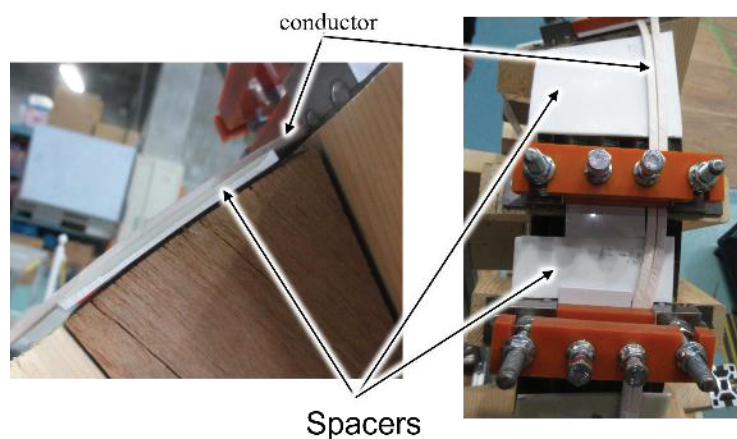


Fig 4.1-4 Insert spacers to fill gap. We inserted flexible ABS plates as spacers, where there is no clamp between the conductor and the vacuum vessel before the winding to eliminate the step between the wood boards. Since there is no step on the actual vacuum vessel, these plates are unnecessary. The ABS is an acrylonitrile-butadiene-styrene resin, which is a kind of the plastic.

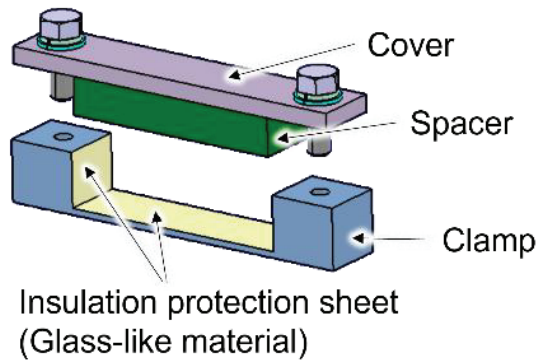


Fig 4.1-5 Design of the clamp for a solid conductor. Size of the conductor is 7.3 mm x 3.3 mm. If the purpose is only to stop the horizontal movement of the conductors, H=6.6 mm is sufficient. The H was increased to create the thread (screw) depth for fixing the cover. A spacer is added to compensate for the higher clamp. In the trial winding, the insulation protection sheet was omitted because we did not care about the damage.

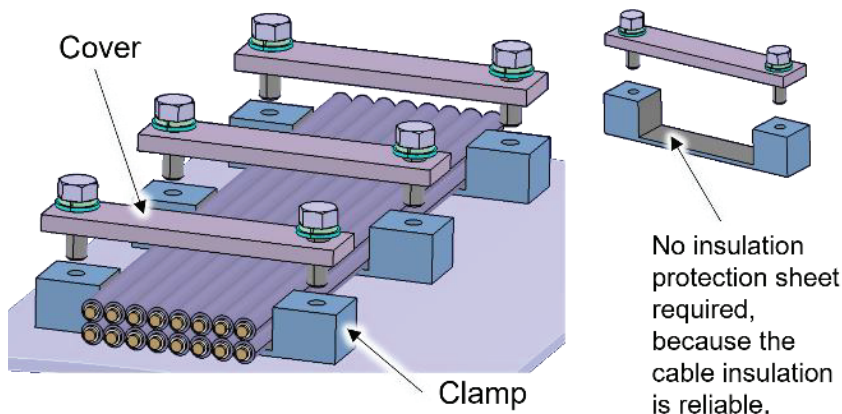
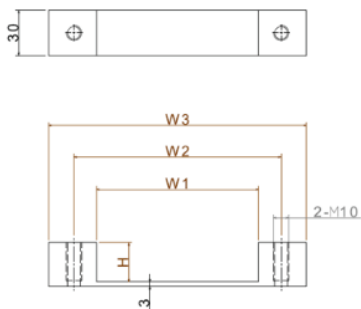


Fig 4.1-6. Design of the clamp for a cable. Size of the conductor is 11mm in diameter. In the trial winding, the clamp for the solid conductor with W1=66 was diverted for cost reduction. The number of the winding was reduced from 8x2 to 6x2 because the width of the clamp was not enough.

Table 4.1-1 Size of the clamps.

	For the solid conductor			For the cable		
	Near terminal	Others	IDEAL	Near terminal	Others	IDEAL
W1	75	66	58.4	99	88	88
W2	100	100		122	122	
W3	130	130		152	152	
H	15	15	6.6	21	21	22



The IDELA indicates the condition of zero gap between conductors.  
The W1 must be widened near the terminal due to layer-to-layer transition.  
Slightly crushed cables assumed to be used.

#### 4.1.2 Trial of winding a square solid conductor as a TFC

Fig 4.1-7 shows copper conductor used for the winding test, of which cross section is 3.3 mm × 7.3 mm. A general coil is made by rotating the take-up (winding) bobbin, but the method cannot be applied to the TFC for the CFQS. The take-up bobbin, which was the vacuum vessel, was fixed and the unwinding bobbin was moved. Since the weight of the bobbin with a conductor is about 20kg, it took physical strength to lift and move it.

As a result of the winding test, the following disadvantages were found.

- The square solid conductor was hard to wind and especially difficult to twist.
- It was necessary to adjust the shape of conductor by hammering it as shown in Fig 4.1-8 and this caused damage to insulator of the conductor as shown in Fig 4.1-9. A general coil bends the conductor using a technique called tension winding, which is a winding method in which the winding bobbin is rotated while the conductor is pulled. This method cannot be applied to the TFC in the CFQS. When winding with a solid conductor, it was also necessary to twist the conductor. We forcibly twisted while bending the conductor by hammering. There were disturbance of conductor alignment and insulation damage. It may be because we added too much striking force to twist the conductor. There is also a concern that the vacuum vessel may be damaged during hammering work.
- In addition, significant gaps were appeared as shown in Fig 4.1-10 at the top and bottom area, because torsion of conductor was large in those area. A gap of about 5 mm was created between the conductor and the clamp, and between the conductor and the flexible plate. Ideally, the gap should be zero. A maximum gap of 5 mm was unavoidable due to the difficulty of correcting the twist of the conductor.
- Winding took a long time because it was difficult to twist the conductor. It may take several weeks to make a single coil.



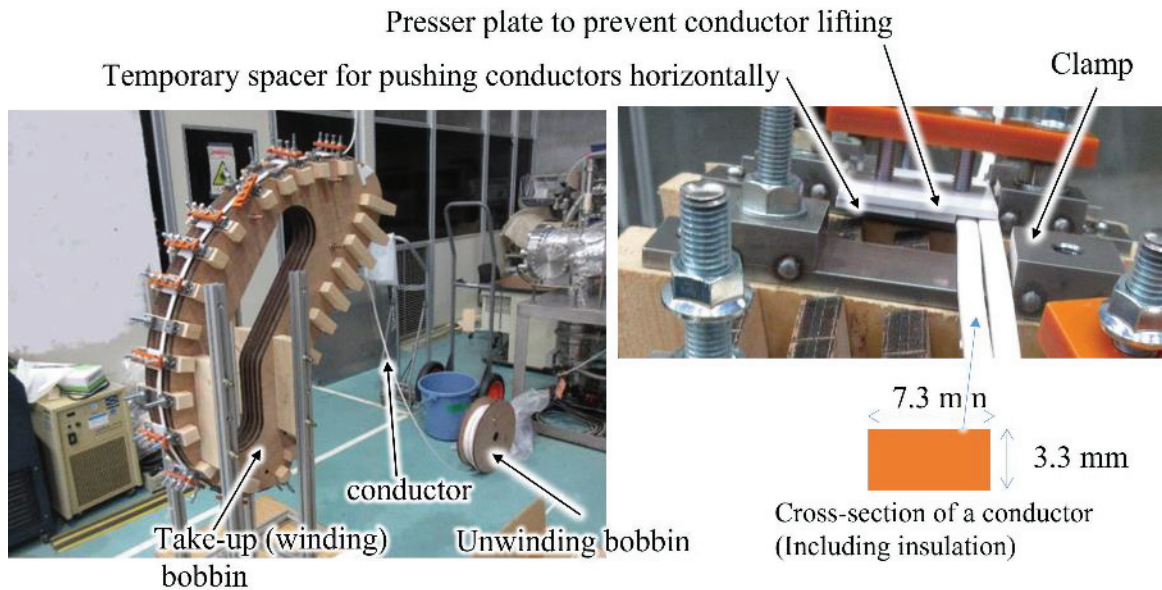


Fig 4.1-7 Winding a solid conductor for the TFC. A general coil is made by rotating the take-up (winding) bobbin, but the method cannot be applied to the TFC for the CFQS. The take-up bobbin, which was the vacuum vessel, was fixed and the unwinding bobbin was moved. Since the weight of the bobbin with a conductor is about 20kg, it took physical strength to lift and move it.

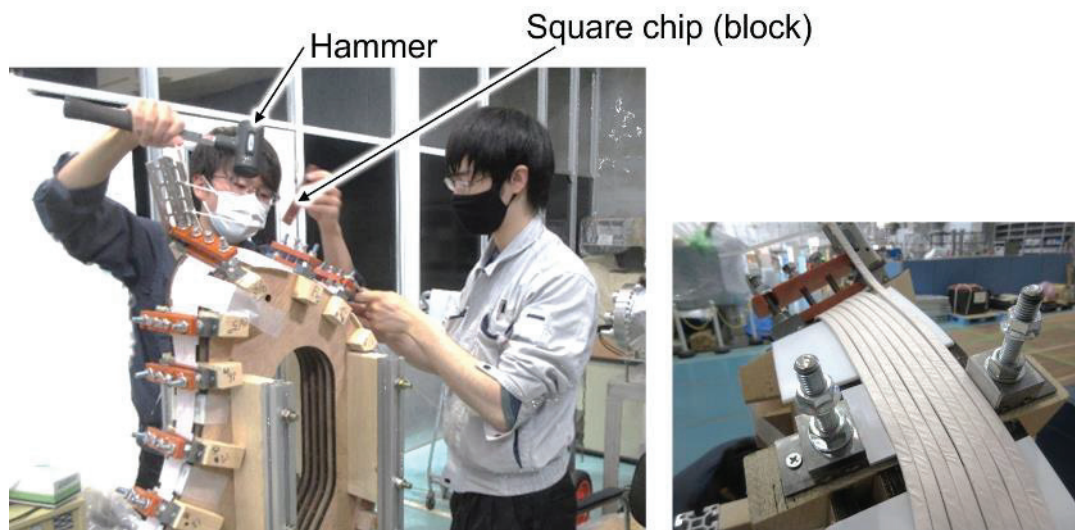


Fig 4.1-8 Conductor bending and twisting methods for the TFC. A general coil bends the conductor using a technique called tension winding, which is a winding method in which the winding bobbin is rotated while the conductor is pulled. This method cannot be applied to the TFC in the CFQS. When winding with a solid conductor, it is also necessary to twist the conductor. We forcibly twisted while bending the conductor by hammering.



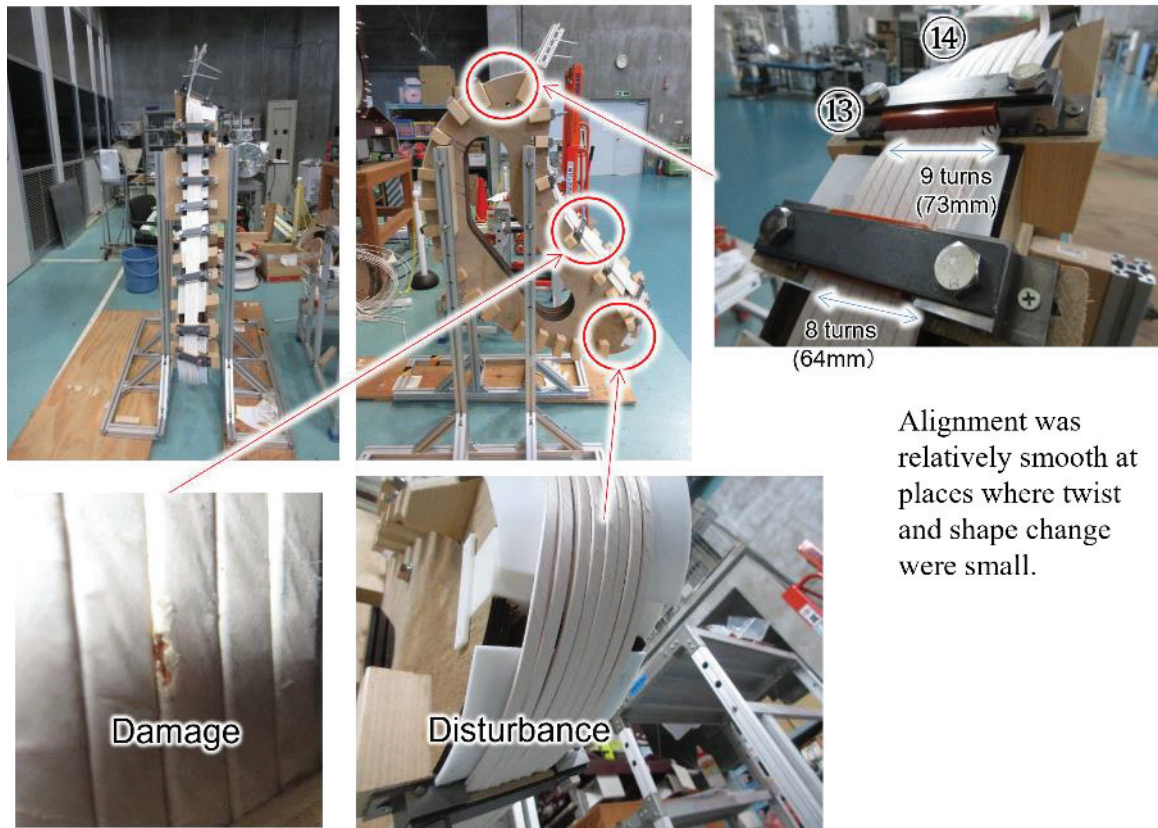


Fig 4.1-9 Visual check after winding the square solid conductor. There were disturbance of conductor alignment and insulation damage. It may be because we added too much striking force to twist the conductor.

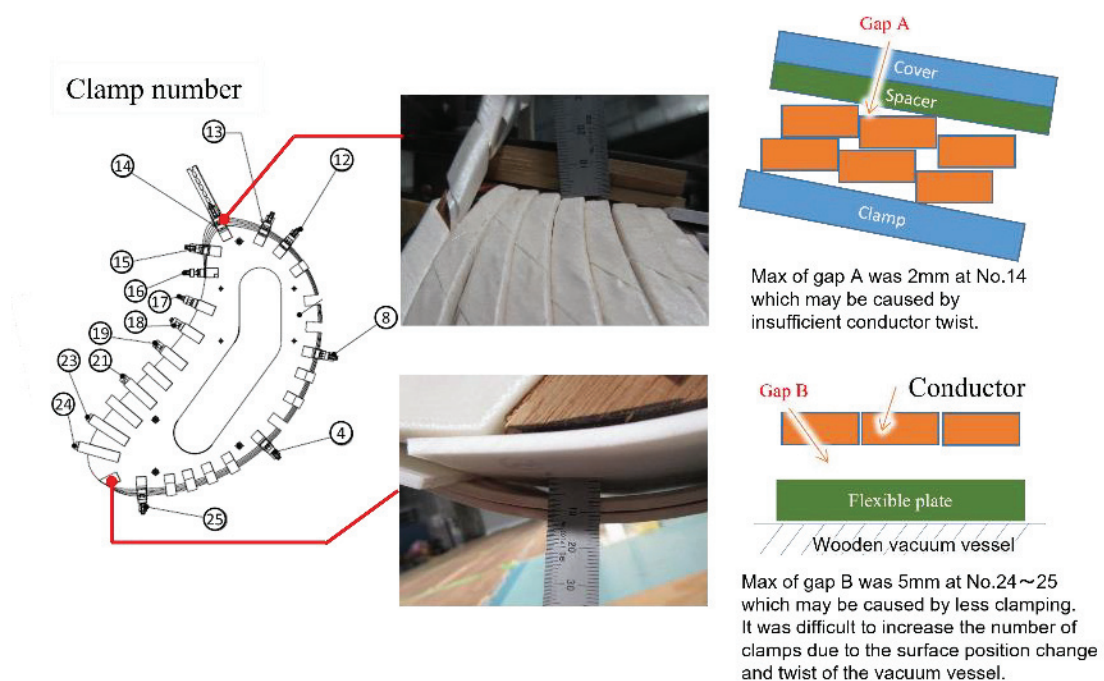


Fig 4.1-10 Gap measurement of the TFC with a solid conductor. Ideally, the gap should be zero. A maximum gap of 5 mm was unavoidable due to the difficulty of correcting the twist of the conductor.

#### 4.1.3 Trial of winding a cable as a TFC

As explained in the previous section, square solid conductors are not easy to wind, so we decided that it would be judged not to produce high-quality coils. Therefore, we tried winding a circular cable.

Fig 4.1-11 shows a cable used for the winding test, of which cross section is 11 mm in diameter. Since the weight of the bundle of a cable was about 12kg, which was about a half of the bobbin with a square solid cable, it was easy to handle the conductor. In addition, the cable was easy to bend, did not need to be twisted, and did not try to return to its original shape after being bent. Therefore, the winding work became much easier.

As a result of the winding test, the following advantages were found.

- It was easy to handle the conductor.
- No hammering was required. So, the risk of damaging the insulation was small.
- As shown in Fig 4.1-12, we could not find any defect.
- As shown in Fig 4.1-13, we could not observe any obvious gaps as with the square solid conductor.
- As shown in Fig 4.1-14, no extra space was required in a guide groove width W1 of clamps, because the cable insulation was flexible. The side spacers for adjusting the gap between the clamp and the cable were unnecessary except near the terminals.

Presser plate to prevent conductor lifting.  
It also stops horizontal movement.

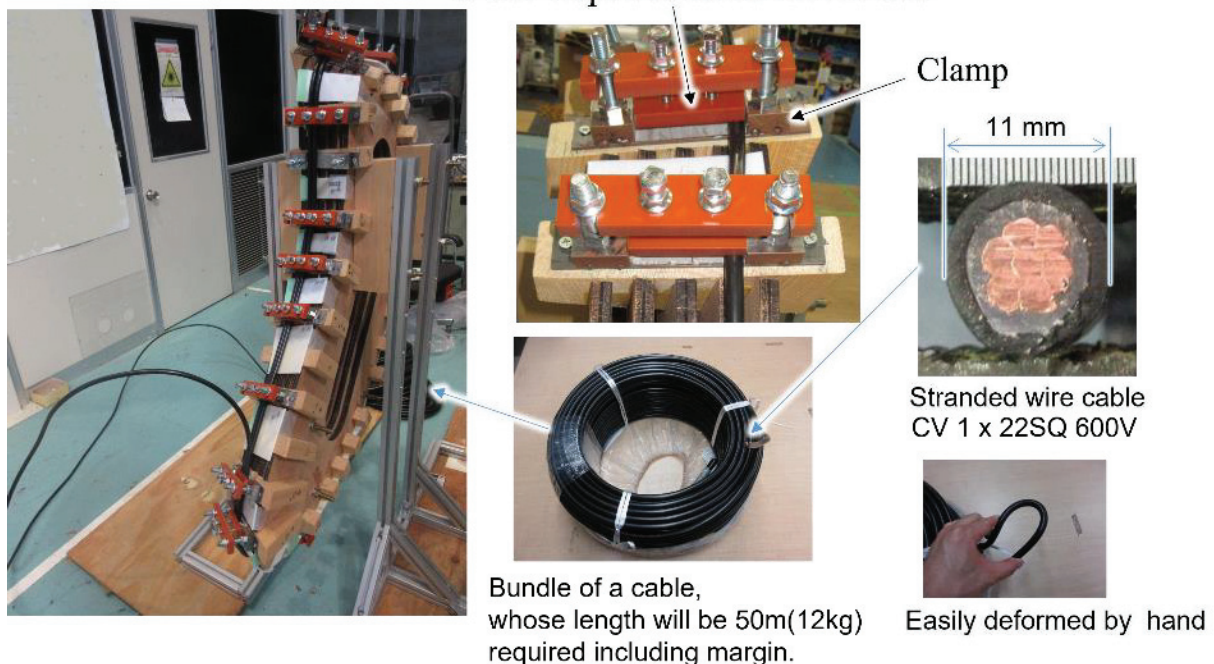


Fig 4.1-11 Winding a cable for the TFC. Winding a cable was much easier than that of the solid conductor. Easily bent by hand. No twist required. Did not return to its original shape. No hammering required. The weight of the bundle of a cable is about 12kg.





Fig 4.1-12 Visual check after winding the cable. We could not find any defect.

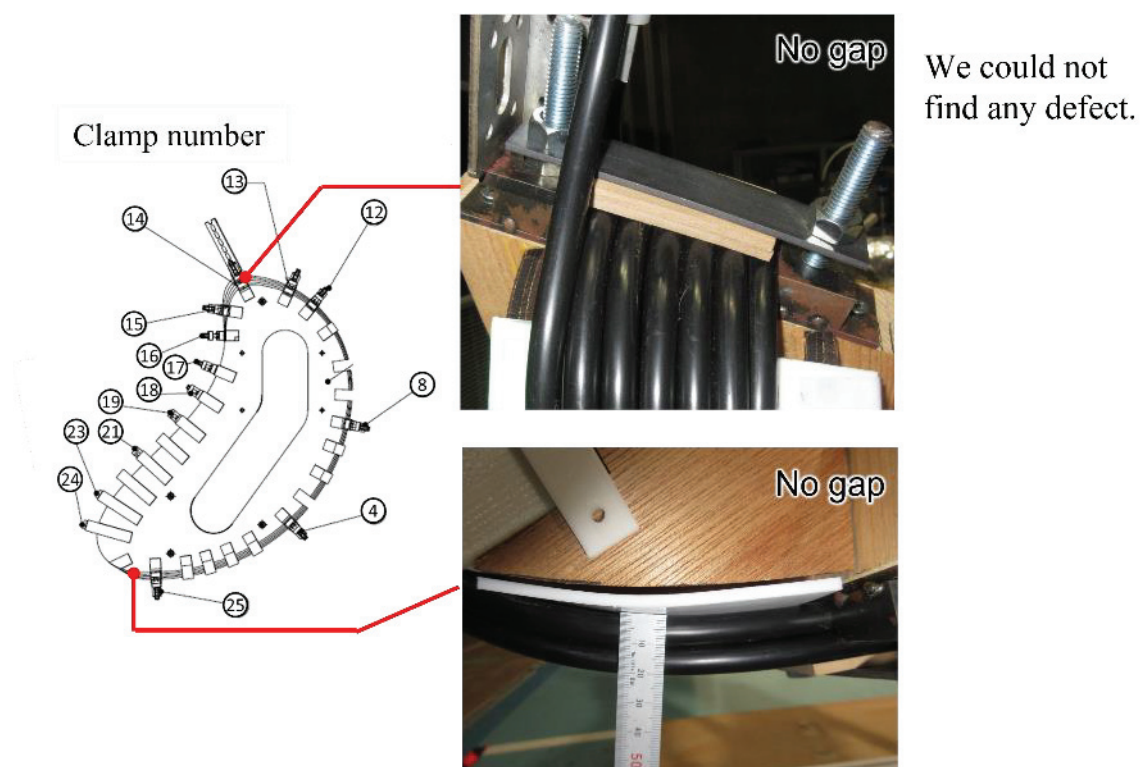
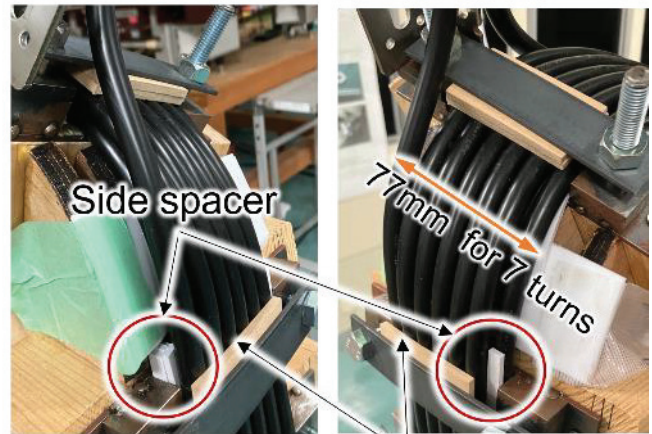


Fig 4.1-13 Gap measurement of the TFC with a cable. No gaps were observed as with the solid conductor.



Away from the terminal



Wooden top apacer  
Near the terminal

Fig 4.1-14 Special report. A guide groove width  $W1$  of clamps and the width of the cables (11 mm x 6) were the same. Cable insulation is flexible, so it can be inserted even if there is no extra in the clamp. The side spacers were required in the clamp only near the terminal to prevent the cable from slipping sideways. The wooden top spacer was inserted between the conductor and the cover because there were no bolts of the appropriate length at the time of testing. If appropriate bolts are prepared when the actual coil is manufactured, the top wooden spacer will not be necessary.

## 4.2 Wooden model of the vacuum vessel for examining the installation of parts in a vacuum vessel

A wooden model of the vacuum vessel was developed. It will be used to examine the installation of parts, such as magnetic measurement, metal limiter and protect plate, and check the workability in the vacuum vessel.

Fig 4.2-1 shows schematic view of the model. 11 wood plates are arranged every 11.25 deg. Each plate is cut out to follow the inner shape of the vacuum vessel. 3 base plates are fixed by 6 pillars at the top, middle and bottom positions. The base plates have grooves into which the wood plates can be inserted. A wood processing company machined these materials. They were delivered to the development and experiment building in NIFS, in which the CHS device was located, and assembled as shown in Fig 4.2-2.

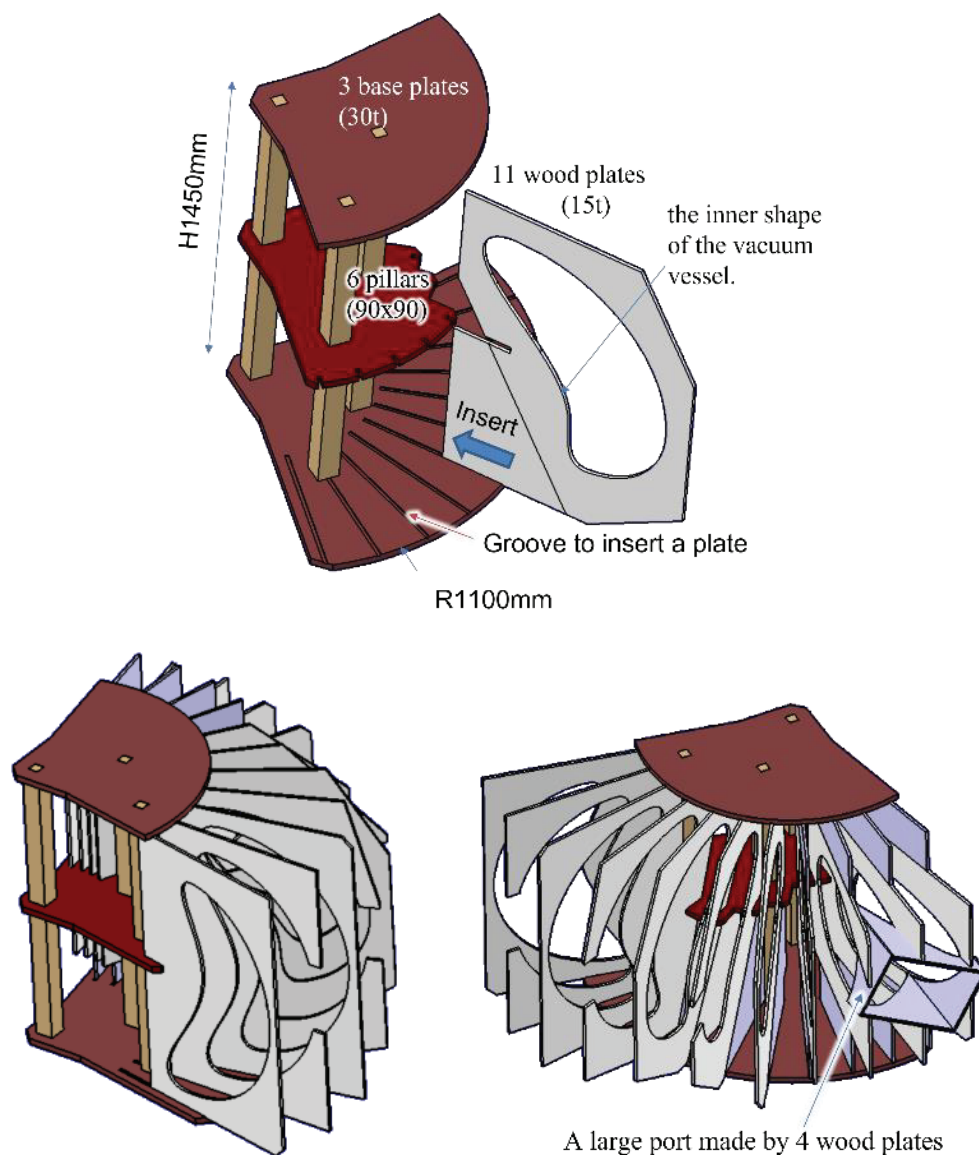


Fig 4.2-1 Schematic view of the model, which is assembled from 24 parts (11 wood plates, 3 base plates, 6 pillars and 4 wood plates for a large port)





Fig 4.2-2 All parts for a model were assembled in NIFS. Each of 24 parts was made by wood processing company.



NIFS-SWJTU JOINT PROJECT FOR CFQS  
~PHYSICS AND ENGINEERING DESIGN~  
VER. 5.1  
2023 AUG.

APPENDIX-A3 (DW)

~DRAWING~

CFQS TEAM



*NIFS; National Institute for Fusion Science*

*SWJTU; Institute of Fusion Science, School of Physical Science and Technology, Southwest Jiaotong University*

*Hefei Keye; Hefei Keye Electrical Physical Equipment Manufacturing Co., Ltd*

## Table of contents

1	CFQS overall view .....	3
2	Modular coil .....	6
3	Toroidal field coil.....	13
4	Poloidal field coil .....	14
5	External current lead .....	16
6	Vacuum vessel .....	18
7	Cage type support structure.....	23
8	Cooling water pipe .....	26

# 1 CFQS overall view

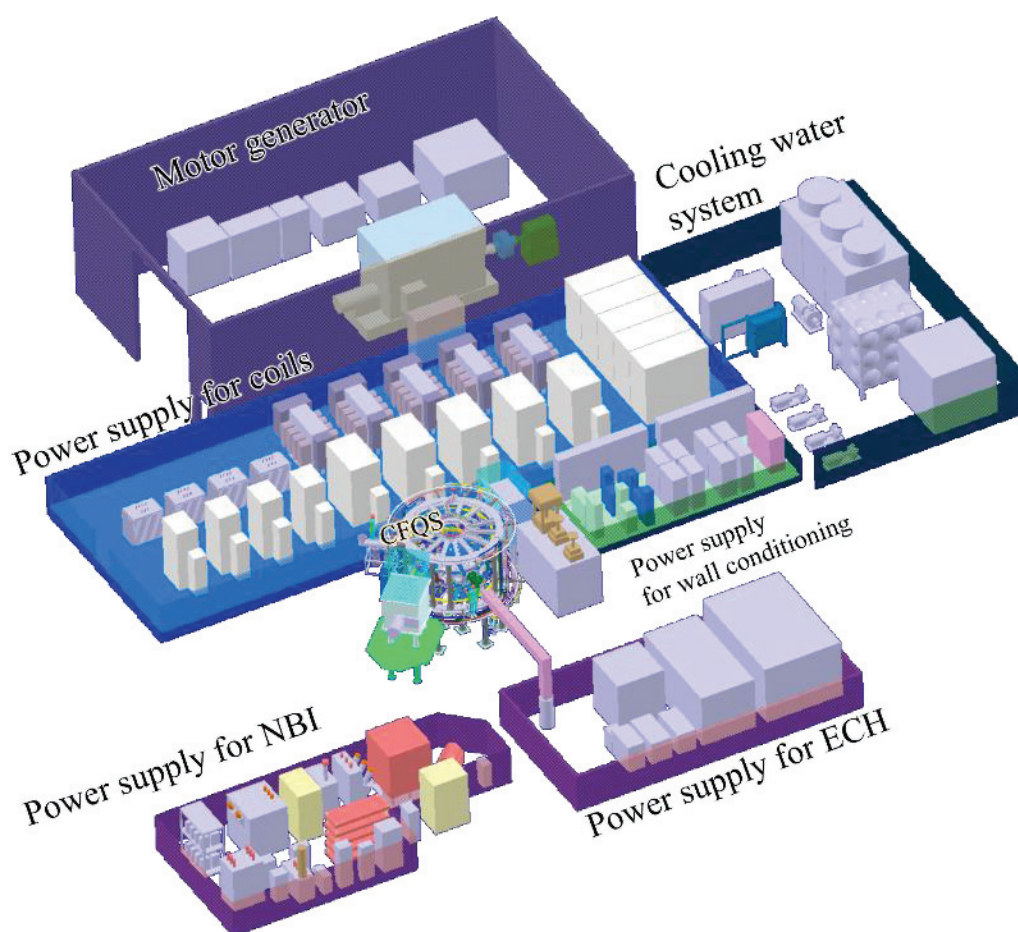
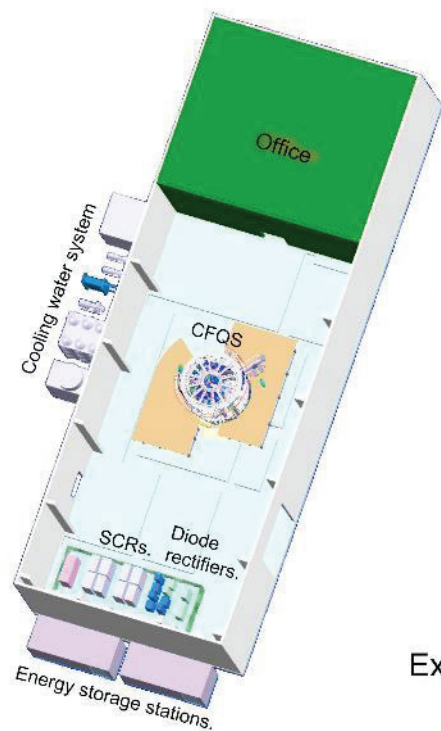
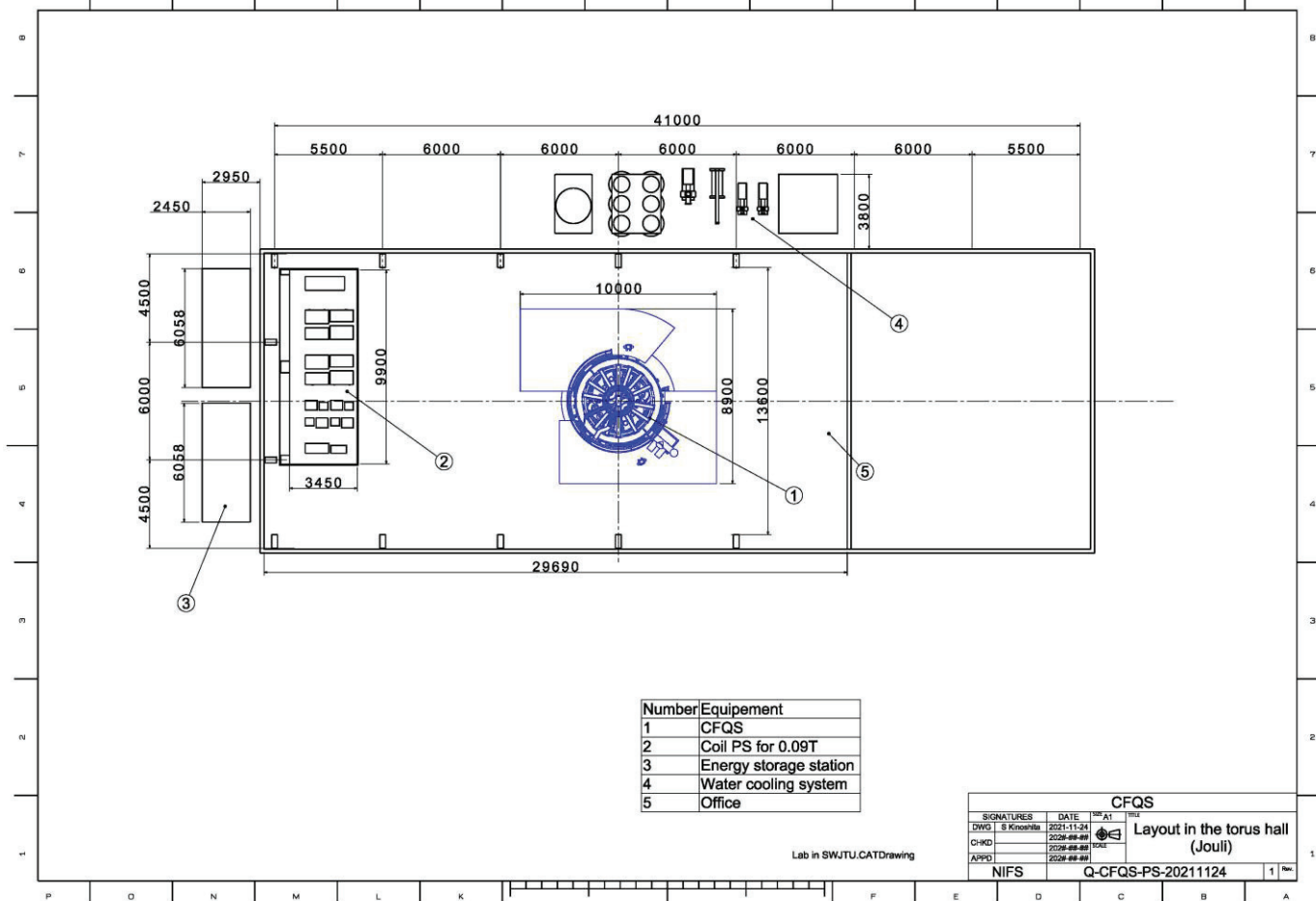
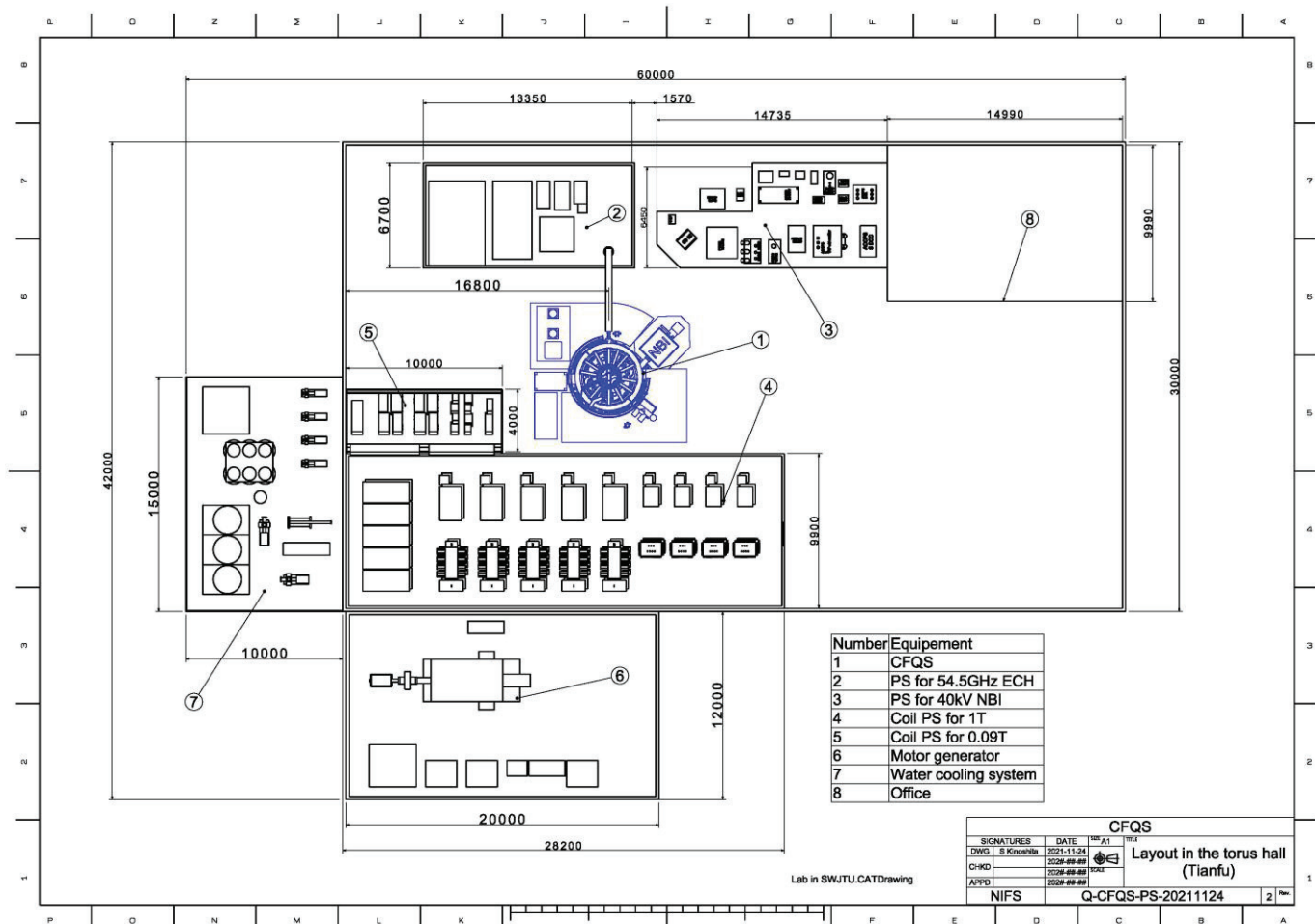


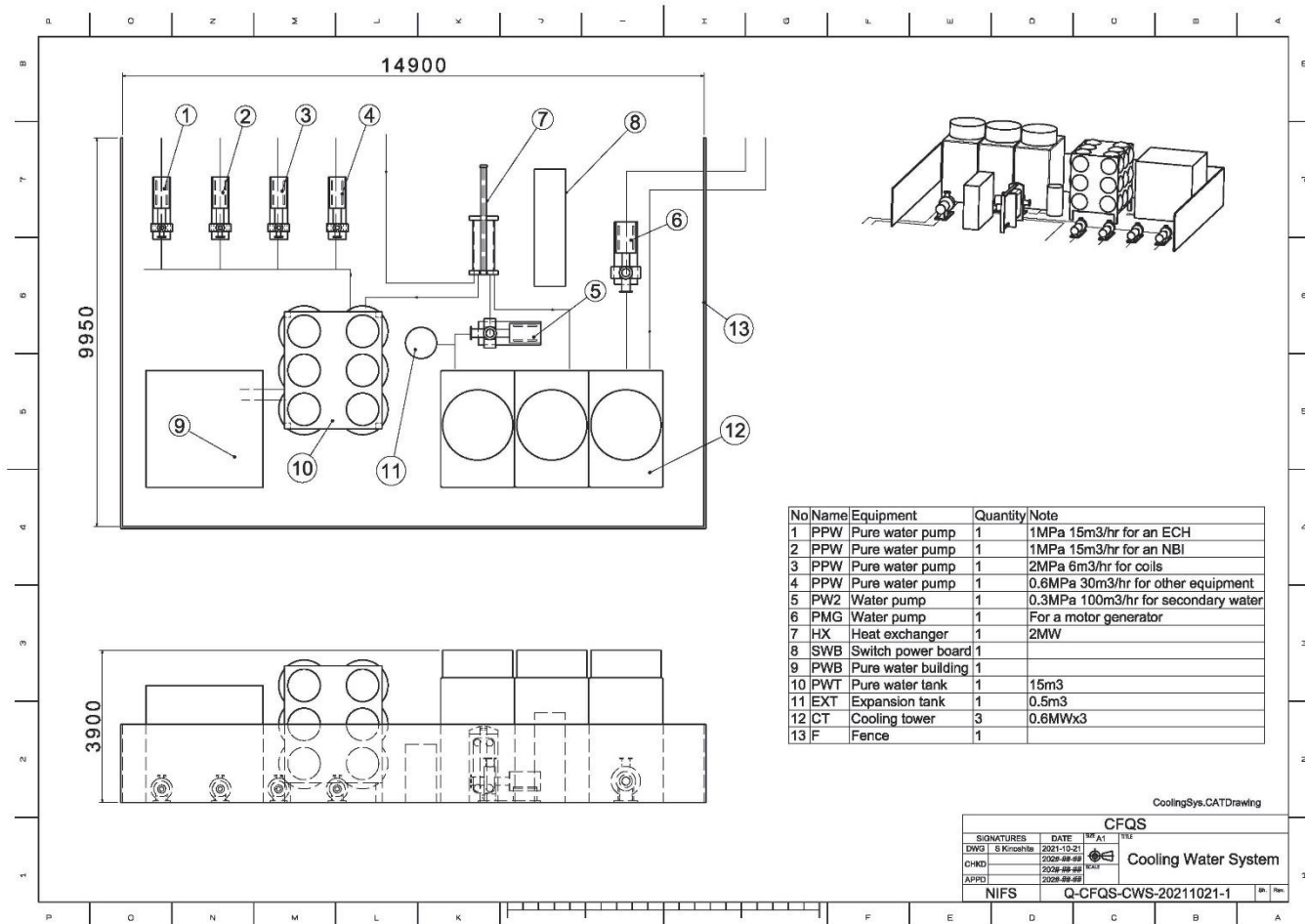
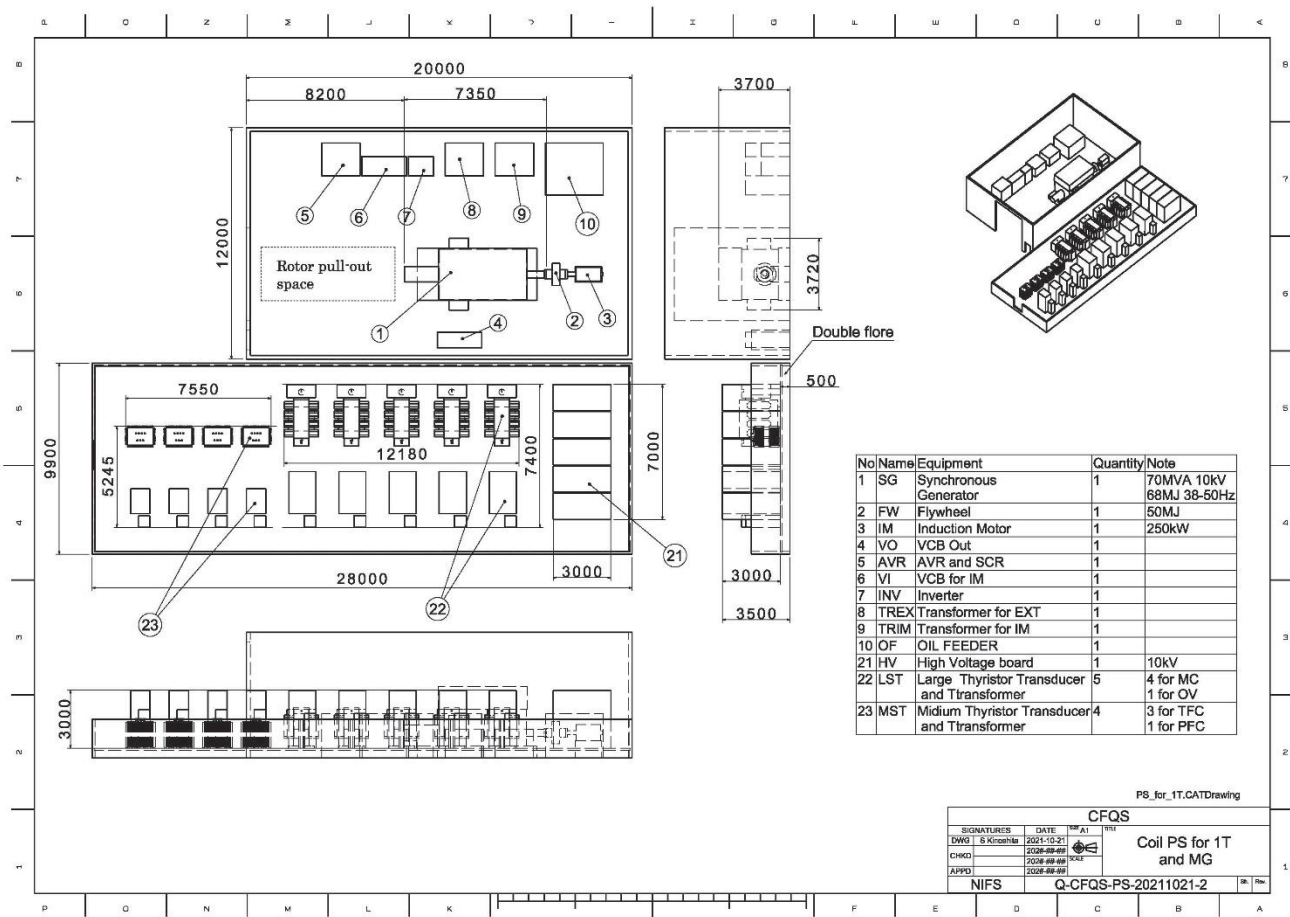
Fig 1-1. Layout of the CFQS for 1T



Experimental building in Jiuli campus

Fig 1-2. Layout of the CFQS for 0.09 T







## 2 Modular coil

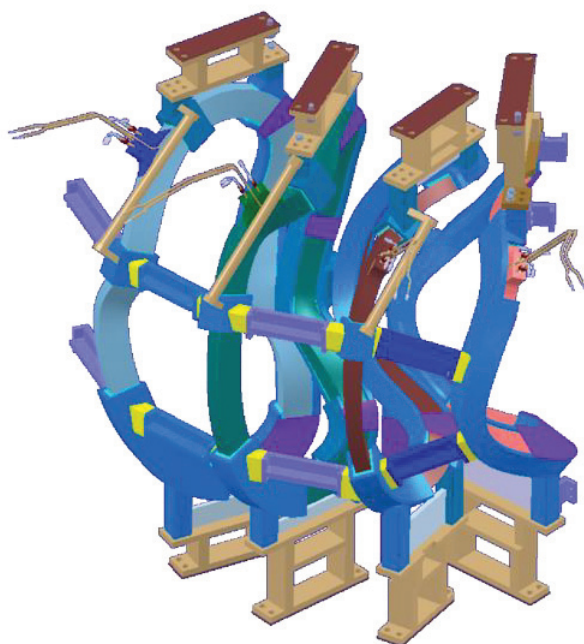


Fig 2-1. Modular coil for 1 T

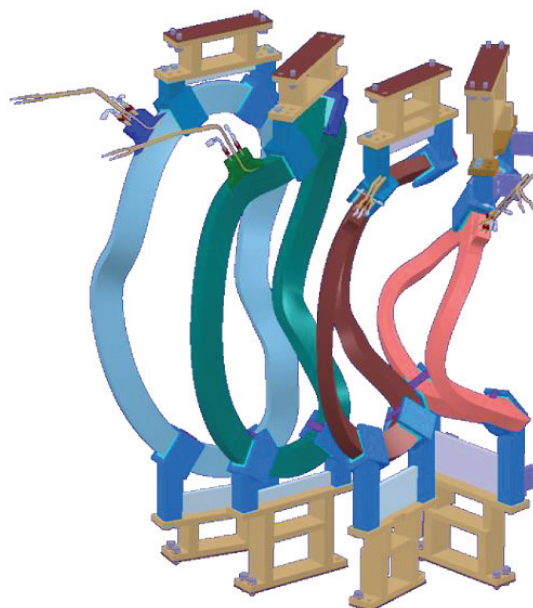
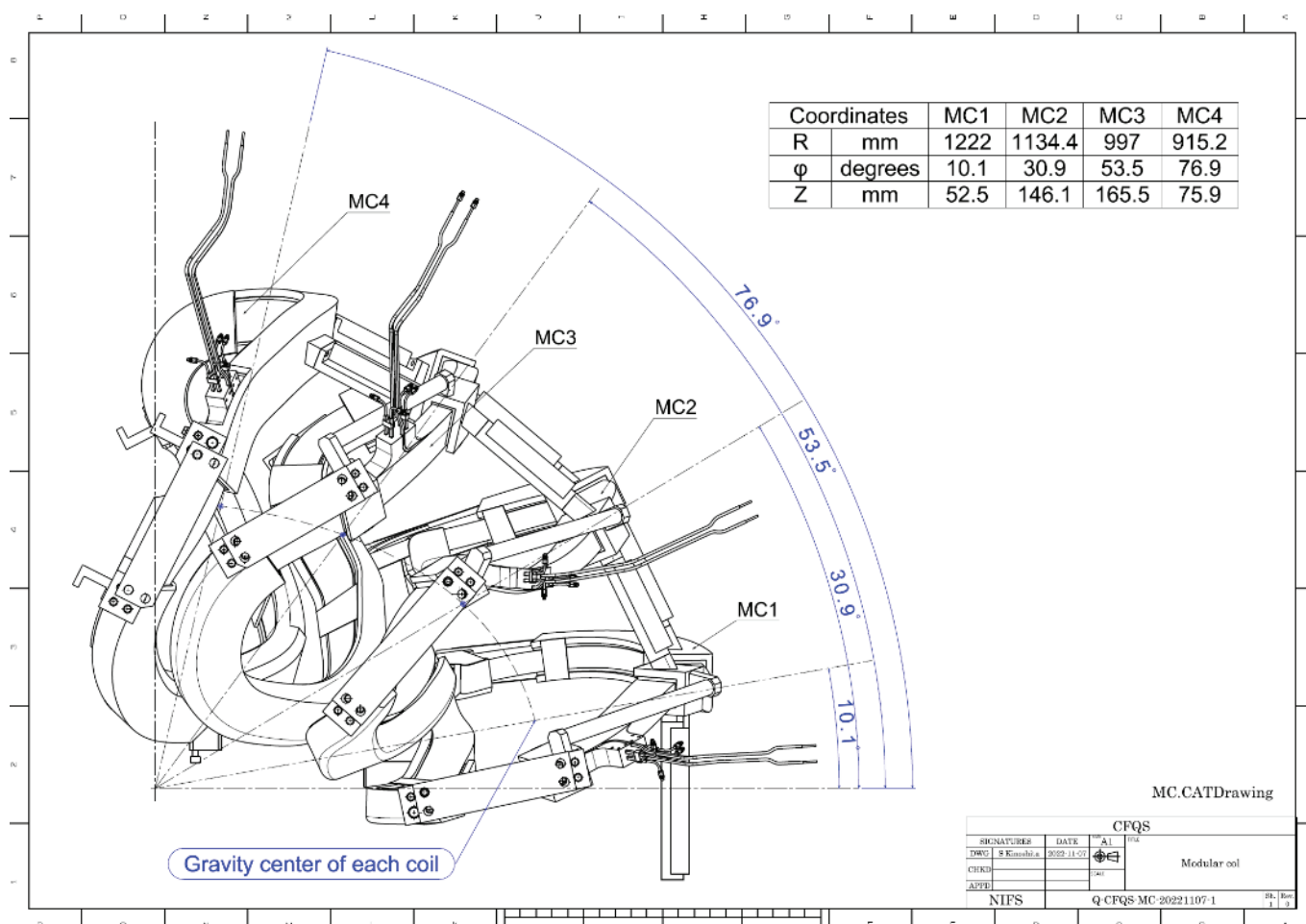
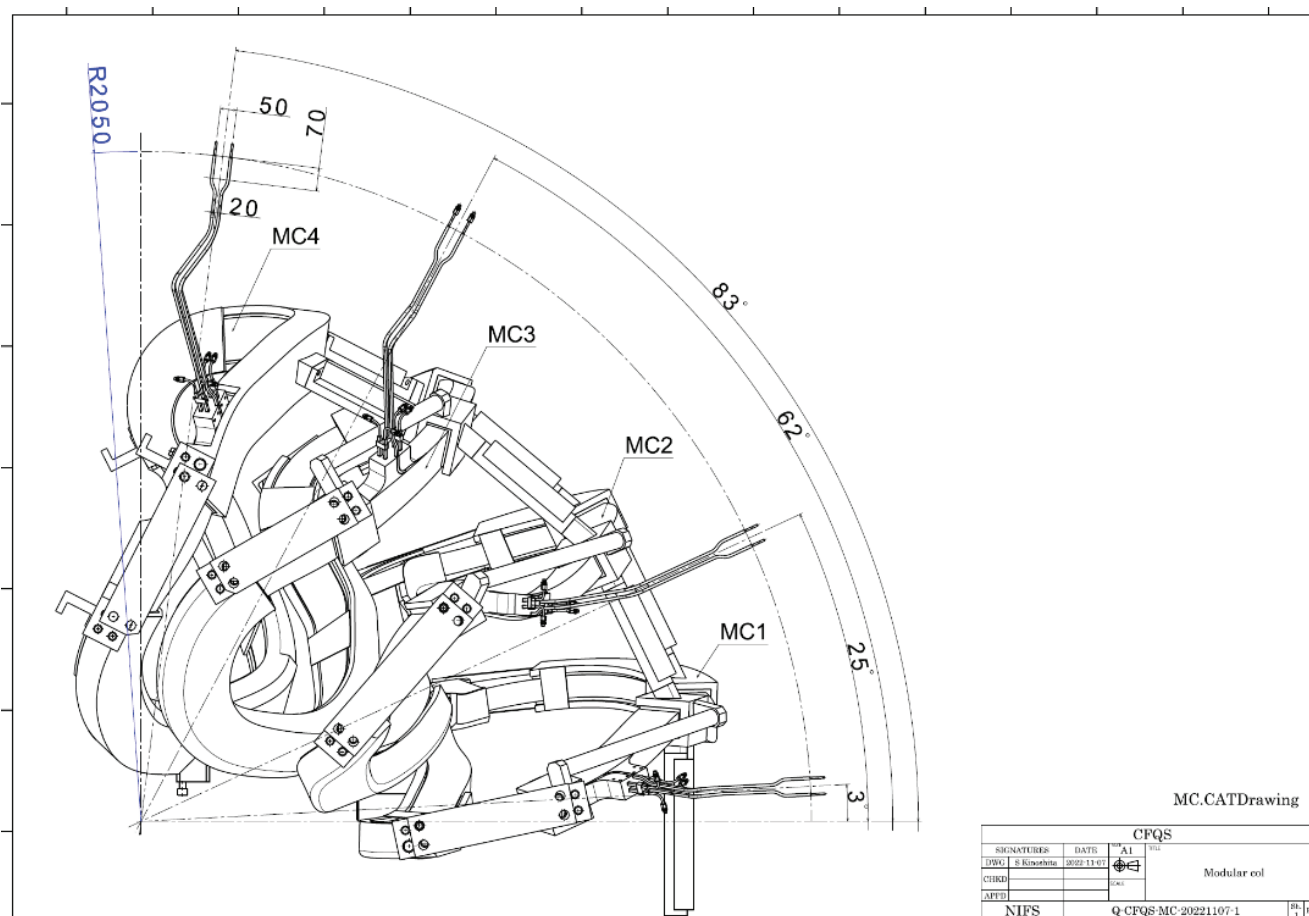
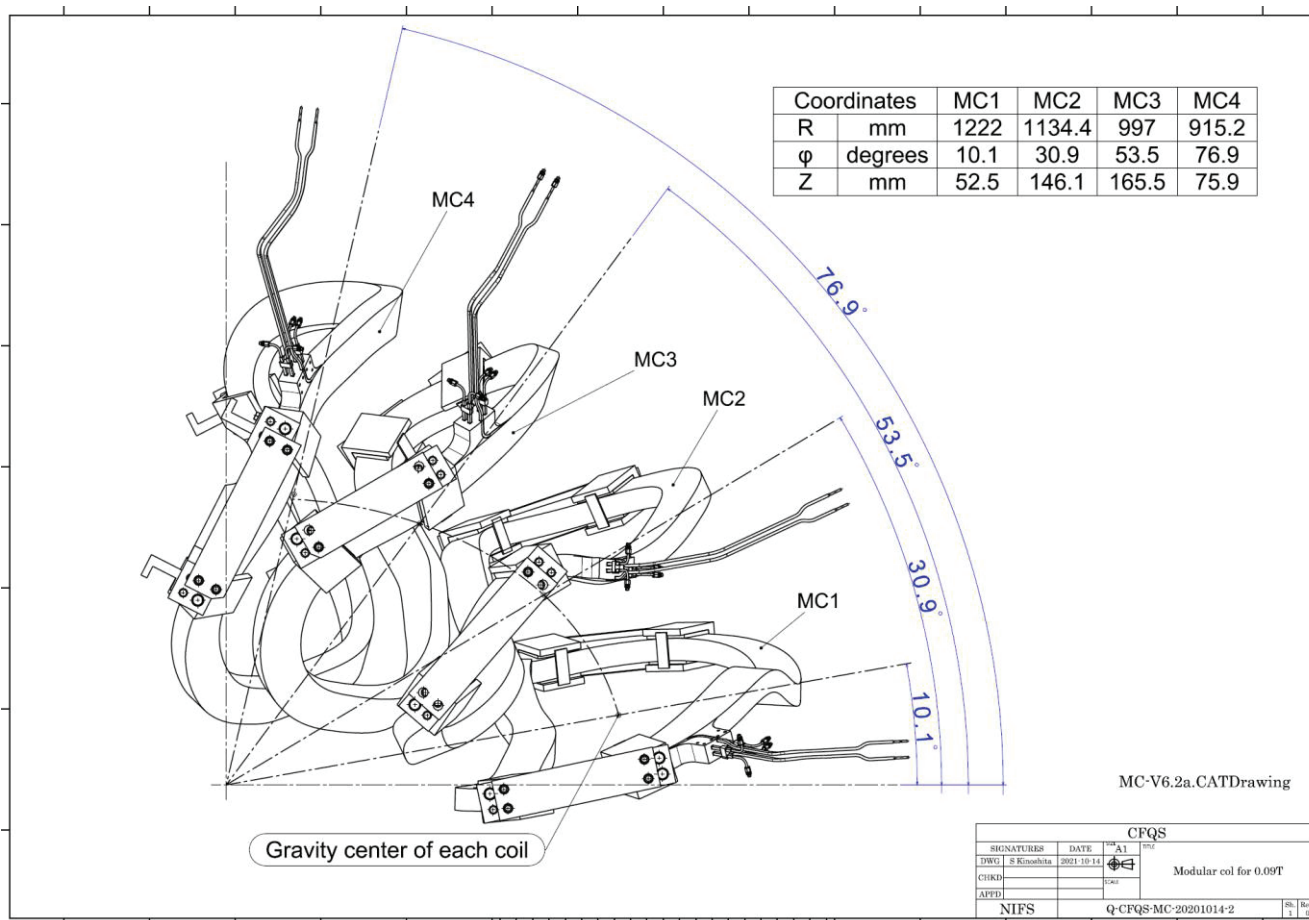
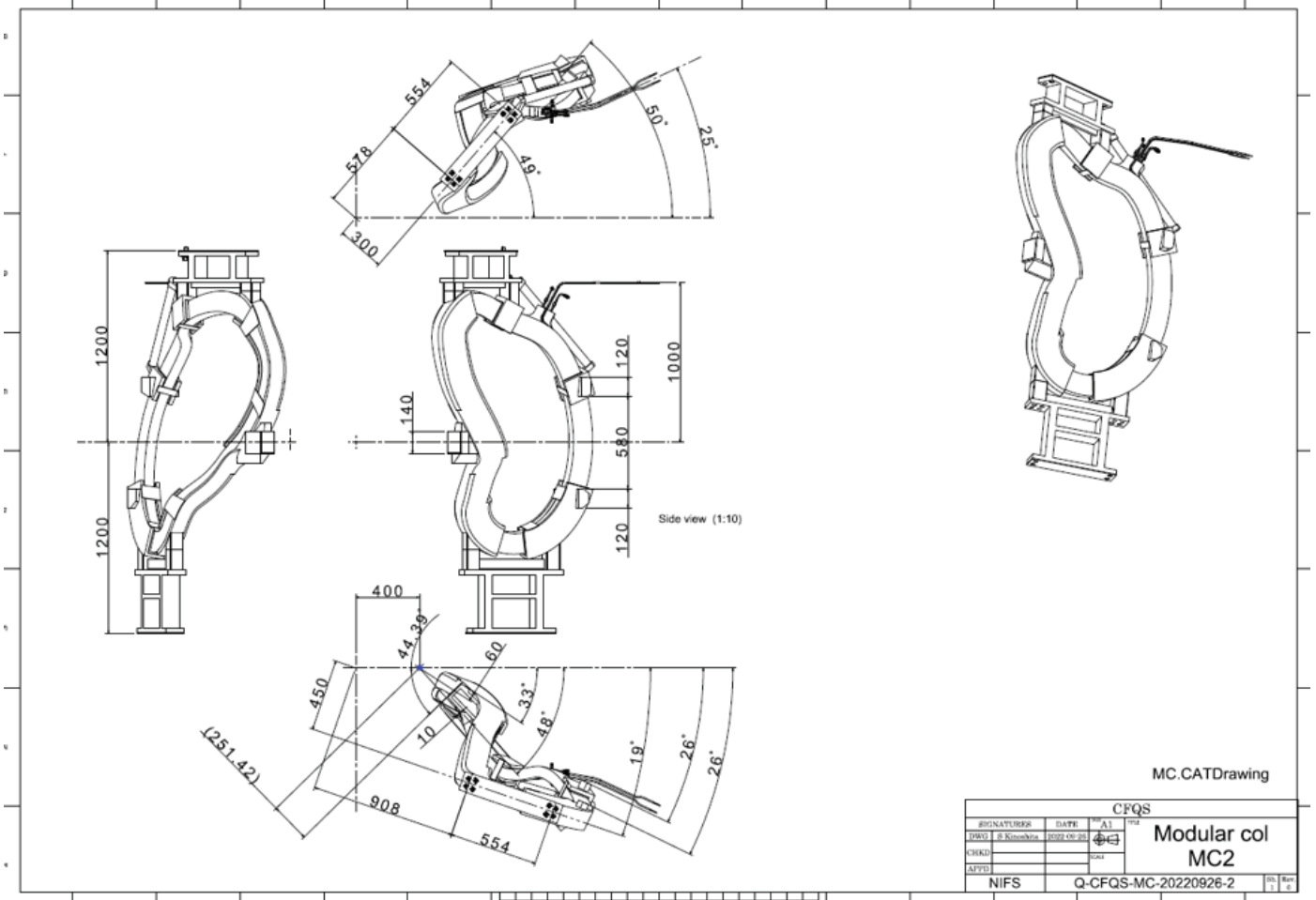
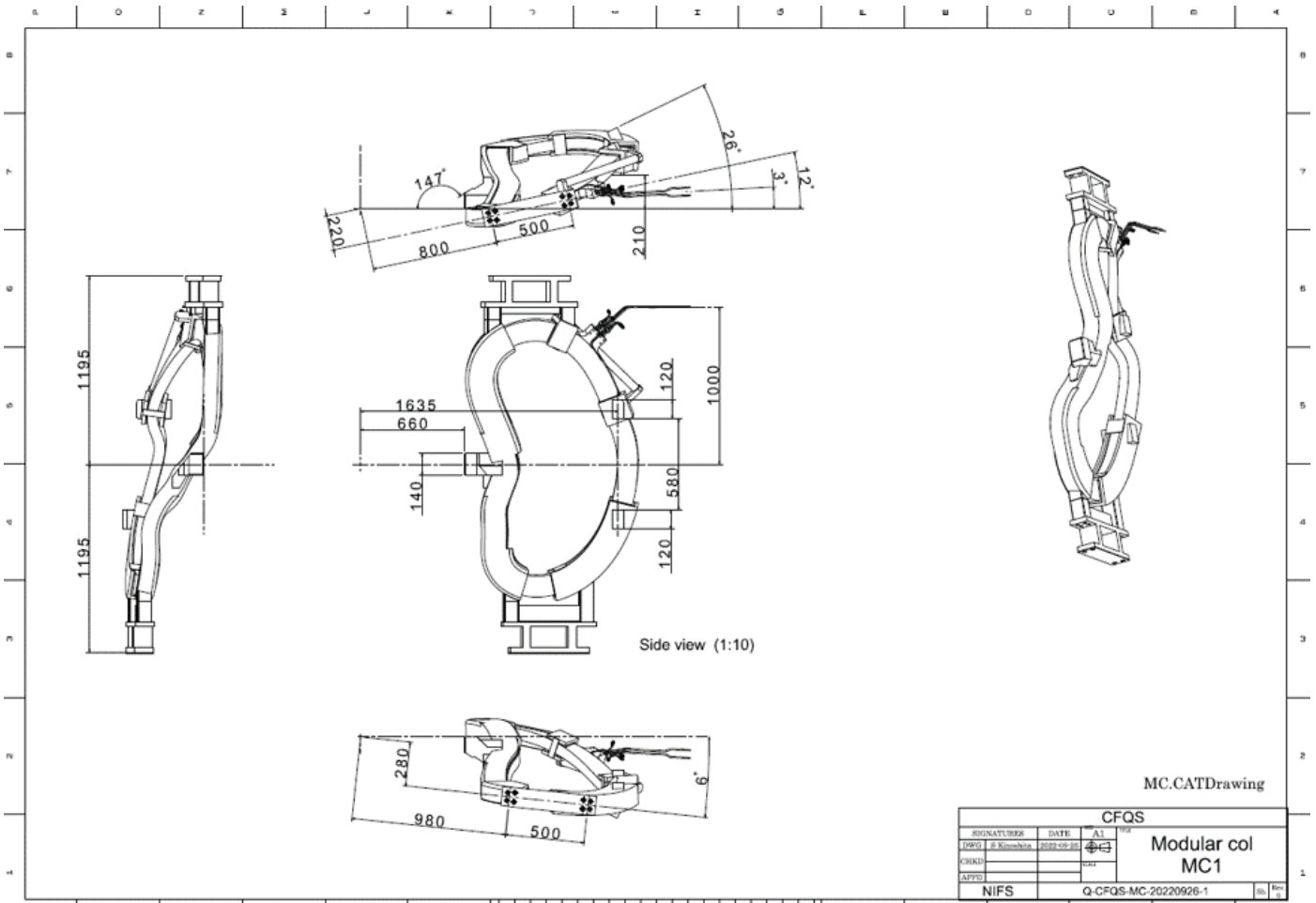


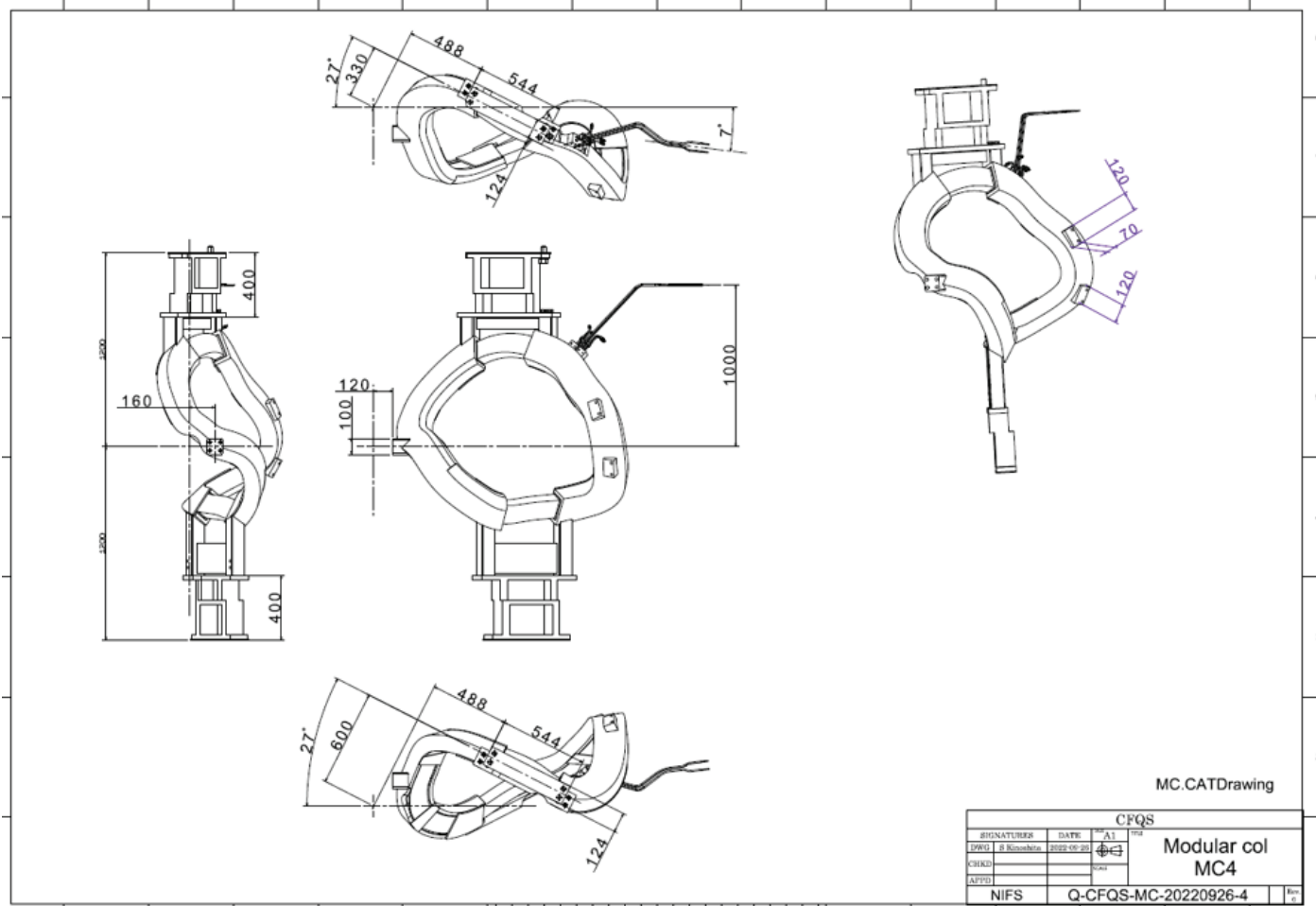
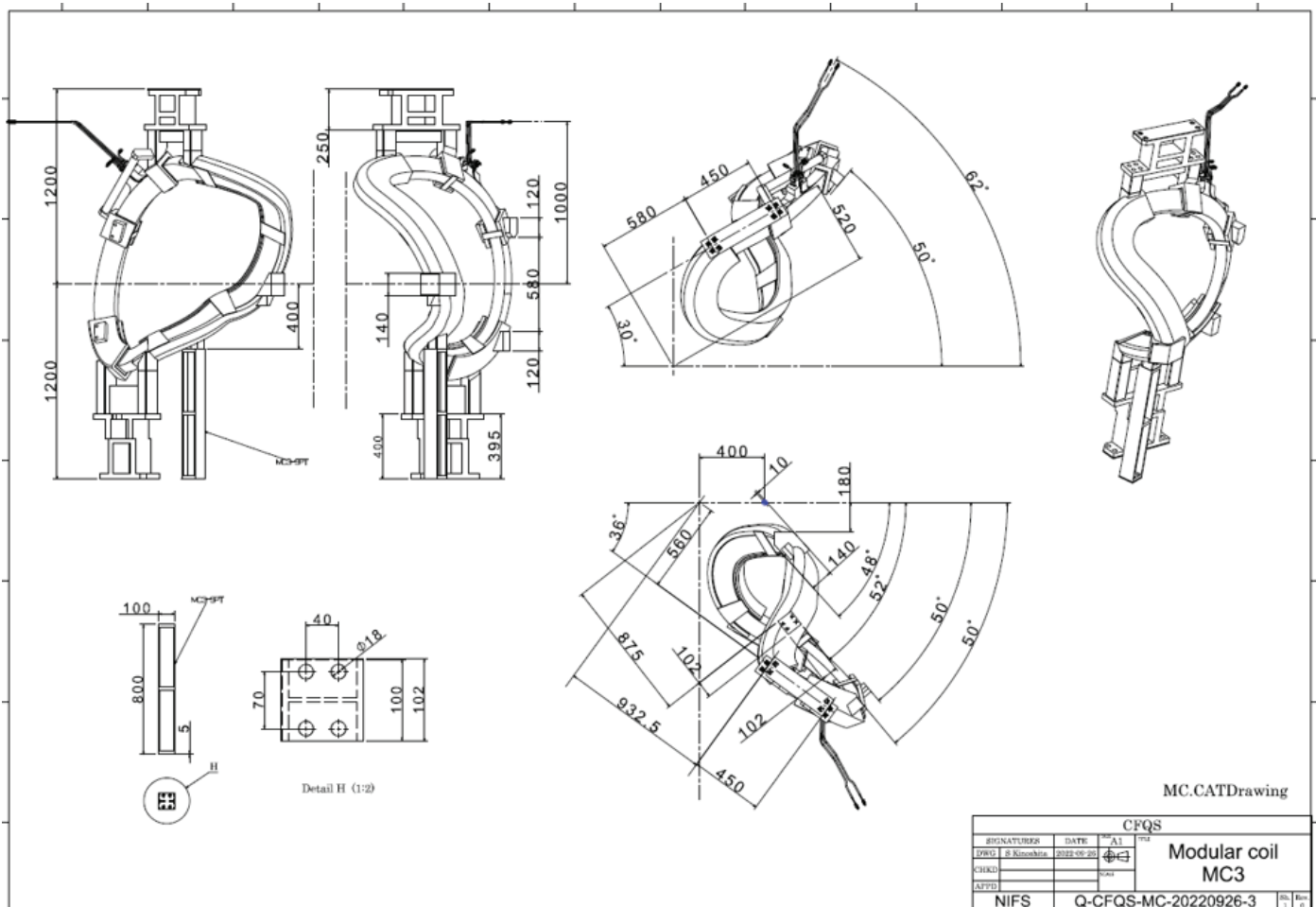
Fig 2-2. Modular coil for 0.09 T

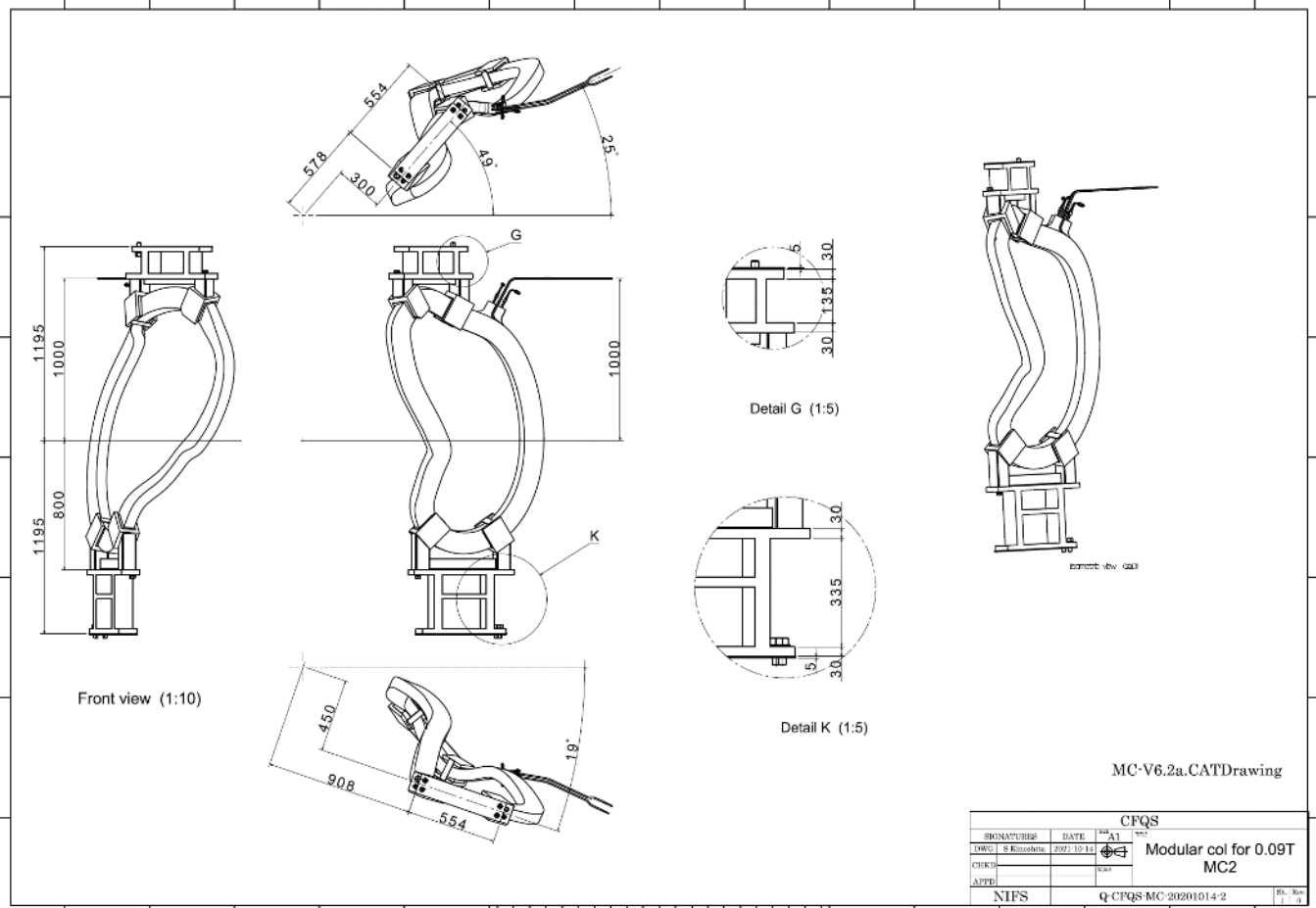
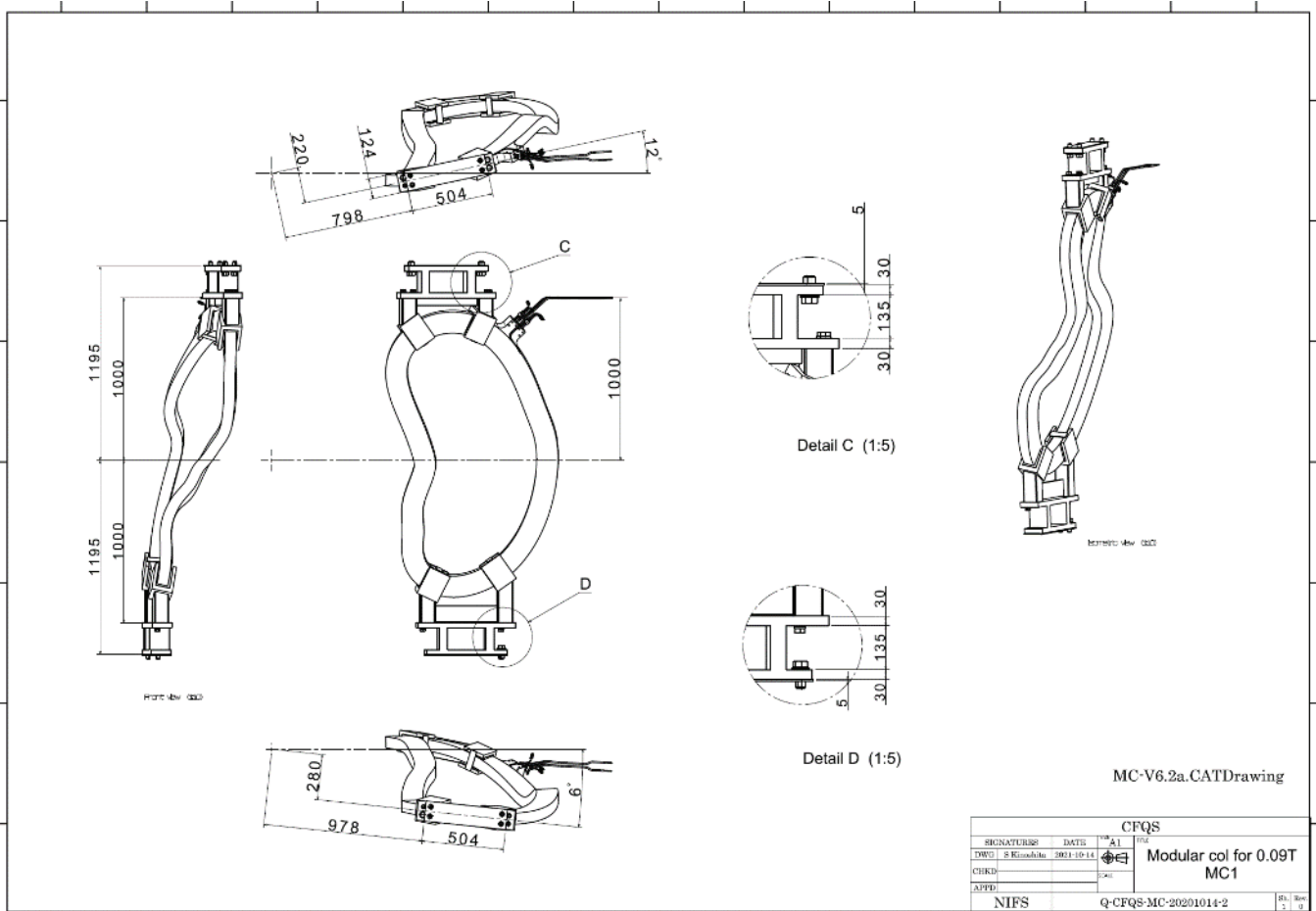


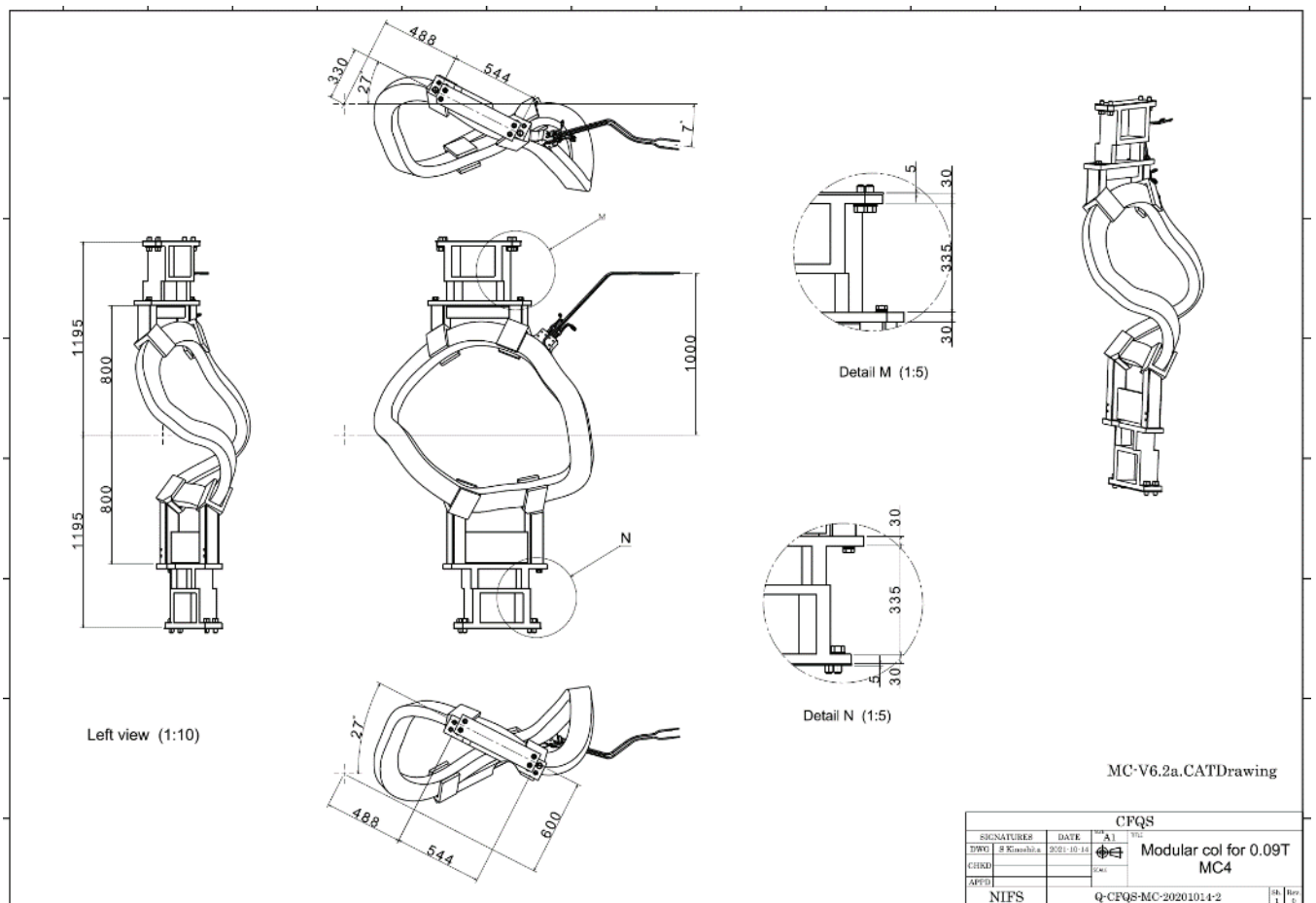
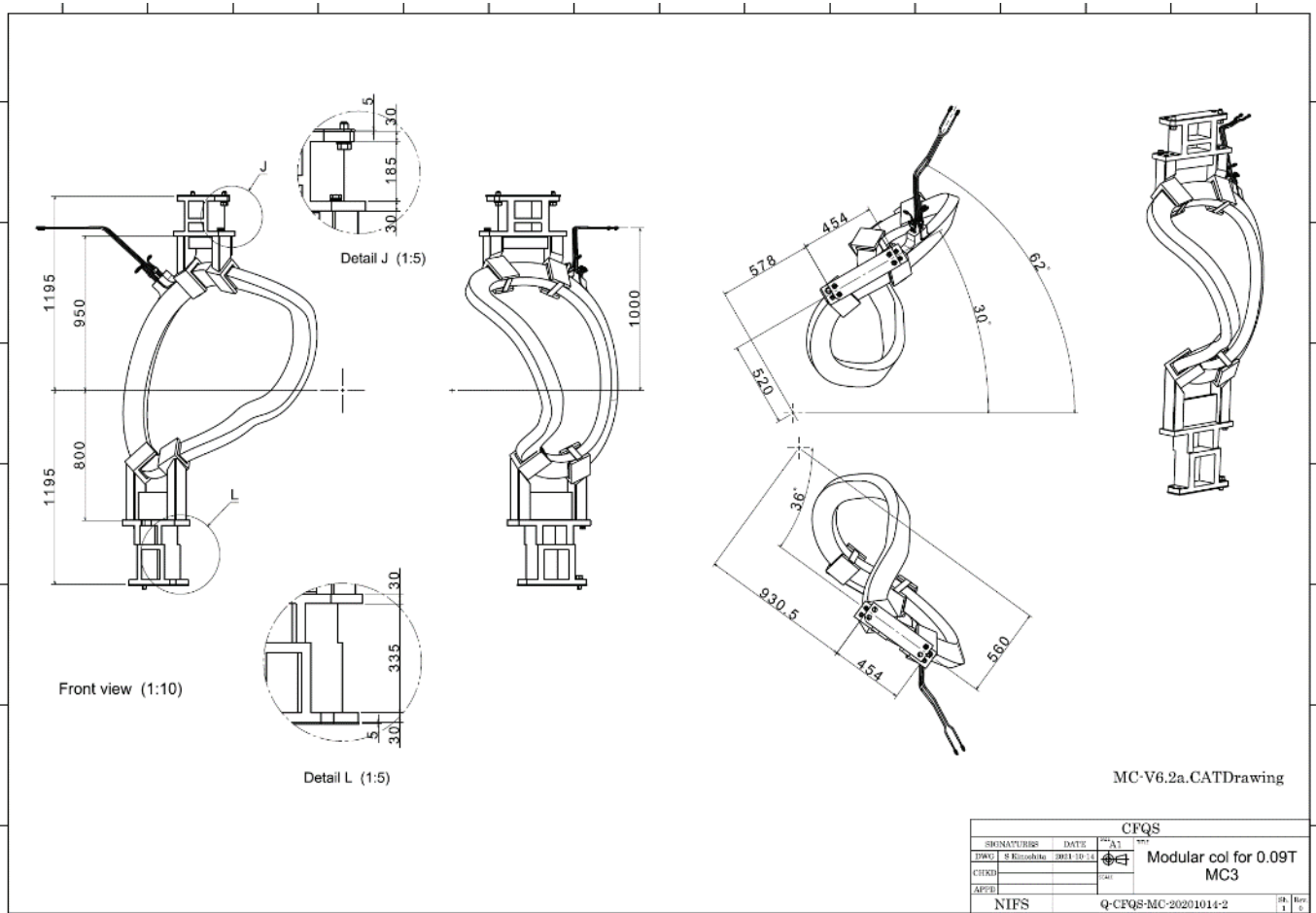




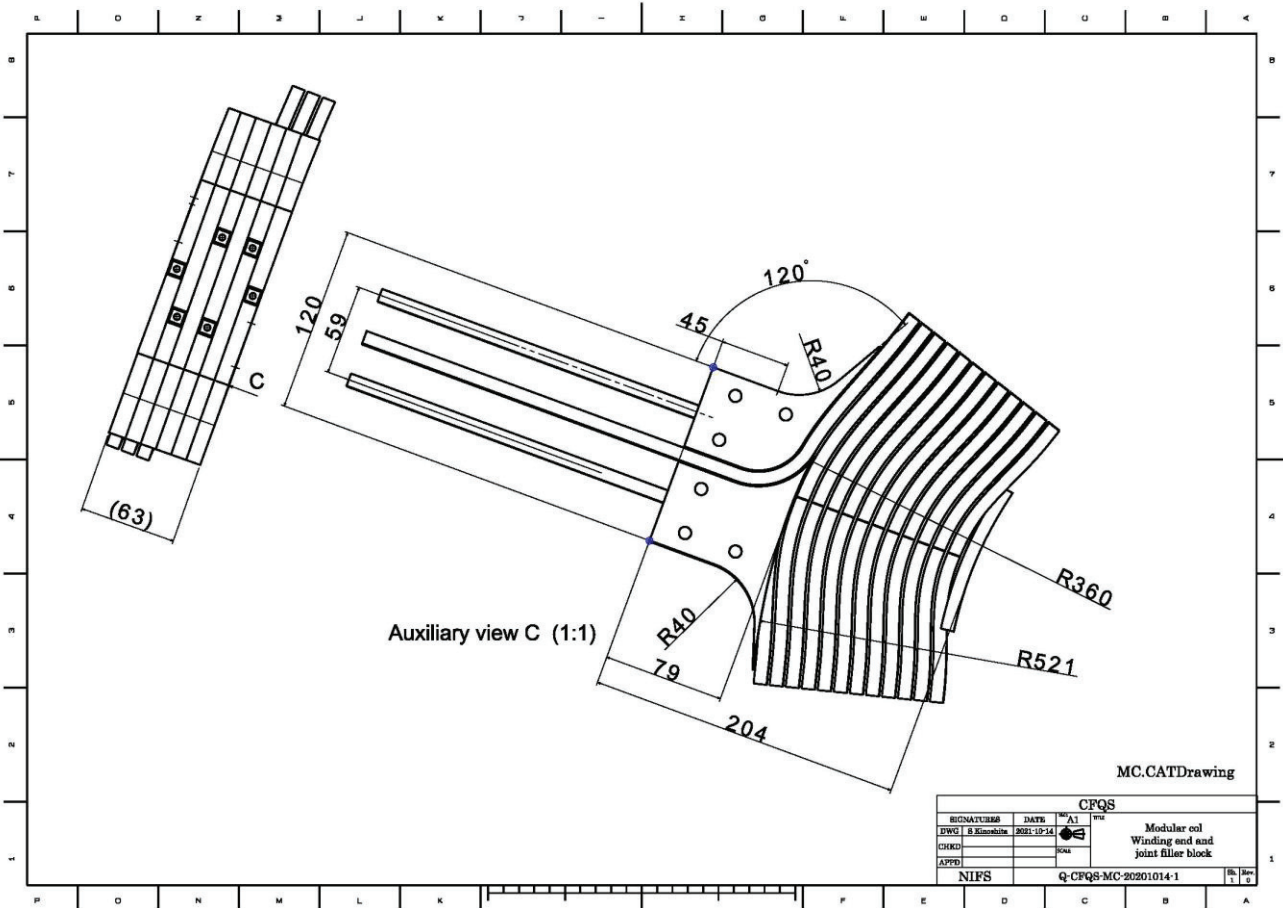
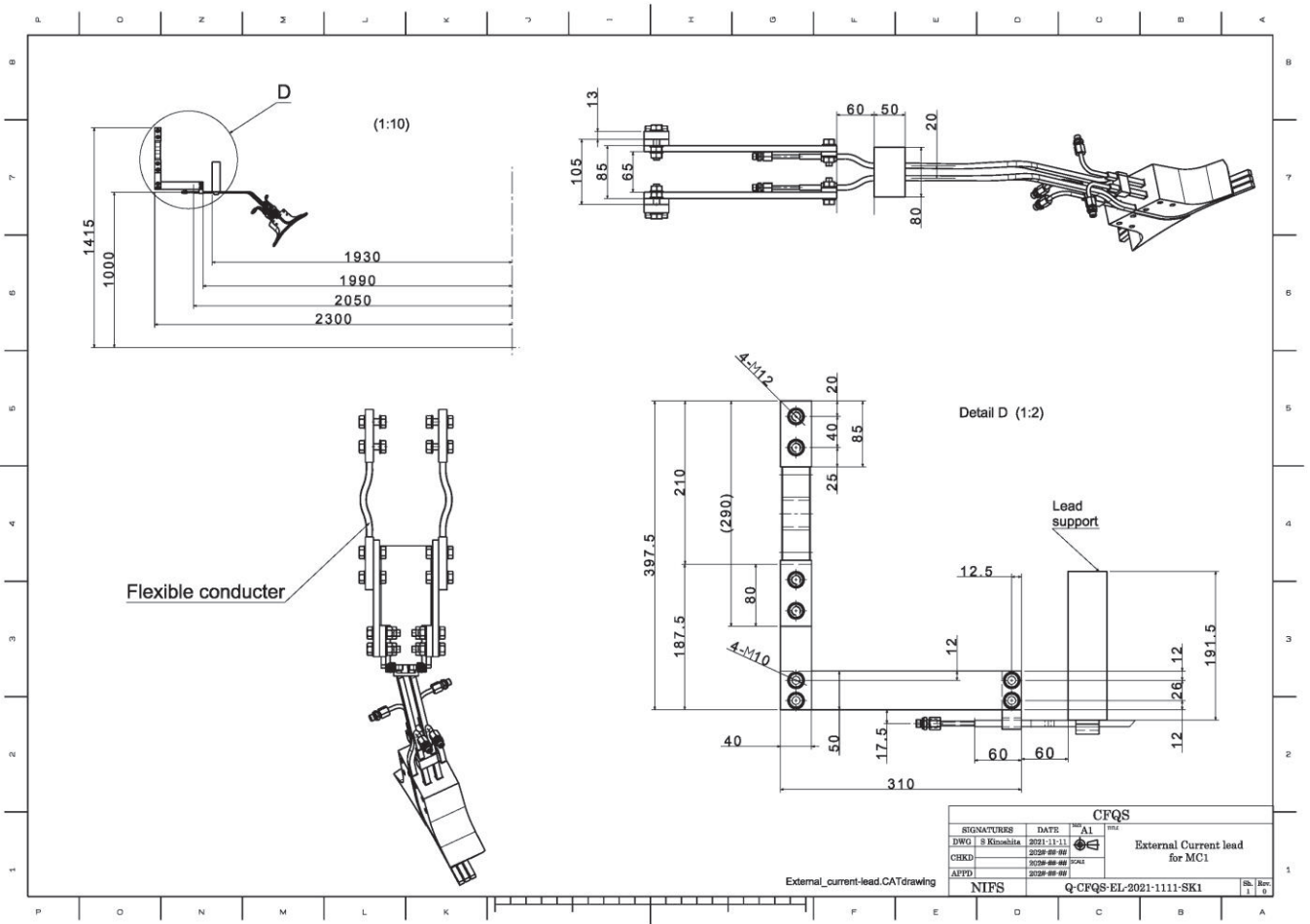














### 3 Toroidal field coil

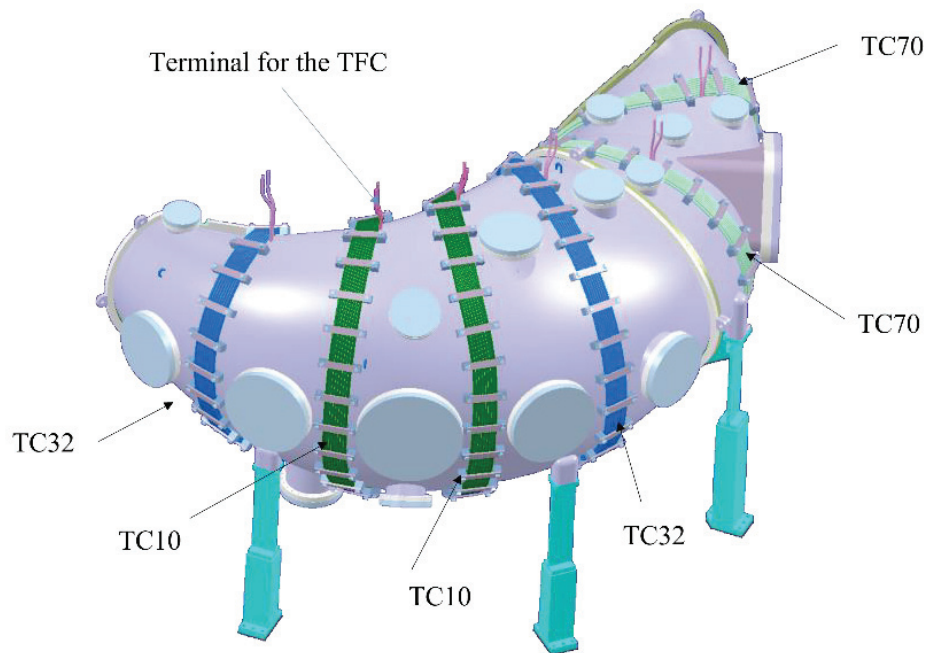
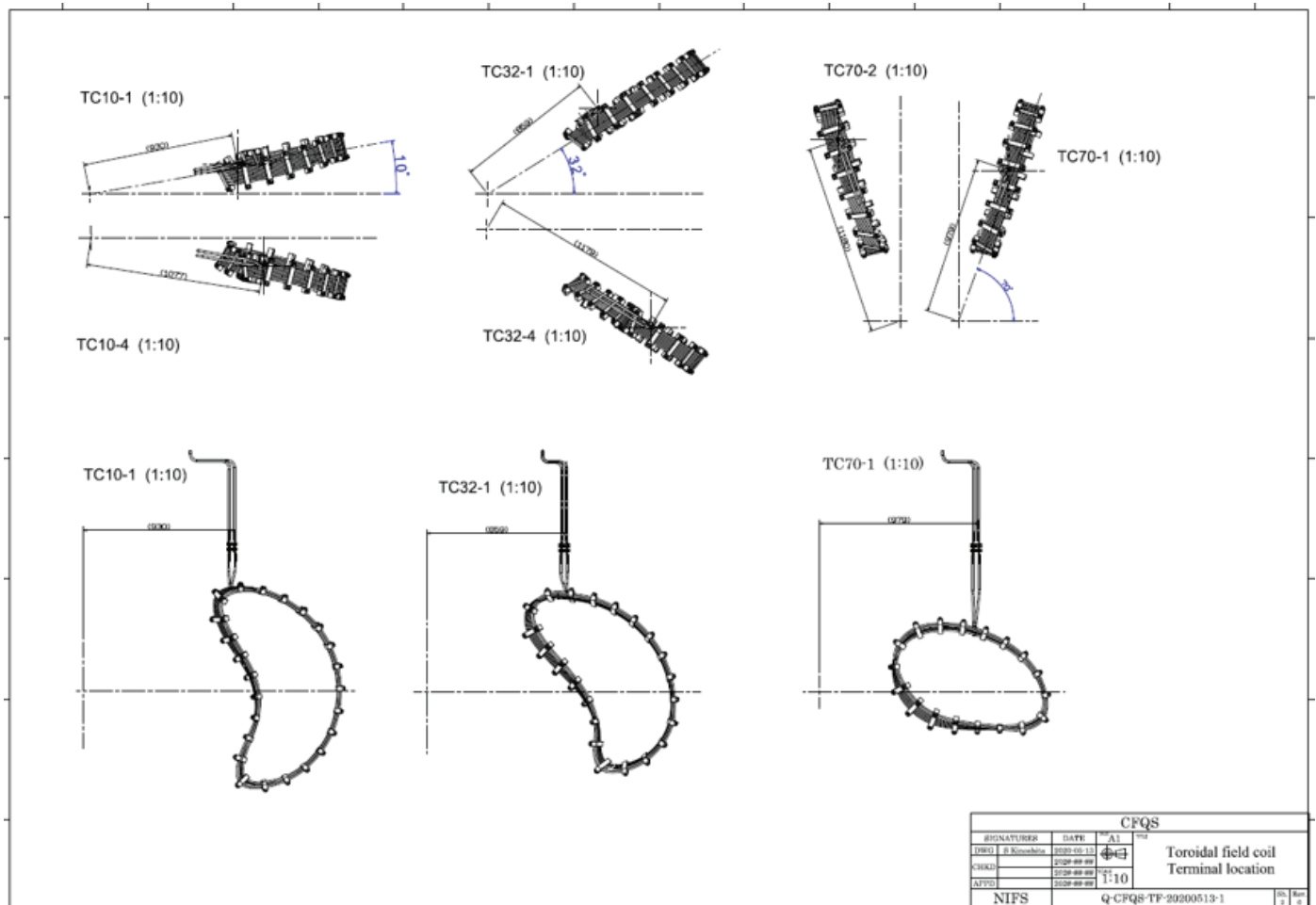
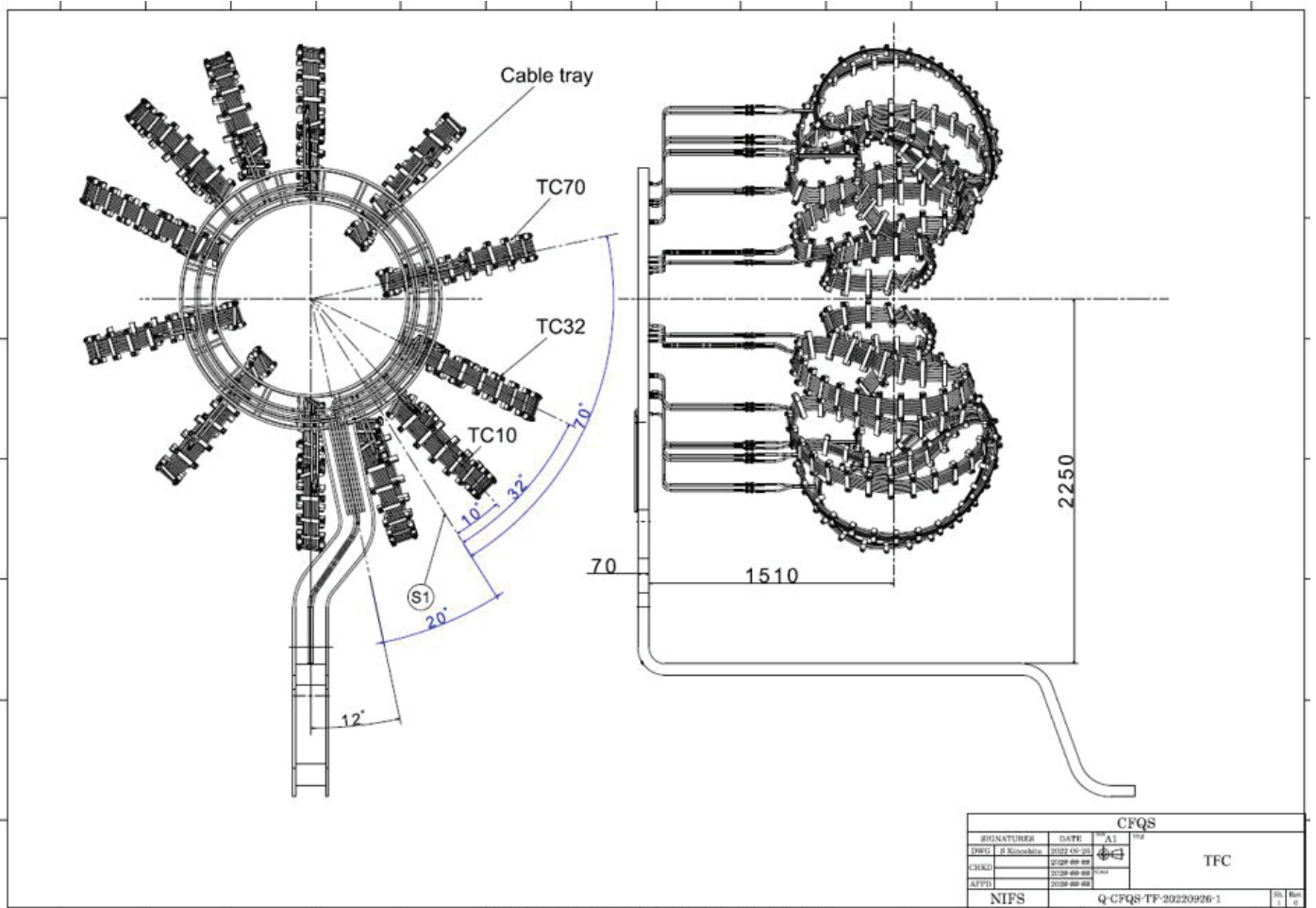


Fig 3-1 VV and TFC





#### 4 Poloidal field coil

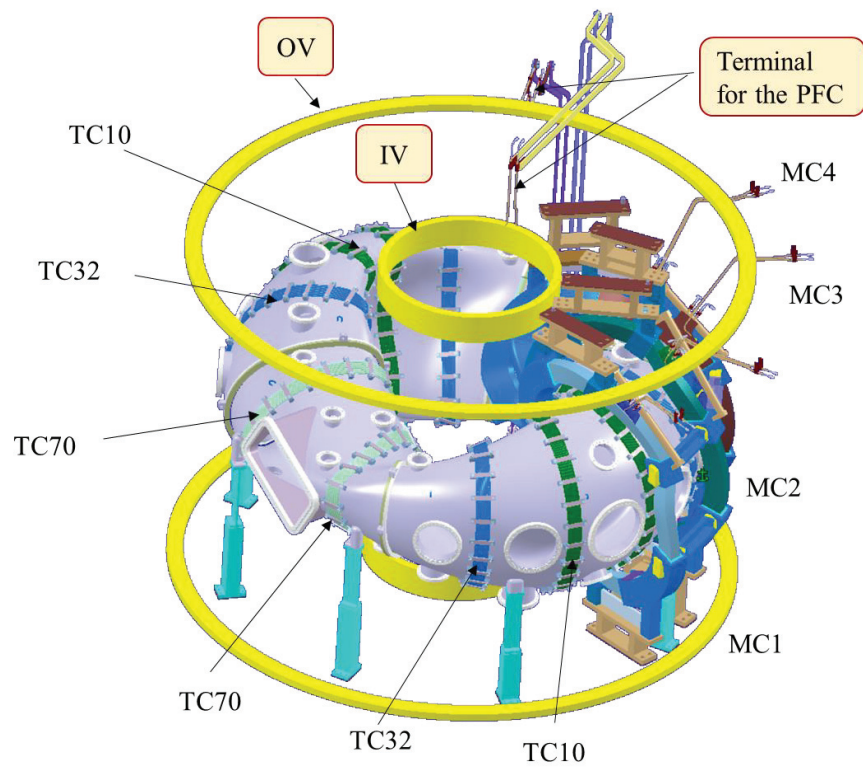
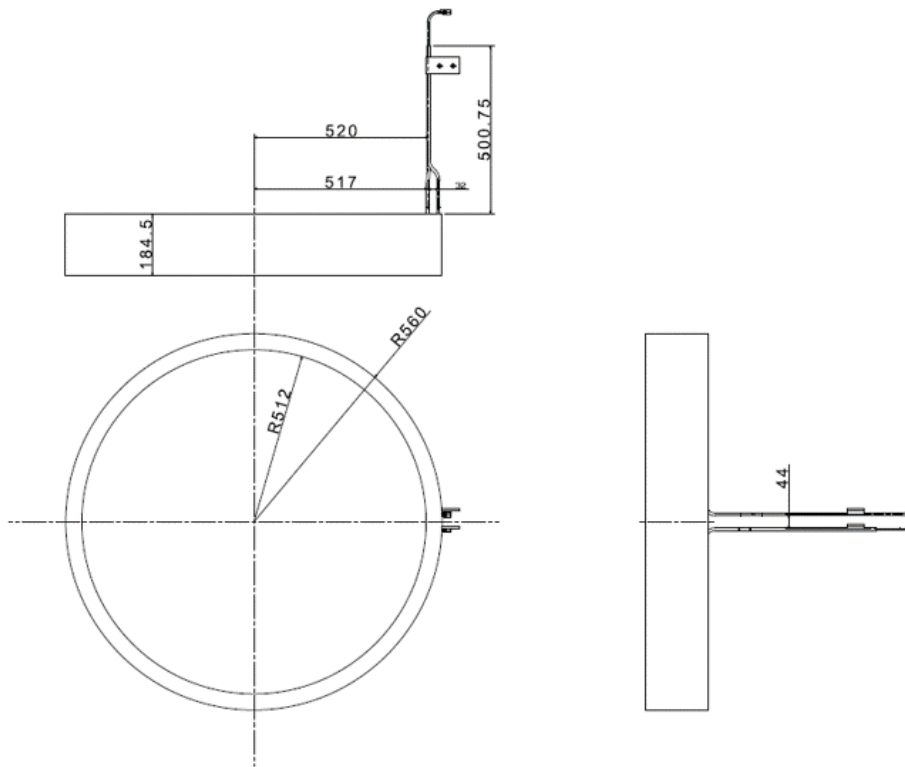
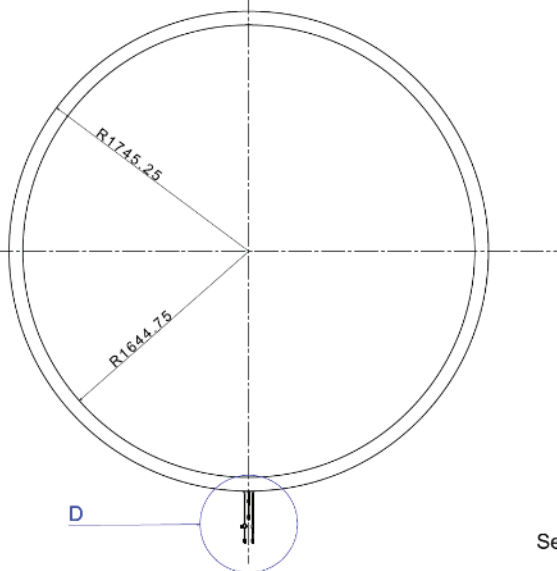


Fig 4-1 PFC

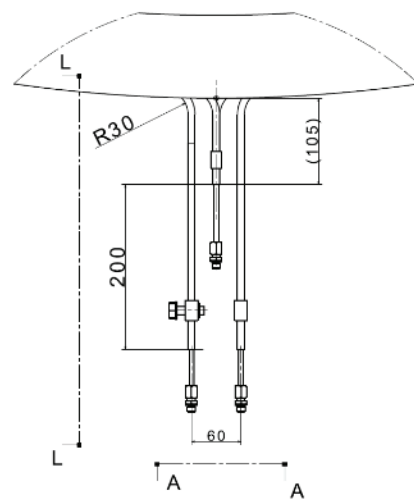
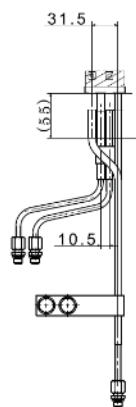
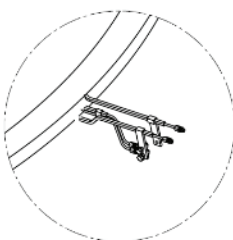


CFQS			
SIGNATURES	DATE	REV	APP
DESIGN: S. Kishimoto	2022-09-20	A1	+
CHECK:			
APPROV:			
NIFS	Q-CFQS-PF-20220926-3		Rev 1.0

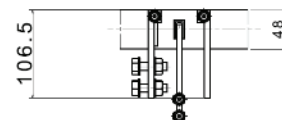


D

Section view L-L (1:2)

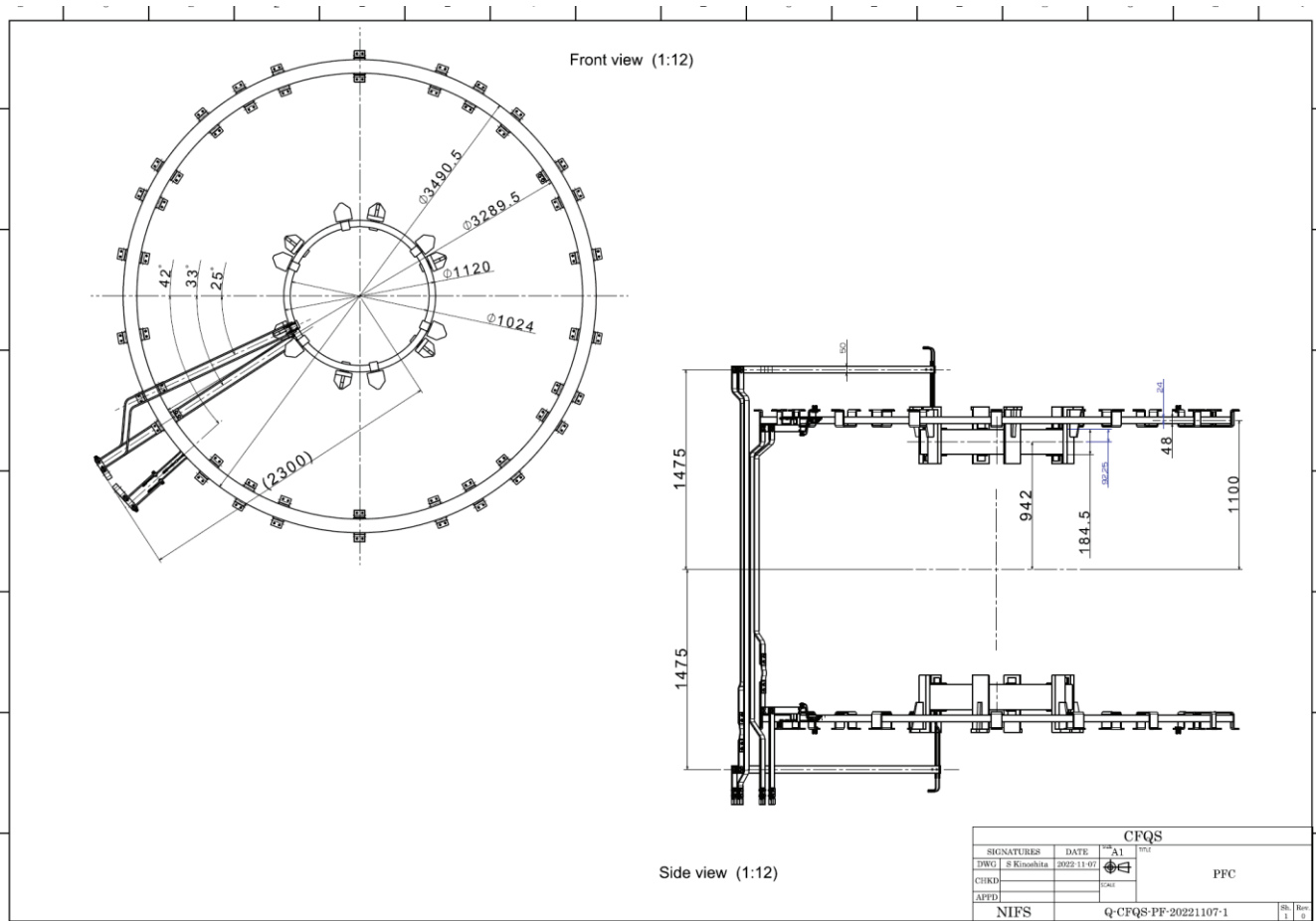


Detail D (1:2)



Section view A-A (1:2)

CFQS			
SIGNATURES	DATE	REV	APP
DESIGN: S. Kishimoto	2022-11-01	A1	+
CHECK:			
APPROV:			
NIFS	Q-CFQS-PF-20221107-2		Rev 1.0



## 5 External current lead

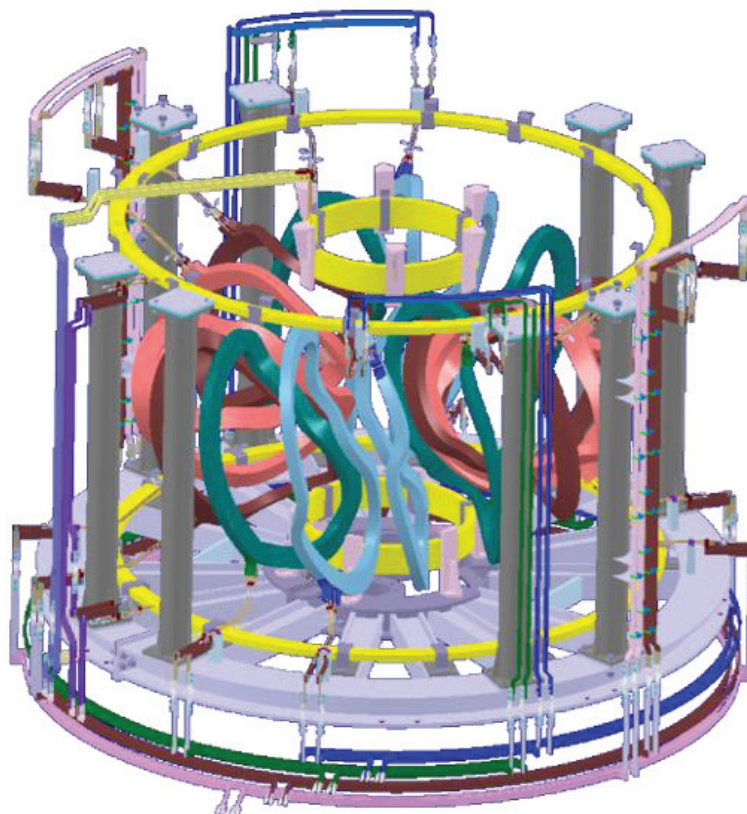
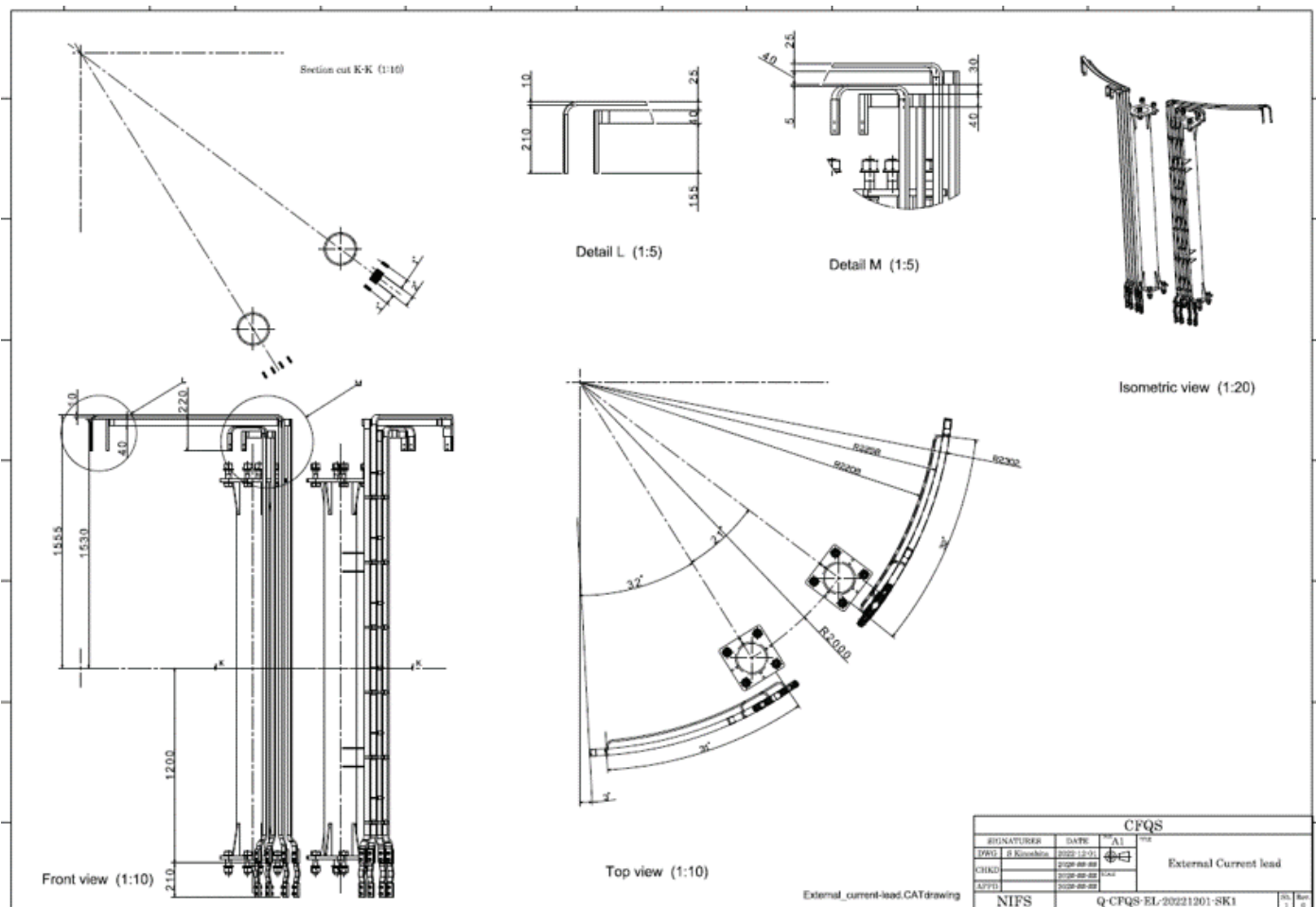
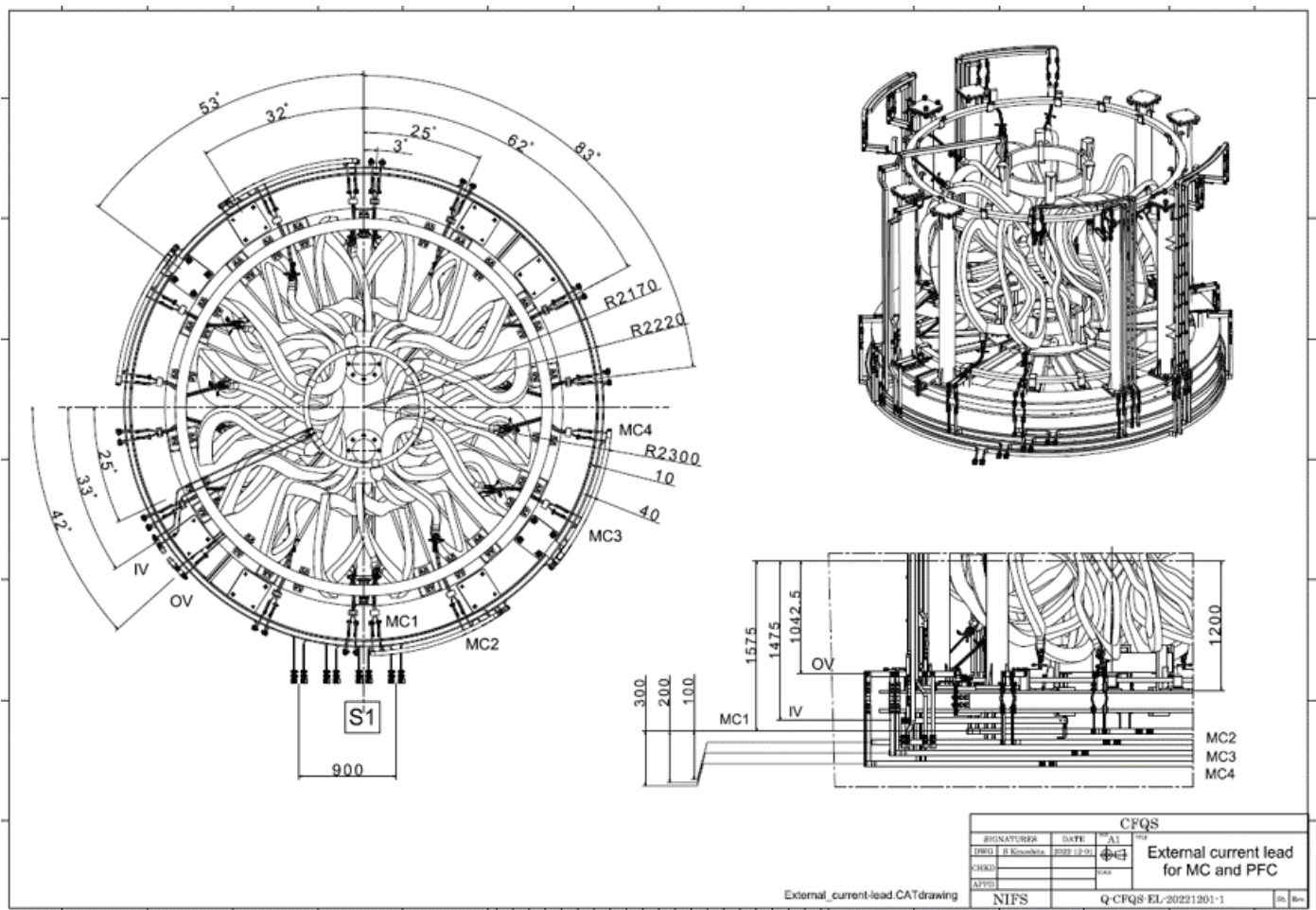


Fig 5-1 Current lead





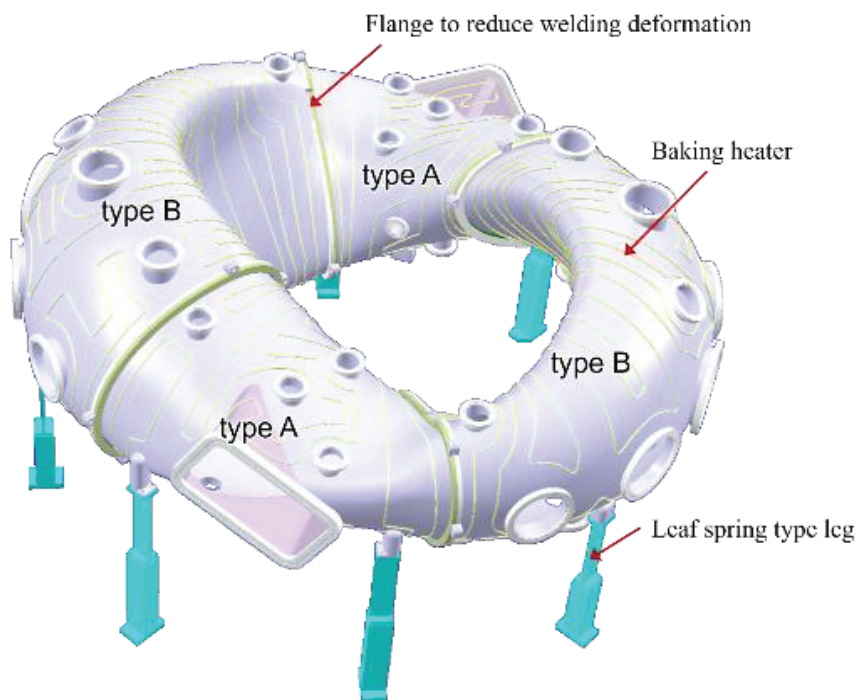
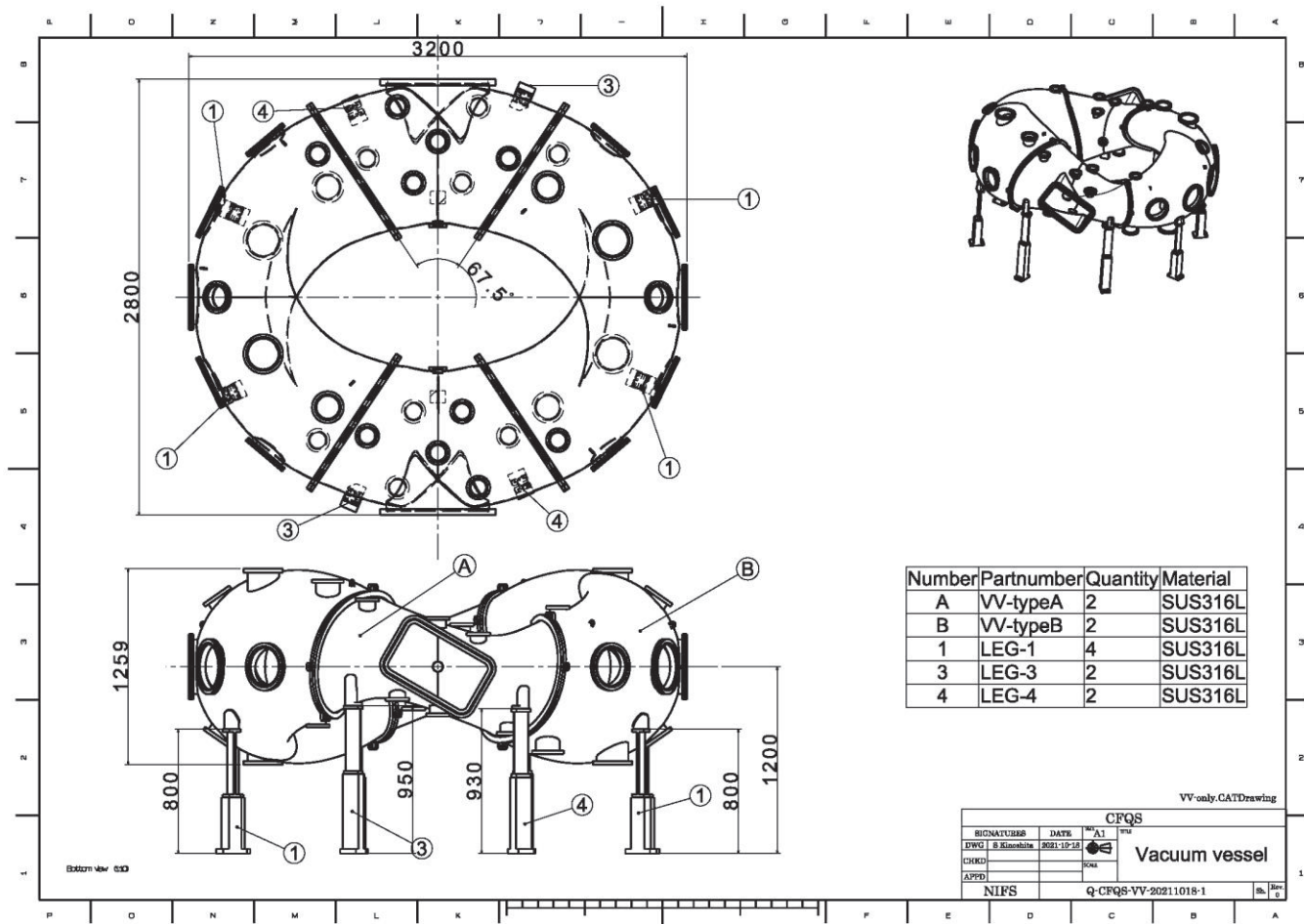
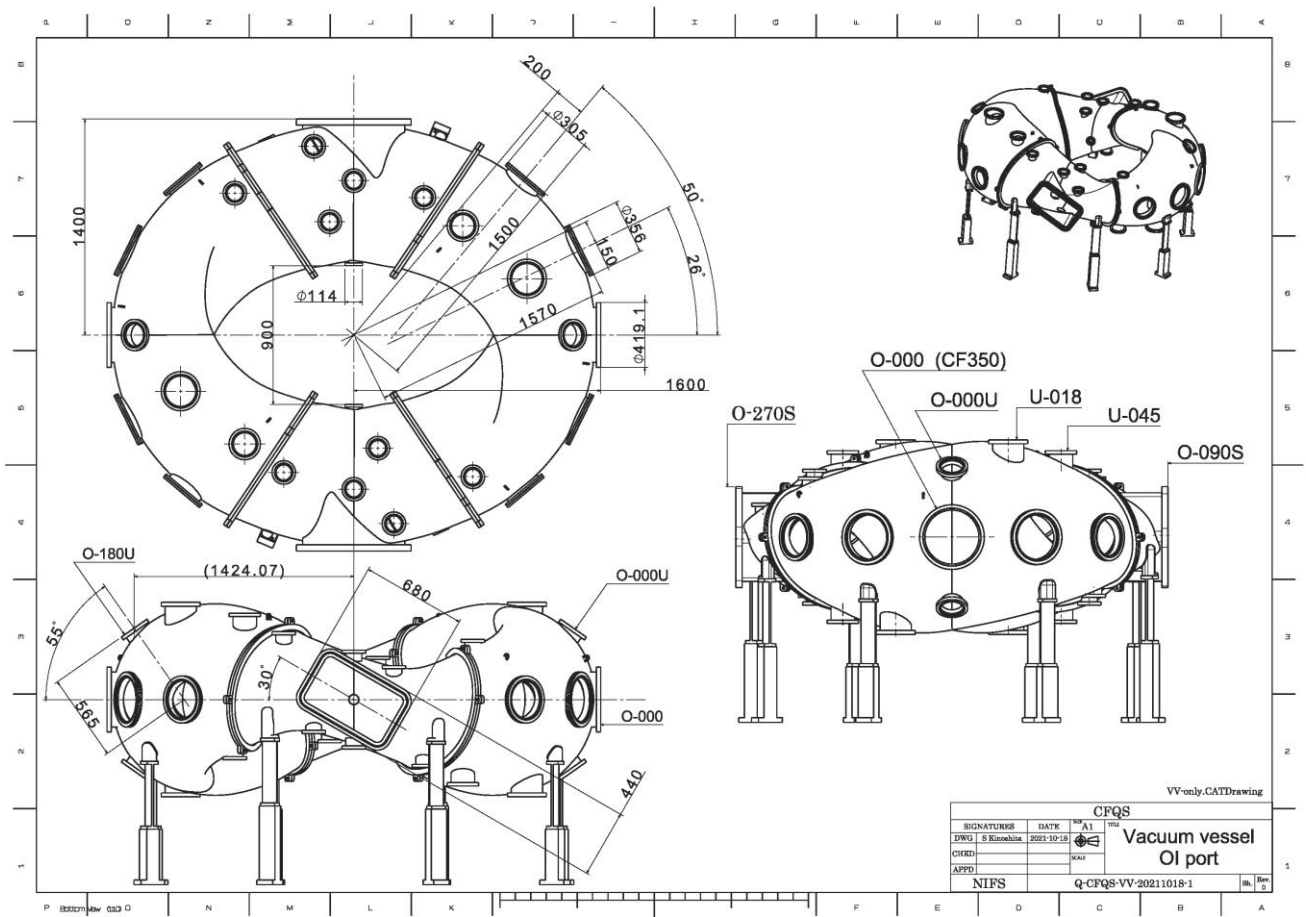
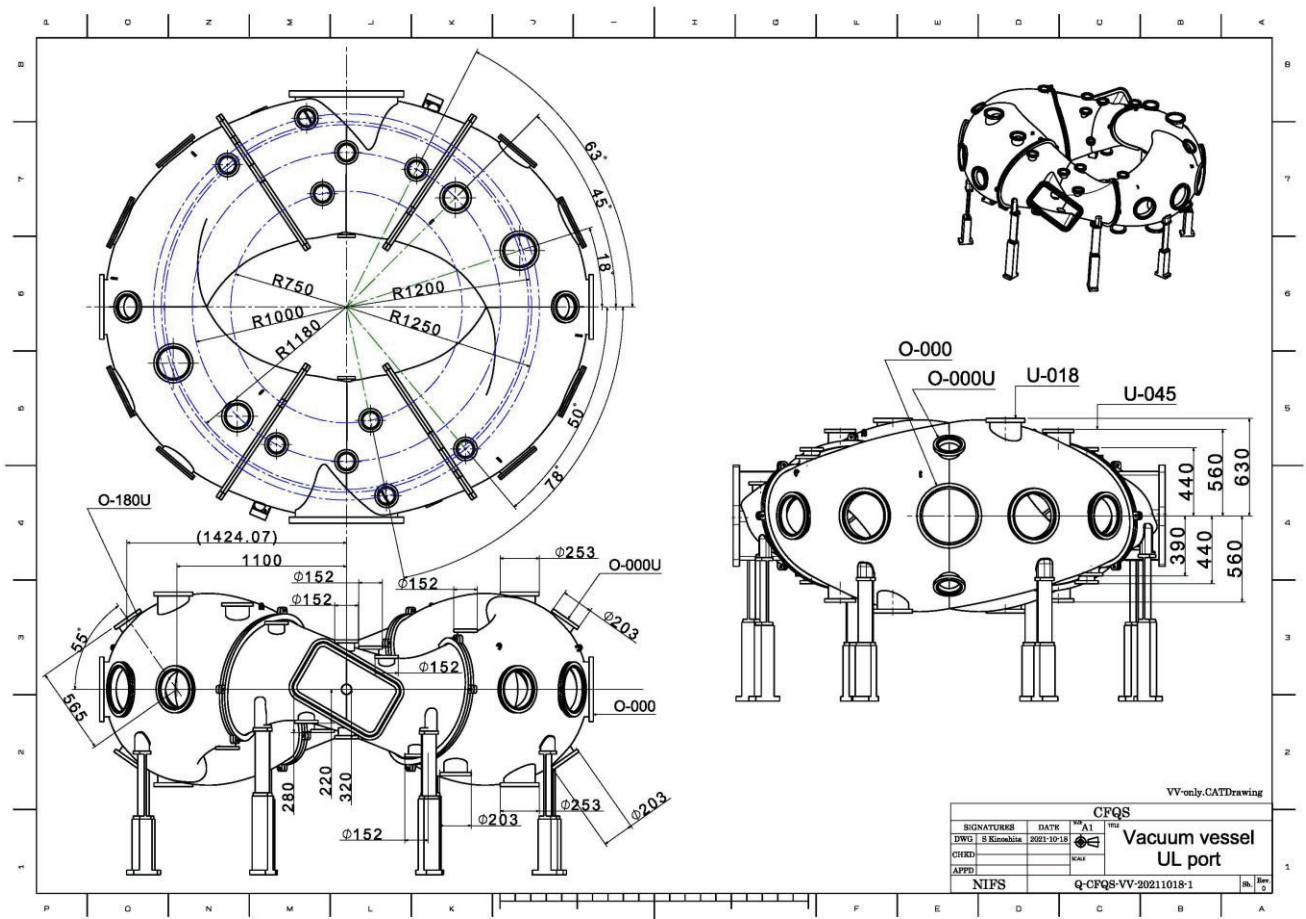
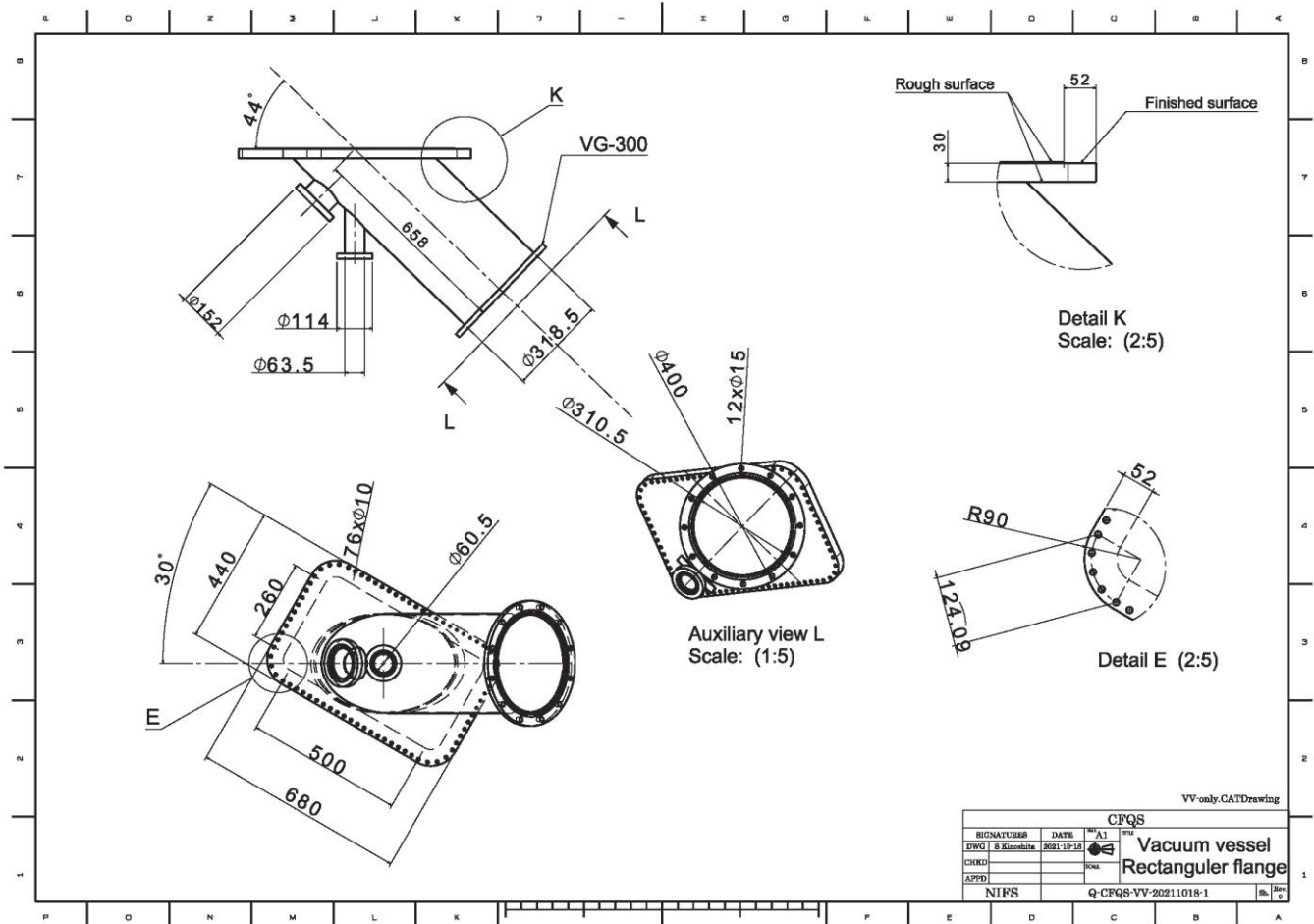
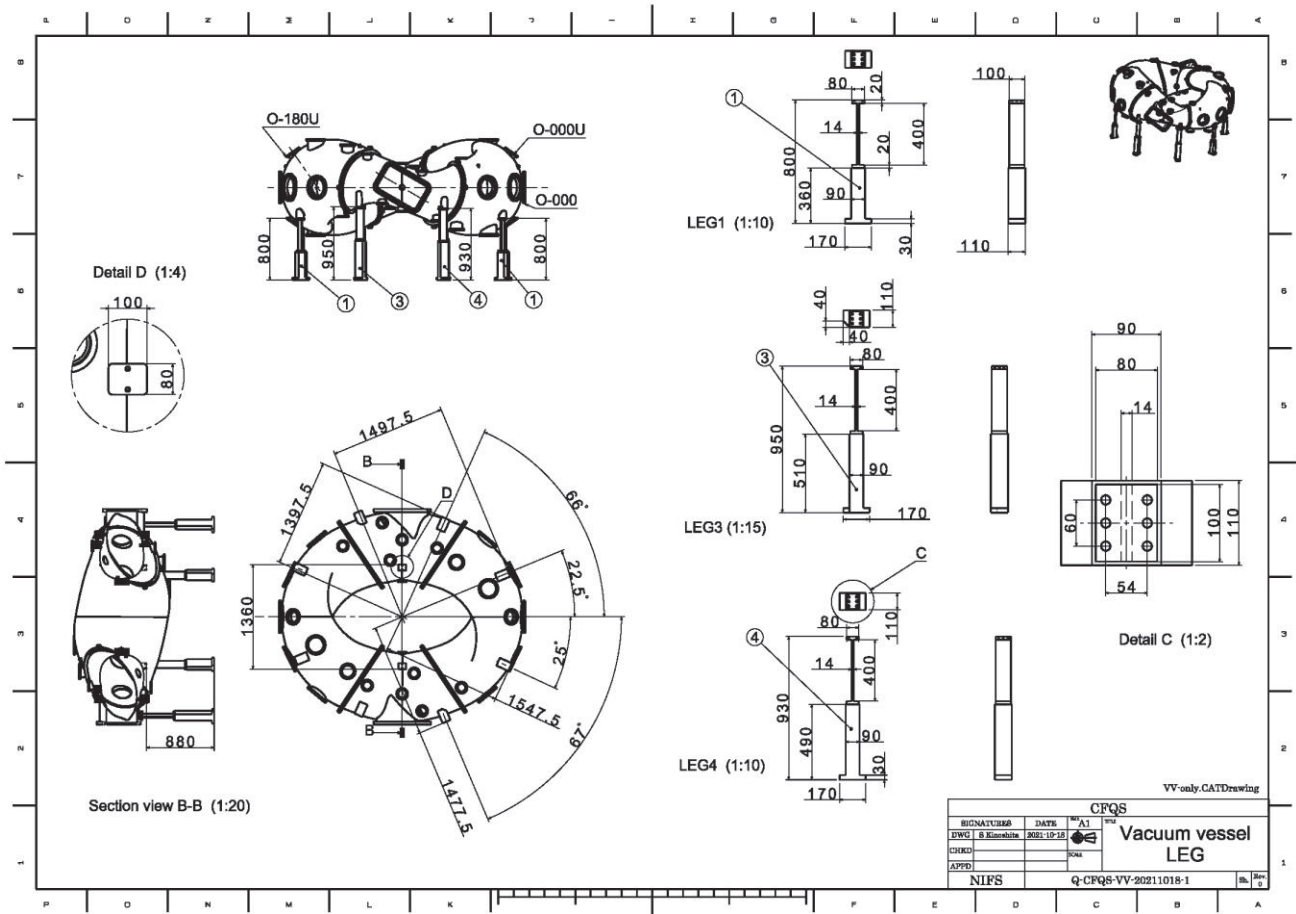


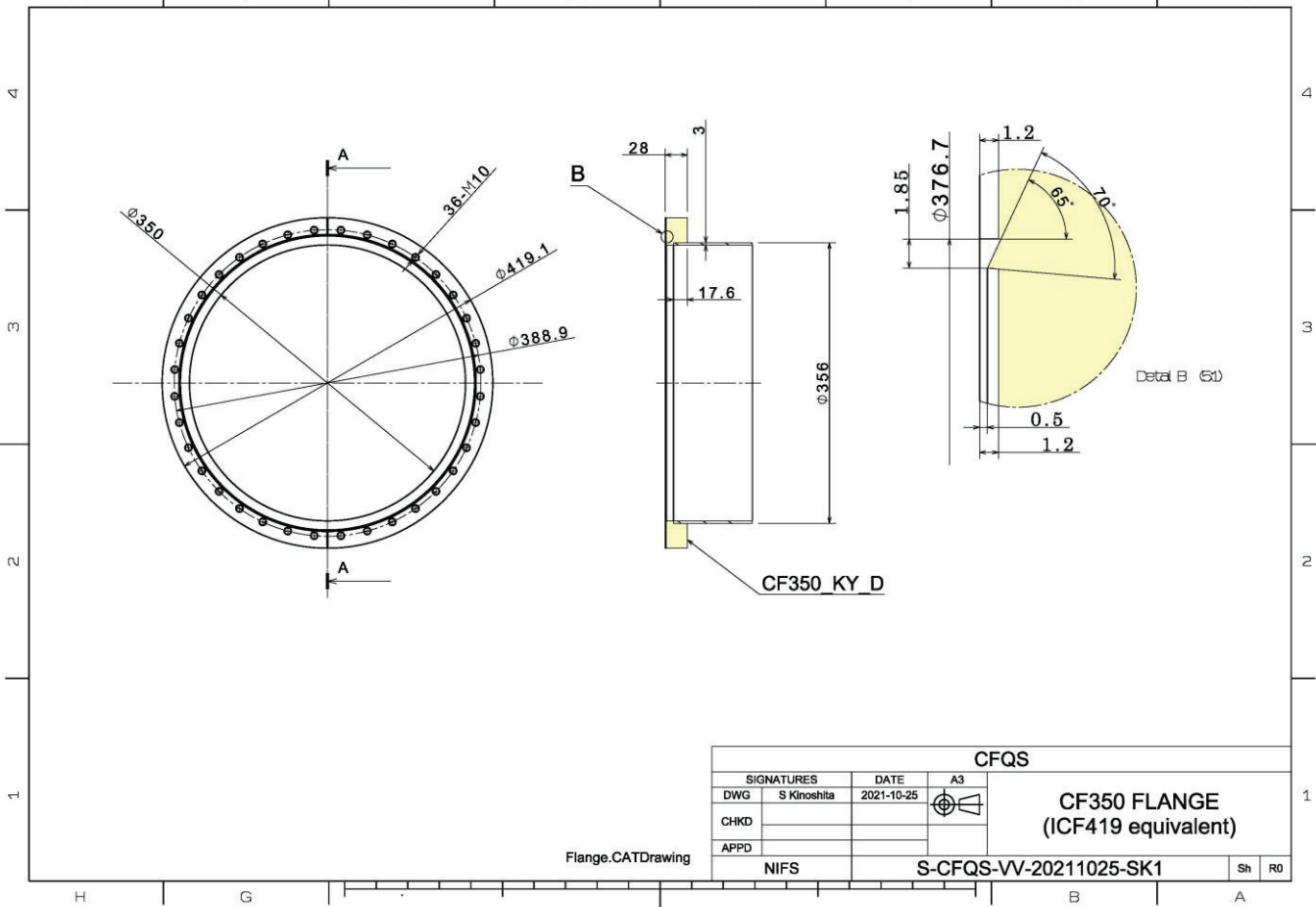
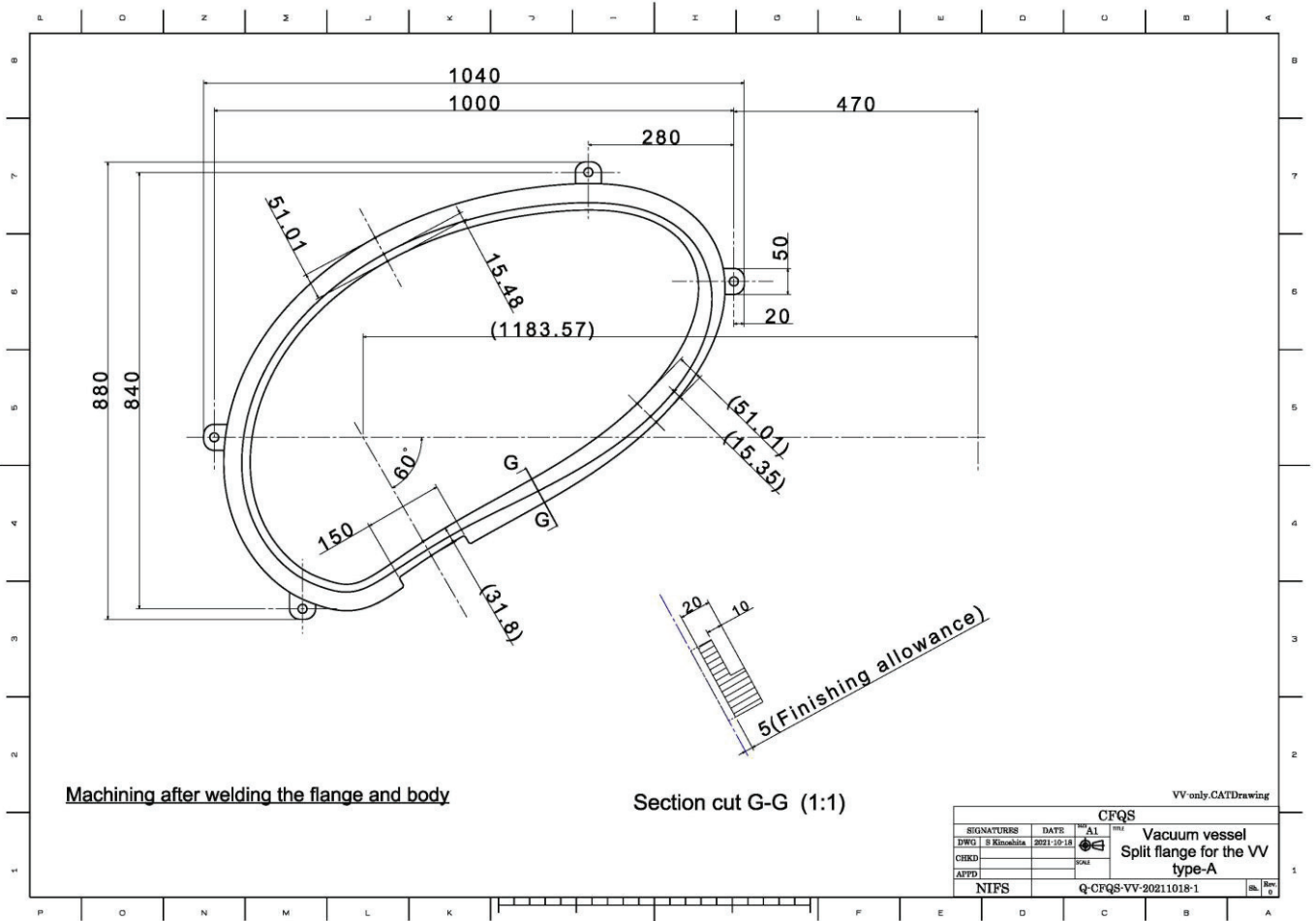
Fig 6-1 Vacuum vessel

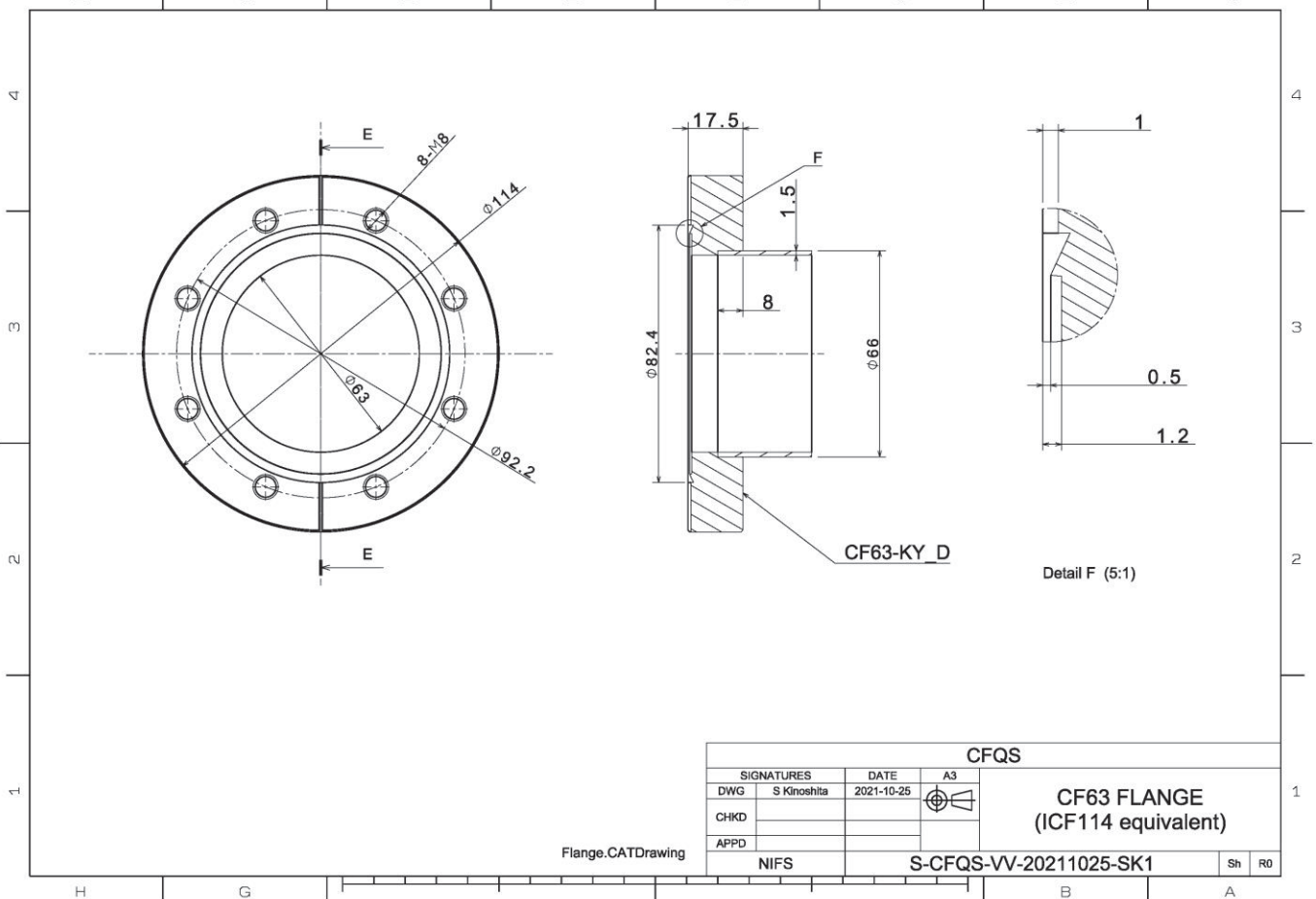
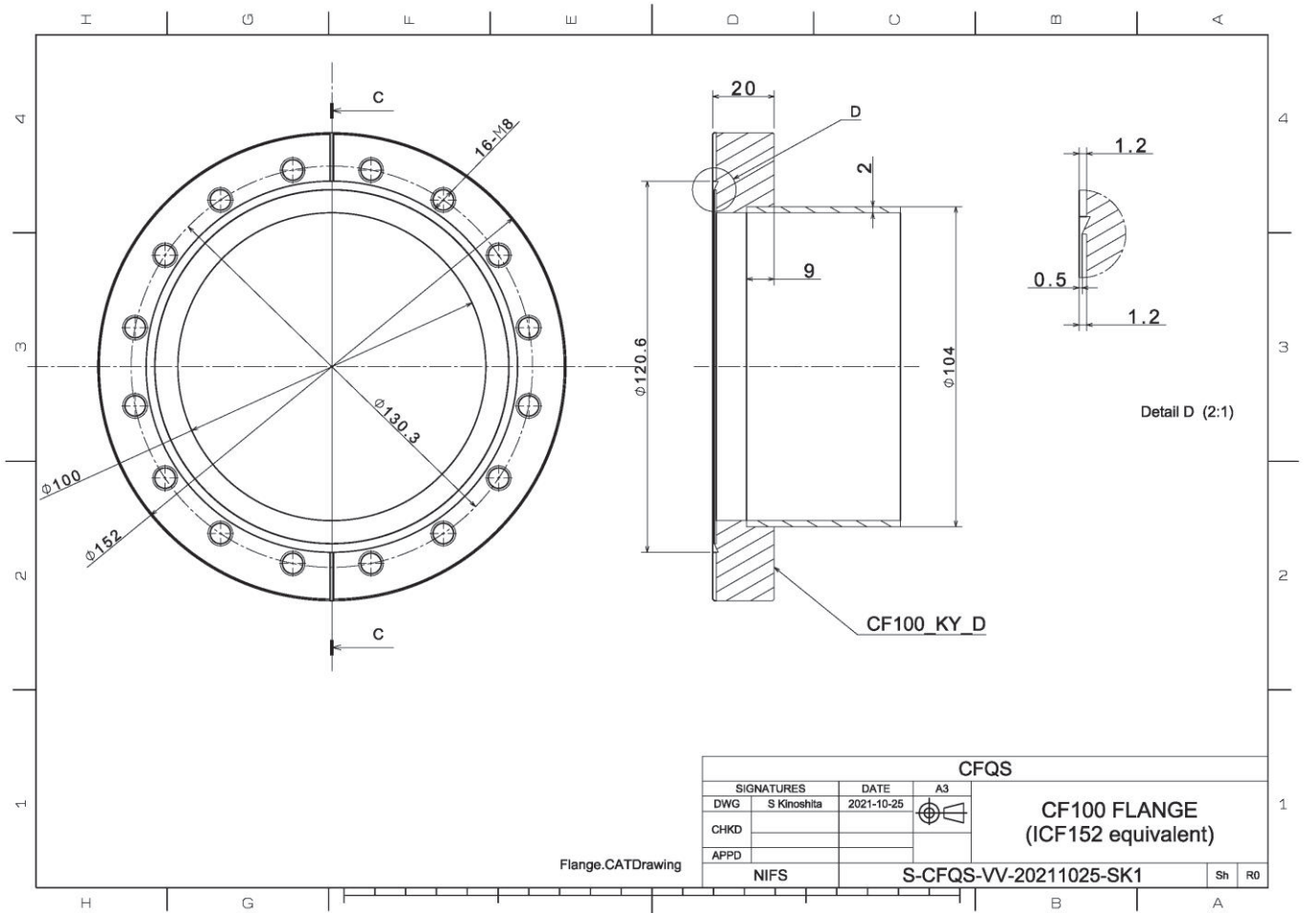














## 7 Cage type support structure

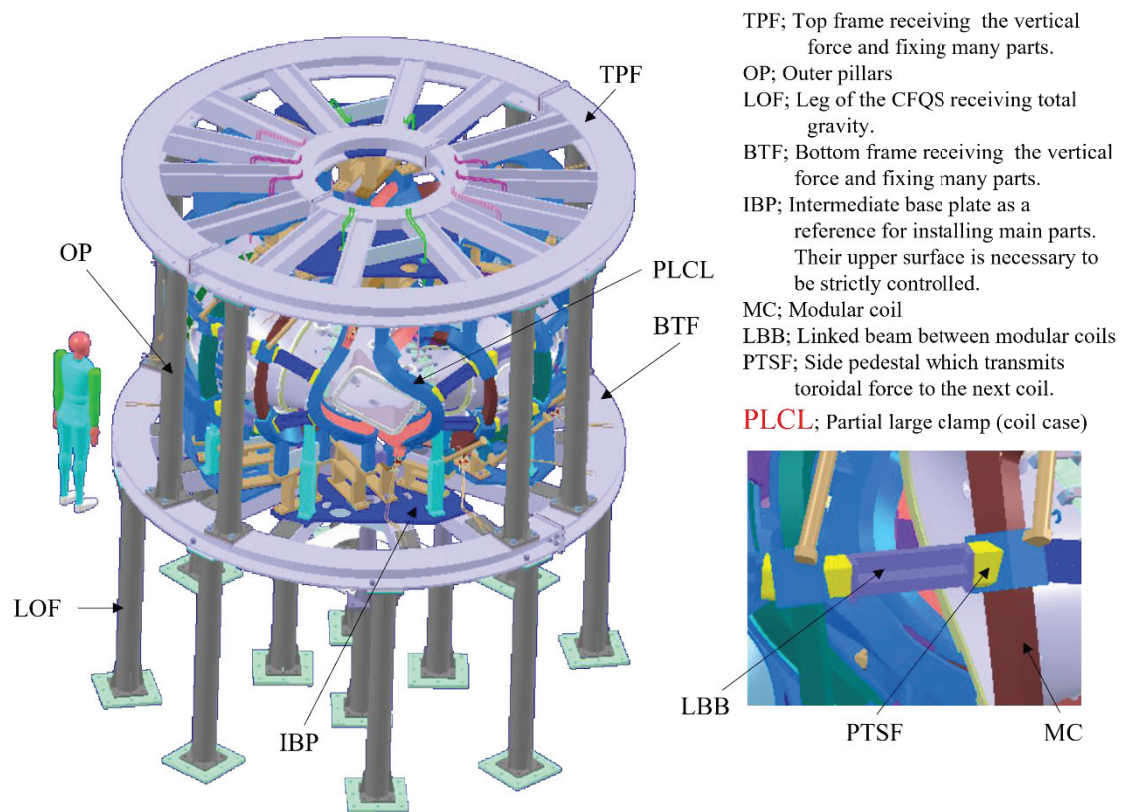
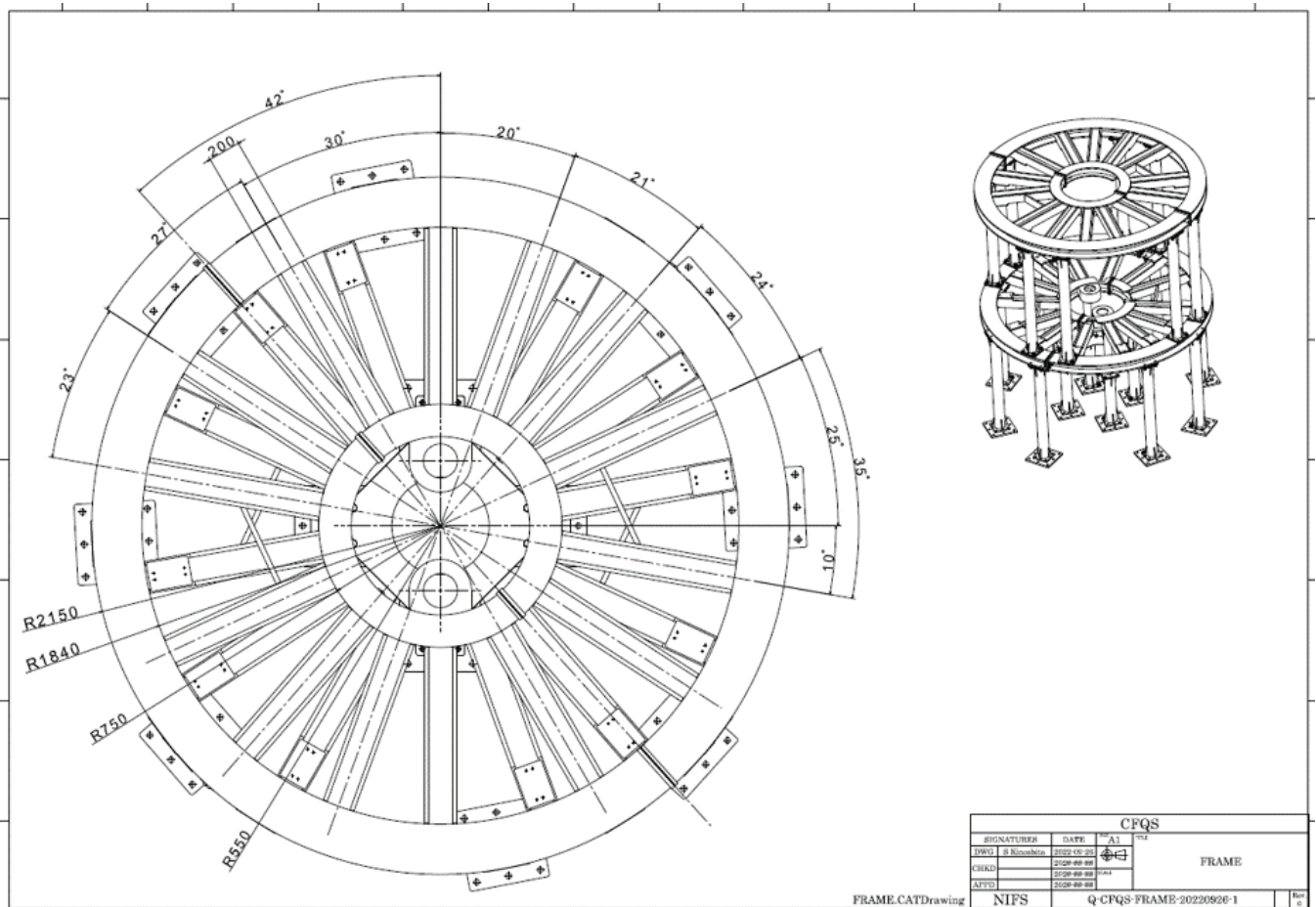
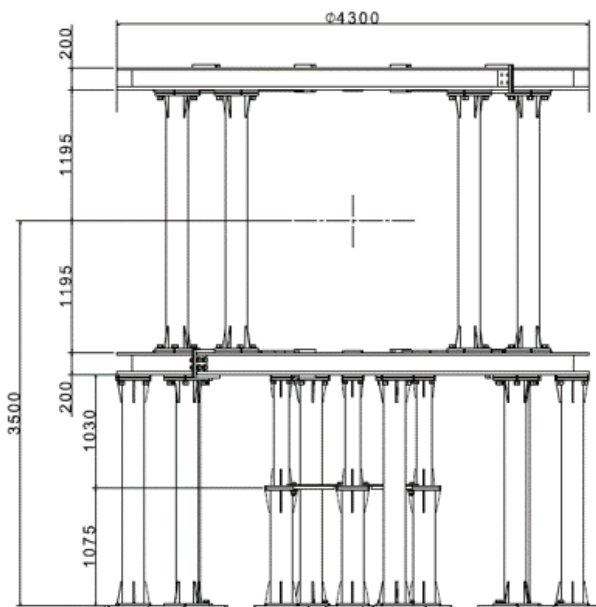


Fig 7-1 Support structure

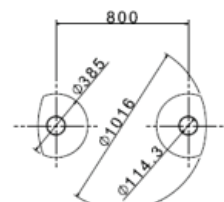
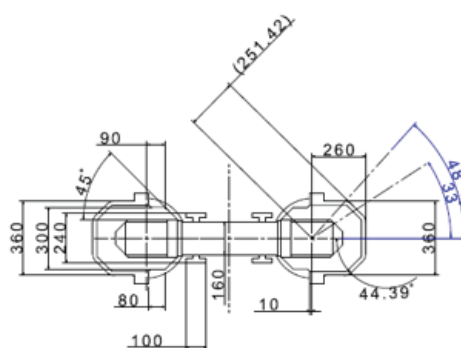




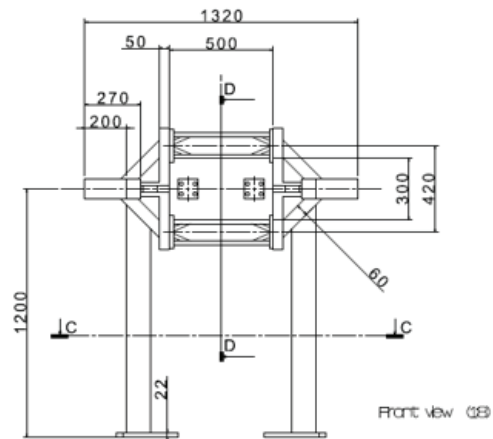
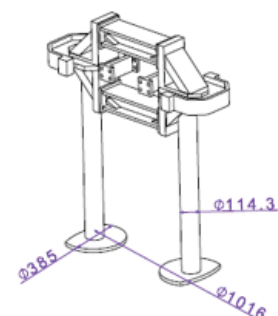
Front view (1:15)

CFQS			
SIGNATURE	DATE	A1	Rev
DESIGNER	2022-08-11		
CHECKED	2022-08-09		
APPROVED	2022-08-09		
NIFS	Q-CFQS-FRAME-20220812-SK	Rev	2

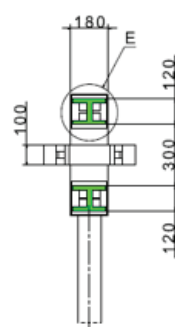
FRAME.CATDrawing



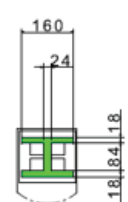
Section view C-C (1:10)



Front view (1:8)



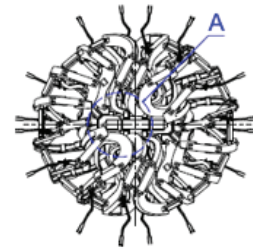
Section view D-D (1:8)



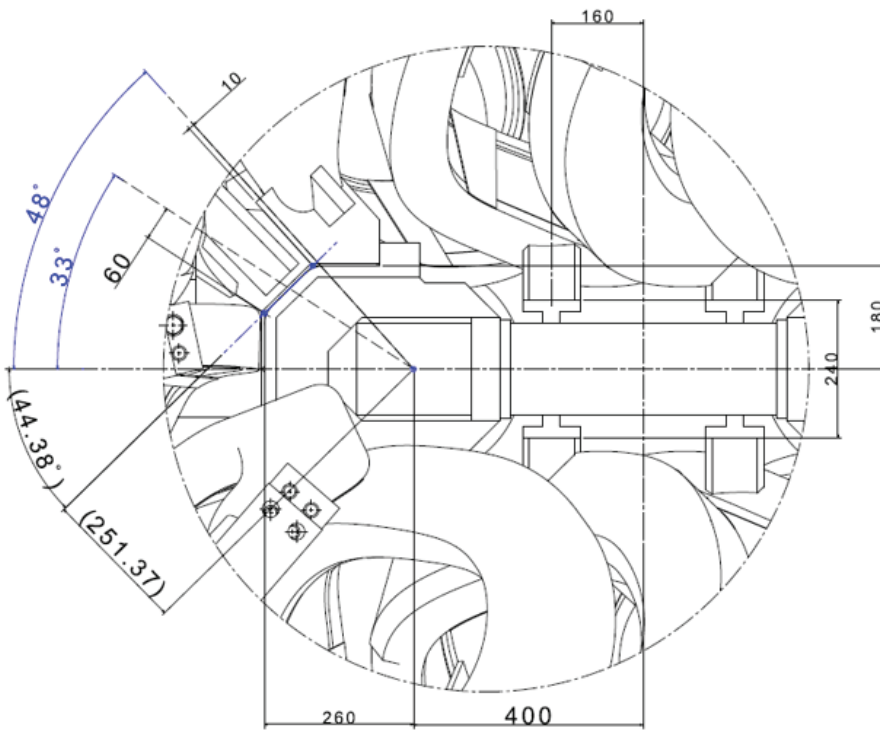
Detail E (1:5)

CFQS			
SIGNATURE	DATE	A1	Rev
DESIGNER	2021-10-20		
CHECKED			
APPROVED			
NIFS	Q-CFQS-SP-20211020-SK1	Rev	2





Top view (1:30)



Detail A (1:3)

MC.CATDrawing

CFQS			
SIGNATURE	DATE	REV	DATE
DWG. R. Kishore	10/22/2022	A1	10/22/2022
CHKD.			
APPR.			
NIFS	Q-CFQS-MC-20220926-5	Rev	

Modular col  
Center support

## 8 Cooling water pipe

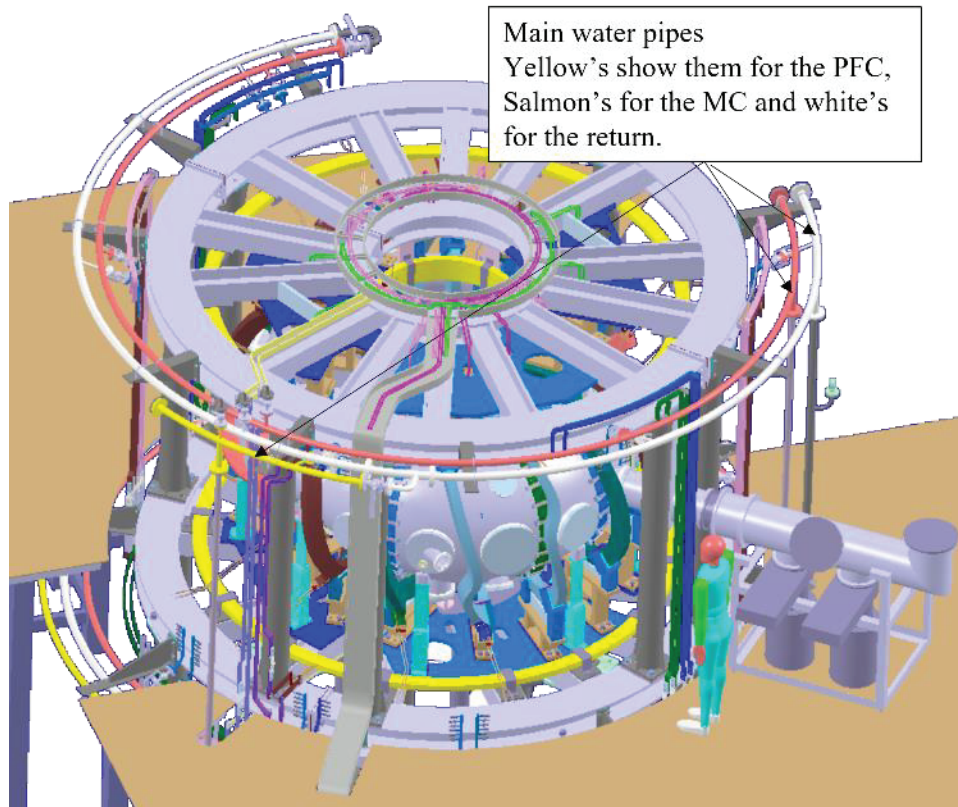
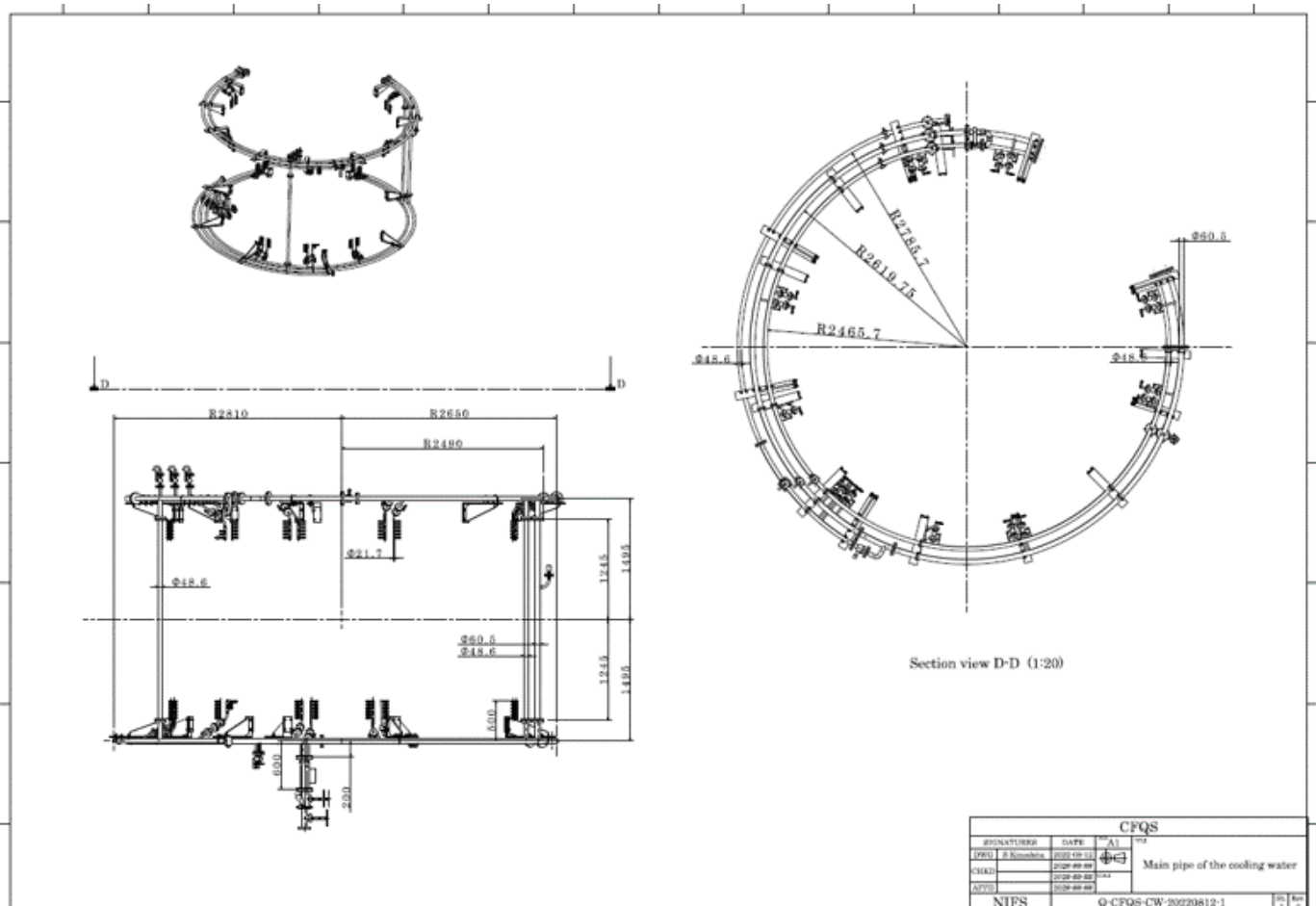


Fig 8-1 Cooling water pipe



NIFS-SWJTU JOINT PROJECT FOR CFQS  
~PHYSICS AND ENGINEERING DESIGN~  
VER. 5.1  
2023. AUG.

APPENDIX-A4 (ST)

~STANDARD INFORMATION~

CFQS Team



*NIFS; National Institute for Fusion Science*

*SWJTU; Institute of Fusion Science, School of Physical Science and Technology, Southwest Jiaotong University*

*Hefei Keye; Hefei Keye Electrical Physical Equipment Manufacturing Co., Ltd*

## Table of Contents

1	Design standard .....	3
1.1	ASME III criterion as a reference .....	3
1.2	Guideline of allowable limit value of stress for the CFQS .....	3
1.3	Consideration on coil accuracy .....	5
1.3.1	Overview .....	5
1.3.2	What should determine the required accuracy of the coil .....	5
1.3.3	Manufacturing accuracy of coil alone .....	6
1.3.4	Accuracy of coil installation .....	7
2	Standard material and accessories .....	8
2.1	Physical property of the metal .....	8
2.1.1	Austenite stainless steel (SUS) .....	8
2.1.2	Oxygen free copper (OFC) .....	8
2.2	Accessories .....	11
2.2.1	Gasket or O-ring for vacuum .....	11
2.2.2	Pipe and flange for the water cooling .....	13
2.2.1	Electrical cable and solderless terminal .....	14
2.2.2	Flexible terminal .....	16
3	Analytical expression .....	17
3.1	Calculation formula of adiabatic temperature rise .....	17
3.2	Calculation formula of a pressure drop and average temperature rise of cooling water .....	18
3.3	Calculation formula and design criteria of lead wires for supplying current to the coil .....	19
4	Power supply for the coil system .....	21
4.1	Power supply system used in the fusion devices .....	21
4.2	Features of the power supply system .....	23
4.2.1	Capacitor bank .....	23
4.2.2	DC motor and generator .....	24
4.2.3	Self-excited induction generator (SEIG) .....	24
4.2.4	Induction motor and synchronous generator .....	24
4.2.5	Variable speed synchronous generator for pumped storage power generation .....	24
5	Coil support structure for torus fusion devices .....	25
5.1	Support structure for the weak magnetic field devices .....	25
5.2	Support structure for the high magnetic field devices .....	26
5.2.1	Set up a central structure, and transmit the electro-magnetic force to it .....	26
5.2.2	Centripetal force support by a donut shape structure .....	27
5.2.3	Supporting centripetal force by the wedge effect .....	29

## 1 Design standard

### 1.1 ASME III criterion as a reference

ASME III defines the following criterion to get allowable limit value of stress. It may be evaluated by the following procedure because it is difficult to distinguish stress components by the FEM calculation.

- $P_m + P_L + P_b + Q < 3 S_m$ , absolute requirement everywhere,
- $P_m < S_m$ , should be satisfied in major area,
- $P_m + P_b < 1.5 S_m$ , local or thermal stress is permitted,
- $P_m + P_b > 1.5 S_m$ , may be permitted in extremely limited area,

Here,  $S_m$  is a design stress strength obtained by the material properties and  $P_m$ ,  $P_L$ ,  $P_b$ ,  $Q$  are stress components obtained by the stress analysis as a von Mises stress. Here technical terms are defined below.

- $S_m$  is a design stress strength that is a reference intensity allowed to load by setting is given as the efficient design. It is obtained from the equation  $S_m = \min (2/3 \sigma_y, 1/3 \sigma_u)$ , where  $\sigma_y$  is a proof stress or offset yield strength that is a stress changing from elastic deformation to permanent deformation.  $\sigma_u$  is a tensile strength that is a maximum tensile stress appearing in the material before breaking.
- $P_m$  is a primary general membrane stress that is an average value of stress in a cross section. Discontinuities and stress concentration are excluded.
- $P_L$  is a primary local membrane stress that is an average value of stress by discontinuities.
- $P_b$  is a primary bending stress that is a stress component proportional to the distance from the centroid in a cross section. Discontinuities and stress concentration are excluded.
- $Q$  is a secondary stress (bending and membrane stress) that is a self-equilibrium stress generated in discontinuity of structure.

### 1.2 Guideline of allowable limit value of stress for the CFQS

Although there is no publicly determined standard for fusion research, it is convenient to define something as guidelines. The stress component of the fusion device is complicated and its analysis not sufficient. So, it is not easy to step in detail on technical standards. We may only follow the basic idea, but we should think about the details flexibly. The fusion research often follows the ASME III. Even in the CFQS project, we will be better to follow the same guideline.

A design guideline in Table 1.2-1 may be used for the CFQS, that is a just guideline, not a necessary and sufficient condition. If it cannot be satisfied, it may be sometimes used on condition that the integrity is confirmed in the periodic inspections.

Table 1.2-1 Design guideline of typical materials for the CFQS.

Material			SUS316	C1020-O (Conductor)	Resin	Composite (Coil)	FRP
Young's Modulus	(GPa)	$E$	198	100	1~3	110	100
Design stress	(MPa)	$S_m$	137	50	-	60	50
Design strain		$\varepsilon$				<0.05%	
Tensile strength	(MPa)	$\sigma_u$	520	230	10~100	-	2000
Yield strength	(MPa)	$\sigma_y$	205	80	-	-	500
Elongation	(%)		40	50	1~2	-	5
Poisson's ratio		$\nu$	0.3	0.34	-	0.3	0.3
Density	(kg/m <sup>3</sup> )	$\rho$	7800	8960	1100	8000	1500
Thermal expansion		$\alpha$	$1.73 \times 10^{-5}$	$1.65 \times 10^{-5}$	$5 \times 10^{-5}$	$1.65 \times 10^{-5}$	$2.0 \times 10^{-5}$
Comments			300k	OFC	after curing	OFC + isolator	Varies

$S_m = \min (2/3 \sigma_y, 1/3 \sigma_u)$ ; ASME III criterion is changed according to operating temperature.

If possible, it is desirable that strain ratio  $\varepsilon$  is less than 0.05 % (110 GPa/60 MPa) for the composite.

Material properties of the coil (that is on copper and insulation composite) differ from structural material. The ASME III should not be strictly applied for them. The strength of the coil is affected by the working method and the heat treatment conditions in addition to the selection of the material. As these data are not released to the public, they need to be acquired by developers themselves through element prototyping and inspection. It is difficult to decide the guidelines when it is not done,

Because it is inconvenient if we have no guidelines, we will temporarily extend the ASME III to the coil, but we also decided to consider its own properties.

- The conductor is very flexible and cannot be cut in a short time even if it exceeds the yield strength.
- The insulation (especially cured resin close to glass) is easy to crack and should be restricted by strain.
- It is more reliable to minimize the deformation of the coil within the measurable range.
- The target of the deformation is 1 mm or less.



## **1.3 Consideration on coil accuracy**

### **1.3.1 Overview**

There is currently a discussion about coil accuracy, so we would like to summarize our thoughts related to it. It is actually exceedingly difficult to determine the required accuracy from the physical point of view of plasma confinement. In reality, the required accuracy has been determined from the engineering point of view of whether or not the device is assembled.

Usually, this provides a guideline for judging whether it is good or bad at each stage of the production process and may be chosen to be smaller than necessary, as a failsafe measure. The value itself has no special meaning. It is not a redundant as soon as a result that exceeds this accuracy is obtained as a new guideline. It will provide us with an opportunity to recheck the data and take some measures before it really becomes worthless.

The purpose of measuring the dimensions is to confirm that there are no design mistakes or errors during manufacturing, as a method of production control. As a result, the effect of improving the accuracy of the coil cannot be expected. Especially high accuracy is not required during the production process. The simplicity of measurement and the certainty that the same result can be obtained by anyone are prioritized over accuracy. When we want to know the actual dimensions for experiments, etc., accurate measurements are often performed after completion.

### **1.3.2 What should determine the required accuracy of the coil**

It should be determined from the physical point of view of plasma confinement, but it is actually exceedingly difficult to determine, and there is no example to identify by studying it. In principle, confinement is expected to worsen if the magnetic field distribution is different from the optimum state. However, it is not known which state is optimal nor how much the difference affects confinement. Therefore, it is not realistic to define the required accuracy of the coil from the viewpoint of plasma confinement.

The relationship between magnetic field ripple in the tokamak and particle confinement has been investigated. It was a problem related to ultra-high speed particles such as alphas, and it does not matter for plasmas of several hundred eV. In particular, since large helical ripples exist in helical systems such as the CFQS and the LHD, it is difficult to consider the effects of small magnetic field fluctuations that are related to coil accuracy.

Although the relationship with plasma confinement is not clear, the only phenomenon that may be inferred from the deterioration of confinement may be related to the question of whether magnetic islands are generated. However, even if there is no coil error, a magnetic island can be created depending on the conditions, so it is not possible to determine whether or not there is an effect from the coil error, based on the presence or absence of the magnetic island.

The Heliotron-E of Kyoto University and the LHD of NIFS had an equilibrium with easily created magnetic islands because there was a magnetic surface with a rotational transform of one. The coil accuracy had become an important issue in such devices. Unless the control coil positively creates an equilibrium with a rational surface, it is believed that the effect of coil accuracy may be small in the CFQS which has no dangerous magnetic surfaces.

The CFQS should experimentally study the effects of MHD instability and neoclassical diffusion. It is thought that detailed research on the effect of the error magnetic field on the confinement time will be possible for the next-generation large-scale equipment with a higher density and temperature.

There are two types of coil accuracy, so we should understand the difference between them.

### **1.3.3 Manufacturing accuracy of coil alone**

It is important to keep in mind that the accuracy of a coil varies, depending on how it is made. It should also be noted that the only way to improve the accuracy of the coil is to change the manufacturing method, and there is no other way.

The coil is produced by winding a conductor and then hardening it with resin. In the process, it is heated from 100 °C to 200 °C, so the conductor expands, and it becomes longer. The amount is about 0.1 %, but since the conductor is exceedingly long, it is quite normal for it to change by several tens of millimeters. Also, when it is cooled, the dimensions try to return to their original size, but the amount of change varies depending on the surrounding conditions and temperature. At the same time, a bending of the conductor occurs, so it is considered that there is no reproducibility in the dimensional fluctuation, due to the temperature change. There is also the meaning of reducing those effects, and in many cases, a metal winding frame is made, and a conductor is wound on it. In that case, since the shape and dimension of the coil are determined by the shape of the winding frame, the dimensional accuracy of the coil is improved. However, it is difficult to achieve accuracy (1/100 mm to 1/10 mm) of machining because there are fluctuations when passing through the heating and cooling process, and when removing the winding frame.

Especially when the required accuracy is fine, it is necessary to reduce the temperature change and integrate the winding frame and the coil conductor. In that case, it should be considered that the manufacturing cost may increase, and the insulation performance may decrease in some cases. Furthermore, since there is a disadvantage that the general VPI method cannot be used, it is necessary to develop insulation technology dedicated to the device.

The Heliotron-J of Kyoto University, and the CHS or the LHD of NIFS used coil cases or vacuum vessels as winding frames. Since this method does not remove the coil from the winding frame, the coil can be completed with an accuracy close to the processing accuracy of the winding frame and the coil accuracy is considered to be about 1 mm. However, since there is no measuring instrument that calculates the dimensions of the coil with an accuracy of millimeters or less, there is no record of its dimensions at the time of completion.

The design concept of PPPL's NCSX is unknown, but as far as the published materials are concerned, like the CHS, the conductor was fixed to the winding frame manufactured with high precision, and a coil with a millimeter order of accuracy was made. The W7-X and the HSX were designed to shape the coil with a winding mould, harden the resin, and then remove the winding mold. The CFQS coil manufacturing method is the same.

The coil accuracy of the W7-X was about  $\pm 5$  on the winding mould and the accuracy after removing it was unknown. Since the coil accuracy of the CFQS is  $\pm 3$  on the winding mould, it is considered to be at the same level as the W-7X.

In starting the engineering design of the CFQS, the coil accuracy was assumed to be 5 mm. There is no basis for the validity of this value, but it was judged that there was no choice but to expect this level of accuracy in order to carry out the engineering design. It seemed difficult to maintain an accuracy of 1 mm or less by the assumed coil manufacturing method. It was estimated that the gap between the coil bodies was too small to accommodate an error of 10 mm or more, considering the need for a coil case and other supports. Therefore, we selected 5 mm as an intermediate value and aimed for a design that could be assembled, even if there was an error of 5 mm. It was found

that the assumption of an error of 5 mm was valid in the test of making the model coil. The current design of the CFQS has dimensions that can be assembled even with an error of 10 mm (the minimum gap between parts is 20 mm), so if the coil is completed with an accuracy of 5 mm, it will be possible to assemble. There is a possibility that an interference of parts may occur locally, but since they are made of metal, it is possible to cut off the interference part. So, it is judged that it can be assembled.

#### 1.3.4 Accuracy of coil installation

Even if a high-precision coil can be made, there is still the possibility that an error will occur when arranging it on the main body of the device. We think that errors during assembly can be corrected by adjustment work. In other words, we designed a coil system to make it possible. A position measuring instrument is required for adjustment. The position accuracy of the marking line is estimated to be 1 mm or less, and the accuracy of 3D measurement in the overall coordinate system is estimated to be about 5 mm. Therefore, if an adjustment with the marking line is possible, we think that it should be used. It is possible to confirm the final result by 3D measurement, but it is not suitable for position adjustment work, because the measurement procedure is too complicated and time-consuming.

There are three degrees of freedom of position, X, Y, Z, and three degrees of freedom of rotation, Rot-X, Rot-Y, Rot-Z, based on the center of gravity in the installation work. They are adjusted to install the coil at the correct position and angle, but if there are no obstacles around it, in principle, the error can be set to 0 within the range of measurement accuracy.

As mentioned earlier, the accuracy of the coil is not a physical problem (it cannot be determined whether it is), so if it can be installed, it is OK for the time being.

The possible displacement to install the coil is estimated as follows.

- ① Position of the vertical direction;  $\Delta Z = \pm 5$  mm (can be controlled by the insulation plate thickness)
- ② Position of the major radius direction;  $\Delta R = 0 \sim 20$  mm
- ③ Position of the toroidal direction,  $\Delta(\phi R) = \pm 5$  mm
- ④ Rotation to the Z axis;  $\Delta(\text{Rot-Z}) = \pm 2$  degrees
- ⑤ Rotation to the R axis;  $\Delta(\text{Rot-R}) = 0$
- ⑥ Rotation to the  $\phi$  axis;  $\Delta(\text{Rot-}\phi) = 0$

Here, ⑤ and ⑥ will be determined by the structure of the coil support legs, so there is no room for adjustment. Only four types of ① to ④ can be adjusted. If we draw appropriate marking lines on the base on which the coil is placed, we may adjust the error to 0, based on their lines. Since ⑤ and ⑥ cannot be adjusted at the time of installation, it is important to accurately attach the support legs to the coil body, which should be done in the process of manufacturing the coil alone. Regarding them, it is possible to finish the upper and lower surfaces of the support legs with an accuracy of 1 mm or less, by machining, after mounting the support legs.

## 2 Standard material and accessories

### 2.1 Physical property of the metal

#### 2.1.1 Austenite stainless steel (SUS)

There are slight differences in mechanical properties due to differences in composition. We should choose them according to our purpose.

The SUS 304 is the most distributed and inexpensive. However, as the permeability may increase, caution is required for nuclear fusion. It turns into magnetic material by bending or rolling. It is better not to use it in a magnetic field. We are worried about distorting the magnetic field profile.

The SUS316 and the SUS316L is more stable than the SUS304. The SUS316L is SUS316 with low carbon and has slightly better cold workability and corrosion resistance but it is a little expensive and a little weaker.

Table 2.1-1 Characteristics of typical SUS materials.

	SUS304(JIS G 4303)	SUS316(JIS G 4305)	SUS316L (JIS G 4305)
Material composition	Cr 18-20 % Ni 8-10.5 % Mn less than 2 % C less than 0.08 %	Cr 16-18 % Ni 10-14 % Mo 2-3 % Mn less than 2 % C less than 0.08 %	Cr 16-18 % Ni 12-15 % Mo 2-3 % Mn less than 2 % C less than 0.03 %
Mechanical properties at room temperature (MPa)	$\sigma_y = 205$ $\sigma_u = 520$ $S_m = 129$	$\sigma_y = 205$ $\sigma_u = 520$ $S_m = 129$	$\sigma_y = 175$ $\sigma_u = 480$ $S_m = 114$
Magnetic permeability	$\mu = 1.004 \sim 1.1$ or more	$\mu = 1.004$	$\mu = 1.004$

#### 2.1.2 Oxygen free copper (OFC)

The physical properties of copper vary greatly with temperature. They are especially important in device design. The temperature dependence of the electrical resistivity is particularly important. Since the design of the normal-conducting coil changes depending on which temperature is assumed, it is necessary to clarify the temperature used in the design. Generally, a resistivity of 75 °C. is often assumed for high-power coil design where temperature rises, and a resistivity of 20 °C. is often assumed for low-power coil design where temperature changes are not a concern.

The formulas for calculating the physical properties of oxygen-free copper are shown below. The attributes of copper obtained in experiments have been introduced in various documents, but we would like to mention that there are some variations due to subtle differences in the copper composition and differences in the experimental temperature range. In the design of this document, 101 % IACS is used unless otherwise specified. 101 % here indicates that the conductivity is 101 % based on standard annealed soft copper.

#### References

- [1] JSME Data Book: Heat Transfer 4<sup>th</sup> Edition, I. Hirata, Journal of the Cryogenic Society of Japan (1970).
- [2] IACS: International annealed copper standard (1914).

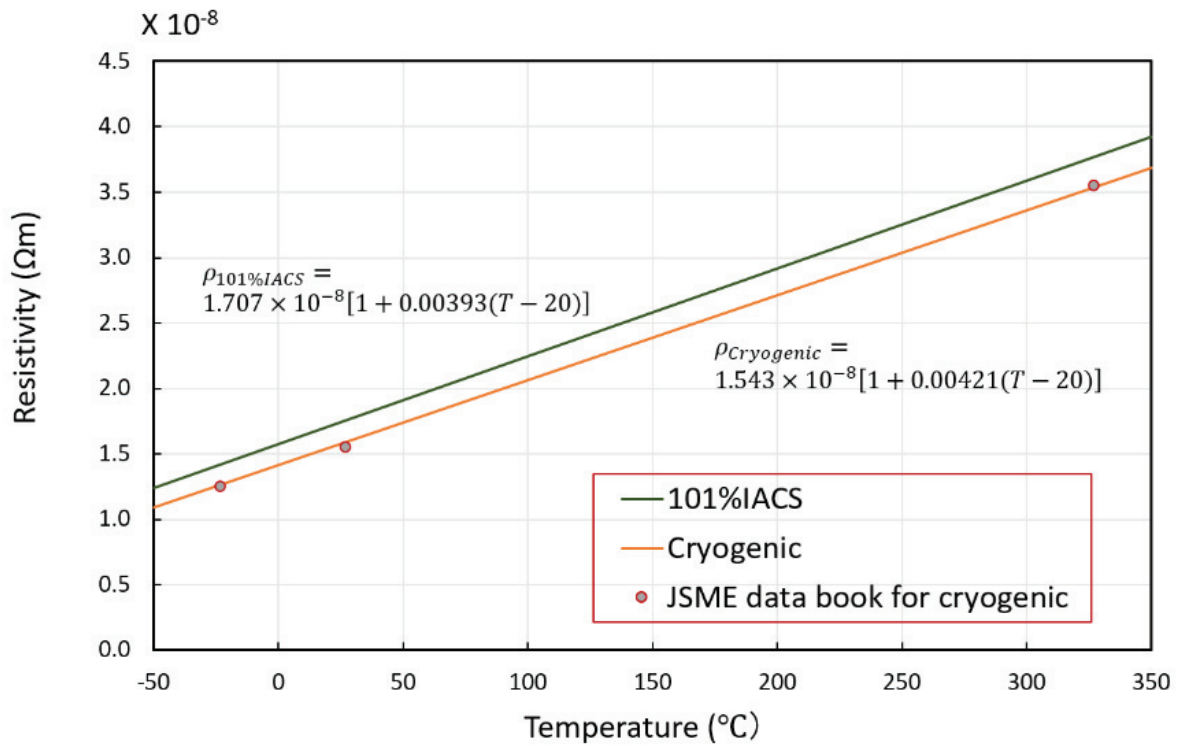


Fig 2.1-1 Temperature dependence of electrical resistivity of copper

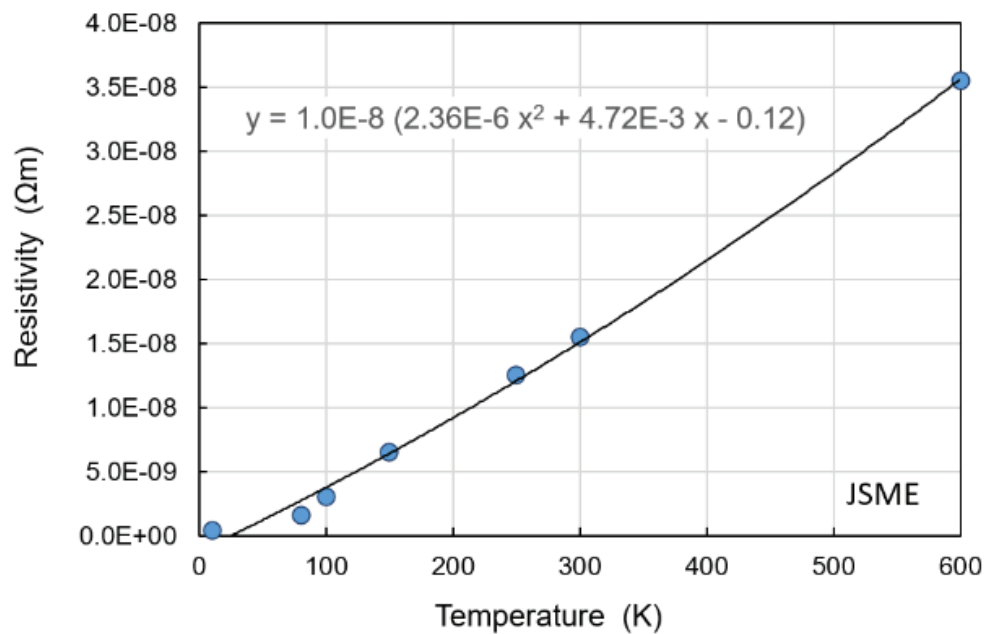


Fig 2.1-2 Temperature dependence of electrical resistivity of copper

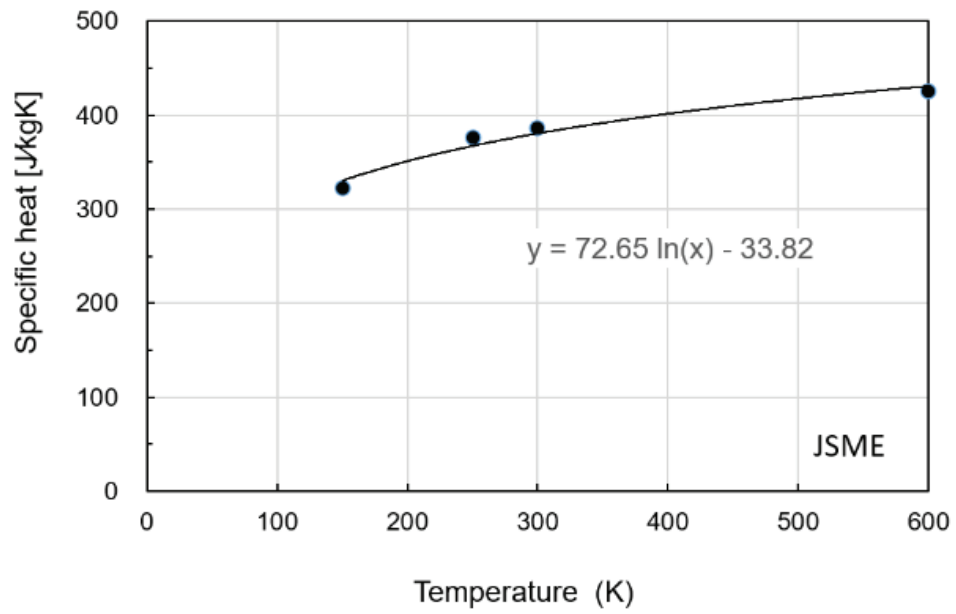


Fig 2.1-3 Temperature characteristics of specific heat of copper

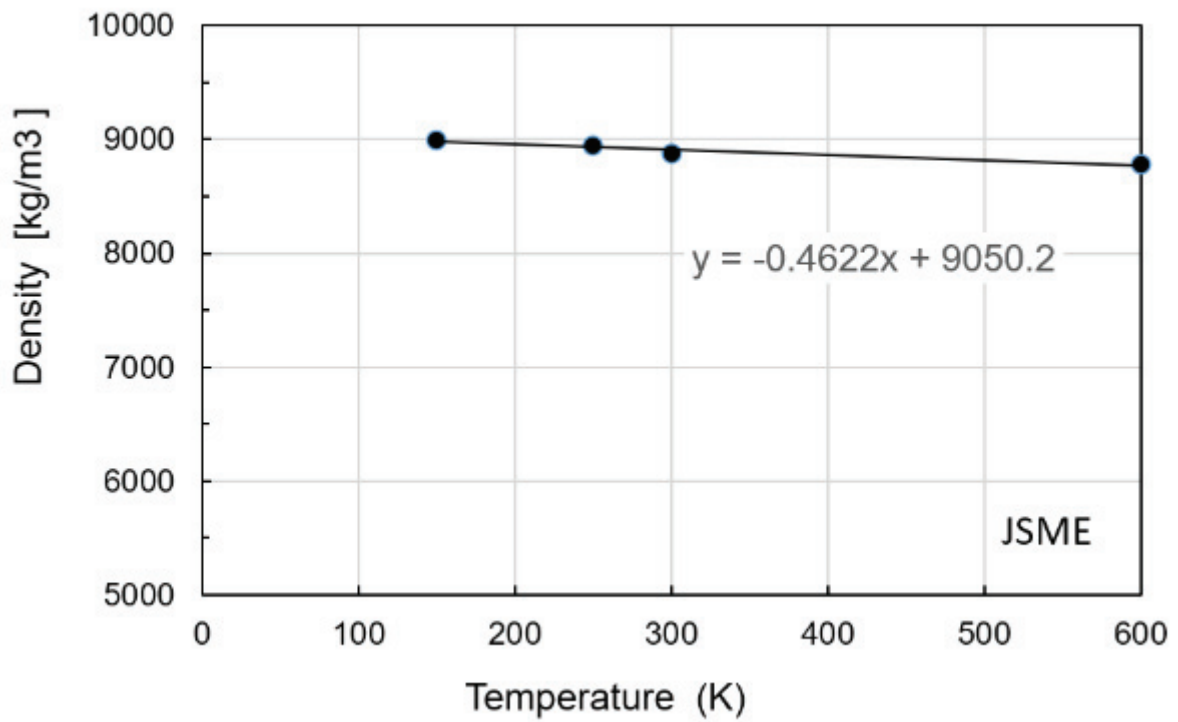


Fig 2.1-4 Temperature characteristics of density of copper



## 2.2 Accessories

### 2.2.1 Gasket or O-ring for vacuum

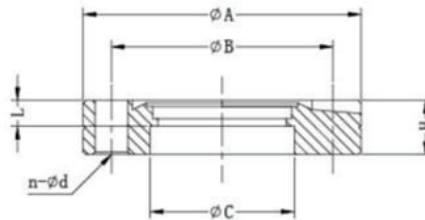
Depending on the operating temperature, it is necessary to select the material of the gasket or O ring properly. The vacuum vessel of the CFQS will use a so-called CF (ConFlat) flange, which is usable over a wide range of temperature range. The CF flanges use an oxygen-free high thermal conductivity copper gasket and knife-edge flange to achieve an ultrahigh vacuum seal. The name "ConFlat" is a registered trademark of Varian, Inc., so "CF" is commonly used by other flange manufacturers. The CF flange is widespread throughout the world, but it should be noted that the name and size are slightly different depending on the country and the manufacturer, and there may be no compatibility.

Deformation of the metal gasket fills small defects in the flange, allowing CF flanges operate down to 10–13 Torr (10–11 Pa) pressure. For stainless-steel CF flanges, baking temperatures of 450 °C can be achieved; the temperature is limited by the choice of gasket material. In North America, flange sizes are given by flange outer diameter in inches, while in Europe and Asia, sizes are given by tube inner diameter in millimeters. In Japan, the outer diameter of the flange is often defined in millimeters. The nominal name of the flange also differs depending on the manufacturer, and is called ICF, UFC, CF, etc. Despite the different naming conventions, the actual flanges are the same. In the CFQS project, we will use the European style of calling the inner diameter of the tube in millimeters. Examples of CF flanges used in the CFQS are shown in Table 2.2-1.

For flanges not standardized as the CF, such as rectangular port flanges, a flange with a groove for rubber O-rings shall be individually designed. The material of the O-ring shall be the fluorine rubber (FKM, Viton), which may be usable in -15 ~ 200 °C but worry about low temperature damage due to liquid nitrogen or cryogenic gas that is sometimes used for evacuation. The Nitrile rubber (NBR), which may be the cheapest, must not be used because it cannot withstand the baking temperature of the vacuum vessel. The usable temperature of the NBR is -50 ~ 80 °C.

Table 2.2-1 CF fixed flanges (example).

Name	O.D (A)	PCD (B)	Thickness (H)	n	d	C	Nominal name of Varian
CF16	33.8	27	7.3	6	4.5	18	ICF34
CF35	69.5	58.7	13	6	6.5	38	ICF70
CF63	113.6	92.2	17.5	8	8.5	66	ICF114
CF100	151.6	130.3	20	16	8.5	104	ICF152
CF150	202.5	181	22	20	8.5	154	ICF203
CF200	253.2	231.8	24.5	24	8.5	205	ICF253
CF250	305	284	24.5	32	8.5	256	ICF305
CF300	355.6	325.7	28.5	32	8.5	306	ICF356
CF350	419.1	388.9	28	36	10.5	356	ICF419



## 2.2.2 Pipe and flange for the water cooling

A pure water cooling system will be used to cool the coils. Non-magnetic SUS piping will be used for the system and the pipe diameter will vary depending on the place in the system. Examples of pipes are shown in .

Table 2.2-2. Unless otherwise specified, the CFQS will use SCH20s in the table.

Table 2.2-2 SUS pipe and flange.

ND		SUS PIPE							20K W FLANGE				
A (mm)	B (Inch)	OD (mm)	Thickness (mm)					Stan dard	OD (mm)	Thick ness (mm)	Number of bolt holes	Bolt hole diameter (mm)	Stan dard
			SCH 5s	SCH 10s	SCH 20s	SCH 40	SCH 80						
6	1/8	10.5	1	1.2	1.5	1.7	2.4						
8	1/4	13.8	1.2	1.65	2	2.2	3						
10	3/8	17.3	1.2	1.65	2	2.3	3.2		90	14	4	15	
15	1/2	21.7	1.65	2.1	2.5	2.8	3.7		95	14	4	15	
20	3/4	27.2	1.65	2.1	2.5	2.9	3.9		100	16	4	15	
25	1	34	1.65	2.8	3	3.4	4.5		125	16	4	19	
32	1-1/4	42.7	1.65	2.8	3	3.6	4.9		135	18	4	19	
40	1-1/2	48.6	1.65	2.8	3	3.7	5.1		140	18	4	19	
50	2	60.5	1.65	2.8	3.5	3.9	5.5		155	18	8	19	
65	2-1/2	76.3	2.1	3	3.5	5.2	7		175	20	8	19	
80	3	89.1	2.1	3	4	5.5	7.6		185	22	8	23	
90	3-1/2	101.6	2.1	3	4	5.7	8.1		195	24	8	23	
100	4	114.3	2.1	3	4	6	8.6		210	24	8	23	
125	5	139.8	2.8	3.4	5	6.6	9.5		250	26	8	25	
150	6	165.2	2.8	3.4	5	7.1	11		280	28	12	25	
200	8	216.3	2.8	4	6.5	8.2	12.7		330	30	12	25	
250	10	267.4	3.4	4	6.5	9.3	15.1		400	34	12	27	
300	12	318.5	4	4.5	6.5	10.3	17.4		445	36	16	27	
350	14	355.6	4	5	8	11.1			490	40	16	33	
400	16	406.4	4.5	5	8	12.7			560	46	16	33	
450	18	457.2	4.5	5	8	14.3			620	48	20	33	
500	20	508	5	5.5	9.5	15.1			675	50	20	33	

ND; Nominal Diameter, OD; Outer Diameter

Unless otherwise specified, the CFQS will use SCH20s for cooling water system and SCH5s for vacuum.

### 2.2.1 Electrical cable and solderless terminal

The MC and the PFC are fabricated with individually designed solid conductors. For other conductors, standard insulated cables will be used. Examples of standard cables are shown in Table 2.2-3.

Table 2.2-3 Electrical cable

Type	Twist	Nominal cross section mm <sup>2</sup>	Finish outer diameter mm	Conductor outer diameter mm	Allowable current A	Density A/mm <sup>2</sup>	Test voltage V	Number of strands	Strand diameter mm
600V IV cable HIV cable	Single wire	0.79	2.6	1	16	20.37	1500		
		1.13	2.8	1.2	19	16.80	1500		
		2.01	3.2	1.6	27	13.43	1500		
		3.14	3.6	2	35	11.14	1500		
		5.31	4.6	2.6	48	9.04	1500		
		8.04	5.6	3.2	62	7.71	1500		
		12.57	6.8	4	81	6.45	2000		
		19.63	8.2	5	107	5.45	2000		
	Stranded wire	0.9	2.8	1.2	17	18.89	1500	7	0.4
		1.25	3	1.35	19	15.20	1500	7	0.45
		2	3.4	1.8	27	13.50	1500	7	0.6
		3.5	4.1	2.4	37	10.57	1500	7	0.8
		5.5	5	3	49	8.91	1500	7	1
		8	6	3.6	61	7.63	1500	7	1.2
		14	7.6	4.8	88	6.29	2000	7	1.6
		22	9.2	6	115	5.23	2000	7	2
		38	11.5	7.8	162	4.26	2500	7	2.6
		60	14	10	217	3.62	2500	19	2
		100	17	13	298	2.98	2500	19	2.6
		150	21	16.1	395	2.63	3000	37	2.3
		200	23	18.2	469	2.35	3000	37	2.6
600V CV cable	Stranded wire	5.5	8	3	58	10.55	1500	7	1
		8	8.6	3.6	72	9.00	1500	7	1.2
		14	9.5	4.4	100	7.14	2000	Circular compression stranded	
		22	11	5.5	130	5.91	2000		
		38	13	7.3	190	5.00	2500		
		60	16	9.3	255	4.25	2500		
		100	19	12	355	3.55	2500		
		150	23	14.7	455	3.03	3000		
		200	26	17	545	2.73	3000		
3300V CV cable	Stranded wire	8	13	3.4	78	9.75	9000		
		14	14	4.4	105	7.50	9000		
		22	15	5.5	140	6.36	9000		
		38	17	7.3	195	5.13	9000		
		60	21	9.3	260	4.33	9000		
		100	23	12	355	3.55	9000		
		150	26	14.7	455	3.03	9000		
		200	30	17	540	2.70	9000		
Type	Explanation						Operating temperature		
IV	Wire insulate by Vinyl						Less than 60°C		
HIV	Heat-proof wire Insulate by Vinyl						Less than 75°C		
CV	Cross-linked polyethylene insulated Vinyl sheathed						Less than 90°C		

Solderless terminals will be used to connect cables. Examples of the terminal are shown in Fig 2.2-1 and Fig 2.2-2. There are many terminals on the market around the world, so suitable ones will be purchased and used.

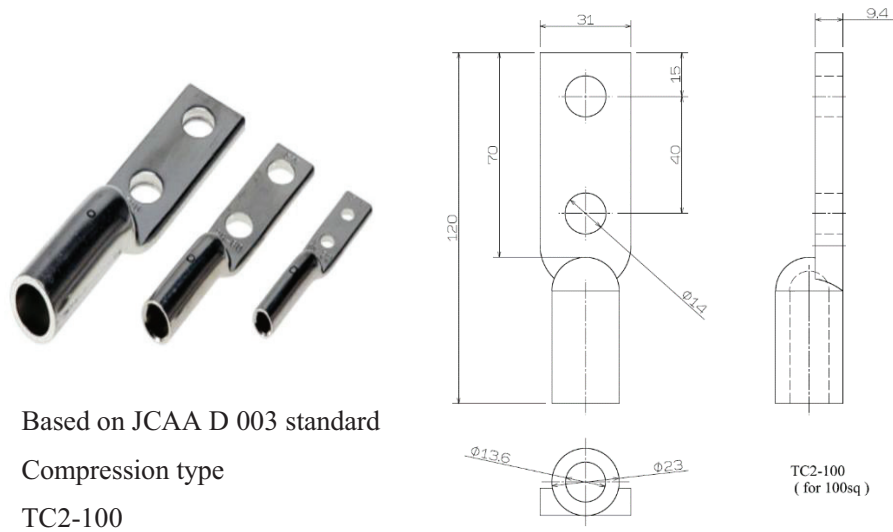


Fig 2.2-1 Compression type solderless terminal TC2-100 for wire 100SQ.

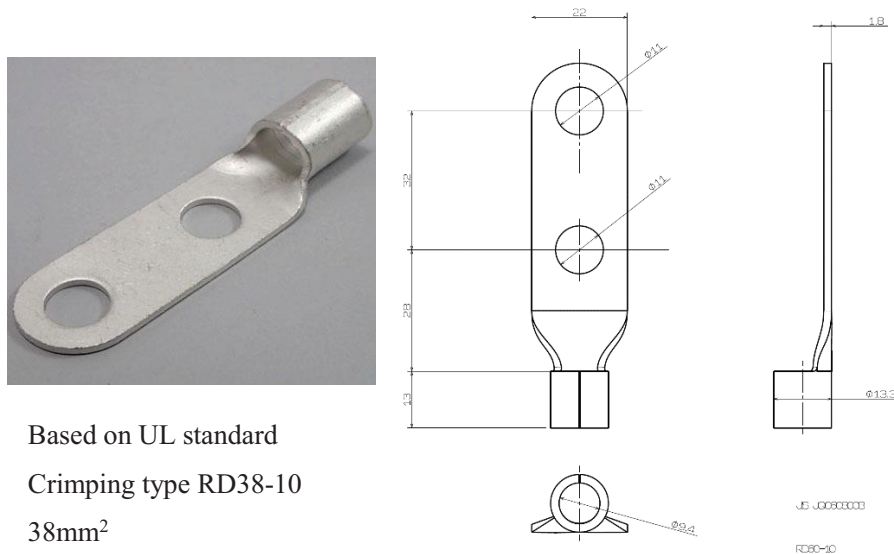


Fig 2.2-2 Crimping type solderless terminal RD38-10 for wire 38SQ.

### 2.2.2 Flexible terminal

Many types are on the market for the purpose of absorbing the amount of displacement due to thermal expansion and contraction, absorbing the vibration generated by electrical equipment, and improving workability during assembly. For convenience, representative dimensions of flexible terminals which are likely to be applicable in the CFQS design are shown as an example.

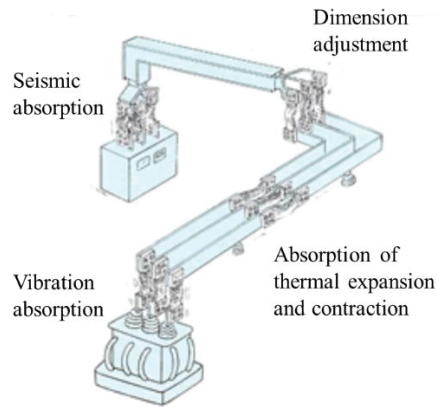
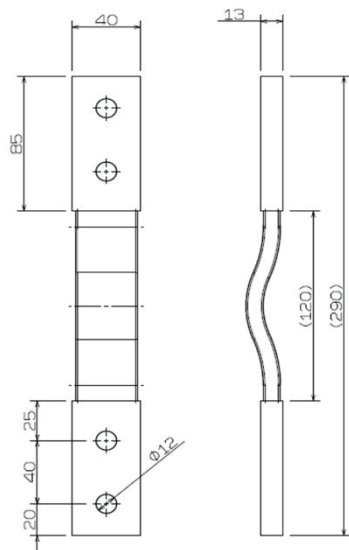


Fig 2.2-3 Application example of flexible terminal.



Nominal cross section 300 mm<sup>2</sup>

Allowable current 770 A

Bolt used M10

Standard length 300 mm

Fig 2.2-4 Example of a standard type of flexible terminal.



### 3 Analytical expression

#### 3.1 Calculation formula of adiabatic temperature rise

The temperature without cooling during pulse operation of the copper coil can be easily evaluated by the following equation. It almost matches the temperature change in a short time, because the standard thermal time constant is much longer than the pulse length. The temperature change of the conductor is obtained from the thermal equation,

$$C \frac{dT}{dt} = Q_h - Q_c ,$$

$$Q_h = I^2 R = (j S_{cu})^2 \times \rho_e L / S_{cu} = j^2 S_{cu} \rho_e L ,$$

$$Q_c = 0 ,$$

where  $C$  is a heat capacity,  $Q_h$  is a heating power and  $Q_c$  is a cooling power.

- Heat capacity of conductor;  $C = m C_p$   $[J/K]$
- Mass of conductor;  $m = L S_{cu} \rho$   $[kg]$
- Density of conductor;  $\rho = 8,911$   $[kg/m^3]$  at room temperature (27 °C)
- Density of conductor;  $\rho = 8,888$   $[kg/m^3]$  at 75 °C
- Specific heat of conductor;  $C_p = 381$   $[J/kgK]$  at room temperature (27 °C)
- Specific heat of conductor;  $C_p = 361$   $[J/kgK]$  at 75 °C
- Resistivity of conductor;  $\rho_e = 1.724 \times 10^{-8}$   $[\Omega m]$  at room temperature (27 °C)
- Resistivity of conductor;  $\rho_e = 1.895 \times 10^{-8}$   $[\Omega m]$  at 75 °C

It is as follows when the physical property value of copper is inputted.

$$\frac{dT}{dt} [K/s] = \frac{Q_h}{C} = \frac{j^2 S_{cu} \rho_e L}{L S_{cu} \rho C_p} = j^2 \frac{\rho_e}{\rho C_p} = j^2 [A/mm^2] \times 5.1 \times 10^{-3} \text{ at } 27^\circ \text{C} ,$$

$$\frac{dT}{dt} [K/s] = \frac{Q_h}{C} = \frac{j^2 S_{cu} \rho_e L}{L S_{cu} \rho C_p} = j^2 \frac{\rho_e}{\rho C_p} = j^2 [A/mm^2] \times 5.9 \times 10^{-3} \text{ at } 75^\circ \text{C} .$$

Here, 75 °C is often used as a typical temperature after heating an electric device, and 27 °C = 300 K is often used as a typical room temperature before heating an electric device.

### 3.2 Calculation formula of a pressure drop and average temperature rise of cooling water

Pressure drop (loss head) of the piping is calculated by the Hazen Williams' equation below.

$$h_f = 10.67 \cdot L \frac{(Q/C)^{1.85}}{D^{4.87}}$$
$$\Delta P = \rho \times g \times h_f$$
$$Q = Au = u \times \frac{(\pi D^2)}{4}$$

where  $h_f$  is the loss head (m),  $L$  is the length of one cooling tube (m),  $Q$  is the flow rate in a tube (m<sup>3</sup>/s),  $C$  is the roughness coefficient (Hazen-Williams-coefficient =100~200), and  $D$  is the inside tube diameter (m).  $g$  is the gravitational acceleration (=9.8 m/s<sup>2</sup>),  $\rho$  is the density of water(=996 kg/m<sup>3</sup>),  $\Delta P$  is the pressure drop ( $P_a$ ),  $A$  is the cross section of cooling hole (m<sup>2</sup>), and  $u$  is the flow velocity(m/s).

Average temperature rise of cooling water is calculated by the equation below.

$$\Delta T_{water} = \frac{\text{Average heat input}}{(\text{Flow rate})(\text{Density})(\text{Specific heat capacity})} = \frac{\Delta W}{t_{period}} \cdot \frac{1}{(Q_0 \rho C_h)}$$

where  $Q_0$  is the flow rate in a tube(m<sup>3</sup>/s),  $\Delta W$  is the heat generation in one pulse(J),  $t_{period}$  is the discharge period(s) and  $C_h$  is the Specific heat capacity of water (= 4186 J/kg K).

### 3.3 Calculation formula and design criteria of lead wires for supplying current to the coil

We will evaluate the lead support design with simplified analysis model as shown in Fig 3.3-1 to Fig 3.3-3.

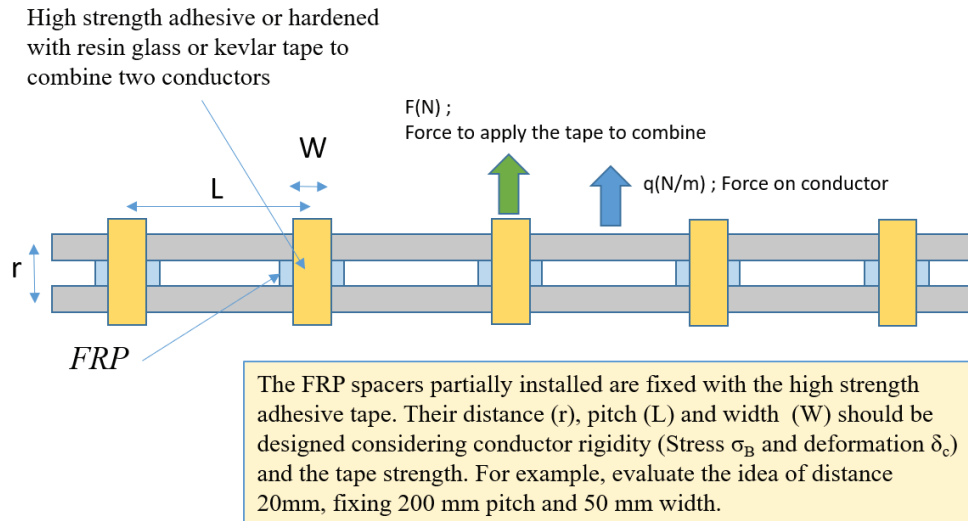


Fig 3.3-1 Simplified analysis model

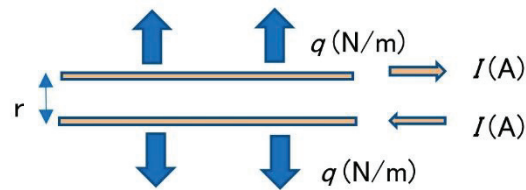


Fig 3.3-2 Definition of repulsive force

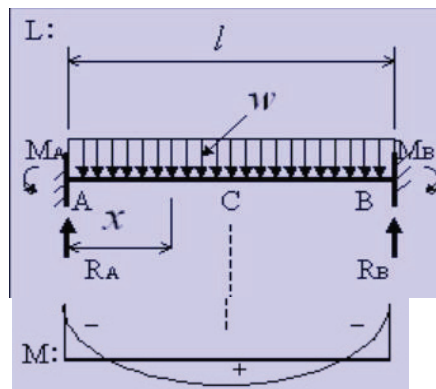


Fig 3.3-3 Deflection and stress distribution of a wire

The lead wire design is as follows.

- Force between parallel straight currents (the repulsive force)

$$q(N/m) = \frac{\mu_0 I^2}{2\pi r},$$

- Maximum stress of the wire with equally distributed load both ends fixed beam

$$\sigma_B(Pa) = \frac{qL^2}{2bh^2} \leq 20 MPa,$$

- Force to apply a part (tape etc.) to combine two wires. The combine part must be designed to endure the force.

$$F(N) = qL,$$

- Deflection of the wire

$$\delta_c(m) = \frac{qL^4}{384EI_x} \leq 2 mm,$$

- Second moment of area (moment of inertia of area) of the wire

$$I_x = \frac{bh^3}{12}.$$

- Lowest natural frequency of the wire

$$f_1 = \frac{4.73^2}{2\pi} \sqrt{\frac{EI_x}{\rho SL^4}} \geq 40 Hz.$$

Where, I (A) is a current, r (m) is a distance between wires, L (m) is the combine part interval, s=b (m) × h (m) is a cross section of wire, E is a longitudinal elastic modulus for the wire, and ρ is a density of the wire. When the wire material is copper of C1020-O,

$$E=100 \text{ GPa},$$

$$\rho = 8,960 \text{ kg/m}^3.$$

## 4 Power supply for the coil system

To apply large current to the coil, a short pulse large capacity power supply is required. Since it is difficult to supply such massive electrical power from the commercial power grids directory due to overload (up to 10MVA), a current source with energy storage function should be employed.

### 4.1 Power supply system used in the fusion devices

Fig 4.1-1 shows the configurations of power supply system with a short pulse large capacity. Of course, AC/DC SCR control converter or rectifiers and PWM chopper circuit system must be utilized for controlling each coil current. The comparison of the power storage system is summarized in Table 4.1-1. The IM and SG type may be the most appropriate power storage system for the CFQS.

Table 4.1-2 shows a capability of the energy stored generators for the fusion devices. Most devices have used the IM and SG type. Discussions for each candidate focusing on capacity, space, cost, and operation control are described in the next section.

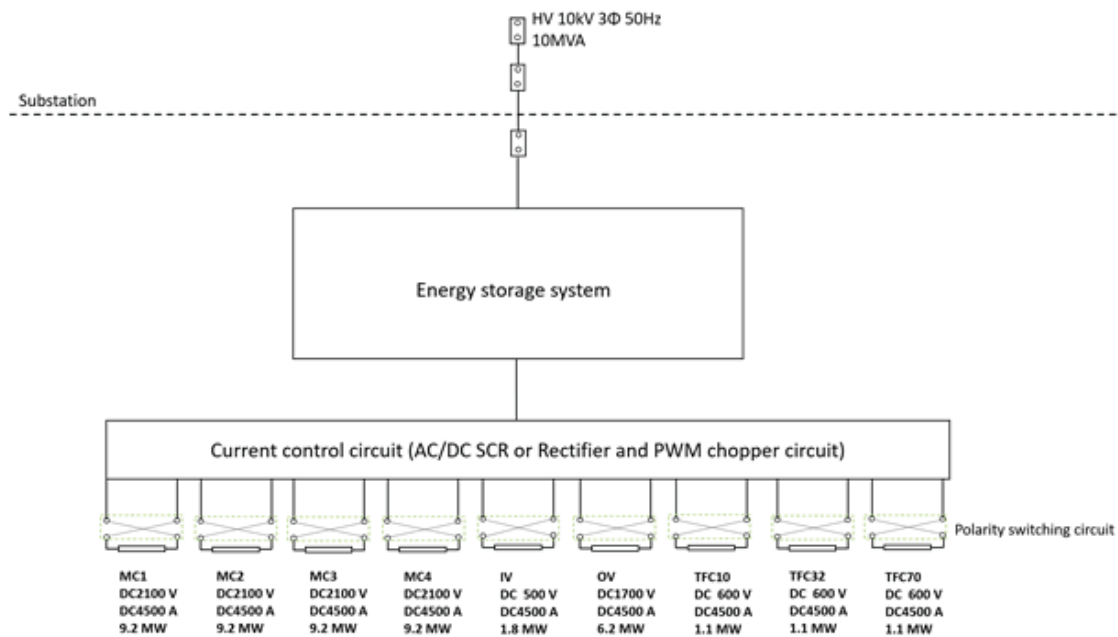


Fig 4.1-1 Configurations of power supply system with a short pulse large capacity.

Table 4.1-1 Comparison of power storage systems.

Power storage candidate	Evaluation	Notes
Capacitor banks	Impractical	It was used in short-pulse experiments in the early days of fusion device development.
Induction motor and synchronous generator (IM and SG)	Appropriate	It has been utilized for various fusion experimental devices. It can store large amount of electrical energy over 100 MJ and supply power with good controllability.
Electric motor that can run as a generator	Marginal	<p>Various motors capable of generator operation have been developed. By switching between the two with time, we can construct an energy storage device.</p> <ul style="list-style-type: none"> <li>• DC motor and generator</li> <li>• SEIG (Self-excited induction generator)</li> <li>• Variable speed synchronous generator for pumped storage power generation</li> </ul>
Others	Impractical	There are various proposals such as batteries, diesel engine-driven generator and superconducting magnetic energy storage (SMES), but they are not yet operational for the fusion device.

Table 4.1-2 Power storage systems for fusion device mainly in Japan.

No	Fusion device	Generator		Drive	
		Capacity	Spec	Capacity	Spec
1	TRIAM-1M Kyushu University	125 MVA 60 MJ	3Φ VSYG 6.6 kV 11 kA 67-59 Hz 670-590 rpm	1.4 MW	3Φ IM
2	Heliotron-J Kyoto University	330 MVA 300 MJ	3Φ VSYG 18 kV 10.58 kA 65-50 Hz 650-500 rpm	3.2 MW	3Φ IM
3	JT-60 HMG QST	400 MVA 2.5 GJ	3Φ VSYG 18 kV 12.83 kA 77.6-54.2 Hz 582-406 rpm	15 MW	3Φ IM
4	JT-60 PMG QST	500 MVA 1.3 GJ	3Φ VSYG 18 kV 16 kA 77.6-54.2 Hz 582-406 rpm	7 MW	3Φ IM
5	JT-60 TMG QST	215 MVA 4 GJ	3Φ VSYG 18 kV 6.9 kA 80-56 Hz 600-420 rpm	19 MW	Inverter drive
6	Gamma 10 University of Tsukuba	250 MVA 800 MJ	3Φ VSYG 18 kV 8 kA 77.6-54.3 Hz 582-407 rpm	2.4 MW	3Φ IM
7	LHD and CHS NIFS	250 MVA 1.4 GJ	3Φ VSYG 18 kV 8 kA 93-58 Hz 701-435 rpm	8.5 MW	3Φ IM
8	HL-2A SWIP, Chengdu (CHS Nagoya University)	125 MVA 200 MJ	3Φ HSYG 3 kV 24 kA 120-96 Hz 3600 rpm	2.5 MW	3Φ IM
9	HL-2A SWIP, Chengdu	300 MVA 1.35 GJ	6Φ VSYG 3 kV 29 kA 100-67 Hz 500-335 rpm	8.5 MW	3Φ IM
10	HL-2A SWIP, Chengdu	90 MVA 250 MJ	3Φ HSYS 1650-1488 rpm	2.5 MW	3Φ IM



No	Fusion device	Generator		Drive	
		Capacity	Spec	Capacity	Spec
11	HSX University of Wisconsin - Madison	84 MVA 42 MWp Over 20 MJ	DCM 30 motors 1.68kV 50kA		DCM
12	PLATO Kyushu University	810 kW <sub>-peak</sub> 2.8 MJ (stored) 384 kJ (release)	3Φ SIM 2 motors 60 Hz-3600 rpm	72 kW	Inverter drive
*	CFQS NSJP	60 MW <sub>-peak</sub> 50 MJ (released) 120 MJ (stored)	3Φ HSYG 10 kV 50-38 Hz 3000 rpm	250 kW	3Φ IM

$$MVA = kV \times kA \times \sqrt{3}$$

Capacity of the above equipment is excessive for the CFQS.

VSYG; Vertical synchronous generator

HSYG; Horizontal synchronous generator

DCM; DC generator and motor

SIM; Self-excited induction generator and motor

IM; Induction motor

## 4.2 Features of the power supply system

### 4.2.1 Capacitor bank

This type has been widely adopted for small fusion devices and its configuration is comparatively simple. However, because high voltage capacitors have small energy density per volume, the problem of installation space for capacitors cannot be ignored. Consequently, capacitor bank is impractical for power supply system with 50MJ of the stored energy.

The size of a capacitor depends on its type. Recently, although the energy storage density of a capacitor is greatly increased such as an electrolytic capacitor with small size, it is limited to 500 V or less. The modular coil of the CFQS is required to be applied over DC 1000 V. Thus, there is no choice but to be selected an oil capacitor with extremely large size.

Total required energy for the MC is approximately 45 MJ with 2100 V. Given 3000 V charging voltage of capacitor bank before discharge and 2700 V after discharge, oil capacitors with about 44.4 F capacity is required. Charging voltage for capacitor bank need to be more than 2400 V even after discharge because of discharge current control. The total required capacitor including capacity of the toroidal field coil (TFC) and the poloidal field coil (PFC) is estimated about 46.8 F 210 MJ based on above voltage conditions. If general oil capacitor with 78 μF, 3510 V rated voltage and size of 0.175 m × 0.620 m = 0.11 m<sup>2</sup> is adopted, total required number of capacitors is about 600,000. Therefore, at least 66,000 m<sup>2</sup> space for capacitors is required. It should not be accommodated in the experimental building. Even though given 10 kV charging voltage is applied to capacitor bank, total required capacitance, number of capacitor and space is estimated about 0.9 F, 10,000, respectively.

Moreover, a pulse width modulation (PWM) switching circuit must be installed between the capacitor bank and coils to control the coil current. Since the switching circuit generates ripples, it is necessary to evaluate the power supply by the combination of the capacitors and the switching circuit.

#### **4.2.2 DC motor and generator**

Since the DC motor is an old technology, procurement of new motors may be difficult. There is no other way but to find for used motors. However, since lifetime of a typical DC motor is limited by a brush, the used motor has relatively high risk of breakdown. Furthermore, over 100 number of DC motors with extremely large installation space may be required to cover the total energy of coils because it is difficult to procurement of over 200 kW used motors. Besides, simultaneous operation control of 100 number of DC motors may be impractical. Thus, the DC motor should be inappropriate for power supply system with 50MJ of the stored energy.

#### **4.2.3 Self-excited induction generator (SEIG)**

Murayama et al. adopted this type for power storage system of a small fusion device [Fusion. Eng. Des. **148**, 111270 (2019)]. The system is utilized squirrel cage IM as a motor/generator (MG) instead of SG. The advantage utilizing the IM with squirrel cage casting structure is robustness derived from the simple structure with no wearing parts except for bearings. Moreover, it can generate electricity with capacitor self-excitation phenomena which does not require excitation control system. However, in the case of CFQS, large installation space for the high voltage capacitors with up to 30 MVAR capacity may be required to obtain the suitable output voltage of SEIG. It is difficult to be accommodated in the experimental building.

Furthermore, we need to compensate the voltage drop of SEIG during the coil energization by connecting additional self-exciting capacitors in parallel at the start of the discharge phase. If additional capacitors are connected to SEIG before the discharge phase, output voltage of SEIG is significantly increased, and it leads to insulation breakdown and overheat. Therefore, high voltage switching devices with high responsiveness and their control systems should be prepared. There may be no achievement of implementation of power supply with SEIG for large or middle-sized fusion device (over 10 MW case).

#### **4.2.4 Induction motor and synchronous generator**

It is a system that slowly accelerates a large flywheel with an induction motor and uses the stored energy to obtain short pulses of high power. It has been utilized for various fusion experimental devices may be most suitable as a large power storage system. It can store large amount of electrical energy over 100 MJ and supply power with good controllability.

#### **4.2.5 Variable speed synchronous generator for pumped storage power generation**

For pumped-storage power generation, large-capacity variable-speed synchronous generators are in operation. It can also be used as an energy storage device since it has both motor and generator functions. In the pumped-storage power generation, energy is accumulated as potential energy of mountain lake water, but in nuclear fusion energy is accumulated as rotational energy of a generator. The idea as an energy storage device is the same as in the induction motor and synchronous generator method. The capacity and the cost may determine which is more suitable, but as the capacity increases, this method may become more advantageous.

## 5 Coil support structure for torus fusion devices

In the torus type device, the method of supporting the electric magnetic force of the coil is especially important. It is not much to say that the structure of the device is determined by which method is applied. The methods applied to various devices are organized below, and the characteristics of each are summarized.

### 5.1 Support structure for the weak magnetic field devices

Fig 5.1-1 shows the support structure for low-field experiments at the CFQS. It has only the upper and lower legs without special structure. This method is only applicable to devices with weak magnetic fields and small electromagnetic forces. There is a possibility that it can be applied to high beta devices such as reverse field pinch, but it is difficult to use in higher magnetic field devices of 1 T. At the CFQS, it may be used for 0.09T low-field experiments in the early stages of the experiment.

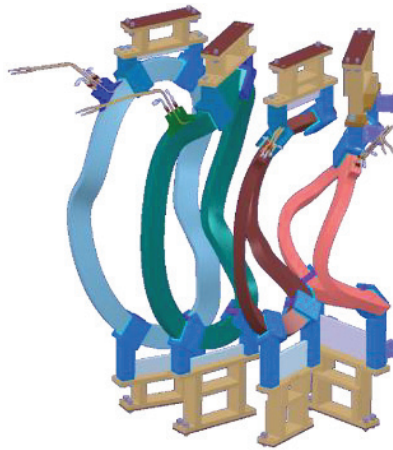


Fig 5.1-1 Support structure for low-field experiments at the CFQS. The modular coil is held stationary only by the upper and lower legs. Deformation of the coil due to electromagnetic force is suppressed by the rigidity of the coil, which is fixed with insulating tape and varnish. It is applicable only when the electromagnetic force is small, and difficult to apply with a strong magnetic field exceeding 1T.

## 5.2 Support structure for the high magnetic field devices

### 5.2.1 Set up a central structure, and transmit the electro-magnetic force to it

In this method, a column or cylinder is constructed in the center of the device and the coils are constructed to it. By canceling the electromagnetic force directed toward the center via the central structure, the movement of the coil is stopped. Since deformation of the coil cannot be stopped by the central structure, it is reinforced by the coil case made of SUS. This method was also used in the tokamak with an iron core as a current transformer in the early days of development. The modern tokamak does not use this method, as the iron core is replaced by an air core current transformer and leaving no space for a central structure.

The W-7X at IPP Germany was designed in this method as shown in Fig 5.2-1. As shown in Fig 5.2-2, the CFQS was also designed by this method. The modular coils are connected by the connecting beams to suppress movement on the outer side of the device. Due to the low aspect ratio, the CFQS did not have enough space to place the ring in the center. Instead, the center pillars and the H-shaped connecting beams are arranged as a center structure.

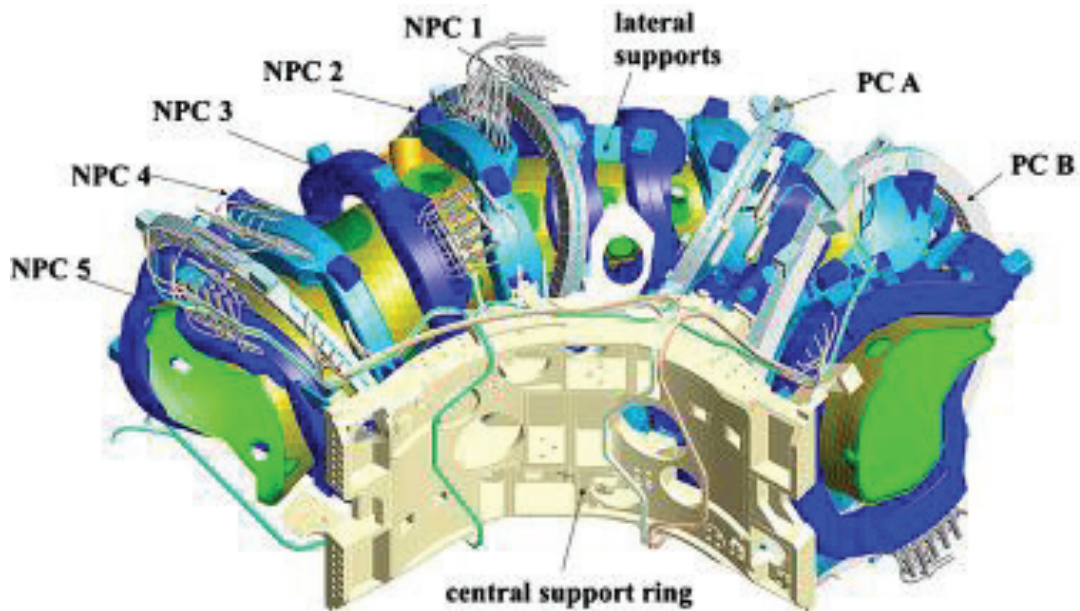


Fig 5.2-1 Support structure for the W-7X at IPP Germany. Reprinted from Fusion engineering and design 84 (2009) pp408-412. Modular coils reinforced with a SUS case are connected to the central support ring.

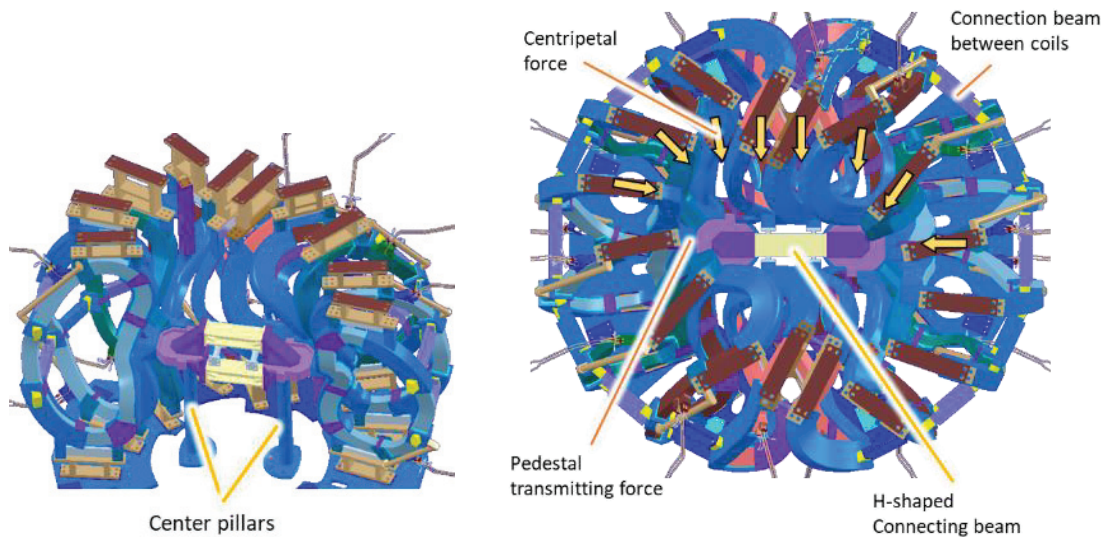


Fig 5.2-2 Support structure for the CFQS. Modular coils reinforced with SUS clamps are connected to the central support structure. The central space is too narrow to place the ring. Instead, the center pillars and the H-shaped connecting beams are arranged as a center structure. The modular coils are connected by the connecting beams to suppress movement on the outer side of the device.

### 5.2.2 Centripetal force support by a donut shape structure

This method is to connect the coils with many metal plates and create a donut shape as a whole. As shown in Fig 5.2-3, the LHD at NIFS Japan was designed in this method. As shown in Fig 5.2-4, the structure of the NCSX was also a type of this method. The method is very robust and may be applicable even for stronger magnetic fields but has the disadvantage of a large amount of structure and difficult final assembly. We considered a design to support the CFQS coil using this method but gave up it because we could not get a large port and the procedure for assembling the whole was difficult.

As shown in Fig 5.2-5, a design that connects adjacent coils with boards is other type of this method. Due to the complex coil geometry, the CFQS is difficult to connect all coils together. Therefore, we designed the CFQS with connection beams added where the coils were close to each other and did not interfere with the port.



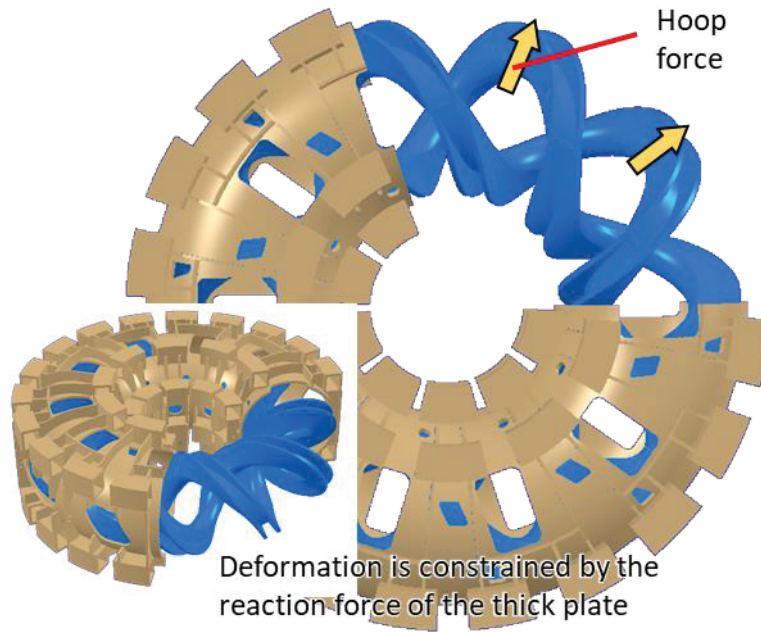


Fig 5.2-3 Support structure for the LHD. A hoop force component is added to the helical coils. In order to suppress the deformation caused by it, the donut shape is made with a thick plate. It is called an electromagnetic force support structure.

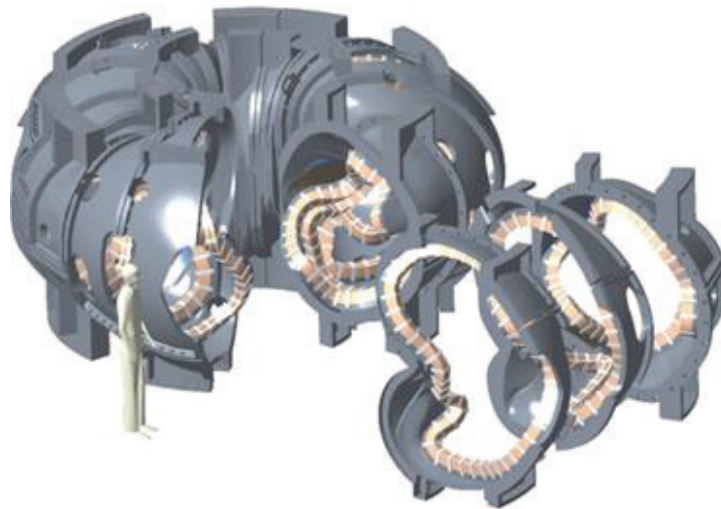


Fig 5.2-4 Support structure for the NCSX planned at PPPL USA. A segmented electromagnetic force support structure is designed. Modular coils are wound inside the segments each. Connecting the segments results in a donut structure. We considered a design to support the CFQS coil using this method but gave up it because we could not get a large port and the procedure for assembling the whole was difficult.



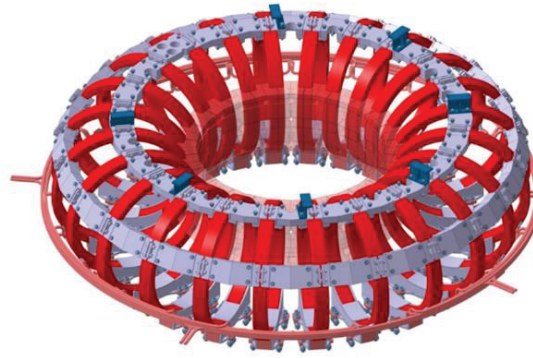


Fig 5.2-5 Support structure for the KTX. Reprinted from a material in 17<sup>th</sup> RFP workshop, Hefei, China (2015). A centripetal force component is added to the toroidal field coils. In order to suppress the deformation caused by it, a donut shape is made by connecting the coils together with many boards. Due to the complex coil geometry, the CFQS is difficult to connect the coils together. Therefore, we designed the CFQS with connection beams added where the coils were close to each other and did not interfere with the port.

### 5.2.3 Supporting centripetal force by the wedge effect

Modern tokamak has a center solenoid for the Joule heating, which makes it difficult to place the central structure in the center of the device. Instead, it has become common to design wedge structures to receive the centripetal force, as shown in Fig 5.2-6. In the case of tokamak, it is known that disruption may create enormous forces on the coil. In order to prevent the coils from overturning, it is standard to connect the coils with shear plates. Due to the complex coil geometry, the CFQS is difficult to fabricate into a wedge structure. The connection beams between coils of the CFQS are not strong, but they also has a function as a shear plate to prevent tilting.

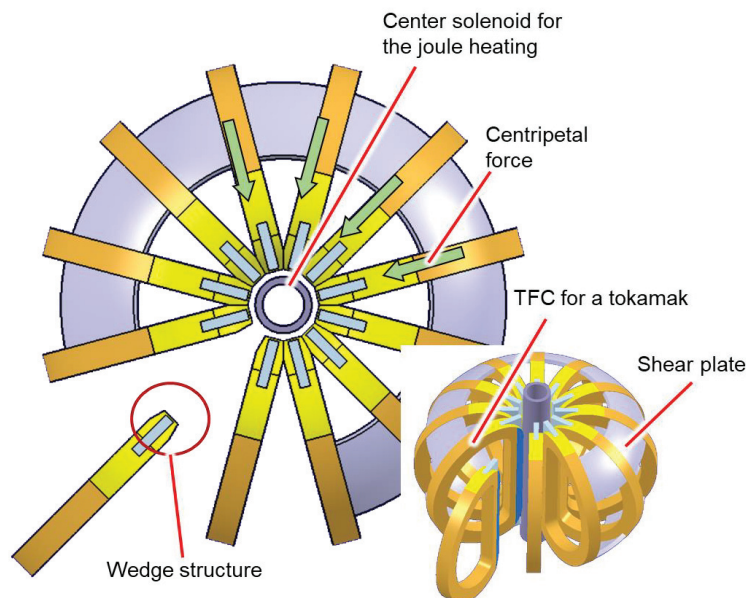


Fig 5.2-6 Support structure for the modern tokamak. Adjacent coils are contacted and supported by the wedge effect. In order to prevent the coils from overturning due to the enormous force, it is common to connect the coils with shear plates. Due to the complex coil geometry, the CFQS is difficult to fabricate into a wedge structure.

NIFS-SWJTU JOINT PROJECT FOR CFQS  
~PHYSICS AND ENGINEERING DESIGN~

VER. 5.1

2023. AUG.

APPENDIX-A5 (PJ)

~RELATED PROJECT~

CFQS Team



*NIFS; National Institute for Fusion Science*

*SWJTU; Institute of Fusion Science, School of Physical Science and Technology, Southwest Jiaotong University*

*Hefei Keye; Hefei Keye Electrical Physical Equipment Manufacturing Co., Ltd*

## Table of Contents

1	Compact helical system CHS.....	3
1.1	Layout of torus hall for the CHS .....	3
1.2	Power system for the CHS .....	5
1.3	Vacuum pumping system for the CHS.....	7
1.4	NBI system for the CHS .....	10
1.5	ECRH system for the CHS.....	15
1.6	Power supply to bake vacuum vessel for the CHS.....	19
1.7	Cooling water system for the CHS.....	20
1.8	Plasma diagnostic system for the CHS .....	21
2	Low aspect ratio RFP RELAX.....	22
2.1	Description of RELAX machine .....	22
2.2	3D tomography from soft X-rays through multi-pinhole disk attached to single view port. ....	22
2.2.1	Principle of 3D tomography .....	22
2.2.2	Numerical trial .....	23
3	Plasma generating device SSHD.....	25
3.1	History of the SSHD .....	25
3.2	Components of the SSHD .....	26
3.3	Plasma measurement with a Langmuir probe .....	28

## 1 Compact helical system CHS

### 1.1 Layout of torus hall for the CHS

The CFQS laboratory will be designed with reference to the structure of the development and experiment building with the CHS installed in NIFS. For reference, the layout of the CHS laboratory is shown below.

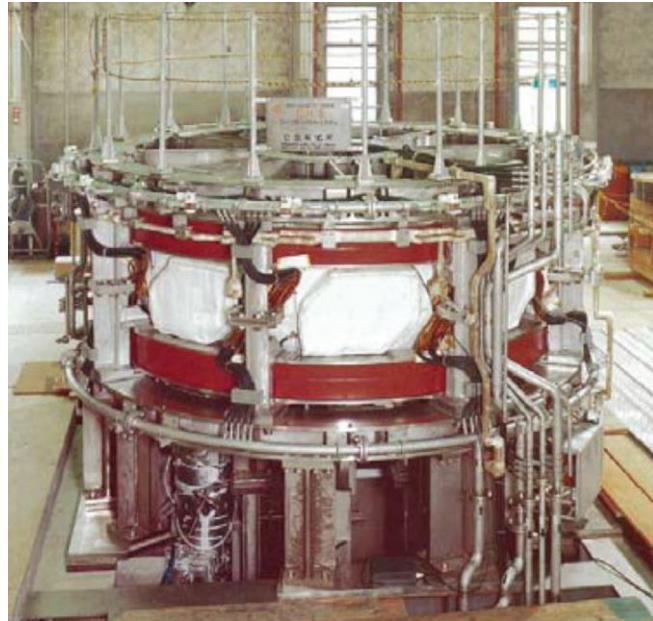


Fig 1.1-1 Body of the CHS (installed in Nagoya University at 1987).

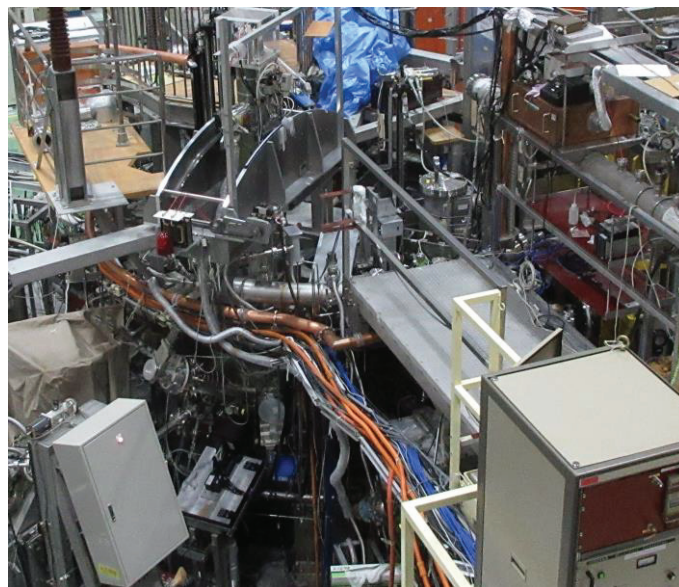


Fig 1.1-2 Body and equipment's of the CHS (installed in NIFS at 2000).

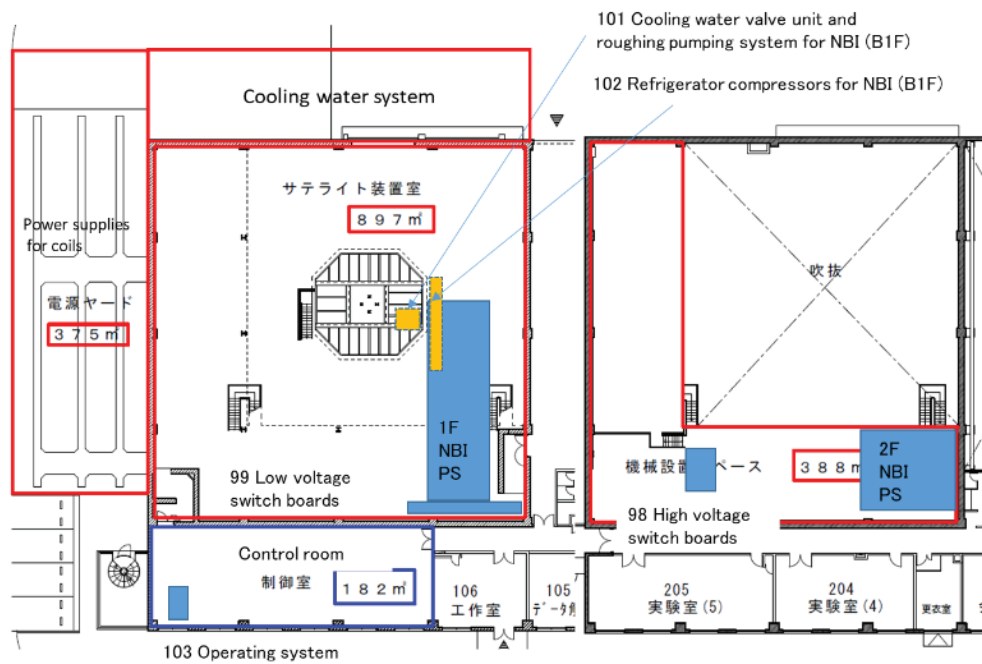


Fig 1.1-3 Layout of torus hall for the CHS in NIFS with the NBI system.

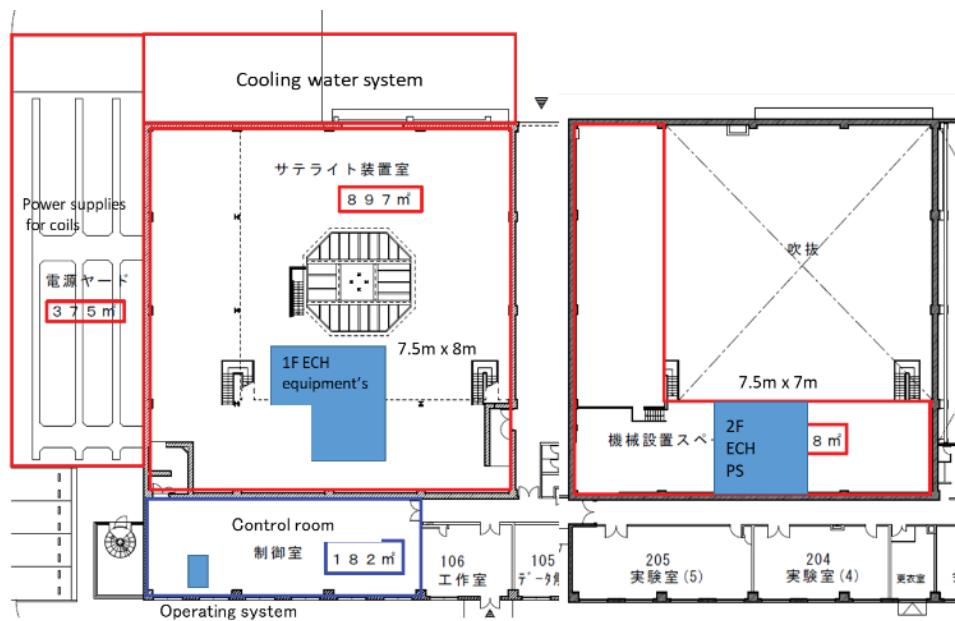


Fig 1.1-4 Layout of torus hall for the CHS in NIFS with the ECRH system.

## 1.2 Power system for the CHS

It should be noted that the commercial voltage is different in Japan and China as shown in Table 1.2-1. To transfer the CHS equipment to CFQS, transformers will be needed to adjust for voltage differences. Table 1.2-2 shows a list of low-voltage power board related to main equipment relocating from the CHS to the CFQS. It is necessary to prepare a power board to supply these voltages with the CFQS. Fig 1.2-1 shows the one-line diagram of the CHS power supply system.

Table 1.2-1 Difference of power environment.

	Frequency	High voltage	Low voltage 1Φ	Low voltage 3Φ
NIFS	60 (West Japan)	6.6 kV	100 V	200 V
China	50	10 kV	220 V	380 V

Table 1.2-2 Load list of low voltage power board KIT-1A-13 for the CHS in NIFS

Row	No	Voltage(V)	System	Use	Load(kVA)
1	u1	200	ECRH	Charger	24
	u4	200	NBI-2	GTO PS	8
	u5	100	ECRH	1Φ SWB	12
	R1	100	NBI-2	AVP CB	1.6
	R2	100	NBI-2	BLA CB	1.6
	R3	100	NBI-2	TCB	1.6
	L9	100	ECRH	CTRL	1.6
	R9	100	ECRH	LN2	0.8
2	R1	200	NBI-2	DCL	16
	R2	200	NBI-2	GTO LV	16
	R3	200	NBI-2	BMAG	16
	R4	200	NBI-2	AVP	4.8
	R5	200	NBI-2	SCR CB	4.8
3	L6	200	NBI-2	DCL CB	8
4	L1	200	NBI-2	SB Gas	8
	R1	200	NBI-2	REFCR	8
	L2	200	NBI-2	REFCR	8
	R2	200	NBI-2	REFCR	8
	L3	200	NBI-2	REFCR	8
	R3	200	NBI-2	REFCR	8
	L4	200	NBI-2	REFCR	8
	R4	200	NBI-2	REFCR	8
	L5	200	NBI-2	REFCR	8
	R5	200	NBI-2	AVP	8
5	L5	200	ECRH	COOL OIL	5.28
	B1	200	ECRH	3Φ SWB	35.2



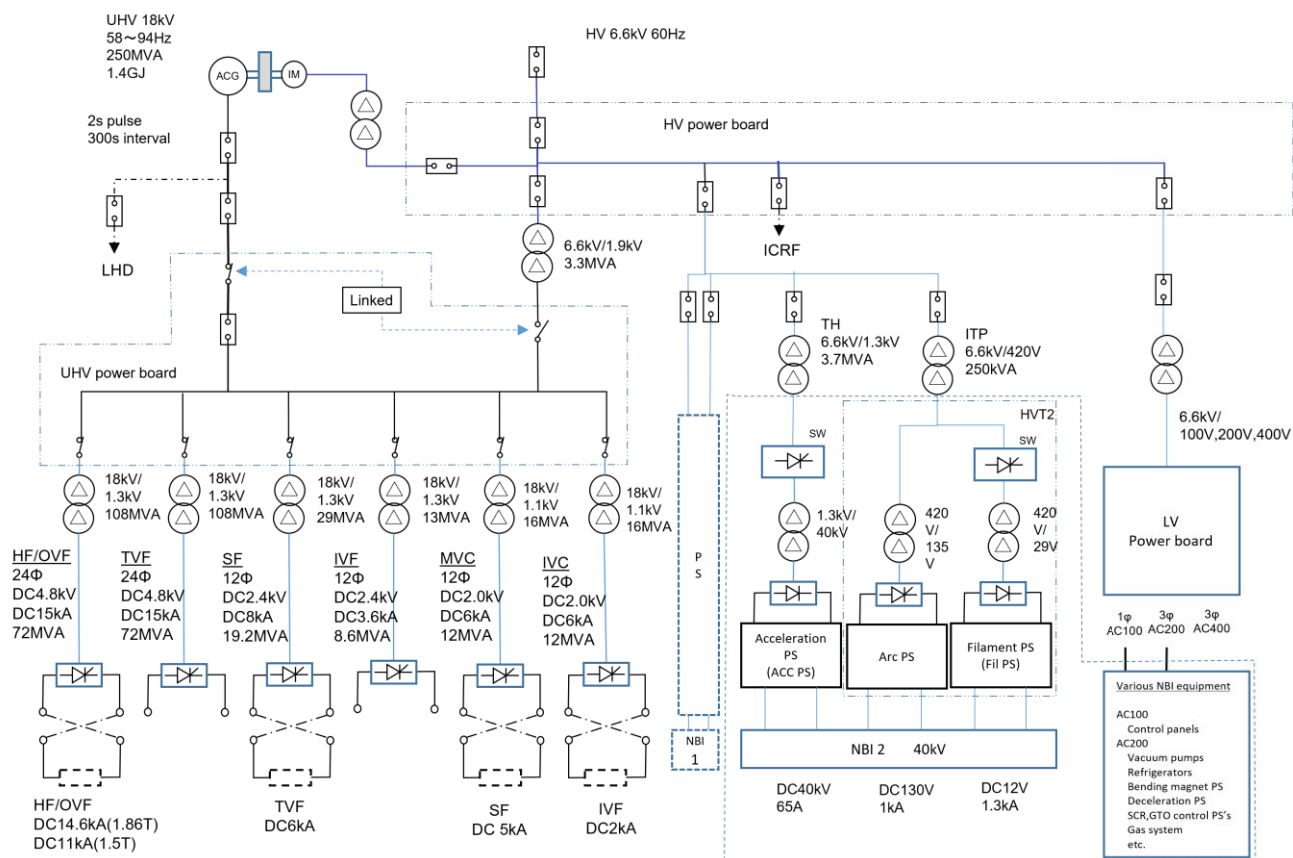


Fig 1.2-1 One line diagram of power supply system for the CHS in NIFS.

### 1.3 Vacuum pumping system for the CHS

We plan to transfer the vacuum pumping unit for CHS in NIFS to CFQS. Their main specification is shown below. To use this unit with CFQS, modification adding some parts will be required.

Table 1.3-1 Main parameters for the vacuum pumping system for the CHS.

No	Item	Contents
1	Input power supply	AC 220 V, 50/60 Hz, 1Φ/3Φ, 20 A (at startup)
2	Cooling water	8 kgf/cm <sup>2</sup> G, 5 ℓ/min or more, 27 °C or less
3	Compressed air	7 kgf/cm <sup>2</sup> G, 20 Nm <sup>3</sup> /h
4	Turbo molecular pump (TMP)	Number of units 2 Model; TH1502VW (Osaka Vacuum Ltd.) Exhaust speed; 1500 ℓ/s Ultimate pressure; $1 \times 10^{-7}$ Pa Cooling method; water cooling Allowable temperature; 120 °C
5	Rotary pump (RP)	Number of units 1 Model; T2063A (Adixen/Alcatel) Exhaust speed; 1420 ℓ/min(60Hz) 1180 ℓ/min(50Hz)

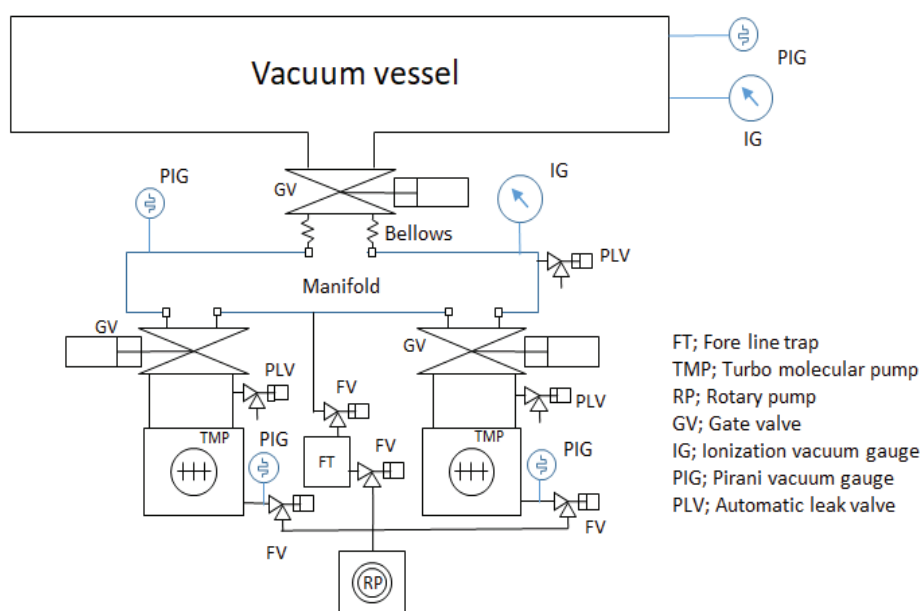
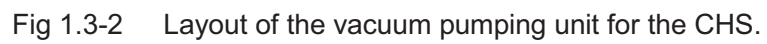


Fig 1.3-1 System diagram of vacuum pumping unit.



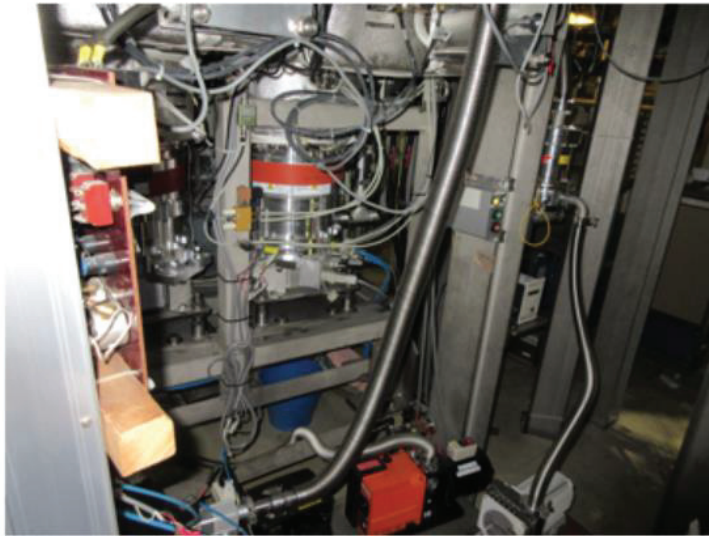
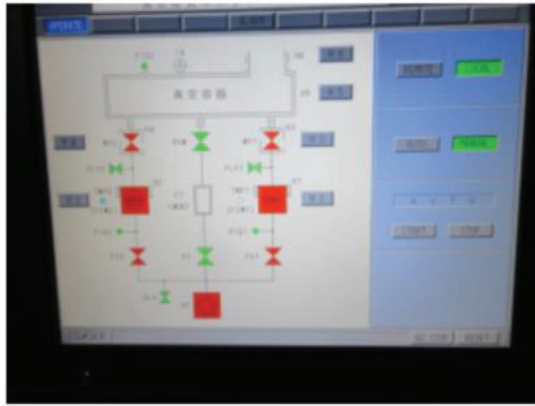


Fig 1.3-3 Picture of vacuum pumping system.

#### 1.4 NBI system for the CHS

There is a plan to transfer the NBI system from the CHS to the CFQS. A configuration of the NBI and power supply for the CHS is shown below.

Table 1.4-1 Power capacity of the CHS NBI-2 system.

No	Item	Voltage	Output Current	Capacity of input transformer
1	Acceleration power supply	AC6.6 kV/DC 40 KV	65 A	3.7 MVA
2	Arc power supply	AC6.6 kV/DC 135 V	1 kA	250 kVA
3	Filament power supply	AC6.6 kV/DC 12 V	1.32 kA	
4	Deceleration power supply	AC 200 V		26 kVA
5	Bending magnet power supply	AC 200 V		20 kVA
6	Refrigerator for cryogenic pump	AC 200 V		64 kVA
7	Low voltage 1Φ (Others)	AC 100 V		4.8 kVA
8	Low voltage 3Φ (Others)	AC 200 V		50 kVA

Table 1.4-2 Technical specifications of the CHS NBI-2 system.

No	Item	Specification
1	Beam specie	H/D
2	Beam energy	20-40 kV
3	Port-through power	1 MW
4	Beam duration	1 s
5	Ion source	Filament-arc discharge with cusp magnets
6	Beam acceleration area	φ 300 mm
7	Aperture radius	φ 5 mm
8	Current density	250 mA/cm <sup>2</sup>
9	Beam optics	Conversing beam via offset aperture
10	Focal length of the beam	3.0 m
11	Beam divergence angle	1 degree
12	Diameter of drift tube	φ 250 mm
13	Neutralization	Gas cell
14	Main vacuum pump	Cryosorption panel (326 m <sup>3</sup> /s)
15	Diagnostics	Calorimetric beam profile measurement

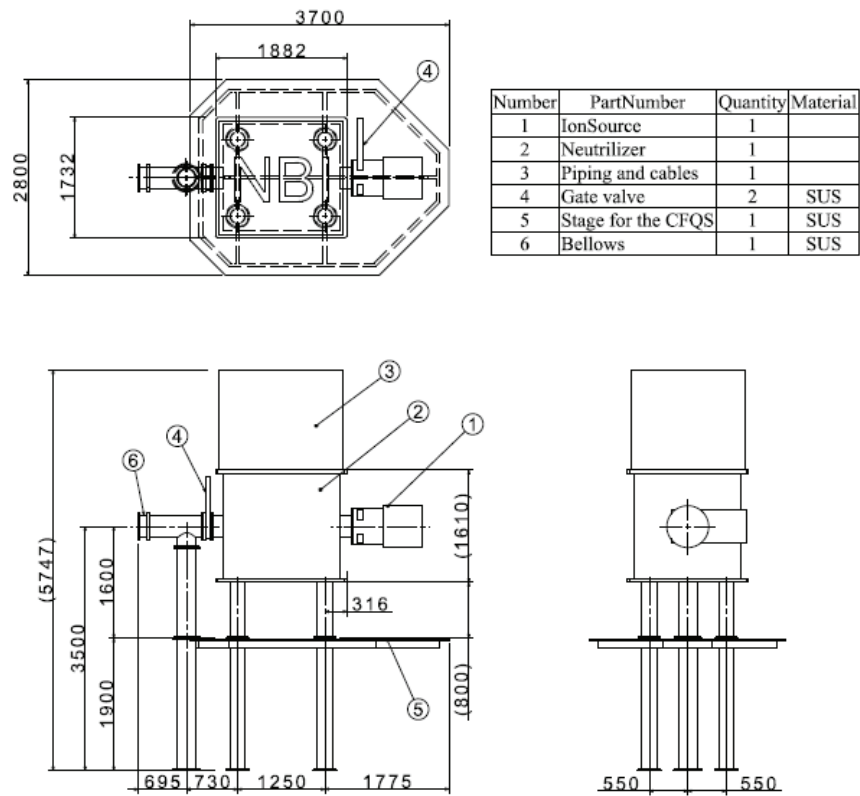


Fig 1.4-1 Ion source of the CHS NBI-2 system.



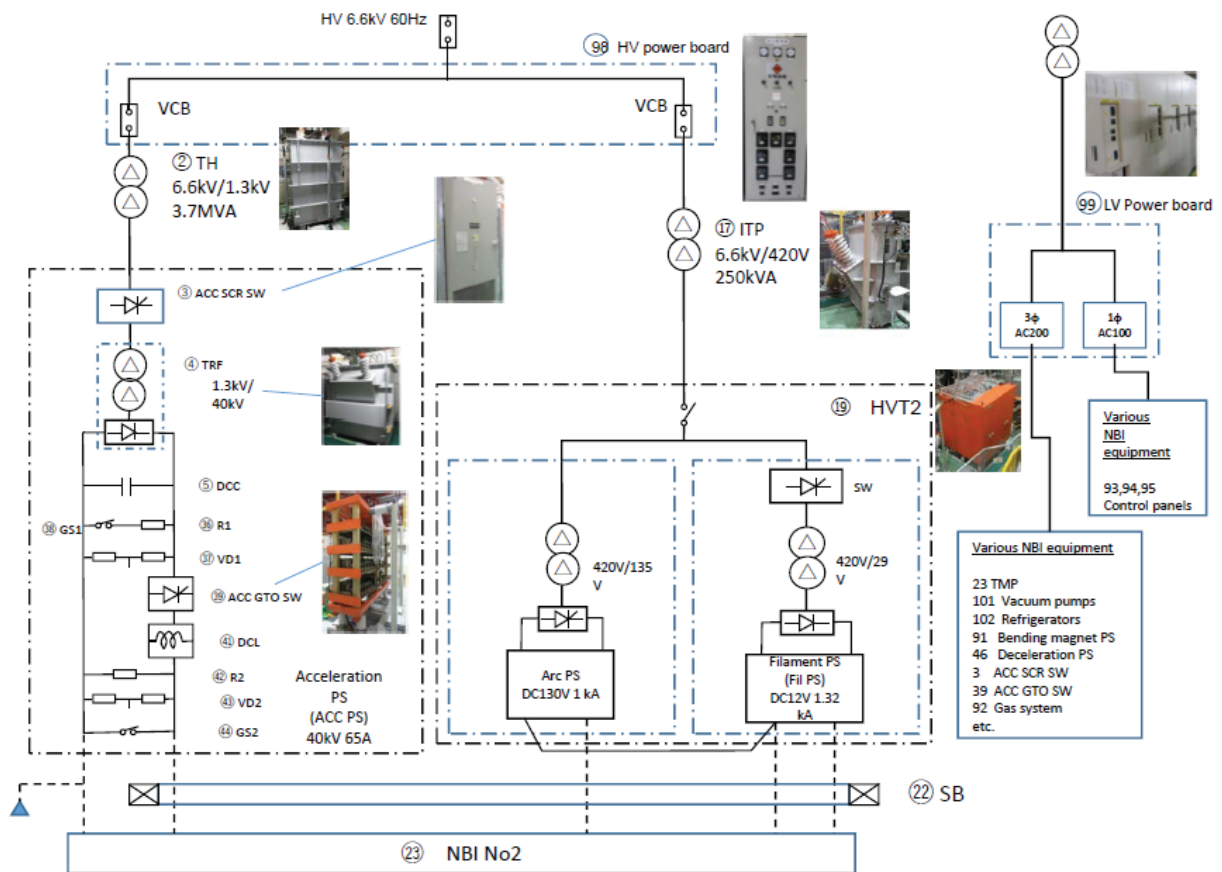


Fig 1.4-2 One-line diagram of the CHS NBI-2 system.

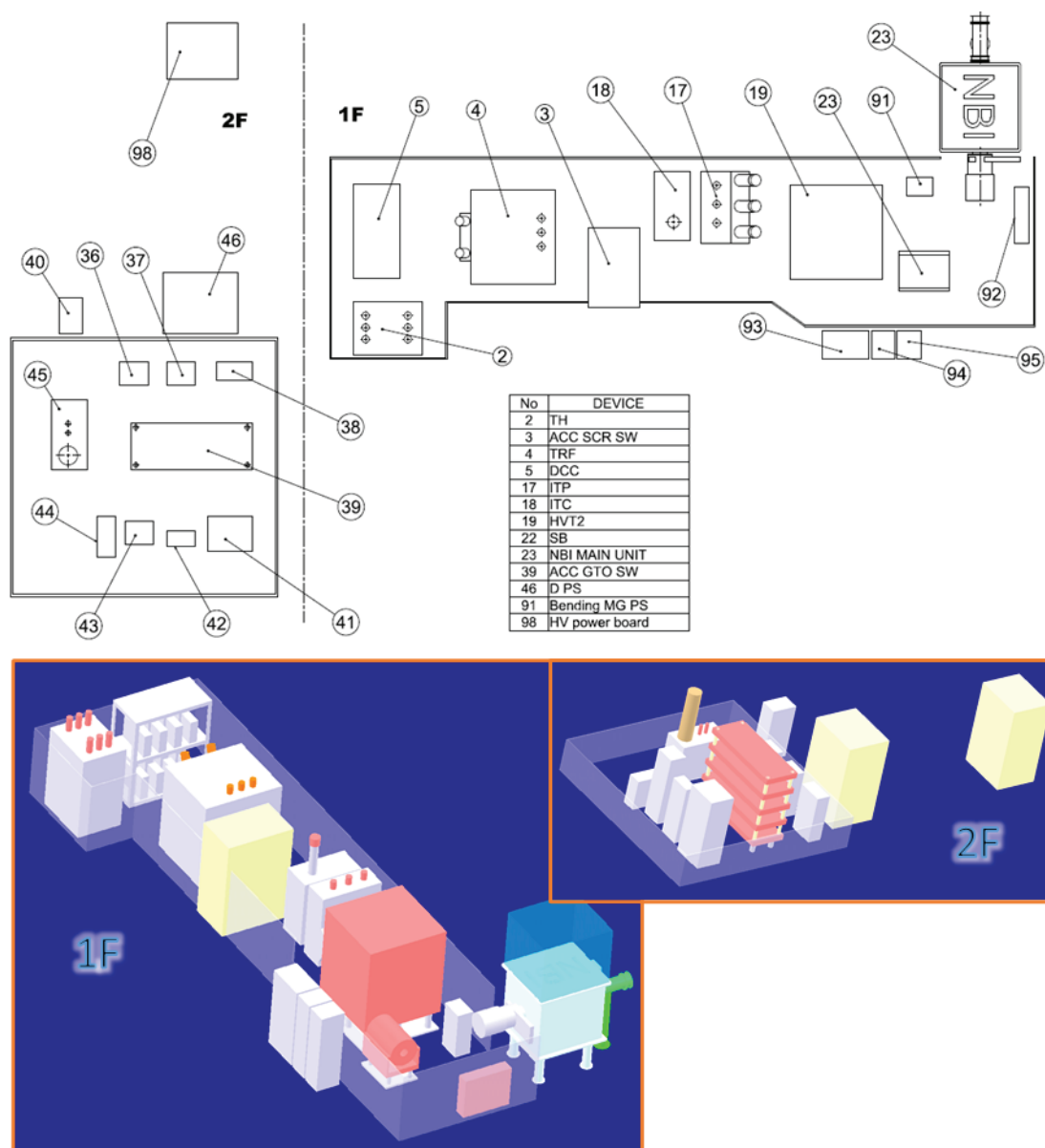


Fig 1.4-3 Layout of the CHS NBI-2 system.

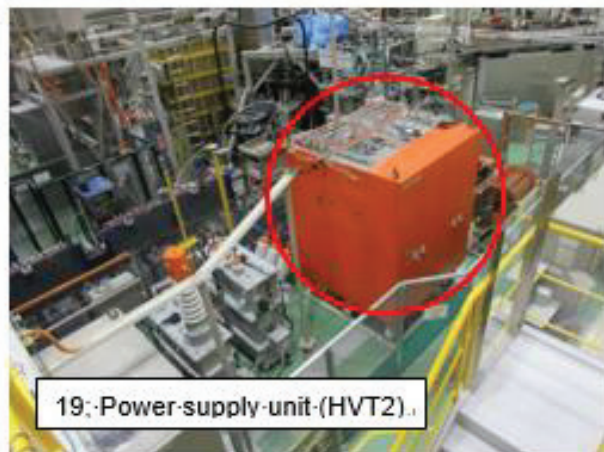
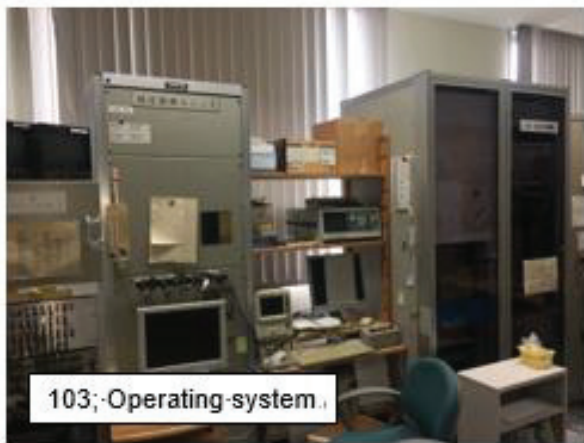


Fig 1.4-4 Picture of main components for the CHS NBI-2 system.

## 1.5 ECRH system for the CHS

There is a plan to transfer the ECRH system from the CHS to the CFQS. However, many parts are obsolete and have not been in operation for a long time and need to be rebuilt for the CFQS. A configuration of the ECRH and power supply for the CHS is shown below.

The EC-waves generated by the gyrotron effectively and locally heat the electrons at a position on the EC-wave beam path where the resonance condition ( $n\omega_{ce} = \omega - k_{\parallel}v_{\parallel}$  and  $\omega_{ce} \equiv eB/m_e$ ) is satisfied. Here, integer  $n$  denotes harmonic number,  $\omega_{ce}$  is electron cyclotron angular frequency,  $e$  is a unit charge of an electron,  $B$  is the strength of magnetic field,  $m_e$  is the mass of an electron with relativistic effect,  $\omega$  is angular frequency of EC-waves, and  $k_{\parallel}$  and  $v_{\parallel}$  are the components of wave number and electron velocity parallel to the magnetic field line, respectively. Applying the frequency of 54.5 GHz, the resonance condition for  $n = 2$  (second harmonic resonance) is satisfied with  $B = 0.97$  T.

In the case of the CHS experiment, the EC-wave power was transmitted from the gyrotron to the CHS vacuum vessel by a quasi-optical transmission line. The transmission line was furnished with focusing and plane mirrors, polarizer mirrors to control transmitted wave's polarization arbitrarily, and vacuum window to keep the vacuum condition in CHS.

By use of the power transmission and injection systems, effective and localized ECRH with power deposition control, electron cyclotron current drive (ECCD), and electron Bernstein wave heating (EBH) will be realized. For that purpose, two dimensionally steerable power injection system with beam focusing was necessary. To realize the power injection system, at least, two mirror antenna system (one is plasma facing 2-D steerable plane mirror, and the other is beam focusing mirror) inside the vacuum vessel was required. The dimensions of the mirrors depend on the focused beam waist size at the plasma core region and the distance between the plasma and the mirrors. The antenna design was optimized under the available circumstance of CHS vacuum vessel design, to realize the beam waist size as small as possible in the plasmas.

Table 1.5-1 Technical specifications of the ECRH for the CHS.

No	Item	Specification
1	Power source	Gyrotron produced by a Russian company, GYCOM
2	Frequency	54.5 GHz
3	Output power	Up to 450 kW
4	Pulse length	0.1 s
5	Resonance condition	1.95 T with fundamental resonance( $n=1$ ) 0.97 T with second harmonic resonance( $n=2$ )
6	Transmission line	Quasi-optical transmission line (Focusing, plane, polarizer, and 2-D steerable mirrors)
7	Magnet	Super conducting magnet with liquid helium replenishment type. It should be replaced to the new one with dedicated refrigerator.
8	Vacuum window	Sapphire window To minimize power reflection at the vacuum window, the thickness of the window $d$ must satisfy a relation: $d = m \lambda_{in}/2$ . Here, $m$ is an integer and $\lambda_{in}$ is wavelength in the window material.

Table 1.5-2 Power supply of the ECRH for the CHS.

No	Item	Specification
1	Type	High voltage capacitor bank with crowbar circuit
2	Charger	Up to 100 kV DC from 200 V AC
3	Capacitor	86 capacitors with 1.5 $\mu$ F each
4	Regulator tube	EIMAC X2062K tetrode tube to supply 70 kV DC. It is old and must be replaced to new one.
5	Ion pumps	DCPS of 3.5kV to keep the vacuum condition inside the gyrotron and the regulator tube
6	Heaters	ACPS of 150 V to generate thermal electron emission at gyrotron cathode
7	Crowbar circuit	High voltage PS used for crowbar-drive works at 8 kV DC
8	Super conducting magnet	SCM requires DCPS of 2 V/33 A

Table 1.5-3 Pure water-cooling system of the ECRH for the CHS.

No	Item	Specification
1	Purpose	Removing heat load on the gyrotron and the regulator tube
2	Cooling collector	100 L/min
3	Cooling body	6 L/min
4	Cooling vacuum window	9 L/min
5	Cooling oil tank	6 L/min
6	Cooling the regulator tube	120 L/min
7	Pressure	0.2 MPa at inlet

### Power Supply for Gyrotrons

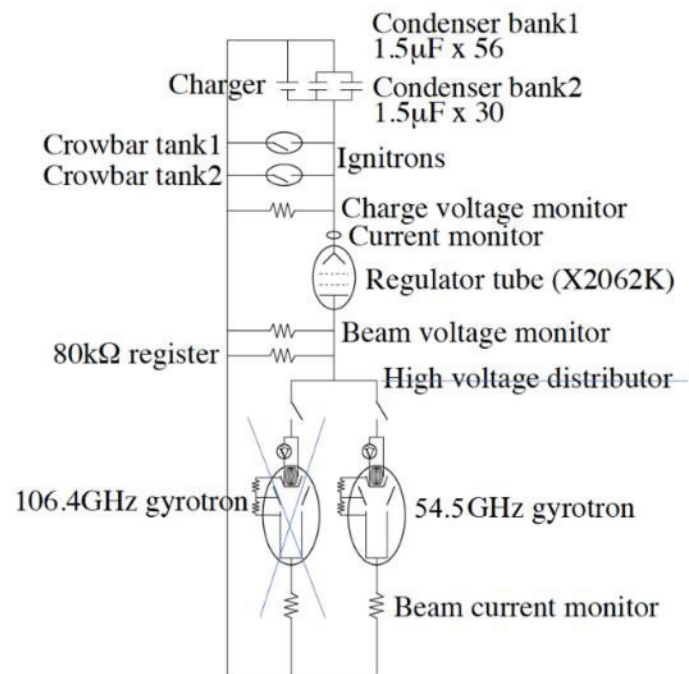


Fig 1.5-1 One-line diagram of the ECRH for the CHS.





Fig 1.5-2 54.5 GHz gyrotron in the ECRH system for the CHS.

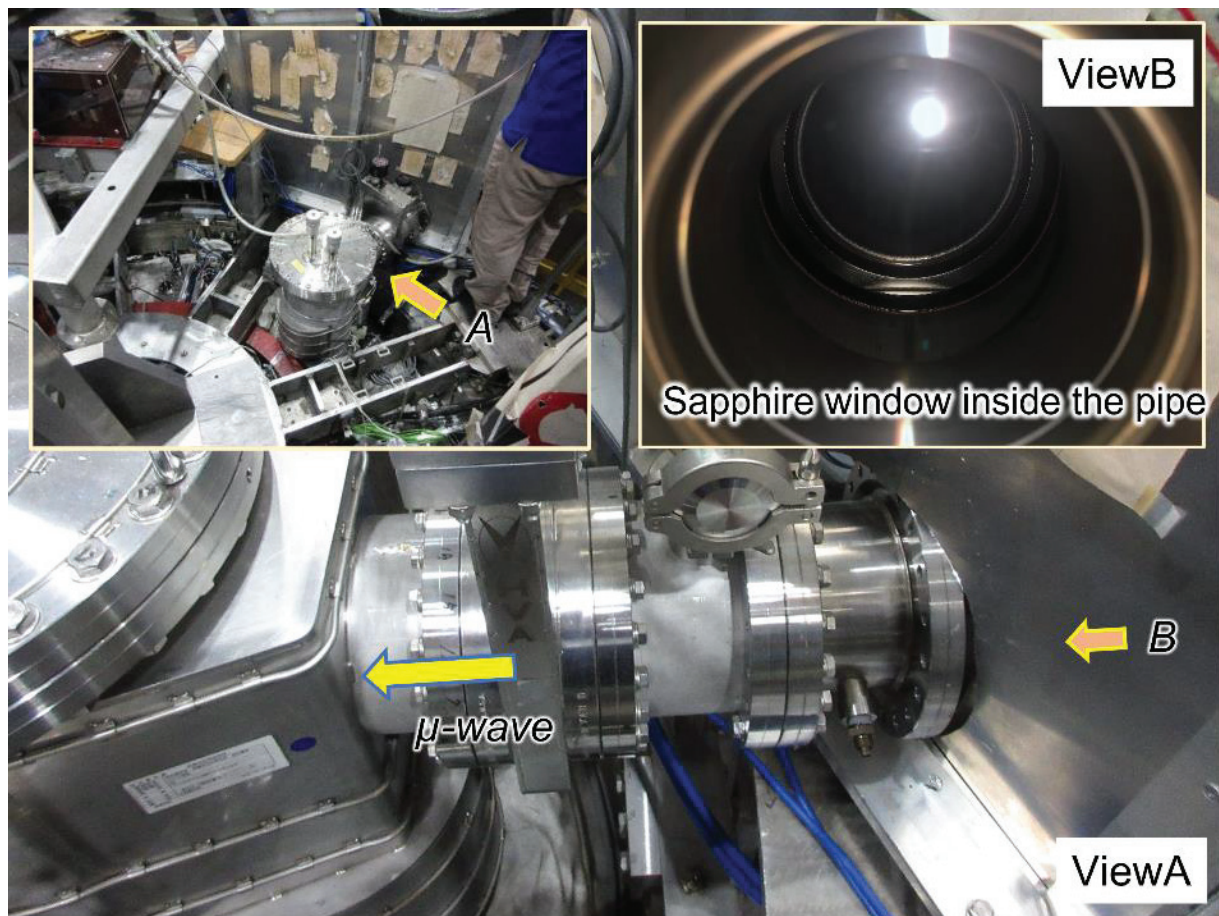


Fig 1.5-3 ECRH power injection mirror antenna vacuum vessel with sapphire window for the CHS.



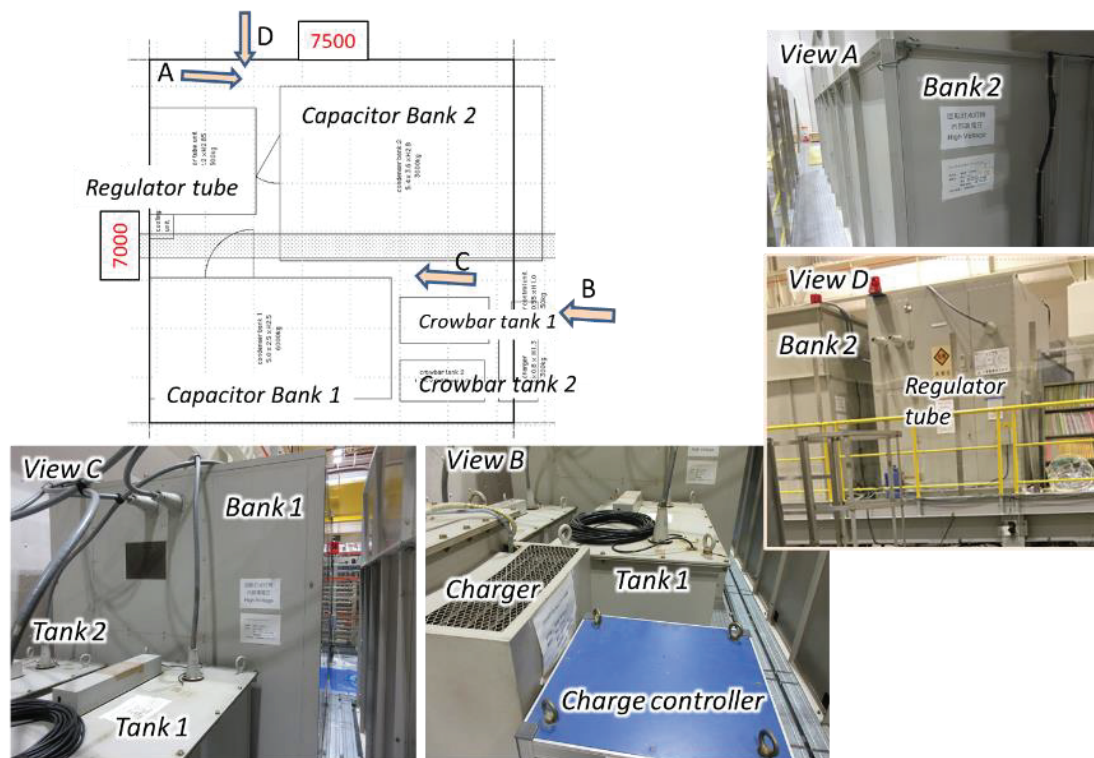


Fig 1.5-4 Power supply for the gyrotron in the ECRH system for the CHS.

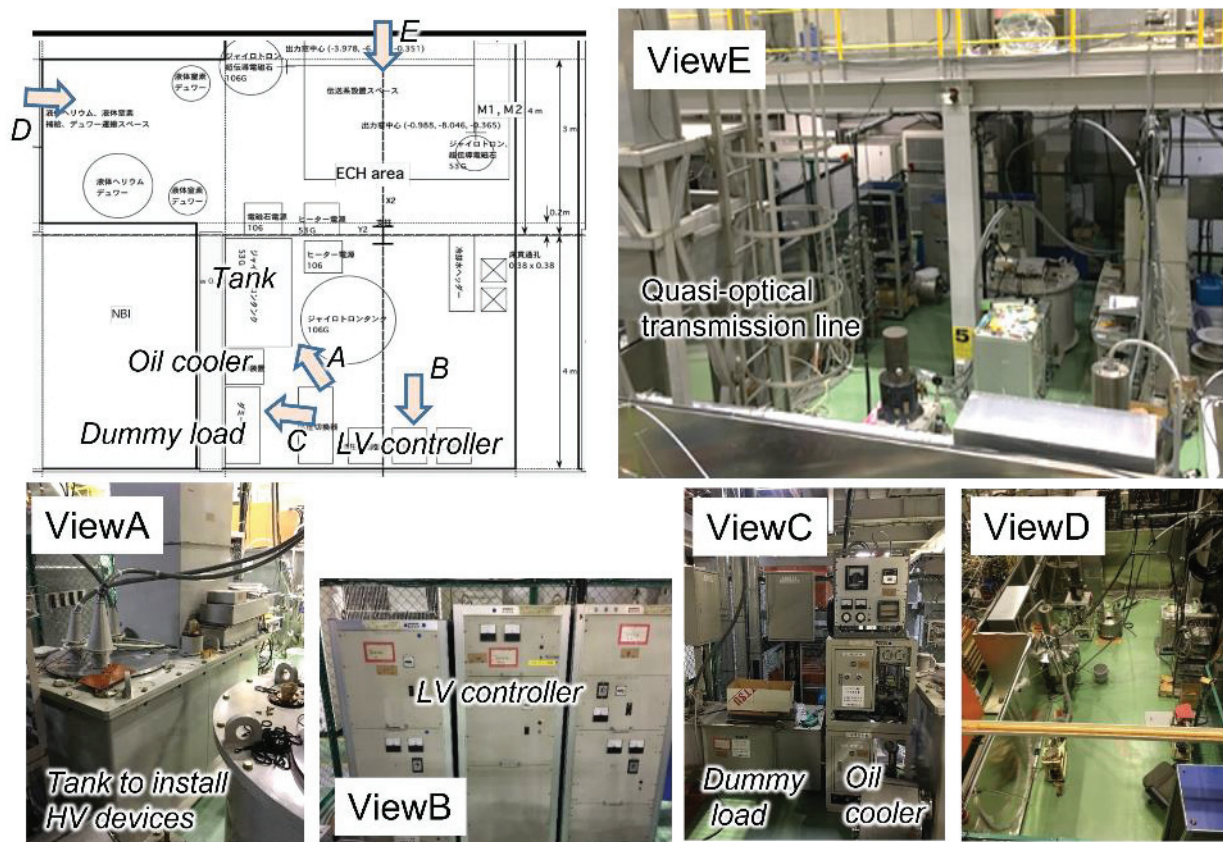


Fig 1.5-5 Some equipments in the ECRH system for the CHS.

## 1.6 Power supply to bake vacuum vessel for the CHS.

The following figure shows the configuration of the baking power supply for the CHS. A similar system will be required for the CFQS.



Fig 1.6-1 Power supply to bake the vacuum vessel for the CHS.

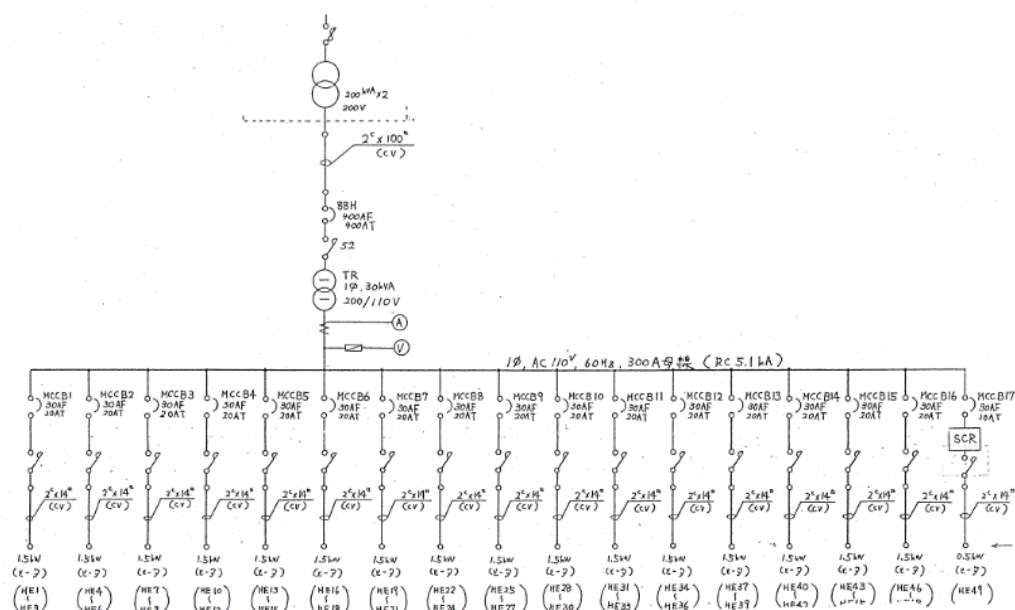


Fig 1.6-2 One line diagram of baking power supply for the CHS.



## 1.7 Cooling water system for the CHS

The following figure shows the configuration of the water-cooling system for the CHS. The CFQS will also require a similar but smaller system.

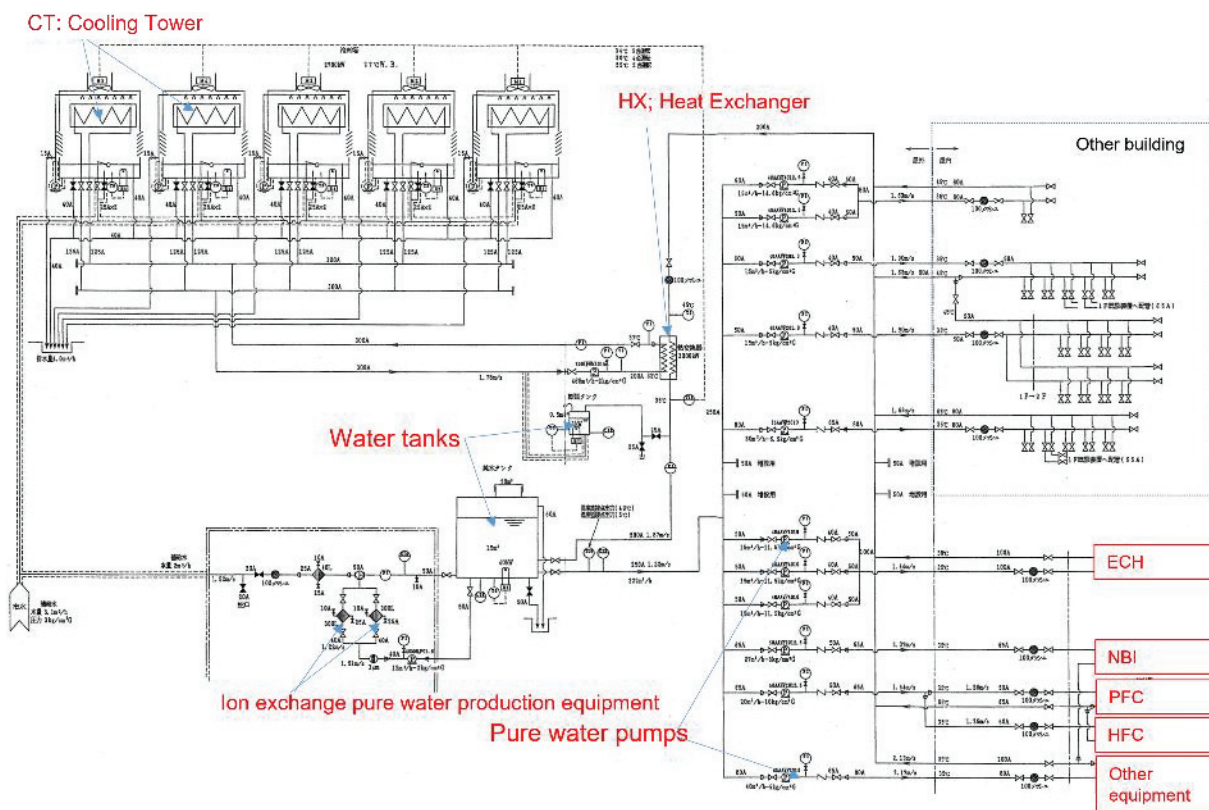


Fig 1.7-1 Cooling water system diagram for the CHS.

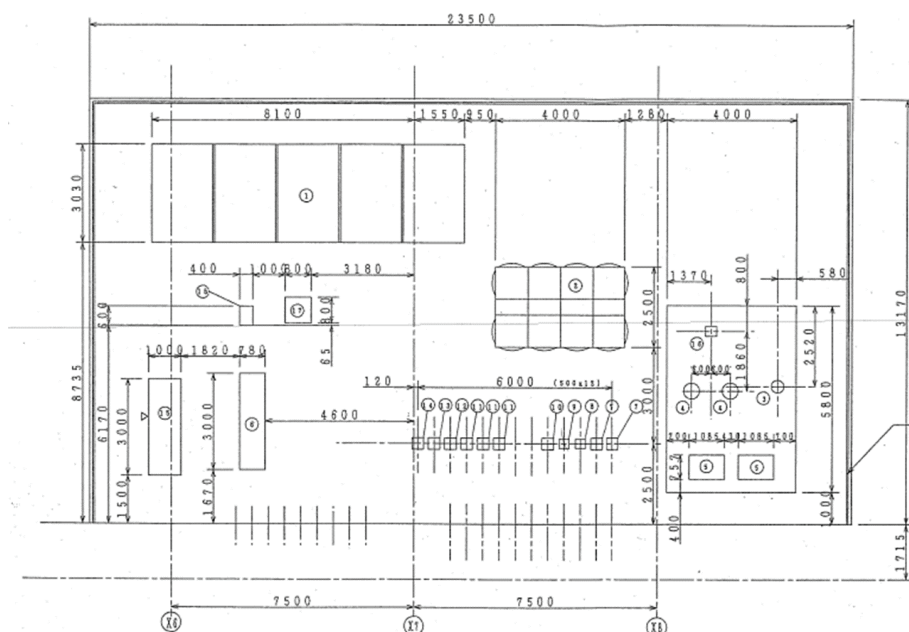


Fig 1.7-2 Layout of cooling water system for the CHS.

## 1.8 Plasma diagnostic system for the CHS

The following figures show the picture of some plasma diagnostic system for the CHS. Similar systems may be required for the CFQS.

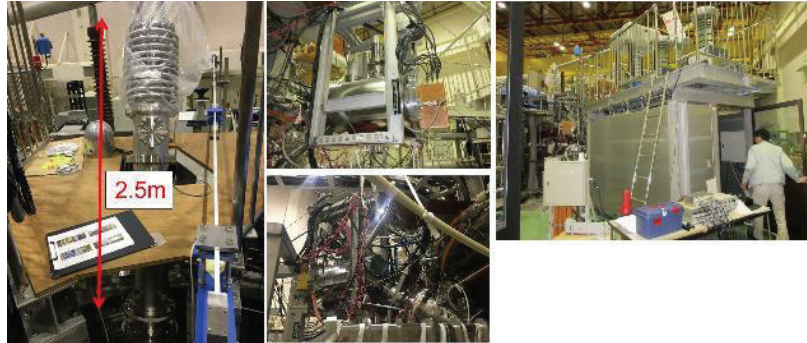


Fig 1.8-1 Heavy ion beam probe to measure turbulence etc. for the CHS.

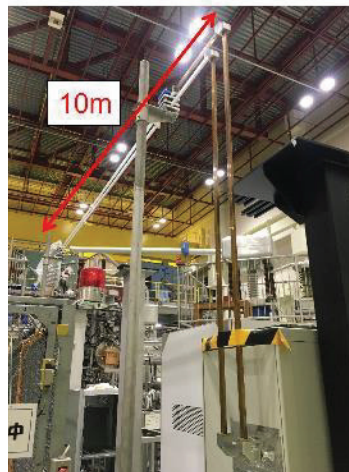


Fig 1.8-2 Microwave interferometer to measure electron density for the CHS.

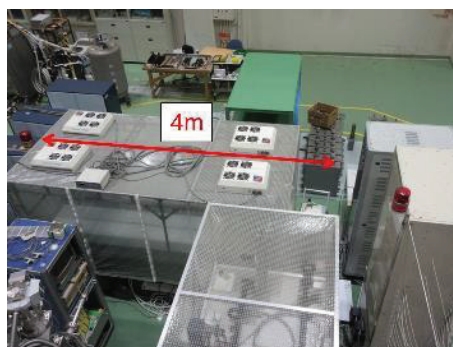


Fig 1.8-3 Thomson scattering system to measure electron temperature for the CHS.

## 2 Low aspect ratio RFP RELAX

### 2.1 Description of RELAX machine

The reversed-field pinch (RFP) is one of the magnetic confinement systems for fusion plasma. Recent progress has led to new concepts for the RFP configurations which are free from magnetic chaos caused by the interaction of tearing modes. One is the quasi-single-helicity (QSH) state where single mode grows to dominate a discharge [2-1]. RELAX of Kyoto institute of technology is an RFP machine ( $R=0.5\text{m}/a=0.25\text{m}$ :  $A=R/a=2$ ) to explore the plasma characteristics in low- $A$  regime [2-2]. In shallow reversal plasmas, the discharge tends to transit between toroidal symmetry state and the QSH state [2-3]. To obtain three-dimensional (3D) structure in such transition, a method of distinguishing the 3D soft X-ray emissivity profile from an image obtained from one view port of limited view area has been developed [2-4].

### 2.2 3D tomography from soft X-rays through multi-pinhole disk attached to single view port.

#### 2.2.1 Principle of 3D tomography

We propose a new method for obtaining three dimensional (3D) tomography of partial toroidal plasmas without assumptions about the magnetic surfaces using a multi-pinhole disk attached to a single viewport. Fig 2.2-1 shows a schematic of the proposed method. The multi-pinhole disk is a disk with several pinholes. All pinholes of the multi-pinhole disk have a finite parallax. Therefore, X-rays emitted from various locations pass out through pinholes and arrives at the screen emerging as an independent 2D image on the corresponding area of the screen. Dividing the 3D space where the plasma exists in the chamber into many small voxels, the emissivity profile of X-ray  $J(x, y, z)$  is denoted as column vector  $J$ . Similarly, the image is also divided into small pixels and denoted as a vector  $I$ . Using  $P$  is a weight coefficient matrix that represents the relationship between pixels and voxels and is determined by the geometric configuration of the device, the obtained image is expressed as  $I = PJ$ .

Assuming that  $J$  consists of a sum of series in terms of orthogonal basis functions as:

$$J = Fs ,$$

where each element of  $s$  and each column vector of  $F$  corresponds to coefficients and basis vectors, respectively. Conversely, by introducing another matrix  $A$  that equal  $PF$ ,  $I$  is consequently expressed by using  $s$  as:

$$I = As .$$

By applying an inversion algorithm such as the least square method to an obtained image, the 3D profile of the emissivity of X-rays  $J$  can be calculated.

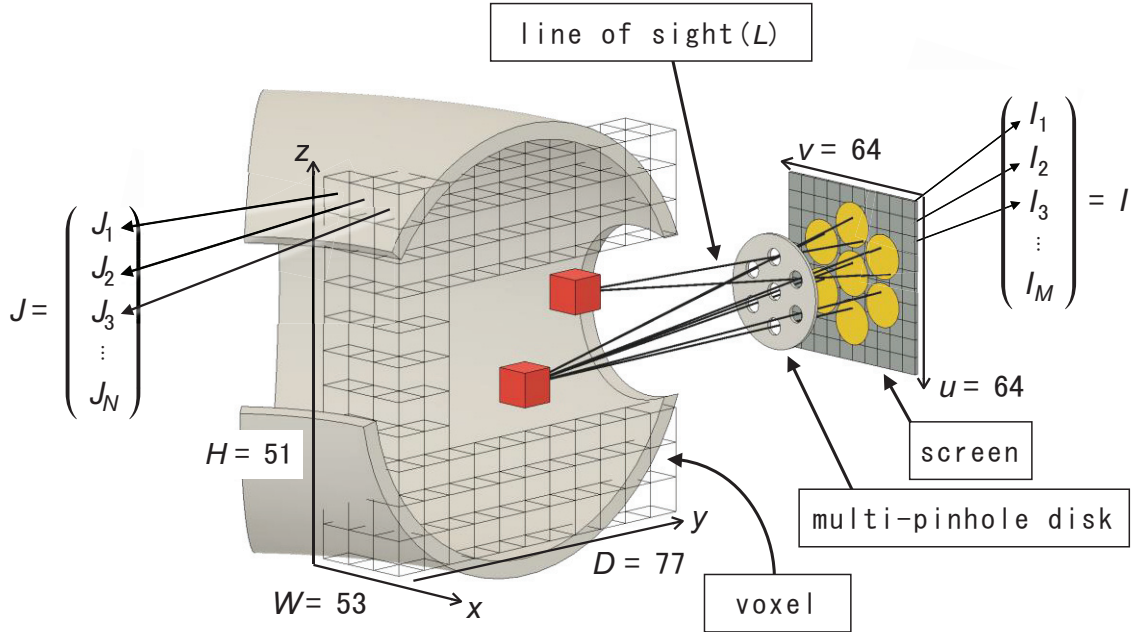


Fig 2.2-1 Schematic of the proposed method for obtaining emissivity profile in a toroidal plasma using a multi-pinhole disk and a screen. The cartesian  $(x, y, z)$  and image  $(u, v)$  coordinates are set on the plasma and the screen, respectively. (Reprinted from [2-4])

### 2.2.2 Numerical trial

We numerically tested whether a test toroidal plasma formed in the RELAX machine could be reconstructed successfully. The test toroidal plasma is asymmetric and has a bean-shaped cross-section with a helical pitch of  $\pi/2$  in the toroidal direction, as shown in Fig 2.2-2(a) and (b) and we arrange seven pinholes on the multi-pinhole disk. In this case, the set of seven images in Fig 2.2-2 (c) is the result. By applying the inversion algorithm to the obtained images,  $J(x, y, z)$  can be inferred as shown in Fig 2.2-2 (d) and (e). Good agreement is observed between the test plasma and the one inferred in Fig 2.2-2 (a) and (d) as well as between Fig 2.2-2 (b) and (e).



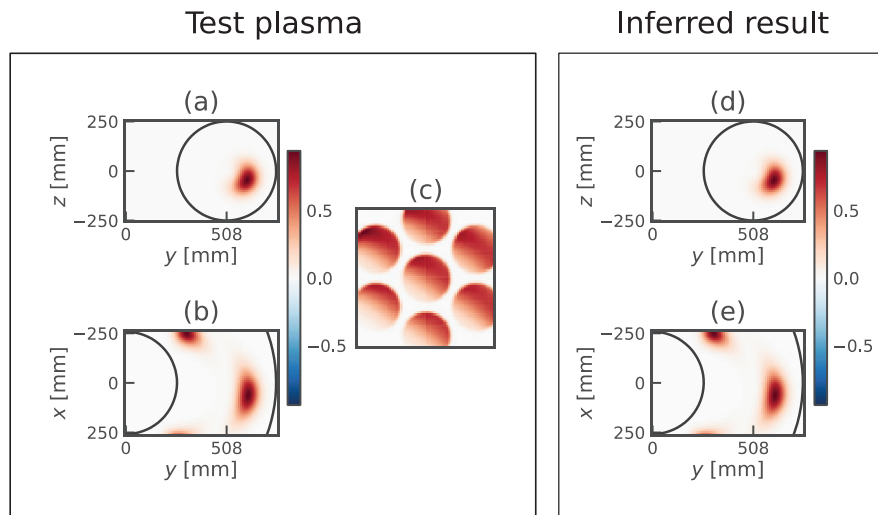


Fig 2.2-2 Comparison of emissivity profile of Test plasma and reconstructed profile. A test spatial profile of emissivity of a toroidal plasma and the seven images obtained in the "Test plasma" window. Conversely, the profile in the "Inferred result" window is a reconstructed result. (Reprinted from [2-4])

## References

- [2-1] R. Lorenzini *et al.*, Nature Physics **5** (2009) 570.
- [2-2] S. Masamune *et al.*, Proc. of the 26th IAEA Fusion Conference EX/P5-22 (2016).
- [2-3] K. Oki *et al.*, Plasma and Fusion Research **7** (2012) 1402028.
- [2-4] S. Inagaki *et al.*, submitted to Opti. Express.

### 3 Plasma generating device SSHD

#### 3.1 History of the SSHD

SSHD is a plasma generating device made at Kyoto University in 1980's as an exhibit and educational tool. It was transferred in 2019 from Kyoto University to NIFS and in 2021 from NIFS to SWJTU. It was used to train technical staff with little experience in handling plasma generators.

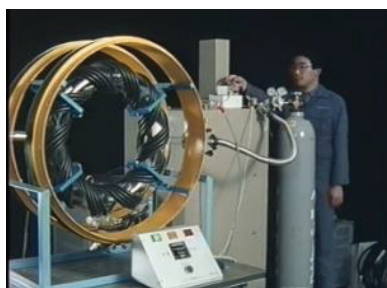


Fig 3.1-1 Demonstration of the SSHD, which was developed for exhibition and education in 1980's at Kyoto University.



Fig 3.1-2 Redevelopment of the SSHD at NIFS. The SSHD was transferred to NIFS in 2019 for the purpose of training technical staff on the handling of plasma equipment.

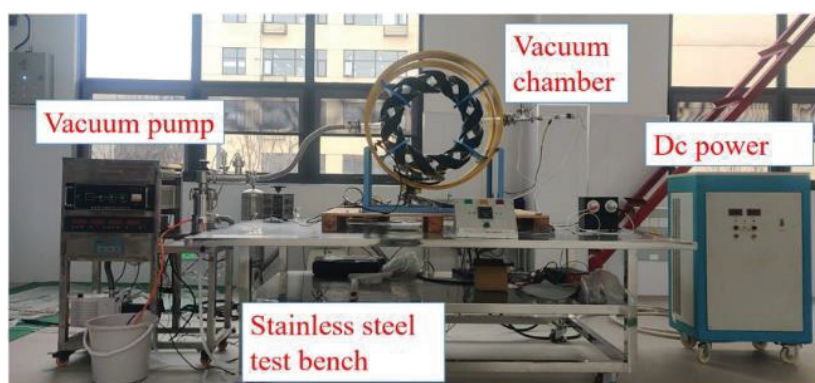


Fig 3.1-3 Redevelopment of the SSHD at SWJTU. The SSHD was transferred to SWJTU in 2021 for the purpose of training technical staff on the handling of plasma equipment.

### 3.2 Components of the SSHD

Main specifications of the SSHD are summarized in Table 3.2-1. Fig 3.2-1 shows main component of the SSHD, including glass vacuum vessel, coil system, and so on. The glass vacuum vessel is torus-shaped with major radius of 250 mm and minor radius of 50 mm and has two helical coils wound around it. Two poloidal coils are wound on yellow rings. When 450 A is applied to the helical coil system, a toroidal magnetic field is about 0.015 T at the center of the vacuum vessel.

Fig 3.2-2 shows radio frequency (RF) oscillator and Fig 3.2-3 shows Geissler tube and induction coil. After igniting the plasma with a Geissler tube, RF wave with 100MHz is supplied to maintain the plasma.

Table 3.2-1 Main specifications of the SSHD

Component	No	Item	Value
Vacuum vessel	1	Shape	Torus with a circular cross section
	2	Major radius	250 mm
	3	Minor radius	50 mm
	4	Material	Glass
	5	Vacuum pressure	$1 \times 10^{-4}$ Pa
	6	Vacuum pumping system	Turbo molecular pump (67l/s)
	7	Exhaust time	10 ~ 30min
	8	Gas type and filling pressure	Ar and $2 \times 10^{-2}$ Pa
Helical coil (In series with the poloidal coil)	9	Shape	Helical
	10	Number of coils	L=2
	11	Pitch number	M=5
	12	Number of turns	4 each
	13	Current	450A
	14	Voltage	5.1V (Including the poloidal coil)
	15	Toroidal magnetic field	0.015T
Poloidal coil	16	Shape	Circular
	17	Number of coils	2
	18	Number of turns	3 each
	19	Current	450A
RF heating coil (Winding parallel to the helical coil)	20	Shape	Helical
	21	Number of coils	2
	22	Number of turns	2 each
Coil power supply	23	Voltage	8V max
	24	Current	500A max
RF power supply	25	Frequency	100MHz
	26	Power (DC input)	193W max (770V, 0.25mA)

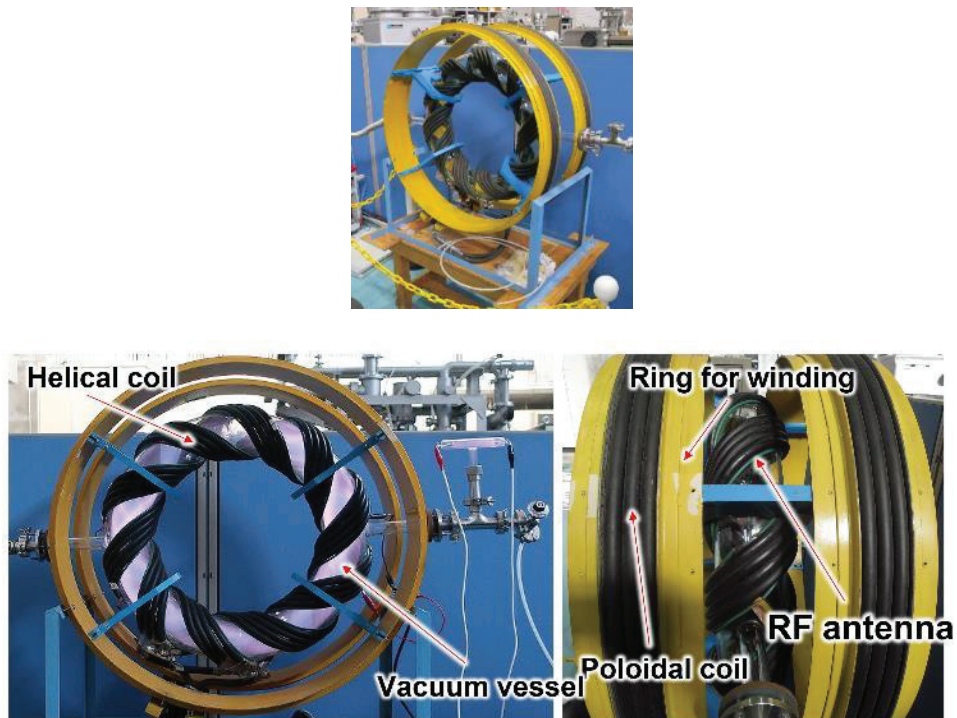


Fig 3.2-1 Vacuum vessel and coil system of the SSHD. The pictures show the helical coil, the vacuum vessel made of glass, the RF antenna, and the poloidal coil.

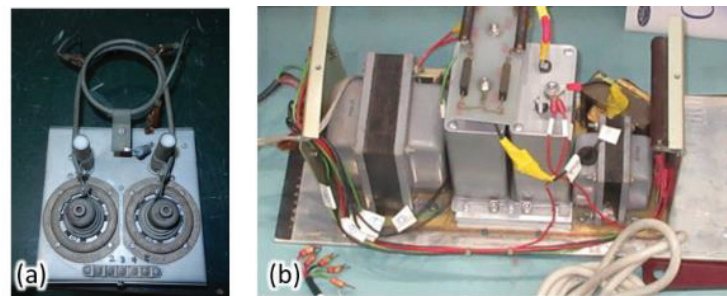


Fig 3.2-2 RF oscillator with 100MHz, which is used to continuously generate plasma. The right picture shows the rectifier circuit, and the left shows the LC resonant circuit for high-frequency oscillation.

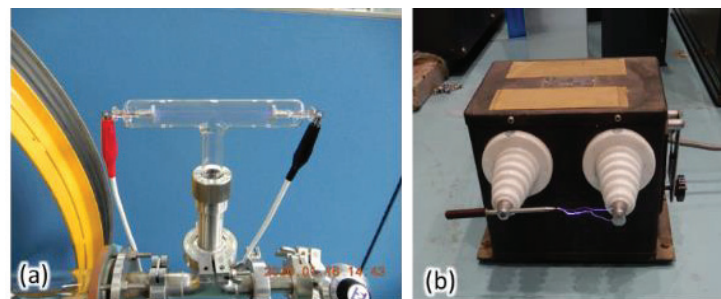


Fig 3.2-3 Plasma igniter.(a) Geissler tube and (b) Induction coil.



### 3.3 Plasma measurement with a Langmuir probe

Plasma experiment with a Langmuir probe was conducted to estimate the plasma parameters. Fig 3.3-1 shows a Langmuir probe, Fig 3.3-2 shows the Langmuir probe inserted into vacuum vessel and plasma. Fig 3.3-3 shows the result of the measurement; electron temperature  $T_e$  and electron density  $n_e$  for different coil current.

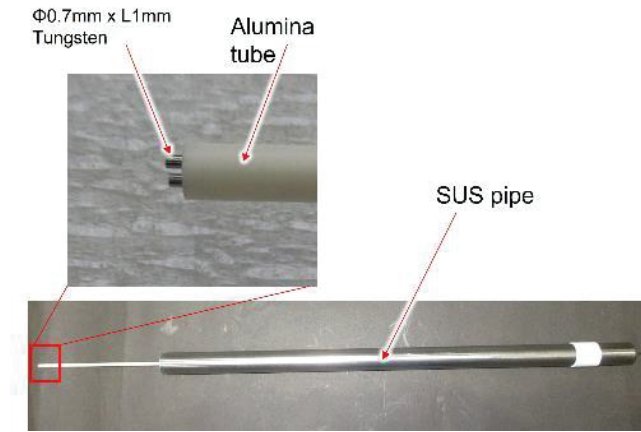


Fig 3.3-1 A Langmuir probe, which was made of two tungsten rods and an alumina sheath. It was used as a single probe with one of two rods.



Fig 3.3-2 The Langmuir probe inserted into the vacuum vessel. It is used to estimate the electron temperature and electron density. The left picture shows the tip of the probe and right shows the plasma around the probe.

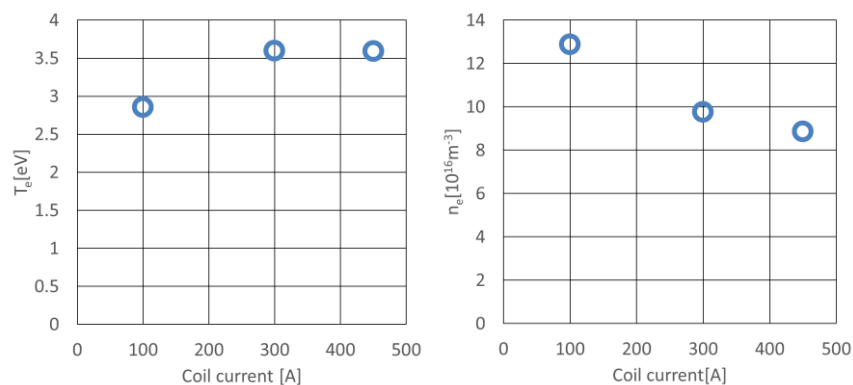


Fig 3.3-3 Electron temperature  $T_e$  and electron density  $n_e$  for different coil current.

## Publication List of NIFS-PROC. Series

- NIFS-PROC-111 Edited by Liquun HU, Shigeru MORITA and Yeong-Kook OH  
Proceeding of A3 Foresight Program Seminar on Critical Physics Issues Specific to Steady State Sustainment of High-Performance Plasmas 12 - 15 December, 2017, Chongqing, China  
Jun. 11, 2018
- NIFS-PROC-112 Edited by E. Kikutani (KEK) and S. Kubo (NIFS)  
Proceedings of the meeting on Archives in Fields of Natural Sciences in FY 2017  
Oct. 18, 2018 (Written in Japanese)
- NIFS-PROC-113 Edited by Koichi Takaki and Tetsuo Ozaki  
Pulsed Power and High-Density Plasma and its Applications  
Feb. 6, 2019
- NIFS-PROC-114 Edited by Daiji Kato, Ling Zhang, and Xiaobin Ding  
The 7th Japan-China-Korea Joint Seminar on Atomic and Molecular Processes in Plasma (AMPP2018)  
May 10, 2019
- NIFS-PROC-115 CFQS Team  
National Institute for Fusion Science, National Institutes of Natural Sciences  
Institute of Fusion Science, School of Physical Science and Technology, Southwest Jiaotong University  
Hefei Keye Electro Physical Equipment Manufacturing Co. Ltd.  
NIFS-SWJTU JOINT PROJECT FOR CFQS -PHYSICS AND ENGINEERING DESIGN-  
VER. 2.1 2019. SEP.  
Nov. 8, 2019
- NIFS-PROC-116 Satoshi Ohdachi, Editor of the Post-CUP Workshop proceeding  
Collected papers at the 2019 Post-CUP Workshop & JSPS-CAS Bilateral Joint Research Projects Workshop,  
24th-26th July, 2019, Nagoya, Japan  
Feb. 21, 2020
- NIFS-PROC-117 Edited by E. Kikutani (KEK) and S. Kubo (NIFS)  
Proceedings of the meetings on Archives in Fields of Natural Sciences in FY2018  
June. 9, 2020 (Written in Japanese)
- NIFS-PROC-118 Edited by Tetsuo Ozaki and Sunao Katsuki  
New Development of Beam Physics and the Application by New Generation Pulsed Power Technology  
June. 29, 2020
- NIFS-PROC-119 CFQS Team  
National Institute for Fusion Science, National Institutes of Natural Sciences  
Institute of Fusion Science, School of Physical Science and Technology, Southwest Jiaotong University  
Hefei Keye Electro Physical Equipment Manufacturing Co. Ltd.  
NIFS-SWJTU JOINT PROJECT FOR CFQS -PHYSICS AND ENGINEERING DESIGN-  
VER. 3.1 2020. NOV.  
Jan. 25, 2021
- NIFS-PROC-120 Edited by Izumi Tsutsui (KEK) and Shin Kubo (NIFS)  
Proceedings of the meetings on Archives in Fields of Natural Sciences in FY2019  
Feb. 25, 2021
- NIFS-PROC-121 Edited by Hiroaki Ito and Tetsuo Ozaki  
Frontier of Advanced Pulsed Power Technology and its Application to Plasma and Particle Beam  
Nov. 08, 2021
- NIFS-PROC-122 CFQS Team  
National Institute for Fusion Science, National Institutes of Natural Sciences  
Institute of Fusion Science, School of Physical Science and Technology, Southwest Jiaotong University  
Hefei Keye Electro Physical Equipment Manufacturing Co. Ltd.  
NIFS-SWJTU JOINT PROJECT FOR CFQS -PHYSICS AND ENGINEERING DESIGN-  
VER. 4.1 2022. JAN.  
Feb. 10, 2022
- NIFS-PROC-123 Edited by Jun Hasegawa and Tetsuo Ozaki  
Recent Developments of Pulsed Power Technology and Plasma Application Research  
Feb. 5, 2023
- NIFS-PROC-124 Edited by Weihua Jiang  
Frontiers of Pulse Power Technology Development  
Feb. 5, 2023
- NIFS-PROC-125 Edited by Koichi Takaki and Tetsuo Ozaki  
Recent trends in technologies of pulse power, high-density plasma and particle beams  
July 1, 2023
- NIFS-PROC-126 CFQS Team  
National Institute for Fusion Science, National Institutes of Natural Sciences  
Institute of Fusion Science, School of Physical Science and Technology, Southwest Jiaotong University  
Hefei Keye Electro Physical Equipment Manufacturing Co. Ltd.  
NIFS-SWJTU JOINT PROJECT FOR CFQS ~PHYSICS AND ENGINEERING DESIGN~  
VER. 5.1 2023. AUG.  
Feb. 8, 2024